TISSUE-ENGINEERED NANOCLAY-BASED BONE-MIMETIC 3D IN VITRO TESTBED FOR STUDYING BREAST CANCER METASTASIS TO BONE

A Dissertation
Submitted to the Graduate Faculty
of the
North Dakota State University
of Agriculture and Applied Science

By

Sumanta Kar

In Partial Fulfillment of the Requirements
for the Degree of
DOCTOR OF PHILOSOPHY

Major Program:
Materials and Nanotechnology

April 2020

Fargo, North Dakota

North Dakota State University
Graduate School

Title

TISSUE-ENGINEERED NANOCLAY-BASED BONE-MIMETIC 3D IN VITRO TESTEBED FOR STUDYING BREAST CANCER METASTASIS TO BONE

By

Sumanta Kar

The Supervisory Committee certifies that this ***disquisition*** complies with North Dakota State University's regulations and meets the accepted standards for the degree of

DOCTOR OF PHILOSOPHY

SUPERVISORY COMMITTEE:

Kalpana S. Katti
Chair

Dinesh R. Katti

Lawrence P. Reynolds

Sangita Sinha

Dali Sun

Approved:

04/08/2020
Date

Erik K. Hobbie
Department Chair

ABSTRACT

Breast cancer shows a high affinity towards the bone, causing bone-related complications leading to poor clinical prognosis. Approximately 80% of breast cancer patients die within five years after primary cancer has metastasized to the bones. The tumor stage strongly influences the survival rates of patients with breast cancer that has spread to bone at the time of diagnosis. There are currently no effective therapeutics available for bone metastases due to the failure of animal models and the scarcity of human bone metastasized samples, as most patients with advance stages of cancer are already in palliative care. Therefore, it is imperative to develop translational models to elucidate disease mechanisms at the cellular and molecular level. Here, we report the development of tissue-engineered nanoclay-based bone-mimetic three-dimensional (3D) *in vitro* model for studying later stages of cancer pathogenesis at the metastatic bone site using osteogenically-differentiated human mesenchymal stem cells (MSCs) and human breast cancer cells (MDA-MB-231 and MCF-7). This 3D model provides an ideal microenvironment suitable for cell-cell and cell-matrix interactions while retaining the behavior of breast cancer cells with different metastatic potential along with mimicking mesenchymal to epithelial transition (MET) of breast cancer cells. Sequential cultures of MSCs with MCF-7 gave rise to tumoroids, while sequential cultures of MSCs with MDA-MB-231 formed disorganized clusters of cells with poor cell-cell adhesion. We further evaluated how cancer-derived factors and cytokines affect bone leading to up to metastasis and conferring drug resistance, respectively. Results showed that Wnt/β-catenin and interleukin-6 (IL-6) mediated IL-6/STAT3 pathways are responsible for bone-related complications and conferring drug resistance, respectively.

Furthermore, we have utilized the 3D *in vitro* model to develop methods for non-invasive and rapid prediction of cancer progression using various biophysical techniques such as

spectroscopy and nanoindentation. Spectroscopy methods showed significant contributions of proteins, lipids, and nucleic acids, while the nanoindentation method showed F-actin mediated softening of cancer cells during cancer progression at the metastatic bone site, respectively. Collectively, 3D *in vitro* model provides an ideal platform for studying the molecular mechanism of breast cancer progression at the metastatic bone site, drug development, and discovery of biomarkers for cancer progression.

ACKNOWLEDGEMENTS

First and foremost, I would like to express my deepest gratitude to my advisor and co-advisor, Prof. Kalpana Katti, and Prof. Dinesh Katti, for their continuous guidance, encouragement, and motivation. I would also like to thank my thesis committee members, Prof. Lawrence Reynolds, Prof. Sangita Sinha, and Prof. Dali Sun, for sharing their precious advice and insights.

I want to acknowledge NDSU grand challenges grant for "Center for Engineered Cancer Test-Beds" for supporting my research work. The scanning electron microscopy experiments conducted in this work are made possible through instrumentation obtained using an MRI grant from the National Science Foundation. Dr. Scott Payne's assistance in the use of electron microscopy is acknowledged. I want to thank Dr. Amber Chevalier Plambeck (Manager of Core Biology Facility at NDSU) and Dr. Pawel Borowicz (Director of Advanced Imaging & Microscopy Laboratory at NDSU) for their help with PCR, Flow Cytometry, and Immunofluorescence Imaging, respectively. Sakshi Taneja from Pharmaceutical Sciences is acknowledged for her help with Western Blotting. Support from ND EPSCoR for tissue engineering laboratory is also acknowledged. Also, I acknowledge Jan Lofberg, Milka Singha, and the Department of Civil and Environmental Engineering for helping me in many aspects during my graduate studies and for providing financial support, respectively.

The members of Prof. Katti's Research Group have been a great source of friendships as well as professional collaboration. The past and present group members that I have had the pleasure to work with or alongside are Mohammad Shahjahan Molla, Anurag Sharma, Keshab Thapa, Krishna Kundu, Nasrullah Faisal, Haneesh Jasuja, Sharad Jaswandkar, and Preetham Ravi.

Finally, and most importantly, I would like to thank my parents for their love, encouragement, and support in all my pursuits. I want to express gratitude to my wife, Sangita, for her unconditional love and support.

DEDICATION

This Dissertation is dedicated to

My beloved father, Dr. Swarup Kumar Kar and

Loving mother, Dr. Kajal Kar.

TABLE OF CONTENTS

ABSTRACT iii

ACKNOWLEDGEMENTS v

DEDICATION vii

LIST OF TABLES xv

LIST OF FIGURES xvi

LIST OF ABBREVIATIONS xxvii

LIST OF APPENDIX FIGURES xxxi

CHAPTER 1. INTRODUCTION 1

1.1. Bone 1

1.1.1. Bone cells 1

1.2. Breast Cancer Bone Metastasis 2

1.3. Current Therapies for Breast Cancer Bone Metastases 6

1.4. 3D Cell Culture Models in Cancer 6

1.5. Tissue-Engineered 3D Models of Breast Cancer Bone Metastases 7

1.6. Nanoclay-based Scaffolds for Bone Tissue Engineering 9

1.7. Wnt/β-catenin Pathway Mediated Osteogenesis at Metastases 11

1.8. IL-6/STAT3 Pathway Mediated Drug Resistance at Metastases 12

1.9. Evaluation of Raman and Infrared Spectroscopy as Diagnostic Tools for Cancer Progression 14

1.10. Cellular Nanomechanics as a Biomarker for Cancer Progression at Metastases 16

1.11. Research Objectives 17

1.12. Organization of this dissertation 18

1.13. References 19

CHAPTER 2. TISSUE-ENGINEERED NANOCLAY-BASED 3D IN VITRO BREAST CANCER MODEL FOR STUDYING BREAST CANCER METASTASIS TO BONE 43

2.1. Introduction 43

2.2. Materials and Methods 46

2.2.1. Preparation of Polycaprolactone (PCL)/*in situ* HAPclay 3D Scaffolds and 2D Films 46

2.2.2. Cell Lines and Culture Media 46

2.2.3. Cell Culture 47

2.2.4. Sequential Culture (SC) with MSCs 47

2.2.5. Cell Viability 47

2.2.6. Alkaline Phosphate (ALP) Activity 48

2.2.7. Cellular Morphology 48

2.2.8. Cellular Migration 48

2.2.9. Quantification of MMP-9 Secretion 49

2.2.10. RNA Extraction and Quantitative RT-PCR Analysis 49

2.2.11. Immunocytochemistry 50

2.2.12. Statistical Analysis 51

2.3. Results 51

2.3.1. Growth of BrCa Cells, MSCs, and Sequential Culture 51

2.3.2. Osteogenesis in MSCs, and Sequential Culture 53

2.3.3. Morphology of Sequential Cultured BrCa Cells 55

2.3.4. *In vitro* Migration of BrCa Cells Towards Bone Scaffolds 55

2.3.5. MMP-9 activity of BrCa Cells, MSCs, and Sequential Culture 55

2.3.6. Invasiveness, Angiogenicity and Bone Homeostasis in Sequential Cultures 57

2.4. Discussion 61

2.5. Conclusion 65

2.6. Acknowledgements 65

2.7. References 66

CHAPTER 3. WNT/β-CATENIN SIGNALING PATHWAY REGULATES OSTEOGENESIS FOR BREAST CANCER BONE METASTASIS: EXPERIMENTS IN AN IN VITRO NANOCLAY SCAFFOLD CANCER TESTEBED 74

3.1. Introduction 74

3.2. Materials and Methods 78

3.2.1. Preparation of Polycaprolactone (PCL)/*in situ* HAPclay 3D Scaffolds 78

3.2.2. Cell Culture 78

3.2.3. Cellular Morphology 79

3.2.4. Gene Expression Studies 79

3.2.5. Immunofluorescence Staining 80

3.2.6. ELISA Assays 81

3.2.7. Alizarin Red S Staining (ARS) and Quantification Assay 81

3.2.8. Western Blot Analysis 81

3.2.9. Statistical Analysis 82

3.3. Results 82

3.3.1. Osteogenic Differentiation of MSCs on Nanoclay-based Scaffolds is Mediated by Wnt/β-catenin Pathway 82

3.3.2. Breast Cancer-derived factors DKK-1 and ET-1 Regulate Wnt/β-catenin Pathway, Leading to Bone Metastasis 86

3.4. Discussion 88

3.5. Conclusion 94

3.6. Acknowledgments 94

3.7. References 95

CHAPTER 4. BONE INTERFACE MODULATES DRUG RESISTANCE IN BREAST CANCER BONE METASTASIS 107

4.1. Introduction 107

4.2. Materials and Methods 111

4.2.1. Cell Lines, Culture Maintenance, and Materials 111

4.2.2. Preparation of PCL/*in situ* HAPclay 3D Scaffolds 112

4.2.3. Cell Culture 112

4.2.4. Cellular Morphology 113

4.2.5. Analysis of Drug Response 113

4.2.6. Flow Cytometric Analysis of Apoptosis 113

4.2.7. ELISA Assay 114

4.2.8. Alizarin Red S Staining (ARS) 114

4.2.9. Gene Expression Studies 114

4.2.10. Immunofluorescence Staining 115

4.2.11. Statistical Analysis 115

4.3. Results and Discussion 116

4.3.1. Bone Tissue Formation on 3D Nanoclay Scaffolds 116

4.3.2. 3D Sequential Culture of MSCs with Breast Cancer Cells Facilitates *in vitro* Growth of *in vivo*-like Tumoroids 116

4.3.3. 3D Sequential Culture of MSCs with Breast Cancer Cells Requires Higher Drug Concentrations than 2D Culture of Breast Cancer Cells to Achieve Comparable Reduction in Cell Viability 117

4.3.4. 3D Sequential Culture of MSCs with Breast Cancer Cells Alters Expression of Apoptosis Regulatory Proteins and Increases Resistance to Apoptosis in Response to Paclitaxel 119

4.3.5. 3D Sequential Culture of MSCs with Breast Cancer Cells Enhances Expression of Multi-Drug Resistance-related Genes 121

4.3.6. 3D Tumor Microenvironment-secreted Cytokine IL-6 may Promote Drug-Resistance against Paclitaxel 121

4.4. Conclusion 126

4.5. Acknowledgements 126

4.6. References 127

CHAPTER 5. QUASI-STATIC AND DYNAMIC NANOMECHANICAL EVALUATION OF BREAST CANCER CELLS WITH PROGRESSION OF METASTASIS TO BONE 137

5.1. Introduction 137

5.2. Materials and Methods 140

5.2.1. Materials, Cell Lines, and Culture Maintenance 140

5.2.2. Preparation of PCL/*in situ* HAPclay 3D Scaffolds 141

5.2.3. Cell Culture 142

5.2.4. Cellular Morphology 142

5.2.5. Quasi-Static Nanoindentation 142

5.2.6. Dynamic Nanoindentation 143

5.2.7. Gene Expression Studies 145

5.2.8. Immunofluorescence Staining 146

5.2.9. Statistical Analysis 147

5.3. Results 147

5.3.1. Cancer Cells Alter Nanomechanical Properties in Response to 3D Culture Conditions 147

5.3.2. Cancer Cells Behave More Liquid-Like When Cultured in 3D Conditions 152

5.3.3. Actin Dynamics Regulate Cellular Nanomechanics During Cancer Progression 155

5.4. Discussion 159

5.5. Conclusion 165

5.6. Acknowledgements 166

5.7. References 166

CHAPTER 6. FOURIER TRASNFORM INFRARED SPECTROSCOPY BASED SPECTRAL BIOMARKERS OF METASTASIZED BREAST CANCER PROGRESSION 181

6.1. Introduction 181

6.2. Materials and Methods 183
6.2.1. Preparation of Polycaprolactone (PCL)/*in situ* HAPclay 3D Scaffolds 183
6.2.2. Cell Lines and Culture Media 184
6.2.3. Cell Culture 184
6.2.4. Sequential Culture (SC) with MSCs 185
6.2.5. Cellular Morphology 185
6.2.6. FTIR Experiments 186
6.2.7. Principal Component Analysis 187
6.2.8. Statistical Analysis 187
6.3. Results and Discussion 187
6.3.1. Cellular Morphology 187
6.3.2. Evaluation of the Potential of FTIR Spectroscopy to Identify the Biomarkers of Cancer Progression on 3D *in vitro* Model 188
6.3.3. Principal Component Analysis 194
6.4. Conclusion 204
6.5. Acknowledgements 205
6.6. References 205
CHAPTER 7. LABEL-FREE DISCRIMINATION OF CANCER CELLS AT DIFFERENT STAGES OF TUMORIGENESIS USING 3D IN VITRO BONE METASTASIS MODEL OF PROSTATE CANCER BY RAMAN IMAGING 221
7.1. Introduction 221
7.2. Materials and Methods 224
7.2.1. Modification of MMT clay 224
7.2.2. Preparation of *in situ* HAPclay 224
7.2.3. Preparation of Polycaprolactone (PCL)/*in situ* HAPClay Scaffolds 224
7.2.4. Cell Culture 225

7.2.5. Raman Imaging 225
7.2.6. Principal Component Analysis (PCA) 227
7.2.7. Cluster Analysis 227
7.2.8. Statistical Analysis 228
7.3. Results and Discussion 228
7.4. Conclusions 239
7.5. Acknowledgments 240
7.6. References 240
CHAPTER 8. SUMMARY AND CONCLUSIONS 248
CHAPTER 9. FUTURE DIRECTIONS 252
9.1. References 255
APPENDIX 257

LIST OF TABLES

Table Page

2.1. The primer sequence used for the quantitative reverse transcription-polymerase chain reaction experiment. 51

3.1. The sequence of primers used for the quantitative real-time PCR experiment. 80

4.1. The sequence of primers used for the quantitative real-time PCR experiment 115

4.2. IC_{50} values of paclitaxel in 2D breast cancer cells (MM 231 & MCF-7) and 3D sequential cultures of MSCs with breast cancer cells (MM 231 & MCF-7). 119

5.1. The sequence of primers used for the quantitative real-time PCR experiment 146

6.1. Assignments of vibrational modes observed in FTIR spectra of monoculture and sequential culture of breast cancer cells..... 191

6.2. Major components of lipid, amide, nucleic acid region in MCF-7 SC..... 196

6.3. Major components of lipid, amide, nucleic acid region in MCF-7 MC 197

6.4. Major components of lipid, amide, nucleic acid region in MM 231 SC 199

6.5. Major components of lipid, amide, nucleic acid region in MM 231 MC 200

7.1. Band assignments for Raman spectra for prostate cancer cells [14, 37-42]. 231

LIST OF FIGURES

Figure Page

1.1. Cancer metastasis involves a series of well-defined steps including cellular detachment or dissemination at the primary site, invasion at basement membrane, intravasation or vascular invasion, circulation or migration through blood vessels or lymph nodes, extravasation, survival, proliferation, angiogenesis, and secondary tumor growth at metastatic site. Epithelial cancer cells undergo epithelial to mesenchymal transition (EMT) to acquire mesenchymal phenotype with increased motility and invasiveness. Newly acquired invasiveness makes the cells disseminate from primary tumors, invade basement membrane, and enter the bloodstream to become circulating tumor cells. These circulating tumor cells migrate into a distant organ (bone), and in response to microenvironment, cells start to colonize to pave the way for secondary micrometastases via Mesenchymal to epithelial transition (MET). When cancer cells undergo MET, they lose their mesenchymal traits followed by gaining of epithelial phenotype. 4

1.2. A gamut of different growth factors and cytokines govern the vicious cycle of bone metastasis, such as vascular endothelial growth factor (VEGF), Interleukin - 8 (IL-8), Interleukin-11 (IL-11), parathyroid hormone-related protein (PTHrP). Studies have identified that these factors mentioned above destabilize the balance between bone resorption and bone formation. RANKL dictates the pathway of osteoclastogenesis, and it causes differentiation of progenitor cells in the bone marrow into osteoclasts. Breast cancer cells secrete PTHrP along with tumor necrosis factor-alpha (TNF-α), which activates RANKL and inhibits osteoprotegerin (OPG), a decoy receptor of RANKL, resulting in bone resorption. Bone resorption increases the secretion of PTHrP by cancer cells, and PTHrP, in turn, upregulates tumor growth factor- β (TGF-β), resulting in severe osteolysis. 5

1.3. Schematic showing the concept of tissue engineering. Cells are isolated from the patient and cultured on two-dimensional (2D) cell culture flask for efficient expansion. Next, the cells are seeded in porous scaffolds together with growth factors to aid regeneration. The scaffolds serve as a mechanical support during tissue growth, and their porous structure provides nutrient supply and helps waste removal. Once a functioning tissue has been successfully engineered, the construct is transplanted on the defect to restore function..... 8

1.4. Schematic showing Wnt/ β-catenin signaling pathway. Wnt signaling is mediated by activation of low-density lipoprotein (LDL) receptor-related protein 5 (LRP-5) and Frizzled 4 (FZD4) by secreted Wnt ligands. (a) In the absence of Wnt signal, β-catenin is phosphorylated by casein kinase 1 (CK1) and the glycogen synthase kinase-3β (GSK-3β)/adenomatous polyposis coli (APC)/Axin 2 complex, leading to ubiquitination and proteasome degradation of β-catenin. (b) In the presence of Wnt signal, the co-receptor LRP5/6 forms complex with Wnt-bound FZD which in turn promotes nuclear translocation of β-catenin and stimulates osteogenesis. 12

1.5. Schematic showing IL-6/STAT3 signaling pathway. Interleukin-6 (IL-6), a pro-inflammatory cytokine produced in the tumor microenvironment by stromal cells, fibroblasts, and cancer cells. Binding of IL-6 to its receptor IL-6R on the cell membrane activates Janus Kinase 2 (JAK2) kinases. Activated JAK2 mediates phosphorylation, dimerization, and nuclear translocation of Signal Transducer and Activator of Transcription 3 (STAT3). STAT3 signaling mediates the expression of various genes, including p53, Bcl-2, multidrug resistance-associated protein 1 (MRP1), and ATP-binding cassette subfamily G member 2 (ABCG2). Bcl-2 and p53 are associated with regulation of apoptosis while overexpression of drug transporters MRP1, ABCG2 has been shown to mediate efflux of drugs from cancer cells, thus decreasing intracellular drug concentration leading to drug resistance. 13

1.6. Schematic representation of energy transitions in Raman and IR spectroscopy. 15

2.1. (A) Schematic showing the steps of sequential culture experiment. (B) Cell viability of 2D and 3D monoculture of MCF 7. (C) Cell viability of 2D and 3D monoculture of MM 231.(D) Cell viability of 3D sequential cultures (3D SC) and MSCs 3D. (n=3; two-way ANOVA followed by *post hoc* Tukey test, $*p < 0.05$, $**p < 0.01$, $***p < 0.001$). 52

2.2. ALP activity of (A) MSCs alone (n=3; one-way ANOVA followed by *post hoc* Tukey test, $*p < 0.05$, $**p < 0.01$, $***p < 0.001$); (B) 3D sequential cultures (SC) of MSCs with breast cancer cells and MSCs 3D. (n=3; two-way ANOVA followed by *post hoc* Tukey test, $*p < 0.05$, $**p < 0.01$, $***p < 0.001$). 53

2.3. Representative immunofluorescence microscope images of MSCs cultured on PCL/*in situ* HAPclay scaffolds after immunostaining for nuclei and Runx2. We found an increase in the Runx2 protein levels at day 4, day 8, and day 16 compared to day 1 but we observed a decrease in the protein levels after day 16. Scale bars: 50 µm. 54

2.4. (A-C) SEM micrographs of sequential culture of MCF-7 cells at days (23+5), (23+10) and (23+15) (White circles/ellipses represent tumoroids); (D-E) sequential culture of MM 231 cells at days (23+5), (23+10) and (23+15). (Black circles/ellipses represent disorganized clusters). (X+Y days: MSCs were cultured on PCL/*in situ* HAPclay scaffolds for X days, then cancer cells were seeded and culture was continued for Y more days). 56

2.5. (A) Schematic showing flowchart of migration assay. (B) Represented images of migrated MM 231 cells (a) control, (b) with bone scaffold; migrated MCF-7 cells (c) control, (d) with bone scaffold. Nuclei are stained with DAPI. The scale bar represents 50 µm. (C) Percent migration of MCF 7 and MM 231 in presence and absence of bone scaffold (control). (n=3; one-way ANOVA followed by *post hoc* Tukey test, $*p < 0.05$, $**p < 0.01$, $***p < 0.001$). 57

2.6. Secretion of MMP-9 in 2D, 3D monocultures of MCF 7 cells (A), MM 231 cells (B), and (C) 3D sequential cultures of cancer cells and MSCs. (n=3; two-way ANOVA followed by *post hoc* Tukey test, *p < 0.05, **p < 0.01, ***p < 0.001)..... 57

2.7. mRNA levels of Twist, Vimentin, E-cad, and FGFR2 in MM 231 3D & MM 231 3D SC (A-B) and (C-D) MCF-7 3D & MCF-7 3D SC. (n=3; Student's unpaired *t-test*, *p < 0.05, **p < 0.01, ***p < 0.001). 58

2.8. mRNA levels of VEGF, HIF-1, RANKL, and ET-1 in MM 231 3D & MM 231 3D SC (A-B) and (C-D) MCF-7 3D & MCF-7 3D SC. (n=3; Student's unpaired *t-test*, *p < 0.05, **p < 0.01, ***p < 0.001). 60

2.9. Representative immunofluorescence microscope images of MM 231 and MCF-7 cells cultured in 2D and 3D sequential culture after immunostaining for nuclei, E-cadherin (A), Vimentin (B), VEGF (C&E) and Cytokeratin 18 (D). Scale bars: 50 µm. 61

2.10. Schematic showing metastatic cascade involved in breast cancer progression and metastasis. Cancer cells at the primary tumor site undergo EMT to generate mesenchymal cells with enhanced motility and invasiveness. The loss of E-cadherin and FGFR2 expressions and gain of Twist1 and Vimentin expressions are hallmarks of epithelial-mesenchymal transition of cancer cells. Newly acquired invasiveness makes the cells invade basement membrane and enter the bloodstream to become circulating tumor cells. These circulating tumor cells migrate into a distant organ (bone), and in response to microenvironment, cells start to colonize to pave the way for secondary micrometastases via MET. When cancer cells undergo MET, they re-express E-cadherin while Twist1 and Vimentin expressions downregulate. HIF-1 and VEGF expressions are also increased due to initiation of blood vessel formation during tumorigenesis. 64

3.1. Schematic showing the steps of sequential culture experiment. 79

3.2. Osteogenic differentiation of MSCs and bone tissue formation on nanoclay-based scaffolds. (a) Quantitative real-time PCR of gene expression for osteogenic markers.RUNX2, ALP, and OCN. (b) OCN released into culture medium, indicative of bone maturation. *p < 0.05, **p < 0.01, and ***p < 0.001 indicate significant difference between 8 days and 23 days MSCs constructs. (c) Immunofluorescence staining for RUNX2 and OCN of 8 days and 23 days MSCs construct. Arrows indicate nuclear translocation of RUNX2. Scale bars, 50 µm. (d) Alizarin Red S staining and quantification absorbance assay of 8 days and 23 days MSCs constructs. Scale bar, 1 mm. $^{\#\#}$p < 0.01, and $^{\#\#\#}$p < 0.001 indicate significant difference between control and MSCs seeded constructs. ***p < 0.001 indicates significant difference between 8 days and 23 days MSCs constructs. 84

3.3. Osteogenesis in nanoclay-based scaffolds is mediated by Wnt/β-catenin signaling pathway. (a) Quantitative real-time PCR of gene expression for Wnt-related factors Wnt5a, β-catenin, AXIN2, FZD4, and LRP5. *$p < 0.05$, **$p < 0.01$ indicate significant difference between 8 days and 23 days MSCs constructs. (b) Immunofluorescence staining for β-catenin of 8 days and 23 days MSCs construct. Arrows indicate nuclear translocation of β-catenin. Scale bars, 50 μm. (c) Expression of β-catenin assessed by western blotting..... 85

3.4. Morphology of breast cancer cells (a) MM 231 and (b) MCF-7 grown on bone-mimetic nanoclay scaffolds. Arrows indicate cells while * indicate scaffold. 86

3.5. Osteogenesis in 3D *in vitro* model of breast cancer bone metastasis. (a) Quantitative real-time PCR of gene expression for late-stage osteogenic marker OCN. (b) OCN released into culture medium, indicative of bone maturation. *$p < 0.05$, ***$p < 0.001$ indicate significant difference between 33 days MSCs and (23+10) days sequential cultures of MSCs with breast cancer cells constructs. (c) Immunofluorescence staining for OCN of 33 days MSCs and (23+10) days sequential cultures of MSCs with breast cancer cells constructs. Scale bars, 50 μm. (d) Alizarin Red S staining and quantification absorbance assay of 33 days MSCs and (23+10) days sequential cultures of MSCs with breast cancer cells constructs. Scale bar, 1 mm. ***$p < 0.001$ indicates significant difference between 33 days MSCs and (23+10) days sequential cultures of MSCs with breast cancer cells constructs. 89

3.6. Wnt/β-catenin signaling regulates osteogenesis in 3D *in vitro* model of breast cancer bone metastasis. (a) Quantitative real-time PCR of gene expression for Wnt-related factors Wnt5a, β-catenin, AXIN2, and LRP5. *$p < 0.05$, **$p < 0.01$, and ***$p < 0.001$ indicate significant difference between 33 days MSCs and (23+10) days sequential cultures of MSCs with breast cancer cells constructs. (b) Immunofluorescence staining for β-catenin of 33 days MSCs and (23+10) days MSCs grown in 1:1 MSCGM: Breast cancer-derived CM. Arrows indicate nuclear translocation of β-catenin. Scale bars, 50 μm. (c) Expression of β-catenin assessed by western blotting..... 90

3.7. Breast cancer-derived factors DKK-1 and ET-1 regulate Wnt/β-catenin signaling pathway. (a) Quantitative real-time PCR of gene expression for DKK-1, and ET-1. (b) DKK-1 and ET-1 released into culture medium. **$p < 0.01$, ***$p < 0.001$ indicate significant difference between (23+10) days sequential cultures of MSCs with MCF-7 and (23+10) days sequential cultures of MSCs with MM 231. (c) Mechanisms of inactivation and stimulation of Wnt/β-catenin signaling pathway by DKK-1 and ET-1, respectively. 91

4.1. (A) Quantitative real-time PCR of gene expression for late-stage osteogenic marker OCN. (B) OCN released into culture medium, indicative of bone maturation.**$p < 0.01$, and ***$p < 0.001$ indicate significant difference between day 0 and day 23 MSCs constructs. (C) Alizarin Red S staining and quantification absorbance assay of day 0 and day 23 MSCs constructs. Scale bar, 1 mm. $^{\#}p < 0.05$, and $^{\#\#\#}p < 0.001$ indicate significant difference between control and MSCs seeded constructs. ***$p < 0.001$ indicates significant difference between day 0 and day 23 MSCs constructs. 117

4.2. (A) Schematic showing the steps of sequential culture experiment. (B) Morphology of breast cancer cells MM 231 and MCF-7 grown on bone-mimetic nanoclay scaffolds. Arrows indicate cells while * indicate scaffold. 118

4.3. (A & B) Cytotoxic effects of paclitaxel in 2D cultures breast cancer cells (MM 231 & MCF-7) and 3D sequential cultures of MSCs with breast cancer cells (MM 231 & MCF-7). Cells were treated with 0.2, 2, 20, and 200 µM of paclitaxel for 48 h. Cell viability was evaluated using a WST-1 assay. Half maximal inhibitory concentration (IC_{50}) values were calculated on Graph Pad Prism using nonlinear regression analysis. 118

4.4. (A & B) Representative dot plot presenting the fluorescence channel analysis of 2D MM 231 & 3D MSCs + MM 231 SC, and 2D MCF-7 & 3D MSCs + MCF-7 SC cells following double staining with Annexin V and Propidium Iodide. Cells were treated with their respective IC_{50} values mentioned in Table 4.2 for 24 h and stained with Annexin V (horizontal) and Propidium Iodide (vertical axis) before analysis with flow cytometry. The percentage of cell apoptosis was calculated by subtracting control (% early apoptosis) from IC_{50} (% early apoptosis) for each culture type. *$p < 0.05$ indicates significant differences between 2D MM 231 and 3D MSCs + MM 231 SC. **$p < 0.01$ indicates significant difference between 2D MCF-7 and 3D MSCs + MCF-7 SC. 120

4.5. (A & B) Quantitative real-time PCR of gene expression for p53 and Bcl-2. *$p < 0.05$, **$p < 0.01$ indicate significant difference between significant difference between 2D cultures of breast cancer cells (MM 231 & MCF-7) and 3D sequential cultures of MSCs with breast cancer cells (MM 231 & MCF-7). Immunofluorescence staining for p53 and Bcl-2 of 2D breast cancer cultures (MM 231 & MCF-7) and 3D sequential cultures of MSCs with breast cancer cells (MM 231 & MCF-7). Arrows indicate nuclear localization of p53. Scale bars, 50 µm. 122

4.6. (A & B) Quantitative real-time PCR of gene expression for MRP1 and ABCG2. *$p < 0.05$ indicates significant difference between significant difference between 2D cultures of breast cancer cells (MM 231 & MCF-7) and 3D sequential cultures of MSCs with breast cancer cells (MM 231 & MCF-7). (C) Immunofluorescence staining for MRP1 of 2D breast cancer cultures (MM 231 & MCF-7) and 3D sequential cultures of MSCs with breast cancer cells (MM 231 & MCF-7). Scale bars, 50 µm. 124

4.7. (A & B) Quantitative real-time PCR of gene expression for IL-6. ELISA Assay for quantification of released IL-6 into culture medium. *$p < 0.05$, **$p < 0.01$ indicate significant difference between 2D cultures of breast cancer cells (MM 231 & MCF-7) and 3D sequential cultures of MSCs with breast cancer cells (MM 231 & MCF-7). Immunofluorescence staining for pSTAT3 (Y705) of 2D breast cancer cultures (MM 231 & MCF-7) and 3D sequential cultures of MSCs with breast cancer cells (MM 231 & MCF-7). Arrows indicate nuclear localization of pSTAT3. Scale bars, 50 µm. (C) Proposed mechanism of IL-6/STAT3 mediated drug-resistance in 3D sequential cultures MSCs with breast cancer cells. 125

5.1. (A) Schematic showing steps of sequential culture MSCs/breast cancer followed by workflow of nanoindentation experiments. Dotted arrow pointing downwards indicates the amount of deformation applied (P) onto cell construct to yield nanomechanical response of cell. (B) Morphology of breast cancer cells MM 231 and MCF-7 grown on 3D bone-mimetic nanoclay scaffolds. Arrows indicate cells while * indicate scaffold. 148

5.2. (A) Representative load-displacement (L-D) curves of MCF-7 as received and 3D bone-mimetic scaffolds-derived MCF-7 cells at the maximum depth of 1000 nm and 2000 nm. (B) Elastic modulus of MCF-7 as received and 3D bone-mimetic scaffolds-derived MCF-7 cells at the maximum depth of 1000 nm and 2000 nm. *$p<0.05$, **$p<0.01$, and ***$p<0.001$ indicate significant difference between MCF-7 as received and 3D bone-mimetic scaffolds-derived MCF-7 cells; $^{\#}p<0.05$, $^{\#\#}p<0.01$, and $^{\#\#\#}p<0.001$ indicate significant difference between scaffolds-derived MCF-7 (d5), and other scaffolds-derived cells (i.e., MCF-7 (d10) and MCF-7 (d15)); $^{\$}p<0.05$, $^{\$\$}p<0.01$, and $^{\$\$\$}p<0.001$ indicate significant difference between scaffolds-derived MCF-7 (d10) and MCF-7 (d15)..... 149

5.3. (A) Representative load-displacement (L-D) curves of MM 231 as received and 3D bone-mimetic scaffolds-derived MM 231 cells at the maximum depth of 1000 nm and 2000 nm. (B) Elastic modulus of MM 231 as received and 3D bone-mimetic scaffolds-derived MM 231 cells at the maximum depth of 1000 nm and 2000 nm. *$p<0.05$, **$p<0.01$, and ***$p<0.001$ indicate significant difference between MM 231 as received and 3D bone-mimetic scaffolds-derived MM 231 cells; $^{\#}p<0.05$, $^{\#\#}p<0.01$, and $^{\#\#\#}p<0.001$ indicate significant difference between scaffolds-derived MM 231 (d5), and other scaffolds-derived cells (i.e., MM 231 (d10) and MM 231 (d15)); $^{\$}p<0.05$, $^{\$\$}p<0.01$, and $^{\$\$\$}p<0.001$ indicate significant difference between scaffolds-derived MM 231 (d10) and MM 231 (d15). 150

5.4. (A) Variation of storage modulus (E') for (i) MCF-7 as received and 3D bone-mimetic scaffolds-derived MCF-7 cells; (ii) MM 231 as received and 3D bone-mimetic scaffolds-derived MM 231 cells. (B) Variation of loss modulus (E'') for (i) MCF-7 as received and 3D bone-mimetic scaffolds-derived MCF-7 cells; (ii) MM 231 as received and 3D bone-mimetic scaffolds-derived MM 231 cells. (C) Variation of loss tangent (tan δ) for (i) MCF-7 as received and 3D bone-mimetic scaffolds-derived MCF-7 cells; (ii) MM 231 as received and 3D bone-mimetic scaffolds-derived MM 231 cells. Intersections with the horizontal dashed line at tan δ =1 of the vertical lines occur at transition frequencies, $\omega_{transition}$..... 154

5.5. Log2 ratios of (A) storage modulus (E'), (B) loss modulus (E''), and (C) loss tangent (tan δ) for MCF-7 and MM 231 across samples (mean ± SD, averaged across frequency). *p<0.05, **p<0.01, and ***p<0.001 indicate significant difference between as received and 3D bone-mimetic scaffolds-derived breast cancer cells; $^{\#}$p<0.05, $^{\#\#}$p<0.01, and $^{\#\#\#}$p<0.001 indicate significant difference between scaffolds-derived breast cancer cells (d5), and other scaffolds-derived breast cancer cells (i.e., (d10) and (d15)); $^{\$}$p<0.05, $^{\$\$}$p<0.01, and $^{\$\$\$}$p<0.001 indicate significant difference between scaffolds-derived breast cancer cells (d10) and (d15). 156

5.6. (A) Representative immunofluorescence images showing distribution of F-actin in (i) MCF-7 as received and MCF-7 cells grown on 3D bone-mimetic scaffolds. Scaffolds grown MCF-7 formed an F-actin band (white arrows) between adjacent cells; (ii) MM 231 as received and MM 231 cells grown on 3D bone-mimetic scaffolds. Scaffolds grown MM 231 neither formed an F-actin band between adjacent cells nor stress-fibers. (B) Quantification of corrected of total cell fluorescence (CTCF) of F-actin for (i) MCF-7 as received and MCF-7 cells grown on 3D bone-mimetic scaffolds; (ii) MM 231 as received and MM 231 cells grown on 3D bone-mimetic scaffolds. *p<0.05, **p<0.01, and ***p<0.001 indicate significant difference between as received and 3D bone-mimetic scaffolds-grown breast cancer cells; $^{\#}$p<0.05, $^{\#\#}$p<0.01, and $^{\#\#\#}$p<0.001 indicate significant difference between scaffolds-grown breast cancer cells (d5), and other scaffolds-grown breast cancer cells (i.e., (d10) and (d15)); $^{\$}$p<0.05, $^{\$\$}$p<0.01, and $^{\$\$\$}$p<0.001 indicate significant difference between scaffolds-grown breast cancer cells (d10) and (d15). 157

5.7. (A) Representative immunofluorescence images showing distribution of tubulin in (i) MCF-7 as received and MCF-7 cells grown on 3D bone-mimetic scaffolds; (ii) MM 231 as received and MM 231 cells grown on 3D bone-mimetic scaffolds. (B) Quantification of corrected of total cell fluorescence (CTCF) of tubulin for (i) MCF-7 as received and MCF-7 cells grown on 3D bone-mimetic scaffolds; (ii) MM 231 as received and MM 231 cells grown on 3D bone-mimetic scaffolds. *p<0.05, **p<0.01, and ***p<0.001 indicate significant difference between as received and 3D bone-mimetic scaffolds-grown breast cancer cells; $^{\#}$p<0.05, $^{\#\#}$p<0.01, and $^{\#\#\#}$p<0.001 indicate significant difference between scaffolds-grown breast cancer cells (d5), and other scaffolds-grown breast cancer cells (i.e., (d10) and (d15)); $^{\$}$p<0.05, $^{\$\$}$p<0.01, and $^{\$\$\$}$p<0.001 indicate significant difference between scaffolds-grown breast cancer cells (d10) and (d15). 158

5.8. Quantitative real-time PCR of gene expression for actin-dynamics related genes CDC42, ARP2, ARP3, N-WASP, CTTN, and CFL2. *p<0.05, **p<0.01, and ***p<0.001 indicate significant difference between MCF-7 as received and MCF-7 cells grown on 3D bone-mimetic scaffolds; $^{\#}$p<0.05, $^{\#\#}$p<0.01, and $^{\#\#\#}$p<0.001 indicate significant difference between MCF-7 (d5) cells grown on 3D bone-mimetic scaffolds, and other MCF-7 cells grown on 3D bone-mimetic scaffolds (i.e., MCF-7 (d10) and MCF-7 (d15)); $^{\$}$p<0.05, $^{\$\$}$p<0.01, and $^{\$\$\$}$p<0.001 indicate significant difference between MCF-7 (d10) and MCF-7 (d15) cells grown on 3D bone-mimetic scaffolds 160

5.9. Quantitative real-time PCR of gene expression for actin-dynamics related genes CDC42, ARP2, ARP3, N-WASP, CTTN, and CFL2. *p<0.05, **p<0.01, and ***p<0.001 indicate significant difference between MM 231 as received and MM 231 cells grown on 3D bone-mimetic scaffolds; $^{\#}$p<0.05, $^{\#\#}$p<0.01, and $^{\#\#\#}$p<0.001 indicate significant difference between MM 231 (d5) cells grown on 3D bone-mimetic scaffolds, and other MM 231 cells grown on 3D bone-mimetic scaffolds (i.e., MM 231 (d10) and MM 231 (d15)); $^{\$}$p<0.05, $^{\$\$}$p<0.01, and $^{\$\$\$}$p<0.001 indicate significant difference between MM 231 (d10) and MM 231 (d15) cells grown on 3D bone-mimetic scaffolds. 161

5.10. (A) In mesenchymal cells, E-cadherin is not present, and the actin cytoskeleton undergoes several changes, leading to a shift of actin and its regulatory proteins and complexes such as N-WASP, cortactin, and Arp2/3 complex from the cortex towards the leading edge to form lamellipodia. In contrast, epithelial cells form tight junctions to create an intracellular barrier separating the tissue from the outside world and adherens junction between adjacent cells that bestow mechanical stability by connecting with the actin cytoskeleton and E-cadherin. Furthermore, E-cadherin maintains adherens junction integrity by providing a basis for sequestration of actin nucleation proteins in non-motile cells. Cortactin, a scaffolding protein, binds to both N-WASP and E-cadherin to recruit Arp2/3 complex to adherens junctions. (B) E-cadherin inhibits CDC42, a small GTPase of the Rho family, which in turn prevents actin interacting regulatory proteins (N-WASP, ARP2/3, and CTTN) from taking part in actin nucleation, at the same time stimulating the activity of actin severing protein CFL2, thereby promoting depolymerization of actin. 163

5.11. (A&B) Quantitative real-time PCR of gene expression for CHD1 for as received MCF-7/MM 231 and MCF-7/MM 231 cells grown 3D bone-mimetic scaffolds. (C) Log2 ratios of CHD1 gene expression of as received and cells grown on 3D bone-mimetic scaffolds for both breast cancer cells. (n=3; one-way ANOVA followed by *post hoc* Tukey test, *$p < 0.05$, **$p < 0.01$, ***$p < 0.001$). 164

6.1. Schematic illustration of the steps of sequential culture experiment. 185

6.2. Schematic representation of the workflow of FTIR experiment. 186

6.3. Representative SEM micrographs of (a) MCF-7 MC, (b) MCF-7 SC, (c) MM 231 MC, and (d) MM 231 SC. 188

6.4. Representative FTIR spectra of (a) MCF-7 SC, (b) MCF-7 MC, (c) MM 231 SC, and (d) MM 231 MC at different incubation times in the region of 3600-930 cm^{-1} 189

6.5. Representative second-derivative spectra of (a) MCF-7 SC, MCF-7 MC, (b) MM 231 SC, MM 231 MC at different incubation times in the region of 3050-930 cm^{-1}. 192

6.6. Representative curve-fitted amide region (1708-1482 cm^{-1}) of MCF-7 MC (a-c), and MCF-7 SC (d-f); lipid region (2990-2800 cm^{-1}) of MCF-7 MC (g-i), and MCF-7 SC (j-l); nucleic acid region (1180-930 cm^{-1}) of MCF-7 MC (m-o), and MCF-7 SC (p-r) for different incubation time. 195

6.7. Representative curve-fitted amide region (1708-1482 cm^{-1}) of MM 231 MC (a-c), and MM 231 SC (d-f); lipid region (2990-2800 cm^{-1}) of MM 231 MC (g-i), and MM 231 SC (j-l); nucleic acid region (1180-930 cm^{-1}) of MM 231 MC (m-o), and MM 231 SC (p-r) for different incubation time. 198

6.8. Intensity ratios of Amide I/Amide II (a and d), CH_2 asymmetric/ CH_2 symmetric stretch (b and e), RNA/DNA (c and f) of monocultures (MC) and sequential cultures of MCF-7 and MM 231, respectively, at different incubation time. (n=3, two-way ANOVA followed by *post hoc* Tukey test,*p<0.05, **p<0.01, and ***p<0.001). 201

6.9. The results of PCA applied to 2 groups of second derivative spectra (MCF-7 MC and MCF-7 SC) in the region of 3050-2800 and 2000-930 cm^{-1} (a), and a PC-1 correlation loading plot (b); the results of PCA applied to 2 groups of second derivative spectra (MM 231 MC and MCF-7 SC) in the region of 3050-2800 and 2000-930 cm^{-1} (c), and a PC-1 correlation loading plot (d); the results of PCA applied to 2 groups of second derivative spectra (MM 231 SC and MCF-7 SC) in the region of 3050-2800 and 2000-930 cm^{-1} (e), and a PC-2 correlation loading plot (f). 203

7.1. Schematic showing sequential culture of MSCs/prostate cancer cells and the workflow of Raman experiment. 225

7.2. (A) Mean Raman spectra of 2D PCa (n=20) and 3D MSCs + PCa SCs (n=20). (B) The corresponding difference spectra calculated from the mean Raman spectra between 2D culture and three different 3D cultures. 230

7.3. (A) PCA score plot spanned by PC1, and PC2 illustrating the intrinsic clustering of 2D PCa and 3D MSCs + PCa SCs. (B) The first two PCs accounting for 92.9% of the total variation in the Raman spectral dataset, revealing the significant Raman spectral features for the classification of cancer cells. 233

7.4. Histogram displaying intensities of Raman bands (A) 1002 cm^{-1}, (B) 1261 cm^{-1}, (C) 1444 cm^{-1}, and (D) 1654 cm^{-1} across samples. (n=20, one-way ANOVA followed by *post hoc* Tukey test, *p<0.05, **p<0.01, and ***p<0.001 indicate significant difference between 2D PCa and 3D MSCs + PCa SCs; $^{\#}$p<0.05, $^{\#\#}$p<0.01, and $^{\#\#\#}$p<0.001 indicate significant difference between day (23+5), and other days of 3D MSCs + PCa SCs; $^{\$}$p<0.05, $^{\$\$}$p<0.01, and $^{\$\$\$}$p<0.001 indicate significant difference between day (23+10) 3D MSCs + PCa SC and day (23+15) 3D MSCs + PCa SC). 234

7.5. Raman mapping images of 2D PCa and three 3D MSCs + PCa SCs for vibrational signatures of: (A) 1002 cm^{-1}, (B) 1261 cm^{-1}, (C) 1444 cm^{-1}, and (D) 1654 cm^{-1}. 235

7.6. Cluster analysis of 2D PCa and PCa cells seeded on bone-mimetic scaffolds for 5, 10 and 15 days, (A) optical images of samples used in Raman Imaging, (B) clusters indicating actin-rich regions colored in red and the red stripe on the top of the image constitutes digitally introduced reference actin, (C) clusters indicating DNA rich regions colored in blue and the blue stripe on the top of the image constitutes digitally introduced reference DNA, (D) average spectra from ten randomly collected spectra from the actin-rich regions on day 15 and the reference spectra for actin, (E) average spectra from ten randomly collected spectra from the DNA rich regions on day 15 and the reference spectra for actin. The bone-mimetic scaffolds are created by seeding MSCs on 3D nanoclay based scaffolds and culturing for 23 days for regeneration of bone tissue. PCa cells are seeded after the MSC culture period of 23 days is completed. The 2D PCa cells indicate PCa cells not seeded on scaffolds. 236

7.7. (A) Reference Actin spectra used for cluster analysis. (B) Cluster map of 3D d(23+15) MSCs+PCa SC indicating actin-rich regions colored in red and the red stripe on the top of the image constitutes digitally introduced reference actin, boxes (a,b, and c) drawn on the cluster map indicate random location on actin-rich region. (C) Spectra from randomly chosen location on actin-region showing similar features as reference actin. 237

7.8. (A) Reference Myosin spectra used for cluster analysis. (B) Cluster map of 3D d(23+15) MSCs+PCa SC indicating myosin-rich regions colored in red and the red stripe on the top of the image constitutes digitally introduced reference myosin, boxes (a,b, and c) drawn on the cluster map indicate random location on myosin-rich region. (C) Spectra from randomly chosen location on myosin-region showing similar features as reference myosin. 238

LIST OF ABBREVIATIONS

MSCs	Mesenchymal Stem Cells.
RUNX2	Runt related transcription factor 2.
DLX5	Distal-less homeobox 5.
OSX	Osterix.
BSP	Bone sialoprotein.
OCN	Osteocalcin.
COL I	Collagen Type I.
M-CSF	Macrophage Colony Stimulating Factor.
RANKL	Receptor Activator of Nuclear factor Kappa B Ligand.
EMT	Epithelial to Mesenchymal transition.
MET	Mesenchymal to Epithelial transition.
VEGF	Vascular Endothelial Growth Factor.
IL-8	Interleukin-8.
IL-11	Interleukin-11.
PTHrP	Parathyroid Hormone-related Protein.
TNF-α	Tumor Necrosis Factor-alpha.
OPG	Osteoprotegerin.
TGF-β	Tumor Growth Factor- β.
HAP	Hydroxyapatite.
PPi	Pyrophosphate.
2D	Two-dimensional.
3D	Three-dimensional.
PLG	Poly-lactide-co-glycolide.

PCN.....Polymer-Clay Nanocomposite.

Na-MMT.....Sodium Montmorillonite.

Chi/PgA.....Chitosan-Polygalacturonic acid.

PCL.....Polycaprolactone.

LRP-5/6.....Low-density lipoprotein receptor-related protein 5/6.

FZD.....Frizzled.

CK1.....Casein Kinase 1.

GSK-3β.....Glycogen Synthase Kinase-3β.

APC.....Adenomatous Polyposis Coli.

DKK-1.....Dickkopf homolog 1.

ET-1.....Endothelin-1.

IL-6.....Interleukin-6.

JAK2.....Janus Kinase 2.

STAT3.....Signal Transducer and Activator of Transcription 3.

MRP1.....Multidrug Resistance-associated Protein 1.

ABCC1.....ATP-binding Cassette Subfamily C Member 1.

ABCG2.....ATP-binding Cassette Subfamily G Member 2.

WASP.....Wiskott - Aldrich syndrome Protein.

ARP2/3.....Actin-related Proteins-2/3.

WAVE2.....Wiskott-Aldrich syndrome protein family member 2.

AFM.....Atomic Force Microscopy.

BrCa.....Breast Cancer.

HBCC.....Human Breast Cancer Cell.

ATCC.....American Type Culture Collection.

DMEM .....Dulbecco’s Modified Eagle Medium.

EMEM.....Eagle’s Minimum Essential Medium.

PBS .....Phosphate Buffered Saline.

UV.....Ultraviolet.

SC.....Sequential Culture.

ALP .....Alkaline Phosphate.

SEM .....Scanning Electron Microscope.

DAPI .....4', 6-diamidino-2-phenylindole.

MMP-9.....Matrix Metalloproteinase 9.

ELISA .....Enzyme-Linked Immunosorbent Assay.

PCR.....Polymerase Chain Reaction.

GAPDH.....Glyceraldehyde 3-Phosphate Dehydrogenase.

FGFR2.....Fibroblast Growth Factor Receptor 2.

HIF-1.....Hypoxia-Inducible Factor 1.

FSG .....Fish Skin Gelatin.

ECM.....Extracellular Matrix.

SDF-1.....Stromal Cell-Derived Factor-1.

TCPS.....Tissue Culture Polystyrene.

PFA .....Paraformaldehyde.

ARS.....Alizarin Red S.

CM .....Conditioned Medium.

ETAR .....Endothelin-A Receptor.

PVA.....Poly (Vinyl Alcohol).

PEG.....Poly (Ethylene Glycol).

FBS .....Fetal Bovine Serum.

IC_{50} .....Half Maximal Inhibitory Concentration.

N-WASP .....Neural-Wiskott-Aldrich Syndrome Protein.

CDC42 .....Cell Division Control protein 42 Homolog.

CTTN .....Cortactin.

CFL2 .....Cofilin-2.

CTCF.....Corrected Total Cell Fluorescence.

L-D.....Load-Displacement.

FTIR.....Fourier Transform Infrared.

PCA.....Principal Component Analysis.

MRI.....Magnetic Resonance Imaging.

LIST OF APPENDIX FIGURES

Figure Page

A1. L-D curves of as received MCF-7 cells at maximum displacement of 1000 nm. 257

A2. L-D curves of scaffolds-derived MCF-7 cells (d5) at maximum displacement of 1000 nm. 261

A3. L-D curves of scaffolds-derived MCF-7 cells (d10) at maximum displacement of 1000 nm. 265

A4. L-D curves of scaffolds-derived MCF-7 cells (d15) at maximum displacement of 1000 nm. 269

A5. L-D curves of as received MCF-7 cells at maximum displacement of 2000 nm. 273

A6. L-D curves of scaffolds-derived MCF-7 cells (d5) at maximum displacement of 2000 nm. 277

A7. L-D curves of scaffolds-derived MCF-7 cells (d10) at maximum displacement of 2000 nm. 281

A8. L-D curves of scaffolds-derived MCF-7 cells (d15) at maximum displacement of 2000 nm. 285

A9. L-D curves of as received MM 231 cells at maximum displacement of 1000 nm. 289

A10. L-D curves of scaffolds-derived MM 231 cells (d5) at maximum displacement of 1000 nm. 293

A11. L-D curves of scaffolds-derived MM 231 cells (d10) at maximum displacement of 1000 nm. 297

A12. L-D curves of scaffolds-derived MM 231 cells (d15) at maximum displacement of 1000 nm. 301

A13. L-D curves of as received MM 231 cells at maximum displacement of 2000 nm. 305

A14. L-D curves of scaffolds-derived MM 231 cells (d5) at maximum displacement of 2000 nm. 309

A15. L-D curves of scaffolds-derived MM 231 cells (d10) at maximum displacement of 2000 nm. 313

A16. L-D curves of scaffolds-derived MM 231 cells (d15) at maximum displacement of 2000 nm. 317

CHAPTER 1. INTRODUCTION

1.1. Bone

Bone is a three-dimensional, highly structured, dynamic tissue with an organized extracellular matrix consisted of organic and inorganic components. It not only provides support and structural integrity to the body but also regulates metabolic activity by governing interactions between bone microarchitecture and heterogeneous population of bone cells, and their aggregate response to various mechanical stimuli such as mechanical loading, fluid flow, and substrate deformation, etc. Bone remodeling is a highly complex process, governed by a gamut of biochemical signaling and mechanical cues generated by its highly structured matrix. Remodeling helps maintain mineral homeostasis and acclimatize to mechanical changes [1, 2]. Osteoblasts, osteoclasts, and osteocytes typically control bone homeostasis. Osteoblasts and osteoclasts independently govern bone formation and bone resorption process, respectively [3]. However, excessive bone formation by osteoblasts without osteoclast activity leads to osteopetrosis [4, 5], while the contrary results in bone loss and osteoporosis [6, 7].

1.1.1. Bone cells

1.1.1.1. Osteoblasts

Osteoblasts are derived from osteoprogenitor lineage of mesenchymal stem cells (MSCs). Induction of osteogenic differentiation is characterized by increased expression of transcription factors such as runt related transcription factor 2 (Runx2), and osterix (Osx), as well as homeobox protein distal-less homeobox 5 (Dlx5) while maturation of osteoblasts is marked by increased expression of Osx and secretion of bone matrix proteins such as bone sialoprotein (BSP) I/II, osteocalcin (OCN), and collagen type I (COL I) [8-14]. Osteoblasts reside along the

bone surface and participate in the deposition and mineralization of the bone matrix during bone remodeling.

1.1.1.2. Osteoclasts

Osteoclasts are derived from mononuclear cells of the hematopoietic stem cell lineage that fuse to form pre-osteoclasts [9]. Macrophage colony stimulating factor (M-CSF) and receptor activator of nuclear factor kappa B ligand (RANKL) secreted by osteoblast, osteoprogenitor mesenchymal cells, and other stromal cells in microenvironment, promote pre-osteoclasts to differentiate into multinucleated, activated osteoclasts that resorb bone during bone remodeling [6, 15]. However, excessive osteoclast activity without bone formation causes osteoporosis, a bone disease characterized by dysfunctional bone matrix with poor mechanical stability leading to bone fractures [16]. In case of bone metastasis, abnormal activation of osteoclasts together with impaired osteoblastic activity leads to osteolytic lesions [17].

1.1.1.3. Osteocytes

Osteocytes are the most abundant cells in the bone matrix derived from the mature osteoblasts, which become embedded in the mineralized bone matrix [18, 19]. They display multiple (up to 50 per cell) cytoplasmic dendritic extensions, which run along narrow canaliculi and establish a connection to neighboring osteocytes, osteoblasts, and the lining cells at the bone surface [12, 20]. Thus, osteocytes act as mechanosensors and provide a means by which bone adapts to mechanical load by changing in microarchitecture, shape, or mass [12].

1.2. Breast Cancer Bone Metastasis

Breast cancer is one most common form of cancer worldwide, and based on current incidence rates, 12.4 % of women born in the United States today may develop breast cancer at some time during their lives [21]. In 2020, an estimated 279,100 cases of breast cancer

will be diagnosed among those 276,480 will be women and 2,620 will be men, respectively. Furthermore, an estimated 42,690 deaths are expected due to breast cancer in 2020 [22]. Breast cancer has the propensity to spread to other organs and bone is the most common site for breast cancer metastases, causing bone-related complications (such as hypercalcemia, excruciating pain, and bone fractures) leading to poor clinical prognosis [17, 23, 24]. Approximately 80% of breast cancer patients die within five years after primary cancer has metastasized to the bones [25]. The survival rate of the patients with breast cancer metastasized to bone is highly influenced by the tumor stage at the time of diagnosis. Breast cancer cells colonize within the bone marrow and impede bone remodeling processes either by activation of osteoclast differentiation or by the promotion of osteoblast activity [26, 27].

Cancer metastasis involves a series of well-defined steps including cellular detachment or dissemination at the primary site, invasion at basement membrane, intravasation or vascular invasion, circulation or migration through blood vessels or lymph nodes, extravasation, survival, proliferation, angiogenesis, and secondary tumor growth at metastatic site [28]. Epithelial cancer cells undergo epithelial to mesenchymal transition (EMT) to acquire mesenchymal phenotype with increased motility and invasiveness. Newly acquired invasiveness makes the cells disseminate from primary tumors, invade basement membrane, and enter the bloodstream to become circulating tumor cells. At the gene level, EMT is characterized by loss of E-cadherin expressions together with increased expressions of Snail, Twist, Slug, and vimentin [29]. These circulating tumor cells migrate into a distant organ (bone), and in response to microenvironment, cells start to colonize to pave the way for secondary micrometastases via mesenchymal to epithelial transition (MET). When cancer cells undergo MET, they lose their mesenchymal traits followed by gaining of epithelial phenotype [30] (Figure 1.1).

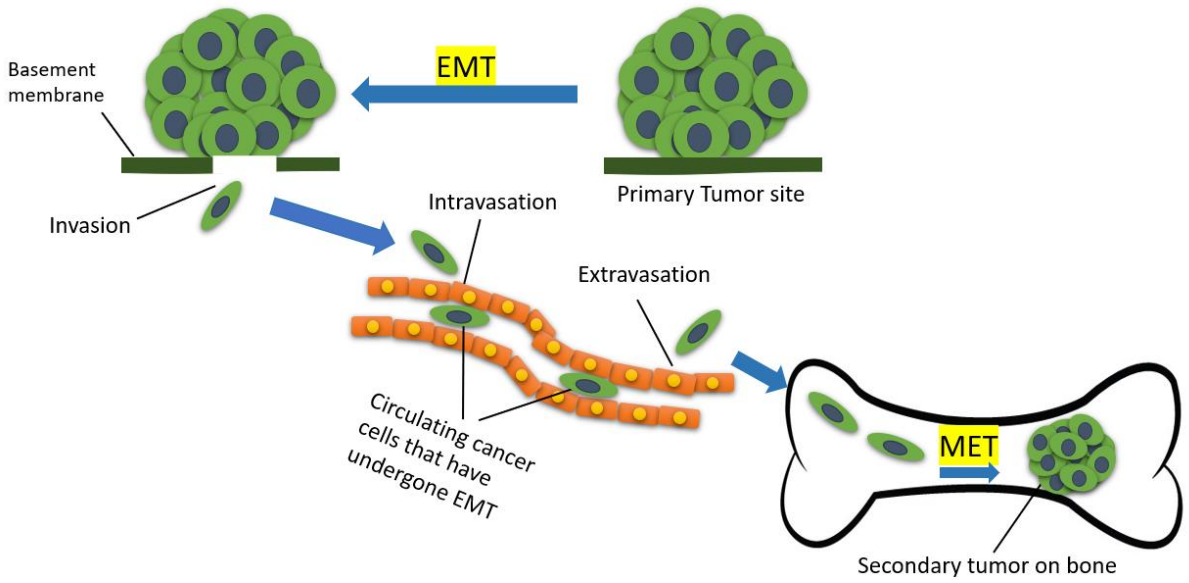

Figure 1.1. Cancer metastasis involves a series of well-defined steps including cellular detachment or dissemination at the primary site, invasion at basement membrane, intravasation or vascular invasion, circulation or migration through blood vessels or lymph nodes, extravasation, survival, proliferation, angiogenesis, and secondary tumor growth at metastatic site. Epithelial cancer cells undergo epithelial to mesenchymal transition (EMT) to acquire mesenchymal phenotype with increased motility and invasiveness. Newly acquired invasiveness makes the cells disseminate from primary tumors, invade basement membrane, and enter the bloodstream to become circulating tumor cells. These circulating tumor cells migrate into a distant organ (bone), and in response to microenvironment, cells start to colonize to pave the way for secondary micrometastases via Mesenchymal to epithelial transition (MET). When cancer cells undergo MET, they lose their mesenchymal traits followed by gaining of epithelial phenotype.

The interactions between the bone microenvironment and breast cancer cells have been shown to contribute towards the development of bone metastases [31]. A gamut of different growth factors and cytokines govern the vicious cycle of bone metastasis, such as vascular endothelial growth factor (VEGF), Interleukin-8 (IL-8), Interleukin-11 (IL-11), parathyroid hormone-related protein (PTHrP). Studies have identified that these factors mentioned above destabilize the balance between bone resorption and bone formation [32, 33].

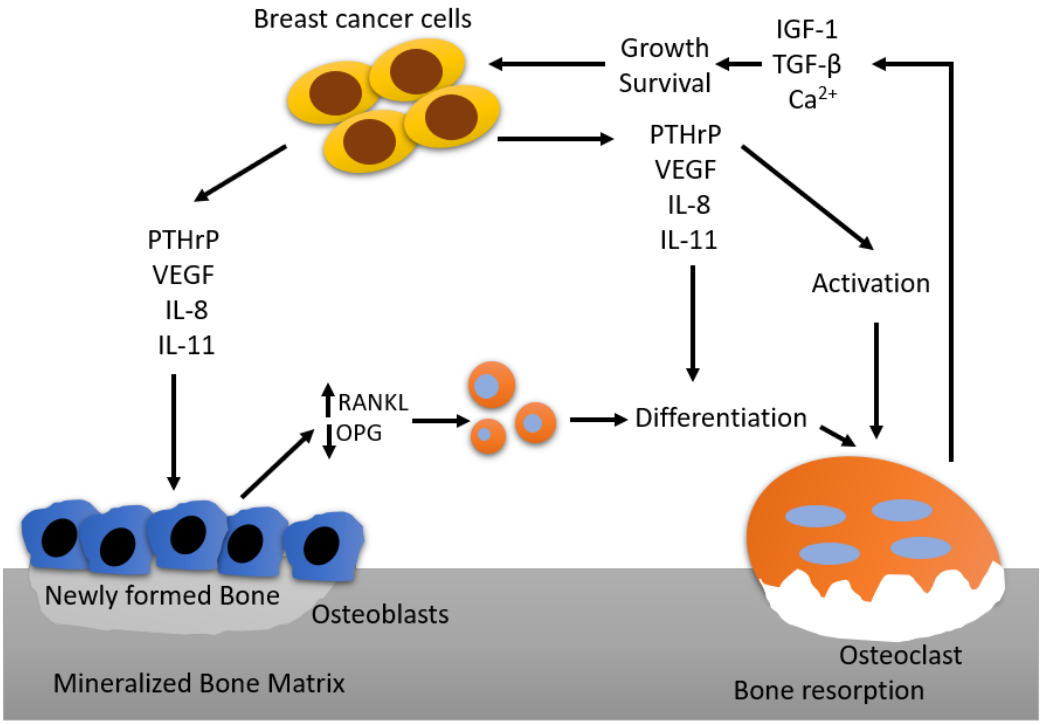

Figure 1.2. A gamut of different growth factors and cytokines govern the vicious cycle of bone metastasis, such as vascular endothelial growth factor (VEGF), Interleukin -8 (IL-8), Interleukin-11 (IL-11), parathyroid hormone-related protein (PTHrP). Studies have identified that these factors mentioned above destabilize the balance between bone resorption and bone formation. RANKL dictates the pathway of osteoclastogenesis, and it causes differentiation of progenitor cells in the bone marrow into osteoclasts. Breast cancer cells secrete PTHrP along with tumor necrosis factor-alpha (TNF-α), which activates RANKL and inhibits osteoprotegerin (OPG), a decoy receptor of RANKL, resulting in bone resorption. Bone resorption increases the secretion of PTHrP by cancer cells, and PTHrP, in turn, upregulates tumor growth factor- β (TGF-β), resulting in severe osteolysis.

RANKL dictates the pathway of osteoclastogenesis, and it causes differentiation of progenitor cells in the bone marrow into osteoclasts [34]. Breast cancer cells secrete PTHrP along with tumor necrosis factor-alpha (TNF-α), which activates RANKL and inhibits osteoprotegerin (OPG), a decoy receptor of RANKL, resulting in bone resorption [35]. Bone resorption increases the secretion of PTHrP by cancer cells, and PTHrP, in turn, upregulates tumor growth factor- β (TGF-β), resulting in severe osteolysis [36] (Figure 1.2). Although improved understanding of the pathophysiology of bone metastases has been useful in

elucidating pathways of cancer using several experimental and animal models, experimental models that faithfully replicate the events that occur in individuals with breast cancer metastasized to the bones are still scarce and limited in unraveling molecular mechanism underlying the later stages of breast cancer pathogenesis to bones.

1.3. Current Therapies for Breast Cancer Bone Metastases

The currently available therapies for patients with bone metastases include bisphosphonate-based treatments to improve bone stability along with pain management, orthopedic surgery to repair bone fractures, and radiotherapy to alleviate pain/or prevent bone fractures [37]. Bisphosphonates are pharmacological agents that help increase bone stability by inhibiting osteoclast-mediated bone resorption activity [38, 39]. Bisphosphonates exhibit a high affinity for hydroxyapatite (HAP) owing to its structural resemblance with pyrophosphate (PPi) [38]. Thus, bisphosphonates primarily get assimilated into the areas of active bone remodeling due to the availability of a large number of HAP binding sites [38]. However, bisphosphonates neither target tumor nor repair bone directly. Recently, Denosumab, a humanized, synthetic monoclonal antibody, has been shown to bind to RANKL, thereby inhibiting the differentiation and activation of premature and mature osteoclasts, respectively, thus impeding bone resorption [40]. Although radiotherapy has long been used for the treatment of localized pain, there have been complaints of increased risk of bone fractures post-radiotherapy [37].

1.4. 3D Cell Culture Models in Cancer

Unraveling the metastatic cascade at the cellular level is the first step towards developing new and effective therapeutic approaches against bone metastases at early stages to improve patient survival rates. Cell culture studies have been an integral part of cancer drug development for decades now. To date, cancer researchers have heavily relied on two-dimensional (2D)

monolayer cell culture systems for the discovery of signaling pathways and drugs. However, conventional 2D monolayer culture systems do not recapitulate cell behavior in a human body where cells exist in a three-dimensional (3D) environment, wherein cell-cell, cell-matrix interactions play a major in regulating the behavior of cancer cells [41, 42]. Although animal models provide a native 3D microenvironment, where human cancer cells can be injected, or human bone fragments can be implanted into immune-deficient animals to create metastatic xenograft; their species difference, immuno-deficiency, and complex disease pathogenesis most often reduce the correlation between clinical trials and animal studies [43, 44]. Therefore, the development of accurate and efficient models to recapitulate cell-cell/cell-matrix interactions to mimic native tumor microenvironment and achieve better drug response is paramount to identify targets for drug development. In recent years, 3D culture systems have received a great deal of attention owing to their ability to mimic *in vivo* tissue microenvironment, leading to altered focal adhesions, growth kinetics, metabolic activity, cytokine production, morphology, genotypic/phenotypic traits**,** and *in vivo*-like drug response [45-51].

1.5. Tissue-Engineered 3D Models of Breast Cancer Bone Metastases

Tissue engineering is an interdisciplinary field of research that combines the principles of engineering and life sciences towards developing biological constructs to augment or restore tissue function [52, 53]. Tissue engineering strategies are relatively less invasive and capable of healing damaged and injured tissues by the natural process as compared to conventional treatments [54]. Cells, growth factors, and scaffolds are critical components of tissue engineering. Scaffolds provide required biophysical and biochemical cues to the cells for tissue formation in a 3D environment similar to *in vivo* environment. A schematic showing the concept of tissue engineering is shown in Figure 1.3 .

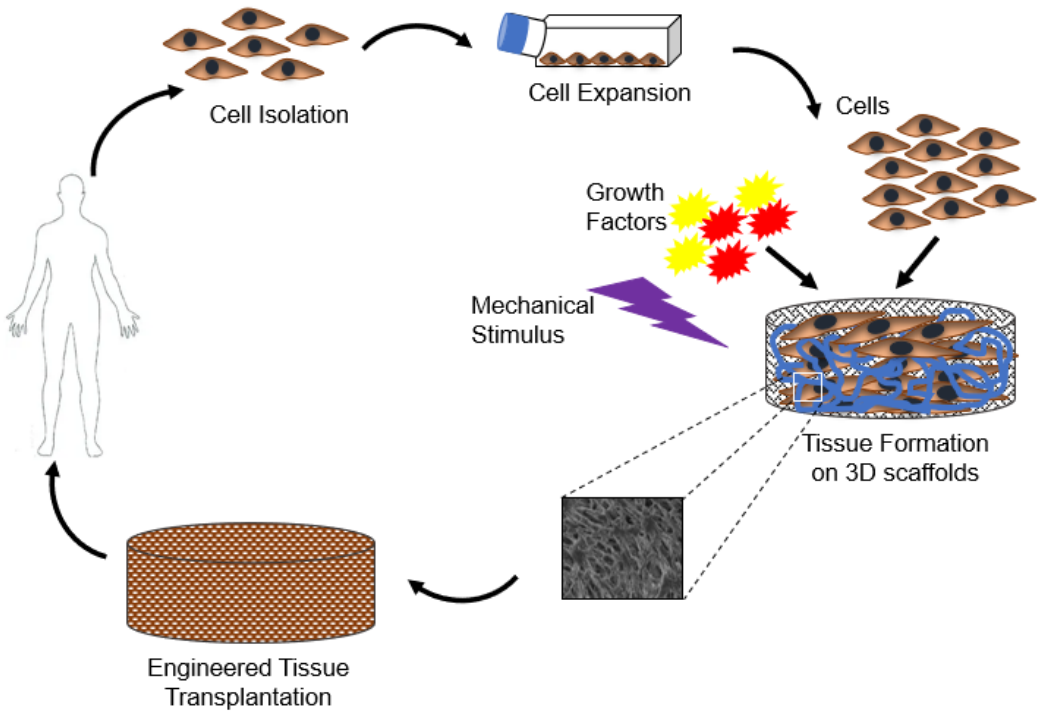

Figure 1.3. Schematic showing the concept of tissue engineering. Cells are isolated from the patient and cultured on two-dimensional (2D) cell culture flask for efficient expansion. Next, the cells are seeded in porous scaffolds together with growth factors to aid regeneration. The scaffolds serve as a mechanical support during tissue growth, and their porous structure provides nutrient supply and helps waste removal. Once a functioning tissue has been successfully engineered, the construct is transplanted on the defect to restore function.

In recent years, tissue engineering approaches have attracted substantial attention owing to its potential to model diseases to delineate the molecular mechanism of disease progression efficiently. There have been a lot of studies focusing on the development of 3D *in vitro* models for studying breast cancer bone metastases to date. For instance, Pathi et al. demonstrated the crucial role of the bone mineral hydroxyapatite in governing breast cancer bone metastasis using porous poly-lactide-co-glycolide (PLG) scaffolds [32]. Further, MSCs-modified bone model was developed to recapitulate metastatic characteristics of various breast cancer cells [55]. Talukdar & Kundu developed 3D silk fibroin-based scaffolds to study interactions between cancer cells and osteoblasts [49] while Mastro et al. showed interactions of cancer cells with bone tissue in real-time with the help of a bioreactor [56]. In another study, silk fibroin scaffolds-based co-

culture model of osteoblasts and breast cancer cells was developed to evaluate the efficacy of targeted delivery of doxorubicin-loaded folate conjugated fibroin nanoparticles [57]. In a recent study, Zhu et al. fabricated a 3D-printed co-culture model of osteoblasts and breast cancer cells to evaluate drug-resistance of breast cancer cells against chemotherapeutic drug 5-Fluorouracil [58]. Although these studies have been able to shed light on disease pathogenesis regarding cytokine production, altered gene/protein expression, and targeted therapies; one of the major limitations of co-culture systems is simultaneous seeding of both cells on scaffolds while colonization of breast cancer cells in bone microenvironment is mediated by chemokines, and growth factors released by already growing bone cells, stromal cells, etc. To this end, we implemented a sequential culture system [48] in which we cultured MSCs on nanoclay scaffolds for 23 days to obtain bone-like extracellular matrix deposition. Then, we seeded breast cancer cells (MDA-MB-231, MCF-7) on the scaffolds bearing newly formed bone to mimic metastatic condition. The details of nanoclay scaffold system will be described in section 1.6.

1.6. Nanoclay-based Scaffolds for Bone Tissue Engineering

The primary focus of tissue engineering has been the development of materials with adequate mechanical properties that favor tissue growth and regeneration. There has been a continuous effort from researchers across the globe to develop composite systems with polymers and nano/micro-sized fillers to tailor properties of polymers, including biodegradability, bioactivity, biocompatibility, surface roughness, and mechanical strength for applications in tissue engineering. Researches related to polymer-clay nanocomposites (PCNs) since 1990 have shown that the addition of clay in small quantities not only improves mechanical strength [59-66] but also influences properties such as biodegradability [67], flammability [68, 69], and gas

permeability [70-72]. PCNs are composites with polymer matrix in which the dispersed phase is the clay particles having at least one of their dimensions in the nanometer range [73, 74].

Modification of clays has been shown to play an essential role in the preparation of nanocomposites due to its ability to alter the final properties of the nanocomposites. Attempts made using both computational and experimental approaches to get more insight into the modification of sodium montmorillonite (Na-MMT) clay with various organic modifiers led to the development of "altered phase" model. This model highlights the effect of interactions among polymer, clay, and organic modifiers on the crystallinity and nanomechanical properties of PCNs [65]. In a related work from our group, it was shown that the backbone chain length and the functional groups in modifiers influenced the crystallinity and nanomechanical properties of PCNs [75]. All these observations prompted us to use unnatural amino acid such as 5-amino valeric acid for modification of clay, which not only increased interlayer d-spacing but also improved its biocompatibility [76]. In a subsequent study, our group biomineralized HAP into intercalated nanoclay galleries to obtain *in situ* HAPclay [77]. We further used *in situ* HAPclay as a reinforcement filler while preparing composites from chitosan-polygalacturonic acid (Chi/PgA) [78] and polycaprolactone (PCL) [79]. It was shown that incorporation of *in situ* HAPclay significantly enhanced mechanical property along with bioactivity of the composites [78, 79]. Studies have been done to evaluate the feasibility of ChiPgA/*in situ* HAPclay composites [78]. Previous studies from our group have reported osteogenic differentiation of human mesenchymal stem cells on *in situ* HAPclay-scaffolds without the use of osteogenic supplements via Wnt/β-catenin pathway [79, 80]. MSCs cultured on nanoclay-based composites mediated mineralization by vesicles containing crystalline calcium minerals [81]. Upon investigation, Ca/P ratio in these vesicles was found to be lower than the

stoichiometric Ca/P ratio of HAP, indicating new bone formation and remodeling of bone [81]. Increasing evidence shows that breast cancer metastasizes to remodeling bone microenvironment, which prompted us to use this system in the present research study.

1.7. Wnt/β-catenin Pathway Mediated Osteogenesis at Metastases

The Wnt/ β-catenin pathway plays a crucial role in the bone regenerative process including fracture healing [82, 83]. Wnt signaling is mediated by activation of low-density lipoprotein (LDL) receptor-related protein 5/6 (LRP-5/6) and Frizzled (FZD) by secreted Wnt ligands [84]. In the absence of Wnt signal, β-catenin is phosphorylated by casein kinase 1 (CK1) and the glycogen synthase kinase-3β (GSK-3β)/adenomatous polyposis coli (APC)/Axin complex, leading to ubiquitination and proteasome degradation of β-catenin [85-87] (Figure 1.4a). In the presence of Wnt signal, the co-receptor LRP5/6 forms complex with Wnt-bound FZD which in turn promotes nuclear translocation of β-catenin and activates of transcription of target genes, such as c-myc, RUNX2, and cyclin D1 [88-90] (Figure 1.4b).

Although Wnt/ β-catenin pathway is well studied for osteogenesis [80, 91-94], little is known about regulation of Wnt/ β-catenin pathway by breast cancer-derived factors such as dickkopf homolog 1 (DKK-1) and endothelin-1 (ET-1) during osteogenesis in breast cancer induced bone metastasis. DKK-1, an inhibitor of canonical Wnt signaling, operates by sequestering LRP-5/6 from FZD and thus blocks Wnt/ β-catenin pathway mediated osteogenesis [95-97].

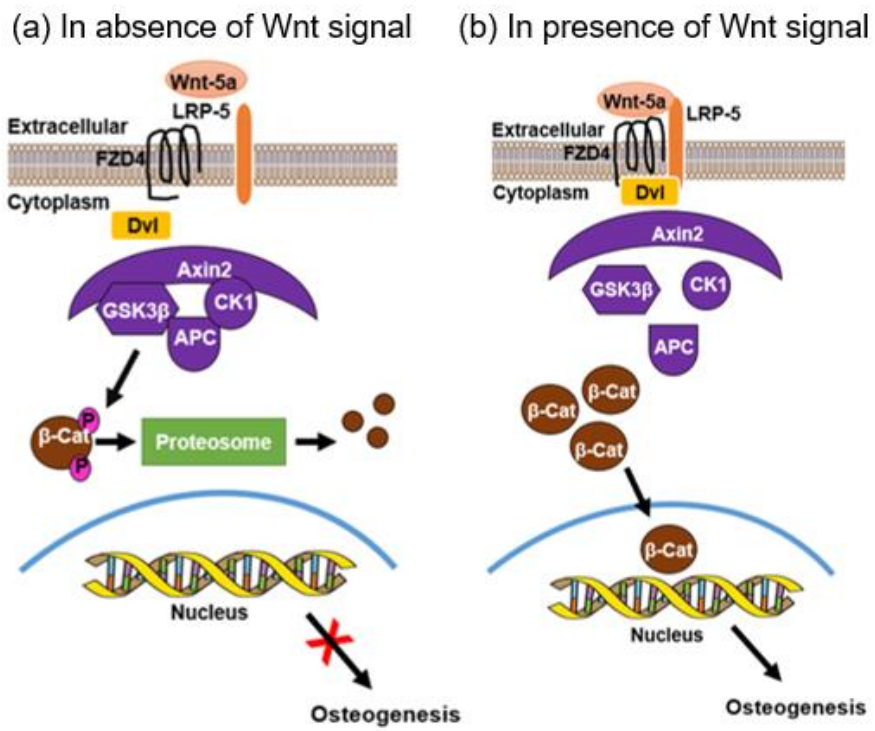

Figure 1.4. Schematic showing Wnt/ β-catenin signaling pathway. Wnt signaling is mediated by activation of low-density lipoprotein (LDL) receptor-related protein 5 (LRP-5) and Frizzled 4 (FZD4) by secreted Wnt ligands. (a) In the absence of Wnt signal, β-catenin is phosphorylated by casein kinase 1 (CK1) and the glycogen synthase kinase-3β (GSK-3β)/adenomatous polyposis coli (APC)/Axin 2 complex, leading to ubiquitination and proteasome degradation of β-catenin. (b) In the presence of Wnt signal, the co-receptor LRP5/6 forms complex with Wnt-bound FZD which in turn promotes nuclear translocation of β-catenin and stimulates osteogenesis.

Increased DKK1 expressions has been associated with osteolytic bone metastases [98]. Breast cancer cells have also been shown to control the secretion of DKK1 during bone metastasis via ET-1. ET-1 has been shown to downregulate secretion of DKK-1, causing increased osteoblastic activity and bone formation [99].

1.8. IL-6/STAT3 Pathway Mediated Drug Resistance at Metastases

Drug resistance has been a major roadblock in successful cancer chemotherapy. Activation of IL-6/STAT3 signaling pathway has been shown to mediate drug resistance in many cancers, including breast [100, 101], ovarian [102], colorectal [103], prostate [104, 105], and gastric cancer [106]. Interleukin-6 (IL-6), a pro-inflammatory cytokine produced in the tumor

microenvironment by stromal cells, fibroblasts, and cancer cells [107]. Binding of IL-6 to its receptor IL-6R on the cell membrane activates Janus Kinase 2 (JAK2) kinases. Activated JAK2 mediates phosphorylation, dimerization, and nuclear translocation of Signal Transducer and Activator of Transcription 3 (STAT3) [108]. STAT3 signaling mediates the expression of various genes, including p53 [109], Bcl-2 [110], multidrug resistance-associated protein 1 (MRP1) or ATP-binding cassette subfamily C member 1 (ABCC1) [111], and ATP-binding cassette subfamily G member 2 (ABCG2) [112]. Bcl-2 and p53 are associated with regulation of apoptosis [113] while overexpression of drug transporters MRP1, ABCG2 has been shown to mediate efflux of drugs from cancer cells, thus decreasing intracellular drug concentration

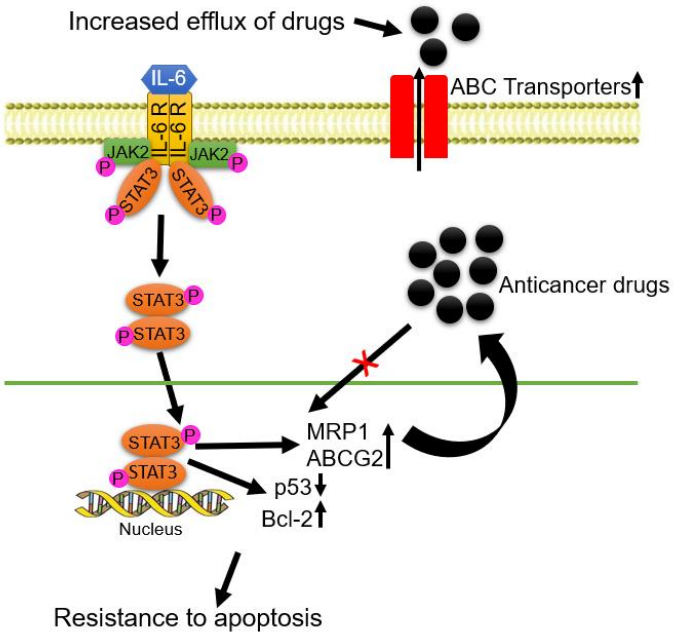

Figure 1.5. Schematic showing IL-6/STAT3 signaling pathway. Interleukin-6 (IL-6), a pro-inflammatory cytokine produced in the tumor microenvironment by stromal cells, fibroblasts, and cancer cells. Binding of IL-6 to its receptor IL-6R on the cell membrane activates Janus Kinase 2 (JAK2) kinases. Activated JAK2 mediates phosphorylation, dimerization, and nuclear translocation of Signal Transducer and Activator of Transcription 3 (STAT3). STAT3 signaling mediates the expression of various genes, including p53, Bcl-2, multidrug resistance-associated protein 1 (MRP1), and ATP-binding cassette subfamily G member 2 (ABCG2). Bcl-2 and p53 are associated with regulation of apoptosis while overexpression of drug transporters MRP1, ABCG2 has been shown to mediate efflux of drugs from cancer cells, thus decreasing intracellular drug concentration leading to drug resistance.

leading to drug resistance [114] (Figure 1.5). ABCC1 and ABCG2 have also been shown to transport a variety of organic anions, including conjugates of sulfate, glucuronide, and glutathione; and various anticancer agents, including mitoxantrone, camptothecins, and anthracyclines, respectively [114].

1.9. Evaluation of Raman and Infrared Spectroscopy as Diagnostic Tools for Cancer Progression

The current gold standard for determining the prognosis of cancer in patients is a basic histopathological examination [115]. Immunohistopathology has also been used extensively for the analysis of biopsy samples in the last decade. Nevertheless, the use of immunohistochemistry is restricted due to the scarcity of large volume of tissue sections for staining and the inability to detect multiple signals at once [116]. Also, the reproducibility and robustness of genomic data remain a concern due to the heterogeneity of tumors [117, 118]. It is, therefore, necessary to develop robust diagnostic and classification tools that have reproducibility and clinical potential.

Raman spectroscopy uses the inelastic scattering of light by an object, and C.V. Raman first documented it in 1928 [119]. When a monochromatic light interacts with a substance, most of the energy is scattered at the same frequency as the incident light (Rayleigh scattering), together with a minimal quantity of photons scattered at frequencies that differ from the incident radiation (inelastic scattering). The fraction of photons scattered from molecules with higher energy than they had before the interaction is called anti-Stokes scattering. In contrast, the photons with reduced energy than those of the incident radiation are termed as Stokes scattering (Figure 1.6). Raman spectroscopy is based on a change in polarizability of a molecule on the absorption of photons (Raman spectroscopy can be used to obtain spectral information from a homo-nuclear molecule), whereas, the complementary IR spectroscopy depends on a change in

the dipole moment. Vibrations of nonpolar, symmetric bonds tend to be active in Raman spectra, whereas polar asymmetric groups are active in IR spectra. For example, O-H vibrations of water give rise to a strong band in IR spectra, whereas Raman water signal is very weak.

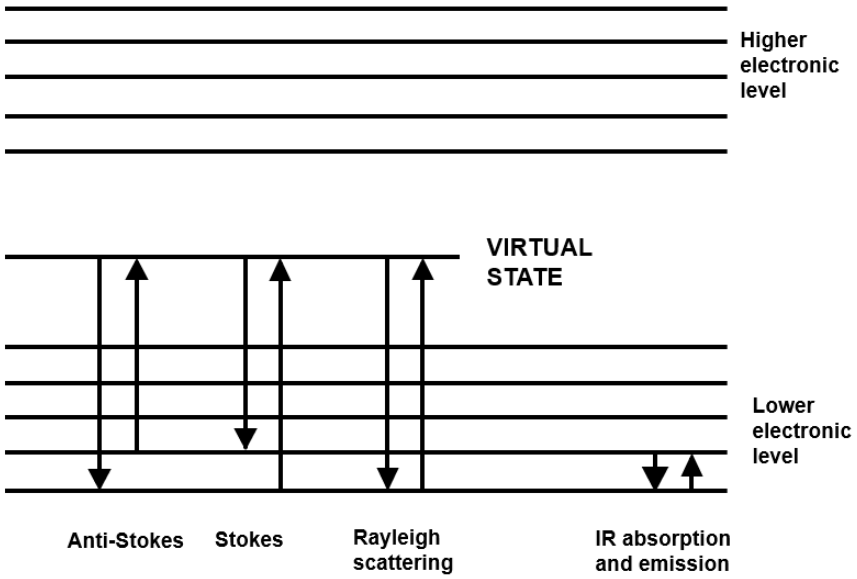

Figure 1.6. Schematic representation of energy transitions in Raman and IR spectroscopy.

Thus, Raman spectroscopy is more suitable for biological applications. However, Raman spectroscopy is inherently weak, with only a small quantity of photons exhibiting Raman scattering (~10^{-6}). Therefore, longer spectral acquisition is required to obtain an adequate signal to noise ratio in Raman as compared to IR spectroscopy. Raman spectroscopy is an information-rich spectroscopic method, like IR, capable of detecting specific groups and the environment-sensitive cell surface composition of biological macromolecules consisting of carbohydrates, proteins, DNA, RNA, and lipids. Thus, Raman and IR spectroscopy methods provide a molecular fingerprint that is especially suited for biological macromolecules in a label-free, rapid, and non-destructive manner [120].

1.10. Cellular Nanomechanics as a Biomarker for Cancer Progression at Metastases

With the advent of new technologies in the realm of nanotechnology, there has been an increasing interest in investigating the mechanical properties of individual cells to delineate disease mechanisms [121, 122]. Increasing evidence supports that altered mechanical properties highly influence cancer pathogenesis and progression at the cellular level. Several studies have reported that cancer cells are softer than their healthy counterparts [123-130], whereas a few studies showed otherwise [131, 132]. It has been shown that dysregulation in the actin cytoskeleton can lead to softening in cancer cells [133-136]. The epithelial monolayer, a multicellular system composed of firmly connected adjacent cells via adherens junctions, has been shown to give rise to most of the human cancers [137, 138]. The actin cytoskeleton of healthy epithelial cells is attached to adherens junctions to counteract internal and external mechanical stimuli and bestow mechanical stability [139, 140]. In contrast, cancerous epithelial cells most often exhibit disruption in stable cell-cell adhesion due to alterations in either adherens junctions or actin cytoskeleton [141-144].

Loss of cell-cell adhesion and gain of the invasive mesenchymal phenotype are hallmarks of epithelial-mesenchymal transition (EMT) of cancer cells, a process that promotes cancer cells to invade the basement membrane; a physical barrier made up of their adjacent cells [29]. Upregulation of several actin-cytoskeletal-associated proteins, including myosin light chain, α-actinin, integrins, and tropomyosin, has been associated with EMT while reduced expression of pseudopod-enriched proteins including Wiskott-Aldrich syndrome protein (WASP) family members, the actin-related proteins-2/3 (Arp2/3) complex, cortactin is associated with reversal of EMT or mesenchymal-epithelial transition (MET) [142, 145-150]. Moreover, altered expression of Arp2/3 complex and Wiskott-Aldrich syndrome protein family member 2 (WAVE2) have

been linked with poor prognosis of breast cancer, indicating a significant role of actin cytoskeleton dynamics in cancer progression [151]. To date, atomic force microscopy (AFM) has widely been used for measuring the mechanical properties of cancer cells [127, 128, 152-167]. However, AFM-based indentation methods have shown limitations in regards to the effects of indentation depth and substrate stiffening [168, 169]. These effects can lead to erroneous results during mechanical measurements of cells. In contrast, nanoindentation, a depth-sensing technique, has been proven to be more efficient in obtaining bulk cellular behavior using controlled strain experiments, which cannot be carried out with low load AFM force curves [170]. Nanoindentation techniques are very useful in probing mechanical properties at lower degrees of length scale with the help of the displacement-controlled nanoindentation module. Nanoindentation techniques have been extensively used to obtain nanoscale mechanical properties of cells [171-173], cell-biomaterials composite [173], soft and mineralized tissues [174-179], biological composites [180-182], and dental materials [183, 184]. Molecular modeling has also been used simultaneously to obtain the mechanics of cancer cells for developing robust predictive methodologies for disease progression [185].

1.11. Research Objectives

The specific objectives of the current research are as follows:

1. To develop a physiologically relevant tissue-engineered nanoclay scaffolds-based 3D *in vitro* model that mimics later stages of breast cancer pathogenesis to bone for anti-cancer therapeutic studies.
2. To study the interactions between breast cancer cells and bone microenvironment.
3. To understand the role of Wnt/β-catenin pathway in osteogenesis at metastases.
4. To evaluate the role of IL-6/STAT3 pathway in drug resistance at metastases.

5. To study the influence of cellular nanomechanics in disease progression at metastases.
6. To evaluate the feasibility of vibrational spectroscopy techniques such as Infrared (IR) and Raman spectroscopy as diagnostic tool for disease progression at metastases.

1.12. Organization of this dissertation

This dissertation is organized into different chapters as follows:

Chapter 1. It initially provides a brief background of bone, breast cancer bone metastasis, and a brief overview of current state in therapeutic-treatments for bone metastases. Then, it shortly describes the importance of 3D cell cultures in cancer research followed by examples of tissue engineered 3D cancer models, and a brief description of development of nanoclay-based scaffolds for bone tissue engineering. Afterward, it describes a brief background of Wnt/β-catenin, IL-6/STAT3 pathways and their involvements in skeletal complications and drug resistance, respectively. The next sections of introduction cover development of methods for non-invasive and rapid prediction of cancer progression at metastases using biophysical techniques such as nanoindentation and spectroscopy (IR & Raman).

Chapter 2. This chapter describes the development of a biologically relevant, 3D tissue-engineered *in vitro* model which mimics mesenchymal to epithelial transition of breast cancer cell at metastatic bone site.

Chapter 3. This chapter describes the critical role of Wnt/β-catenin pathway in regulating bone-related complications in breast cancer bone metastasis.

Chapter 4. This chapter describes cytokine-mediated drug resistance in 3D tissue-engineered model of breast cancer bone metastasis.

Chapter 5. This chapter describes the significant role of actin cytoskeleton in governing cellular nanomechanics leading up to breast cancer progression at metastatic bone site.

Chapter 6. This chapter describes the feasibility of Infrared spectroscopy in evaluating breast cancer progression at metastatic bone site.

Chapter 7. This chapter demonstrates Raman spectroscopy as a powerful imaging method for prostate cancer bone metastasis diagnosis.

Chapter 8. This chapter presents summary and major conclusions of the research presented in this dissertation.

Chapter 9. The future directions for the research in this field are discussed in this chapter.

1.13. References

[1] D.B. Burr, Targeted and nontargeted remodeling, Bone 30(1) (2002) 2-4.

[2] A.M. Parfitt, Targeted and nontargeted bone remodeling: relationship to basic multicellular unit origination and progression, Bone 30(1) (2002) 5-7.

[3] N.A. Sims, T.J. Martin, Coupling the activities of bone formation and resorption: a multitude of signals within the basic multicellular unit, BoneKEy reports 3 (2014).

[4] F. Lazner, M. Gowen, D. Pavasovic, I. Kola, Osteopetrosis and osteoporosis: two sides of the same coin, Human molecular genetics 8(10) (1999) 1839-1846.

[5] C. Sobacchi, A. Schulz, F.P. Coxon, A. Villa, M.H. Helfrich, Osteopetrosis: genetics, treatment and new insights into osteoclast function, Nature Reviews Endocrinology 9(9) (2013) 522-536.

[6] B.F. Boyce, D.E. Hughes, K.R. Wright, L. Xing, A. Dai, Recent advances in bone biology provide insight into the pathogenesis of bone diseases, Laboratory investigation; a journal of technical methods and pathology 79(2) (1999) 83-94.

[7] A. Klibanski, L. Adams-Campbell, T.L. Bassford, S.N. Blair, S.D. Boden, K. Dickersin, D.R. Gifford, L. Glasse, S.R. Goldring, K. Hruska, Osteoporosis prevention, diagnosis, and therapy, Journal of the American Medical Association 285(6) (2001) 785-795.

[8] P. Ducy, R. Zhang, V. Geoffroy, A.L. Ridall, G. Karsenty, Osf2/Cbfa1: a transcriptional activator of osteoblast differentiation, cell 89(5) (1997) 747-754.

[9] R. Florencio-Silva, G.R.d.S. Sasso, E. Sasso-Cerri, M.J. Simões, P.S. Cerri, Biology of bone tissue: structure, function, and factors that influence bone cells, BioMed research International 2015 (2015).

[10] T. Komori, H. Yagi, S. Nomura, A. Yamaguchi, K. Sasaki, K. Deguchi, Y. Shimizu, R.T. Bronson, Y.H. Gao, M. Inada, M. Sato, R. Okamoto, Y. Kitamura, S. Yoshiki, T. Kishimoto, Targeted disruption of Cbfa1 results in a complete lack of bone formation owing to maturational arrest of osteoblasts, Cell 89(5) (1997) 755-764.

[11] T. Komori, Runx2, a multifunctional transcription factor in skeletal development, Journal of cellular biochemistry 87(1) (2002) 1-8.

[12] K. Nakashima, X. Zhou, G. Kunkel, Z. Zhang, J.M. Deng, R.R. Behringer, B. De Crombrugghe, The novel zinc finger-containing transcription factor osterix is required for osteoblast differentiation and bone formation, Cell 108(1) (2002) 17-29.

[13] H. Hu, M.J. Hilton, X. Tu, K. Yu, D.M. Ornitz, F. Long, Sequential roles of Hedgehog and Wnt signaling in osteoblast development, Development 132(1) (2005) 49-60.

[14] D.A. Glass Ii, P. Bialek, J.D. Ahn, M. Starbuck, M.S. Patel, H. Clevers, M.M. Taketo, F. Long, A.P. McMahon, R.A. Lang, Canonical Wnt signaling in differentiated osteoblasts controls osteoclast differentiation, Developmental cell 8(5) (2005) 751-764.

[15] J.C. Crockett, D.J. Mellis, D.I. Scott, M.H. Helfrich, New knowledge on critical osteoclast formation and activation pathways from study of rare genetic diseases of osteoclasts: focus on the RANK/RANKL axis, Osteoporosis International 22(1) (2011) 1-20.

[16] X. Feng, J.M. McDonald, Disorders of bone remodeling, Annual Review of Pathology: Mechanisms of Disease 6 (2011) 121-145.

[17] Y.-C. Chen, D.M. Sosnoski, A.M. Mastro, Breast cancer metastasis to the bone: mechanisms of bone loss, Breast Cancer Res 12(6) (2010) 215.

[18] L.F. Bonewald, The amazing osteocyte, Journal of bone and mineral research 26(2) (2011) 229-238.

[19] A.M. Parfitt, Bone-forming cells in clinical conditions. in Bone. Volume 1: the osteoblast and osteocyte. B.K. Hall, (Ed.), Telford Press and CRC Press. Boca Raton, 1990, pp 351–429.

[20] S.C. Manolagas, Choreography from the tomb: an emerging role of dying osteocytes in the purposeful, and perhaps not so purposeful, targeting of bone remodeling, IBMS BoneKEy 3 (2006) 5.

[21] A.M. Noone, N. Howlader, M. Krapcho, D. Miller, A. Brest, M. Yu, J. Ruhl, Z. Tatalovich, A. Mariotto, D.R. Lewis, SEER cancer statistics review, 1975-2015, Bethesda, MD: National Cancer Institute (2018).

[22] R.L. Siegel, K.D. Miller, A. Jemal, Cancer statistics, 2020, CA: A Cancer Journal for Clinicians 70(1) (2020) 7-30.

[23] W. Kozlow, T.A. Guise, Breast cancer metastasis to bone: mechanisms of osteolysis and implications for therapy, Journal of mammary gland biology and neoplasia 10(2) (2005) 169-180.

[24] T.A. Guise, W.M. Kozlow, A. Heras-Herzig, S.S. Padalecki, J.J. Yin, J.M. Chirgwin, Molecular mechanisms of breast cancer metastases to bone, Clinical breast cancer 5 Suppl(2) (2005) S46-53.

[25] A. Marturano-Kruik, M.M. Nava, K. Yeager, A. Chramiec, L. Hao, S. Robinson, E. Guo, M.T. Raimondi, G. Vunjak-Novakovic, Human bone perivascular niche-on-a-chip for studying metastatic colonization, Proceedings of the National Academy of Sciences 115(6) (2018) 1256-1261.

[26] O.S. Nielsen, A.J. Munro, I.F. Tannock, Bone metastases: pathophysiology and management policy, Journal of Clinical Oncology 9(3) (1991) 509-524.

[27] R.D. Rubens, Bone metastases—the clinical problem, European Journal of Cancer 34(2) (1998) 210-213.

[28] P. Gassmann, J. Haier, The tumor cell–host organ interface in the early onset of metastatic organ colonisation, Clinical & experimental metastasis 25(2) (2008) 171-181.

[29] R. Kalluri, R.A. Weinberg, The basics of epithelial-mesenchymal transition, The Journal of clinical investigation 119(6) (2009) 1420-1428.

[30] D. Yao, C. Dai, S. Peng, Mechanism of the mesenchymal–epithelial transition and its relationship with metastatic tumor formation, Molecular cancer research 9(12) (2011) 1608-1620.

[31] Y.B. Kang, P.M. Siegel, W.P. Shu, M. Drobnjak, S.M. Kakonen, C. Cordon-Cardo, T.A. Guise, J. Massague, A multigenic program mediating breast cancer metastasis to bone, Cancer Cell 3(6) (2003) 537-549.

[32] S.P. Pathi, C. Kowalczewski, R. Tadipatri, C. Fischbach, A Novel 3-D Mineralized Tumor Model to Study Breast Cancer Bone Metastasis, Plos One 5(1) (2010) 10.

[33] S.P. Pathi, D.D.W. Lin, J.R. Dorvee, L.A. Estroff, C. Fischbach, Hydroxyapatite nanoparticle-containing scaffolds for the study of breast cancer bone metastasis, Biomaterials 32(22) (2011) 5112-5122.

[34] A. Leibbrandt, J.M. Penninger, RANK/RANKL: Regulators of Immune Responses and Bone Physiology, Annals of the New York Academy of Sciences 1143 (2008) 123-150.

[35] D.H. Jones, T. Nakashima, O.H. Sanchez, I. Kozieradzki, S.V. Komarova, I. Sarosi, S. Morony, E. Rubin, R. Sarao, C.V. Hojilla, Regulation of cancer cell migration and bone metastasis by RANKL, Nature 440(7084) (2006) 692-696.

[36] J.L. Sanders, N. Chattopadhyay, O. Kifor, T. Yamaguchi, R.R. Butters, E.M. Brown, Extracellular calcium-sensing receptor expression and its potential role in regulating parathyroid hormone-related peptide secretion in human breast cancer cell lines, Endocrinology 141(12) (2000) 4357-4364.

[37] M.J. Wolanczyk, K. Fakhrian, I.A. Adamietz, Radiotherapy, bisphosphonates and surgical stabilization of complete or impending pathologic fractures in patients with metastatic bone disease, Journal of Cancer 7(1) (2016) 121.

[38] M.T. Drake, B.L. Clarke, S. Khosla, Bisphosphonates: mechanism of action and role in clinical practice, Elsevier, pp. 1032-1045.

[39] D. Simos, C.L. Addison, I. Kuchuk, B. Hutton, S. Mazzarello, M. Clemons, Bone-targeted agents for the management of breast cancer patients with bone metastases, Journal of clinical medicine 2(3) (2013) 67-88.

[40] E. Prommer, Palliative oncology: denosumab, American Journal of Hospice and Palliative Medicine® 32(5) (2015) 568-572.

[41] E. Cukierman, R. Pankov, D.R. Stevens, K.M. Yamada, Taking cell-matrix adhesions to the third dimension, Science 294(5547) (2001) 1708-1712.

[42] E. Cukierman, R. Pankov, K.M. Yamada, Cell interactions with three-dimensional matrices, Current opinion in cell biology 14(5) (2002) 633-640.

[43] A. Nyga, U. Cheema, M. Loizidou, 3D tumour models: novel in vitro approaches to cancer studies, Journal of Cell Communication and Signaling 5(3) (2011) 239-248.

[44] K.L. Kretschmann, A.L. Welm, Mouse models of breast cancer metastasis to bone, Cancer and Metastasis Reviews 31(3-4) (2012) 579-583.

[45] J.T. Erler, V.M. Weaver, Three-dimensional context regulation of metastasis, Clinical & experimental metastasis 26(1) (2009) 35-49.

[46] K.R. Levental, H. Yu, L. Kass, J.N. Lakins, M. Egeblad, J.T. Erler, S.F.T. Fong, K. Csiszar, A. Giaccia, W. Weninger, Matrix crosslinking forces tumor progression by enhancing integrin signaling, Cell 139(5) (2009) 891-906.

[47] M.S. Samuel, V. Poltavets, S.M. Pitson, M. Kochetkova, The role of the extracellular matrix and its molecular and cellular regulators in cancer cell plasticity, Frontiers in oncology 8 (2018) 431.

[48] S. Kar, M.D.S. Molla, D.R. Katti, K.S. Katti, Tissue-engineered nanoclay-based 3D in vitro breast cancer model for studying breast cancer metastasis to bone, Journal of tissue engineering and regenerative medicine 13(2) (2019) 119-130.

[49] S. Talukdar, S.C. Kundu, Engineered 3D Silk-Based Metastasis Models: Interactions Between Human Breast Adenocarcinoma, Mesenchymal Stem Cells and Osteoblast-Like Cells, Advanced Functional Materials 23(42) (2013) 5249-5260.

[50] S. Talukdar, S.C. Kundu, A non-mulberry silk fibroin protein based 3D in vitro tumor model for evaluation of anticancer drug activity, Advanced Functional Materials 22(22) (2012) 4778-4788.

[51] S. Talukdar, M. Mandal, D.W. Hutmacher, P.J. Russell, C. Soekmadji, S.C. Kundu, Engineered silk fibroin protein 3D matrices for in vitro tumor model, Biomaterials 32(8) (2011) 2149-2159.

[52] R. Langer, J.P. Vacanti, C.A. Vacanti, A. Atala, L.E. Freed, G. Vunjak-Novakovic, Tissue engineering: biomedical applications, Tissue engineering 1(2) (1995) 151-161.

[53] R.S. Langer, J.P. Vacanti, Tissue engineering: the challenges ahead, Scientific American 280(4) (1999) 86-89.

[54] A.J. Salgado, O.P. Coutinho, R.L. Reis, Bone tissue engineering: state of the art and future trends, Macromolecular bioscience 4(8) (2004) 743-765.

[55] W. Zhu, M. Wang, Y.B. Fu, N.J. Castro, S.W. Fu, L.G. Zhang, Engineering a biomimetic three-dimensional nanostructured bone model for breast cancer bone metastasis study, Acta Biomaterialia 14 (2015) 164-174.

[56] A.M. Mastro, E.A. Vogler, A Three-Dimensional Osteogenic Tissue Model for the Study of Metastatic Tumor Cell Interactions with Bone, Cancer Research 69(10) (2009) 4097-4100.

[57] B. Subia, T. Dey, S. Sharma, S.C. Kundu, Target Specific Delivery of Anticancer Drug in Silk Fibroin Based 3D Distribution Model of Bone-Breast Cancer Cells, Acs Applied Materials & Interfaces 7(4) (2015) 2269-2279.

[58] W. Zhu, B. Holmes, R.I. Glazer, L.G. Zhang, 3D printed nanocomposite matrix for the study of breast cancer bone metastasis, Nanomedicine: Nanotechnology, Biology and Medicine 12(1) (2016) 69-79.

[59] A. Okada, M. Kawasumi, A. Usuki, Y. Kojima, T. Kurauchi, O. Kamigaito, Synthesis and properties of nylon-6/clay hybrids, pp. 45-50.

[60] E.P. Giannelis, Polymer layered silicate nanocomposites, Advanced materials 8(1) (1996) 29-35.

[61] S.T. Lim, C.H. Lee, H.J. Choi, M.S. Jhon, Solidlike transition of melt-intercalated biodegradable polymer/clay nanocomposites, Journal of Polymer Science Part B: Polymer Physics 41(17) (2003) 2052-2061.

[62] H.-M. Park, W.-K. Lee, C.-Y. Park, W.-J. Cho, C.-S. Ha, Environmentally friendly polymer hybrids Part I Mechanical, thermal, and barrier properties of thermoplastic starch/clay nanocomposites, Journal of Materials Science 38(5) (2003) 909-915.

[63] M. Pramanik, S.K. Srivastava, B.K. Samantaray, A.K. Bhowmick, Rubber–clay nanocomposite by solution blending, Journal of applied polymer science 87(14) (2003) 2216-2220.

[64] S. Wang, Y. Hu, Z. Wang, T. Yong, Z. Chen, W. Fan, Synthesis and characterization of polycarbonate/ABS/montmorillonite nanocomposites, Polymer Degradation and Stability 80(1) (2003) 157-161.

[65] D. Sikdar, S.M. Pradhan, D.R. Katti, K.S. Katti, B. Mohanty, Altered phase model for polymer clay nanocomposites, Langmuir 24(10) (2008) 5599-5607.

[66] D. Sikdar, K.S. Katti, D.R. Katti, Molecular interactions alter clay and polymer structure in polymer clay nanocomposites, Journal of Nanoscience and Nanotechnology 8(4) (2008) 1638-1657.

[67] S. Sinha Ray, K. Yamada, M. Okamoto, K. Ueda, Polylactide-layered silicate nanocomposite: a novel biodegradable material, Nano Letters 2(10) (2002) 1093-1096.

[68] J.W. Gilman, Flammability and thermal stability studies of polymer layered-silicate (clay) nanocomposites, Applied clay science 15(1-2) (1999) 31-49.

[69] J.W. Gilman, C.L. Jackson, A.B. Morgan, R. Harris, E. Manias, E.P. Giannelis, M. Wuthenow, D. Hilton, S.H. Phillips, Flammability properties of polymer− layered-silicate nanocomposites. Polypropylene and polystyrene nanocomposites, Chemistry of materials 12(7) (2000) 1866-1873.

[70] K. Yano, A. Usuki, A. Okada, T. Kurauchi, O. Kamigaito, Synthesis and properties of polyimide–clay hybrid, Journal of Polymer Science Part A: Polymer Chemistry 31(10) (1993) 2493-2498.

[71] P.B. Messersmith, E.P. Giannelis, Synthesis and barrier properties of poly (ε-caprolactone)-layered silicate nanocomposites, Journal of Polymer Science Part A: Polymer Chemistry 33(7) (1995) 1047-1057.

[72] R. Xu, E. Manias, A.J. Snyder, J. Runt, New biomedical poly (urethane urea)− layered silicate nanocomposites, Macromolecules 34(2) (2001) 337-339.

[73] S.S. Ray, M. Okamoto, Polymer/layered silicate nanocomposites: a review from preparation to processing, Progress in polymer science 28(11) (2003) 1539-1641.

[74] K. Müller, E. Bugnicourt, M. Latorre, M. Jorda, Y. Echegoyen Sanz, J.M. Lagaron, O. Miesbauer, A. Bianchin, S. Hankin, U. Bölz, Review on the processing and properties of polymer nanocomposites and nanocoatings and their applications in the packaging, automotive and solar energy fields, Nanomaterials 7(4) (2017) 74.

[75] D. Sikdar, D.R. Katti, K.S. Katti, B. Mohanty, Influence of backbone chain length and functional groups of organic modifiers on crystallinity and nanomechanical properties of intercalated clay-polycaprolactam nanocomposites, International Journal of Nanotechnology 6(5-6) (2009) 468-492.

[76] K.S. Katti, A.H. Ambre, N. Peterka, D.R. Katti, Use of unnatural amino acids for design of novel organomodified clays as components of nanocomposite biomaterials, Philosophical Transactions of the Royal Society of London A: Mathematical, Physical and Engineering Sciences 368(1917) (2010) 1963-1980.

[77] A. Ambre, K.S. Katti, D.R. Katti, In situ mineralized hydroxyapatite on amino acid modified nanoclays as novel bone biomaterials, Materials Science and Engineering: C 31(5) (2011) 1017-1029.

[78] A.H. Ambre, D.R. Katti, K.S. Katti, Nanoclays mediate stem cell differentiation and mineralized ECM formation on biopolymer scaffolds, Journal of Biomedical Materials Research Part A 101(9) (2013) 2644-2660.

[79] A.H. Ambre, D.R. Katti, K.S. Katti, Biomineralized hydroxyapatite nanoclay composite scaffolds with polycaprolactone for stem cell-based bone tissue engineering, Journal of Biomedical Materials Research Part A 103(6) (2015) 2077-2101.

[80] S. Kar, H. Jasuja, D.R. Katti, K.S. Katti, Wnt/β-catenin Signaling Pathway Regulates Osteogenesis for Breast Cancer Bone Metastasis: Experiments in an In Vitro Nanoclay Scaffold Cancer Testbed, ACS Biomaterials Science & Engineering (2019) https://doi.org/10.1021/acsbiomaterials.9b00923.

[81] K.S. Katti, A.H. Ambre, S. Payne, D.R. Katti, Vesicular delivery of crystalline calcium minerals to ECM in biomineralized nanoclay composites, Materials Research Express 2(4) (2015) 13.

[82] Y. Chen, B.A. Alman, Wnt pathway, an essential role in bone regeneration, Journal of cellular biochemistry 106(3) (2009) 353-362.

[83] Y. Chen, H.C. Whetstone, A.C. Lin, P. Nadesan, Q. Wei, R. Poon, B.A. Alman, Beta-catenin signaling plays a disparate role in different phases of fracture repair: implications for therapy to improve bone healing, PLoS medicine 4(7) (2007) e249.

[84] M.L. Johnson, M.A. Kamel, The Wnt signaling pathway and bone metabolism, Current opinion in rheumatology 19(4) (2007) 376-382.

[85] J. Behrens, Cross-regulation of the Wnt signalling pathway: a role of MAP kinases, J Cell Sci 113(6) (2000) 911-919.

[86] Q. Eastman, R. Grosschedl, Regulation of LEF-1/TCF transcription factors by Wnt and other signals, Current opinion in cell biology 11(2) (1999) 233-240.

[87] S. Ikeda, S. Kishida, H. Yamamoto, H. Murai, S. Koyama, A. Kikuchi, Axin, a negative regulator of the Wnt signaling pathway, forms a complex with GSK-3β and β-catenin and

promotes GSK-3β-dependent phosphorylation of β-catenin, The EMBO journal 17(5) (1998) 1371-1384.

[88] T.-C. He, A.B. Sparks, C. Rago, H. Hermeking, L. Zawel, L.T. Da Costa, P.J. Morin, B. Vogelstein, K.W. Kinzler, Identification of c-MYC as a target of the APC pathway, Science 281(5382) (1998) 1509-1512.

[89] T. Gaur, C.J. Lengner, H. Hovhannisyan, R.A. Bhat, P.V.N. Bodine, B.S. Komm, A. Javed, A.J. Van Wijnen, J.L. Stein, G.S. Stein, Canonical WNT signaling promotes osteogenesis by directly stimulating Runx2 gene expression, Journal of Biological Chemistry 280(39) (2005) 33132-33140.

[90] O. Tetsu, F. McCormick, β-Catenin regulates expression of cyclin D1 in colon carcinoma cells, Nature 398(6726) (1999) 422.

[91] T. Cai, D. Sun, Y. Duan, P. Wen, C. Dai, J. Yang, W. He, WNT/β-catenin signaling promotes VSMCs to osteogenic transdifferentiation and calcification through directly modulating Runx2 gene expression, Experimental cell research 345(2) (2016) 206-217.

[92] W. Liu, A. Konermann, T. Guo, A. Jäger, L. Zhang, Y. Jin, Canonical Wnt signaling differently modulates osteogenic differentiation of mesenchymal stem cells derived from bone marrow and from periodontal ligament under inflammatory conditions, Biochimica et Biophysica Acta (BBA)-General Subjects 1840(3) (2014) 1125-1134.

[93] W. Zhang, D. Huang, F. Zhao, W. Gao, L. Sun, X. Li, X. Chen, Synergistic effect of strontium and silicon in strontium-substituted sub-micron bioactive glass for enhanced osteogenesis, Materials Science and Engineering: C 89 (2018) 245-255.

[94] J. Guan, J. Zhang, S. Guo, H. Zhu, Z. Zhu, H. Li, Y. Wang, C. Zhang, J. Chang, Human urine-derived stem cells can be induced into osteogenic lineage by silicate bioceramics via activation of the Wnt/β-catenin signaling pathway, Biomaterials 55 (2015) 1-11.

[95] B. Mao, W. Wu, Y. Li, D. Hoppe, P. Stannek, A. Glinka, C. Niehrs, LDL-receptor-related protein 6 is a receptor for Dickkopf proteins, Nature 411(6835) (2001) 321.

[96] V.E. Ahn, M.L.-H. Chu, H.-J. Choi, D. Tran, A. Abo, W.I. Weis, Structural basis of Wnt signaling inhibition by Dickkopf binding to LRP5/6, Developmental cell 21(5) (2011) 862-873.

[97] W. Balemans, E. Piters, E. Cleiren, M. Ai, L. Van Wesenbeeck, M.L. Warman, W. Van Hul, The binding between sclerostin and LRP5 is altered by DKK1 and by high-bone mass LRP5 mutations, Calcified tissue international 82(6) (2008) 445-453.

[98] G. Bu, W. Lu, C.C. Liu, K. Selander, T. Yoneda, C. Hall, E.T. Keller, Y. Li, Breast cancer-derived Dickkopf1 inhibits osteoblast differentiation and osteoprotegerin expression: implication for breast cancer osteolytic bone metastases, International journal of cancer 123(5) (2008) 1034-1042.

[99] G.A. Clines, K.S. Mohammad, Y. Bao, O.W. Stephens, L.J. Suva, J.D. Shaughnessy Jr, J.W. Fox, J.M. Chirgwin, T.A. Guise, Dickkopf homolog 1 mediates endothelin-1-stimulated new bone formation, Molecular endocrinology 21(2) (2007) 486-498.

[100] J.-J. Qin, L. Yan, J. Zhang, W.-D. Zhang, STAT3 as a potential therapeutic target in triple negative breast cancer: a systematic review, Journal of Experimental & Clinical Cancer Research 38(1) (2019) 195.

[101] P. Aryappalli, S.S. Al-Qubaisi, S. Attoub, J.A. George, K. Arafat, K.B. Ramadi, Y.A. Mohamed, M.M. Al-Dhaheri, A. Al-Sbiei, M.J. Fernandez-Cabezudo, The IL-6/STAT3

signaling pathway is an early target of manuka honey-induced suppression of human breast cancer cells, Frontiers in oncology 7 (2017) 167.

[102] Y. Wang, X. Zong, S. Mitra, A.K. Mitra, D. Matei, K.P. Nephew, IL-6 mediates platinum-induced enrichment of ovarian cancer stem cells, JCI insight 3(23) (2018).

[103] Z.-Y. Wang, J.-A. Zhang, X.-J. Wu, Y.-F. Liang, Y.-B. Lu, Y.-C. Gao, Y.-C. Dai, S.-Y. Yu, Y. Jia, X.-X. Fu, IL-6 inhibition reduces STAT3 activation and enhances the antitumor effect of carboplatin, Mediators of inflammation 2016 (2016).

[104] S. Huang, Q. Liu, Q. Liao, Q. Wu, B. Sun, Z. Yang, X. Hu, M. Tan, L. Li, Interleukin-6/signal transducer and activator of transcription 3 promotes prostate cancer resistance to androgen deprivation therapy via regulating pituitary tumor transforming gene 1 expression, Cancer science 109(3) (2018) 678-687.

[105] S.O. Lee, W. Lou, M. Hou, F. De Miguel, L. Gerber, A.C. Gao, Interleukin-6 promotes androgen-independent growth in LNCaP human prostate cancer cells, Clinical Cancer Research 9(1) (2003) 370-376.

[106] I.-H. Ham, H.J. Oh, H. Jin, C.A. Bae, S.-M. Jeon, K.S. Choi, S.-Y. Son, S.-U. Han, R.A. Brekken, D. Lee, Targeting interleukin-6 as a strategy to overcome stroma-induced resistance to chemotherapy in gastric cancer, Molecular cancer 18(1) (2019) 68.

[107] J. Bromberg, T.C. Wang, Inflammation and cancer: IL-6 and STAT3 complete the link, Cancer cell 15(2) (2009) 79-80.

[108] C.-W. Ni, H.-J. Hsieh, Y.-J. Chao, D.L. Wang, Interleukin-6-induced JAK2/STAT3 signaling pathway in endothelial cells is suppressed by hemodynamic flow, American Journal of Physiology-Cell Physiology 287(3) (2004) C771-C780.

[109] G. Niu, K.L. Wright, Y. Ma, G.M. Wright, M. Huang, R. Irby, J. Briggs, J. Karras, W.D. Cress, D. Pardoll, Role of Stat3 in regulating p53 expression and function, Molecular and cellular biology 25(17) (2005) 7432-7440.

[110] H.-J. Choi, J.-S. Han, Overexpression of phospholipase D enhances Bcl-2 expression by activating STAT3 through independent activation of ERK and p38MAPK in HeLa cells, Biochimica et Biophysica Acta (BBA)-Molecular Cell Research 1823(6) (2012) 1082-1091.

[111] W.-H. Liu, M.-T. Chen, M.-L. Wang, Y.-Y. Lee, G.-Y. Chiou, C.-S. Chien, P.-I. Huang, Y.-W. Chen, M.-C. Huang, S.-H. Chiou, Cisplatin-selected resistance is associated with increased motility and stem-like properties via activation of STAT3/Snail axis in atypical teratoid/rhabdoid tumor cells, Oncotarget 6(3) (2015) 1750.

[112] J. Zhou, F. Chen, J. Xiao, C. Li, Y. Liu, Y. Ding, P. Wan, X. Wang, J. Huang, Z. Wang, Enhanced functional properties of corneal epithelial cells by coculture with embryonic stem cells via the integrin β1-FAK-PI3K/Akt pathway, The international journal of biochemistry & cell biology 43(8) (2011) 1168-1177.

[113] J. Prochazkova, V. Lichnovsky, D. Kylarova, B. Erdosova, P. Vranka, Involvement of p53 and Bcl-2 family proteins in regulating programmed cell death and proliferation in human embryogenesis, General physiology and biophysics 23(2) (2004) 209-229.

[114] Y.-L. Sun, A. Patel, P. Kumar, Z.-S. Chen, Role of ABC transporters in cancer chemotherapy, Chinese journal of cancer 31(2) (2012) 51.

[115] A.S.Y. Leong, Z. Zhuang, The changing role of pathology in breast cancer diagnosis and treatment, Pathobiology 78(2) (2011) 99-114.

[116] M. Smolina, E. Goormaghtigh, Infrared imaging of MDA-MB-231 breast cancer cell line phenotypes in 2D and 3D cultures, Analyst 140(7) (2015) 2336-2343.

[117] P.K. Tan, T.J. Downey, E.L. Spitznagel Jr, P. Xu, D. Fu, D.S. Dimitrov, R.A. Lempicki, B.M. Raaka, M.C. Cam, Evaluation of gene expression measurements from commercial microarray platforms, Nucleic acids research 31(19) (2003) 5676-5684.

[118] D.E. Ingber, Can cancer be reversed by engineering the tumor microenvironment?, Elsevier, pp. 356-364.

[119] C.V. Raman, K.S. Krishnan, A new type of secondary radiation, Nature 121(3048) (1928) 501-502.

[120] M. Diem, A. Mazur, K. Lenau, J. Schubert, B. Bird, M. Miljković, C. Krafft, J. Popp, Molecular pathology via IR and Raman spectral imaging, Journal of biophotonics 6(11-12) (2013) 855-886.

[121] M.M. Yallapu, K.S. Katti, D.R. Katti, S.R. Mishra, S. Khan, M. Jaggi, S.C. Chauhan, The roles of cellular nanomechanics in cancer, Medicinal research reviews 35(1) (2015) 198-223.

[122] D.R. Katti, K.S. Katti, S. Molla, S. Kar, Biomechanics of Cells as Potential Biomarkers for Diseases: A New Tool in Mechanobiology, in: R. Narayan (Ed.), Encyclopedia of Biomedical Engineering, Elsevier, Amsterdam, 2019, pp. 1-21.

[123] M.F. Coughlin, D.R. Bielenberg, G. Lenormand, M. Marinkovic, C.G. Waghorne, B.R. Zetter, J.J. Fredberg, Cytoskeletal stiffness, friction, and fluidity of cancer cell lines with different metastatic potential, Clinical & experimental metastasis 30(3) (2013) 237-250.

[124] V. Swaminathan, K. Mythreye, E.T. O'Brien, A. Berchuck, G.C. Blobe, R. Superfine, Mechanical Stiffness Grades Metastatic Potential in Patient Tumor Cells and in Cancer Cell Lines, Cancer Research 71(15) (2011) 5075-5080.

[125] J. Guck, S. Schinkinger, B. Lincoln, F. Wottawah, S. Ebert, M. Romeyke, D. Lenz, H.M. Erickson, R. Ananthakrishnan, D. Mitchell, Optical deformability as an inherent cell marker for testing malignant transformation and metastatic competence, Biophysical journal 88(5) (2005) 3689-3698.

[126] E.C. Faria, N. Ma, E. Gazi, P. Gardner, M. Brown, N.W. Clarke, R.D. Snooka, Measurement of elastic properties of prostate cancer cells using AFM, Analyst 133(11) (2008) 1498-1500.

[127] Q.S. Li, G.Y.H. Lee, C.N. Ong, C.T. Lim, AFM indentation study of breast cancer cells, Biochemical and Biophysical Research Communications 374(4) (2008) 609-613.

[128] M. Lekka, P. Laidler, D. Gil, J. Lekki, Z. Stachura, A.Z. Hrynkiewicz, Elasticity of normal and cancerous human bladder cells studied by scanning force microscopy, European Biophysics Journal with Biophysics Letters 28(4) (1999) 312-316.

[129] J. Hu, Y. Zhou, J.D. Obayemi, J. Du, W.O. Soboyejo, An investigation of the viscoelastic properties and the actin cytoskeletal structure of triple negative breast cancer cells, Journal of the mechanical behavior of biomedical materials 86 (2018) 1-13.

[130] S.E. Cross, Y.S. Jin, J. Tondre, R. Wong, J. Rao, J.K. Gimzewski, AFM-based analysis of human metastatic cancer cells, Nanotechnology 19(38) (2008).

[131] M.J. Rosenbluth, W.A. Lam, D.A. Fletcher, Force microscopy of nonadherent cells: A comparison of leukemia cell deformability, Biophysical Journal 90(8) (2006) 2994-3003.

[132] G. Zhang, M. Long, Z.-Z. Wu, W.-Q. Yu, Mechanical properties of hepatocellular carcinoma cells, World journal of gastroenterology 8(2) (2002) 243.

[133] J. Stricker, T. Falzone, M.L. Gardel, Mechanics of the F-actin cytoskeleton, Journal of biomechanics 43(1) (2010) 9-14.

[134] G. Bao, S. Suresh, Cell and molecular mechanics of biological materials, Nature materials 2(11) (2003) 715-725.

[135] D.A. Fletcher, R.D. Mullins, Cell mechanics and the cytoskeleton, Nature 463(7280) (2010) 485-492.

[136] S. Suresh, Biomechanics and biophysics of cancer cells, Acta biomaterialia 3(4) (2007) 413-438.

[137] B. De Craene, G. Berx, Regulatory networks defining EMT during cancer initiation and progression, Nature Reviews Cancer 13(2) (2013) 97-110.

[138] E. Dejana, Endothelial cell–cell junctions: happy together, Nature reviews Molecular cell biology 5(4) (2004) 261-270.

[139] H.T. Morris, L.M. Machesky, Actin cytoskeletal control during epithelial to mesenchymal transition: focus on the pancreas and intestinal tract, British journal of cancer 112(4) (2015) 613-620.

[140] R.W. Style, R. Boltyanskiy, G.K. German, C. Hyland, C.W. MacMinn, A.F. Mertz, L.A. Wilen, Y. Xu, E.R. Dufresne, Traction force microscopy in physics and biology, Soft matter 10(23) (2014) 4047-4055.

[141] M.F. Olson, E. Sahai, The actin cytoskeleton in cancer cell motility, Clinical & experimental metastasis 26(4) (2009) 273.

[142] H. Yamaguchi, J. Condeelis, Regulation of the actin cytoskeleton in cancer cell migration and invasion, Biochimica et Biophysica Acta (BBA)-Molecular Cell Research 1773(5) (2007) 642-652.

[143] T. Okegawa, R.-C. Pong, Y. Li, J.-T. Hsieh, The role of cell adhesion molecule in cancer progression and its application in cancer therapy, Acta Biochimica Polonica 51(2) (2004) 445-457.

[144] U. Cavallaro, G. Christofori, Cell adhesion in tumor invasion and metastasis: loss of the glue is not enough, Biochimica et Biophysica Acta (BBA)-Reviews on Cancer 1552(1) (2001) 39-45.

[145] J. Haynes, J. Srivastava, N. Madson, T. Wittmann, D.L. Barber, Dynamic actin remodeling during epithelial–mesenchymal transition depends on increased moesin expression, Molecular biology of the cell 22(24) (2011) 4750-4764.

[146] J. Liu, G. Hu, D. Chen, A.Y. Gong, G.S. Soori, T.J. Dobleman, X.-M. Chen, Suppression of SCARA5 by Snail1 is essential for EMT-associated cell migration of A549 cells, Oncogenesis 2(9) (2013) e73-e73.

[147] J. Shankar, A. Messenberg, J. Chan, T.M. Underhill, L.J. Foster, I.R. Nabi, Pseudopodial actin dynamics control epithelial-mesenchymal transition in metastatic cancer cells, Cancer research 70(9) (2010) 3780-3790.

[148] J. Shankar, I.R. Nabi, Actin cytoskeleton regulation of epithelial mesenchymal transition in metastatic cancer cells, PloS one 10(3) (2015).

[149] C. Le Clainche, M.-F. Carlier, Regulation of actin assembly associated with protrusion and adhesion in cell migration, Physiological reviews 88(2) (2008) 489-513.

[150] S.K. Wu, G.A. Gomez, M. Michael, S. Verma, H.L. Cox, J.G. Lefevre, R.G. Parton, N.A. Hamilton, Z. Neufeld, A.S. Yap, Cortical F-actin stabilization generates apical–lateral patterns of junctional contractility that integrate cells into epithelia, Nature cell biology 16(2) (2014) 167-178.

[151] K. Iwaya, K. Norio, K. Mukai, Coexpression of Arp2 and WAVE2 predicts poor outcome in invasive breast carcinoma, Modern pathology 20(3) (2007) 339-343.

[152] A. Calzado-Martín, M. Encinar, J. Tamayo, M. Calleja, A. San Paulo, Effect of actin organization on the stiffness of living breast cancer cells revealed by peak-force modulation atomic force microscopy, ACS nano 10(3) (2016) 3365-3374.

[153] N. Schierbaum, J. Rheinlaender, T.E. Schäffer, Viscoelastic properties of normal and cancerous human breast cells are affected differently by contact to adjacent cells, Acta biomaterialia 55 (2017) 239-248.

[154] W.W. Xu, R. Mezencev, B. Kim, L.J. Wang, J. McDonald, T. Sulchek, Cell Stiffness Is a Biomarker of the Metastatic Potential of Ovarian Cancer Cells, Plos One 7(10) (2012).

[155] A.N. Ketene, E.M. Schmelz, P.C. Roberts, M. Agah, The effects of cancer progression on the viscoelasticity of ovarian cell cytoskeleton structures, Nanomedicine-Nanotechnology Biology and Medicine 8(1) (2012) 93-102.

[156] M. Nikkhah, J.S. Strobl, R. De Vita, M. Agah, The cytoskeletal organization of breast carcinoma and fibroblast cells inside three dimensional (3-D) isotropic silicon microstructures, Biomaterials 31(16) (2010) 4552-4561.

[157] J.S. Strobl, M. Nikkhah, M. Agah, Actions of the anti-cancer drug suberoylanilide hydroxamic acid (SAHA) on human breast cancer cytoarchitecture in silicon microstructures, Biomaterials 31(27) (2010) 7043-7050.

[158] M. Nikkhah, J.S. Strobl, E.M. Schmelz, M. Agah, Evaluation of the influence of growth medium composition on cell elasticity, Journal of Biomechanics 44(4) (2011) 762-766.

[159] N. Nguyen, Y. Shao, A. Wineman, J. Fu, A. Waas, Atomic force microscopy indentation and inverse analysis for non-linear viscoelastic identification of breast cancer cells, Mathematical biosciences 277 (2016) 77-88.

[160] Y. Nematbakhsh, K.T. Pang, C.T. Lim, Correlating the viscoelasticity of breast cancer cells with their malignancy, Convergent Science Physical Oncology 3(3) (2017) 034003.

[161] Y.M. Efremov, W.-H. Wang, S.D. Hardy, R.L. Geahlen, A. Raman, Measuring nanoscale viscoelastic parameters of cells directly from AFM force-displacement curves, Scientific reports 7(1) (2017) 1-14.

[162] Y.H. Chim, L.M. Mason, N. Rath, M.F. Olson, M. Tassieri, H. Yin, A one-step procedure to probe the viscoelastic properties of cells by Atomic Force Microscopy, Scientific reports 8(1) (2018) 1-12.

[163] M. Lekka, D. Gil, K. Pogoda, J. Dulińska-Litewka, R. Jach, J. Gostek, O. Klymenko, S. Prauzner-Bechcicki, Z. Stachura, J. Wiltowska-Zuber, Cancer cell detection in tissue sections using AFM, Archives of biochemistry and biophysics 518(2) (2012) 151-156.

[164] G. Coceano, M.S. Yousafzai, W. Ma, F. Ndoye, L. Venturelli, I. Hussain, S. Bonin, J. Niemela, G. Scoles, D. Cojoc, E. Ferrari, Investigation into local cell mechanics by atomic force microscopy mapping and optical tweezer vertical indentation, Nanotechnology 27(6) (2016).

[165] X. Guo, K. Bonin, K. Scarpinato, M. Guthold, The effect of neighboring cells on the stiffness of cancerous and non-cancerous human mammary epithelial cells, New Journal of Physics 16(10) (2014) 105002.

[166] J.R. Staunton, B.L. Doss, S. Lindsay, R. Ros, Correlating confocal microscopy and atomic force indentation reveals metastatic cancer cells stiffen during invasion into collagen I matrices, Scientific reports 6 (2016).

[167] S. Nawaz, P. Sánchez, K. Bodensiek, S. Li, M. Simons, I.A.T. Schaap, Cell visco-elasticity measured with AFM and optical trapping at sub-micrometer deformations, PloS one 7(9) (2012).

[168] D. Kirmizis, S. Logothetidis, Atomic force microscopy probing in the measurement of cell mechanics, International journal of nanomedicine 5 (2010) 137.

[169] K. Haase, A.E. Pelling, Investigating cell mechanics with atomic force microscopy, Journal of The Royal Society Interface 12(104) (2015) 20140970.

[170] J. Domke, S. Dannohl, W.J. Parak, O. Muller, W.K. Aicher, M. Radmacher, Substrate dependent differences in morphology and elasticity of living osteoblasts investigated by atomic force microscopy, Colloids and Surfaces B-Biointerfaces 19(4) (2000) 367-379.

[171] J. Arfsten, C. Bradtmöller, I. Kampen, A. Kwade, Compressive testing of single yeast cells in liquid environment using a nanoindentation system, Journal of Materials Research 23(12) (2008) 3153-3160.

[172] R. Khanna, K.S. Katti, D.R. Katti, Experiments in nanomechanical properties of live osteoblast cells and cell–biomaterial interface, Journal of Nanotechnology in Engineering and Medicine 2(4) (2011) 041005.

[173] R. Khanna, D.R. Katti, K.S. Katti, AFM and Nanoindentation Studies of Bone Nodules on Chitosan-Polygalacturonic Acid-Hydroxyapatite Nanocomposites, Cmes-Computer Modeling in Engineering & Sciences 87(6) (2012) 530-555.

[174] D.M. Ebenstein, L.A. Pruitt, Nanoindentation of soft hydrated materials for application to vascular tissues, Journal of Biomedical Materials Research Part A: An Official Journal of The Society for Biomaterials, The Japanese Society for Biomaterials, and The Australian Society for Biomaterials and the Korean Society for Biomaterials 69(2) (2004) 222-232.

[175] O. Franke, M. Göken, M.A. Meyers, K. Durst, A.M. Hodge, Dynamic nanoindentation of articular porcine cartilage, Materials science and engineering: C 31(4) (2011) 789-795.

[176] M.E. Roy, J.Y. Rho, T.Y. Tsui, N.D. Evans, G.M. Pharr, Mechanical and morphological variation of the human lumbar vertebral cortical and trabecular bone, Journal of biomedical materials research 44(2) (1999) 191-197.

[177] K.S. Katti, C. Gu, D.R. Katti, Anisotropic properties of human cortical bone with osteogenesis imperfecta, Biomechanics and modeling in mechanobiology 15(1) (2016) 155-167.

[178] C. Gu, D.R. Katti, K.S. Katti, Dynamic nanomechanical behaviour of healthy and OI human cortical bone, Bioinspired, Biomimetic and Nanobiomaterials 4(1) (2015) 15-25.

[179] C. Gu, D.R. Katti, K.S. Katti, Microstructural and photoacoustic infrared spectroscopic studies of human cortical bone with osteogenesis imperfecta, Jom 68(4) (2016) 1116-1127.

[180] K.S. Katti, B. Mohanty, D.R. Katti, Nanomechanical properties of nacre, Journal of Materials Research 21(5) (2006) 1237-1242.

[181] B. Mohanty, K.S. Katti, D.R. Katti, D. Verma, Dynamic nanomechanical response of nacre, Journal of materials research 21(8) (2006) 2045-2051.

[182] B. Mohanty, K.S. Katti, D.R. Katti, Experimental investigation of nanomechanics of the mineral-protein interface in nacre, Mechanics Research Communications 35(1-2) (2008) 17-23.

[183] G. Balooch, G.W. Marshall, S.J. Marshall, O.L. Warren, S.A.S. Asif, M. Balooch, Evaluation of a new modulus mapping technique to investigate microstructural features of human teeth, Journal of biomechanics 37(8) (2004) 1223-1232.

[184] J.H. Kinney, S.J. Marshall, G.W. Marshall, The mechanical properties of human dentin: a critical review and re-evaluation of the dental literature, Critical Reviews in Oral Biology & Medicine 14(1) (2003) 13-29.

[185] D.R. Katti, K.S. Katti, Cancer cell mechanics with altered cytoskeletal behavior and substrate effects: A 3D finite element modeling study, Journal of the mechanical behavior of biomedical materials 76 (2017) 125-134.

CHAPTER 2. TISSUE-ENGINEERED NANOCLAY-BASED 3D IN VITRO BREAST CANCER MODEL FOR STUDYING BREAST CANCER METASTASIS TO BONE[1]

This chapter describes the development of a biologically relevant, 3D tissue-engineered *in vitro* model which mimics mesenchymal to epithelial transition of breast cancer cell at metastatic bone site. The contents of this chapter have been published in S. Kar, MD S Molla, D.R. Katti, K.S. Katti; "Tissue-engineered nanoclay-based 3D *in vitro* breast cancer model for studying breast cancer metastasis to bone", Journal of Tissue Engineering and Regenerative Medicine 13 (2) (2019) 119-130.

2.1. Introduction

Breast cancer (BrCa) is the most common form of cancer worldwide and based on current incident rates, 12.4% of women born in the United States today may develop breast cancer at some time during their lives [1]. In 2018, an estimated 266,120 cases of breast cancer will be diagnosed including 263,57o women and 2550 men. Furthermore, an estimated 41400 deaths are expected due to breast cancer in 2018 [2]. BrCa has the propensity to spread to other organs and bone is the most common site for breast cancer metastases [3]. Approximately 70% breast cancer patients eventually develop bone metastasis [4]. BrCa mediated bone metastasis results into either osteolytic lesions which typically induce a vicious cycle by inhibiting osteoblastic activity while stimulating osteoclastic activity or osteoblastic lesions which promote osteoblasts to rapidly produce an excess bone matrix, leading to mechanically unstable and dysfunctional bone matrix [5]. The interaction between cancer cells and the host microenvironment has been responsible for the establishment of metastatic lesions [4].

[1]This chapter was co-authored by S. Kar, MD. S Molla, D.R. Katti, and K.S. Katti. Sumanta Kar had the primary responsibility for preparing samples, conducting all tests, and drafting this chapter. Kalpana Katti and Dinesh Katti directed the research orientation and revised this chapter.

To study the bone metastasis, numerous 2D models and *in vivo* animal models have been developed. However, these models suffer from severe limitations, such as controllability, reproducibility, and flexibility of design [6]. In a 2D system, the cells lose their *in vivo* morphology, and this affects the cell-cell and cell-matrix interactions [7]. As a result, it fails to recapitulate the *in vivo* cancer microenvironment. *In vivo* animal models contain their own set of limitations, such as expensive, time-consuming and most often lead to uncertain pathogenesis of bone metastasis after injection of tumor cells [8], and often result in the death of animals before bone metastasis. To address the above-mentioned drawbacks of traditional cancer models along with the lack of availability of human bone metastasized breast cancer samples necessitates the need for reliable 3D *in vitro* models of metastasis. There have been a lot of studies on the development of 3D models for breast cancer bone metastases to date. For instance, Pathi et al. demonstrated the crucial role of the bone mineral hydroxyapatite in governing breast cancer bone metastasis [9]. Further, MSCs modified bone model was developed to recapitulate metastatic characteristics of various breast cancer cells has been developed [10]. The role of hydroxyapatite (HAP) nanoparticles in regulating breast cancer bone metastasis have been studied using degradable scaffolds [11] while 3D silk fibroin-based scaffolds have been used to evaluate direct and indirect interactions between tumor cells and osteoblasts [12]. Mastro et al. showed interactions of cancer cells with bone tissue in real time with the help of a bioreactor [13]. Also, Holen et al. reported the use of the 3D model to evaluate tumor cell-bone cell interactions [14]. In a recent study, polyurethane foam scaffolds models have also been used to create 3D models for breast cancer bone metastasis [15]. However, none of these studies have been able to shed on light on the mechanism that governs later stage of breast cancer pathogenesis in bone. Therefore, the primary goal of this study is to develop a 3D *in vitro* model

which mimics later stage of cancer pathogenesis in bone using nanoclay based scaffolds, developed in our previous study for bone tissue engineering [16]. Our group has previously investigated nanoclays for preparation of bone tissue engineering scaffolds [16-18]. These studies are based on a simulation-based design methodology for design of polymer clay nanocomposites [19-22].

There have also been a few studies on the use of commercially available nanoclays in preparation of bone tissue engineering scaffolds [23-25]. Our previous studies showed osteogenic differentiation of human bone marrow mesenchymal stem cells (MSCs), and MSCs mediated mineralization through the biomimetic process of vesicular delivery on nanoclay based scaffolds without the use of osteogenic supplements [16, 26]. We have previously shown early colonization stage of prostate cancer bone metastasis using the sequential culture of MSCs with prostate cancer cells on nanoclay based scaffolds [27-29].

In this study, we hypothesized, that sequential culture of MSCs with BrCa cells on our bone mimetic porous scaffolds recapitulate native microenvironment for BrCa metastasis. To corroborate this hypothesis, we sequential cultured MSCs with two BrCa cell lines MCF-7 and MDA-MB-231 and evaluated cellular growth, osteogenesis, morphology, migration, MMP-9 activity, gene, and protein expressions. The collective observations from this study suggest a successful development of a biologically relevant, 3D tissue-engineered *in vitro* breast cancer model for bone metastasis using nanoclay based scaffolds.

2.2. Materials and Methods

2.2.1. Preparation of Polycaprolactone (PCL)/*in situ* HAPclay 3D Scaffolds and 2D Films

We started off with modifying Na-MMT (Clay Minerals Respiratory at the University of Missouri, Columbia) with 5-aminovaleric acid (Sigma-Aldrich) following the procedure described in prior studies to increase the d-spacing of Na-MMT clay [30]. Further, we biomineralized HAP on modified clay (*in situ* HAPclay) using the methodology illustrated in our previous study [31]. Briefly, we used a wet-precipitation method to prepare *in situ* HAPclay from Na_2HPO_4 and $CaCl_2$ (J.T. Baker). Finally, 3D PCL/*in situ* HAPclay scaffolds were prepared using freeze extraction method described in our previous study [32]Ambre, Katti, & Katti, 2015). In brief, polycaprolactone (PCL) (average Mn 80,000; Sigma Aldrich) was dissolved in 1, 4 dioxane (Sigma-Aldrich) and then 10 wt. % *in situ* HAPclay was added into it to prepare the solution for the scaffolds. The same solution was subjected to room temperature evaporation for the preparation of PCL/*in situ* HAPClay 2D films.

2.2.2. Cell Lines and Culture Media

Human bone marrow Mesenchymal stem cells (MSCs) were obtained from Lonza (PT-2501) and maintained in MSCGM Bulletkit medium (Lonza, PT-3001). Human breast cancer cell (HBCC) lines MDA-MB-231 (shortened as -MM 231) (ATCC HTB-26) (highly metastatic) and MCF-7 (ATCC HTB-22) (low metastatic) were purchased from American Type Culture Collection (ATCC) maintained in medium comprised of 90% Dulbecco's Modified Eagle medium DMEM-F-12(1:1) from Hyclone, 10% FBS (ATCC), and 1% Pen-Strep antibiotic solution (Gibco); and Eagle's Minimum Essential Medium (EMEM) (ATCC), 10% FBS (ATCC), 0.01 mg/ml human recombinant insulin (Invitrogen) and 1% Pen-Strep Solution

(Gibco), respectively. All cell cultures were maintained at 37 ºC and 5% CO_2 in a humidified incubator.

2.2.3. Cell Culture

PCL/*in situ* HAPclay scaffolds were cut into small pieces (with a diameter of 12 mm and thickness of 3 mm) and placed in 24-well plates. Before cell seeding, scaffolds were sterilized under UV light for 45 min, kept in 70% ethanol for 12 h, washed with PBS, and then stored in humidified incubator immersed in culture medium for 24 h until further use. For all the monocultures, 5 x 10^4 number of cells were seeded per scaffold with 500 µl of culture medium. For 2D cultures, an equal number of cells were seeded on PCL/*in situ* HAPclay films.

2.2.4. Sequential Culture (SC) with MSCs

A schematic describing the sequential culture system is shown in Figure 2.1A. Human bone marrow mesenchymal cells (MSCs) were seeded on scaffolds (5 x 10^4 number of MSCs in 500 µl culture medium). After 23 days, 5 x 10^4 HBCCs were seeded per scaffold on the top of the MSCs, and the culture was continued for different periods of time. For SC, 1:1 ratio of MSCs and HBCCs (MM 231 & MCF-7) media was used. The media was changed every 3 days, and for all the experiments 500 µl of the media was used per scaffold.

2.2.5. Cell Viability

Cell viability and proliferation was determined using WST-1 (Roche) as per the manufacturer's protocol. In brief, cell-seeded scaffolds were removed from the culture medium at predetermined time points, washed with PBS and placed in a new 24-well plate with a solution consisting of 450 µl DMEM-12 (1:1) and 50 µl WST-1 reagent per well and incubated for 4 h in a humidified incubator. Then scaffolds were removed from the 24-well plates and the intensity of

yellow color, which directly represents the quantity of live cells, was measured at 450 nm using a microplate spectrophotometer (Bio-Rad).

2.2.6. Alkaline Phosphate (ALP) Activity

ALP assay was performed for MSCs, MM 231 3D SC and MCF-7 3D SC. Samples were washed with PBS and placed in 24-well plates with 850 µl Triton X-100 (1% v/v solution) (Sigma-Aldrich, X-100) per well and two freeze-thaw cycles (-70 ºC to 37 ºC) were used to obtain cell lysates. 250 µl of cell lysates were added to 250 µl of p-nitrophenyl phosphate (Sigma Aldrich, N7653) in a new 24-well plate per well and then incubated for 1 h at room temperature. Subsequently, 70 µl of 3N NaOH was added to each well and absorbance was taken at 405 nm using a microplate spectrophotometer (Bio-Rad).

2.2.7. Cellular Morphology

Cell adhesion to scaffolds and cell-scaffold interaction was determined using JEOL JSM-6490LV scanning electron microscope (SEM). Samples were removed from the culture medium, washed with PBS, and fixed with 2.5% glutaraldehyde. Subsequently treated with ethanol series (10% v/v, 30% v/v, 50% v/v, 70% v/v, and 100% v/v) (5 mins each stage) to dehydrate and then dried using hexamethyldisilazane. Samples were then coated with gold and mounted on SEM stub to observe under scanning electron microscope (SEM).

2.2.8. Cellular Migration

Cancer cells were trypsinized from 25 cm^2 flasks, and $1.5x10^4$ cells were seeded into each Transwell insert (Corning) of 8.0 µm pore size in serum-containing media. The cells were allowed to migrate towards the serum-containing media in the lower chamber (control) or bone scaffold immersed in serum-containing media in the lower chamber as shown in Figure 2.5A. After 16 h, cells were fixed with 4% paraformaldehyde and permeabilized with 0.2% TritonX-

100 for 5 min. The nuclei of the cells were stained with 4', 6-diamidino-2-phenylindole (DAPI) for 5 min and 5X images were acquired using Zeiss Axio Observer Z1 LSM 700 and analyzed using ImagePro.

2.2.9. Quantification of MMP-9 Secretion

The amount of MMP-9 released by sequential, mono- and 2D cultures of MM 231, MCF-7, and MSCs in the conditioned medium at the predetermined time points was determined using MMP-9 ELISA assay according to the protocol provided by Boster Biological Technology Co. Briefly, the antibody specific for MMP-9 was pre-coated onto the wells of a microplate. The standards and samples were pipetted into the wells. After removal of any unbound substances, the biotin-conjugated antibody specific for MMP-9 was added to the wells. After washing avidin-conjugated peroxidase was added to the wells. Following a wash to remove any unbound avidin-enzyme reagent, tetramethylbenzidine solution was added to the wells, and the blue color was developed in proportion to the amount of the proteins. The absorbance was determined at 450 nm, and the concentration of released MMP-9 was determined using a standard curve.

2.2.10. RNA Extraction and Quantitative RT-PCR Analysis

Total RNA was extracted and quantified from cells cultured on PCL/*in situ* HAPclay 2D films and 3D scaffolds using Direct-zol RNA MiniPrep kit (Zymo Research) and Nanodrop ND 2000 (Nanodrop products, Wilmington DE, USA) spectrophotometer, respectively. Further, cDNA was reverse transcribed from 2 μg of RNA using random primers and M-MLV reverse transcriptase from Promega. SYBR Green Master Mix (Thermo Fisher Scientific) was used for template amplification with a primer for each of the transcripts by following manufacturer's protocol in a 7500 Fast Real-Time PCR system (Applied Biosystems). The thermal profile of the SYBR Green real-time PCR program consisted of 2 min at 50 °C, 10 min at 95 °C, 40 cycles of

15 s at 95 °C and 1 min at 60 °C, and a dissociation stage at the end of the run from 60 °C to 95 °C. The gene expressions of Glyceraldehyde 3-phosphate dehydrogenase (GAPDH), E-Cadherin (E-cad), vascular endothelial growth factor (VEGF), Receptor activator of nuclear factor kappa-B ligand (RANKL), fibroblast growth factor receptor 2 (FGFR2), Hypoxia-inducible factor 1 (HIF-1), Twist, Vimentin, and Endothelin-1 (ET-1) was studied in the 3D monocultures of BrCa cells (MCF-7 3D, MM 231 3D) at days 10, and 3D sequential cultures of MSCs with BrCa cells (MCF-7 3D SC, MM 231 3D SC) at days 33 (23+10). GAPDH served as the housekeeping gene while 2D cancer cultures (MM 231 and MCF-7) (at day 10) served as control. Target gene expressions were calculated as $2^{-\Delta\Delta Ct}$. The primer sequences used in this experiment are listed in Table 2.1.

2.2.11. Immunocytochemistry

MM 231 3D SC, MCF-7 3D SC and control 2D BrCa samples were fixed with 4% paraformaldehyde (PFA) for 30 min and permeabilized with 0.2% TritonX-100 in PBS for 5 min. For immunofluorescence, the fixed and permeabilized samples were blocked with 0.2% fish skin gelatin (FSG) for 45 min and incubated with a primary antibody overnight at 4 °C. Vimentin, VEGFA, E-cadherin, Cytokeratin 18, and Runx2 (all antibodies were obtained from Abcam) antibodies were diluted in a blocking buffer (0.2% FSG in PBS containing 0.02% Tween20). All the primary antibodies were used at a dilution of 1:150. Alexa Flour 488 or Alexa Flour 647 conjugated secondary antibodies corresponding to the origin of the primary antibody were added at a dilution of 1:250 and incubated for 45 min at 25 °C. The nuclei of the cells were stained with DAPI. Zeiss Axio Observer Z1 LSM 700 was used for inverted confocal microscopy, and Imaris software was used for image analysis.

2.2.12. Statistical Analysis

All data were expressed as mean ± standard deviation (SD). Statistical comparisons between two groups were done using Student's unpaired *t-test* while multiple comparisons were done using one-way/two-way ANOVA followed by *post hoc* Tukey test (GraphPad Prism v7.04). Differences at p values of less than 0.05 were considered statistically significant (*), p values less than 0.01 were considered statistically highly significant (**), and p values less than 0.001 were considered statistically very highly significant (***). All error bars were presented as SD.

Table 2.1. The primer sequence used for the quantitative reverse transcription-polymerase chain reaction experiment.

Gene	Forward primer	Reverse primer
GAPDH	5'-CATCTTCTTTTGCGTCGCCA-3'	5'-TTAAAAGCAGCCCTGGTGACC-3'
E-cadherin	5'-AAG TGA CCG ATGATGAT-3'	5'-CTC TGT CCA TCT CAG CG-3'
VEGF	5'-GAC AAG AAA ATC CCT GTGGGC-3'	5'-AAC GCG AGT CTG TGT TTT TGC-3'
RANKL	5'-CAACATATCGTTGGATCACAGCA-3'	5'GACAGACTCACTTTATGGGAACC-3'
HIF-1	5'CATAAAGTCTGCAACATGGAAGGT3'	5'ATTTGATGGGTGAGGAATGGGTT-3'
Endothelin-1	5'-AGAGTGTGTCTACTTCTGCCA-3'	5'-CTTCCAAGTCCATACGGAACAA-3'
Twist1	5'-GTCCGCAGTCTTACGAGGAG -3'	5'-CCAGCTTGAGGGTCTGAATC -3'
Vimentin	5'-GAGAACTTTGCCGTTGAAGC -3'	5'-TCCAGCAGCTTCCTGTAGGT -3'
FGFR2	5'-GAGAAGGAGATCACGGCTTC-3'	5'-AAGTCTGGCTTCTTGGTCGT-3'

2.3. Results

2.3.1. Growth of BrCa Cells, MSCs, and Sequential Culture

Initially, we compared cell growth and viability of 2D and 3D monoculture system at days 5, 10 and 15. The highest cell growth was observed at day 15 on the 2D monoculture as well as on 3D monoculture matrices for both BrCa cell lines. Nevertheless, the overall growth profile observed in 3D monoculture was higher than that achieved in the 2D [Figure 2.1(B-C)].

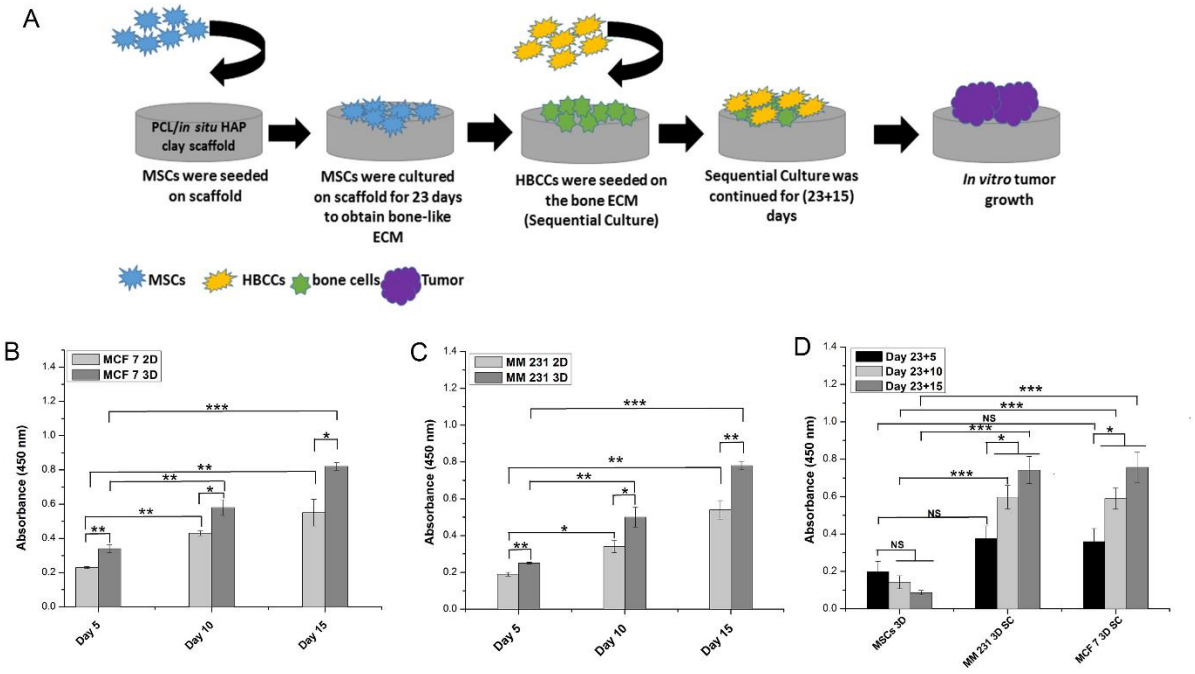

Figure 2.1. (A) Schematic showing the steps of sequential culture experiment. (B) Cell viability of 2D and 3D monoculture of MCF 7. (C) Cell viability of 2D and 3D monoculture of MM 231.(D) Cell viability of 3D sequential cultures (3D SC) and MSCs 3D. (n=3; two-way ANOVA followed by *post hoc* Tukey test, *$p < 0.05$,.**$p < 0.01$,.***$p < 0.001$).

For sequential culture, 3D scaffolds were first seeded with MSCs and the cells were allowed to differentiate, and regenerate bone tissue for 23 days[16]. Subsequently, BrCa cells were seeded on the bone mimetic scaffolds and cell viability assay was performed at days 5, 10 and 15 after seeding of cancer cells and results were compared with control MSCs. The cell viability of 3D sequential cultures of MSCs with BrCa cells (MCF -7 3D SC, MM 231 3D SC) significantly increased over time as compared to MSCs while MSCs showed insignificant differences in cell viability over time. The highest cell growth for sequential cultures of MSCs with BrCa cells was observed at day 38 (23+15) (Figure 2.1D).

2.3.2. Osteogenesis in MSCs, and Sequential Culture

ALP is a well-known osteogenic marker [33]. At first, we performed ALP assay on MSCs seeded constructs to see if MSCs were converting into bone cells. It has previously been shown that the ALP levels diminish when extracellular matrix (ECM) formation comes into effect [34]. In line with this observation, we saw a significant increase in ALP levels at day 8 compared to day 4. Nevertheless, ALP activity starts to decrease after day 16 (Figure 2.2A).

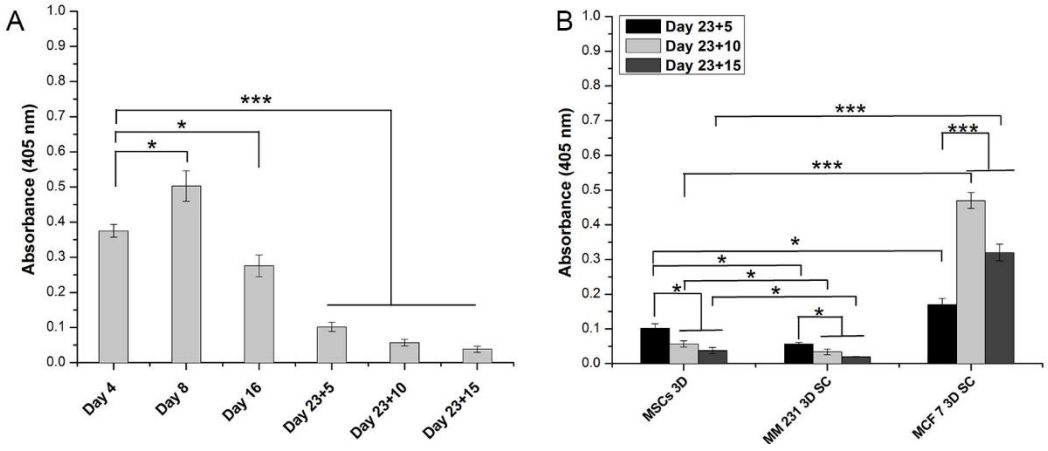

Figure 2.2. ALP activity of (A) MSCs alone (n=3; one-way ANOVA followed by *post hoc* Tukey test, *$p < 0.05$,.**$p < 0.01$,.***$p < 0.001$); (B) 3D sequential cultures (SC) of MSCs with breast cancer cells and MSCs 3D. (n=3; two-way ANOVA followed by *post hoc* Tukey test, *$p < 0.05$, **$p < 0.01$, ***$p < 0.001$).

We further performed immunocytochemistry to analyze protein levels of runt-related protein 2 (Runx2), a transcription factor involved in the initial stages of osteoblastic differentiation. Runx2 induces the differentiation of multipotent mesenchymal cells into immature osteoblasts, directing the formation of immature bone but the protein levels of Runx2 in osteoblasts reduces during bone development, and osteoblasts acquire mature phenotypes required for mature bone formation [35-37]. In accordance with these observations, we found an increase in the protein levels at day 4, day 8, and day 16 compared to day 1 but we observed a decrease in the protein levels after day 16 (Figure 2.3).

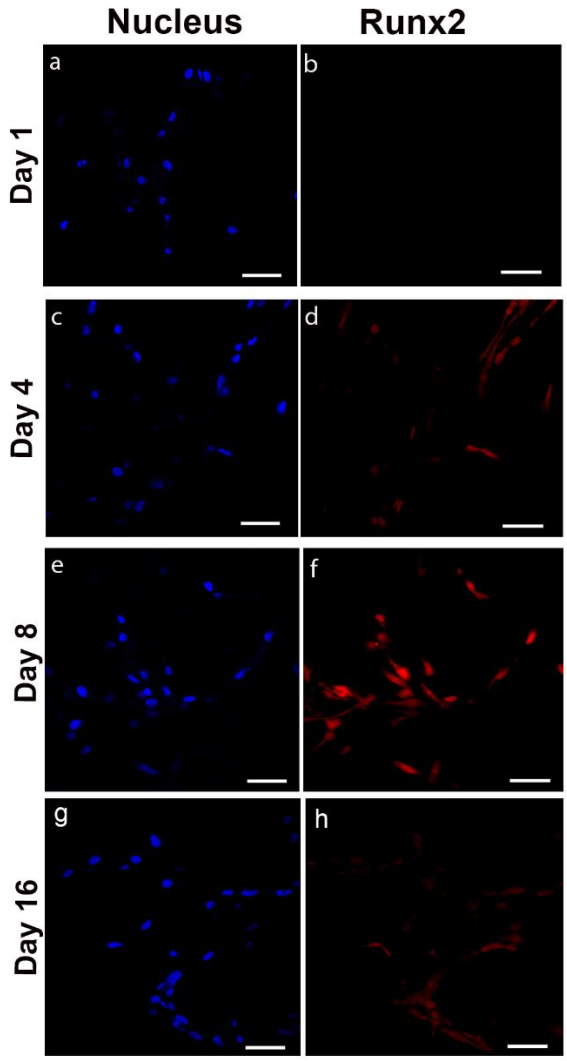

Figure 2.3. Representative immunofluorescence microscope images of MSCs cultured on PCL/*in situ* HAPclay scaffolds after immunostaining for nuclei and Runx2. We found an increase in the Runx2 protein levels at day 4, day 8, and day 16 compared to day 1 but we observed a decrease in the protein levels after day 16. Scale bars: 50 µm.

Next, we evaluated ALP activity of sequential culture of MSCs with BrCa cells to evaluate the effect of BrCa cells on the osteogenesis. ALP activity of MSCs 3D, MM 231 3D SC, MCF-7 3D SC is shown in Figure 2.2. We observed a significant reduction in ALP levels of MM 231 3D SC compared to MSCs 3D over time (Figure 2.2B). In contrast, the MCF-7 3D SC showed a substantial ALP production over time compared to MSCs 3D; day 33 (23+10) being the highest as compared to other days (Figure 2.2B).

2.3.3. Morphology of Sequential Cultured BrCa Cells

To investigate the evolution of the morphology of cells over time upon culturing on PCL/*in situ* HAPclay scaffolds, SEM imaging was performed. The sequential culture of MSCs with MCF-7 not only gave rise to well-defined 3D tumoroids with distinguishable cellular boundaries but also the size of tumoroids (several 100 μm) was observed to increase over time [Figure 2.4(A-C)]. Similarly, the sequential culture of MSCs with MM 231 showed good interaction with bone scaffolds and formed disorganized clusters of cells with poor cell-cell adhesion owing to its inherent property [Figure 2.4(D-F)].

2.3.4. *In vitro* Migration of BrCa Cells Towards Bone Scaffolds

To evaluate whether 3D bone scaffolds could influence the migratory properties of BrCa cells, we performed migration assay followed by DAPI staining of nuclei of cells (Figure 2.5B). We observed a significant increase in migration of MM 231 and MCF-7 cells in the presence of bone scaffolds as compared to controls. MM 231 cells showed overall highest migration (Figure 2.5C).

2.3.5. MMP-9 activity of BrCa Cells, MSCs, and Sequential Culture

Matrix metalloproteinases (MMPs) are a family of zinc-dependent endopeptidases that are known to degrade extracellular matrix components. Matrix metalloproteinase 9 (MMP-9), also known as gelatinase B, is an MMP that plays a crucial role in tumor progression by aiding angiogenesis and stromal remodeling [38]. As seen in [Figure 2.6(A-B)], the MMP-9 activity was observed to be higher in cancer cells cultured on 3D than 2D systems. MSCs 3D showed no secretion of MMP-9 at day 28 (23+5) while a little secretion of MMP-9 was observed at day 33 (23+10). On the other hand, MM 231 3D SC showed a significant increase in MMP-9 secretion

over time while MCF-7 3D SC showed a substantial reduction in MMP-9 secretion with time (Figure 2.6C).

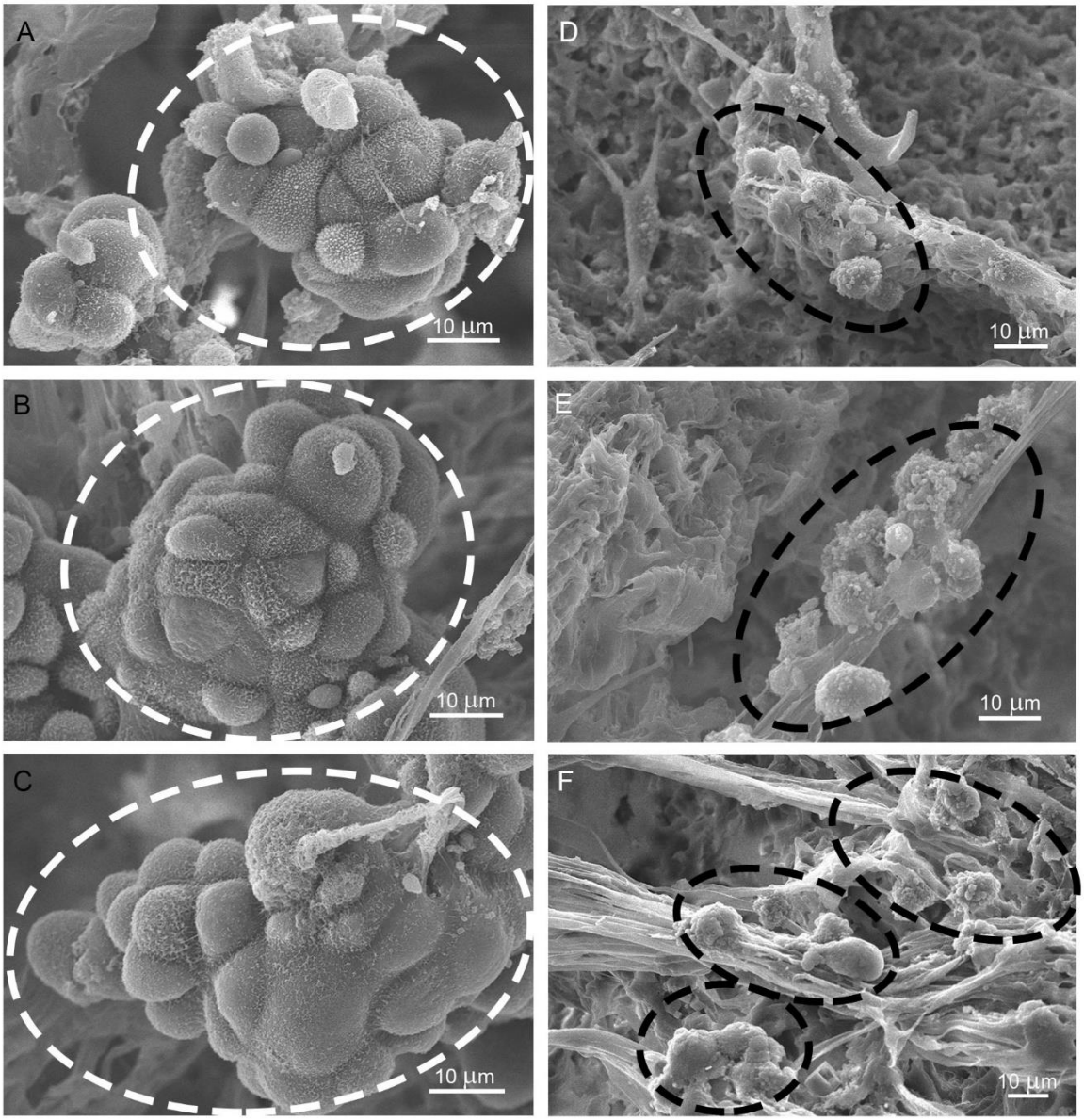

Figure 2.4. (A-C) SEM micrographs of sequential culture of MCF-7 cells at days (23+5), (23+10) and (23+15) (White circles/ellipses represent tumoroids); (D-E) sequential culture of MM 231 cells at days (23+5), (23+10) and (23+15). (Black circles/ellipses represent disorganized clusters). (X+Y days: MSCs were cultured on PCL/*in situ* HAPclay scaffolds for X days, then cancer cells were seeded and culture was continued for Y more days).

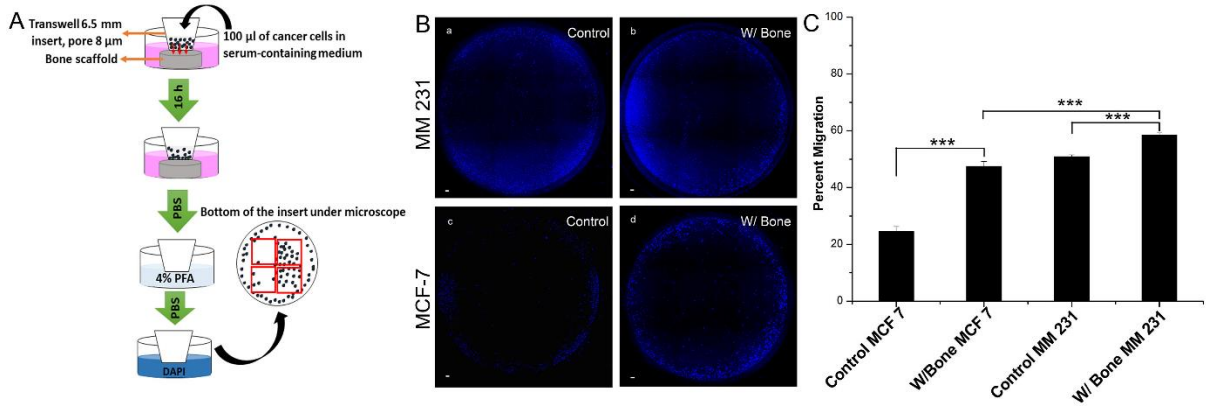

Figure 2.5. (A) Schematic showing flowchart of migration assay. (B) Represented images of migrated MM 231 cells (a) control, (b) with bone scaffold; migrated MCF-7 cells (c) control, (d) with bone scaffold. Nuclei are stained with DAPI. The scale bar represents 50 µm. (C) Percent migration of MCF 7 and MM 231 in presence and absence of bone scaffold (control). (n=3; one-way ANOVA followed by *post hoc* Tukey test, *p < 0.05, **p < 0.01, ***p < 0.001).

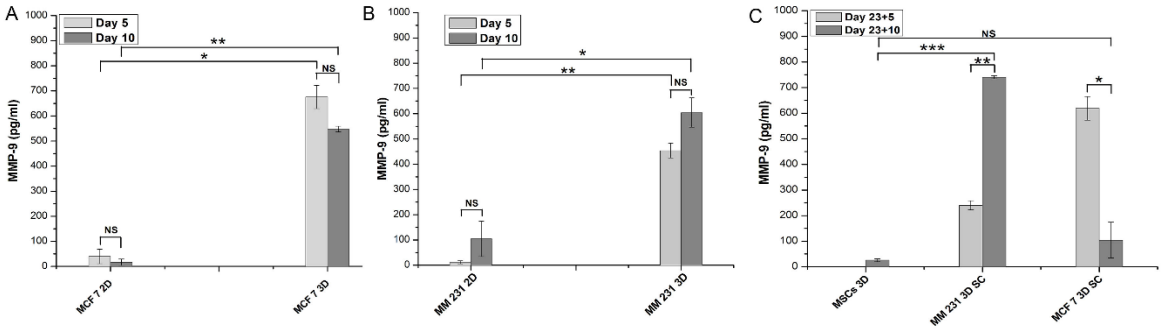

Figure 2.6. Secretion of MMP-9 in 2D, 3D monocultures of MCF 7 cells (A), MM 231 cells (B), and (C) 3D sequential cultures of cancer cells and MSCs. (n=3; two-way ANOVA followed by *post hoc* Tukey test, *p < 0.05, **p < 0.01, ***p < 0.001).

2.3.6. Invasiveness, Angiogenicity and Bone Homeostasis in Sequential Cultures

In most of the cases, metastasis at the primary site is initiated by an event known as epithelial-mesenchymal transition (EMT) while mesenchymal-epithelial transition (MET) plays a key role in the early phase of metastatic cancer cell colonization [39]. The loss of epithelial properties and the gain of mesenchymal features during EMT are believed to aid the invasion and migration of cells from the primary tumor to the site of metastasis [40].

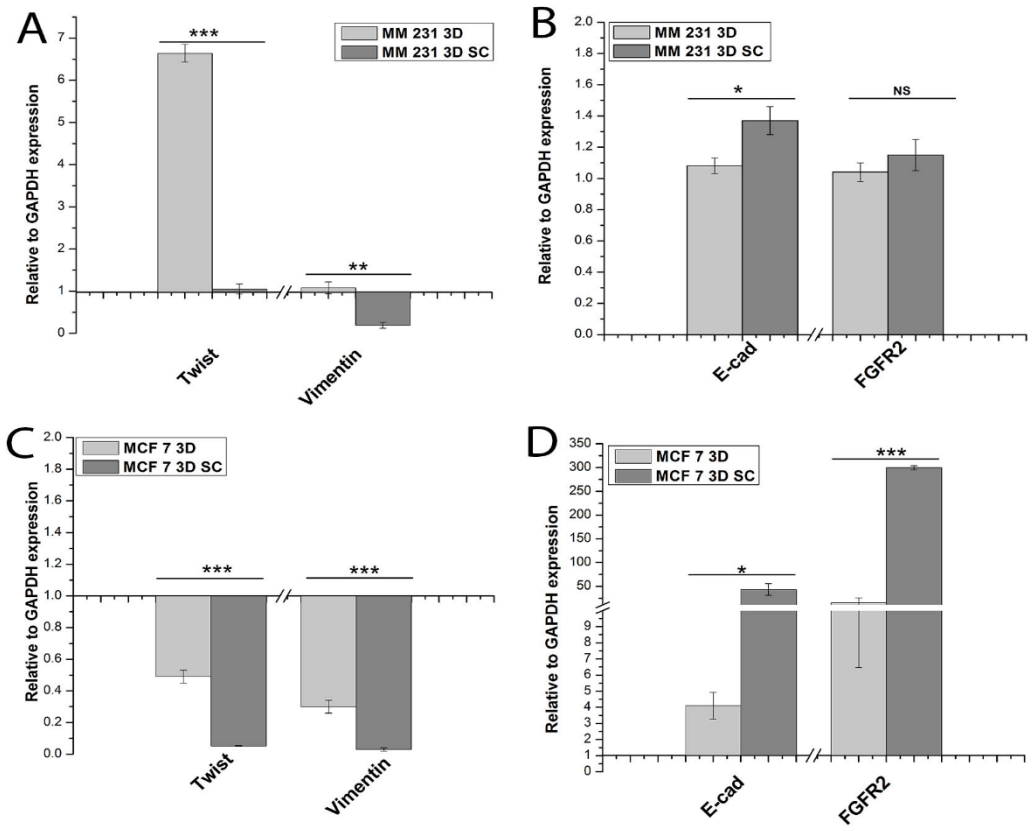

Figure 2.7. mRNA levels of Twist, Vimentin, E-cad, and FGFR2 in MM 231 3D & MM 231 3D SC (A-B) and (C-D) MCF-7 3D & MCF-7 3D SC. (n=3; Student's unpaired *t-test*, $*p < 0.05$, $**p < 0.01$, $***p < 0.001$).

To investigate if sequentially culturing MSCs with BrCa cells altered the invasiveness of BrCa cells, we analyzed the mRNA levels of known EMT markers such as Twist1 and Vimentin. Twist1 is a transcription factor that has been shown to induce EMT [41] while Vimentin [42] is an intermediary filament that is highly expressed in mesenchymal cells. The mRNA levels of Twist1 and Vimentin were significantly downregulated in MM 231 3D SC compared to MM 231 3D (Figure 2.7A). Similarly, Vimentin was not detected at the protein level in MM 231 cells grown on 3D SC while it was present in 2D cells (Figure 2.9B). MCF 7 cells do not express Twist1 and Vimentin. We observed further downregulation of these genes in both MCF-7 3D and MCF-7 3D SC (Figure 2.7C).

E-cadherin is a cell adhesion molecule that plays a key role in the formation of homotypic junctions across epithelial cells [43]. The loss of E-cadherin is associated with epithelial to mesenchymal transition of cancer cells [44]. Also, FGFR2 is highly expressed in the epithelial phenotype of cancer cells during colonization at the secondary metastatic site [45]. We observed a significant increase in mRNA levels of both E-cadherin and FGFR2 in MCF 7 3D SC as opposed to MCF-7 3D (Figure 2.7D).

It should be noted that MM 231 cells are known to express low levels of E-cadherin because of hypermethylation of the promoter [46]. Interestingly, we observed a significant increase in the mRNA levels of E-cadherin in MM 231 3D SC as compared to MM 231 3D (Figure 2.7B). Similarly, increased expression of E-cadherin was detected at the protein level in MM 231 cells grown on 3D SC compared to those on 2D (Figure 2.9A). However, we observed insignificant differences in the mRNA expression levels of FGFR2 between MM 231 3D SC and MM 231 3D (Figure 2.7B). We further analyzed protein level expression cytokeratins that are predominantly expressed in epithelial cells. [47]. We observed an increased expression of cytokeratin 18 at the protein level in the sequential culture of MSCs with MCF-7 cells compared to those on 2D (Figure 2.9D). Hence, the gene expression and immunostaining results showed upregulation of MET markers along with downregulation of EMT markers in MM 231 3D SC and demonstrated overexpression of MET markers in MCF 7 3D SC, thus indicating the formation of MET of breast cancer on 3D *in vitro* model. Vascular endothelial growth factor (VEGF) and hypoxia-inducible factor-1 (HIF-1) are well-known markers of angiogenesis. To evaluate whether culturing MSCs sequentially with BrCa cells increased the angiogenicity of BrCa cells, we quantified the mRNA levels of VEGF and HIF-1. MM 231 3D SC and MCF 7 3D

SC showed a significant increase in VEGF mRNA levels as compared to MM 231 3D and MCF-7 3D, respectively [Figure 2.8(A, C)].

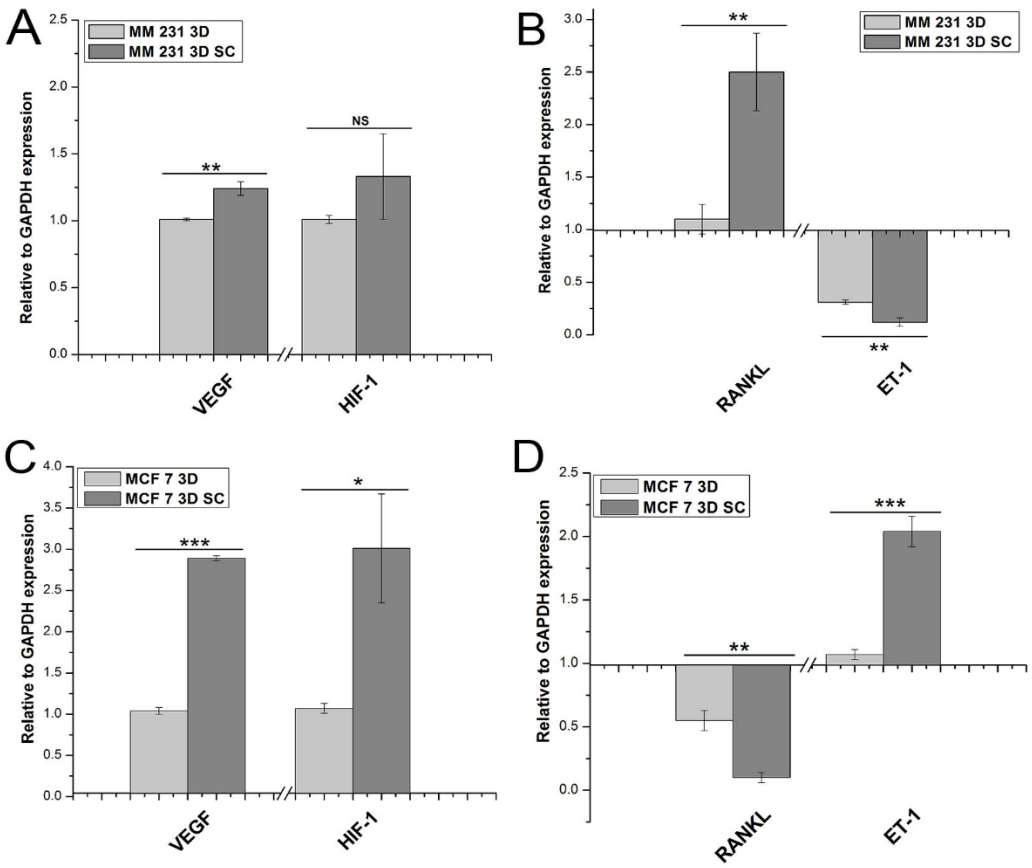

Figure 2.8. mRNA levels of VEGF, HIF-1, RANKL, and ET-1 in MM 231 3D & MM 231 3D SC (A-B) and (C-D) MCF-7 3D & MCF-7 3D SC. (n=3; Student's unpaired *t-test*, $*p < 0.05$, $**p < 0.01$, $***p < 0.001$).

Similarly, increased expressions of VEGF were detected at the protein levels in the sequential culture of both BrCa cells compared to 2D [Figure 2.9(C, E)]. MM 231 3D SC showed insignificant differences in HIF-1 mRNA levels while MCF-7 3D SC showed significant increase in HIF-1 levels compared to their respective controls [Figure 2.8(A, C)]. Previous studies have shown that receptor activator of nuclear factor kappa-B ligand (RANKL) and endothelin-1 (ET-1) mediate formation of osteoblastic and osteolytic metastatic lesions, respectively [48, 49].

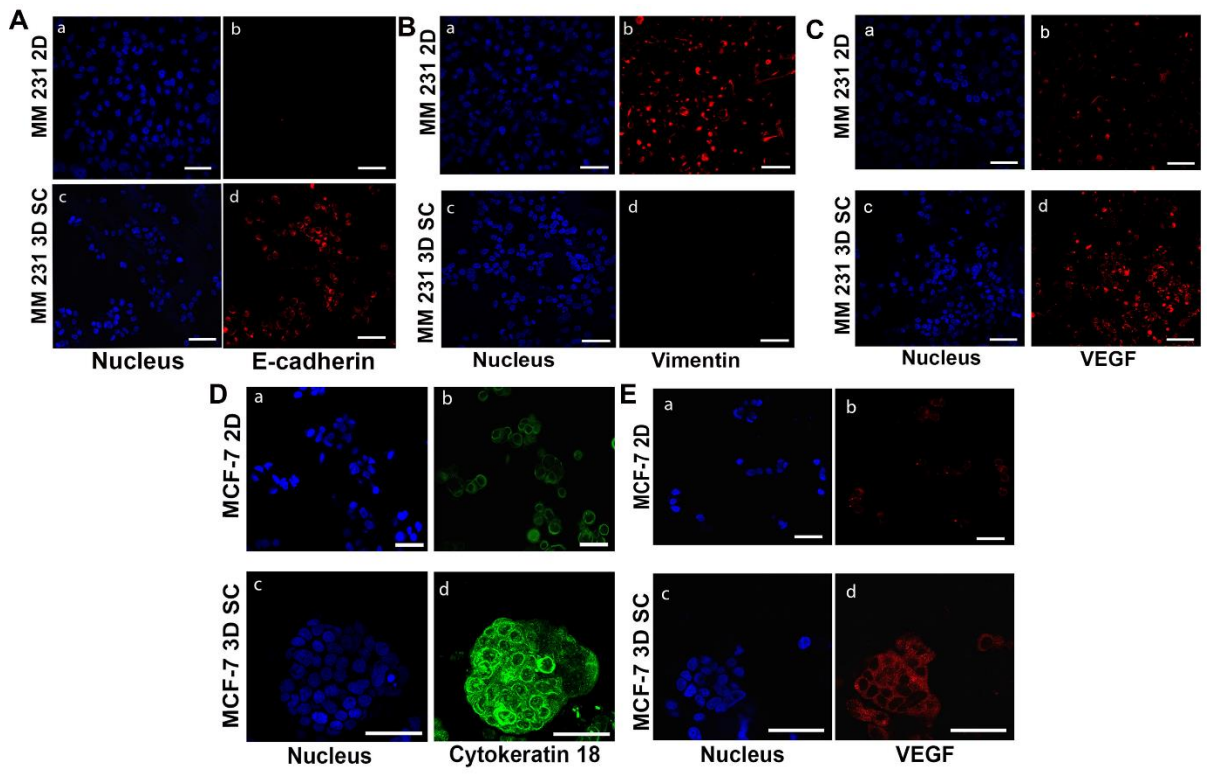

Figure 2.9. Representative immunofluorescence microscope images of MM 231 and MCF-7 cells cultured in 2D and 3D sequential culture after immunostaining for nuclei, E-cadherin (A), Vimentin (B), VEGF (C&E) and Cytokeratin 18 (D). Scale bars: 50 µm.

RT-PCR results showed that RANKL expression was significantly enhanced in the sequential culture of MSCs with MM 231 cells while sequential the culture of MSCs with MCF-7 cells demonstrated significantly enhanced expression of ET-1 compared to their respective controls [Figure 2.8(B, D)].

2.4. Discussion

In recent years, 3D cell culture system has received a great deal of attention owing to its unique ability to mimic the *in vivo* like microenvironment [50]. Existing 3D models of breast cancer bone metastasis have used either mineral or mineral reinforced polymer matrix to mimic tumor microenvironment. However, none of these models have not been able to recreate the later stage of cancer pathogenesis in bone. In contrast, our scaffolds allow MSCs cells to deposit bone

ECM which eventually helps in recapitulating the bone microenvironment. It has previously been shown that the presence of MSCs increases the growth of tumor cells *in vitro* and *in vivo* [51]. Furthermore, a recent study showed that MSCs could migrate to orthopedically implanted human breast tumors, leading to the promotion of BrCa cell bone metastasis *in vivo* [52]. A similar phenomenon was observed in our engineered bone model via sequential culturing of MSCs and BrCa cells on nanoclay scaffolds. Our 3D nanoclay scaffolds allowed cellular attachment, ECM secretion, and growth in 3D, which on prolonged culture gave rise to tumoroids.

The growth of cancer cells in the bone depends on the interaction between cancer cells and the host cells in the bone microenvironment. The complex bone microenvironment produces a gamut of cytokines and growth factors favorable for cancer cells. Their interaction with bone cells further induces the release of cytokines that promote cancer growth [53]. Furthermore, BrCa mediated bone metastasis involves cellular migration of cancer cells from the primary tumor site to bone. The presence of chemokines, growth factors make the bone microenvironment an ideal milieu for tumor-homing [5]. Our results show that deposited ECM with biochemical cues maximizes the migration of BrCa cells. It has previously been reported that chemokine receptors such as CXCR4, CXCR7 are highly expressed on the surface of BrCa cells, and their ligands are expressed at bone [4]. The stromal cell-derived factor-1 (SDF-1) [54] and osteopontin [55] have also been shown to be involved in the chemotactic migration of BrCa to bone.

We also demonstrated that the sequential culture of MSCs with BrCa cells upregulated the expression of MET related genes while downregulating EMT related genes. VEGF is a potent angiogenic stimulator that is highly expressed in many solid tumors resulting in poor

prognosis of the disease [56]. A hypoxic core region is developed when a solid tumor is formed inducing transcription of HIF-1 via stimulation of VEGF [57].Therefore, proangiogenic factors such as VEGF, and HIF-1 encourage the growth and colonization of BrCa cells on bone microenvironment to aid skeletal dissemination. The genes related to angiogenesis (VEGF and HIF-1) were also upregulated in the sequential culture of MSCs with BrCa cells. BrCa mediated bone metastasis results in either osteolytic or osteoblastic lesions. It has previously been documented that ET-1 and RANKL mediate formation of osteoblastic and osteolytic metastatic lesions, respectively [48, 49].

We observed upregulation of osteolytic metastasis marker RANKL in the sequential culture of MSCs with MM 231 cells while the sequential culture of MSCs with MCF-7 cells showed upregulation of osteoblastic metastasis marker ET-1. Earlier studies have demonstrated that an increase in MMP-9 expression is also related to osteolytic metastasis mediated by MM 231 cells [58]. A similar phenomenon was observed in our study when MSCs were sequential cultured with MM 231 cells on nanoclay scaffolds. In contrast, the sequential culture of MSCs with MCF-7 showed a significant reduction in MMP-9 secretion, and this could be due to the induction of osteoblastic metastasis. Previous studies have shown that MM 231-conditioned medium inhibits the differentiation of osteoblasts while MCF-7-conditioned medium promotes it [59-61]. In line with these observations, we found a significant decrease in the ALP levels of sequential culture of MSCs with MM 231 cells while sequential culture of MSCs with MCF-7 cells exhibited a significant increase in ALP levels over time. Hence, ALP assay results further strengthen our observation on MMP-9 assay and gene expression analysis. Together, these results indicate that the 3D *in vitro* model retains and recapitulates the behavior of BrCa cells based on their metastatic abilities.

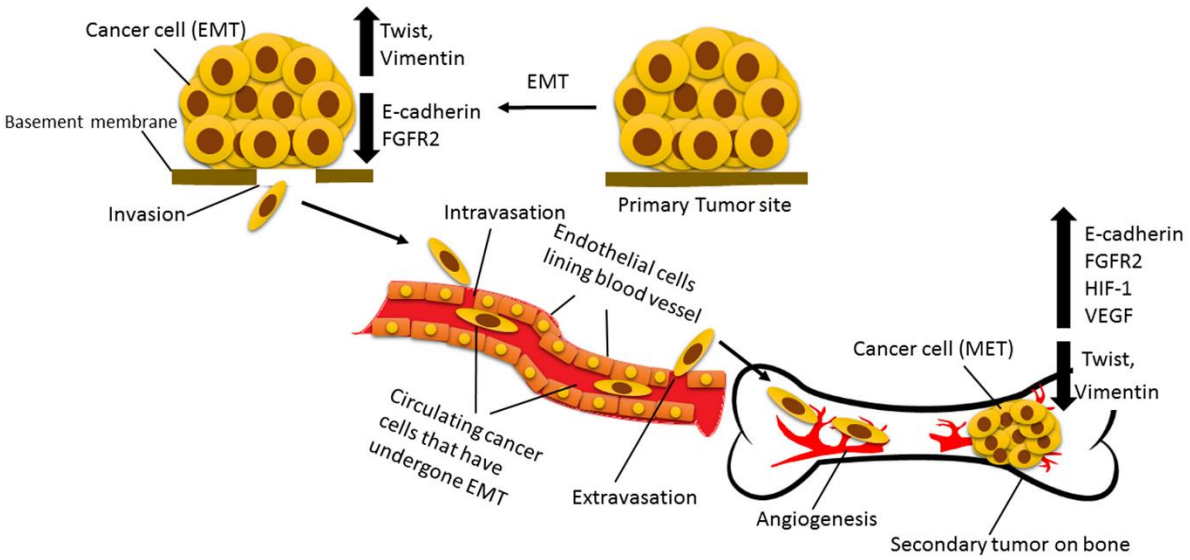

Figure 2.10. Schematic showing metastatic cascade involved in breast cancer progression and metastasis. Cancer cells at the primary tumor site undergo EMT to generate mesenchymal cells with enhanced motility and invasiveness. The loss of E-cadherin and FGFR2 expressions and gain of Twist1 and Vimentin expressions are hallmarks of epithelial-mesenchymal transition of cancer cells. Newly acquired invasiveness makes the cells invade basement membrane and enter the bloodstream to become circulating tumor cells. These circulating tumor cells migrate into a distant organ (bone), and in response to microenvironment, cells start to colonize to pave the way for secondary micrometastases via MET. When cancer cells undergo MET, they re-express E-cadherin while Twist1 and Vimentin expressions downregulate. HIF-1 and VEGF expressions are also increased due to initiation of blood vessel formation during tumorigenesis.

In summary, the novel 3D *in vitro* tumor model provides a unique microenvironment mimicking the physiological cell-cell and cell-matrix interactions, leading to more appropriate BrCa cell behavior in the later stage of cancer metastasis in bone. The unique and distinct behavior of various cells lines including the metastatic MM 231 and the low metastatic MCF-7 was observed at the bone metastasis site. The changes to migratory capabilities and invasiveness of MM 231 in comparison to tumor growth with MCF-7 was directly observed on the 3D model. The metastatic cascade responsible for breast cancer bone metastasis based on our results is given in Figure 2.10. Further experiments need to be carried out to verify the suitability of our model for studying initial stages in metastatic progression, i.e. cellular/tumoral dormancy. In the

future, we plan to increase the complexity of our system by incorporating immunological, hematopoietic, and vascular elements that are known to have key roles in regulating metastatic progression.

2.5. Conclusion

This study marked a successful development of a biologically relevant, 3D tissue-engineered breast cancer model for studying bone metastasis using nanoclay based scaffolds. Here we demonstrate that the *in vitro* model can retain and recapitulate metastatic ability of various BrCa cells, thus providing a promising tool for future BrCa metastasis study. The model was able to be mimic MET stage of cancer metastasis, thus providing a platform for analyzing the biochemical cues that underlie disease progression. Collectively, this 3D *in vitro* model demonstrates a potential to serve as a testbed for studying later stage of breast cancer pathogenesis in bone.

2.6. Acknowledgements

Authors acknowledge support from NDSU Grand Challenges grant for ‘CECT-Center for Engineered Cancer Test-Beds’. The scanning electron microscopy experiments conducted in this work are made possible through instrumentation obtained using MRI grant from National Science Foundation. Mr. Scott Payne’s assistance in use of electron microscopy is acknowledged. Dr. Tao Wang, manager of core biology facility at NDSU is acknowledged for help in use of the qRT PCR experiments. Support from ND EPSCoR for tissue engineering laboratory is also acknowledged. Dr. Pawel Borowicz from Advanced Imaging and Microscopy Laboratory is acknowledged for help in use of fluorescence imaging.

2.7. References

[1] N. Howlader, A. Noone, M. Krapcho, J. Garshell, D. Miller, S.F. Altekruse, C.L. Kosary, M. Yu, J. Ruhl, Z. Tatalovich, A. Mariotto, D.R. Lewis, H.S. Chen, E.J. Feuer, K.A. Cronin, SEER Cancer Statistics Review, 1975-2012, National Cancer Institute. Bethesda, MD, 2015.

[2] R.L. Siegel, K.D. Miller, A. Jemal, Cancer statistics, 2018, CA: a cancer journal for clinicians 68(1) (2018) 7-30.

[3] Y.-C. Chen, D.M. Sosnoski, A.M. Mastro, Breast cancer metastasis to the bone: mechanisms of bone loss, Breast Cancer Res 12(6) (2010) 215.

[4] Y.B. Kang, P.M. Siegel, W.P. Shu, M. Drobnjak, S.M. Kakonen, C. Cordon-Cardo, T.A. Guise, J. Massague, A multigenic program mediating breast cancer metastasis to bone, Cancer Cell 3(6) (2003) 537-549.

[5] A.M. Sitarski, M.R. Reagan, 3D Tissue Engineered *in vitro* Models of Cancer in Bone, ACS Biomaterials Science & Engineering 4(2) (2018) 324-336.

[6] N. Pouliot, H.B. Pearson, A. Burrows, Investigating metastasis using *in vitro* platforms, (2000).

[7] E. Cukierman, R. Pankov, D.R. Stevens, K.M. Yamada, Taking cell-matrix adhesions to the third dimension, Science 294(5547) (2001) 1708-1712.

[8] J.K. Simmons, B.E. Hildreth, W. Supsavhad, S.M. Elshafae, B.B. Hassan, W.P. Dirksen, R.E. Toribio, T.J. Rosol, Animal Models of Bone Metastasis, Veterinary Pathology 52(5) (2015) 827-841.

[9] S.P. Pathi, D.D.W. Lin, J.R. Dorvee, L.A. Estroff, C. Fischbach, Hydroxyapatite nanoparticle-containing scaffolds for the study of breast cancer bone metastasis, Biomaterials 32(22) (2011) 5112-5122.

[10] W. Zhu, M. Wang, Y.B. Fu, N.J. Castro, S.W. Fu, L.G. Zhang, Engineering a biomimetic three-dimensional nanostructured bone model for breast cancer bone metastasis study, Acta Biomaterialia 14 (2015) 164-174.

[11] D.D. Lin, S.P. Pathi, C. Fischbach-Teschl, L.A. Estroff, The effects of hydroxyapatite nanoparticles on breast cancer bone metastasis in 3-D scaffolds, Bone 48 (2011) S253.

[12] S. Talukdar, S.C. Kundu, Engineered 3D Silk-Based Metastasis Models: Interactions Between Human Breast Adenocarcinoma, Mesenchymal Stem Cells and Osteoblast-Like Cells, Advanced Functional Materials 23(42) (2013) 5249-5260.

[13] A.M. Mastro, E.A. Vogler, A Three-Dimensional Osteogenic Tissue Model for the Study of Metastatic Tumor Cell Interactions with Bone, Cancer Research 69(10) (2009) 4097-4100.

[14] I. Holen, F. Nutter, J.M. Wilkinson, C.A. Evans, P. Avgoustou, P.D. Ottewell, Human breast cancer bone metastasis *in vitro* and *in vivo*: a novel 3D model system for studies of tumour cell-bone cell interactions, Clinical & experimental metastasis 32(7) (2015) 689-702.

[15] V. Angeloni, N. Contessi, C. De Marco, S. Bertoldi, M.C. Tanzi, M.G. Daidone, S. Fare, Polyurethane foam scaffold as *in vitro* model for breast cancer bone metastasis, Acta biomaterialia 63 (2017) 306-316.

[16] A.H. Ambre, D.R. Katti, K.S. Katti, Biomineralized hydroxyapatite nanoclay composite scaffolds with polycaprolactone for stem cell-based bone tissue engineering, Journal of Biomedical Materials Research Part A 103(6) (2015) 2077-2101.

[17] K.S. Katti, D.R. Katti, R. Dash, Synthesis and characterization of a novel chitosan/montmorillonite/hydroxyapatite nanocomposite for bone tissue engineering, Biomedical Materials 3(3) (2008) 034122.

[18] A.H. Ambre, D.R. Katti, K.S. Katti, Nanoclays mediate stem cell differentiation and mineralized ECM formation on biopolymer scaffolds, Journal of Biomedical Materials Research Part A 101(9) (2013) 2644-2660.

[19] D. Sikdar, K.S. Katti, D.R. Katti, Molecular Interactions Alter Clay and Polymer Structure in Polymer Clay Nanocomposites, Journal of Nanoscience and Nanotechnology 8(4) (2008) 1638-1657.

[20] D. Sikdar, S.M. Pradhan, D.R. Katti, K.S. Katti, B. Mohanty, Altered phase model for polymer clay nanocomposites, Langmuir 24(10) (2008) 5599-5607.

[21] D. Sikdar, D.R. Katti, K.S. Katti, B. Mohanty, Influence of backbone chain length and functional groups of organic modifiers on crystallinity and nanomechanical properties of intercalated clay-polycaprolactam nanocomposites, International Journal of Nanotechnology 6(5-6) (2009) 468-492.

[22] D. Sikdar, K. Katti, D. Katti, Molecular interactions alter clay and polymer structure in polymer clay nanocomposites, Journal of Nanoscience and Nanotechnology 8(4) (2008) 1638-1657.

[23] A.J. Mieszawska, J.G. Llamas, C.A. Vaiana, M.P. Kadakia, R.R. Naik, D.L. Kaplan, Clay enriched silk biomaterials for bone formation, Acta Biomaterialia 7(8) (2011) 3036-3041.

[24] A.K. Gaharwar, S.M. Mihaila, A. Swami, A. Patel, S. Sant, R.L. Reis, A.P. Marques, M.E. Gomes, A. Khademhosseini, Bioactive Silicate Nanoplatelets for Osteogenic Differentiation of Human Mesenchymal Stem Cells, Advanced Materials 25(24) (2013) 3329-3336.

[25] S. Kar, T. Kaur, A. Thirugnanam, Microwave-assisted synthesis of porous chitosan-modified montmorillonite-hydroxyapatite composite scaffolds, International Journal of Biological Macromolecules 82 (2016) 628-636.

[26] K.S. Katti, A.H. Ambre, S. Payne, D.R. Katti, Vesicular delivery of crystalline calcium minerals to ECM in biomineralized nanoclay composites, Materials Research Express 2(4) (2015).

[27] S. Molla, D.R. Katti, K.S. Katti, *In vitro* design of mesenchymal to epithelial transition of prostate cancer metastasis using 3D nanoclay bone-mimetic scaffolds, Journal of tissue engineering and regenerative medicine 12(3) (2018) 727-737.

[28] K.S. Katti, M. Molla, F. Karandish, M.K. Haldar, S. Mallik, D.R. Katti, Sequential culture on biomimetic nanoclay scaffolds forms three-dimensional tumoroids, Journal of Biomedical Materials Research Part A 104(7) (2016) 1591-1602.

[29] K.S. Katti, D.R. Katti, M.S. Molla, S. Kar, Evaluation of Cancer Tumors in 3D Porous Bone Mimetic Scaffolds, Poromechanics VI, pp. 881-888.

[30] K.S. Katti, A.H. Ambre, N. Peterka, D.R. Katti, Use of unnatural amino acids for design of novel organomodified clays as components of nanocomposite biomaterials, Philosophical Transactions of the Royal Society of London A: Mathematical, Physical and Engineering Sciences 368(1917) (2010) 1963-1980.

[31] A. Ambre, K.S. Katti, D.R. Katti, In situ mineralized hydroxyapatite on amino acid modified nanoclays as novel bone biomaterials, Materials Science and Engineering: C 31(5) (2011) 1017-1029.

[32] A.H. Ambre, D.R. Katti, K.S. Katti, Biomineralized hydroxyapatite nanoclay composite scaffolds with polycaprolactone for stem cell-based bone tissue engineering, Journal of Biomedical Materials Research Part A 103(6) (2015) 2077-2101.

[33] Y. Gotoh, K. Hiraiwa, M. Nagayama, *In vitro* mineralization of osteoblastic cells derived from human bone, Bone and mineral 8(3) (1990) 239-250.

[34] R.A. Thibault, L. Scott Baggett, A.G. Mikos, F.K. Kasper, Osteogenic differentiation of mesenchymal stem cells on pregenerated extracellular matrix scaffolds in the absence of osteogenic cell culture supplements, Tissue Engineering Part A 16(2) (2009) 431-440.

[35] Z. Maruyama, C.A. Yoshida, T. Furuichi, N. Amizuka, M. Ito, R. Fukuyama, T. Miyazaki, H. Kitaura, K. Nakamura, T. Fujita, Runx2 determines bone maturity and turnover rate in postnatal bone development and is involved in bone loss in estrogen deficiency, Developmental dynamics: an official publication of the American Association of Anatomists 236(7) (2007) 1876-1890.

[36] T. Komori, Regulation of osteoblast differentiation by Runx2, Osteoimmunology, Springer2009, pp. 43-49.

[37] T. Komori, Runx2, a multifunctional transcription factor in skeletal development, Journal of cellular biochemistry 87(1) (2002) 1-8.

[38] A.R. Farina, A.R. Mackay, Gelatinase B/MMP-9 in tumour pathogenesis and progression, Cancers 6(1) (2014) 240-296.

[39] T. Brabletz, EMT and MET in metastasis: where are the cancer stem cells?, Cancer cell 22(6) (2012) 699-701.

[40] D.X. Nguyen, P.D. Bos, J. Massagué, Metastasis: from dissemination to organ-specific colonization, Nature Reviews Cancer 9(4) (2009) 274-284.

[41] J. Yang, S.A. Mani, J.L. Donaher, S. Ramaswamy, R.A. Itzykson, C. Come, P. Savagner, I. Gitelman, A. Richardson, R.A. Weinberg, Twist, a master regulator of morphogenesis, plays an essential role in tumor metastasis, cell 117(7) (2004) 927-939.

[42] A. Satelli, S. Li, Vimentin in cancer and its potential as a molecular target for cancer therapy, Cellular and molecular life sciences 68(18) (2011) 3033-3046.

[43] S. Hirano, A. Nose, K. Hatta, A. Kawakami, M. Takeichi, Calcium-dependent cell-cell adhesion molecules (cadherins): subclass specificities and possible involvement of actin bundles, The Journal of cell biology 105(6) (1987) 2501-2510.

[44] A. Wells, C. Yates, C.R. Shepard, E-cadherin as an indicator of mesenchymal to epithelial reverting transitions during the metastatic seeding of disseminated carcinomas, Clinical & experimental metastasis 25(6) (2008) 621-628.

[45] C.L. Chaffer, J.P. Brennan, J.L. Slavin, T. Blick, E.W. Thompson, E.D. Williams, Mesenchymal-to-epithelial transition facilitates bladder cancer metastasis: role of fibroblast growth factor receptor-2, Cancer research 66(23) (2006) 11271-11278.

[46] Y.L. Chao, C.R. Shepard, A. Wells, Breast carcinoma cells re-express E-cadherin during mesenchymal to epithelial reverting transition, Molecular cancer 9(1) (2010) 179.

[47] M.H. Sawaf, J.P. Ouhayoun, A.H. Shabana, N. Forest, Cytokeratins, markers of epithelial cell differentiation: expression in normal epithelia, Pathologie-biologie 40(6) (1992) 655-665.

[48] T.A. Guise, J.J. Yin, K.S. Mohammad, Role of endothelin-1 in osteoblastic bone metastases, Cancer 97(S3) (2003) 779-784.

[49] H.A. Azim, N.S. Kamal, H.A. Azim, Bone metastasis in breast cancer: the story of RANK-ligand, Journal of the Egyptian National Cancer Institute 24(3) (2012) 107-114.

[50] C. Fischbach, R. Chen, T. Matsumoto, T. Schmelzle, J.S. Brugge, P.J. Polverini, D.J. Mooney, Engineering tumors with 3D scaffolds, Nature methods 4(10) (2007) 855-860.

[51] K. Suzuki, R. Sun, M. Origuchi, M. Kanehira, T. Takahata, J. Itoh, A. Umezawa, H. Kijima, S. Fukuda, Y. Saijo, Mesenchymal stromal cells promote tumor growth through the enhancement of neovascularization, Molecular Medicine 17(7-8) (2011) 579.

[52] R.H. Goldstein, M.R. Reagan, K. Anderson, D.L. Kaplan, M. Rosenblatt, Human bone marrow–derived MSCs can home to orthotopic breast cancer tumors and promote bone metastasis, Cancer research 70(24) (2010) 10044-10050.

[53] D.M. Sosnoski, V. Krishnan, W.J. Kraemer, C. Dunn-Lewis, A.M. Mastro, Changes in cytokines of the bone microenvironment during breast cancer metastasis, International journal of breast cancer 2012 (2012).

[54] T.A. Guise, How metastases home to bone: The attraction of chemokines, BoneKEy-Osteovision (2002).

[55] G.M. Pio, Y. Xia, M.M. Piaseczny, J.E. Chu, A.L. Allan, Soluble bone-derived osteopontin promotes migration and stem-like behavior of breast cancer cells, PloS one 12(5) (2017) e0177640.

[56] S.E. Aldridge, T.W.J. Lennard, J.R. Williams, M.A. Birch, Vascular endothelial growth factor acts as an osteolytic factor in breast cancer metastases to bone, British journal of cancer 92(8) (2005) 1531-1537.

[57] Z.-j. Liu, G.L. Semenza, H.-f. Zhang, Hypoxia-inducible factor 1 and breast cancer metastasis, Journal of Zhejiang University Science B 16(1) (2015) 32-43.

[58] B. Liu, J. Cui, J. Sun, J. Li, X. Han, J. Guo, M. Yi, N. Amizuka, X. Xu, M. Li, Immunolocalization of MMP9 and MMP2 in osteolytic metastasis originating from MDA-MB-231 human breast cancer cells, Molecular medicine reports 14(2) (2016) 1099-1106.

[59] R.R. Mercer, C. Miyasaka, A.M. Mastro, Metastatic breast cancer cells suppress osteoblast adhesion and differentiation, Clinical & experimental metastasis 21(5) (2004) 427-435.

[60] G.L. Barnes, K.E. Hebert, M. Kamal, A. Javed, T.A. Einhorn, J.B. Lian, G.S. Stein, L.C. Gerstenfeld, Fidelity of Runx2 activity in breast cancer cells is required for the generation of metastases-associated osteolytic disease, Cancer research 64(13) (2004) 4506-4513.

[61] W.-W. Shen, W.-G. Chen, F.-Z. Liu, X. Hu, H.-K. Wang, Y. Zhang, T.-W. Chu, Breast cancer cells promote osteoblastic differentiation via Sema 3A signaling pathway *in vitro*, International journal of clinical and experimental pathology 8(2) (2015) 1584.

CHAPTER 3. WNT/β-CATENIN SIGNALING PATHWAY REGULATES OSTEOGENESIS FOR BREAST CANCER BONE METASTASIS: EXPERIMENTS IN AN IN VITRO NANOCLAY SCAFFOLD CANCER TESTEBED[2]

This chapter describes the critical role of Wnt/β-catenin pathway in regulating bone-related complications in breast cancer bone metastasis. The contents of this chapter have been published in S. Kar, H. Jasuja, D.R. Katti, K.S. Katti; "Wnt/β-catenin Signaling Pathway Regulates Osteogenesis for Breast Cancer Bone Metastasis: Experiments in an *In Vitro* Nanoclay Scaffold Cancer Testbed", ACS Biomaterials Science and Engineering (2019).

3.1. Introduction

Breast cancer shows a high affinity towards the bone, causing bone-related complications leading to poor clinical prognosis [1]. Approximately 80% of breast cancer patients die within five years after primary cancer has metastasized to the bones [2]. The survival rate of the patients with breast cancer metastasized to bone is highly influenced by the tumor stage at the time of diagnosis. The interactions between the bone microenvironment and breast cancer cells have been shown to contribute towards the development of bone metastases [3]. Breast cancer cells colonize within the bone marrow and impede bone remodeling processes either by activation of osteoclast differentiation or by the promotion of osteoblast activity [4, 5]. Unraveling the metastatic cascade at the cellular level would help us develop new and effective therapeutic approaches to detect bone metastases at early stages to improve patient survival rates. To better understand the metastatic cascade within the bone, *in vivo* mouse models and two-dimensional (2D) *in vitro* models have been developed. *In vivo* mouse models offer a natural three-

[2] This chapter was co-authored by S. Kar, H. Jasuja, D.R. Katti, and K.S. Katti. Sumanta Kar had the primary responsibility for preparing samples, conducting all tests, and drafting this chapter. Kalpana Katti and Dinesh Katti directed the research orientation and revised this chapter.

dimensional (3D) microenvironment [6], where human-derived cancer cells can be injected, or human bone fragments can be implanted into immune-deficient animals to create metastatic xenograft [7]; however, these animal models are expensive, do not possess an immune system, exhibit low efficiency in generating metastases [8]. In contrast to *in vivo* models, 2D *in vitro* models offer simplicity and low-cost platform for cancer research. There have been a few studies to recapitulate cancer-induced bone metastasis using 2D *in vitro* models. Breast cancer cells were co-cultured with osteoblast to evaluate the role osteoblasts in proliferation and migration of cancer cells [9, 10]; also, conditioned media has been extensively used to assess the paracrine effect of cancer cells secreted cytokines [11-13].

However, 2D *in vitro* models simplify the inherent 3D microenvironment of cancer cells due to lack of spatial cues. In contrast, 3D *in vitro* models represent a more physiologically relevant environment, better at recapitulating the *in vivo* interactions between cancer cells and bone microenvironment, leading to improved predictions [14]. There have been a lot of studies focusing on the development of 3D *in vitro* models for studying breast cancer bone metastases to date. Recent studies have shown a significant role of the hydroxyapatite (HAP) in regulating breast cancer bone metastasis using porous poly-lactide-co-glycolide (PLG) scaffolds [15]. In another study, 3D model was created by depositing bone-related proteins from differentiated mesenchymal stem cells on chitosan/HAP scaffolds to study metastatic abilities of breast cancer cells [16]. Talukdar & Kundu developed 3D silk fibroin-based scaffolds to study interactions between cancer cells and osteoblasts [17]. Although most studies are based on static experiments, some works on the interactions between 3D bone tissue and cancer cells in real time on a bioreactor system [18] are also reported. Other materials reported for development of scaffolds include polyurethane foams [19]. Although these studies have been useful in

elucidating some individual characteristics of the bone environment, further studies need to be carried out to develop a true bone-mimetic environment. To this end, we have developed a 3D *in vitro* model of breast cancer bone metastasis using nanoclay-based scaffolds along with osteogenically differentiated human mesenchymal stem cells (MSCs) and human breast cancer cells (MCF-7 and MDA-MB-231). We have investigated engineered nanoclays extensively [20-22] in the context of simulation based design of polymer clay nanocomposites and also reported their application for bone tissue engineering [23]. We have previously reported osteogenic induction of MSCs, and MSCs mediated mineralization via vesicular delivery on nanoclay based scaffolds/composites without the use of osteogenic supplements [23, 24]. Nanoclay based scaffolds are highly porous with pore sizes of 100-300 μm and possess a compressive modulus of 2.495 MPa[23] which is higher than the modulus (~1.1 kPa) of mesenchymal stem cells [25], however, lower than that of tissue culture polystyrene (TCPS) (~5 GPa) [26]. These reasons mentioned above make nanoclay based scaffold an ideal candidate for recapitulating bone-mimicking microenvironment.

Recently, we have reported late stage of prostate and breast cancer pathogenesis to bone using sequential culture of MSCs with human prostate and breast cancer cells on nanoclay based scaffolds, respectively [27-31]. We have also evaluated the feasibility of the developed 3D *in vitro* model of breast cancer bone metastasis for spectral biomarker discovery using FT-IR spectroscopy [32]. Commercially available nanoclays have also been used for preparation of bone tissue engineering scaffolds [33-36]. Overall, the testbed developed using the nanoclays enables many evaluations of cancer metastasis including changes in morphological, and critical pathways at metastasis to bone.

The Wnt/ β-catenin pathway plays a crucial role in the bone regenerative process including fracture healing [37, 38]. Wnt signaling is mediated by activation of low-density lipoprotein (LDL) receptor-related protein 5/6 (LRP-5/6) and Frizzled (FZD) by secreted Wnt ligands [39]. In the absence of Wnt signal, β-catenin is phosphorylated by casein kinase 1 (CK1) and the glycogen synthase kinase-3β (GSK-3β)/adenomatous polyposis coli (APC)/Axin complex, leading to ubiquitination and proteasome degradation of β-catenin [40-42]. In the presence of Wnt signal, the co-receptor LRP5/6 forms complex with Wnt-bound FZD which in turn promotes nuclear translocation of β-catenin and activates of transcription of target genes, such as c-myc, cyclin D1, and RUNX2 [43-45]. Although Wnt/ β-catenin pathway is well studied for osteogenesis [46-56], little is known about regulation of Wnt/ β-catenin pathway by breast cancer -derived factors such as dickkopf homolog 1 (DKK-1) and endothelin-1 (ET-1) during osteogenesis in breast cancer induced bone metastasis. DKK-1, an inhibitor of canonical Wnt signaling, operates by sequestering LRP-5/6 from FZD and thus blocks Wnt/ β-catenin pathway mediated osteogenesis [57-59]. Increased DKK1 expressions has been associated with osteolytic bone metastases mediated by MDA-MB-231[60]. Breast cancer cells have also been shown to control the secretion of DKK1 during bone metastasis via ET-1. ET-1 has been shown to downregulate secretion of DKK-1, causing increased osteoblastic activity and bone formation [61]. Researchers have shown that breast cell lines T47D, MCF-7, and ZR75-1 secreted ET-1 and caused osteoblastic metastases, while osteolytic breast cancer cell line MDA-MB-231 did not secrete ET-1 [62].

In the present study, we hypothesized that Wnt/β-catenin pathway might be responsible for osteogenesis in breast cancer bone metastasis. Here we aim at investigating the role of Wnt/β-

catenin pathway on osteogenesis in 3D utilizing the *in vitro* model of breast cancer bone metastasis.

3.2. Materials and Methods

3.2.1. Preparation of Polycaprolactone (PCL)/*in situ* HAPclay 3D Scaffolds

Preparation of PCL/*in situ* HAPclay scaffolds is described elsewhere [23]. In brief, PCL/ *in situ* HAPclay scaffolds were prepared by adding 10% *in situ* HAPclay to polycaprolactone (PCL), using freeze-extraction method. HAPclay was prepared by *in situ* biomineralization of hydroxyapatite (HAP) into intercalated nanoclay galleries resulted due to modification of Na-MMT clay (Clay Minerals Respiratory at the University of Missouri, Columbia) by 5-aminovaleric acid [63-65].

3.2.2. Cell Culture

Human MSCs (Lonza) were cultured in MSCGM™ Bulletkit™ medium (Lonza, PT-3001). Human breast cancer cell lines MCF-7 and MDA-MB 231 (shortened as MM 231) (ATCC) were cultured in Eagle's Minimum Essential Medium (EMEM), 10% FBS, 0.01 mg/ml human recombinant insulin and 1% P/S ; and 90% Dulbecco's Modified Eagle medium/Nutrient Mixture F-12 DMEM-F-12(1:1), 10% FBS, and 1% P/S, respectively. Prior to cell culture, PCL/*in situ* HAPclay scaffolds (12 mm diameter and thickness of 3 mm) were sterilized under UV light for 45 mins, immersed in 70% ethanol for 12 h, washed in phosphate buffered saline (PBS), and kept in humidified 5% CO_2 incubator at 37 ºC immersed in culture medium for 24 h. For the sequential culture, MSCs were seeded at a density of 5 x 10^4 cells per scaffold (1.47 x 10^5 cells/cm^3 of scaffold) and cultured for 23 days to obtain bone extracellular matrix (ECM) formation on scaffolds. Further, breast cancer cells MM 231/MCF-7 were seeded on the newly

formed bone ECM in the 3D scaffolds at a density of 5 x 10^4 cells per scaffold (1.47 x 10^5 cells/cm^3 of scaffold) and maintained in 1:1 MSCs and breast cancer cell medium [Figure 3.1].

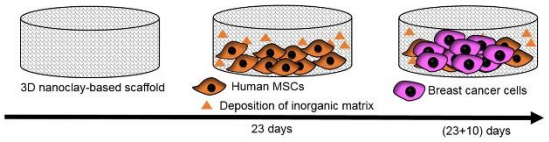

Figure 3.1. Schematic showing the steps of sequential culture experiment.

3.2.3. Cellular Morphology

Cell-seeded scaffolds were fixed with 2.5% glutaraldehyde, dehydrated in a graded ethanol series (10%, 30%, 50%, 70%, and 100%), and dried in hexamethyldisilazane. Then, the samples were gold sputter coated and observed in SEM (JEOL JSM-6490LV) to evaluate cell morphology.

3.2.4. Gene Expression Studies

RNA was isolated from cell-seeded scaffolds using Direct-zol RNA MiniPrep kit (Zymo Research). Then, cDNA was synthesized using 2 µg of RNA, random primers, and M-MLV reverse transcriptase (Promega) in thermal cycler (Applied Biosystems). Real-time polymerase chain reaction (PCR) experiment was performed using 7500 Fast Real-Time PCR system (Applied Biosystems). Forward primer, reverse primer, SYBR Green dye, and cDNA were added to make a final volume of 20 µl and run using a thermal profile with a holding stage (2 min at 50 °C, 10 min at 95 °C) and a cycling stage (40 cycles of 15 s at 95 °C, and 1 min at 60 °C). The mRNA expressions of alkaline phosphatase (ALP), Runt Related Transcription Factor 2 (RUNX2), Osteocalcin (OCN), Wnt5a, β-catenin, FZD4, AXIN2, and LRP5 were quantified and normalized to housekeeping gene glyceraldehyde-3-phosphate-dehydrogenase (GAPDH). Target

gene expressions were analyzed using comparative C_t method ($2^{-\Delta\Delta Ct}$). Table 3.1 lists the sequence of primers used.

Table 3.1. The sequence of primers used for the quantitative real-time PCR experiment.

Gene	Forward primer	Reverse primer
GAPDH	5'-CATCTTCTTTTGCGTCGCCA-3'	5'-TTAAAAGCAGCCCTGGTGACC-3'
ALP	5'-TCAACACCAACGTGGCTAAG -3'	5'-CACAATGCCCACAGATTTCC-3'
OCN	5'-GTG ACG AGT TGG CTG ACC-3'	5'-TGG AGA GGA GCA GAA CTG G-3'
Wnt-5a	5'-TCT CAG CCC AAG CAA CAA GG-3'	5'-GCC AGC ATC ACA TCA CAA CAC-3'
DKK-1	5'-CCA GAC CAT TGA CAA CTA CC-3'	5'-CAG GCG AGA CAG ATT TGC-3'
ET-1	5'-AGAGTGTGTCTACTTCTGCCA-3'	5'-CTTCCAAGTCCATACGGAACAA-3'
AXIN2	5'-GGA GAA ATG CGT GGA TAC C -3'	5'-GCT GCT TGG AGA CAA TGC -3'
β-catenin	5'-GGC AGC AAC AGT CTT ACC -3'	5'- TCC ACA TCC TCT TCC TCA -3'
LRP5	5'-GTTCGGTCTGACGCAGTACA-3'	5'-GTCCATCACGAAGTCCAGGT-3'
RUNX2	5'- GTC TCA CTG CCT CTC ACT TG-3'	5'- CAC ACA TCT CCT CCC TTC TG-3'
FZD4	5'-CAT CTC TCA TCC CTT TCC C-3'	5'-GCC TAC TCT CAT AGT CTT CC-3'

3.2.5. Immunofluorescence Staining

Cell-seeded scaffolds were washed in PBS, fixed in 4% paraformaldehyde (PFA) for 30 min, and permeabilized in 0.2% TritonX-100 in PBS for 5 min. Then, the samples were blocked with 0.2% fish skin gelatin (FSG) for 45 min, followed by incubation with primary antibody overnight at 4 °C. RUNX2 (Abcam), OCN (Santa Cruz), E-cadherin (Abcam), and β-catenin (Santa Cruz) antibodies were diltuted in a blocking buffer (0.2% FSG in PBS containing 0.02% Tween20) at a dilution of 1:150. Finally, Alexa Flour 488/647 conjugated secondary antibodies corresponding to the origin of the used primary antibodies were added for 45 min at 25 °C. The nuclei were counterstained with DAPI. The stained samples were observed under confocal microscope (Zeiss Axio Observer Z1 LSM 700).

3.2.6. ELISA Assays

The amount of OCN (Invitrogen), DKK-1(RayBiotech), and ET-1 (RayBiotech) released in the cell culture media was determined using the ELISA assay kits following the manufacturer's instructions. To this end, we kept the cell-seeded scaffolds in a serum-free medium for 48 h before protein harvest.

3.2.7. Alizarin Red S Staining (ARS) and Quantification Assay

Cell-seeded scaffolds were fixed with 4% paraformaldehyde for 30 min and washed with PBS 2-3 times to remove residual fixative agent. 2% Alizarin Red S (ARS) staining solution of 50 µl was dropped on the washed scaffold and kept it for 2 min 30 sec. After 2 min and 30 sec, the scaffold was washed using PBS many times in order to remove the unbound stain and dried at room temperature for imaging. Photos were taken at 20X magnification. For quantification, stained samples were immersed into 700 µl of 10% acetic acid solution and incubated at room temperature for 5 min to solubilize the stain. The absorbance of the released Alizarin Red S stain was measured at 405 nm.

3.2.8. Western Blot Analysis

Total protein was extracted from cell-seeded scaffolds using a mammalian cell extraction kit following the manufacturer's instructions (Biovision) and protein concentration was estimated using Bradford's reagent (Thermo Fisher). Further, 100 µg of total protein per sample was loaded per lane and resolved through SDS-polyacrylamide gel electrophoresis in 8-16% separating gel. The resolved proteins were transferred on to 0.2 µm nitrocellulose membrane (Bio-Rad) and blocked for 1 h with 5% bovine serum albumin (BSA) in PBS with 0.05% Tween-20 (PBST) (Alfa Aesar). The membranes were washed with PBST and incubated with primary mouse monoclonal antibody against human β-catenin (Santa Cruz; 1:250 dilutions) at 4 °C

overnight. The protein expression of β-catenin was studied relative to β-actin which was used as loading control (mouse monoclonal against human β-actin, (Abgent; 1:1000 dilutions). The blots were washed and incubated with horse radish peroxidase (HRP)-conjugated secondary goat anti-mouse IgG (Azure Biosystems, 1:10000 dilutions) for 1 h. After a brief washing step, the blots were visualized using enhanced chemiluminescence method (Amersham ECL Prime Western Blotting Detection Reagent, GE Healthcare) through a gel documentation system (Alpha Innotech FluorChem FC2 Imaging System).

3.2.9. Statistical Analysis

All the experiments were carried out in triplicates (n = 3) unless otherwise mentioned, and the data are presented as mean ± standard derivation. The statistical significance (p-value) among multiple comparisons was determined using one-way ANOVA followed by appropriate *post hoc* test while statistical significance (p-value) between two groups was determined using Student's unpaired *t-test*, using GraphPad Prism v7.04.

3.3. Results

3.3.1. Osteogenic Differentiation of MSCs on Nanoclay-based Scaffolds is Mediated by Wnt/β-catenin Pathway

To evaluate the induction of osteogenic differentiation in MSCs on nanoclay-based scaffolds, we examined the expressions of bone-specific genes (ALP, RUNX2, and OCN). ALP is an early stage osteogenic marker [66] while RUNX2 is a transcription factor that governs the early stages of osteoblastic differentiation [67, 68]. RUNX2 has been shown to promote the differentiation of mesenchymal cells into immature osteoblasts; however, the levels of RUNX2 reduces when osteoblasts undergo maturation [69, 70]. ALP expression has also been shown to downregulate during maturation of osteoblasts and formation of extracellular matrix (ECM) [71].

OCN is a late stage bone marker, and the expression of OCN increases during osteoblast maturation [72]. In accordance with these previous observations, we found increased gene expressions of ALP and RUNX2 at 8 days, indicating induction of osteogenic differentiation of MSCs; however, the expressions of ALP and RUNX2 were downregulated by ~2-fold along with a ~2-fold increase in OCN expression at 23 days, suggesting maturation of tissue-engineered bone [Figure 3.2(a)]. We further confirmed gene expressions results with immunostaining of RUNX2, OCN, and quantified release of OCN in culture medium using ELISA. We noticed intense staining of RUNX2 at 8 days while it was reduced at 23 days along with intense staining of OCN, as shown in Figure 3.2(c). We also observed a significant increase in release of OCN (~20 ng/ml) at 23 days as opposed to 8 days (~3.38 ng/ml) [Figure 3.2(b)]. Next, we evaluated calcium deposition on scaffolds using ARS staining. ARS showed dispersed and limited calcium deposition at 8 days while enhanced calcium deposition was observed at 23 days, which was further confirmed by quantification of released of ARS [Figure 3.2(d)]. The Wnt/β-catenin signaling pathway has been shown to play a critical role in various stages of osteogenesis [37]. In order to evaluate if Wnt/β-catenin signaling pathway is activated during osteogenesis on the nanoclay-based scaffolds, we analyzed the expressions of Wnt/β-catenin pathway-specific genes (Wnt5a, β-catenin, AXIN2, FZD4, and LRP5). Wnt5a is a member of the Wnt family that plays a critical role in bone osteogenesis, while AXIN2 is a direct target gene of Wnt ligand binding and activation of the Wnt pathway [73, 74]. Wnt/β-catenin pathway suggests Wnt-FZD-LRP complex formation in the presence of the Wnt ligand. Further, Wnt-FZD-LRP complex inhibits cytoplasmic degradation of β-catenin while promoting nuclear translocation of β-catenin to initiate transcription of bone-specific genes [44].

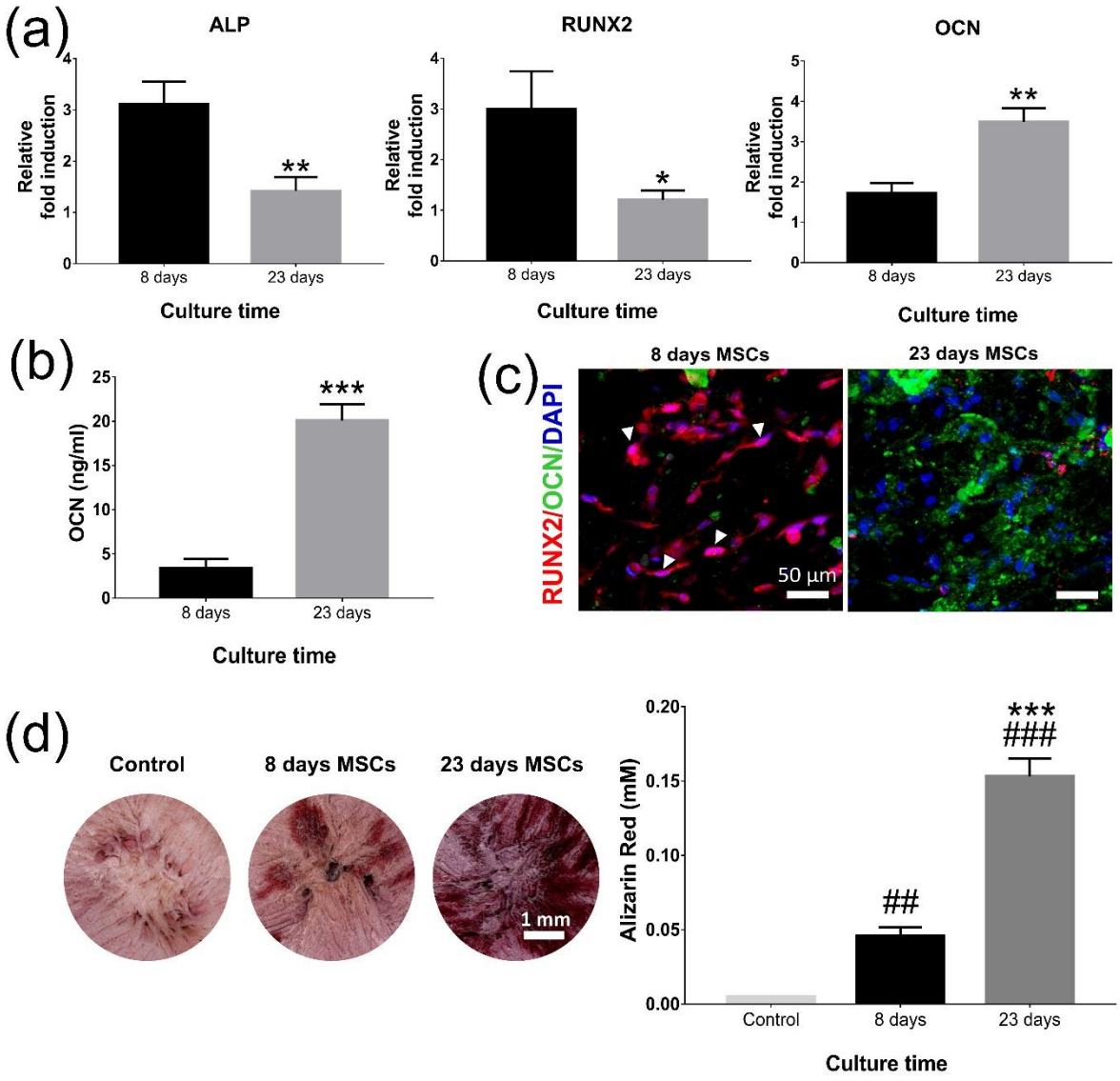

Figure 3.2. Osteogenic differentiation of MSCs and bone tissue formation on nanoclay-based scaffolds. (a) Quantitative real-time PCR of gene expression for osteogenic markers RUNX2, ALP, and OCN. (b) OCN released into culture medium, indicative of bone maturation. *$p < 0.05$, **$p < 0.01$, and ***$p < 0.001$ indicate significant difference between 8 days and 23 days MSCs constructs. (c) Immunofluorescence staining for RUNX2 and OCN of 8 days and 23 days MSCs construct. Arrows indicate nuclear translocation of RUNX2. Scale bars, 50 µm. (d) Alizarin Red S staining and quantification absorbance assay of 8 days and 23 days MSCs constructs. Scale bar, 1 mm. $^{\#\#}p < 0.01$, and $^{\#\#\#}p < 0.001$ indicate significant difference between control and MSCs seeded constructs. ***$p < 0.001$ indicates significant difference between 8 days and 23 days MSCs constructs.

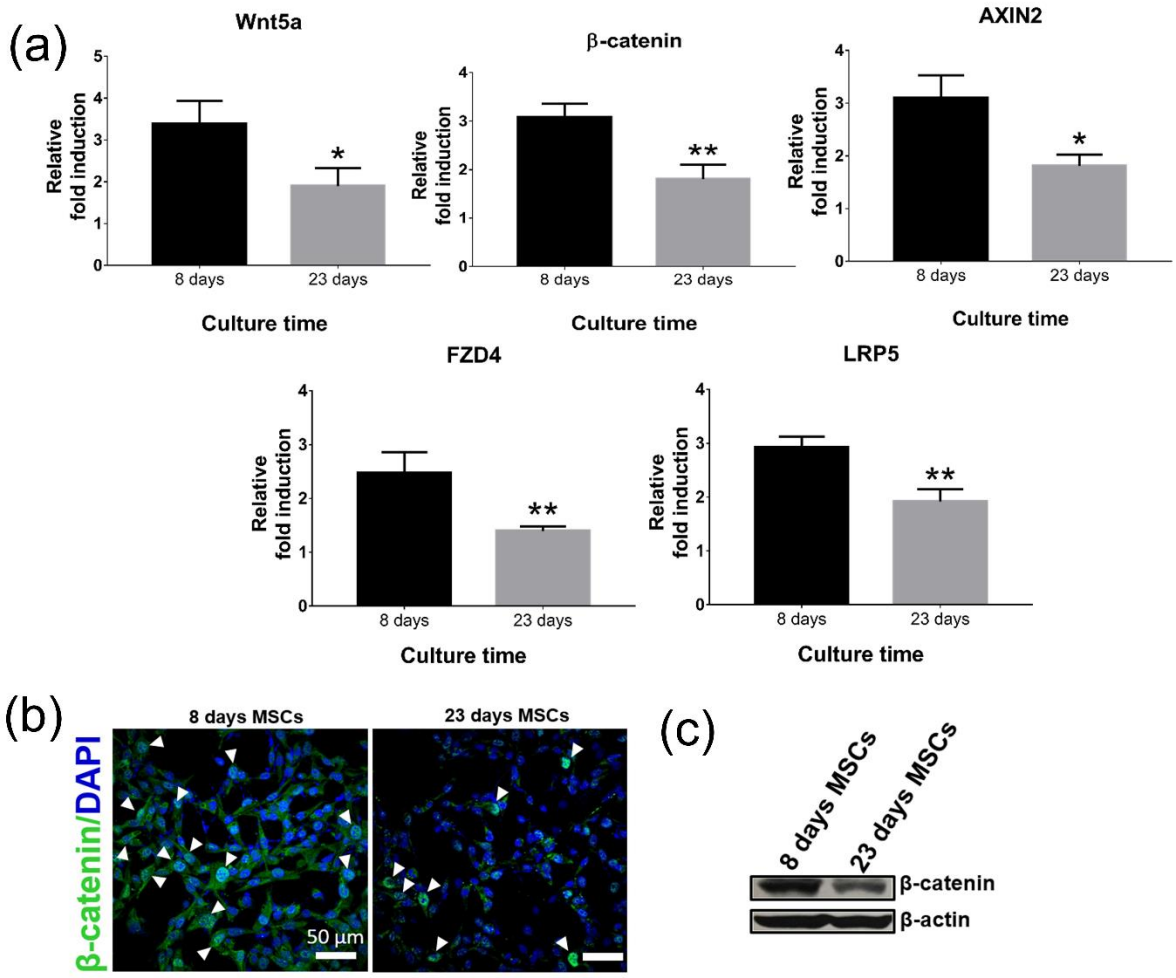

Figure 3.3. Osteogenesis in nanoclay-based scaffolds is mediated by Wnt/β-catenin signaling pathway. (a) Quantitative real-time PCR of gene expression for Wnt-related factors Wnt5a, β-catenin, AXIN2, FZD4, and LRP5. *$p < 0.05$, **$p < 0.01$ indicate significant difference between 8 days and 23 days MSCs constructs. (b) Immunofluorescence staining for β-catenin of 8 days and 23 days MSCs construct. Arrows indicate nuclear translocation of β-catenin. Scale bars, 50 μm. (c) Expression of β-catenin assessed by western blotting.

It has previously been shown that β-catenin regulates early stages of osteogenic differentiation; however, the expression of β-catenin reduces during maturation of bone [75, 76]. In line with these observations, we noticed upregulated expressions of Wnt-related factors (Wnt5a, β-catenin, AXIN2, FZD4, and LRP5) at 8 days while the expressions of all genes evaluated went d own by ~1.25-fold at 23 days [Figure 3.3(a)], which was further substantiated by immunostaining (nuclear translocation) [Figure 3.3(b)] and western blot of β-catenin [Figure

3.3(c)], indicating activation of Wnt/β-catenin signaling pathway on nanoclay scaffolds during osteogenesis.

3.3.2. Breast Cancer-derived factors DKK-1 and ET-1 Regulate Wnt/β-catenin Pathway, Leading to Bone Metastasis

Breast cancer bone metastasis most often leads to either osteolytic lesion by activation of osteoclast differentiation or osteoblastic lesions by promotion of osteoblastic activity, leading to a weakened bone matrix with poor mechanical stability [77].

In the present study, we chose two breast cancer cell lines MM 231 and MCF-7. We observed very distinct behavior of two breast cancer cells on bone scaffolds, as shown in Figure 3.4. Sequential culture of MSCs with MCF-7 (MSCs + MCF-7 SC) gave rise to tumoroids with distinguishable cellular boundaries [Figure 3.4(b)] while sequential culture of MSCs with MM 231 (MSCs + MM 231 SC) showed formation of disorganized aggregates of cells [Figure 3.4(a)].

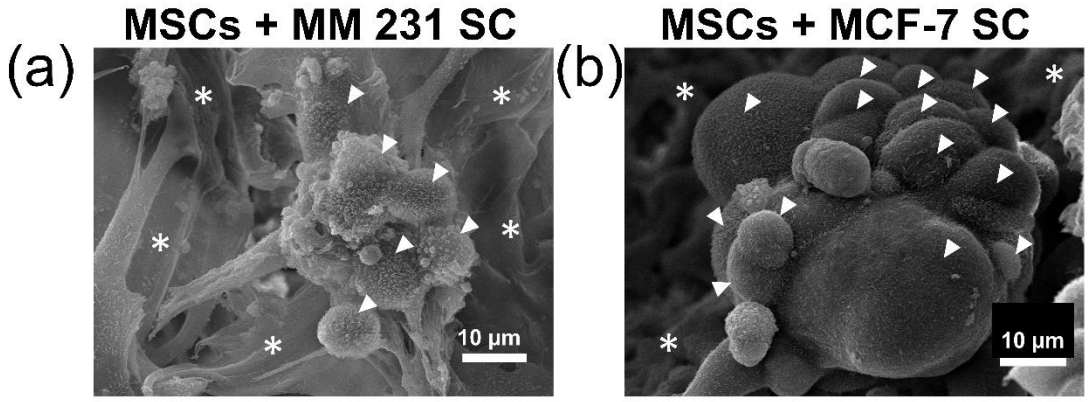

Figure 3.4. Morphology of breast cancer cells (a) MM 231 and (b) MCF-7 grown on bone-mimetic nanoclay scaffolds. Arrows indicate cells while * indicate scaffold.

Further, to evaluate the effect of breast cancer cells on tissue-engineered bone, we analyzed the expression of late-stage bone marker OCN. We noticed a ~1.2-fold increase in OCN expression with MSCs + MCF-7 SC while MSCs + MM 231 SC exhibited a ~3-fold

downregulation of OCN, as compared to MSCs, which was substantiated by immunostaining and quantification of OCN release in culture medium [Figure 3.5(a-c)]. In addition, we assessed calcium deposition on sequential culture constructs using ARS and observed intense calcium deposition on MSCs + MCF-7 SC, whereas MSCs + MM 231 SC showed abrogated calcium deposition, compared to MSCs [Figure 3.5(d)].

Next, we assessed the expressions of Wnt-related factors (Wnt5a, β-catenin, AXIN2, and LRP5) to identify whether Wnt/β-catenin signaling pathway is involved in osteogenesis during bone metastasis. We noticed a ~2.2-fold increase in the expressions of Wnt-related factors in MSCs + MCF-7 SC while MSCs + MM 231 SC showed a ~1-fold downregulation in the expressions of Wnt-related factors, compared to MSCs, indicating upregulation and downregulation of β-catenin in the sequential culture of breast cancer cells MCF-7 and MM231, respectively [Figure 3.6(a)]. To further validate our results, we performed western blot experiments of β-catenin and found results in good agreement with gene expression [Figure 3.6(c)].

To evaluate whether breast cancer cells can modulate expression of β-catenin in MSCs, we cultured MSCs for another 10 days in (1:1) MSCGM and breast cancer-derived conditioned medium (CM) after bone formation at 23 days. Interestingly, we observed re-activation of β-catenin expression when MSCs were treated with MCF-7 CM and while treating MSCs with MM 231 CM diminished β-catenin expression as shown by immunostaining [Figure 3.6(b)].

Breast cancer has been shown to contribute towards formation of osteolytic and osteoblastic bone metastases under the influence of DKK-1 and ET-1, respectively [60, 62]. DKK-1 is an inhibitor of Wnt signaling, operates by sequestering LRP-5/6 from the receptor FZD and thus blocks Wnt/ β-catenin signaling mediated osteogenesis [57-59], whereas ET-1 has

been shown to promote Wnt/ β-catenin signaling, leading to osteogenesis [78]. To determine whether DKK-1 and ET-1 are involved in the regulation of Wnt/β-catenin signaling pathway, we evaluated the expressions of these factors. We found upregulated expression of ET-1 in MSCs + MCF-7 SC, whereas MSCs + MM 231 SC exhibited higher levels of DKK-1, which was substantiated by quantifying release of these factors in culture media using ELISA assay [Figure 3.7(a, b)]. Taken together, breast-cancer derived factors DKK-1 and ET-1 seem to regulate Wnt/β-catenin pathway, leading to bone metastasis.

3.4. Discussion

It is well known that metastatic breast cancer cells colonize within the bone marrow and disrupt bone remodeling, either by activation of osteoclast differentiation or by the promotion of osteoblast activity.

Given the multifaceted role of the Wnt/β-catenin pathway in bone regeneration, we hypothesized that regulation of the Wnt/β-catenin pathway might influence the types of bone metastasis. Therefore, the primary goal of the study is to understand the influence of Wnt/β-catenin pathway in osteogenesis during breast cancer mediated bone metastases *in vitro*. Due to the scarcity of availability of human breast cancer metastasized bone samples and *in vivo* mouse models for spontaneous breast cancer bone metastasis, we developed a 3D *in vitro* model using nanoclay-based scaffolds along with osteogenically differentiated MSCs and human breast cancer cells. We have previously reported uniform bone-like ECM formation on nanoclay scaffolds at 23 days when seeded with MSCs [23]. In a recent study, we reported that migration of breast cancer cells were significantly enhanced in the presence of bone-mimetic scaffolds [30]. Also, growing cancer cells on bone ECM led to formation of *in vivo* like tumoroids as shown in Figure 3.4(b).

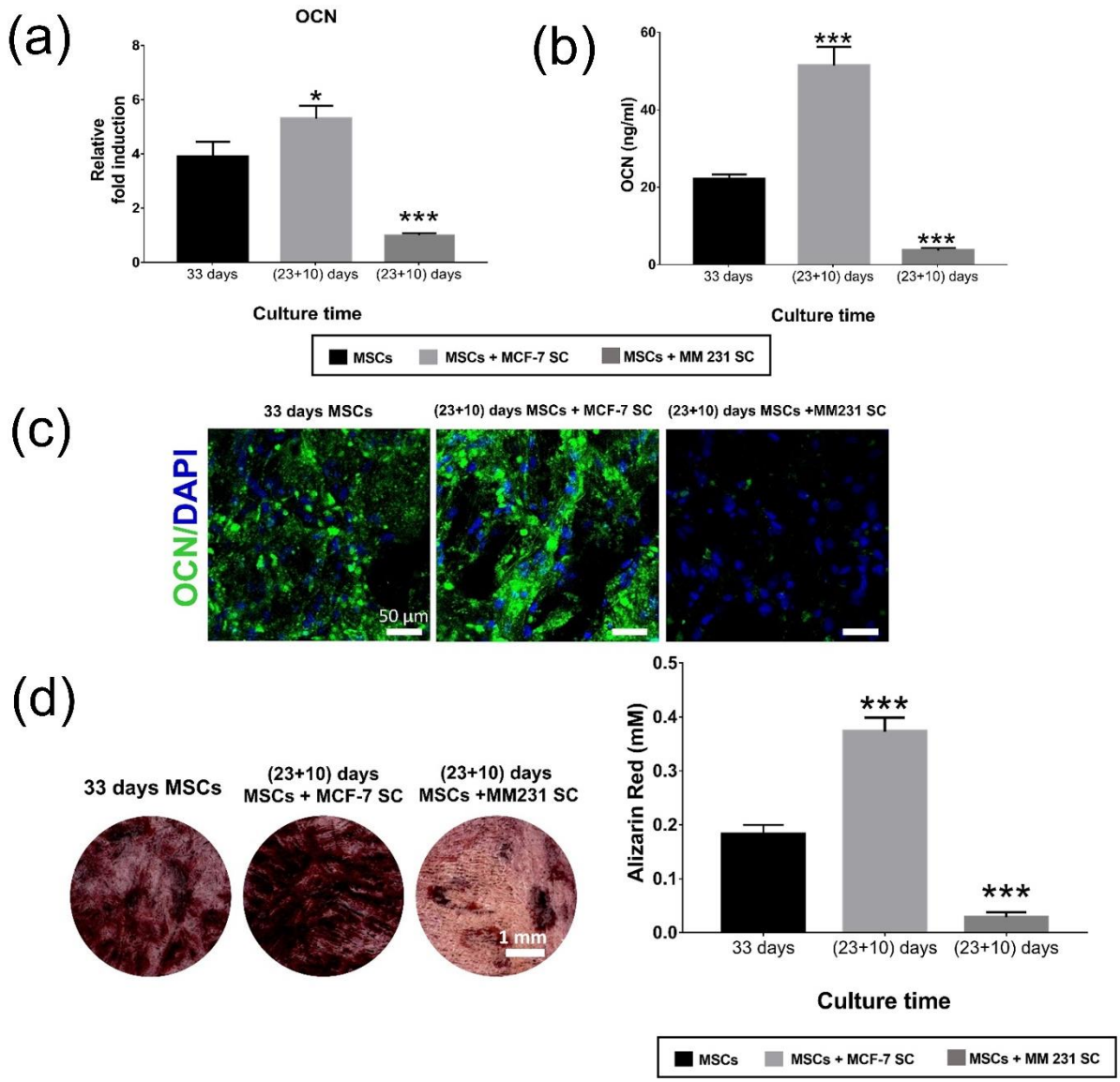

Figure 3.5. Osteogenesis in 3D *in vitro* model of breast cancer bone metastasis. (a) Quantitative real-time PCR of gene expression for late-stage osteogenic marker OCN. (b) OCN released into culture medium, indicative of bone maturation. *$p < 0.05$, ***$p < 0.001$ indicate significant difference between 33 days MSCs and (23+10) days sequential cultures of MSCs with breast cancer cells constructs. (c) Immunofluorescence staining for OCN of 33 days MSCs and (23+10) days sequential cultures of MSCs with breast cancer cells constructs. Scale bars, 50 µm. (d) Alizarin Red S staining and quantification absorbance assay of 33 days MSCs and (23+10) days sequential cultures of MSCs with breast cancer cells constructs. Scale bar, 1 mm. ***$p < 0.001$ indicates significant difference between 33 days MSCs and (23+10) days sequential cultures of MSCs with breast cancer cells constructs.

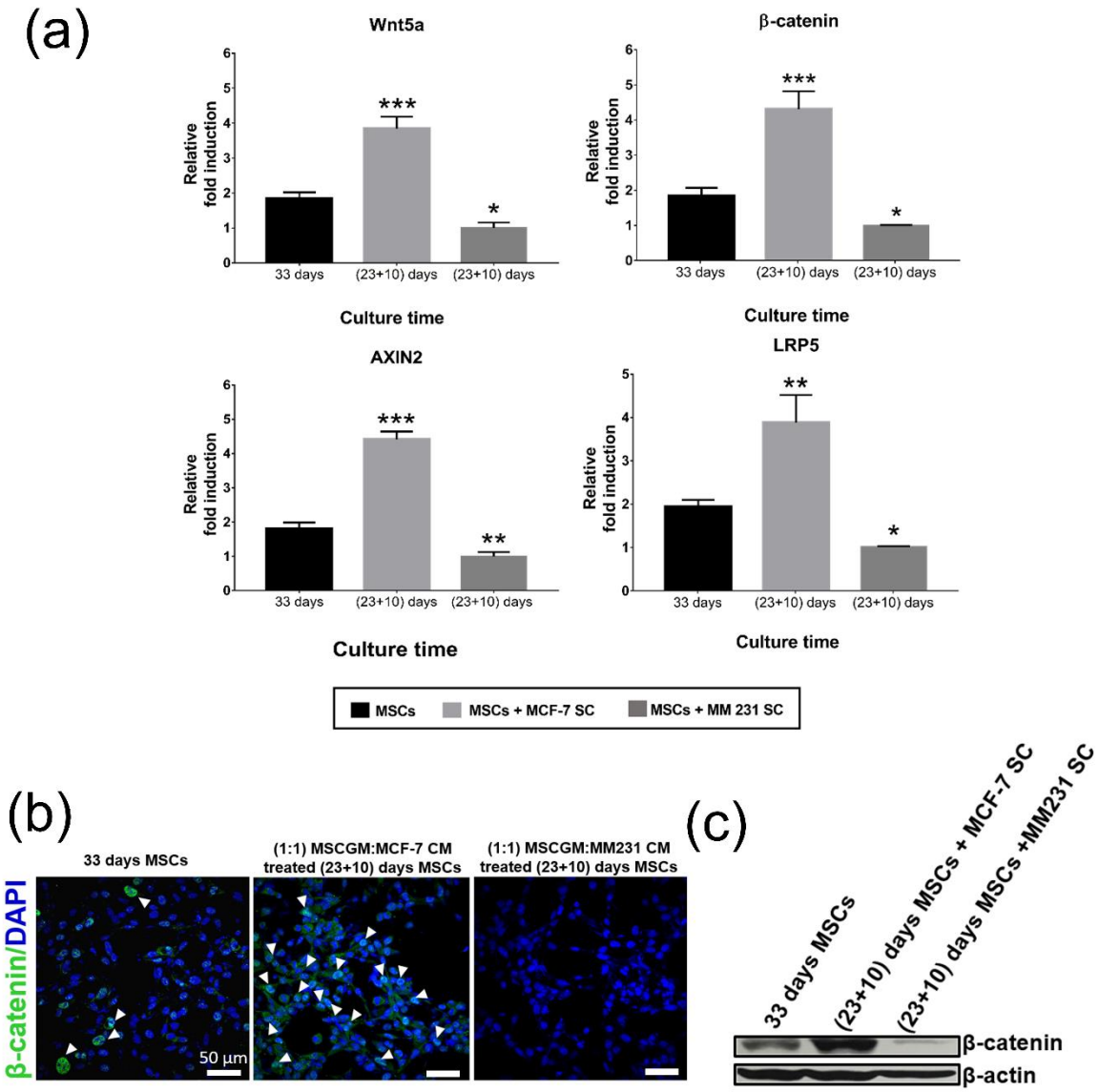

Figure 3.6. Wnt/β-catenin signaling regulates osteogenesis in 3D *in vitro* model of breast cancer bone metastasis. (a) Quantitative real-time PCR of gene expression for Wnt-related factors Wnt5a, β-catenin, AXIN2, and LRP5. *$p < 0.05$, **$p < 0.01$, and***$p < 0.001$ indicate significant difference between 33 days MSCs and (23+10) days sequential cultures of MSCs with breast cancer cells constructs. (b) Immunofluorescence staining for β-catenin of 33 days MSCs and (23+10) days MSCs grown in 1:1 MSCGM: Breast cancer-derived CM. Arrows indicate nuclear translocation of β-catenin. Scale bars, 50 µm. (c) Expression of β-catenin assessed by western blotting.

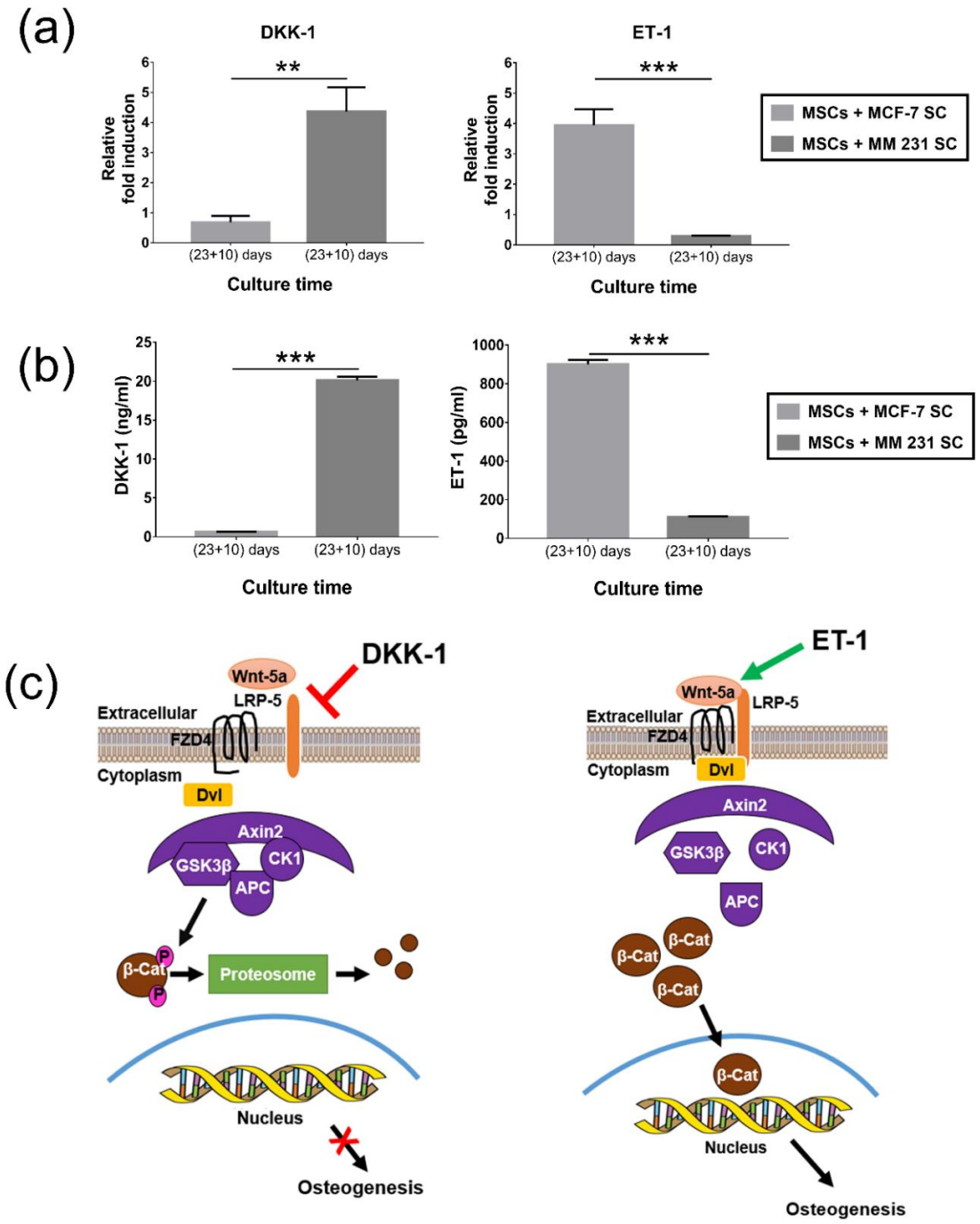

Figure 3.7. Breast cancer-derived factors DKK-1 and ET-1 regulate Wnt/β-catenin signaling pathway. (a) Quantitative real-time PCR of gene expression for DKK-1, and ET-1. (b) DKK-1 and ET-1 released into culture medium. $^{**}p < 0.01$, $^{***}p < 0.001$ indicate significant difference between (23+10) days sequential cultures of MSCs with MCF-7 and (23+10) days sequential cultures of MSCs with MM 231. (c) Mechanisms of inactivation and stimulation of Wnt/β-catenin signaling pathway by DKK-1 and ET-1, respectively.

Collectively, these observations demonstrate successful recapitulation of metastatic condition *in vitro* on nanoclay scaffolds. To this end, we cultured MSCs for 23 days on nanoclay-based scaffolds to obtain bone-like ECM formation by deposition of inorganic matrix from osteogenically differentiated MSCs [Figure 3.2(d)]; after this step, we seeded human breast cancer cells on the obtained bone-like tissue model to mimic *in vivo* metastatic spreading condition [Figure 3.1].

In the present study, we confirmed activation of Wnt/β-catenin pathway during bone formation on nanoclay-based scaffolds [Figure 3.3]. Activation of Wnt/β-catenin pathway in MSCs could be attributed to the released silicate ions from nanoclay. The nanoclays are 2:1 phyllosilicates with one octahedral alumina sheet sandwiched between two tetrahedral silica sheets [79]. Silicate containing bioglass and bioceramics have also been reported to stimulate osteoblastic differentiation via Wnt/β-catenin pathway [47, 50, 54, 80]. Breast cancer has been shown to form both osteolytic and osteoblastic bone metastases under the influence of DKK-1 and ET-1, respectively [60, 62]. In the present study, we observed that MSCs + MCF-7 SC resulted in increased bone formation as shown by increased expression of OCN and intensive calcium deposition [Figure 3.5(c, d)]. It is noteworthy to mention that we also found enhanced expression of Wnt-related factors (Wnt-5a, β-catenin, AXIN2, and LRP5) in the MSCs + MCF-7 SC, suggesting involvement of Wnt/β-catenin pathway in regulating osteogenesis during bone metastasis. The activation of Wnt/β-catenin pathway has been well-documented in literature for osteoblast differentiation *in vitro* and bone formation *in vivo* [38, 81, 82]. It is therefore not surprising that Wnt/β-catenin pathway may play a role in increased bone formation during bone metastasis. We further noticed that MSCs + MCF-7 SC express higher levels of ET-1 [Figure 3.7(a,b)] and previous studies have demonstrated that up-regulation of ET-1 resulted in

osteoblastic metastases [62]. In a recent study, ET-1 has been shown to promote osteogenic differentiation of periodontal ligament stem cells via Wnt/ β-catenin pathway [78]. In another study, ET-1 has been shown to activate β-catenin signaling through the endothelin-A receptor (ETAR)/β-arrestin complex in ovarian cancer metastasis [83]. Hence, it seems likely that up-regulation of ET-1 may contribute towards activation of the Wnt/β-catenin pathway in MSCs + MCF-7 SC, leading to increased bone formation.

Next, the inactivation of Wnt/β-catenin pathway by breast-cancer derived DKK-1 resulted in inhibition of bone formation in MSCs + MM 231 SC, as indicated by abrogated calcium deposition and reduced OCN expression [Figure 3.5(c, d)]. Our results are in good agreement with previous studies on the inhibitory effect of DKK-1 on osteoblast differentiation *in vitro* and bone formation *in vivo* [37, 60, 84-86]. Hence, inhibited bone formation in our model is mediated through down-regulation of osteoblast differentiation by DKK-1 induced inactivation of Wnt/β-catenin pathway. In summary, our 3D *in vitro* model allows investigation of the interactions between breast cancer cells and bone and facilitates quantification of bone formation with different breast cancer cells. Most importantly, the model exhibited both inhibited and excessive bone formation with different cell lines, mimicking bone lesions observed in breast cancer patients. Therefore, this model is suitable for studying cellular mechanisms underlying the change during bone metastasis. However, it should be noted that our model does not take the early phases of bone metastases, such as local invasion, intravasation, dissemination via circulation, and extravasation into consideration. Thus, our data suggested that Wnt/β-catenin pathway regulates osteogenesis at secondary bone site. Future studies are planned to evaluate whether this pathway also governs in the early phases of breast cancer bone metastasis.

3.5. Conclusion

The present study suggests that osteogenesis in 3D *in vitro* model of breast cancer bone metastasis is mediated by Wnt/β-catenin signaling pathway. MCF-7 cells secrete ET-1, which promotes osteoblastic differentiation via Wnt/β-catenin signaling and incudes bone-forming activity, leading to excessive bone formation. Inactivation of Wnt/β-catenin signaling by MM 231 secreted DKK-1 leads to inhibited bone formation through down-regulation of osteoblast differentiation. Further, 3D *in vitro* model exhibited mixed bone lesions with different cell types, mimicking bone lesions observed in breast cancer patients. However, it should be noted that this model omits early stages of breast cancer bone metastasis. More studies should be carried out to understand the underlying molecular mechanism of Wnt-dependent pathways in tumor-harboring bone microenvironment before developing any therapeutic strategies for bone metastasis. *In vitro* breast cancer model thus presents a viable testbed for studying metastasis.

3.6. Acknowledgments

This research study was financially supported by NDSU Grand Challenges grant for 'Center for Engineered Cancer Test-Beds' (CECT). Dr. Scott Payne, Dr. Tao Wang, and Dr. Pawel Borowicz are acknowledged for their help with Scanning electron microscopy, PCR, and immunofluorescence imaging, respectively. Sakshi Taneja from Pharmaceutical Sciences is acknowledged for her help with Western Blot. Support from ND EPSCoR and NSF is also acknowledged for tissue engineering laboratory and scanning electron microscope, respectively.

3.7. References

[1] W. Kozlow, T.A. Guise, Breast cancer metastasis to bone: mechanisms of osteolysis and implications for therapy, Journal of mammary gland biology and neoplasia 10(2) (2005) 169-180.

[2] A. Marturano-Kruik, M.M. Nava, K. Yeager, A. Chramiec, L. Hao, S. Robinson, E. Guo, M.T. Raimondi, G. Vunjak-Novakovic, Human bone perivascular niche-on-a-chip for studying metastatic colonization, Proceedings of the National Academy of Sciences 115(6) (2018) 1256-1261.

[3] Y. Kang, P.M. Siegel, W. Shu, M. Drobnjak, S.M. Kakonen, C. Cordón-Cardo, T.A. Guise, J. Massagué, A multigenic program mediating breast cancer metastasis to bone, Cancer cell 3(6) (2003) 537-549.

[4] O.S. Nielsen, A.J. Munro, I.F. Tannock, Bone metastases: pathophysiology and management policy, Journal of Clinical Oncology 9(3) (1991) 509-524.

[5] R.D. Rubens, Bone metastases—the clinical problem, European Journal of Cancer 34(2) (1998) 210-213.

[6] A. Fantozzi, G. Christofori, Mouse models of breast cancer metastasis, Breast Cancer Research 8(4) (2006) 212.

[7] A. Nyga, U. Cheema, M. Loizidou, 3D tumour models: novel *in vitro* approaches to cancer studies, Journal of cell communication and signaling 5(3) (2011) 239.

[8] K.L. Kretschmann, A.L. Welm, Mouse models of breast cancer metastasis to bone, Cancer and Metastasis Reviews 31(3-4) (2012) 579-583.

[9] C. Arrigoni, P. De Luca, M. Gilardi, S. Previdi, M. Broggini, M. Moretti, Direct but not indirect co-culture with osteogenically differentiated human bone marrow stromal cells

increases RANKL/OPG ratio in human breast cancer cells generating bone metastases, Molecular cancer 13(1) (2014) 238.

[10] M. Rajski, B. Vogel, F. Baty, C. Rochlitz, M. Buess, Global gene expression analysis of the interaction between cancer cells and osteoblasts to predict bone metastasis in breast cancer, PloS one 7(1) (2012) e29743.

[11] C. Liverani, L. Mercatali, C. Spadazzi, F. La Manna, A. De Vita, N. Riva, S. Calpona, M. Ricci, A. Bongiovanni, E. Gunelli, CSF-1 blockade impairs breast cancer osteoclastogenic potential in co-culture systems, Bone 66 (2014) 214-222.

[12] X. Chen, J. Lu, Y. Ji, A. Hong, Q. Xie, Cytokines in osteoblast-conditioned medium promote the migration of breast cancer cells, Tumor Biology 35(1) (2014) 791-798.

[13] D. Denoyer, N. Kusuma, A. Burrows, X. Ling, L. Jupp, R.L. Anderson, N. Pouliot, Bone-derived soluble factors and laminin-511 cooperate to promote migration, invasion and survival of bone-metastatic breast tumor cells, Growth Factors 32(2) (2014) 63-73.

[14] C. Fischbach, R. Chen, T. Matsumoto, T. Schmelzle, J.S. Brugge, P.J. Polverini, D.J. Mooney, Engineering tumors with 3D scaffolds, Nature Methods 4(10) (2007) 855-860.

[15] S.P. Pathi, C. Kowalczewski, R. Tadipatri, C. Fischbach, A Novel 3-D Mineralized Tumor Model to Study Breast Cancer Bone Metastasis, Plos One 5(1) (2010) 10.

[16] W. Zhu, M. Wang, Y.B. Fu, N.J. Castro, S.W. Fu, L.G. Zhang, Engineering a biomimetic three-dimensional nanostructured bone model for breast cancer bone metastasis study, Acta Biomaterialia 14 (2015) 164-174.

[17] S. Talukdar, S.C. Kundu, Engineered 3D Silk-Based Metastasis Models: Interactions Between Human Breast Adenocarcinoma, Mesenchymal Stem Cells and Osteoblast-Like Cells, Advanced Functional Materials 23(42) (2013) 5249-5260.

[18] A.M. Mastro, E.A. Vogler, A Three-Dimensional Osteogenic Tissue Model for the Study of Metastatic Tumor Cell Interactions with Bone, Cancer Research 69(10) (2009) 4097-4100.

[19] V. Angeloni, N. Contessi, C. De Marco, S. Bertoldi, M.C. Tanzi, M.G. Daidone, S. Fare, Polyurethane foam scaffold as *in vitro* model for breast cancer bone metastasis, Acta biomaterialia 63 (2017) 306-316.

[20] D. Sikdar, S.M. Pradhan, D.R. Katti, K.S. Katti, B. Mohanty, Altered phase model for polymer clay nanocomposites, Langmuir 24(10) (2008) 5599-5607.

[21] D. Sikdar, K.S. Katti, D.R. Katti, Molecular interactions alter clay and polymer structure in polymer clay nanocomposites, Journal of Nanoscience and Nanotechnology 8(4) (2008) 1638-1657.

[22] D. Sikdar, D.R. Katti, K.S. Katti, B. Mohanty, Influence of backbone chain length and functional groups of organic modifiers on crystallinity and nanomechanical properties of intercalated clay-polycaprolactam nanocomposites, International Journal of Nanotechnology 6(5-6) (2009) 468-492.

[23] A.H. Ambre, D.R. Katti, K.S. Katti, Biomineralized hydroxyapatite nanoclay composite scaffolds with polycaprolactone for stem cell-based bone tissue engineering, Journal of Biomedical Materials Research Part A 103(6) (2015) 2077-2101.

[24] K.S. Katti, A.H. Ambre, S. Payne, D.R. Katti, Vesicular delivery of crystalline calcium minerals to ECM in biomineralized nanoclay composites, Materials Research Express 2(4) (2015) 13.

[25] N.I. Nikolaev, T. Müller, D.J. Williams, Y. Liu, Changes in the stiffness of human mesenchymal stem cells with the progress of cell death as measured by atomic force microscopy, Journal of biomechanics 47(3) (2014) 625-630.

[26] R. Khanna, K.S. Katti, D.R. Katti, Experiments in nanomechanical properties of live osteoblast cells and cell–biomaterial interface, Journal of Nanotechnology in Engineering and Medicine 2(4) (2011) 041005.

[27] K.S. Katti, M. Molla, F. Karandish, M.K. Haldar, S. Mallik, D.R. Katti, Sequential culture on biomimetic nanoclay scaffolds forms three-dimensional tumoroids, Journal of Biomedical Materials Research Part A 104(7) (2016) 1591-1602.

[28] S. Molla, D.R. Katti, K.S. Katti, *In vitro* design of mesenchymal to epithelial transition of prostate cancer metastasis using 3D nanoclay bone-mimetic scaffolds, Journal of tissue engineering and regenerative medicine 12(3) (2018) 727-737.

[29] K.S. Katti, D.R. Katti, M.S. Molla, S. Kar, Evaluation of Cancer Tumors in 3D Porous Bone Mimetic Scaffolds, Poromechanics VI, pp. 881-888.

[30] S. Kar, M.D.S. Molla, D.R. Katti, K.S. Katti, Tissue-engineered nanoclay-based 3D *in vitro* breast cancer model for studying breast cancer metastasis to bone, Journal of tissue engineering and regenerative medicine 13(2) (2019) 119-130.

[31] M.D.S. Molla, D.R. Katti, K.S. Katti, An *in vitro* model of prostate cancer bone metastasis for highly metastatic and non-metastatic prostate cancer using nanoclay bone-mimetic scaffolds, MRS Advances 4(21) (2019) 1207-1213.

[32] S. Kar, D.R. Katti, K.S. Katti, Fourier transform infrared spectroscopy based spectral biomarkers of metastasized breast cancer progression, Spectrochimica Acta Part A: Molecular and Biomolecular Spectroscopy 208 (2019) 85-96.

[33] A.K. Gaharwar, S.M. Mihaila, A. Swami, A. Patel, S. Sant, R.L. Reis, A.P. Marques, M.E. Gomes, A. Khademhosseini, Bioactive silicate nanoplatelets for osteogenic differentiation of human mesenchymal stem cells, Advanced materials 25(24) (2013) 3329-3336.

[34] S. Kar, T. Kaur, A. Thirugnanam, Microwave-assisted synthesis of porous chitosan–modified montmorillonite–hydroxyapatite composite scaffolds, International journal of biological macromolecules 82 (2016) 628-636.

[35] A.K. Gaharwar, S. Mukundan, E. Karaca, A. Dolatshahi-Pirouz, A. Patel, K. Rangarajan, S.M. Mihaila, G. Iviglia, H. Zhang, A. Khademhosseini, Nanoclay-enriched poly (ε-caprolactone) electrospun scaffolds for osteogenic differentiation of human mesenchymal stem cells, Tissue Engineering Part A 20(15-16) (2014) 2088-2101.

[36] A.J. Mieszawska, J.G. Llamas, C.A. Vaiana, M.P. Kadakia, R.R. Naik, D.L. Kaplan, Clay enriched silk biomaterials for bone formation, Acta biomaterialia 7(8) (2011) 3036-3041.

[37] Y. Chen, B.A. Alman, Wnt pathway, an essential role in bone regeneration, Journal of cellular biochemistry 106(3) (2009) 353-362.

[38] Y. Chen, H.C. Whetstone, A.C. Lin, P. Nadesan, Q. Wei, R. Poon, B.A. Alman, Beta-catenin signaling plays a disparate role in different phases of fracture repair: implications for therapy to improve bone healing, PLoS medicine 4(7) (2007) e249.

[39] M.L. Johnson, M.A. Kamel, The Wnt signaling pathway and bone metabolism, Current opinion in rheumatology 19(4) (2007) 376-382.

[40] J. Behrens, Cross-regulation of the Wnt signalling pathway: a role of MAP kinases, J Cell Sci 113(6) (2000) 911-919.

[41] Q. Eastman, R. Grosschedl, Regulation of LEF-1/TCF transcription factors by Wnt and other signals, Current opinion in cell biology 11(2) (1999) 233-240.

[42] S. Ikeda, S. Kishida, H. Yamamoto, H. Murai, S. Koyama, A. Kikuchi, Axin, a negative regulator of the Wnt signaling pathway, forms a complex with GSK-3β and β-catenin and promotes GSK-3β-dependent phosphorylation of β-catenin, The EMBO journal 17(5) (1998) 1371-1384.

[43] T.-C. He, A.B. Sparks, C. Rago, H. Hermeking, L. Zawel, L.T. Da Costa, P.J. Morin, B. Vogelstein, K.W. Kinzler, Identification of c-MYC as a target of the APC pathway, Science 281(5382) (1998) 1509-1512.

[44] T. Gaur, C.J. Lengner, H. Hovhannisyan, R.A. Bhat, P.V.N. Bodine, B.S. Komm, A. Javed, A.J. Van Wijnen, J.L. Stein, G.S. Stein, Canonical WNT signaling promotes osteogenesis by directly stimulating Runx2 gene expression, Journal of Biological Chemistry 280(39) (2005) 33132-33140.

[45] O. Tetsu, F. McCormick, β-Catenin regulates expression of cyclin D1 in colon carcinoma cells, Nature 398(6726) (1999) 422.

[46] T. Cai, D. Sun, Y. Duan, P. Wen, C. Dai, J. Yang, W. He, WNT/β-catenin signaling promotes VSMCs to osteogenic transdifferentiation and calcification through directly modulating Runx2 gene expression, Experimental cell research 345(2) (2016) 206-217.

[47] J. Guan, J. Zhang, S. Guo, H. Zhu, Z. Zhu, H. Li, Y. Wang, C. Zhang, J. Chang, Human urine-derived stem cells can be induced into osteogenic lineage by silicate bioceramics via activation of the Wnt/β-catenin signaling pathway, Biomaterials 55 (2015) 1-11.

[48] W. Liu, A. Konermann, T. Guo, A. Jäger, L. Zhang, Y. Jin, Canonical Wnt signaling differently modulates osteogenic differentiation of mesenchymal stem cells derived from

bone marrow and from periodontal ligament under inflammatory conditions, Biochimica et Biophysica Acta (BBA)-General Subjects 1840(3) (2014) 1125-1134.

[49] Z. Zhang, Z. Li, C. Zhang, J. Liu, Y. Bai, S. Li, C. Zhang, Biomimetic intrafibrillar mineralized collagen promotes bone regeneration via activation of the Wnt signaling pathway, International journal of nanomedicine 13 (2018) 7503.

[50] W. Zhang, D. Huang, F. Zhao, W. Gao, L. Sun, X. Li, X. Chen, Synergistic effect of strontium and silicon in strontium-substituted sub-micron bioactive glass for enhanced osteogenesis, Materials Science and Engineering: C 89 (2018) 245-255.

[51] L. Li, X. Peng, Y. Qin, R. Wang, J. Tang, X. Cui, T. Wang, W. Liu, H. Pan, B. Li, Acceleration of bone regeneration by activating Wnt/β-catenin signalling pathway via lithium released from lithium chloride/calcium phosphate cement in osteoporosis, Scientific reports 7 (2017) 45204.

[52] Y. Wang, X. Zhang, J. Shao, H. Liu, X. Liu, E. Luo, Adiponectin regulates BMSC osteogenic differentiation and osteogenesis through the Wnt/β-catenin pathway, Scientific reports 7(1) (2017) 3652.

[53] K. Tao, D. Xiao, J. Weng, A. Xiong, B. Kang, H. Zeng, Berberine promotes bone marrow-derived mesenchymal stem cells osteogenic differentiation via canonical Wnt/β-catenin signaling pathway, Toxicology letters 240(1) (2016) 68-80.

[54] C. Wu, P. Han, M. Xu, X. Zhang, Y. Zhou, G. Xue, J. Chang, Y. Xiao, Nagelschmidtite bioceramics with osteostimulation properties: material chemistry activating osteogenic genes and WNT signalling pathway of human bone marrow stromal cells, Journal of Materials Chemistry B 1(6) (2013) 876-885.

[55] G. Li, J. Liu, Y. Wang, K. Yang, M. Zhao, Y. Xiao, X. Wen, L. Liu, LNGFR targets the Wnt/β-catenin pathway and promotes the osteogenic differentiation in rat ectomesenchymal stem cells, Scientific reports 7(1) (2017) 11021.

[56] F. Zhang, K. Luo, Z. Rong, Z. Wang, F. Luo, Z. Zhang, D. Sun, S. Dong, J. Xu, F. Dai, Periostin upregulates Wnt/β-catenin signaling to promote the osteogenesis of CTLA4-modified human bone marrow-mesenchymal stem cells, Scientific reports 7 (2017) 41634.

[57] B. Mao, W. Wu, Y. Li, D. Hoppe, P. Stannek, A. Glinka, C. Niehrs, LDL-receptor-related protein 6 is a receptor for Dickkopf proteins, Nature 411(6835) (2001) 321.

[58] V.E. Ahn, M.L.-H. Chu, H.-J. Choi, D. Tran, A. Abo, W.I. Weis, Structural basis of Wnt signaling inhibition by Dickkopf binding to LRP5/6, Developmental cell 21(5) (2011) 862-873.

[59] W. Balemans, E. Piters, E. Cleiren, M. Ai, L. Van Wesenbeeck, M.L. Warman, W. Van Hul, The binding between sclerostin and LRP5 is altered by DKK1 and by high-bone mass LRP5 mutations, Calcified tissue international 82(6) (2008) 445-453.

[60] G. Bu, W. Lu, C.C. Liu, K. Selander, T. Yoneda, C. Hall, E.T. Keller, Y. Li, Breast cancer-derived Dickkopf1 inhibits osteoblast differentiation and osteoprotegerin expression: implication for breast cancer osteolytic bone metastases, International journal of cancer 123(5) (2008) 1034-1042.

[61] G.A. Clines, K.S. Mohammad, Y. Bao, O.W. Stephens, L.J. Suva, J.D. Shaughnessy Jr, J.W. Fox, J.M. Chirgwin, T.A. Guise, Dickkopf homolog 1 mediates endothelin-1-stimulated new bone formation, Molecular endocrinology 21(2) (2007) 486-498.

[62] T.A. Guise, J.J. Yin, K.S. Mohammad, Role of endothelin-1 in osteoblastic bone metastases, Cancer 97(S3) (2003) 779-784.

[63] A. Ambre, K.S. Katti, D.R. Katti, In situ mineralized hydroxyapatite on amino acid modified nanoclays as novel bone biomaterials, Materials Science and Engineering: C 31(5) (2011) 1017-1029.

[64] A.H. Ambre, K.S. Katti, D.R. Katti, Nanoclay based composite scaffolds for bone tissue engineering applications, Journal of Nanotechnology in Engineering and Medicine 1(3) (2010) 031013.

[65] K.S. Katti, A.H. Ambre, N. Peterka, D.R. Katti, Use of unnatural amino acids for design of novel organomodified clays as components of nanocomposite biomaterials, Philosophical Transactions of the Royal Society of London A: Mathematical, Physical and Engineering Sciences 368(1917) (2010) 1963-1980.

[66] Y. Gotoh, K. Hiraiwa, M. Nagayama, *In vitro* mineralization of osteoblastic cells derived from human bone, Bone and mineral 8(3) (1990) 239-250.

[67] T. Komori, H. Yagi, S. Nomura, A. Yamaguchi, K. Sasaki, K. Deguchi, Y. Shimizu, R.T. Bronson, Y.H. Gao, M. Inada, M. Sato, R. Okamoto, Y. Kitamura, S. Yoshiki, T. Kishimoto, Targeted disruption of Cbfa1 results in a complete lack of bone formation owing to maturational arrest of osteoblasts, Cell 89(5) (1997) 755-764.

[68] F. Otto, A.P. Thornell, T. Crompton, A. Denzel, K.C. Gilmour, I.R. Rosewell, G.W.H. Stamp, R.S.P. Beddington, S. Mundlos, B.R. Olsen, P.B. Selby, M.J. Owen, Cbfa1, a candidate gene for cleidocranial dysplasia syndrome, is essential for osteoblast differentiation and bone development, Cell 89(5) (1997) 765-771.

[69] T. Komori, Runx2, a multifunctional transcription factor in skeletal development, Journal of cellular biochemistry 87(1) (2002) 1-8.

[70] T. Komori, Regulation of osteoblast differentiation by Runx2, Osteoimmunology, Springer2009, pp. 43-49.

[71] R.A. Thibault, L. Scott Baggett, A.G. Mikos, F.K. Kasper, Osteogenic differentiation of mesenchymal stem cells on pregenerated extracellular matrix scaffolds in the absence of osteogenic cell culture supplements, Tissue Engineering Part A 16(2) (2009) 431-440.

[72] W. Huang, S. Yang, J. Shao, Y.-P. Li, Signaling and transcriptional regulation in osteoblast commitment and differentiation, Frontiers in bioscience: a journal and virtual library 12 (2007) 3068.

[73] M. Lohi, A.S. Tucker, P.T. Sharpe, Expression of Axin2 indicates a role for canonical Wnt signaling in development of the crown and root during pre-and postnatal tooth development, Developmental Dynamics 239(1) (2010) 160-167.

[74] H.M.I. Yu, B. Jerchow, T.J. Sheu, B. Liu, F. Costantini, J.E. Puzas, W. Birchmeier, W. Hsu, The role of Axin2 in calvarial morphogenesis and craniosynostosis, Development 132(8) (2005) 1995-2005.

[75] T. Pflug, U. Huynh-Do, S. Rudloff, Reduced β-catenin expression affects patterning of bone primordia, but not bone maturation, Biology open 6(5) (2017) 582-588.

[76] S.L. Holmen, C.R. Zylstra, A. Mukherjee, R.E. Sigler, M.-C. Faugere, M.L. Bouxsein, L. Deng, T.L. Clemens, B.O. Williams, Essential role of β-catenin in postnatal bone acquisition, Journal of Biological Chemistry 280(22) (2005) 21162-21168.

[77] A.M. Sitarski, M.R. Reagan, 3D Tissue Engineered *in vitro* Models of Cancer in Bone, ACS Biomaterials Science & Engineering 4(2) (2018) 324-336.

[78] L. Liang, W. Zhou, N. Yang, J. Yu, H. Liu, ET-1 promotes differentiation of periodontal ligament stem cells into osteoblasts through ETR, MAPK, and Wnt/β-catenin signaling pathways under inflammatory microenvironment, Mediators of inflammation 2016 (2016).

[79] R.T. Martin, S.W. Bailey, D.D. Eberl, D.S. Fanning, S. Guggenheim, H. Kodama, D.R. Pevear, J. Środoń, F.J. Wicks, Report of the clay minerals society nomenclature committee: revised classification of clay materials, Clays and Clay Minerals 39(3) (1991) 333-335.

[80] P. Han, C. Wu, Y. Xiao, The effect of silicate ions on proliferation, osteogenic differentiation and cell signalling pathways (WNT and SHH) of bone marrow stromal cells, Biomaterials Science 1(4) (2013) 379-392.

[81] G. Bain, T. Müller, X. Wang, J. Papkoff, Activated β-catenin induces osteoblast differentiation of C3H10T1/2 cells and participates in BMP2 mediated signal transduction, Biochemical and biophysical research communications 301(1) (2003) 84-91.

[82] T.P. Hill, D. Später, M.M. Taketo, W. Birchmeier, C. Hartmann, Canonical Wnt/β-catenin signaling prevents osteoblasts from differentiating into chondrocytes, Developmental cell 8(5) (2005) 727-738.

[83] L. Rosanò, R. Cianfrocca, S. Masi, F. Spinella, V. Di Castro, A. Biroccio, E. Salvati, M.R. Nicotra, P.G. Natali, A. Bagnato, β-Arrestin links endothelin A receptor to β-catenin signaling to induce ovarian cancer cell invasion and metastasis, Proceedings of the National Academy of Sciences 106(8) (2009) 2806-2811.

[84] Y. Yang, Wnts and wing: Wnt signaling in vertebrate limb development and musculoskeletal morphogenesis, Birth Defects Research Part C: Embryo Today: Reviews 69(4) (2003) 305-317.

[85] K.L. Clines, G.A. Clines, DKK1 and Kremen Expression Predicts the Osteoblastic Response to Bone Metastasis, Translational oncology 11(4) (2018) 873-882.

[86] Y. Chen, H.Y. Shi, S.R. Stock, P.H. Stern, M. Zhang, Regulation of breast cancer-induced bone lesions by β-catenin protein signaling, Journal of Biological Chemistry 286(49) (2011) 42575-42584.

CHAPTER 4. BONE INTERFACE MODULATES DRUG RESISTANCE IN BREAST CANCER BONE METASTASIS[3]

This chapter describes cytokine-mediated drug resistance in 3D tissue-engineered model of breast cancer bone metastasis. The contents of this chapter have been submitted for publication.

4.1. Introduction

Breast cancer, in the advanced stage, metastasizes to the bones. It is estimated that 80-90% of breast cancer patients eventually develop and die of bone metastases [1]. Metastatic breast cancer cells interact with the bone cells to support their growth, proliferation, and chemoresistance [2]. There is currently no effective therapeutics available in clinic for bone metastases due to lack of models that could replicate the molecular events that occur in individuals with breast cancer metastasized to the bones, and failure of the scientific community to identify therapeutic targets for drug discovery. To date, cancer researchers have heavily relied on two-dimensional (2D) monolayer cell culture systems for discovery of signaling pathways and drugs. However, conventional 2D monolayer culture systems do not recapitulate cell behavior in a human body where cells exist in a three-dimensional (3D) environment, wherein cell-cell, cell-matrix interactions play a major in regulating the behavior of cancer cells [3, 4]. Although animal models provide a native 3D microenvironment for studying the molecular mechanism of various pathological processes to some extent, their species difference, immuno-deficiency, and complex disease pathogenesis most often reduce the correlation between clinical trials and animal studies. Approximately 95% of anti-cancer drug discovery attempts have failed

[3]This chapter was co-authored by S. Kar, D.R. Katti, and K.S. Katti. Sumanta Kar had the primary responsibility for preparing samples, conducting all tests, and drafting this chapter. Kalpana Katti and Dinesh Katti directed the research orientation and revised this chapter.

in the recent past due to variations in drug response between animal models and human trials [5]. Therefore, the development of accurate and efficient models to recapitulate cell-cell/cell-matrix interactions to mimic native tumor microenvironment and achieve better drug response is paramount for new drug discovery.

In recent years, 3D culture systems have received a great deal of attention owing to their ability to mimic *in vivo* tissue microenvironment, leading to improved drug response. Human adipose tissue-derived extracellular matrix scaffolds [6], decellularized porcine lung scaffolds [7], chitosan scaffolds [8], porous poly(vinyl alcohol) (PVA) and chitosan micro particles [9], microfluidics-based multicellular tumor spheroids [10], poly(ethylene glycol) (PEG)-fibrinogen hydrogel microspheres [11] have been used as *in vitro* models of breast cancer for drug screening. 3D co-culture systems have also been used in a few studies to develop *in vitro* models of breast cancer bone metastasis for evaluating drug response. For instance, Talukdar and Kundu co-cultured osteoblasts, mesenchymal stem cells (MSCs), and breast cancer cells on silk-fibroin scaffolds to simulate bone metastatic milieu and assess efficacy of anti-cancer drugs [12]. In another study, silk fibroin scaffolds-based co-culture model of osteoblasts and breast cancer cells was developed to evaluate the efficacy of targeted delivery of doxorubicin loaded folate conjugated fibroin nanoparticles [13]. In a recent study, Zhu et al. fabricated 3D-printed co-culture model of osteoblasts and breast cancer cells to evaluate drug-resistance of breast cancer cells against chemotherapeutic drug 5-Fluorouracil [14]. Although these studies have been able to shed light on disease pathogenesis regarding cytokine production, altered gene/protein expression, and targeted therapies; one of the major limitations of co-culture systems is simultaneous seeding of both cells on scaffolds while colonization of breast cancer cells in bone microenvironment is mediated by chemokines, and growth factors released by already growing

bone cells, stromal cells etc. In addition, the bone microenvironment is not created at the time of cancer cell arrival and thus the bone metastasis condition is not recapitulated. Recent studies based on X-ray experiments have also indicated that initiation of metastasis occurs at immature bone sites [15]. Further, the migration pattern of breast cancer cells (MDA-MB 231) is influenced by substrate anisotrpy [16]. To this end, we implemented a sequential culture system on nanoclay scaffolds to provide a microenvironment conducive to bone metastases [17-20]. Nanoclay scaffolds have high porosity with interconnected pores [21] which contribute to the high surface area-to-volume ratio for cell-biomaterials interaction [22]. Nanoclay scaffolds also have high compressive strength (~2.495 MPa) which can provide matrix stiffness, leading to improved focal adhesions, cytokine production, and metastatic dissemination of breast cancer [23-25]. Furthermore, we have observed earlier, that nanoclay scaffolds provide an acquiescent environment for long term culture of cancer cells, and cancer cells cultured on these scaffolds show *in vivo* like tumor morphology [17], which might contribute towards drug resistance and tumor aggression. Human MSCs are also reported to differentiate into osteoblasts on nanoclay scaffolds [21]. These observations mentioned above make nanoclay scaffolds a good candidate as testbeds to study breast cancer bone metastasis.

We have used both computational and experimental approaches to design polymer-clay nanocomposites (PCNs) for bone tissue engineering applications [21, 26-29]. A few studies also reported the use of commercially available nanoclays for bone tissue engineering applications [30-33]. In our previous study, we demonstrated mineralized bone-like tissue formation via vesicular delivery by osteogenically differentiated MSCs on nanoclay scaffolds without the use of osteogenic supplements [21, 34]. We have recently shown mesenchymal to epithelial transition of prostate and breast cancer cells in sequential culture of MSCs with prostate and

breast cancer cells on nanoclay scaffolds, respectively [17-20, 35, 36]. In another study, we showed involvement of Wnt/β-catenin Signaling in breast cancer mediated osteogenesis at metastatic bone site [37]. We also reported spectral biomarkers of breast cancer progression at metastatic bone site using non-invasive IR spectroscopy [38]. In a recent study, the role of prostate cancer phenotype on bone mineralization at metastases was also described [39].

Paclitaxel (PTX), a chemotherapeutic drug that binds to beta-tubulin and stabilizes microtubule breakdown, leading to cell cycle arrest at G2/M phase [40]. It is currently used in the treatment for many cancers, including breast, lung, ovarian, bladder, and prostate cancer [41-43]. However, in recent years, resistance to paclitaxel has become a major clinical issue, leading to treatment failures and recurrences in patients. Despite many attempts, the mechanism of paclitaxel is yet to be demystified. Studies have shown that resistance can occur from altered expression of apoptosis regulatory proteins (p53, Bcl-2) [44, 45], and overexpression of ATP binding cassette (ABC) transporters/ multidrug resistance-related proteins such as multidrug resistance-associated protein 1 (MRP1), ATP-binding cassette subfamily G member 2 (ABCG2) [46, 47].

Interleukin-6 (IL-6), a pro-inflammatory cytokine produced in the tumor microenvironment by stromal cells, fibroblasts, and cancer cells [48]. Binding of IL-6 to its receptor IL-6R on the cell membrane activates Janus Kinase 2 (JAK2) kinases. Activated JAK2 mediates phosphorylation, dimerization, and nuclear translocation of Signal Transducer and Activator of Transcription 3 (STAT3)[49]. STAT3 signaling mediates the expression of various genes, including p53[50], Bcl-2[51], MRP1[52], and ABCG2 [53]. Bcl-2 and p53 are associated with regulation of apoptosis [54] while overexpression of drug transporters MRP1, ABCG2 has been shown to mediate efflux of drugs from cancer cells, thus decreasing intracellular drug

concentration leading to drug-resistance [55]. Activation of IL-6/STAT3 signaling pathway has been shown to mediate chemoresistance in many cancers, including breast [56, 57], ovarian [58], colorectal [59], prostate [60, 61], and gastric cancer [62]. To our knowledge, no studies have been carried out to establish the role of cytokines such as IL-6 in acquired drug resistance of breast cancer cells in the context of bone metastasis to date.

In the present study, we hypothesized that the 3D *in vitro* model would provide better physiological and biological cues to recapitulate *in vivo* bone metastatic microenvironment in regards to cytokine-mediated drug resistance than 2D monolayer cultures. Thus, this study aimed to develop an effective 3D *in vitro* model with enhanced resistance to paclitaxel using 3D bone-mimetic nanoclay scaffolds, to shed light on the underlying mechanism of drug resistance in breast cancer bone metastasis.

4.2. Materials and Methods

4.2.1. Cell Lines, Culture Maintenance, and Materials

Polycaprolactone (PCL) (average Mn 80,000), 5-aminovaleric acid, paclitaxel, cell proliferation reagent WST-1, calcium chloride ($CaCl_2$), sodium phosphate (Na_2HPO_4), fish skin gelatin (FSG), TritonX-100, Tween20, 4′,6-diamidino-2-phenylindole (DAPI), and 1,4-dioxane were purchased from Sigma Aldrich. Na-MMT clay was obtained from Clay Minerals Respiratory at the University of Missouri. Human mesenchymal stem cells (MSCs) (PT-2501) (Lonza) were maintained in complete growth medium (MSCGM™ SingleQuots™ (PT-4105) was added to MSC basal medium (MSCBM™, PT-3238) to obtain complete growth medium) from Lonza. Human breast cancer cell lines MDA-MB-231 (HTB-26) (shortened as MM 231), MCF-7 (HTB-22), Fetal Bovine Serum (FBS), and Eagle's Minimum Essential Medium (EMEM) were purchased from American Type Culture Collection (ATCC). Hyclone™ Dulbecco's Modified

Eagle medium Nutrient Mixture F-12 DMEM-F-12(1:1), Corning™ Phosphate Buffered Saline (PBS), and 4% Paraformaldehyde in PBS (PFA) were purchased from VWR. Gibco™ penicillin-streptomycin antibiotic solution (P/S), Gibco™ human recombinant insulin, Applied Biosystems™ Fast SYBR Green, and human Osteocalcin (OCN) ELISA kit were purchased from Invitrogen. MM 231 cells were cultured in DMEM-F-12(1:1), 10% FBS, and 1% P/S. MCF-7 cells were grown in Eagle's Minimum Essential Medium (EMEM), 10% FBS, 0.01 mg/ml human recombinant insulin, and 1% P/S. All cell cultures were maintained at 37 ºC and 5% CO_2 in a humidified incubator. Human Interleukin-6 (IL-6) ELISA and ApoScreen® Annexin V-FITC kits were purchased from RayBiotech and SouthernBiotech, respectively. Direct-zol RNA MiniPrep kit was purchased from Zymo Research. Anti-pSTAT3 (Y705) (Abcam), anti-MRP1 (Abcam), anti-p53 (Novus), anti-Bcl-2 (Novus) primary antibodies, secondary antibodies, and other reagents used were of analytical grade.

4.2.2. Preparation of PCL/*in situ* HAPclay 3D Scaffolds

PCL/*in situ* HAPclay scaffolds were prepared as previously reported [21]. In brief, we modified clay with 5-aminovaleric acid as described previously to increase d-spacing of clay [29, 63]. Then, we biomineralized hydroxyapatite (HAP) into intercalated nanoclay galleries to obtain *in situ* HAPclay. Further, we dissolved PCL in 1, 4-dioxane, added 10% *in situ* HAPclay to PCL solution, subjected the resultant solution to freeze-extraction to obtain *in situ* HAPclay scaffolds, as described previously [21].

4.2.3. Cell Culture

Scaffolds (~12 mm diameter and ~3 mm thickness) were sterilized under UV light for 45 mins followed by immersion in 70% ethanol for 12 h. Then, scaffolds were washed in PBS, placed in 24-well plates containing culture medium, and stored in humidified 5% CO_2 incubator

at 37 ºC until further use. Scaffolds were seeded with 5 x 10^4 MSCs per scaffold and cultured for 23 days to obtain bone-like extracellular matrix (ECM) formation. Then, we seeded 5 x 10^4 breast cancer cells (MM 231/MCF-7) per scaffold on bone ECM formed on the scaffolds and cultured in 1:1 MSCs and breast cancer cell medium [Figure 4.2(A)]. For 2D cultures, 5 x 10^4 breast cancer cells (MM 231/MCF-7) were cultured on tissue culture polystyrene (TCPS).

4.2.4. Cellular Morphology

Cell-seeded scaffolds were first fixed with 2.5% glutaraldehyde overnight followed by dehydration in a series of ethanol washes (10%, 30%, 50%, 70%, and 100%). Then, samples were dried in hexamethyldisilazane, gold sputter coated before imaging in with a JSM-6490LV SEM (JEOL, Tokyo, Japan).

4.2.5. Analysis of Drug Response

3D sequential cultures of MSCs with breast cancer cells (at day (23+10)) and 2D cultures breast cancer cells (at day 10) were serum starved for 24 h, and subsequently treated with 0.2, 2, 20, and 200 µM of paclitaxel for 48 h. Cell viability of drug treated and control (untreated) samples was determined using a WST-1 assay. Half maximal inhibitory concentration (IC_{50}) values for 2D and 3D cultures were calculated with Graph Pad Prism (v7.04) using nonlinear regression analysis.

4.2.6. Flow Cytometric Analysis of Apoptosis

After treating 2D cultures of breast cancer cells and 3D sequential cultures of MSCs with breast cancer cells for 24 h with their respective IC_{50} concentrations, cells were harvested, thoroughly washed in cold PBS, resuspended cells in cold Annexin Binding Buffer to a concentration of 1 x 10^6 cells/ml, labeled with Propidium Iodide (PI) and Fluorescein

isothiocyanate (FITC)- conjugated Annexin V, and analyzed using BD Accuri C6 Flow cytometer. Data were analyzed using ACEA NovoExpress™ software.

4.2.7. ELISA Assay

Cell-seeded scaffolds and 2D cultures were serum-starved for 48 h before harvesting of protein. Culture medium was collected from scaffolds, at day 0 (MSCs), at day 23 (MSCs), at day (23+10) (MSCs + breast cancer cells sequential cultures), and 2D breast cancer cultures (at day 10), and assayed for OCN and IL-6 content, respectively, by ELISA kits according to manufacturer's instructions.

4.2.8. Alizarin Red S Staining (ARS)

ARS staining was performed according to the procedure described earlier [35]. Briefly, Cell-seeded scaffolds were fixed in 4% paraformaldehyde for 30 min, washed in PBS, and stained with 2% Alizarin Red S (ARS) for 2.5 min. Then, stained scaffolds were washed in PBS, dried at room temperature, and observed under stereoscopic zoom microscope (Ash Technologies). We further solubilized the stain and quantified it using a microplate absorbance reader at 405 nm.

4.2.9. Gene Expression Studies

Total RNA was isolated from cell-seeded scaffolds and 2D cultures using Direct-zol RNA MiniPrep kit. Isolated RNA was reverse transcribed to synthesize cDNA using M-MLV reverse transcriptase (Promega), random primers, and thermal cycler (Applied Biosystems). Further, Real-Time Polymerase Chain Reaction (RT-PCR) was performed using forward primer, reverse primer, cDNA, SYBR Green dye, and a thermal profile with a holding stage (2 min at 50 °C, 10 min at 95 °C) and a cycling stage (40 cycles of 15 s at 95 °C, and 1 min at 60 °C) on 7500 Fast Real-Time System (Applied Biosystems). The mRNA expression of OCN was

evaluated at day 0 and day 23 in MSCs grown in scaffolds. We also analyzed the mRNA expression of IL-6, p53, Bcl-2, MRP1, and ABCG2 evaluated in 2D monolayer cultures of breast cancer cells (at day 10) and 3D sequential cultures of MSCs with breast cancer cells (at day (23+10)). All the mRNA expressions were normalized to housekeeping gene glyceraldehyde-3-phosphate dehydrogenase (GAPDH). Target gene expressions were calculated using comparative C_t method ($2^{-\Delta\Delta Ct}$). Table 4.1 lists the sequence of primers used.

Table 4.1. The sequence of primers used for the quantitative real-time PCR experiment

Gene	Forward primer	Reverse primer
GAPDH	5'-CATCTTCTTTTGCGTCGCCA-3'	5'-TTAAAAGCAGCCCTGGTGACC-3'
p53	5'CGGGATCCATGGAGGAGCCGCAGTCAGAT-3'	5'CCGCTCGAGTTTCTGGGAAGGGACAGAAGA-3'
Bcl-2	5'-GGCTGGGATGCCTTTGTG-3'	5'-CAGCCAGGAGAAATCAAACAGA-3'
MRP1	5' GTCGGGGCATATTCCTGGC-3'	5' GGGCATCCTCTTTTAAGGCTG-3'
ABCG2	5'-TGGCTGTCATGGCTTCAGTA-3'	5'-GCCACGTGATTCTTCCACAA-3
IL-6	5′-GATGGCTGAAAAAGATGGATGC-3′	5′-TGGTTGGGTCAGGGGTGGTT-3′
OCN	5'-GTG ACG AGT TGG CTG ACC-3'	5'-TGG AGA GGA GCA GAA CTG G-3'

4.2.10. Immunofluorescence Staining

Cell-seeded scaffolds and 2D cultures were fixed in 4% paraformaldehyde in PBS for 30 min, permeabilized in 0.2% TritonX-100 in PBS for 5 min, and blocked with 0.2% FSG for 45 min. Then, the samples were incubated overnight at 4 °C with primary antibodies diluted in a blocking buffer (0.2% FSG in PBS containing 0.02% Tween20) at a dilution of 1:100. The samples were subsequently incubated with Alexa Flour 488 conjugated secondary antibodies corresponding to origin of the primary antibodies used for 45 mins at 25 °C. Nuclei were stained with DAPI. The stained samples were observed with Zeiss AxioObserver.Z1 LSM 700.

4.2.11. Statistical Analysis

Data are presented as mean ± standard derivation (n=3). Statistical significance (p-value) among multiple comparisons was determined using one-way ANOVA followed by *post*

hoc Tukey test, while statistical significance (p-value) between two groups was determined using unpaired *Student's t-test*, using GraphPad Prism v7.04. $p<0.05$ was considered statistically significant.

4.3. Results and Discussion

4.3.1. Bone Tissue Formation on 3D Nanoclay Scaffolds

To evaluate bone formation on 3D nanoclay scaffolds, we analyzed mRNA expression of late -stage bone marker OCN and observed a ~3-fold increase at day 23 [Figure 4.1(A)] as opposed to day 0, which was further substantiated by quantification of OCN release in culture medium [Figure 4.1(B)]. Our observations are in good agreements with previous findings on OCN being a major regulator of osteoblasts maturation [64]. We also assessed calcium deposition on scaffolds using ARS staining and noticed intense ARS staining at day 23 as compared to day 0, confirming deposition of inorganic matrix by osteogenically differentiated MSCs on nanoclay scaffolds, which was further substantiated by quantification of released ARS [Figure 4.1(C)].

4.3.2. 3D Sequential Culture of MSCs with Breast Cancer Cells Facilitates *in vitro* Growth of *in vivo*-like Tumoroids

To evaluate morphology of cancer cells grown in sequential cultures with MSCs, we performed SEM imaging. Sequential culture of MSCs with MCF-7 gave rise to tumoroids while sequential culture of MSCs with MM 231 showed poorly connected disorganized cellular clusters as shown in Figure 4.2(B).

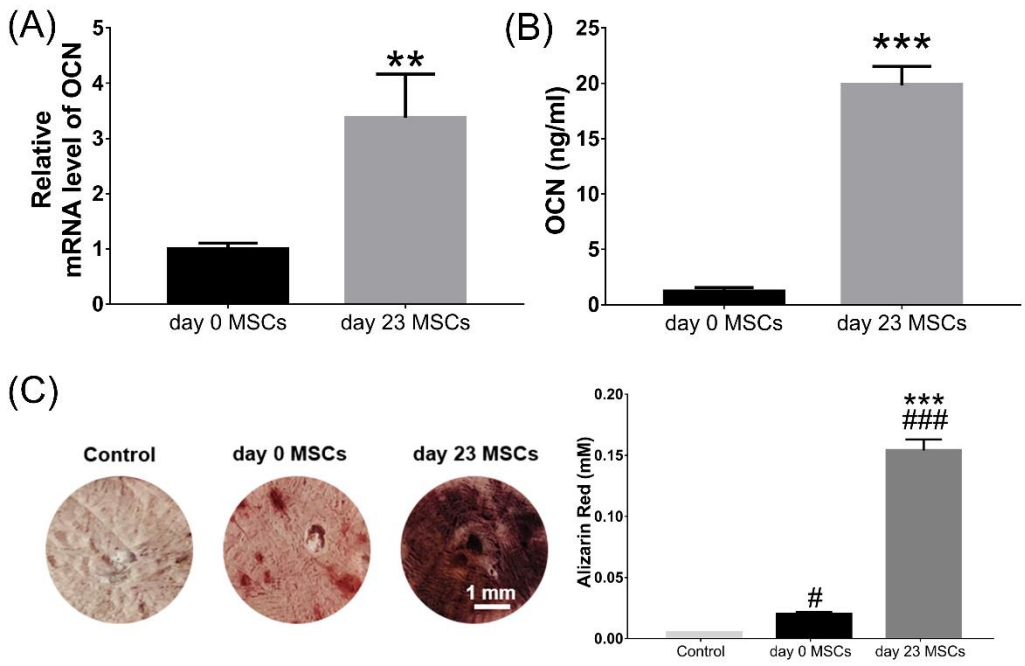

Figure 4.1. (A) Quantitative real-time PCR of gene expression for late-stage osteogenic marker OCN. (B) OCN released into culture medium, indicative of bone maturation. **$p < 0.01$, and ***$p < 0.001$ indicate significant difference between day 0 and day 23 MSCs constructs. (C) Alizarin Red S staining and quantification absorbance assay of day 0 and day 23 MSCs constructs. Scale bar, 1 mm. $^{\#}p < 0.05$, and $^{\#\#\#}p < 0.001$ indicate significant difference between control and MSCs seeded constructs. ***$p < 0.001$ indicates significant difference between day 0 and day 23 MSCs constructs.

4.3.3. 3D Sequential Culture of MSCs with Breast Cancer Cells Requires Higher Drug Concentrations than 2D Culture of Breast Cancer Cells to Achieve Comparable Reduction in Cell Viability

The cytotoxic effect of paclitaxel on 2D and 3D cultures was evaluated using a WST-1 assay. Cells were treated with 0.2, 2, 20, and 200 µM of paclitaxel for 48 h.

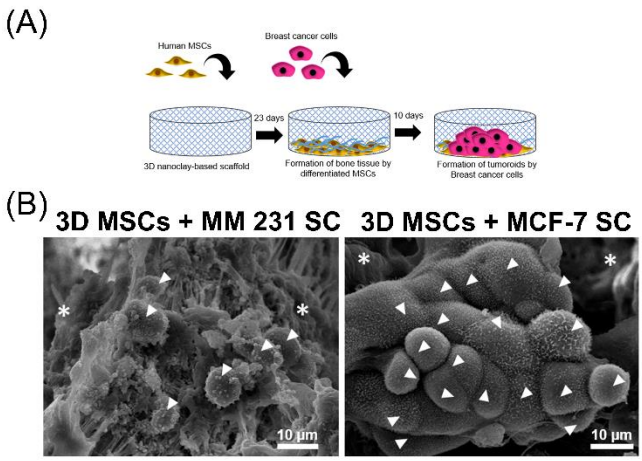

Figure 4.2. (A) Schematic showing the steps of sequential culture experiment. (B) Morphology of breast cancer cells MM 231 and MCF-7 grown on bone-mimetic nanoclay scaffolds. Arrows indicate cells while * indicate scaffold.

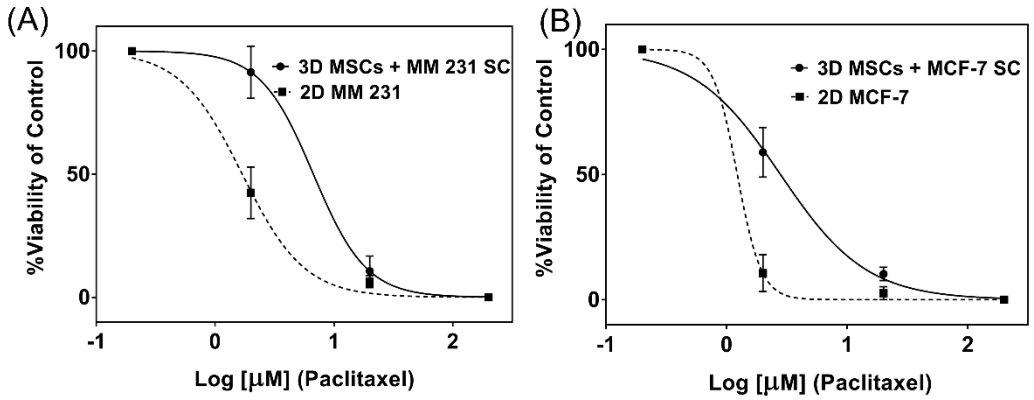

Figure 4.3. (A & B) Cytotoxic effects of paclitaxel in 2D cultures breast cancer cells (MM 231 & MCF-7) and 3D sequential cultures of MSCs with breast cancer cells (MM 231 & MCF-7). Cells were treated with 0.2, 2, 20, and 200 µM of paclitaxel for 48 h. Cell viability was evaluated using a WST-1 assay. Half maximal inhibitory concentration (IC_{50}) values were calculated on Graph Pad Prism using nonlinear regression analysis.

We observed a dose-dependent cytotoxic effect of paclitaxel on both 2D and 3D cultures of MM 231 and MCF-7 cells. IC_{50} was calculated from dose-response study using curve-fitting. Paclitaxel inhibited the proliferation of 2D MM 231 and 3D MSCs +MM 231 SC, with IC_{50} values of 1.69 µM and 6.71 µM, respectively, following 48 h incubation. Further, IC_{50} values for 2D MCF-7 and 3D MSCs + MCF-7 SC were 1.23 µM and 2.80 µM, respectively [Figure 4.3 &

Table 4.2]. Overall, these data demonstrate that 3D sequential culture of MSCs with breast cancer required higher concentrations of paclitaxel than 2D culture of breast cancer cells to achieve comparable reduction in cell viability.

Table 4.2. IC_{50} values of paclitaxel in 2D breast cancer cells (MM 231 & MCF-7) and 3D sequential cultures of MSCs with breast cancer cells (MM 231 & MCF-7).

Type of Culture	IC_{50} (μM)
2D MM 231	1.69
2D MCF-7	1.23
3D MSCs +MM 231 SC	6.71
3D MSCs +MCF-7 SC	2.80

$IC_{50,}$ half maximal inhibitory concentration.

4.3.4. 3D Sequential Culture of MSCs with Breast Cancer Cells Alters Expression of Apoptosis Regulatory Proteins and Increases Resistance to Apoptosis in Response to Paclitaxel

To assess the ability of paclitaxel to induce apoptosis in 2D and 3D cultures, cells were subjected to their respective IC_{50} concentrations of paclitaxel for 24 h, followed by flow cytometric analysis of apoptosis using Annexin V-FITC apoptosis assay. As shown in Figure 4.4, apoptosis assay showed a substantial difference between 2D and 3D cultures regarding the rate of apoptosis induction. The rate of apoptosis to paclitaxel was 15.64 ± 0.99 % (versus 9.44 ± 0.84 % in 3D MSCs + MM 231 SC) and 28.57 ± 0.60 % (versus 10.6 ± 0.91 % in 3D MSCs + MCF-7 SC) in 2D cultures of MM 231 and MCF-7, respectively, indicating a significant increase in resistance to apoptosis in response to paclitaxel in 3D sequential cultures of MSCs with breast cancer cells, compared to 2D cultures.

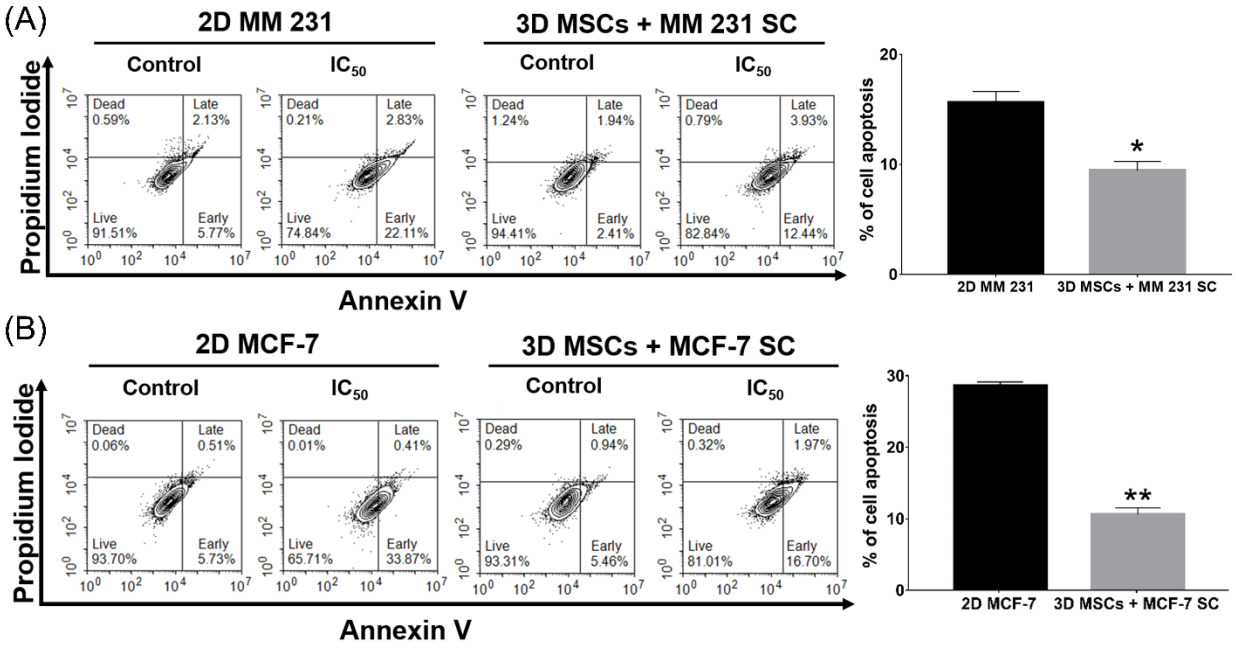

Figure 4.4. (A & B) Representative dot plot presenting the fluorescence channel analysis of 2D MM 231 & 3D MSCs + MM 231 SC, and 2D MCF-7 & 3D MSCs + MCF-7 SC cells following double staining with Annexin V and Propidium Iodide. Cells were treated with their respective IC_{50} values mentioned in Table 4.2 for 24 h and stained with Annexin V (horizontal) and Propidium Iodide (vertical axis) before analysis with flow cytometry. The percentage of cell apoptosis was calculated by subtracting control (% early apoptosis) from IC_{50} (% early apoptosis) for each culture type. *$p < 0.05$ indicates significant differences between 2D MM 231 and 3D MSCs + MM 231 SC. **$p < 0.01$ indicates significant difference between 2D MCF-7 and 3D MSCs + MCF-7 SC.

To determine the mechanism of resistance to apoptosis in 3D cultures, we analyzed the expression of anti-apoptotic Bcl-2 and tumor suppressor p53 proteins. We observed a ~3.42-fold increase in Bcl-2 expression along with a ~3.15-fold downregulation in p53 expression at mRNA levels in 3D MSCs + MM 231 SC, as compared to 2D cultures while 3D MSCs + MCF-7 SC exhibited a ~2.70-fold increase in Bcl-2 expression accompanied by a ~2.20-fold downregulation in p53 expression at mRNA levels as opposed to 2D cultures [Figure 4.5] . We further performed immunostaining of Bcl-2 and p53 and found results to be in good agreement with mRNA expression [Figure 4.5].

4.3.5. 3D Sequential Culture of MSCs with Breast Cancer Cells Enhances Expression of Multi-Drug Resistance-related Genes

Multidrug resistance has long been a major roadblock in successful cancer chemotherapy. Increasing evidence supports that overexpression of ABC drug transporters such as MRP1, ABCG2 mediate efflux of drugs from cancer cells, thus decreasing intracellular drug concentration leading to drug-resistance [46, 47, 65]. To investigate the effects of 3D bone-mimetic microenvironment on the expression of multi-drug resistance-related genes, we examined the expression of MRP1 and ABCG2 on cells grown in 2D and 3D sequential cultures. We found a ~1.80-fold and a ~1.89-fold increase in MRP1 and ABCG2 expression at mRNA levels, respectively, in 3D MSCs + MM 231 SC while 3D MSCs + MCF-7 SC exhibited a ~1.62-fold increase in MRP1 expression together with a ~1.89-fold upregulation in ABCG2 expression at mRNA levels, as compared to their respective 2D cultures [Figure 4.6 (A), (B)]. We also performed immunostaining of MRP1 and found results in good agreement with mRNA levels [Figure 4.6(C)].

4.3.6. 3D Tumor Microenvironment-secreted Cytokine IL-6 may Promote Drug-Resistance against Paclitaxel

The observations mentioned above prompted us to evaluate the involvement of STAT3 signaling because all the genes evaluated in present study are directly or indirectly related to STAT3 signaling pathway [52, 53, 66]. Further, tumor microenvironment releases various cytokines including IL-6, and IL-6 has been shown to activate IL-6/STAT3 signaling [48, 49].

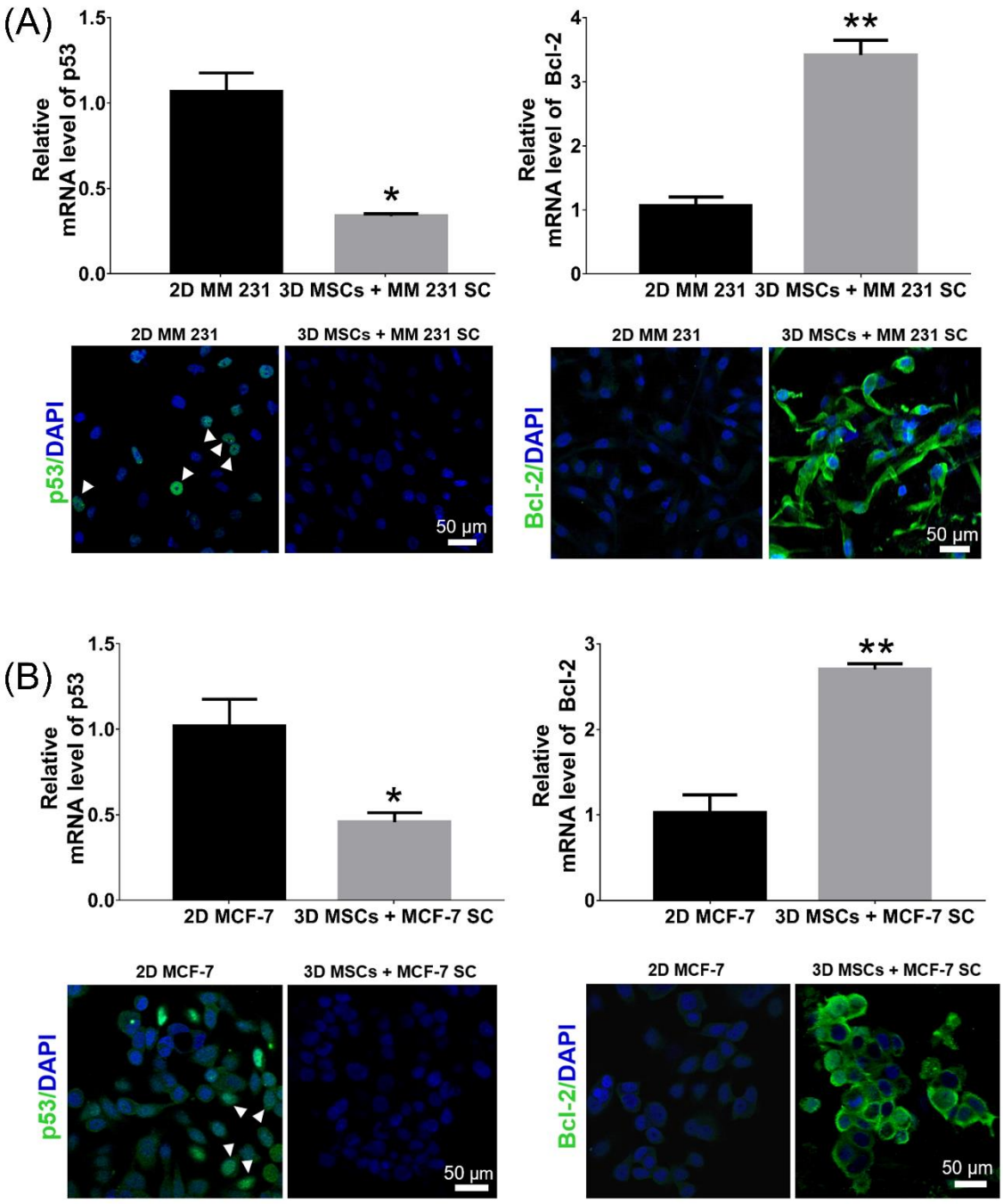

Figure 4.5. (A & B) Quantitative real-time PCR of gene expression for p53 and Bcl-2. *$p < 0.05$, **$p < 0.01$ indicate significant difference between significant difference between 2D cultures of breast cancer cells (MM 231 & MCF-7) and 3D sequential cultures of MSCs with breast cancer cells (MM 231 & MCF-7). Immunofluorescence staining for p53 and Bcl-2 of 2D breast cancer cultures (MM 231 & MCF-7) and 3D sequential cultures of MSCs with breast cancer cells (MM 231 & MCF-7). Arrows indicate nuclear localization of p53. Scale bars, 50 µm.

Previous studies have shown the involvement of IL-6/STAT3 signaling pathway in mediating chemoresistance in breast cancer [56, 57]. Also, a few recent studies illustrated that growing cells in 3D cultures could lead to elevated levels of cytokine production, which can have a significant influence on signaling pathways [67, 68]. In accordance with these observations, we noticed a ~2.10-fold and a ~1.23-fold increase in IL-6 mRNA levels, respectively, in 3D MSCs + MM 231 SC and 3D MSCs + MCF-7 SC as compared to their respective 2D cultures, which was further substantiated by quantifying release of IL-6 in culture medium [Figure 4.7(A, B)].

We further observed intense immunostaining of pSTAT3 (Y705) in 3D sequential cultures of MSCs with both breast cancer cells as opposed to their respective 2D cultures, confirming to activation of STAT3 [Figure 4.7(A),(B)]. In summary, our results showed that breast cancer cells grown in 3D bone-mimetic scaffolds exhibited altered physiological and biochemical properties including increased drug resistance, inhibited rate of apoptosis, enhanced expression of multidrug resistance-related genes, and elevated levels of cytokine and its downstream effectors associated with drug resistance, as opposed to 2D monolayer cultures. Most importantly, STAT3, a potential biomarker for chemoresistance in many cancers, was activated in our 3D breast cancer bone metastasis model. Thus, our data suggest that the 3D *in vitro* model is a promising testbed for screening new therapeutics for breast cancer bone metastasis.

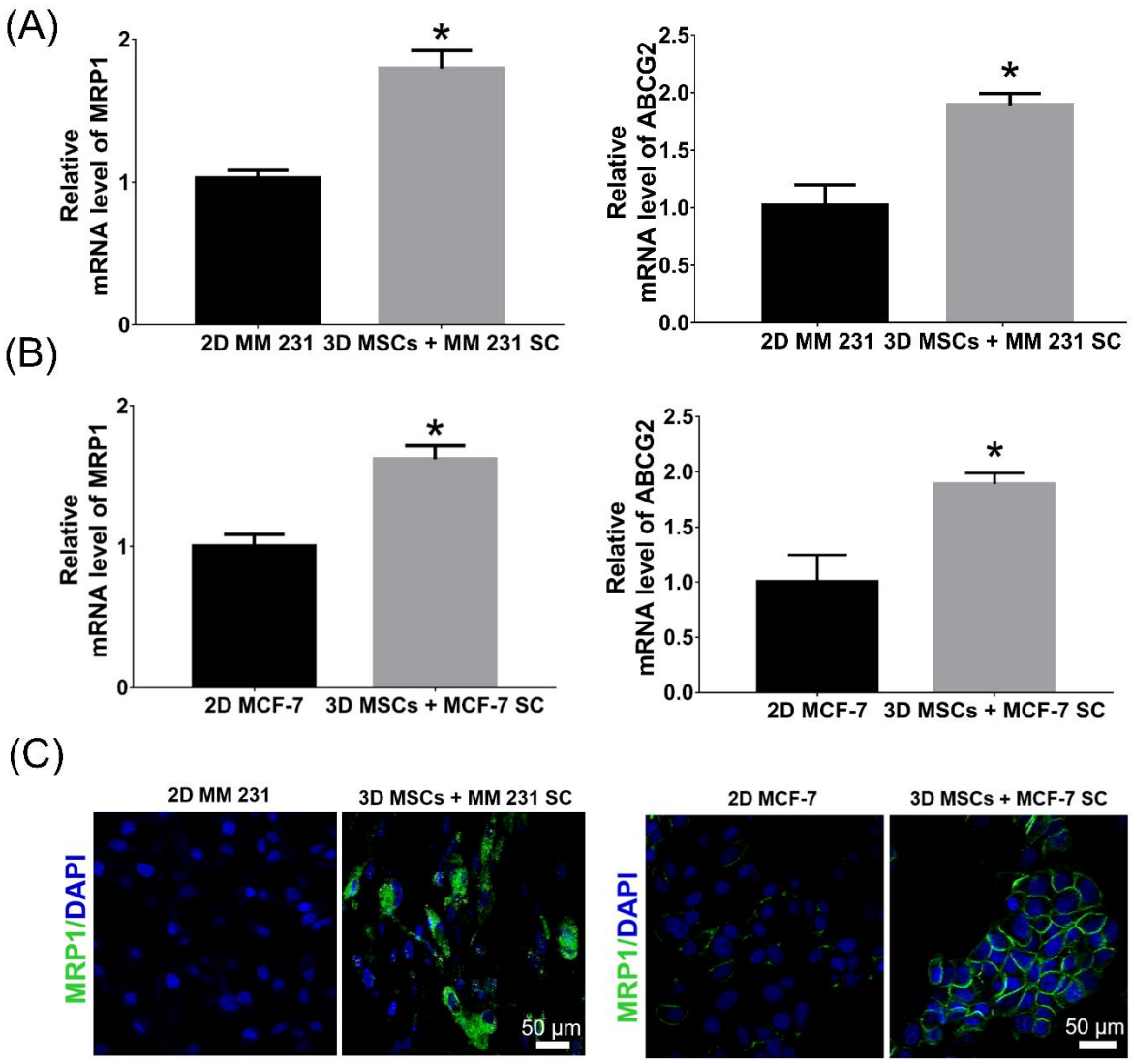

Figure 4.6. (A & B) Quantitative real-time PCR of gene expression for MRP1 and ABCG2. *$p < 0.05$ indicates significant difference between significant difference between 2D cultures of breast cancer cells (MM 231 & MCF-7) and 3D sequential cultures of MSCs with breast cancer cells (MM 231 & MCF-7). (C) Immunofluorescence staining for MRP1 of 2D breast cancer cultures (MM 231 & MCF-7) and 3D sequential cultures of MSCs with breast cancer cells (MM 231 & MCF-7). Scale bars, 50 µm.

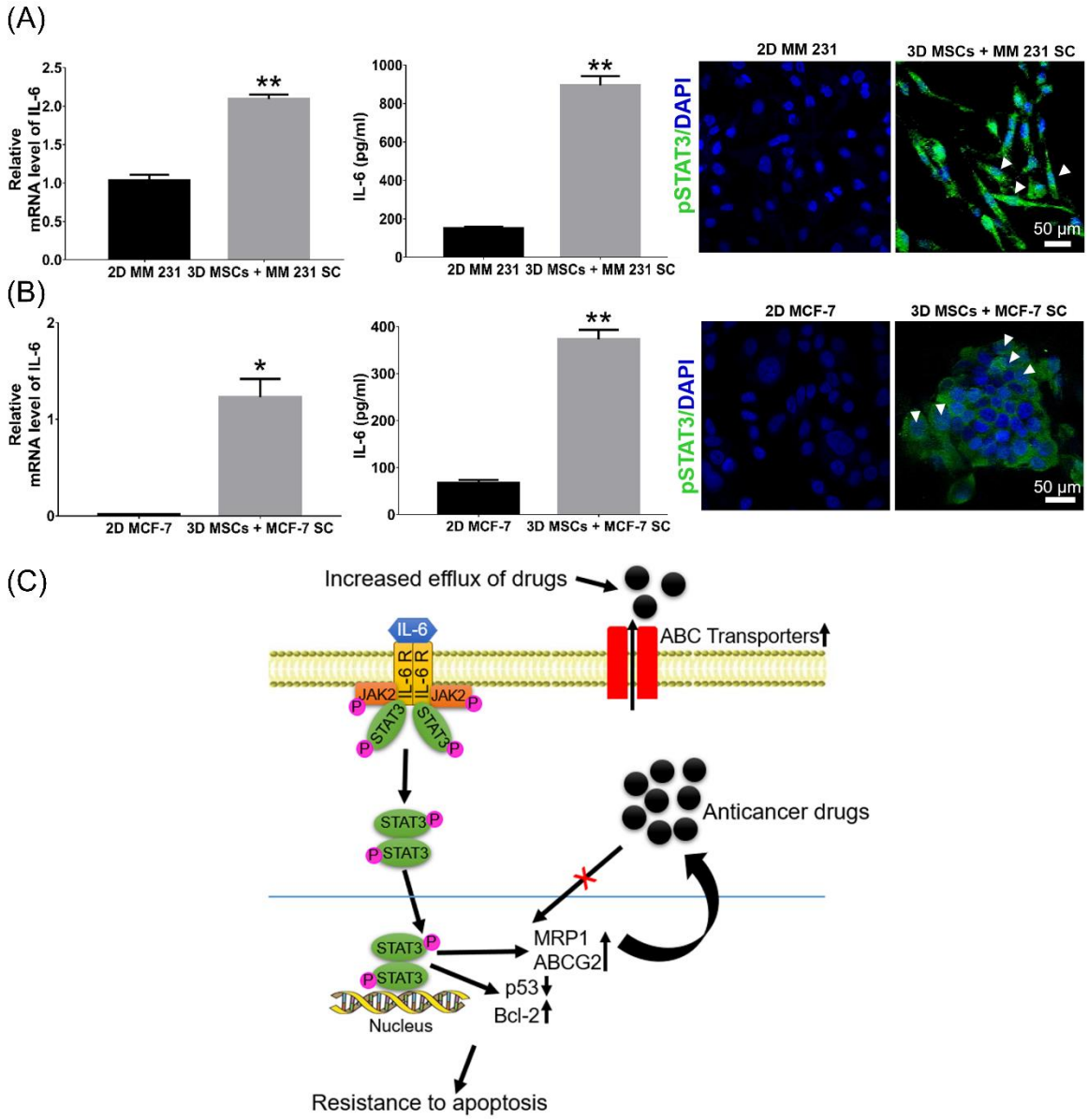

Figure 4.7. (A & B) Quantitative real-time PCR of gene expression for IL-6. ELISA Assay for quantification of released IL-6 into culture medium. *$p < 0.05$, **$p < 0.01$ indicate significant difference between 2D cultures of breast cancer cells (MM 231 & MCF-7) and 3D sequential cultures of MSCs with breast cancer cells (MM 231 & MCF-7). Immunofluorescence staining for pSTAT3 (Y705) of 2D breast cancer cultures (MM 231 & MCF-7) and 3D sequential cultures of MSCs with breast cancer cells (MM 231 & MCF-7). Arrows indicate nuclear localization of pSTAT3. Scale bars, 50 µm. (C) Proposed mechanism of IL-6/STAT3 mediated drug-resistance in 3D sequential cultures MSCs with breast cancer cells.

4.4. Conclusion

In the present study, we have used a previously developed *in vitro* model using 3D bone-mimetic nanoclay scaffolds that mimic *in vivo* bone metastatic microenvironment to evaluate drug efficacy demonstrating the use of the scaffold as a breast cancer metastasis testbed. Enhanced drug resistance to paclitaxel was observed at the bone metastasis site as compared to the cells not at the bone site. Our results showed that breast cancer cells grown at 3D metastatic bone site not only require higher drug concentrations than 2D cultures to achieve a comparable reduction in cell viability but also exhibited increased resistance to apoptosis in response to paclitaxel. Upon exploring the underlying mechanism of drug resistance, we noticed that elevated levels of IL-6 secretion in the breast cancer culture at 3D metastatic bone site activated STAT3 signaling, which inhibited apoptosis by upregulating expression of anti-apoptotic Bcl-2 along with a substantial reduction in expression of tumor suppressor gene p53 and upregulated expression of multidrug resistance-related genes (MRP1, ABCG2) rendering cancer cells grown in 3D cultures drug-resistant. Taken together, our data demonstrate that the 3D bone-mimetic nanoclay scaffolds-based *in vitro* tumor model is a promising testbed for screening new therapeutics for breast cancer bone metastasis. Also, our results indicate that the bone interface at metastasis of breast cancer modulates drug resistance in breast cancer cells.

4.5. Acknowledgements

Authors acknowledge the financial support from NDSU Grand Challenges grant for the ‘Center for Engineered Cancer Test-Beds’ (CECT) for completion of this research study. We also acknowledge Dr. Scott Payne for his help with SEM imaging. We want to acknowledge the support from ND EPSCoR for tissue engineering laboratory.

4.6. References

[1] A. Lipton, R. Uzzo, R.J. Amato, G.K. Ellis, B. Hakimian, G.D. Roodman, M.R. Smith, The science and practice of bone health in oncology: managing bone loss and metastasis in patients with solid tumors, Journal of the National Comprehensive Cancer Network 7(Suppl 7) (2009) S-1.

[2] Y. Kang, P.M. Siegel, W. Shu, M. Drobnjak, S.M. Kakonen, C. Cordón-Cardo, T.A. Guise, J. Massagué, A multigenic program mediating breast cancer metastasis to bone, Cancer cell 3(6) (2003) 537-549.

[3] E. Cukierman, R. Pankov, D.R. Stevens, K.M. Yamada, Taking cell-matrix adhesions to the third dimension, Science 294(5547) (2001) 1708-1712.

[4] E. Cukierman, R. Pankov, K.M. Yamada, Cell interactions with three-dimensional matrices, Current opinion in cell biology 14(5) (2002) 633-640.

[5] J.A. DiMasi, H.G. Grabowski, Economics of new oncology drug development, Journal of Clinical Oncology 25(2) (2007) 209-216.

[6] L.W. Dunne, Z. Huang, W.X. Meng, X.J. Fan, N.Y. Zhang, Q.X. Zhang, Z.G. An, Human decellularized adipose tissue scaffold as a model for breast cancer cell growth and drug treatments, Biomaterials 35(18) (2014) 4940-4949.

[7] W. Li, X. Hu, S. Yang, S. Wang, C. Zhang, H. Wang, Y.Y. Cheng, Y. Wang, T. Liu, K. Song, A novel tissue-engineered 3D tumor model for anti-cancer drug discovery, Biofabrication 11(1) (2018) 015004.

[8] H.K. Dhiman, A.R. Ray, A.K. Panda, Three-dimensional chitosan scaffold-based MCF-7 cell culture for the determination of the cytotoxicity of tamoxifen, Biomaterials 26(9) (2005) 979-986.

[9] J.L. Horning, S.K. Sahoo, S. Vijayaraghavalu, S. Dimitrijevic, J.K. Vasir, T.K. Jain, A.K. Panda, V. Labhasetwar, 3-D tumor model for in vitro evaluation of anticancer drugs, Molecular pharmaceutics 5(5) (2008) 849-862.

[10] C.S. Shin, B. Kwak, B. Han, K. Park, Development of an in vitro 3D tumor model to study therapeutic efficiency of an anticancer drug, Molecular pharmaceutics 10(6) (2013) 2167-2175.

[11] S. Pradhan, J.M. Clary, D. Seliktar, E.A. Lipke, A three-dimensional spheroidal cancer model based on PEG-fibrinogen hydrogel microspheres, Biomaterials 115 (2017) 141-154.

[12] S. Talukdar, S.C. Kundu, Engineered 3D Silk-Based Metastasis Models: Interactions Between Human Breast Adenocarcinoma, Mesenchymal Stem Cells and Osteoblast-Like Cells, Advanced Functional Materials 23(42) (2013) 5249-5260.

[13] B. Subia, T. Dey, S. Sharma, S.C. Kundu, Target Specific Delivery of Anticancer Drug in Silk Fibroin Based 3D Distribution Model of Bone-Breast Cancer Cells, Acs Applied Materials & Interfaces 7(4) (2015) 2269-2279.

[14] W. Zhu, B. Holmes, R.I. Glazer, L.G. Zhang, 3D printed nanocomposite matrix for the study of breast cancer bone metastasis, Nanomedicine: Nanotechnology, Biology and Medicine 12(1) (2016) 69-79.

[15] F. He, A.E. Chiou, H.C. Loh, M. Lynch, B.R. Seo, Y.H. Song, M.J. Lee, R. Hoerth, E.L. Bortel, B.M. Willie, G.N. Duda, L.A. Estroff, A. Masic, W. Wagermaier, P. Fratzl, C. Fischbach, Multiscale characterization of the mineral phase at skeletal sites of breast cancer metastasis, Proceedings of the National Academy of Sciences of the United States of America 114(40) (2017) 10542-10547.

[16] J. Dai, Y. Yang, J. Gong, Y. Yao, Biointerface anisotropy modulates migration of breast cancer cell, Colloids and Surfaces: B In press, available online (2020).

[17] S. Kar, M.D.S. Molla, D.R. Katti, K.S. Katti, Tissue-engineered nanoclay-based 3D in vitro breast cancer model for studying breast cancer metastasis to bone, Journal of tissue engineering and regenerative medicine 13(2) (2019) 119-130.

[18] K.S. Katti, M. Molla, F. Karandish, M.K. Haldar, S. Mallik, D.R. Katti, Sequential culture on biomimetic nanoclay scaffolds forms three-dimensional tumoroids, Journal of Biomedical Materials Research Part A 104(7) (2016) 1591-1602.

[19] S. Molla, D.R. Katti, K.S. Katti, In vitro design of mesenchymal to epithelial transition of prostate cancer metastasis using 3D nanoclay bone-mimetic scaffolds, Journal of tissue engineering and regenerative medicine (2017).

[20] K.S. Katti, D.R. Katti, M.S. Molla, S. Kar, Evaluation of Cancer Tumors in 3D Porous Bone Mimetic Scaffolds, Poromechanics VI, pp. 881-888.

[21] A.H. Ambre, D.R. Katti, K.S. Katti, Biomineralized hydroxyapatite nanoclay composite scaffolds with polycaprolactone for stem cell-based bone tissue engineering, Journal of Biomedical Materials Research Part A 103(6) (2015) 2077-2101.

[22] A. Kramschuster, L.-S. Turng, 17—Fabrication of tissue engineering scaf-folds, Handbook of Biopolymers and Biodegradable Plastics: Properties, Processing and Applications 427 (2012).

[23] J.T. Erler, V.M. Weaver, Three-dimensional context regulation of metastasis, Clinical & experimental metastasis 26(1) (2009) 35-49.

[24] K.R. Levental, H. Yu, L. Kass, J.N. Lakins, M. Egeblad, J.T. Erler, S.F.T. Fong, K. Csiszar, A. Giaccia, W. Weninger, Matrix crosslinking forces tumor progression by enhancing integrin signaling, Cell 139(5) (2009) 891-906.

[25] M.S. Samuel, V. Poltavets, S.M. Pitson, M. Kochetkova, The role of the extracellular matrix and its molecular and cellular regulators in cancer cell plasticity, Frontiers in oncology 8 (2018) 431.

[26] D. Sikdar, S.M. Pradhan, D.R. Katti, K.S. Katti, B. Mohanty, Altered phase model for polymer clay nanocomposites, Langmuir 24(10) (2008) 5599-5607.

[27] D. Sikdar, K.S. Katti, D.R. Katti, Molecular interactions alter clay and polymer structure in polymer clay nanocomposites, Journal of Nanoscience and Nanotechnology 8(4) (2008) 1638-1657.

[28] D. Sikdar, D.R. Katti, K.S. Katti, B. Mohanty, Influence of backbone chain length and functional groups of organic modifiers on crystallinity and nanomechanical properties of intercalated clay-polycaprolactam nanocomposites, International Journal of Nanotechnology 6(5-6) (2009) 468-492.

[29] A. Ambre, K.S. Katti, D.R. Katti, In situ mineralized hydroxyapatite on amino acid modified nanoclays as novel bone biomaterials, Materials Science and Engineering: C 31(5) (2011) 1017-1029.

[30] A.K. Gaharwar, S.M. Mihaila, A. Swami, A. Patel, S. Sant, R.L. Reis, A.P. Marques, M.E. Gomes, A. Khademhosseini, Bioactive silicate nanoplatelets for osteogenic differentiation of human mesenchymal stem cells, Advanced materials 25(24) (2013) 3329-3336.

[31] A.K. Gaharwar, S. Mukundan, E. Karaca, A. Dolatshahi-Pirouz, A. Patel, K. Rangarajan, S.M. Mihaila, G. Iviglia, H. Zhang, A. Khademhosseini, Nanoclay-enriched poly (ε-caprolactone) electrospun scaffolds for osteogenic differentiation of human mesenchymal stem cells, Tissue Engineering Part A 20(15-16) (2014) 2088-2101.

[32] S. Kar, T. Kaur, A. Thirugnanam, Microwave-assisted synthesis of porous chitosan–modified montmorillonite–hydroxyapatite composite scaffolds, International journal of biological macromolecules 82 (2016) 628-636.

[33] A.J. Mieszawska, J.G. Llamas, C.A. Vaiana, M.P. Kadakia, R.R. Naik, D.L. Kaplan, Clay enriched silk biomaterials for bone formation, Acta biomaterialia 7(8) (2011) 3036-3041.

[34] K.S. Katti, A.H. Ambre, S. Payne, D.R. Katti, Vesicular delivery of crystalline calcium minerals to ECM in biomineralized nanoclay composites, Materials Research Express 2(4) (2015) 13.

[35] S. Kar, K.S. Katti, D.R. Katti, Engineered nanoclay based bone-mimetic 3D in vitro test-bed for bone metastasis of breast cancer, Transactions of the Annual Meeting of the Society for Biomaterials and the Annual International Biomaterials Symposium 40 (2019) 641.

[36] M.D.S. Molla, D.R. Katti, K.S. Katti, An in vitro model of prostate cancer bone metastasis for highly metastatic and non-metastatic prostate cancer using nanoclay bone-mimetic scaffolds, MRS Advances 4(21) (2019) 1207-1213.

[37] S. Kar, H. Jasuja, D.R. Katti, K.S. Katti, Wnt/β-catenin Signaling Pathway Regulates Osteogenesis for Breast Cancer Bone Metastasis: Experiments in an In Vitro Nanoclay Scaffold Cancer Testbed, ACS Biomaterials Science & Engineering (2019). https://doi.org/10.1021/acsbiomaterials.9b00923

[38] S. Kar, D.R. Katti, K.S. Katti, Fourier transform infrared spectroscopy based spectral biomarkers of metastasized breast cancer progression, Spectrochimica Acta Part A: Molecular and Biomolecular Spectroscopy 208 (2019) 85-96.

[39] M.D.S. Molla, D.R. Katti, J. Iswara, R. Venkatesan, R. Paulmurugan, K.S. Katti, Prostate cancer phenotype influences bone mineralization at metastasis: A study using an in vitro prostate cancer metastasis testbed, JBMR Plus 4(2) (2020) e10256.

[40] M.A. Jordan, K. Wendell, S. Gardiner, W.B. Derry, H. Copp, L. Wilson, Mitotic block induced in HeLa cells by low concentrations of paclitaxel (Taxol) results in abnormal mitotic exit and apoptotic cell death, Cancer research 56(4) (1996) 816-825.

[41] M. Markman, Pharmaceutical management of ovarian cancer, Drugs 68(6) (2008) 771-789.

[42] M. Tubiana-Hulin, How to maximize the efficacy of taxanes in breast cancer, Cancer treatment reviews 31 (2005) S3-S9.

[43] J.A. Yared, K.H.R. Tkaczuk, Update on taxane development: new analogs and new formulations, Drug design, development and therapy 6 (2012) 371.

[44] S. Sharifi, J. Barar, M.S. Hejazi, N. Samadi, Roles of the Bcl-2/Bax ratio, caspase-8 and 9 in resistance of breast cancer cells to paclitaxel, Asian Pac J Cancer Prev 15(20) (2014) 8617-22.

[45] R.M. Elledge, S.A.W. Fuqua, G.M. Clark, P. Pujol, D.C. Allred, W.L. McGuire, Prognostic significance of p53 gene alterations in node-negative breast cancer, Breast cancer research and treatment 26(3) (1993) 225-235.

[46] B. Fazeny-Dörner, M. Piribauer, C. Wenzel, N. Fakhrai, C. Pirker, W. Berger, R. Sedivy, M. Rudas, M. Filipits, I. Okamoto, Cytogenetic and comparative genomic hybridization

findings in four cases of breast cancer after neoadjuvant chemotherapy, Cancer genetics and cytogenetics 146(2) (2003) 161-166.

[47] N.V. Litviakov, N.V. Cherdyntseva, M.M. Tsyganov, E.V. Denisov, E.Y. Garbukov, M.K. Merzliakova, V.V. Volkomorov, S.V. Vtorushin, M.V. Zavyalova, E.M. Slonimskaya, Changing the expression vector of multidrug resistance genes is related to neoadjuvant chemotherapy response, Cancer chemotherapy and pharmacology 71(1) (2013) 153-163.

[48] J. Bromberg, T.C. Wang, Inflammation and cancer: IL-6 and STAT3 complete the link, Cancer cell 15(2) (2009) 79-80.

[49] C.-W. Ni, H.-J. Hsieh, Y.-J. Chao, D.L. Wang, Interleukin-6-induced JAK2/STAT3 signaling pathway in endothelial cells is suppressed by hemodynamic flow, American Journal of Physiology-Cell Physiology 287(3) (2004) C771-C780.

[50] G. Niu, K.L. Wright, Y. Ma, G.M. Wright, M. Huang, R. Irby, J. Briggs, J. Karras, W.D. Cress, D. Pardoll, Role of Stat3 in regulating p53 expression and function, Molecular and cellular biology 25(17) (2005) 7432-7440.

[51] H.-J. Choi, J.-S. Han, Overexpression of phospholipase D enhances Bcl-2 expression by activating STAT3 through independent activation of ERK and p38MAPK in HeLa cells, Biochimica et Biophysica Acta (BBA)-Molecular Cell Research 1823(6) (2012) 1082-1091.

[52] W.-H. Liu, M.-T. Chen, M.-L. Wang, Y.-Y. Lee, G.-Y. Chiou, C.-S. Chien, P.-I. Huang, Y.-W. Chen, M.-C. Huang, S.-H. Chiou, Cisplatin-selected resistance is associated with increased motility and stem-like properties via activation of STAT3/Snail axis in atypical teratoid/rhabdoid tumor cells, Oncotarget 6(3) (2015) 1750.

[53] J. Zhou, F. Chen, J. Xiao, C. Li, Y. Liu, Y. Ding, P. Wan, X. Wang, J. Huang, Z. Wang, Enhanced functional properties of corneal epithelial cells by coculture with embryonic stem cells via the integrin β1-FAK-PI3K/Akt pathway, The international journal of biochemistry & cell biology 43(8) (2011) 1168-1177.

[54] J. Prochazkova, V. Lichnovsky, D. Kylarova, B. Erdosova, P. Vranka, Involvement of p53 and Bcl-2 family proteins in regulating programmed cell death and proliferation in human embryogenesis, General physiology and biophysics 23(2) (2004) 209-229.

[55] Y.-L. Sun, A. Patel, P. Kumar, Z.-S. Chen, Role of ABC transporters in cancer chemotherapy, Chinese journal of cancer 31(2) (2012) 51.

[56] P. Aryappalli, S.S. Al-Qubaisi, S. Attoub, J.A. George, K. Arafat, K.B. Ramadi, Y.A. Mohamed, M.M. Al-Dhaheri, A. Al-Sbiei, M.J. Fernandez-Cabezudo, The IL-6/STAT3 signaling pathway is an early target of manuka honey-induced suppression of human breast cancer cells, Frontiers in oncology 7 (2017) 167.

[57] J.-J. Qin, L. Yan, J. Zhang, W.-D. Zhang, STAT3 as a potential therapeutic target in triple negative breast cancer: a systematic review, Journal of Experimental & Clinical Cancer Research 38(1) (2019) 195.

[58] Y. Wang, X. Zong, S. Mitra, A.K. Mitra, D. Matei, K.P. Nephew, IL-6 mediates platinum-induced enrichment of ovarian cancer stem cells, JCI insight 3(23) (2018).

[59] Z.-Y. Wang, J.-A. Zhang, X.-J. Wu, Y.-F. Liang, Y.-B. Lu, Y.-C. Gao, Y.-C. Dai, S.-Y. Yu, Y. Jia, X.-X. Fu, IL-6 inhibition reduces STAT3 activation and enhances the antitumor effect of carboplatin, Mediators of inflammation 2016 (2016).

[60] S. Huang, Q. Liu, Q. Liao, Q. Wu, B. Sun, Z. Yang, X. Hu, M. Tan, L. Li, Interleukin-6/signal transducer and activator of transcription 3 promotes prostate cancer resistance to

androgen deprivation therapy via regulating pituitary tumor transforming gene 1 expression, Cancer science 109(3) (2018) 678-687.

[61] S.O. Lee, W. Lou, M. Hou, F. De Miguel, L. Gerber, A.C. Gao, Interleukin-6 promotes androgen-independent growth in LNCaP human prostate cancer cells, Clinical Cancer Research 9(1) (2003) 370-376.

[62] I.-H. Ham, H.J. Oh, H. Jin, C.A. Bae, S.-M. Jeon, K.S. Choi, S.-Y. Son, S.-U. Han, R.A. Brekken, D. Lee, Targeting interleukin-6 as a strategy to overcome stroma-induced resistance to chemotherapy in gastric cancer, Molecular cancer 18(1) (2019) 68.

[63] K.S. Katti, A.H. Ambre, N. Peterka, D.R. Katti, Use of unnatural amino acids for design of novel organomodified clays as components of nanocomposite biomaterials, Philosophical Transactions of the Royal Society of London A: Mathematical, Physical and Engineering Sciences 368(1917) (2010) 1963-1980.

[64] W. Huang, S. Yang, J. Shao, Y.-P. Li, Signaling and transcriptional regulation in osteoblast commitment and differentiation, Frontiers in bioscience: a journal and virtual library 12 (2007) 3068.

[65] Y. Hee Choi, A.-M. Yu, ABC transporters in multidrug resistance and pharmacokinetics, and strategies for drug development, Current pharmaceutical design 20(5) (2014) 793-807.

[66] R.L. Carpenter, H.-W. Lo, STAT3 target genes relevant to human cancers, Cancers 6(2) (2014) 897-925.

[67] M.C. Regier, S.I. Montanez-Sauri, M.P. Schwartz, W.L. Murphy, D.J. Beebe, K.E. Sung, The influence of biomaterials on cytokine production in 3D cultures, Biomacromolecules 18(3) (2017) 709-718.

[68] E. Redondo-Castro, C.J. Cunningham, J. Miller, H. Brown, S.M. Allan, E. Pinteaux, Changes in the secretome of tri-dimensional spheroid-cultured human mesenchymal stem cells in vitro by interleukin-1 priming, Stem cell research & therapy 9(1) (2018) 11.

CHAPTER 5. QUASI-STATIC AND DYNAMIC NANOMECHANICAL EVALUATION OF BREAST CANCER CELLS WITH PROGRESSION OF METASTASIS TO BONE[4]

This chapter describes the significant role of actin cytoskeleton in governing cellular nanomechanics leading up to breast cancer progression at metastatic bone site. The contents of this chapter have been submitted for publication.

5.1. Introduction

With the advent of novel nanomechanics experimental and modeling methodologies, there has been an increasing interest in investigating the mechanical properties of individual cells to delineate disease mechanisms [1, 2]. Increasing evidence supports that altered mechanical properties highly influence cancer pathogenesis and progression at the cellular level. Several studies have reported that cancer cells are softer than their healthy counterparts [3-10], whereas a few studies showed otherwise [11, 12]. It has been shown that dysregulation in the actin cytoskeleton can lead to softening in cancer cells [13-16]. The epithelial monolayer, a multicellular system composed of firmly connected adjacent cells via adherens junctions, has been shown to give rise to most of the human cancers [17, 18]. The actin cytoskeleton of healthy epithelial cells is attached to adherens junctions to counteract internal and external mechanical stimuli and bestow mechanical stability [19, 20]. In contrast, cancerous epithelial cells most often exhibit disruption in stable cell-cell adhesion due to alterations in either adherens junctions or actin cytoskeleton [21-24]. In addition, a few studies have compared distribution of the actin cytoskeleton in breast cancer cells with normal breast cells using fluorescence staining [7, 9, 25, 26].

[4] This chapter was co-authored by S. Kar, D.R. Katti, and K.S. Katti. Sumanta Kar had the primary responsibility for preparing samples, conducting all tests, and drafting this chapter. Kalpana Katti and Dinesh Katti directed the research orientation and revised this chapter.

Loss of cell-cell adhesion and gain of the invasive mesenchymal phenotype are hallmarks of epithelial-mesenchymal transition (EMT) of cancer cells, a process that promotes cancer cells to invade the basement membrane; a physical barrier made up of their adjacent cells [27]. Upregulation of several actin-cytoskeletal-associated proteins, including myosin light chain, α-actinin, integrins, and tropomyosin, has been associated with EMT while reduced expression of pseudopod-enriched proteins including Wiskott-Aldrich syndrome protein (WASP) family members, the actin-related proteins-2/3 (Arp2/3) complex, cortactin is associated with reversal of EMT or mesenchymal-epithelial transition (MET) [22, 28-33]. Moreover, altered expression of Arp2/3 complex and Wiskott-Aldrich syndrome protein family member 2 (WAVE2) have been linked with poor prognosis of breast cancer, indicating a significant role of actin cytoskeleton dynamics in cancer progression [34].

To date, various methods have been used to measure mechanical properties of cells, including atomic force microscopy (AFM) [7, 8, 25, 26, 35-48], optical tweezers [45, 48-53], micropipette aspiration [54-57], magnetic twisting cytometry [58-60], high-frequency microrheology [61, 62], and particle-tracking microrheology [63, 64]. Despite their extensive usage, a few of them possess drawbacks, including the effects of indentation depth and substrate stiffening in AFM [65, 66], stress-induced loading in micropipette aspirations[56, 57], and laser-induced thermal loading in optical tweezers [67]. These effects can lead to erroneous results during mechanical measurements of cells. To this end, our group had previously developed a nanoindentation-based technique as an alternative method for measurements of cellular mechanical properties [68, 69].

Nanoindentation is a depth-sensing technique and has been proven to be more efficient in obtaining bulk cellular behavior using controlled strain experiments, which cannot be carried out

with low load AFM force curves [70]. Nanoindentation techniques are very useful in probing mechanical properties at lower degrees of length scale with the help of the displacement-controlled nanoindentation module. Nanoindentation techniques have been extensively used to obtain nanoscale mechanical properties of cells [68, 69, 71], cell-biomaterials composite [69], soft and mineralized tissues [72-77], biological composites [78-80], and dental materials [81, 82]. Molecular modeling has also been used simultaneously to obtain the mechanics of cancer cells for developing robust predictive methodologies for disease progression [83].

Breast cancer is the most prevalent cancer types among women, and it becomes incurable once the disease has metastasized to the bones. Changes in cellular shape and architecture facilitate the colonization of metastatic breast cancer at bone marrow space. Due to the scarcity of accurate and efficient models to replicate stages of cancer progression for early detection, most of the patients (80%) with breast cancer metastasized to the bones die within five years [84]. Moreover, no studies have been done to evaluate the changes in the mechanical properties of breast cancer cells during cancer progression at the bone site, owing to the lack of suitable models to recapitulate the molecular events. In recent years, three-dimensional (3D) culture systems have attracted substantial attention due to their ability to recapitulate *in vivo* tumor microenvironment by providing enough spatial and biophysical cues to mimic molecular events that occur during disease progression as compared to two-dimensional (2D) cellular models. Moreover, 3D culture systems eliminate issues that exist in animal models regarding immunodeficiency, species difference, and uncertain disease pathogenesis [85-87].

Recently, we have developed a nanoclay-based 3D *in vitro* model for breast cancer bone metastasis, mimicking MET of breast cancer in sequential culture of osteogenically differentiated human mesenchymal stem cells (MSCs) and human breast cancer cells [88]. In our previous

studies, we have reported osteogenesis and mineralization in nanoclay-based composites by MSCs without the use of osteogenic supplements [89, 90]. In another study, we showed MET of prostate cancer cells in sequential culture of MSCs with prostate cancer cells [91, 92]. Recent studies from our group also showed the influence of breast/prostate cancer-derived factors on osteogenesis at metastases [93, 94].

In the present study, we hypothesized that breast cancer cells grown on 3D bone-mimetic scaffolds would exhibit changes in elastic and viscoelastic properties over time due to alterations in actin cytoskeleton dynamics and organization during disease progression. To this end, we evaluated mechanical properties of breast cancer cells grown on 3D bone-mimetic scaffolds using quasi-static and dynamic nanoindentation methods, and correlated changes in elastic and viscoelastic properties with dysregulation in actin cytoskeleton dynamics using fluorescence staining and mRNA expression of actin cytoskeleton-related genes.

5.2. Materials and Methods

5.2.1. Materials, Cell Lines, and Culture Maintenance

Na-MMT clay was procured from Clay Minerals Respiratory at the University of Missouri. Calcium chloride ($CaCl_2$), polycaprolactone (PCL) (average Mn 80,000), 1,4-dioxane, sodium phosphate (Na_2HPO_4), Tween20, 4′,6-diamidino-2-phenylindole (DAPI), fish skin gelatin (FSG), 5-aminovaleric acid, and TritonX-100 were purchased from Sigma Aldrich. Human mesenchymal stem cells (MSCs) (PT-2501) were purchased from Lonza (Walkersville, MD) and maintained in complete growth medium (MSCGM™ SingleQuots™ (PT-4105) was added to MSC basal medium (MSCBM™, PT-3238) to obtain complete growth medium). Human breast cancer cell lines MCF-7 (HTB-22), MDA-MB-231 (HTB-26) (shortened as MM 231), Eagle's Minimum Essential Medium (EMEM), and Fetal Bovine Serum (FBS) were purchased

from American Type Culture Collection (ATCC). Corning™ Phosphate Buffered Saline (PBS), Hyclone™ Dulbecco's Modified Eagle medium Nutrient Mixture F-12 DMEM-F-12(1:1), and Alfa Aesar™ Paraformaldehyde, 4% in PBS (PFA) were purchased from VWR. Rhodamine Phalloidin, Gibco™ human recombinant insulin, Gibco™ penicillin-streptomycin antibiotic solution (P/S), Applied Biosystems™ Fast SYBR Green, and Gibco™ TrypLE™ Express Enzyme (1X), phenol red were purchased from Invitrogen. MCF-7 cells were maintained in Eagle's Minimum Essential Medium (EMEM), 10% FBS, 0.01 mg/ml human recombinant insulin, and 1% P/S whereas MM 231 cells were cultured in DMEM-F-12(1:1), 10% FBS, and 1% P/S. All cell cultures were maintained at 37 ºC and 5% CO_2 in a humidified incubator. Direct-zol RNA MiniPrep kit (Zymo Research), anti-Tubulin (Abcam) primary antibody, secondary antibody, and other reagents used were of analytical grade.

5.2.2. Preparation of PCL/*in situ* HAPclay 3D Scaffolds

PCL/*in situ* HAPclay scaffolds were synthesized following the procedure described elsewhere [89]. Briefly, we modified clay with 5-aminovaleric acid to increase the d-spacing of clay followed by biomineralized of hydroxyapatite (HAP) into intercalated nanoclay galleries to obtain *in situ* HAPclay according to the procedure reported in our previous studies [95-97]. Next, 10% *in situ* HAPclay was added to PCL solution to get a composite mixture, which was further subjected to freeze-extraction to synthesize PCL/*in situ* HAPclay scaffolds. Scaffolds were cut into cylindrical shape (~12 mm diameter and ~ 3 mm thickness), sterilized under UV light for 45 mins, submerged in 70% ethanol for 12 h, washed in PBS to remove excess ethanol, and stored in 5% CO_2 incubator at 37 ºC immersed in 24-well plates containing culture medium for 24 h before cell seeding.

5.2.3. Cell Culture

MSCs were seeded at a density of 5 x 10^4 per scaffold and cultured for 23 days to deposit bone-like extracellular matrix (ECM) onto scaffolds. Then, scaffolds with newly formed bone were seeded with 5 x 10^4 breast cancer cells (MCF-7/ MM 231) per scaffold and maintained in 1:1 MSCs and breast cancer cell medium. Breast cancer cells (MCF-7/MM 231) cultured on 2D tissue culture polystyrene (TCPS) are called “as received” throughout the study.

5.2.4. Cellular Morphology

Cell-seeded scaffold constructs were fixed with 2.5% glutaraldehyde followed by dehydration in a graded series of ethanol solution (10%, 30%, 50%, 70%, and 100%) and drying in hexamethyldisilazane. Then, samples were gold sputter coated and observed with a JSM-6490LV SEM (JEOL, Tokyo, Japan).

5.2.5. Quasi-Static Nanoindentation

The quasi-static nanomechanical characterization of live breast cancer cells (MCF-7/MM 231) was conducted using Triboscope™, Hysitron (Minneapolis, MN) equipped with multimode AFM (Nanoscope IIIa controller and J-type piezo scanner system) (Veeco Metrology, Santa Barbara, CA) and a Berkovich diamond indenter fluid tip (three-sided pyramidal; 100-200 nm tip radius) on displacement-controlled mode at maximum displacements of 1000 nm and 2000 nm at a loading and unloading rate of 100 nm/s. To carry out the tests in presence of culture medium, we grew the breast cancer cells on TCPS and then glued the TCPS with cells onto a 3D-printed holder (~12 mm diameter and ~3 mm height) and filled it fresh culture medium (EMEM + 2% FBS (MCF-7), DMEM-F12 + 2% FBS (MM 231)), which was further glued to a steel disc. The holder containing cell-seeded TCPS sample was placed onto the nanoindentation stage, and the whole assembly was maintained at 37 °C using a MultiMode™ low-temperature heater from

Veeco Metrology (Santa Barbara, CA) during the experiment. All the indentation tests were completed within two hours. For cells grown on 3D scaffolds, cells were extracted using TrypLE™ Express Enzyme, and seeded onto TCPS before performing nanoindentation tests. Cellular nanomechanical response was calculated following methodologies described in our previous studies [68, 69].

Using Oliver & Pharr method [98], the elastic modulus (E) of cells was calculated from load-displacement (L-D) curves. In this method, initial unloading portion of the L-D curve is fitted to power-law function followed by differentiation of power-law relation to obtain contact stiffness. The reduced elastic modulus (E_r) of cancer cells was calculated from the stiffness and contact area. Elastic modulus (E) of cells was further determined from the reduced modulus (E_r) and Poisson ratio (υ) of 0.50 was used for biological systems using the following equation:

$$\frac{1}{E_r} = \frac{(1-v^2)}{E} + \frac{(1-v_i^2)}{E_i}$$

Where, υ and E are Poisson's ratio and the elastic modulus of the sample, respectively; and υ_i and E_i are respective properties of the indenter. For diamond, υ_i = 0.07 and E_i = 1141 GPa. For each measured sample, at least 20 cells were measured. Data is reported as mean ± Standard Deviation (SD).

5.2.6. Dynamic Nanoindentation

The dynamic nano-mechanical response of live cancer cells was obtained by using frequency sweep mode of nano-DMA module (Triboscope™, Hysitron equipped with multimode AFM (Nanoscope IIIa controller and J-type piezo scanner system) (Veeco Metrology, Santa Barbara, CA). In this mode, the oscillating dynamic load of 1 µN was superimposed on a quasi-static load of 1000 µN over a frequency range of 10-250 Hz. The dynamic nanoindentation tests

were performed using the same setup and Berkovich diamond indenter, as described in section 5.2.5.

In dynamic nanoindentation tests, the displacement amplitude, load amplitude, and phase lag were measured to calculate the storage modulus (E'), loss modulus (E''), and loss tangent (tan δ) of cancer cells. During dynamic nanoindentation tests, the sample is subjected to a small oscillatory load (P) with a known load amplitude (P_0) and frequency (ω). During the test, the alternating displacement response is measured at the same testing frequency using a lock-in amplifier. The sinusoidal behavior of the load (P) and the resulting displacement (X_0) is related by the following expression:

$$P = P_0 + \sin \omega t$$

$$X = X_0 + \sin (\omega t - \varphi)$$

Where, t is the time and φ is the phase difference between load amplitude (P_0) and displacement amplitude (X_0), respectively. In a dynamic nanoindentation test, the observed response (i.e., the damping coefficient and the stiffness) is the aggregate response of the instrument and the sample being tested. Therefore, the response of the instrument must be subtracted from the aggregate response to obtain the true dynamic properties of sample. Hence, the stiffness (k_i), damping coefficient (C_i), and mass (m) of the indenter are obtained by air calibration before experiment followed by real-time correction of the aggregate response for the response of the instrument. Storage modulus (E') is given by the in-phase elastic response of the sample, and loss modulus (E'') is a measure of viscoelastic response of the sample/energy being dissipated during the test. The storage modulus (E'), loss modulus (E''), and loss tangent (tan δ) are determined by the following expressions:

$$E' = \frac{k\sqrt{\pi}}{2\sqrt{A_c}}$$

$$E'' = \frac{\omega C\sqrt{\pi}}{2\sqrt{A_c}}$$

$$\tan\delta = \frac{E''}{E'} = \frac{\omega C}{k}$$

Where, *C* and *k* are the damping coefficient and the stiffness of the sample, respectively, and A_c is the projected contact area of indenter on the surface of sample. For each measured sample, at least 20 cells were measured. Data is reported as mean ± SD.

5.2.7. Gene Expression Studies

We began with extracting total RNA from cell-seeded scaffolds and 2D cultures using the Direct-zol RNA MiniPrep kit. Then, we reverse-transcribed the extracted RNA to synthesize cDNA using random primers, M-MLV reverse transcriptase (Promega) on a thermal cycler (Applied Biosystems). Next, we performed Real-Time Polymerase Chain Reaction (RT-PCR) was using cDNA, SYBR Green dye, forward primer, reverse primer on a 7500 Fast Real-Time System (Applied Biosystems). The thermal profile used for the run was comprised of a holding stage (2 min at 50 °C, 10 min at 95 °C) and a cycling stage (40 cycles of 15 s at 95 °C, and 1 min at 60 °C). The mRNA expressions of Neural-Wiskott-Aldrich syndrome protein (N-WASP), Cell division control protein 42 homolog (CDC42), ARP2, ARP3, Cortactin (CTTN), E-cadherin (CDH1), and Cofilin-2 (CFL2) were quantified and normalized to housekeeping gene glyceraldehyde-3-phosphate-dehydrogenase (GAPDH). Target gene expressions were determined using comparative C_t method ($2^{-\Delta\Delta Ct}$). Table 5.1 lists the sequence of primers used. All the experiments were repeated on triplicate samples.

Table 5.1. The sequence of primers used for the quantitative real-time PCR experiment

Gene	Forward primer	Reverse primer
GAPDH	5'-CATCTTCTTTTGCGTCGCCA-3'	5'-TTAAAAGCAGCCCTGGTGACC-3'
N-WASP	5' -ACTGTTAGACCAGATACG ACAGGGT-3'	5'-TGCAGGTGTTGGTGGTGT AGA-3'
ARP2	5'-GGAGTTGGTGTTGCTGAAT-3'	5'-TAGTAGACCCTCCAGAAAGC-3'
ARP3	5'-CAATCCTTGGAAACTGCTA-3'	5'-CCATTTTGACCCATCTGTA-3'
CDC42	5'-ATGCAGACAATTAAGTGTG TTGTTGTGGGCGA-3'	5'- TCATAGCAGCACACACC TGCGGCTCTTCTT-3'
CTTN	5'-AAAGCTTCAGCAGGCCAC-3'	5'-TTTGGTCCTGTTTCAAGT TCC-3'
CFL2	5'-AGTGCCACAGAGCCGAAG-3'	5'TCATCATTCACTGTAACTCCAGAAG-3'
CDH1	5'-AAG TGA CCG ATGATGAT-3'	5'-CTC TGT CCA TCT CAG CG-3'

5.2.8. Immunofluorescence Staining

Cells grown on scaffolds and 2D cultures were fixed with paraformaldehyde, 4% in PBS for 30 min, permeabilized with TritonX-100, 0.2% in PBS for 5 min, and blocked with FSG, 0.2% in PBS for 45 min. Then, the samples were incubated overnight at 4 °C with primary antibody diluted in a blocking buffer (0.2% FSG in PBS containing 0.02% Tween20) at a dilution of 1:150. Next, the samples were incubated with Alexa Flour 488 conjugated secondary antibody corresponding to origin of the primary antibody used for 45 mins at 25 °C. The actin cytoskeleton and Nuclei were stained with Rhodamine Phalloidin and DAPI, respectively. The stained samples were observed under Zeiss AxioObserver.Z1 LSM 700. Images were processed with Image J software and the quantitative analysis of both actin and tubulin fluorescence was performed on at least 5-6 cells for each sample evaluated by calculating the corrected total cell fluorescence (CTCF) of each signal as follows:

$$\text{CTCF} = \text{Integrated density of selected cell} - (\text{Area of selected cell} \times \text{Mean fluorescence of background})$$

5.2.9. Statistical Analysis

Data is reported as mean ± SD. Statistical significance (p-value) among multiple comparisons was determined using one-way ANOVA followed by *post hoc* Tukey test while Student's unpaired *t-test* was used to determine statistical significance (p-value) between two groups, using GraphPad Prism v7.04. $p<0.05$ was considered statistically significant.

5.3. Results

5.3.1. Cancer Cells Alter Nanomechanical Properties in Response to 3D Culture Conditions

In the present study, we have created a 3D *in vitro* model for breast cancer bone metastasis, mimicking MET of breast cancer in sequential culture of osteogenically differentiated MSCs and breast cancer cells, according to procedure described in our previous studies. Briefly, MSCs were cultured on 3D scaffolds for 23 days to generate bone tissue. Then, human breast cancer cells were seeded on the newly formed bone matrix (Figure 5.1A). The morphology of cancer cells grown in sequential cultures with MSCs on 3D scaffolds was obtained using SEM. We observed formation of tumoroids with distinguishable cellular boundaries by MCF-7 cells, whereas MM 231 cells formed disordered cellular aggregates as shown in Figure 5.1B.

To evaluate the nanomechanical response of cancer cells grown on TCPS and scaffolds, we performed displacement-controlled nanoindentation experiments at maximum displacements of 1000 nm and 2000 nm using Triboscope™, Hysitron (Minneapolis, MN) equipped with multimode AFM (Nanoscope IIIa controller and J-type piezo scanner system) (Veeco Metrology, Santa Barbara, CA) and a Berkovich diamond indenter fluid tip ((three-sided pyramidal; 100–200 nm tip radius).

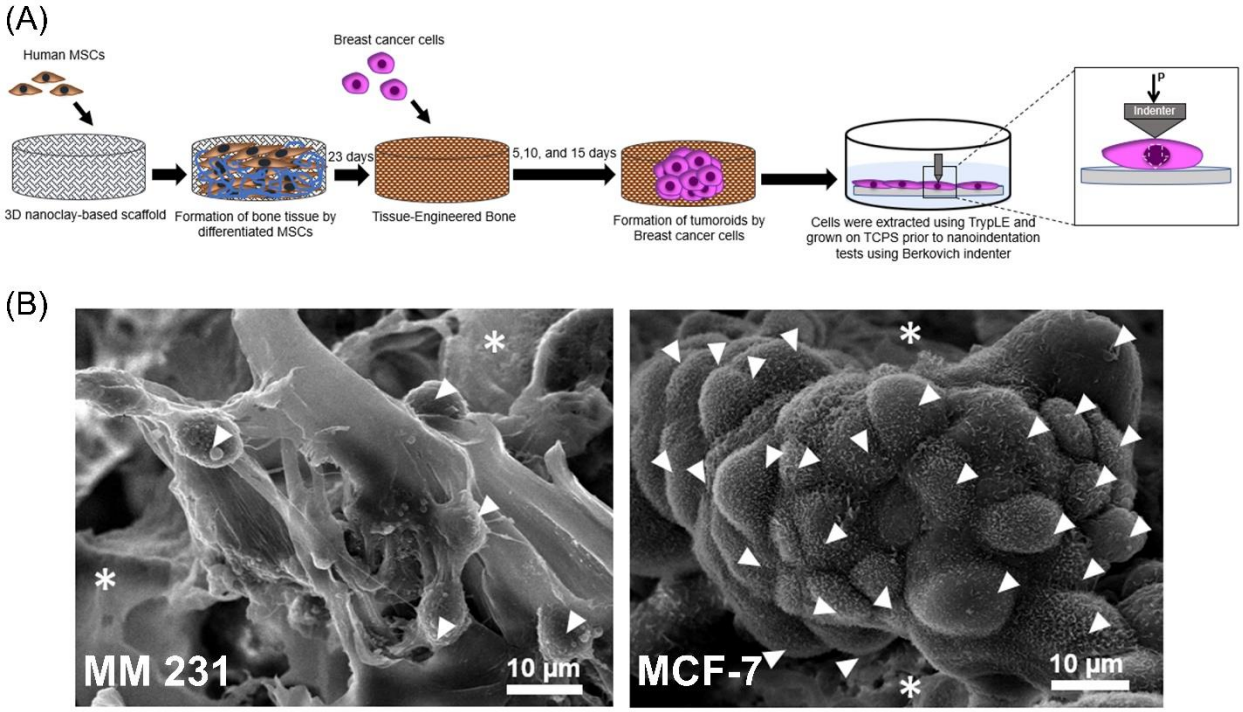

Figure 5.1. (A) Schematic showing steps of sequential culture MSCs/breast cancer followed by workflow of nanoindentation experiments. Dotted arrow pointing downwards indicates the amount of deformation applied (P) onto cell construct to yield nanomechanical response of cell. (B) Morphology of breast cancer cells MM 231 and MCF-7 grown on 3D bone-mimetic nanoclay scaffolds. Arrows indicate cells while * indicate scaffold.

Although earlier studies have used blunt tips for indenting human biological tissue samples [72], several recent studies have shown that cell stiffness measured by sharp indenters is comparable to stiffness measured by blunt tips [99, 100]. Also, sharper tips can get information on the localized mechanical properties from deeper penetration into the probed sample with little to no detrimental effect easily compared to blunt tips [68, 100]. These facts mentioned above made us use Berkovich tip in the present study. Nanomechanical properties of soft biological samples such as cells, tissues obtained by indentation experiments are usually described by elastic modulus [7, 47, 68, 101, 102]. In the present study, we used Oliver and Pharr analysis method [98] to derive the elastic modulus of the breast cancer cells.

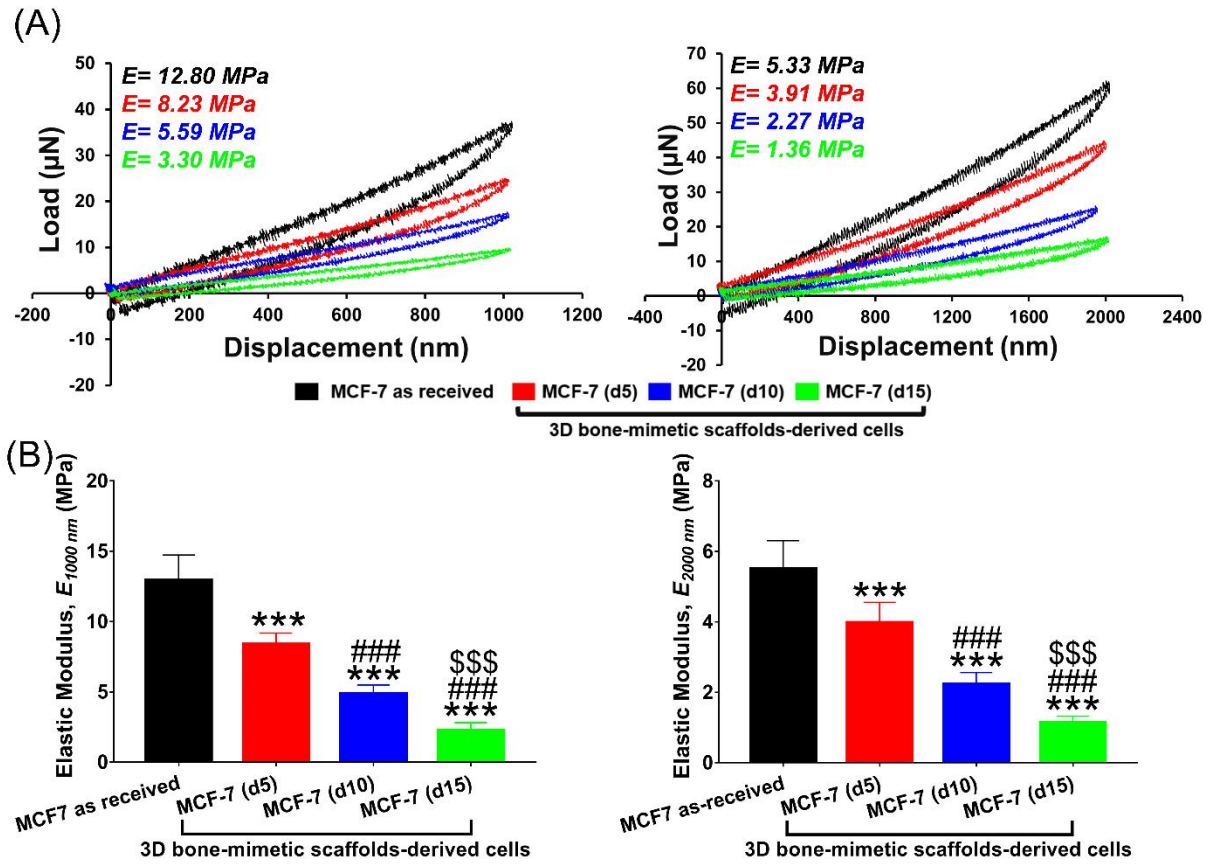

Figure 5.2. (A) Representative load-displacement (L-D) curves of MCF-7 as received and 3D bone-mimetic scaffolds-derived MCF-7 cells at the maximum depth of 1000 nm and 2000 nm. (B) Elastic modulus of MCF-7 as received and 3D bone-mimetic scaffolds-derived MCF-7 cells at the maximum depth of 1000 nm and 2000 nm. *p<0.05, **p<0.01, and ***p<0.001 indicate significant difference between MCF-7 as received and 3D bone-mimetic scaffolds-derived MCF-7 cells; $^{\#}$p<0.05, $^{\#\#}$p<0.01, and $^{\#\#\#}$p<0.001 indicate significant difference between scaffolds-derived MCF-7 (d5), and other scaffolds-derived cells (i.e., MCF-7 (d10) and MCF-7 (d15)); $^{\$}$p<0.05, $^{\$\$}$p<0.01, and $^{\$\$\$}$p<0.001 indicate significant difference between scaffolds-derived MCF-7 (d10) and MCF-7 (d15).

Indentation depth has been shown to influence the measurement of elastic modulus of cells. AFM-based indentation studies on cells are usually performed at an indentation depth of ~300-500 nm [100]. The mechanical properties observed at shallow indentation arises from cellular membrane and peripheral structures, whereas, at deeper indentation (~1000-2000 nm), the bulk mechanical property of cell can be obtained [68, 70]. It was reported that shallow indentation showed no significant difference between cancerous and healthy cells, whereas

deeper indentation resulted in a substantial reduction of cancerous compared to their healthy counterparts [103].

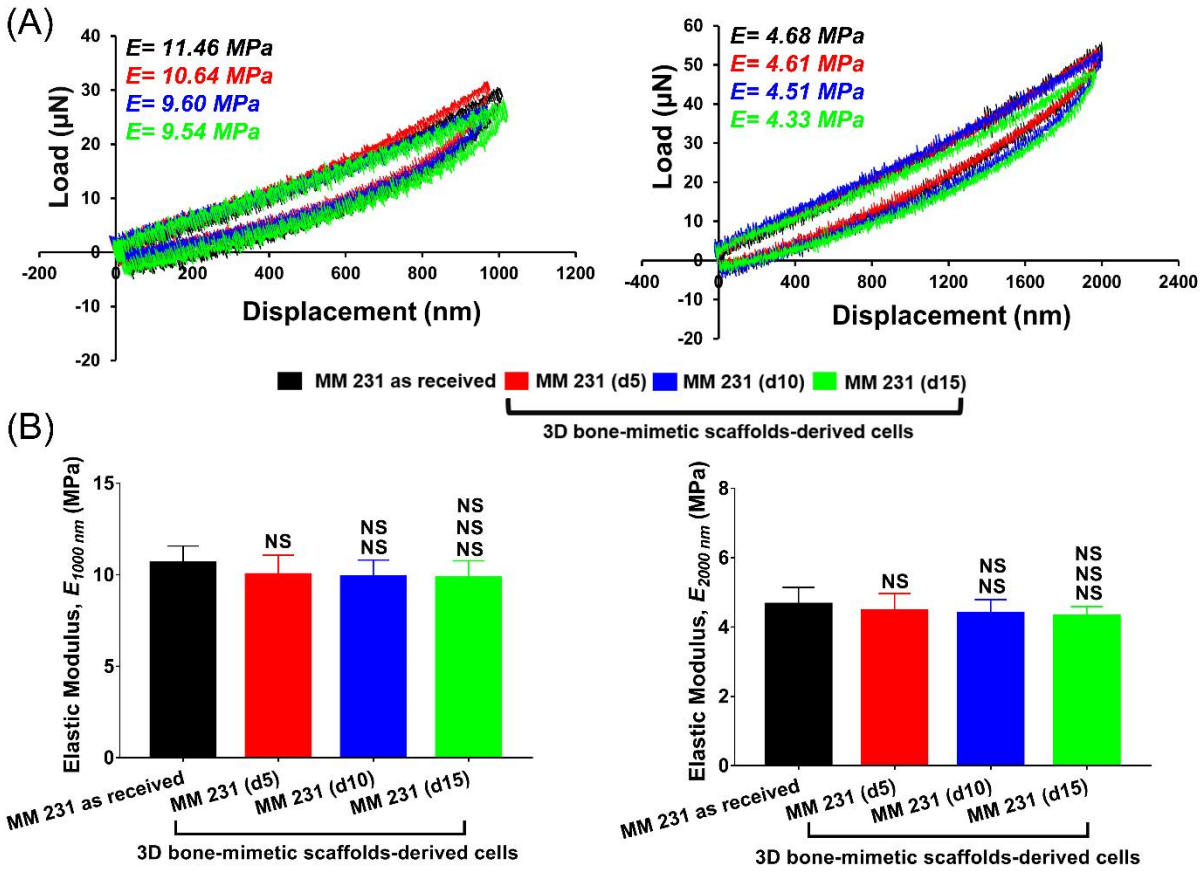

Figure 5.3. (A) Representative load-displacement (L-D) curves of MM 231 as received and 3D bone-mimetic scaffolds-derived MM 231 cells at the maximum depth of 1000 nm and 2000 nm. (B) Elastic modulus of MM 231 as received and 3D bone-mimetic scaffolds-derived MM 231 cells at the maximum depth of 1000 nm and 2000 nm. *p<0.05, **p<0.01, and ***p<0.001 indicate significant difference between MM 231 as received and 3D bone-mimetic scaffolds-derived MM 231 cells; $^{\#}$p<0.05, $^{\#\#}$p<0.01, and $^{\#\#\#}$p<0.001 indicate significant difference between scaffolds-derived MM 231 (d5), and other scaffolds-derived cells (i.e., MM 231 (d10) and MM 231 (d15)); $^{\$}$p<0.05, $^{\$\$}$p<0.01, and $^{\$\$\$}$p<0.001 indicate significant difference between scaffolds-derived MM 231 (d10) and MM 231 (d15).

Keeping these facts mentioned above in mind, we used two different indentation depths, 1000 nm, and 2000 nm, for displacement controlled nanoindentation experiments. Since the sizes of most of the breast cancer cells observed were ≥20 μm, an indentation depth >2000 nm was not used to avoid substrate effect on the measured elastic moduli [104].

The representative load-displacement (L-D) curves for as received and 3D bone-mimetic scaffolds-derived MCF-7 cells at the indentation depth 1000 nm and 2000 nm are shown in Figure 5.2A, and the respective elastic modulus or *E* values are given in Figure 5.2B. We observed that both $E_{1000\,nm}$ and $E_{2000\,nm}$ of scaffolds-derived MCF-7 cells are significantly lower than that of MCF-7 as received cells. We further observed a significant decrease within the scaffolds-derived MCF-7 cells with increasing number of days. It is noteworthy to mention that elastic modulus decreased with increasing indentation depth. At 1000 nm, the mean elastic modulus of MCF-7 as received, and scaffolds-derived MCF-7 (d5), MCF-7 (d10), and MCF-7 (d15) were 12.92 ± 1.81 MPa, 8.37 ± 0.81 MPa, 4.85 ± 0.65 MPa, and 2.25 ± 0.57 MPa, respectively. At 2000 nm, the mean elastic modulus of MCF-7 as received, and scaffolds-derived MCF-7 (d5), MCF-7 (d10), and MCF-7 (d15) were 5.50 ± 0.83 MPa, 3.98 ± 0.54 MPa, 2.23 ± 0.32 MPa, and 1.14 ± 0.18 MPa, respectively. The representative L-D curves for as received and 3D bone-mimetic scaffolds-derived MM 231 cells at the indentation depth 1000 nm and 2000 nm are shown in Figure 5.3A, and the respective elastic modulus or *E* values are indicated in Figure 5.3B. There was no significant difference between elastic moduli of as-received and 3D bone-mimetic scaffolds-derived MM 231 cells at both 1000 nm and 2000 nm. Interestingly, we observed insignificant changes within elastic moduli of scaffolds-derived MM 231 cells. We once again observed reduction in elastic modulus with increasing indentation depth. At 1000 nm, the mean elastic modulus of MM 231 as received, and scaffolds-derived MM 231 (d5), MM 231 (d10), and MM 231 (d15) were 10.62 ± 0.95 MPa, 10.00 ± 1.07 MPa, 9.88 ± 0.93 MPa, and 9.82 ± 0.94 MPa, respectively. At 2000 nm, the mean elastic modulus of MM 231 as received, and scaffolds-derived MM 231 (d5), MM 231 (d10), and MM 231 (d15) were 4.65 ± 0.49 MPa, 4.46 ± 0.52 MPa, 4.39 ± 0.41 MPa, and 4.31 ± 0.27 MPa, respectively. Overall, MCF-7 showed

progressive reduction in elastic modulus as compared to MM 231 when cultured in 3D bone-mimetic scaffolds.

5.3.2. Cancer Cells Behave More Liquid-Like When Cultured in 3D Conditions

To assess the evolution in viscoelastic properties of live cancer cells during disease progression, we performed dynamic nanoindentation using frequency sweep mode of nano-DMA module (Triboscope™, Hysitron equipped with multimode AFM (Nanoscope IIIa controller and J-type piezo scanner system) (Veeco Metrology, Santa Barbara, CA). In this mode, the oscillating dynamic load of 1 μN was superimposed on a quasi-static load of 1000 μN over a frequency range of 10-250 Hz. The storage modulus (E'), loss modulus (E''), and loss tangent (tan δ) of as-received and scaffolds-derived breast cancer cells (MCF-7 and MM 231) are shown in Figure 5.4(A, B, and C). Storage moduli of both cells across samples were found to be in same range as elastic moduli reported in the previous section. For example, storage modulus of MCF-7 as received, and scaffolds-derived MCF-7 (d5), MCF-7 (d10), and MCF-7 (d15) were ~13-14 MPa, ~6-8 MPa, ~3-6 MPa, and ~3-4 MPa, respectively [Figure 5.4A(i)]. In the case of MM 231, storage modulus of as-received and scaffolds-derived d5, d10, and d15 were ~8-10 MPa, ~6-9 MPa, ~5-7 MPa, and ~5-7 MPa, respectively [Figure 5.4A(ii)]. Loss moduli values for both cells across samples were in the same range. For instance, loss moduli of as-received MCF-7/MM 231, and scaffolds-derived MCF-7/MM 231 (d5), MCF-7/MM 231 (d10), and MCF-7/MM231 (d15) cells were ~3-5 MPa, ~2-4 MPa, ~2-4 MPa, and ~2-3 MPa, respectively (Figure 5.4B). It should be noted that both storage and loss moduli of both cells across conditions seem to be independent of frequency. Interestingly, we found an increase in loss tangent tan δ with increasing frequency for both cells grown in TCPS (as received) (Figure 5.4C). In other words,

cells became more viscous (higher loss tangent, tan δ indicates more viscous behavior) at higher frequencies.

Next, we assessed whether growing cells on scaffolds altered viscoelastic properties of the cells. For scaffolds-derived MCF-7 (d5), we noticed an increase in tan δ with increasing frequency, but it never went beyond the value of 1. Interestingly, tan δ values were found to be higher than 1 for both MCF-7 (d10) and MCF-7 (d15) at 199 Hz (and beyond) and 165 Hz (and beyond), respectively. The frequency at which cells transition from solid-like to liquid-like (more viscous) (tan δ =1) is termed as transition frequency ($\omega_{transition}$), as shown by the intersecting dashed lines [Figure 5.4C(i)]. Based on transition frequency, scaffolds-derived MCF-7 (d15) was found to be more liquid-like as compared to MCF-7 (d10). In case of scaffolds-derived MM 231 cells, we observed no significant increase in tan δ values over time [Figure 5.4C(ii)]. Also, we could not determine the transition frequency for MM 231 as tan δ values never went beyond 1. It should be noted that our results are in good agreement with recent studies done on breast cancer cells using high-frequency microrheology based methods [61, 62], AFM indentation studies [26]. To compare the storage modulus (E'), loss modulus (E''), and loss tangent (tan δ) of as received and scaffolds-derived breast cancer cells (MCF-7 and MM 231), we calculated log2 ratios of E',E'', and tan δ for MCF-7 and MM 231 across samples (averaged across frequency) (Figure 5.5). We observed a significant decrease in the storage of modulus of scaffolds-derived MCF-7 over scaffolds-derived MM 231 cells over time, as compared to their respective as-received counterparts (Figure 5.5A).

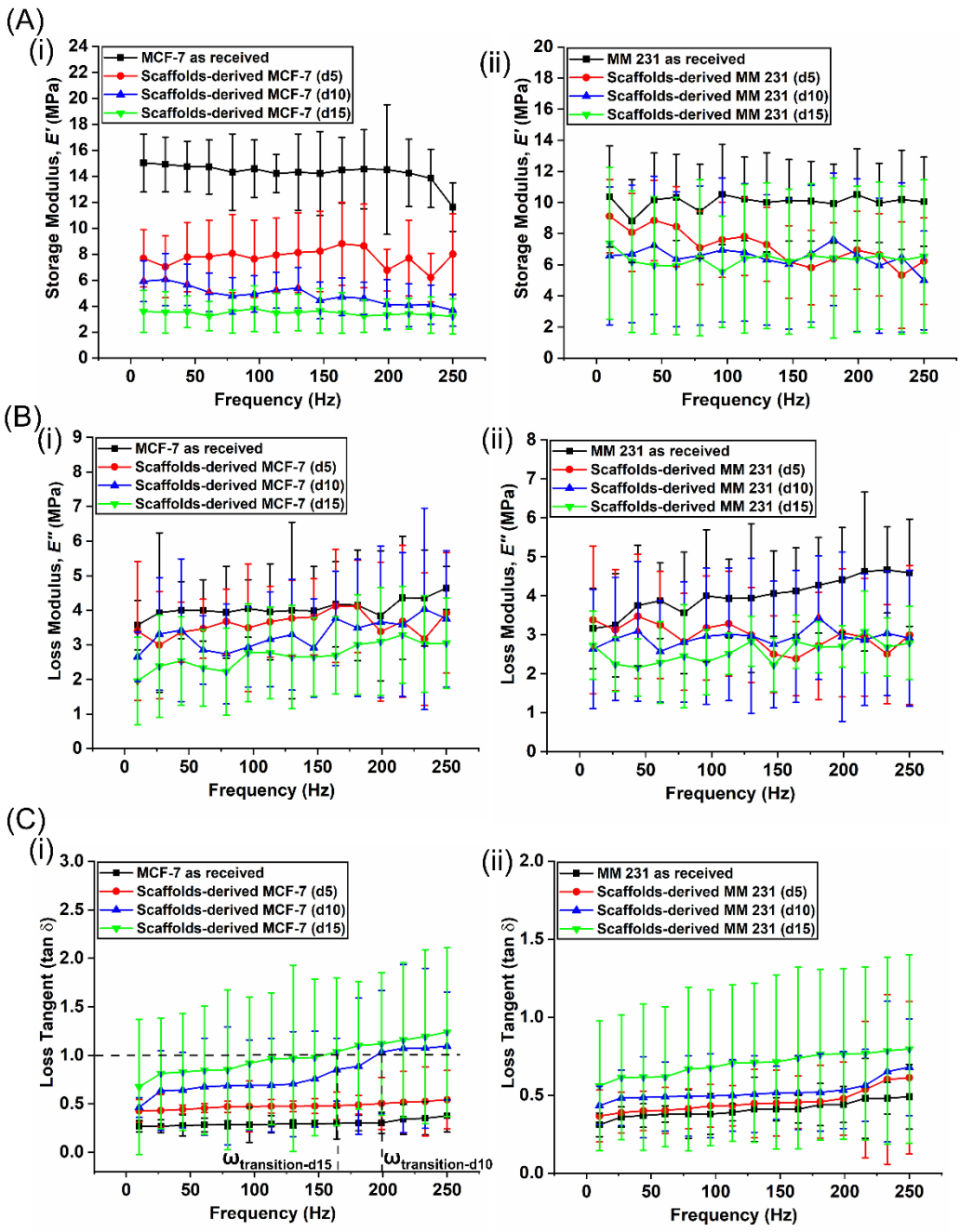

Figure 5.4. (A) Variation of storage modulus (*E'*) for (i) MCF-7 as received and 3D bone-mimetic scaffolds-derived MCF-7 cells; (ii) MM 231 as received and 3D bone-mimetic scaffolds-derived MM 231 cells. (B) Variation of loss modulus (*E''*) for (i) MCF-7 as received and 3D bone-mimetic scaffolds-derived MCF-7 cells; (ii) MM 231 as received and 3D bone-mimetic scaffolds-derived MM 231 cells. (C) Variation of loss tangent (tan δ) for (i) MCF-7 as received and 3D bone-mimetic scaffolds-derived MCF-7 cells; (ii) MM 231 as received and 3D bone-mimetic scaffolds-derived MM 231 cells. Intersections with the horizontal dashed line at tan δ =1 of the vertical lines occur at transition frequencies, $\omega_{transition}$.

In case of loss modulus, scaffolds-derived MCF-7 showed a significant increase over scaffolds-derived MM 231 at day 5, compared to their respective as received counterparts. We observed insignificant changes at day 10 and day 15 in regards to loss modulus as both cells were approaching liquid-like phase during the experiment (Figure 5.5B). Also, we found a substantial increase in tan δ of scaffolds-derived MCF-7 cells over scaffolds-derived MM 231 over time (Figure 5.5C), further confirming our observation in Figure 5.4. Overall, MCF-7 cells showed more liquid-like behavior as compared to MM 231 cells when cultured in 3D bone-mimetic scaffolds.

5.3.3. Actin Dynamics Regulate Cellular Nanomechanics During Cancer Progression

To investigate whether the observed changes in elastic moduli and viscoelastic properties were correlated to structural rearrangements of cytoskeletal components, we performed immunofluorescence staining on as received and scaffolds-grown counterparts of both cancer cells. Representative immunofluorescence images of F-actin and tubulin stained as-received MCF-7/MM 231 and MCF-7/MM 231 cells grown on 3D-bone-mimetic scaffolds are shown in Figures 5.6 and 5.7. The confocal images showed a significant reduction in density of F-actin in scaffolds-grown MCF-7 cells compared to MCF-7 as received cells, but regardless of culture type, there was no significant difference in the density of tubulin [Figures 5.6A(i), 5.7A(i)]. Furthermore, the F-actin network of as received MCF-7 consisted of evenly distributed short fibers, whereas MCF-7 cells grown on scaffolds showed the formation of thin F-actin band between adjacent cells (indicated by small white arrows in Figure 5.6A(i)). To further validate our observation, we calculated corrected total cell fluorescence (CTCF) of F-actin and tubulin for as-received and scaffolds-grown MCF-7 cells.

We found 60.47%, 79.44%, and 95.60% reduction in the concentration of F-actin from as received to scaffolds-grown MCF-7 (d5), MCF-7 (d10), and MCF-7 (d15), respectively [Figure 5.6B(i)]; however, we observed no significant changes in the concentration of tubulin, as shown in Figure 5.7A(i) and B(i).

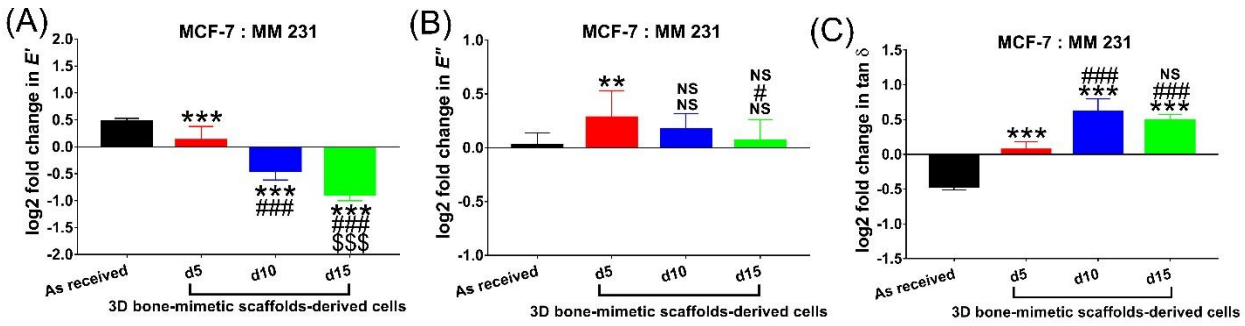

Figure 5.5. Log2 ratios of (A) storage modulus (E'), (B) loss modulus (E''), and (C) loss tangent (tan δ) for MCF-7 and MM 231 across samples (mean ± SD, averaged across frequency). *p<0.05, **p<0.01, and ***p<0.001 indicate significant difference between as received and 3D bone-mimetic scaffolds-derived breast cancer cells; $^{\#}$p<0.05, $^{\#\#}$p<0.01, and $^{\#\#\#}$p<0.001 indicate significant difference between scaffolds-derived breast cancer cells (d5), and other scaffolds-derived breast cancer cells (i.e., (d10) and (d15)); $^{\$}$p<0.05, $^{\$\$}$p<0.01, and $^{\$\$\$}$p<0.001 indicate significant difference between scaffolds-derived breast cancer cells (d10) and (d15).

As-received MM 231 cells exhibited an F-actin network consisted of short fibers [Figure 5.6A (ii)]. The organization of actin cytoskeleton did not change significantly from as received to scaffolds-grown MM 231 cells. MM 231 cells grown on scaffolds neither formed stress fibers nor an F-actin band between adjacent cells, as shown in Figure 5.6A(ii). We once again observed no significant changes in tubulin intensity between as received and scaffolds-grown MM 231 cells [Figure 5.7A (ii)]. Furthermore, quantitative analysis of F-actin [Figure 5.6B(ii)] and tubulin [Figure 5.7B(ii)] fluorescence performed on as-received and scaffolds-grown MM 231 cells showed good agreement with the observations made in Figures 5.6A(ii) and 5.7A(ii). It was previously shown that actin filaments affect the mechanical properties of cells and not microtubules [38, 105]. In accordance with the previous reports, we only observed changes in F-actin concentration while concentration of tubulin remained unchanged.

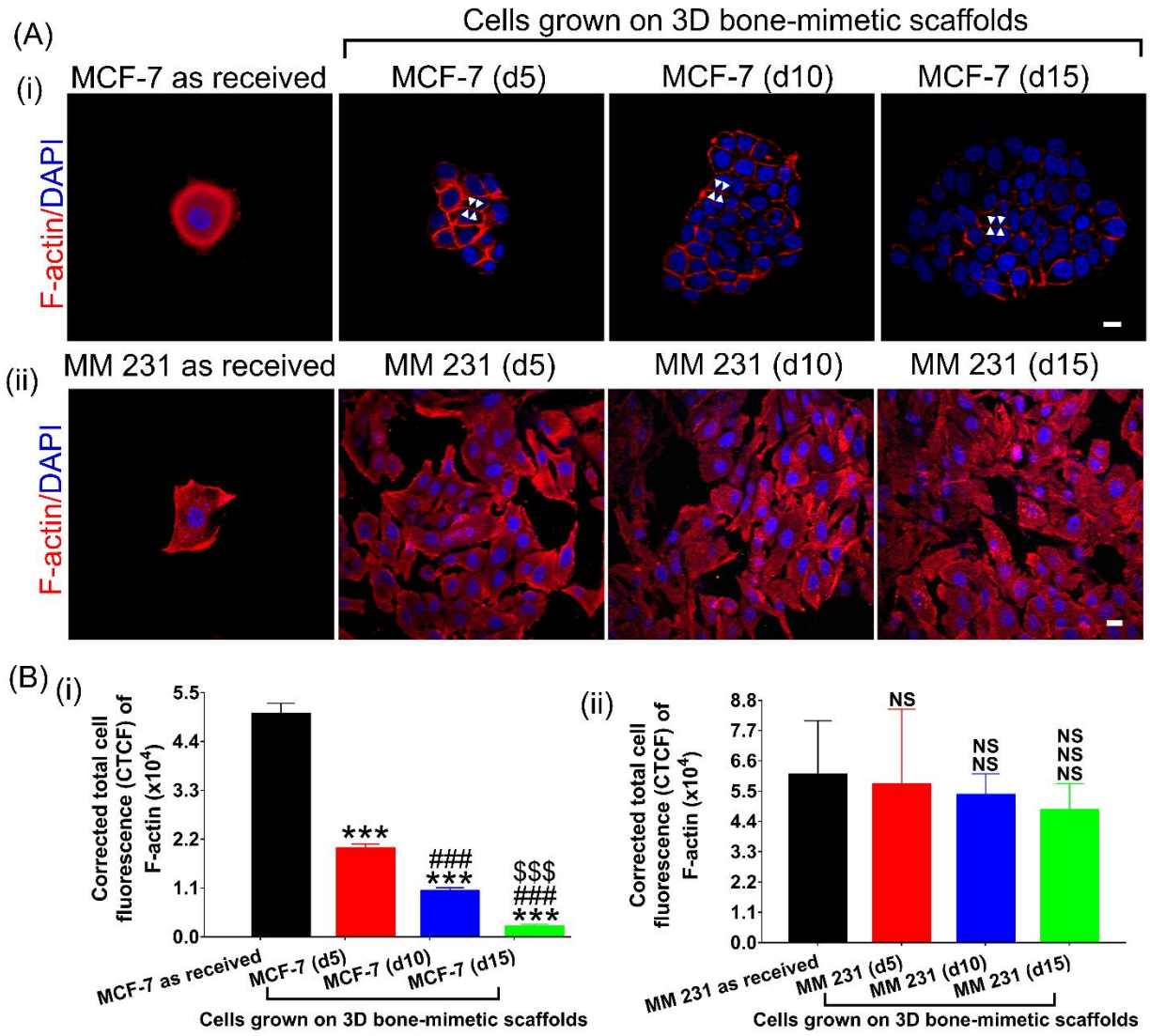

Figure 5.6. (A) Representative immunofluorescence images showing distribution of F-actin in (i) MCF-7 as received and MCF-7 cells grown on 3D bone-mimetic scaffolds. Scaffolds grown MCF-7 formed an F-actin band (white arrows) between adjacent cells; (ii) MM 231 as received and MM 231 cells grown on 3D bone-mimetic scaffolds. Scaffolds grown MM 231 neither formed an F-actin band between adjacent cells nor stress-fibers. (B) Quantification of corrected of total cell fluorescence (CTCF) of F-actin for (i) MCF-7 as received and MCF-7 cells grown on 3D bone-mimetic scaffolds; (ii) MM 231 as received and MM 231 cells grown on 3D bone-mimetic scaffolds. *$p<0.05$, **$p<0.01$, and ***$p<0.001$ indicate significant difference between as received and 3D bone-mimetic scaffolds-grown breast cancer cells; $^{\#}p<0.05$, $^{\#\#}p<0.01$, and $^{\#\#\#}p<0.001$ indicate significant difference between scaffolds-grown breast cancer cells (d5), and other scaffolds-grown breast cancer cells (i.e., (d10) and (d15)); $^{\$}p<0.05$, $^{\$\$}p<0.01$, and $^{\$\$\$}p<0.001$ indicate significant difference between scaffolds-grown breast cancer cells (d10) and (d15).

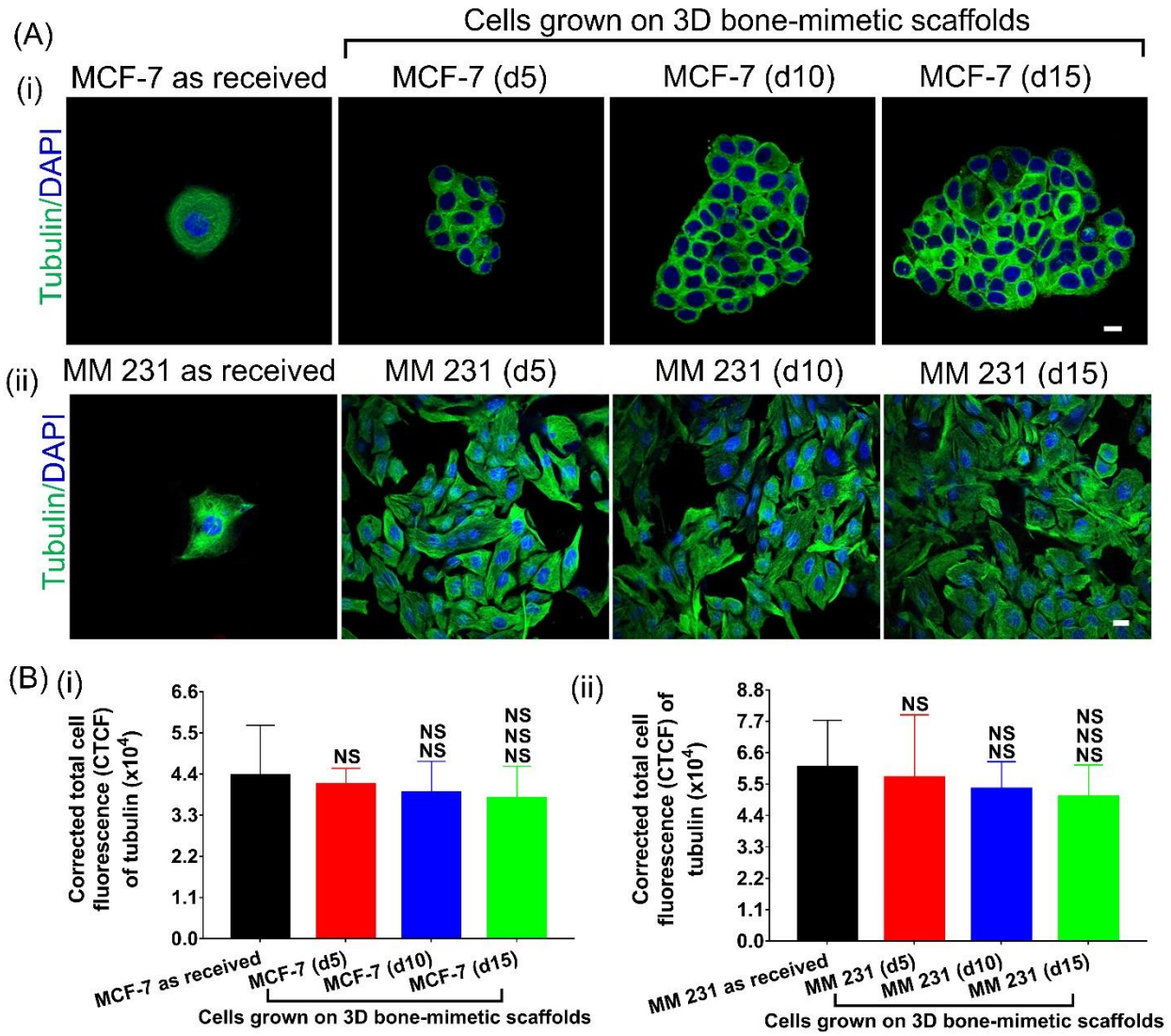

Figure 5.7. (A) Representative immunofluorescence images showing distribution of tubulin in (i) MCF-7 as received and MCF-7 cells grown on 3D bone-mimetic scaffolds; (ii) MM 231 as received and MM 231 cells grown on 3D bone-mimetic scaffolds. (B) Quantification of corrected of total cell fluorescence (CTCF) of tubulin for (i) MCF-7 as received and MCF-7 cells grown on 3D bone-mimetic scaffolds; (ii) MM 231 as received and MM 231 cells grown on 3D bone-mimetic scaffolds. *p<0.05, **p<0.01, and ***p<0.001 indicate significant difference between as received and 3D bone-mimetic scaffolds-grown breast cancer cells; $^{\#}$p<0.05, $^{\#\#}$p<0.01, and $^{\#\#\#}$p<0.001 indicate significant difference between scaffolds-grown breast cancer cells (d5), and other scaffolds-grown breast cancer cells (i.e., (d10) and (d15)); $^{\$}$p<0.05, $^{\$\$}$p<0.01, and $^{\$\$\$}$p<0.001 indicate significant difference between scaffolds-grown breast cancer cells (d10) and (d15).

The observations mentioned above prompted us to evaluate the expression of genes related to actin dynamics. The schematic diagram shown in Figure 5.10A shows how actin regulatory proteins mediate the reorganization of the actin cytoskeleton during MET. We evaluated the expression of CDC42, ARP2, ARP3, N-WASP, CTTN, and CFL2 at the mRNA level. Figure 5.8 shows the expression of these genes for both as-received and scaffolds-grown MCF-7 cells. CDC42, ARP2, ARP3, N-WASP, and CTTN showed reduction at the mRNA level by ~1.70-2.20 fold, ~3-4 fold, and ~9-12 fold in scaffolds-grown MCF-7 (d5), MCF-7 (d10), and MCF-7 (d15), respectively, compared to as received MCF-7. Interestingly, we observed an upregulation in CFL2 expression level by ~2.58 fold, ~4.42 fold, and ~9.37 fold in scaffolds-grown MCF-7 (d5), MCF-7 (d10), and MCF-7 (d15), respectively, compared to as received MCF-7. In the case of MM 231, we observed no significant changes in expression levels of all the evaluated for both as-received and scaffolds-grown cells over time, as shown in Figure 5.9. Taken together, actin dynamics seem to regulate cellular nanomechanics during cancer progression, and MCF-7 cells exhibited a substantial reorganization of actin cytoskeleton when cultured in 3D bone-mimetic scaffolds as compared to MM 231 cells.

5.4. Discussion

In the present study, we investigated nanomechanical properties of as-received and 3D bone-mimetic scaffolds-derived breast cancer cells (MCF-7 and MM 231).We found that scaffolds-grown MCF-7 cells exhibited dramatic changes in elastic modulus and demonstrated liquid-like behavior over time compared to MCF-7 as received cells.

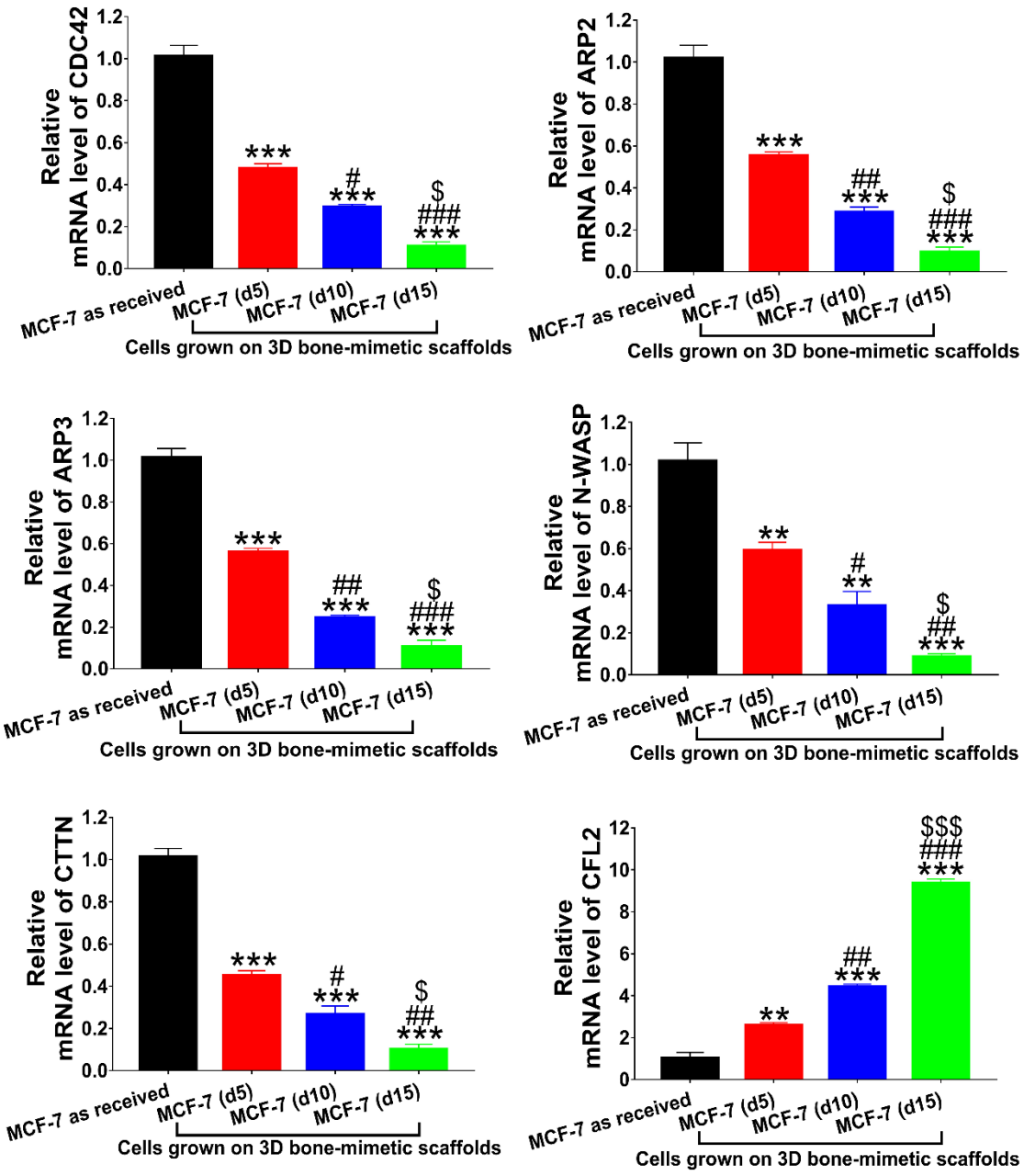

Figure 5.8. Quantitative real-time PCR of gene expression for actin-dynamics related genes CDC42, ARP2, ARP3, N-WASP, CTTN, and CFL2. *p<0.05, **p<0.01, and ***p<0.001 indicate significant difference between MCF-7 as received and MCF-7 cells grown on 3D bone-mimetic scaffolds; #p<0.05, $^{\#\#}$p<0.01, and $^{\#\#\#}$p<0.001 indicate significant difference between MCF-7 (d5) cells grown on 3D bone-mimetic scaffolds, and other MCF-7 cells grown on 3D bone-mimetic scaffolds (i.e., MCF-7 (d10) and MCF-7 (d15)); $^{\$}$p<0.05, $^{\$\$}$p<0.01, and $^{\$\$\$}$p<0.001 indicate significant difference between MCF-7 (d10) and MCF-7 (d15) cells grown on 3D bone-mimetic scaffolds

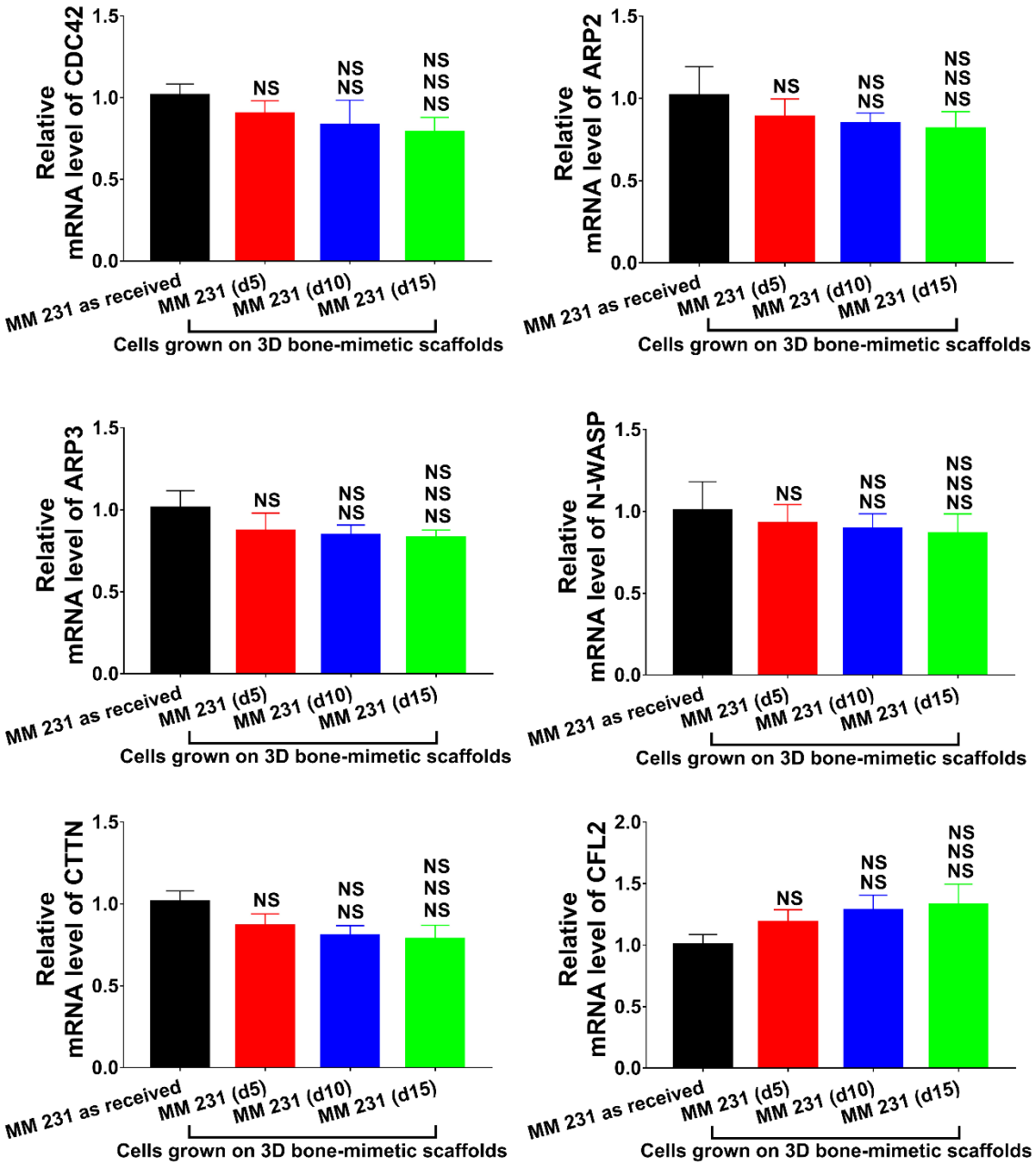

Figure 5.9. Quantitative real-time PCR of gene expression for actin-dynamics related genes CDC42, ARP2, ARP3, N-WASP, CTTN, and CFL2. *p<0.05, **p<0.01, and ***p<0.001 indicate significant difference between MM 231 as received and MM 231 cells grown on 3D bone-mimetic scaffolds; $^{\#}$p<0.05, $^{\#\#}$p<0.01, and $^{\#\#\#}$p<0.001 indicate significant difference between MM 231 (d5) cells grown on 3D bone-mimetic scaffolds, and other MM 231 cells grown on 3D bone-mimetic scaffolds (i.e., MM 231 (d10) and MM 231 (d15)); $^{\$}$p<0.05, $^{\$\$}$p<0.01, and $^{\$\$\$}$p<0.001 indicate significant difference between MM 231 (d10) and MM 231 (d15) cells grown on 3D bone-mimetic scaffolds.

In contrast, scaffolds-grown MM 231 cells neither showed significant changes in elastic modulus nor exhibited liquid-like behavior over time as compared to as-received MM 231 cells. Larger loss tangent values of MCF-7 cells compared to MM 231 cells is consistent with results from a previous study conducted using AFM [26].

Scaffolds-grown MCF-7 cells were softer and had a larger loss tangent (a measure of liquid-like behavior) than as-received MCF-7 cells [Figures 5.2 and 5.4C(i)] whereas elastic moduli and loss tangent values were similar for as-received and scaffolds-grown MM 231 cells [Figures 5.3 and 5.4C(ii)]. It was reported that dysregulation in actin cytoskeletal dynamics is associated with an increased liquidity or liquid-like behavior (represented by higher loss tangent), while elastic moduli increase with stabilization of the F-actin network [106, 107].

Actin cytoskeleton dynamics have been shown to play a critical role during transition between mesenchymal and epithelial states. In the mesenchymal state, E-cadherin is not present, and the actin cytoskeleton undergoes several changes, leading to a shift of actin and its regulatory proteins and complexes such as N-WASP, cortactin, and Arp2/3 complex from the cortex towards the leading edge to form lamellipodia [19]. In contrast, epithelial cells form tight junctions to create an intracellular barrier separating the tissue from the outside world and adherens junction between adjacent cells that bestow mechanical stability by connecting with the actin cytoskeleton and E-cadherin. Furthermore, E-cadherin maintains integrity of adherens junctions by providing a basis for sequestration of actin nucleation proteins in non-motile cells. Cortactin, a scaffolding protein, binds to both N-WASP and E-cadherin to recruit Arp2/3 complex to adherens junctions [19, 33]. Although the Rho family small GTPase CDC42 has been shown to regulate most of the changes in the mesenchymal state [108], overexpression of E-cadherin (in the epithelial state) has been associated with inhibition of CDC42[30, 109].

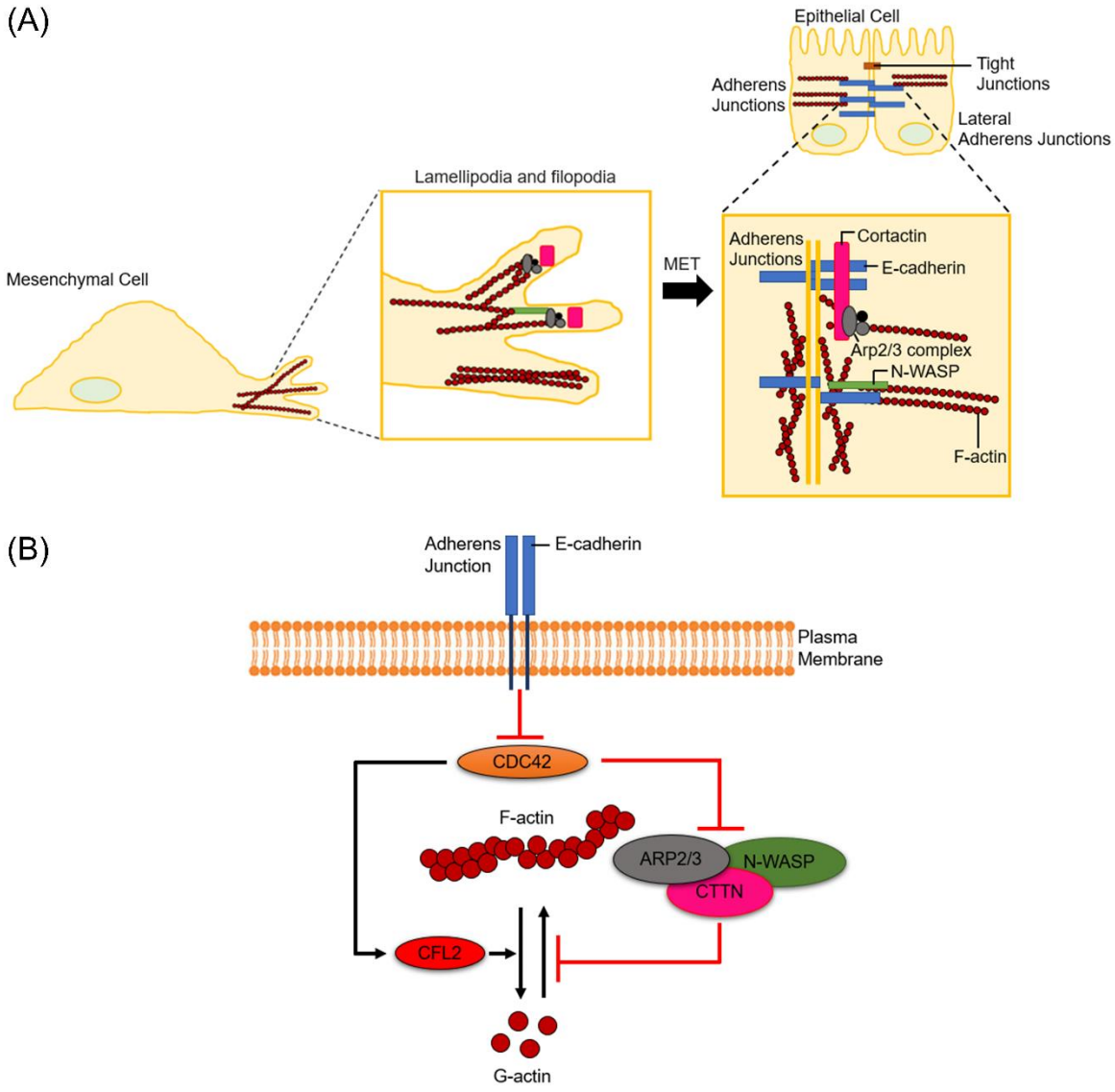

Figure 5.10. (A) In mesenchymal cells, E-cadherin is not present, and the actin cytoskeleton undergoes several changes, leading to a shift of actin and its regulatory proteins and complexes such as N-WASP, cortactin, and Arp2/3 complex from the cortex towards the leading edge to form lamellipodia. In contrast, epithelial cells form tight junctions to create an intracellular barrier separating the tissue from the outside world and adherens junction between adjacent cells that bestow mechanical stability by connecting with the actin cytoskeleton and E-cadherin. Furthermore, E-cadherin maintains adherens junction integrity by providing a basis for sequestration of actin nucleation proteins in non-motile cells. Cortactin, a scaffolding protein, binds to both N-WASP and E-cadherin to recruit Arp2/3 complex to adherens junctions. (B) E-cadherin inhibits CDC42, a small GTPase of the Rho family, which in turn prevents actin interacting regulatory proteins (N-WASP, ARP2/3, and CTTN) from taking part in actin nucleation, at the same time stimulating the activity of actin severing protein CFL2, thereby promoting depolymerization of actin.

It is evident from the observations mentioned above that the degree of F-actin reduction is closely related to the expression of E-cadherin. We have previously reported enhanced expression of E-cadherin in scaffolds-grown breast cancer cells during MET [88]. This prompted us to calculate the log2 ratios of E-cadherin expression in scaffolds-grown MM 231/MCF-7 compared to their respective controls, and we observed a 95.44% increase in E-cadherin expression in scaffolds-grown MCF-7 cells compared to scaffolds-grown MM 231 cells (Figure 5.11C).

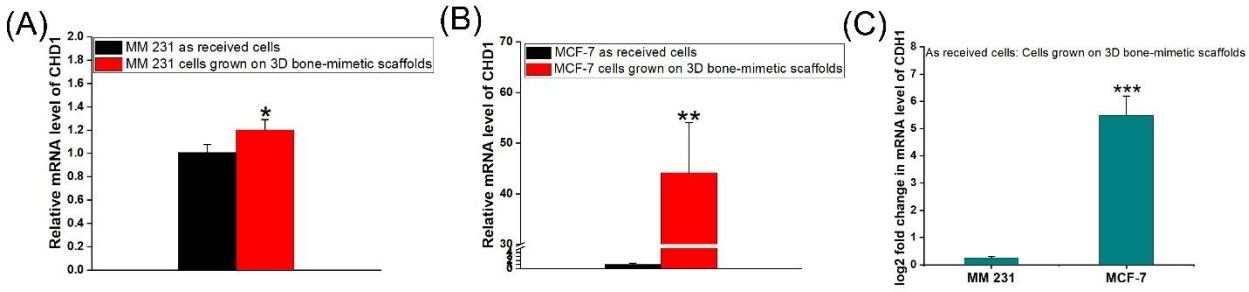

Figure 5.11. (A&B) Quantitative real-time PCR of gene expression for CHD1 for as received MCF-7/MM 231 and MCF-7/MM 231 cells grown 3D bone-mimetic scaffolds. (C) Log2 ratios of CHD1 gene expression of as received and cells grown on 3D bone-mimetic scaffolds for both breast cancer cells. (n=3; one-way ANOVA followed by *post hoc* Tukey test, $*p < 0.05$, $**p < 0.01$, $***p < 0.001$).

Hence, overexpression of E-cadherin inhibits CDC42, a small GTPase of the Rho family, which in turn prevents actin interacting regulatory proteins (N-WASP, ARP2/3, and CTTN) from participating in actin nucleation, at the same time stimulating the activity of actin severing protein CFL2, thereby promoting depolymerization of F-actin (Figure 5.10B). This explains the significant reduction of F-actin in scaffolds-grown MCF-7 cells compared to scaffolds-grown MM 231 cells. Methods described in the study could be translated into clinical studies in the form of elastography. Elastography is a non-invasive medical imaging technique that maps the stiffness and elastic properties of a tissue. It uses low frequency vibration during ultrasound or magnetic resonance imaging (MRI) to measure stiffness of organs inside the body.

In summary, we reported the evolution of nanomechanical properties of breast cancer cells at metastases using quasi-static and dynamic nanoindentation methods. Our results demonstrated that the reduction of elastic modulus of scaffolds-derived MCF-7 cells was induced by depolymerization and reorganization of F-actin to the adherens junctions, whereas scaffolds-derived MM 231 cells showed insignificant changes in elastic modulus and F-actin reorganization over time, as opposed to their respective as-received counterparts. Together, our data indicate that the mechanical properties of breast cancer cells could be used as a possible biomarker of breast cancer progression at metastases.

5.5. Conclusion

In the present study, we investigated the nanomechanical properties of as-received and 3D bone-mimetic scaffolds-derived breast cancer cells (MCF-7 and MM 231). We found that scaffolds-grown MCF-7 cells exhibited dramatic changes in elastic modulus and demonstrated liquid-like behavior over time compared to MCF-7 as received cells. In contrast, scaffolds-grown MM 231 cells neither showed significant differences in elastic modulus nor exhibited liquid-like behavior over time as compared to as-received MM 231 cells. Scaffolds-grown MCF-7 cells were softer and had a larger loss tangent (a measure of liquid-like behavior) than as-received MCF-7 cells, whereas elastic moduli and loss tangent values were similar for as-received and scaffolds-grown MM 231 cells. From immunofluorescence and gene expression analysis results, we observed that the significant reduction in elastic modulus together with increased liquid-like behavior of scaffolds-derived MCF-7 cells compared to MCF-7 as received cells, was induced by depolymerization and reorganization of F-actin to the adherens junctions. In contrast, scaffolds-derived MM 231 cells showed insignificant changes in F-actin reorganization over time, as opposed to their as-received counterparts. The significant reduction of F-actin during progression

of metastasis in MCF-7 cells at bone indicates a critical role of the highly viscoelastic cytoplasm in MCF-7, leading to overall increase in loss tangent. The MM-231 cell line does not exhibit this behavior. It is interesting to note that the pathogenesis of the two cell cells is quite different clinically and here we demonstrate the use of a bone scaffold testbed to create metastasis that can be captured through nanomechanical evolution. Collectively, our data indicate that the nanomechanical properties of breast cancer cells could be used as a possible biomarker of breast cancer progression at metastases.

5.6. Acknowledgements

This research was supported by funds from NDSU Grand Challenge Initiative for "Center for Engineered Cancer Beds". The authors acknowledge use of instruments in Electron Microscopy Center, Core Biology Facility, and Advanced Imaging & Microscopy Lab at NDSU. Support from ND EPSCoR for tissue engineering laboratory is also acknowledged. The nanoindentation equipment used in this study was obtained through NSF Instrumentation for Materials Research Grant.

5.7. References

[1] M.M. Yallapu, K.S. Katti, D.R. Katti, S.R. Mishra, S. Khan, M. Jaggi, S.C. Chauhan, The roles of cellular nanomechanics in cancer, Medicinal research reviews 35(1) (2015) 198-223.

[2] D.R. Katti, K.S. Katti, S. Molla, S. Kar, Biomechanics of Cells as Potential Biomarkers for Diseases: A New Tool in Mechanobiology, in: R. Narayan (Ed.), Encyclopedia of Biomedical Engineering, Elsevier, Amsterdam, 2019, pp. 1-21.

[3] M.F. Coughlin, D.R. Bielenberg, G. Lenormand, M. Marinkovic, C.G. Waghorne, B.R. Zetter, J.J. Fredberg, Cytoskeletal stiffness, friction, and fluidity of cancer cell lines with different metastatic potential, Clinical & experimental metastasis 30(3) (2013) 237-250.

[4] V. Swaminathan, K. Mythreye, E.T. O'Brien, A. Berchuck, G.C. Blobe, R. Superfine, Mechanical Stiffness Grades Metastatic Potential in Patient Tumor Cells and in Cancer Cell Lines, Cancer Research 71(15) (2011) 5075-5080.

[5] J. Guck, S. Schinkinger, B. Lincoln, F. Wottawah, S. Ebert, M. Romeyke, D. Lenz, H.M. Erickson, R. Ananthakrishnan, D. Mitchell, Optical deformability as an inherent cell marker for testing malignant transformation and metastatic competence, Biophysical journal 88(5) (2005) 3689-3698.

[6] E.C. Faria, N. Ma, E. Gazi, P. Gardner, M. Brown, N.W. Clarke, R.D. Snooka, Measurement of elastic properties of prostate cancer cells using AFM, Analyst 133(11) (2008) 1498-1500.

[7] Q.S. Li, G.Y.H. Lee, C.N. Ong, C.T. Lim, AFM indentation study of breast cancer cells, Biochemical and Biophysical Research Communications 374(4) (2008) 609-613.

[8] M. Lekka, P. Laidler, D. Gil, J. Lekki, Z. Stachura, A.Z. Hrynkiewicz, Elasticity of normal and cancerous human bladder cells studied by scanning force microscopy, European Biophysics Journal with Biophysics Letters 28(4) (1999) 312-316.

[9] J. Hu, Y. Zhou, J.D. Obayemi, J. Du, W.O. Soboyejo, An investigation of the viscoelastic properties and the actin cytoskeletal structure of triple negative breast cancer cells, Journal of the mechanical behavior of biomedical materials 86 (2018) 1-13.

[10] S.E. Cross, Y.-S. Jin, J. Rao, J.K. Gimzewski, Nanomechanical analysis of cells from cancer patients, Nature nanotechnology 2(12) (2007) 780-783.

[11] M.J. Rosenbluth, W.A. Lam, D.A. Fletcher, Force microscopy of nonadherent cells: A comparison of leukemia cell deformability, Biophysical Journal 90(8) (2006) 2994-3003.

[12] G. Zhang, M. Long, Z.-Z. Wu, W.-Q. Yu, Mechanical properties of hepatocellular carcinoma cells, World journal of gastroenterology 8(2) (2002) 243.

[13] J. Stricker, T. Falzone, M.L. Gardel, Mechanics of the F-actin cytoskeleton, Journal of biomechanics 43(1) (2010) 9-14.

[14] G. Bao, S. Suresh, Cell and molecular mechanics of biological materials, Nature materials 2(11) (2003) 715-725.

[15] D.A. Fletcher, R.D. Mullins, Cell mechanics and the cytoskeleton, Nature 463(7280) (2010) 485-492.

[16] S. Suresh, Biomechanics and biophysics of cancer cells, Acta biomaterialia 3(4) (2007) 413-438.

[17] B. De Craene, G. Berx, Regulatory networks defining EMT during cancer initiation and progression, Nature Reviews Cancer 13(2) (2013) 97-110.

[18] E. Dejana, Endothelial cell–cell junctions: happy together, Nature reviews Molecular cell biology 5(4) (2004) 261-270.

[19] H.T. Morris, L.M. Machesky, Actin cytoskeletal control during epithelial to mesenchymal transition: focus on the pancreas and intestinal tract, British journal of cancer 112(4) (2015) 613-620.

[20] R.W. Style, R. Boltyanskiy, G.K. German, C. Hyland, C.W. MacMinn, A.F. Mertz, L.A. Wilen, Y. Xu, E.R. Dufresne, Traction force microscopy in physics and biology, Soft matter 10(23) (2014) 4047-4055.

[21] M.F. Olson, E. Sahai, The actin cytoskeleton in cancer cell motility, Clinical & experimental metastasis 26(4) (2009) 273.

[22] H. Yamaguchi, J. Condeelis, Regulation of the actin cytoskeleton in cancer cell migration and invasion, Biochimica et Biophysica Acta (BBA)-Molecular Cell Research 1773(5) (2007) 642-652.

[23] T. Okegawa, R.-C. Pong, Y. Li, J.-T. Hsieh, The role of cell adhesion molecule in cancer progression and its application in cancer therapy, Acta Biochimica Polonica 51(2) (2004) 445-457.

[24] U. Cavallaro, G. Christofori, Cell adhesion in tumor invasion and metastasis: loss of the glue is not enough, Biochimica et Biophysica Acta (BBA)-Reviews on Cancer 1552(1) (2001) 39-45.

[25] A. Calzado-Martín, M. Encinar, J. Tamayo, M. Calleja, A. San Paulo, Effect of actin organization on the stiffness of living breast cancer cells revealed by peak-force modulation atomic force microscopy, ACS nano 10(3) (2016) 3365-3374.

[26] N. Schierbaum, J. Rheinlaender, T.E. Schäffer, Viscoelastic properties of normal and cancerous human breast cells are affected differently by contact to adjacent cells, Acta biomaterialia 55 (2017) 239-248.

[27] R. Kalluri, R.A. Weinberg, The basics of epithelial-mesenchymal transition, The Journal of clinical investigation 119(6) (2009) 1420-1428.

[28] J. Haynes, J. Srivastava, N. Madson, T. Wittmann, D.L. Barber, Dynamic actin remodeling during epithelial–mesenchymal transition depends on increased moesin expression, Molecular biology of the cell 22(24) (2011) 4750-4764.

[29] J. Liu, G. Hu, D. Chen, A.Y. Gong, G.S. Soori, T.J. Dobleman, X.-M. Chen, Suppression of SCARA5 by Snail1 is essential for EMT-associated cell migration of A549 cells, Oncogenesis 2(9) (2013) e73-e73.

[30] J. Shankar, I.R. Nabi, Actin cytoskeleton regulation of epithelial mesenchymal transition in metastatic cancer cells, PloS one 10(3) (2015).

[31] J. Shankar, A. Messenberg, J. Chan, T.M. Underhill, L.J. Foster, I.R. Nabi, Pseudopodial actin dynamics control epithelial-mesenchymal transition in metastatic cancer cells, Cancer research 70(9) (2010) 3780-3790.

[32] C. Le Clainche, M.-F. Carlier, Regulation of actin assembly associated with protrusion and adhesion in cell migration, Physiological reviews 88(2) (2008) 489-513.

[33] S.K. Wu, G.A. Gomez, M. Michael, S. Verma, H.L. Cox, J.G. Lefevre, R.G. Parton, N.A. Hamilton, Z. Neufeld, A.S. Yap, Cortical F-actin stabilization generates apical–lateral patterns of junctional contractility that integrate cells into epithelia, Nature cell biology 16(2) (2014) 167-178.

[34] K. Iwaya, K. Norio, K. Mukai, Coexpression of Arp2 and WAVE2 predicts poor outcome in invasive breast carcinoma, Modern pathology 20(3) (2007) 339-343.

[35] W. Xu, R. Mezencev, B. Kim, L. Wang, J. McDonald, T. Sulchek, Cell stiffness is a biomarker of the metastatic potential of ovarian cancer cells, PloS one 7(10) (2012).

[36] A.N. Ketene, E.M. Schmelz, P.C. Roberts, M. Agah, The effects of cancer progression on the viscoelasticity of ovarian cell cytoskeleton structures, Nanomedicine-Nanotechnology Biology and Medicine 8(1) (2012) 93-102.

[37] M. Nikkhah, J.S. Strobl, E.M. Schmelz, M. Agah, Evaluation of the influence of growth medium composition on cell elasticity, Journal of Biomechanics 44(4) (2011) 762-766.

[38] M. Nikkhah, J.S. Strobl, R. De Vita, M. Agah, The cytoskeletal organization of breast carcinoma and fibroblast cells inside three dimensional (3-D) isotropic silicon microstructures, Biomaterials 31(16) (2010) 4552-4561.

[39] J.S. Strobl, M. Nikkhah, M. Agah, Actions of the anti-cancer drug suberoylanilide hydroxamic acid (SAHA) on human breast cancer cytoarchitecture in silicon microstructures, Biomaterials 31(27) (2010) 7043-7050.

[40] N. Nguyen, Y. Shao, A. Wineman, J. Fu, A. Waas, Atomic force microscopy indentation and inverse analysis for non-linear viscoelastic identification of breast cancer cells, Mathematical biosciences 277 (2016) 77-88.

[41] Y. Nematbakhsh, K.T. Pang, C.T. Lim, Correlating the viscoelasticity of breast cancer cells with their malignancy, Convergent Science Physical Oncology 3(3) (2017) 034003.

[42] Y.M. Efremov, W.-H. Wang, S.D. Hardy, R.L. Geahlen, A. Raman, Measuring nanoscale viscoelastic parameters of cells directly from AFM force-displacement curves, Scientific reports 7(1) (2017) 1-14.

[43] Y.H. Chim, L.M. Mason, N. Rath, M.F. Olson, M. Tassieri, H. Yin, A one-step procedure to probe the viscoelastic properties of cells by Atomic Force Microscopy, Scientific reports 8(1) (2018) 1-12.

[44] M. Lekka, D. Gil, K. Pogoda, J. Dulińska-Litewka, R. Jach, J. Gostek, O. Klymenko, S. Prauzner-Bechcicki, Z. Stachura, J. Wiltowska-Zuber, Cancer cell detection in tissue sections using AFM, Archives of biochemistry and biophysics 518(2) (2012) 151-156.

[45] G. Coceano, M.S. Yousafzai, W. Ma, F. Ndoye, L. Venturelli, I. Hussain, S. Bonin, J. Niemela, G. Scoles, D. Cojoc, E. Ferrari, Investigation into local cell mechanics by

atomic force microscopy mapping and optical tweezer vertical indentation, Nanotechnology 27(6) (2016).

[46] X. Guo, K. Bonin, K. Scarpinato, M. Guthold, The effect of neighboring cells on the stiffness of cancerous and non-cancerous human mammary epithelial cells, New Journal of Physics 16(10) (2014) 105002.

[47] J.R. Staunton, B.L. Doss, S. Lindsay, R. Ros, Correlating confocal microscopy and atomic force indentation reveals metastatic cancer cells stiffen during invasion into collagen I matrices, Scientific reports 6 (2016).

[48] S. Nawaz, P. Sánchez, K. Bodensiek, S. Li, M. Simons, I.A.T. Schaap, Cell visco-elasticity measured with AFM and optical trapping at sub-micrometer deformations, PloS one 7(9) (2012).

[49] M.S. Yousafzai, G. Coceano, S. Bonin, J. Niemela, G. Scoles, D. Cojoc, Investigating the effect of cell substrate on cancer cell stiffness by optical tweezers, Journal of biomechanics 60 (2017) 266-269.

[50] G. Hong-Lian, L. Chun-Xiang, D. Jian-Fa, J. Yu-Qiang, H. Xue-Hai, L. Zhao-Lin, C. Bing-Ying, Z. Dao-Zhong, Mechanical properties of breast cancer cell membrane studied with optical tweezers, Chinese Physics Letters 21(12) (2004) 2543.

[51] M.S. Yousafzai, G. Coceano, A. Mariutti, F. Ndoye, L. Amin, J. Niemela, S. Bonin, G. Scoles, D. Cojoc, Effect of neighboring cells on cell stiffness measured by optical tweezers indentation, Journal of biomedical optics 21(5) (2016) 057004.

[52] M. Dao, C.T. Lim, S. Suresh, Mechanics of the human red blood cell deformed by optical tweezers, Journal of the Mechanics and Physics of Solids 51(11-12) (2003) 2259-2280.

[53] H. Zhang, K.-K. Liu, Optical tweezers for single cells, Journal of The Royal Society Interface 5(24) (2008) 671-690.

[54] W.R. Trickey, F.P.T. Baaijens, T.A. Laursen, L.G. Alexopoulos, F. Guilak, Determination of the Poisson's ratio of the cell: recovery properties of chondrocytes after release from complete micropipette aspiration, Journal of biomechanics 39(1) (2006) 78-87.

[55] M. Sato, M.J. Levesque, R.M. Nerem, Micropipette aspiration of cultured bovine aortic endothelial cells exposed to shear stress, Arteriosclerosis, Thrombosis, and Vascular Biology 7(3) (1987) 276-286.

[56] R.M. Hochmuth, Micropipette aspiration of living cells, Journal of biomechanics 33(1) (2000) 15-22.

[57] E. Evans, A. Yeung, Apparent viscosity and cortical tension of blood granulocytes determined by micropipet aspiration, Biophysical journal 56(1) (1989) 151-160.

[58] B. Fabry, G.N. Maksym, R.D. Hubmayr, J.P. Butler, J.J. Fredberg, Implications of heterogeneous bead behavior on cell mechanical properties measured with magnetic twisting cytometry, Journal of magnetism and magnetic materials 194(1-3) (1999) 120-125.

[59] N. Wang, D.E. Ingber, Probing transmembrane mechanical coupling and cytomechanics using magnetic twisting cytometry, Biochemistry and Cell Biology 73(7-8) (1995) 327-335.

[60] M. Puig-De-Morales, M. Grabulosa, J. Alcaraz, J. Mullol, G.N. Maksym, J.J. Fredberg, D. Navajas, Measurement of cell microrheology by magnetic twisting cytometry with frequency domain demodulation, Journal of Applied Physiology 91(3) (2001) 1152-1159.

[61] A. Rigato, A. Miyagi, S. Scheuring, F. Rico, High-frequency microrheology reveals cytoskeleton dynamics in living cells, Nature physics 13(8) (2017) 771-775.

[62] J.R. Staunton, W.Y. So, C.D. Paul, K. Tanner, High-frequency microrheology in 3D reveals mismatch between cytoskeletal and extracellular matrix mechanics, Proceedings of the National Academy of Sciences 116(29) (2019) 14448-14455.

[63] S. Yamada, D. Wirtz, S.C. Kuo, Mechanics of living cells measured by laser tracking microrheology, Biophysical journal 78(4) (2000) 1736-1747.

[64] Y. Tseng, T.P. Kole, D. Wirtz, Micromechanical mapping of live cells by multiple-particle-tracking microrheology, Biophysical journal 83(6) (2002) 3162-3176.

[65] D. Kirmizis, S. Logothetidis, Atomic force microscopy probing in the measurement of cell mechanics, International journal of nanomedicine 5 (2010) 137.

[66] K. Haase, A.E. Pelling, Investigating cell mechanics with atomic force microscopy, Journal of The Royal Society Interface 12(104) (2015) 20140970.

[67] E.J.G. Peterman, F. Gittes, C.F. Schmidt, Laser-induced heating in optical traps, Biophysical journal 84(2) (2003) 1308-1316.

[68] R. Khanna, K.S. Katti, D.R. Katti, Experiments in nanomechanical properties of live osteoblast cells and cell–biomaterial interface, Journal of Nanotechnology in Engineering and Medicine 2(4) (2011) 041005.

[69] R. Khanna, D.R. Katti, K.S. Katti, AFM and Nanoindentation Studies of Bone Nodules on Chitosan-Polygalacturonic Acid-Hydroxyapatite Nanocomposites, Cmes-Computer Modeling in Engineering & Sciences 87(6) (2012) 530-555.

[70] J. Domke, S. Dannohl, W.J. Parak, O. Muller, W.K. Aicher, M. Radmacher, Substrate dependent differences in morphology and elasticity of living osteoblasts investigated by atomic force microscopy, Colloids and Surfaces B-Biointerfaces 19(4) (2000) 367-379.

[71] J. Arfsten, C. Bradtmöller, I. Kampen, A. Kwade, Compressive testing of single yeast cells in liquid environment using a nanoindentation system, Journal of Materials Research 23(12) (2008) 3153-3160.

[72] D.M. Ebenstein, L.A. Pruitt, Nanoindentation of soft hydrated materials for application to vascular tissues, Journal of Biomedical Materials Research Part A: An Official Journal of The Society for Biomaterials, The Japanese Society for Biomaterials, and The Australian Society for Biomaterials and the Korean Society for Biomaterials 69(2) (2004) 222-232.

[73] O. Franke, M. Göken, M.A. Meyers, K. Durst, A.M. Hodge, Dynamic nanoindentation of articular porcine cartilage, Materials science and engineering: C 31(4) (2011) 789-795.

[74] M.E. Roy, J.Y. Rho, T.Y. Tsui, N.D. Evans, G.M. Pharr, Mechanical and morphological variation of the human lumbar vertebral cortical and trabecular bone, Journal of biomedical materials research 44(2) (1999) 191-197.

[75] K.S. Katti, C. Gu, D.R. Katti, Anisotropic properties of human cortical bone with osteogenesis imperfecta, Biomechanics and modeling in mechanobiology 15(1) (2016) 155-167.

[76] C. Gu, D.R. Katti, K.S. Katti, Dynamic nanomechanical behaviour of healthy and OI human cortical bone, Bioinspired, Biomimetic and Nanobiomaterials 4(1) (2015) 15-25.

[77] C. Gu, D.R. Katti, K.S. Katti, Microstructural and photoacoustic infrared spectroscopic studies of human cortical bone with osteogenesis imperfecta, Jom 68(4) (2016) 1116-1127.

[78] B. Mohanty, K.S. Katti, D.R. Katti, D. Verma, Dynamic nanomechanical response of nacre, Journal of materials research 21(8) (2006) 2045-2051.

[79] K.S. Katti, B. Mohanty, D.R. Katti, Nanomechanical properties of nacre, Journal of Materials Research 21(5) (2006) 1237-1242.

[80] B. Mohanty, K.S. Katti, D.R. Katti, Experimental investigation of nanomechanics of the mineral-protein interface in nacre, Mechanics Research Communications 35(1-2) (2008) 17-23.

[81] G. Balooch, G.W. Marshall, S.J. Marshall, O.L. Warren, S.A.S. Asif, M. Balooch, Evaluation of a new modulus mapping technique to investigate microstructural features of human teeth, Journal of biomechanics 37(8) (2004) 1223-1232.

[82] J.H. Kinney, S.J. Marshall, G.W. Marshall, The mechanical properties of human dentin: a critical review and re-evaluation of the dental literature, Critical Reviews in Oral Biology & Medicine 14(1) (2003) 13-29.

[83] D.R. Katti, K.S. Katti, Cancer cell mechanics with altered cytoskeletal behavior and substrate effects: A 3D finite element modeling study, Journal of the mechanical behavior of biomedical materials 76 (2017) 125-134.

[84] A. Marturano-Kruik, M.M. Nava, K. Yeager, A. Chramiec, L. Hao, S. Robinson, E. Guo, M.T. Raimondi, G. Vunjak-Novakovic, Human bone perivascular niche-on-a-chip for studying metastatic colonization, Proceedings of the National Academy of Sciences 115(6) (2018) 1256-1261.

[85] A. Fantozzi, G. Christofori, Mouse models of breast cancer metastasis, Breast Cancer Research 8(4) (2006) 212.

[86] A. Nyga, U. Cheema, M. Loizidou, 3D tumour models: novel in vitro approaches to cancer studies, Journal of Cell Communication and Signaling 5(3) (2011) 239-248.

[87] K.L. Kretschmann, A.L. Welm, Mouse models of breast cancer metastasis to bone, Cancer and Metastasis Reviews 31(3-4) (2012) 579-583.

[88] S. Kar, M.D.S. Molla, D.R. Katti, K.S. Katti, Tissue-engineered nanoclay-based 3D in vitro breast cancer model for studying breast cancer metastasis to bone, Journal of tissue engineering and regenerative medicine 13(2) (2019) 119-130.

[89] A.H. Ambre, D.R. Katti, K.S. Katti, Biomineralized hydroxyapatite nanoclay composite scaffolds with polycaprolactone for stem cell-based bone tissue engineering, Journal of Biomedical Materials Research Part A 103(6) (2015) 2077-2101.

[90] K.S. Katti, A.H. Ambre, S. Payne, D.R. Katti, Vesicular delivery of crystalline calcium minerals to ECM in biomineralized nanoclay composites, Materials Research Express 2(4) (2015) 13.

[91] S. Molla, D.R. Katti, K.S. Katti, In vitro design of mesenchymal to epithelial transition of prostate cancer metastasis using 3D nanoclay bone-mimetic scaffolds, Journal of tissue engineering and regenerative medicine 12(3) (2018).727-737

[92] M.D.S. Molla, D.R. Katti, K.S. Katti, An in vitro model of prostate cancer bone metastasis for highly metastatic and non-metastatic prostate cancer using nanoclay bone-mimetic scaffolds, MRS Advances 4(21) (2019) 1207-1213.

[93] M.D.S. Molla, D.R. Katti, J. Iswara, R. Venkatesan, R. Paulmurugan, K.S. Katti, Prostate cancer phenotype influences bone mineralization at metastasis: A study using an in vitro prostate cancer metastasis testbed, JBMR Plus.4(2) (2020) e10256

[94] S. Kar, H. Jasuja, D.R. Katti, K.S. Katti, Wnt/β-catenin Signaling Pathway Regulates Osteogenesis for Breast Cancer Bone Metastasis: Experiments in an in vitro Nanoclay Scaffold Cancer Testbed, ACS Biomaterials Science & Engineering (2019). https://doi.org/10.1021/acsbiomaterials.9b00923

[95] A. Ambre, K.S. Katti, D.R. Katti, In situ mineralized hydroxyapatite on amino acid modified nanoclays as novel bone biomaterials, Materials Science and Engineering: C 31(5) (2011) 1017-1029.

[96] A.H. Ambre, K.S. Katti, D.R. Katti, Nanoclay based composite scaffolds for bone tissue engineering applications, Journal of Nanotechnology in Engineering and Medicine 1(3) (2010) 031013.

[97] K.S. Katti, A.H. Ambre, N. Peterka, D.R. Katti, Use of unnatural amino acids for design of novel organomodified clays as components of nanocomposite biomaterials, Philosophical Transactions of the Royal Society of London A: Mathematical, Physical and Engineering Sciences 368(1917) (2010) 1963-1980.

[98] W.C. Oliver, G.M. Pharr, An improved technique for determining hardness and elastic modulus using load and displacement sensing indentation experiments, Journal of materials research 7(6) (1992) 1564-1583.

[99] Y.-W. Chiou, H.-K. Lin, M.-J. Tang, H.-H. Lin, M.-L. Yeh, The influence of physical and physiological cues on atomic force microscopy-based cell stiffness assessment, PloS one 8(10) (2013).

[100] N. Gavara, A beginner's guide to atomic force microscopy probing for cell mechanics, Microscopy research and technique 80(1) (2017) 75-84.

[101] Z. Zhou, C. Zheng, S. Li, X. Zhou, Z. Liu, Q. He, N. Zhang, A. Ngan, B. Tang, A. Wang, AFM nanoindentation detection of the elastic modulus of tongue squamous carcinoma cells with different metastatic potentials, Nanomedicine: Nanotechnology, Biology and Medicine 9(7) (2013) 864-874.

[102] K. Iida, R. Sakai, S. Yokoyama, N. Kobayashi, S. Togo, H.Y. Yoshikawa, A. Rawangkan, K. Namiki, M. Suganuma, Cell softening in malignant progression of human lung cancer cells by activation of receptor tyrosine kinase AXL, Scientific reports 7(1) (2017) 1-11.

[103] K. Pogoda, J. Jaczewska, J. Wiltowska-Zuber, O. Klymenko, K. Zuber, M. Fornal, M. Lekka, Depth-sensing analysis of cytoskeleton organization based on AFM data, European Biophysics Journal 41(1) (2012) 79-87.

[104] R. Saha, W.D. Nix, Effects of the substrate on the determination of thin film mechanical properties by nanoindentation, Acta materialia 50(1) (2002) 23-38.

[105] C. Rotsch, M. Radmacher, Drug-induced changes of cytoskeletal structure and mechanics in fibroblasts: An atomic force microscopy study, Biophysical Journal 78(1) (2000) 520-535.

[106] B. Fabry, A.H. Klemm, S. Kienle, T.E. Schäffer, W.H. Goldmann, Focal adhesion kinase stabilizes the cytoskeleton, Biophysical journal 101(9) (2011) 2131-2138.

[107] A. Mott, G. Lenormand, J. Costales, J.J. Fredberg, B.A. Burleigh, Modulation of host cell mechanics by Trypanosoma cruzi, Journal of cellular physiology 218(2) (2009) 315-322.

[108] E.F. Woodham, L.M. Machesky, Polarised cell migration: intrinsic and extrinsic drivers, Current opinion in cell biology 30 (2014) 25-32.

[109] L. Asnaghi, W.C. Vass, R. Quadri, P.M. Day, X. Qian, R. Braverman, A.G. Papageorge, D.R. Lowy, E-cadherin negatively regulates neoplastic growth in non-small cell lung cancer: role of Rho GTPases, Oncogene 29(19) (2010) 2760-2771.

CHAPTER 6. FOURIER TRASNFORM INFRARED SPECTROSCOPY BASED SPECTRAL BIOMARKERS OF METASTASIZED BREAST CANCER PROGRESSION[5]

This chapter describes the feasibility of infrared spectroscopy in evaluating breast cancer progression at metastatic bone site. The contents of this chapter have been published in S. Kar, D.R. Katti, K.S. Katti; "Fourier transform infrared spectroscopy based spectral biomarkers of metastasized breast cancer progression", Spectrochimica Acta Part A: Molecular and Biomolecular Spectroscopy 208, 85-96.

6.1. Introduction

Breast cancer is a global health issue and the second leading cause of cancer death in women. Women born in the western countries such as United States are at elevated risk (1 in 8 women or 12.4%) of developing breast cancer at some time during their lives[1]. According to latest cancer statistics, in 2018, an estimated 266,120 cases of breast cancer will be diagnosed including 263,570 women and 2,550 men [2]. Bone is the most common site for breast cancer metastases, and approximately 30-85% breast cancer patients eventually develop bone metastasis [3, 4]. The crosstalk between breast cancer cells and bone microenvironment has been instrumental in the development and progression of bone metastases [4]. There is still insufficient knowledge about the underlying mechanisms that govern bone metastasis; this deficiency hinders new therapeutic development. Basic histopathological examination of breast cancer tissue samples has been the gold standard in determining the prognosis of cancer patients [5]. Immunohistopathology have been used extensively to analysis of biopsy samples in the last

[5] This chapter was co-authored by S. Kar, D.R. Katti, and K.S. Katti. Sumanta Kar had the primary responsibility for preparing samples, conducting all tests, and drafting this chapter. Kalpana Katti and Dinesh Katti directed the research orientation and revised this chapter.

decade. However, immunohistochemistry methods have certain limitations such as the volume of tissue section available for staining; one cannot use more than a few probes/antibodies on a tissue section [6]. Genomic level characterization has also been used to obtain information on the biology of breast cancer [7, 8]. However, the reproducibility and robustness of gene expression data remain a concern[9] owing to the heterogeneity of tumors[10]. It is, therefore, necessary to develop new methods to understand cancer progression.

In recent years, Fourier Transform Infrared (FTIR) spectroscopy has been widely used in the field of biomedical sciences, especially cancer diagnostics, owing to its non-invasiveness, and reproducibility. FTIR has also been successfully used to evaluate bone mineralogy and diseases [11-15] and evaluate bio-nano interfaces in biological structures [16]. FTIR spectroscopy can detect a change of functional groups in biological molecules from the interaction between the IR radiation and the covalent bonds of the biological molecules. IR spectroscopy harnesses the fact that molecules have specific frequencies at which they vibrate corresponding to distinct energy levels. The most significant differences in the spectrum of biological molecules have been observed within the mid-infrared range (4000-400 cm^{-1}). FTIR have been used to analyze biological cells and tissues including bone [14, 15, 17, 18] , skin [19, 20], colon [21-23], lung [24-28], breast [6, 29-38], heart [39-41], liver [40, 42-44], prostate [45-51], gastric [52-54], oral [55-58] and cervical tissues [59-62]. Furthermore, this technique has been used in cancer grading [29, 30, 50], in anticancer drug investigations [63-66], studies on the effect of breast cancer cells on fibroblasts [67], and analysis of biological fluids of normal and cancer origin [68-76]. However, to our knowledge, FTIR has never been applied till date to evaluate the biochemical changes in cancer cells during breast cancer bone metastasis because of the complexity of sample itself and lack of samples of patients. One possible approach to

overcome this problem is to obtain IR spectra of well-characterized cell lines in 3D culture. Therefore, the primary goal of this study is to identify biochemical changes that underlie cancer progression on 3D *in vitro* model of breast cancer bone metastasis using FTIR.

Our hypothesis was that sequential culture of MSCs with breast cancer cells would be able to emulate cancer progression *in vitro*. To this end, we cultured MSCs on PCL/*in situ* HAPclay scaffolds to obtain new bone formation as described in our previous studies [77]. The scaffold preparation utilized the Altered phase theory [78] of polymer clay nanocomposites that was developed in our group to tailor the scaffold properties with clay modifications [79-81]. Further, breast cancer cells were seeded on newly formed bone to recapitulate bone metastasis a method also previously applied to build *in vitro* metastasis models of prostate [82-84].

In the present study, we aim to identify infrared excitations that significantly discriminate 3D sequential culture from 3D monoculture and apply principal component analysis to determine whether samples form cluster (sub-group) according to variation in wavenumber signal. The collective observations from this study suggest successful application of FTIR to identify biochemical changes in cancer cells during breast cancer bone metastasis. This works lays the foundation for further studies to evaluate whether FTIR can be used as non-invasive and cost-effective method for screening of biochemical changes in cancer cells during bone metastases.

6.2. Materials and Methods

6.2.1. Preparation of Polycaprolactone (PCL)/*in situ* HAPclay 3D Scaffolds

We began with modifying Na-MMT (Clay Minerals Respiratory at the University of Missouri, Columbia) with 5-aminovaleric acid (Sigma-Aldrich) following the procedure described in prior studies to increase the d-spacing of Na-MMT clay [85]. We further mineralized hydroxyapatite (HAP) on modified clay (*in situ* HAPclay) using the

biomineralization procedure illustrated in our previous study[86, 87]. Briefly, we used wet precipitation method to obtain *in situ* HAPclay from Na_2HPO_4 and $CaCl_2$ (J.T. Baker). Finally, 3D PCL/*in situ* HAPclay scaffolds were prepared using freeze extraction method described in our previous study [77]. Further, polycaprolactone (PCL) (average Mn 80,000; Sigma Aldrich) was dissolved in 1, 4 dioxane (Sigma-Aldrich) and then 10 wt. % *in situ* HAPclay was mixed into it to prepare the solution for the scaffolds.

6.2.2. Cell Lines and Culture Media

Human bone marrow Mesenchymal stem cells (MSCs) were purchased from Lonza (PT-2501) and maintained in MSCGM Bulletkit medium (Lonza, PT-3001). Human breast cancer cell (HBCC) lines MDA-MB-231 (shortened as -MM 231) (ATCC HTB-26) (highly metastatic) and MCF-7 (ATCC HTB-22) (low metastatic) were obtained from American Type Culture Collection (ATCC) maintained in medium comprised of 90% Dulbecco's Modified Eagle medium DMEM-F-12(1:1) from Hyclone, 10% FBS (ATCC), and 1% Pen-Strep antibiotic solution (Gibco); and Eagle's minimum Essential Medium (EMEM) (ATCC), 10% FBS (ATCC), 0.01 mg/ml human recombinant insulin (Invitrogen) and 1% Pen-Strep Solution (Gibco), respectively. All cell cultures were maintained at 37 ºC and 5% CO_2 in a humidified incubator.

6.2.3. Cell Culture

PCL/*in situ* HAPclay scaffolds were cut into circular discs having a diameter of 12 mm and thickness of 3 mm and placed in 24-well plates. Before cell seeding, scaffolds were sterilized under UV light for 45 min, kept in 70% ethanol for 12 h, washed in PBS, and then stored in humidified incubator immersed in culture medium for 24 h until further use. For all the

monocultures (MC), 5 x 10^4 number of cells were seeded per scaffold with 500 µl of culture medium.

6.2.4. Sequential Culture (SC) with MSCs

Human bone marrow mesenchymal cells (MSCs) were seeded on scaffolds (5 x 10^4 number of MSCs in 500 µl culture medium). After 23 days, 5 x 10^4 HBCCs were seeded onto scaffolds that were previously seeded with MSCs, and the culture was continued for different periods of time. For SC, 1:1 ratio of MSCs and HBCCs (MM 231 & MCF-7) media was used. The media was changed every 3 days, and for all the experiments 500 µl of the media was used per scaffold. The process is illustrated in Scheme 6.1.

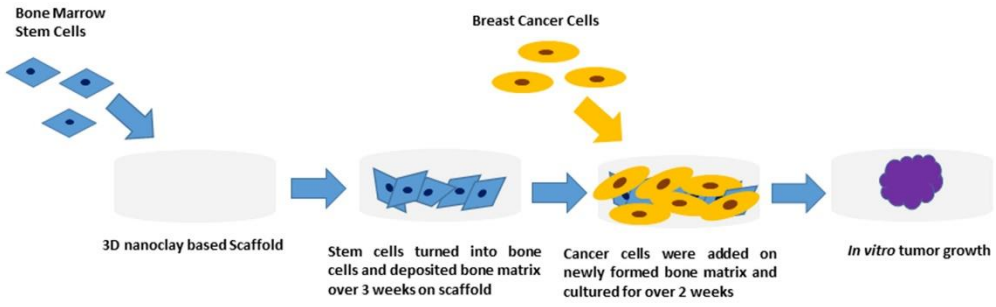

Figure 6.1. Schematic illustration of the steps of sequential culture experiment.

6.2.5. Cellular Morphology

Morphology and adhesion of cancer cells in absence (MC) and presence (SC) of bone were determined using JEOL JSM-6490LV scanning electron microscope (SEM). Samples were removed from the culture medium, washed in PBS, and fixed with 2.5% glutaraldehyde. Subsequently, samples were treated with ethanol series (10% v/v, 30% v/v, 50% v/v, 70% v/v, and 100% v/v) allowed to dehydrate and then dried using hexamethyldisilazane. Fixed samples were then coated with gold and mounted on SEM stubs to observe under SEM.

6.2.6. FTIR Experiments

The FTIR spectroscopic experiments were performed on NEXUS TM 870 FTIR spectrometer from Nicolet with KBr beam splitter in the range of 3600-930 cm^{-1} at a spectral resolution of 4 cm^{-1}, 32 scans, using a ZnSe window. Experiments are conducted in transmission mode. To prepare sample for FTIR, cells grown on scaffolds were harvested using TrypLE™ Express Enzyme (Gibco) for 5 min. Retrieved cells were centrifuged, washed in PBS, and seeded onto ZnSe window at a cell density of 1x 10^5. Cell-seeded window was kept for 2 days until cells reach 80-90% confluency. Window was then removed from culture plate and washed in PBS for 10 min. Cells were fixed in 4% paraformaldehyde in phosphate buffered saline (PBS) for 10 min at room temperature, washed in PBS 2-3 times to remove residual paraformaldehyde from the surface. GRAMS/32 software was used for spectral analysis. The center positions for each sub-band in curve-fitting were determined by second-derivative analysis and the shapes of the underlying bands were chosen by Gaussian algorithm. The number of bands for curve-fitting analysis was chosen from second-derivative spectra. For each variant, three samples were analyzed. The overall experimental workflow is presented in Figure 6.2. Assignments for all the deconvoluted bands in Figures 6.6 and 6.7 are presented in Table 6.1. Slight changes in the position of deconvoluted bands in Figures 6.6 and 6.7 are represented with "~"; for instance, 2850-2854 cm^{-1} bands are written as ~2854 cm^{-1}.

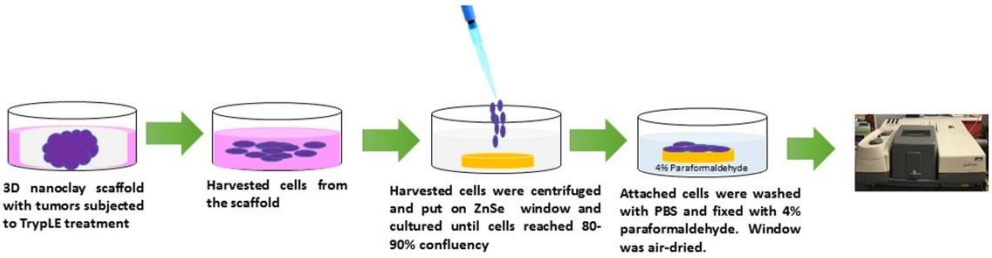

Figure 6.2. Schematic representation of the workflow of FTIR experiment.

6.2.7. Principal Component Analysis

Principal Component Analysis (PCA) is an unsupervised statistical method that enables a variable reduction by building linear combinations of spectral absorbance that vary together. The first principal component (PC1) accounts for most of the data variance while the second principal component (PC2) explains the residual variance and is uncorrelated to the first one. The projection (score) of each spectrum on the different PCs indicates the importance of the contribution of that PC to the spectrum. Prior to PCA analysis, second-derivative spectra were imported and stored in a data matrix containing 1100 rows (different wavenumbers) and 18 columns (spectral intensities). PCA was performed in the spectral region of 3050-2800 and 2000-930 cm^{-1} using a covariance matrix. (PCA for Spectroscopy, Origin Pro 2018).

6.2.8. Statistical Analysis

All intensity ratio data were expressed as mean ± standard deviation and were verified by Two-way ANOVA followed by *post hoc* Tukey test for multiple comparisons (GraphPad Prism, v7.04). Differences at p values of less than 0.05 were considered statistically significant (*), p values less than 0.01 were considered statistically highly significant (**), and p values less than 0.001 were considered statistically very highly significant (***).

6.3. Results and Discussion

6.3.1. Cellular Morphology

We performed SEM to investigate the morphology of cancer cells in monoculture and sequential culture on 3D nanoclay scaffolds. The monoculture of MCF-7 cells showed good cell attachment and spreading but did not form dense tumoroids as shown in Figure 6.3a. On the contrary, the sequential culture of MSCs with MCF-7 cells resulted into well-defined 3D tumoroids with distinguishable cellular boundaries, tight junctions, and hypoxic core regions as

shown in Figure 6.3b. MM 231 MC (Figure 6.3c) allowed cellular infiltration along with forming small cellular aggregates while the sequential culture of MM 231 (Figure 6.3d) showed disorganized clusters of cells with poor cell-cell adhesion which could be explained by their inherent properties.

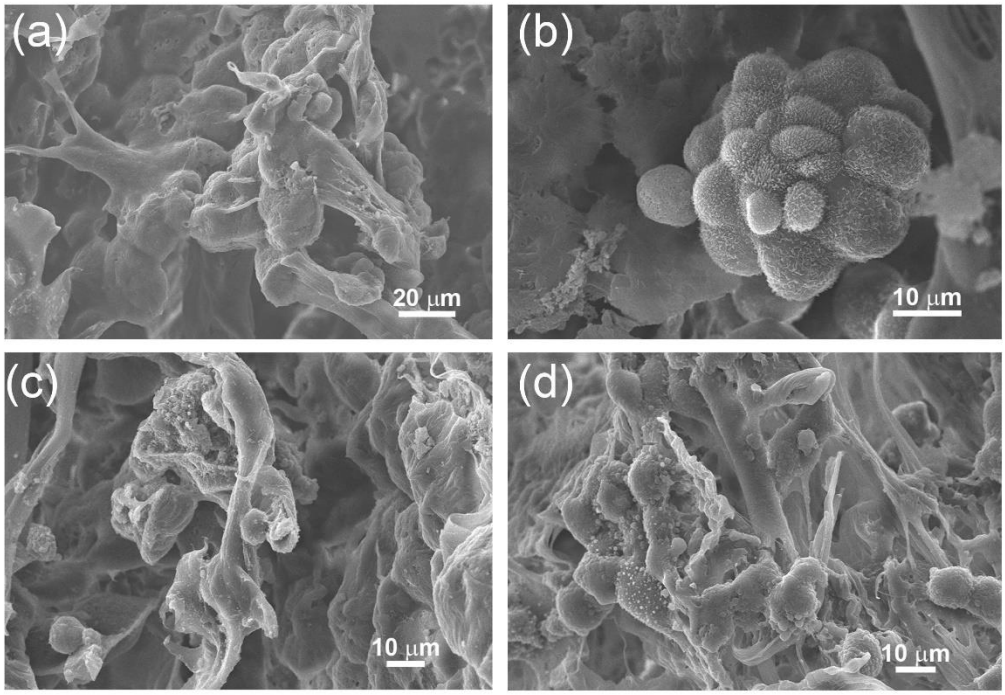

Figure 6.3. Representative SEM micrographs of (a) MCF-7 MC, (b) MCF-7 SC, (c) MM 231 MC, and (d) MM 231 SC.

6.3.2. Evaluation of the Potential of FTIR Spectroscopy to Identify the Biomarkers of Cancer Progression on 3D *in vitro* Model

Figure 6.4 shows the representative spectra of all monoculture and sequential culture of cancer cells in the range of 3600-930 cm^{-1}. These spectra show major absorption features of lipids, proteins, and nucleic acids. Figure 6.5 shows the second derivative spectra of all samples in the region 3050-2800 and 2000-930 cm^{-1}. The second derivative spectra show minor differences in spectral band shapes and show major absorption features for lipids, proteins, and nucleic acids. This is widely used to eliminate the baseline contribution and to obtain resolving

bands, which are often broad and overlapped. Table 6.1 summarizes the band wavenumber and their assignments observed in the FTIR spectra of cancer cells.

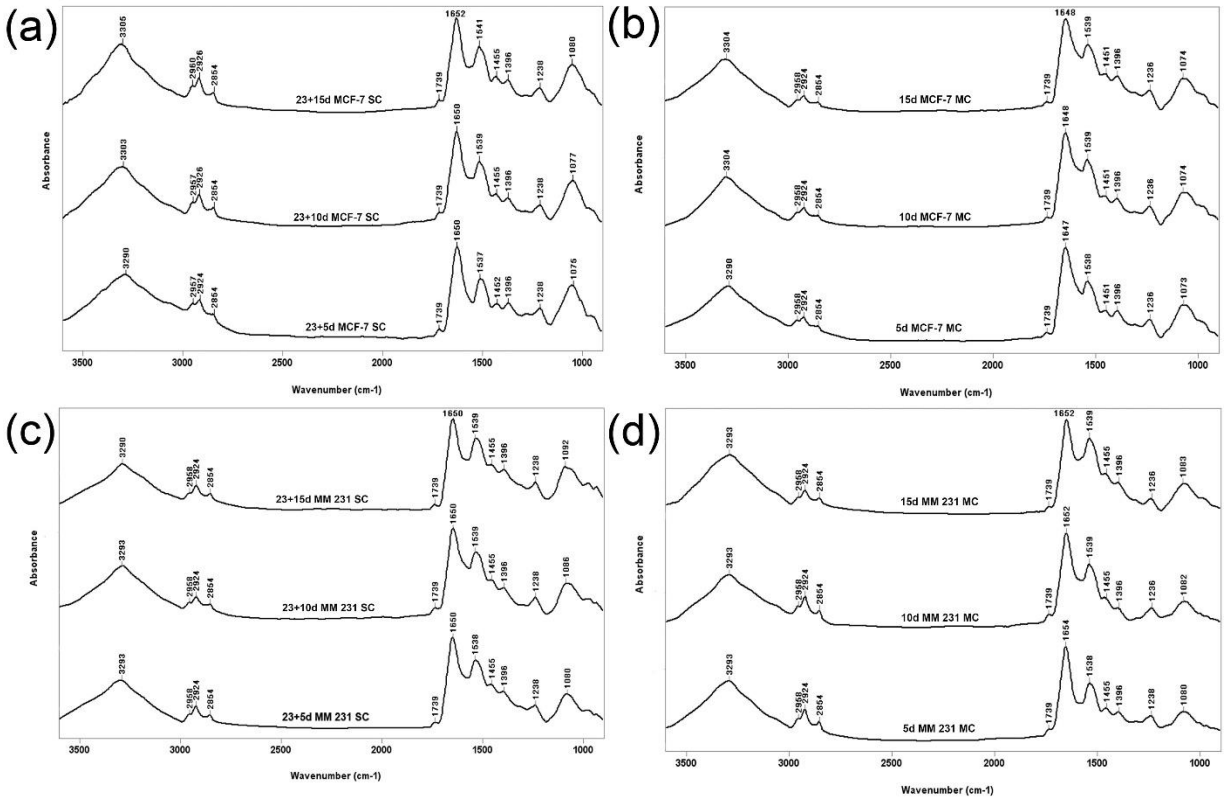

Figure 6.4. Representative FTIR spectra of (a) MCF-7 SC, (b) MCF-7 MC, (c) MM 231 SC, and (d) MM 231 MC at different incubation times in the region of 3600-930 cm^{-1}.

6.3.2.1 Lipids

The spectral region 3050–2800 cm^{-1} (Figures 6.4 and 6.5) primarily corresponds to lipids and proteins. There are mainly four bands observed for lipids, attributed to the asymmetric and symmetric stretching vibrations of CH_2 and CH_3 groups that are found at ~2959 (CH_3 asymmetric stretch), ~2926 (CH_2 asymmetric stretch), ~2877 (CH_3 symmetric stretch), and ~2854 cm^{-1} (CH_2 symmetric stretch), respectively. The bands corresponding to CH_2 groups are attributed to saturated chains in lipids whereas the methyl (CH_3) bands are attributed to the methyl groups in lipids and proteins. Also, the bands observed at ~1738 cm^{-1} and ~1455 cm^{-1} are

attributed to the carbonyl (C=O) stretch of cholesterol esters and CH_2 bending mode of lipids of the cells, respectively (Figures 6.4 and 6.6).

The bands related to CH_2 asymmetric (~2926 cm^{-1}) and CH_2 symmetric stretch (~2854 cm^{-1}) and their ratios have previously been used to calculate lipids content and to differentiate between cancerous and normal tissues, cells [38, 53, 106-110]. In the present study, we calculated intensity (area) ratios of these two lipid bands of cancer cells in monoculture and sequential cultures using curve-fitting as shown in Figures 6.6(g-l) and 6.7(g-l) and the areas are presented in Tables 6.2-6.5. We observed a significant decrease in the intensity ratios of the sequential culture of cancer cells while monoculture showed insignificant differences [Figure 6.8(b, e)]. The decrease in lipids can result from the fact that triglycerides contain a substantial proportion of methylene and fat; progression and growth of cancer requires nutrition and energy; therefore, they might utilize lipids to supply nutrition and energy, which can cause the lipids not to be accumulated in cancer cells during cancer progression [107].

6.3.2.2. Proteins

Proteins are one of the major constituents in all cells, thus their vibration bands are easily observed in FTIR spectroscopy. Protein bands are predominantly observed in the 1800-1500 cm^{-1} spectral region (Figures 6.4 and 6.5). The infrared spectra of proteins exhibit two major bands, the amide I and amide II. These two amide bands are positioned at approximately 1650 cm^{-1} and 1540 cm^{-1}. These are most widely used in studies on protein secondary structures and assigned primarily to C=O stretching and NH bending modes. The changes in the amide I band reflect the differences in strengths of the hydrogen bonding, coupling between inter and intra molecular dipoles, which in turn makes amide I band sensitive to secondary conformational changes [111].

Table 6.1. Assignments of vibrational modes observed in FTIR spectra of monoculture and sequential culture of breast cancer cells

Wavenumber (cm^{-1})	Assignment	Reference
3290-3303	N-H stretch (Amide A): proteins	[49, 88]
2957-2959	CH_3 asymmetric stretch: proteins, lipids, triglycerides	[37]
2921-2926	CH_2 asymmetric stretch: mainly saturated lipids, proteins, triglycerides	[37]
2892-2898	≡C-H stretch: methine groups of aliphatic chains	[89]
2873-2877	CH_3 symmetric stretch: mainly proteins, lipids, triglycerides	[37]
2850-2854	CH_2 symmetric stretch: mainly lipids, proteins, triglycerides, fatty acids	[37]
1738-1739	C=O stretch: triglycerides, phospholipids, cholesterol esters	[37]
1700-1702	C=O stretch: guanine	[90]
1717	C=O stretch: thymine	[90]
1686-1692	C=O stretch + N-H bend: proteins (anti-parallel β-pleated sheet and β-turns structures)	[91, 92]
1648-1660	Amide I: proteins (α-helix structure)	[49, 91, 93, 94]
1630	Amide I: proteins (β-pleated sheet structures)	[37, 92]
1609	N-H scissoring mode: adenine	[95]
1582-1594	C=N stretch: arginine proteins	[96]
1537-1564	N-H bend + C-N stretch (amide II): proteins	[48, 92, 97, 98]
1510-1515	Ring C-C stretch: tyrosine proteins	[96]
1445-1455	CH_2, CH_3 deformation modes: mainly lipids, proteins	[28, 52, 91]
1392-1396	COO^- symmetric stretch: Fatty acids, amino acids	[37, 97]
1232-1262	PO^{2-} asymmetric stretch: nucleic acids, proteins	[58, 90, 92, 95, 99]
1155-1160	C=O stretch: ribose (RNA)	[100, 101]
1108-1120	C=O stretch: ribose ring (RNA)	[90, 100, 101]
1073-1092	PO^{2-} symmetric stretch: nucleic acids (DNA)	[28, 49, 52, 58, 90, 95, 97, 98]
1048-1066	C=O stretch: ribose ring (nucleic acids)	[37, 90, 99]
1024-1030	COH deformation: nucleic acids (DNA)	[100-104]
985-997	C=O stretch, Uracil ring motions: nucleic acids (RNA)	[90, 100, 101]
962-970	Symmetric stretching mode of dianionic phosphate monoesters of phosphorylated proteins or cellular nucleic acids: DNA	[97, 100, 101, 105]

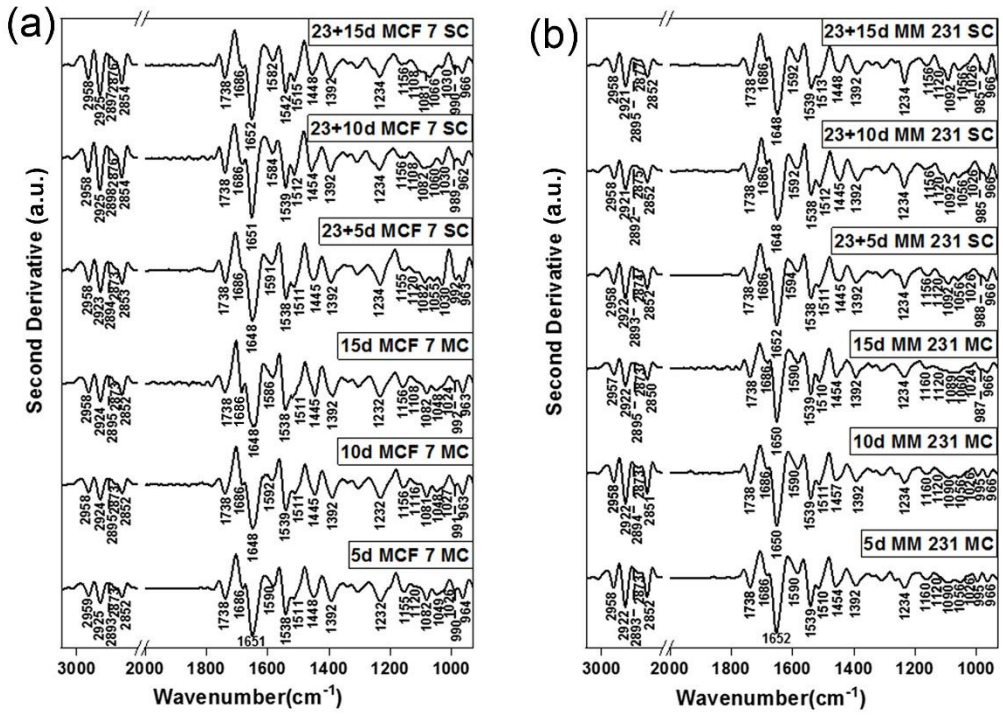

Figure 6.5. Representative second-derivative spectra of (a) MCF-7 SC, MCF-7 MC, (b) MM 231 SC, MM 231 MC at different incubation times in the region of 3050-930 cm^{-1}.

Amide I band has been extensively used to quantify and identity changes associated with α-helical (1648–1660 cm^{-1}), β-plated sheet (1630 cm^{-1}), β-turns, and anti-parallel β-plated sheet (1686–1692 cm^{-1}) structures of proteins [112]. Also, the band observed in the region of ~1396 cm^{-1} is attributed to the COO^- symmetric stretch of the side chains of free amino acid residues of proteins (Figures 6.4 and 6.5). Previous studies have used intensity ratios of amide I and amide II to obtain protein content and to differentiate between cancerous and normal tissues, cells [38, 106]. In the present study, we calculated intensity (area) ratios of amide I and amide II using curve fitting [Figures 6.6(a-f) and 6.7(a-f) and Tables 6.2-6.5]. We observed a significant increase in the intensity ratios of amide I and amide II over time in the sequential culture of cancer cells while monocultures showed inappreciable differences over time [Figure 6.8(a, d)]. The increase of the protein absorptions in the sequential culture of cancer cells indicating that a

few C-O bonds from proteins and hydrogen bonds in the C-OH groups of amino acids may have got destroyed during cancer progression [38, 106].

6.3.2.3 Nucleic acids

The bands observed in the spectral region of 1300-930 cm^{-1} (Figures 6.4 and 6.5) mainly corresponds to proteins and nucleic acids (RNA and DNA). DNA, RNA, and phosphorylated proteins exhibit two bands at approximately 1232-1238 cm^{-1} and 1073-1092 cm^{-1} attributed to PO_2^- asymmetric stretch and PO_2^- symmetric stretch, respectively (Figures 6.4 and 6.5). Nucleic acid also shows specific bands at ~1160 (C=O stretch of ribose from RNA), ~1120 (C=O stretch of ribose from RNA), ~1066 (C=O stretch of ribose from nucleic acids), ~1030 (C-OH deformation: nucleic acids), ~997 (RNA, uracil motions), and ~970 (symmetric stretching mode of dianionic phosphate monoesters of phosphorylated proteins or cellular nucleic acids arising from DNA) cm^{-1} (Figure 6.5 and Table 6.1). It is noteworthy to mention that shifts seen in C=O bands (Figure 6.5 and Table 6.1) are mainly mediated through hydrogen bonding. The spectral region of 1180-930 cm^{-1} was chosen for curve fitting to obtain the area of the bands mentioned above [Figures 6.6(m-r) and 6.7(m-r) and Tables 6.2-6.5]. The intensity (area) ratio of ~1120/~1030 cm^{-1} represents RNA/DNA for cancer cells in the present study. The RNA/DNA band ratio is used to obtain information about the transcriptional status of the cells [113]. Our results showed a significant increase in the RNA/DNA ratio for sequential culture cancer cells as opposed to monoculture [Figure 6.8(c, f)]. These results could be explained by the higher metabolic activity of the cancer cells during cancer progression in sequential culture.

6.3.3. Principal Component Analysis

To perform a clear assessment of spectral variance across the samples studied we employed principal component analysis whose score and loading plots revealed subtle differences appearing due to the cancer progression.

6.3.3.1. MCF-7 MC versus MCF-7 SC

Figure 6.9a shows a clear separation between second derivatives of FTIR spectra of MCF-7 MC and MCF-7 sequential culture SC in the PC-1 versus PC-2 score plot. The data reported in Figure 6.9a explained more than 91% of the spectral variance. The loading plot shown in Figure 6.9b indicates that the largest changes in the sequential culture of cancer cells are associated with proteins and nucleic acids. Along PC-1, the discriminating positively correlated loadings are found for monoculture at 1648,1538 while negatively correlated loadings are characteristic for sequential culture, and they are observed at 1564, 1700 and 1609 cm^{-1}.

It is noteworthy to mention that negative loadings at 1700 and 1609 cm^{-1} arise from C=O stretching vibrations of guanine and adenine, respectively. Conformational changes in the DNA may explain this during cancer progression [114]. The phosphate bands could be used as markers of changes of conformational states of nucleic acids. The PC-1 loading plot also shows that the nucleic acid bands at 1232, 1082 and 964 cm^{-1} discriminate monoculture from sequential culture (1262 and 989 cm^{-1}) in the spectral region below 1400 cm^{-1}.

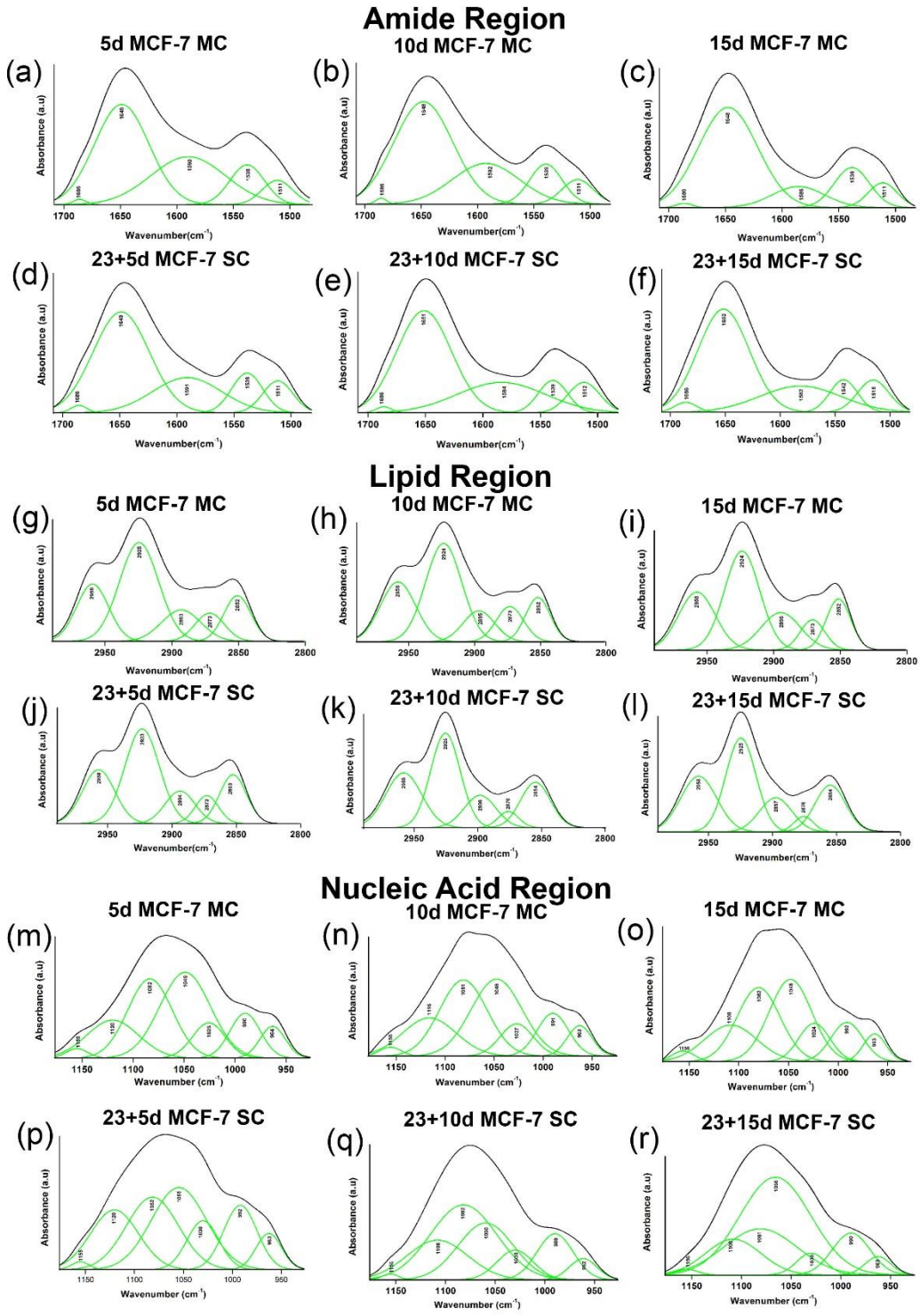

Figure 6.6. Representative curve-fitted amide region (1708-1482 cm^{-1}) of MCF-7 MC (a-c), and MCF-7 SC (d-f); lipid region (2990-2800 cm^{-1}) of MCF-7 MC (g-i), and MCF-7 SC (j-l); nucleic acid region (1180-930 cm^{-1}) of MCF-7 MC (m-o), and MCF-7 SC (p-r) for different incubation time.

Table 6.2. Major components of lipid, amide, nucleic acid region in MCF-7 SC

Lipid Region					
Position (cm^{-1}) (23+5d MCF-7 SC)	Area	Position (cm^{-1}) (23+10d MCF-7 SC)	Area	Position (cm^{-1}) (23+15d MCF-7 SC)	Area
2958	0.13±0.0090	2958	0.16±0.0100	2958	0.16±0.0100
2923	0.27±0.0200	2925	0.23±0.0200	2925	0.23±0.0100
2894	0.07±0.0060	2898	0.11±0.0200	2897	0.10±0.0100
2873	0.05±0.0050	2876	0.05±0.0090	2876	0.05±0.0090
2853	0.10±0.0070	2854	0.11±0.0060	2854	0.12±0.0040
Amide Region					
Position (cm^{-1}) (23+5d MCF-7 SC)	Area	Position (cm^{-1}) (23+10d MCF-7 SC)	Area	Position (cm^{-1}) (23+15d MCF-7 SC)	Area
1686	0.14±0.0200	1686	0.13±0.0030	1686	0.14±0.0020
1648	4.71±0.1300	1651	7.13±0.0700	1652	7.26±0.0400
1591	2.01±0.2000	1584	1.71±0.0200	1582	1.44±0.0400
1538	1.09±0.1500	1539	1.28±0.0600	1542	1.27±0.0400
1511	0.75±0.0600	1512	1.17±0.0800	1515	1.35±0.0100
Nucleic Acid Region					
Position (cm^{-1}) (23+5d MCF-7 SC)	Area	Position (cm^{-1}) (23+10d MCF-7 SC)	Area	Position (cm^{-1}) (23+15d MCF-7 SC)	Area
1155	0.04±0.0002	1156	0.03±0.0020	1156	0.03±0.0500
1120	0.90±0.0600	1108	0.82±0.0200	1108	0.81±0.0500
1082	1.01±0.1600	1082	1.52±0.0300	1081	1.01±0.0600
1055	1.27±0.2100	1060	0.98±0.0300	1066	1.80±0.0300
1030	0.54±0.0700	1030	0.33±0.0300	1030	0.25±0.0200
992	0.63±0.0900	989	0.57±0.0400	990	0.43±0.0300
963	0.27±0.0300	962	0.15±0.0300	963	0.11±0.0300

Table 6.3. Major components of lipid, amide, nucleic acid region in MCF-7 MC

Lipid Region					
Position (cm^{-1}) (5d MCF-7 MC)	Area	Position (cm^{-1}) (10d MCF-7 MC)	Area	Position (cm^{-1}) (15d MCF-7 MC)	Area
2959	0.15±0.0030	2958	0.15±0.0020	2958	0.16±0.0070
2925	0.32±0.0050	2924	0.33±0.0070	2924	0.37±0.0100
2893	0.09±0.0100	2895	0.11±0.0200	2895	0.11±0.0030
2873	0.06±0.0100	2873	0.07±0.0200	2873	0.08±0.0030
2852	0.11±0.0100	2852	0.11±0.0800	2852	0.13±0.0040
Amide Region					
Position (cm^{-1}) (5d MCF-7 MC)	Area	Position (cm^{-1}) (10d MCF-7 MC)	Area	Position (cm^{-1}) (15d MCF-7 MC)	Area
1686	0.07±0.0100	1686	0.07±0.0040	1686	0.09±0.0200
1651	4.77±0.1300	1648	6.37±0.1500	1648	6.43±0.0500
1590	3.16±0.0500	1592	2.50±0.3600	1586	1.13±0.1100
1538	1.30±0.1000	1539	1.52±0.1900	1538	1.53±0.1400
1511	0.72±0.1200	1511	0.74±0.0600	1511	0.78±0.0600
Nucleic Acid Region					
Position (cm^{-1}) (5d MCF-7 MC)	Area	Position (cm^{-1}) (10d MCF-7 MC)	Area	Position (cm^{-1}) (15d MCF-7 MC)	Area
1155	0.06±0.0100	1156	0.07±0.0030	1156	0.08±0.0010
1120	0.63±0.0400	1116	0.81±0.0200	1108	0.83±0.0200
1082	1.13±0.0800	1081	1.45±0.0600	1082	1.38±0.0300
1049	1.18±0.1500	1048	1.37±0.1900	1048	1.31±0.0600
1026	0.37±0.0500	1027	0.49±0.0600	1024	0.49±0.0300
990	0.47±0.0500	991	0.58±0.0400	992	0.45±0.0060
964	0.23±0.0200	963	0.29±0.0100	963	0.23±0.0070

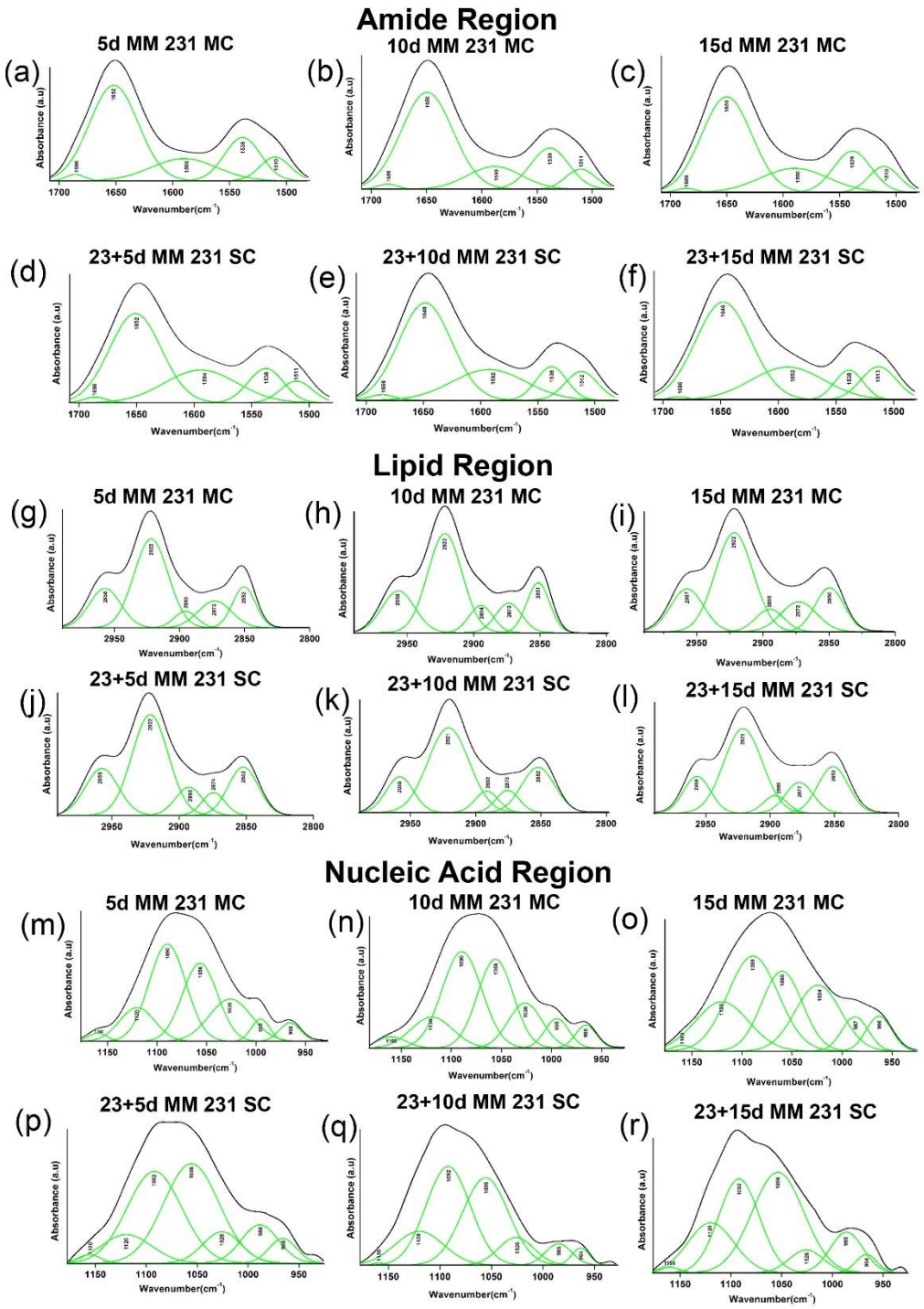

Figure 6.7. Representative curve-fitted amide region (1708-1482 cm^{-1}) of MM 231 MC (a-c), and MM 231 SC (d-f); lipid region (2990-2800 cm^{-1}) of MM 231 MC (g-i), and MM 231 SC (j-l); nucleic acid region (1180-930 cm^{-1}) of MM 231 MC (m-o), and MM 231 SC (p-r) for different incubation time.

Table 6.4. Major components of lipid, amide, nucleic acid region in MM 231 SC

Lipid Region					
Position (cm^{-1}) (23+5d MM 231 SC)	Area	Position (cm^{-1}) (23+10d MM 231 SC)	Area	Position (cm^{-1}) (23+15d MM 231 SC)	Area
2958	0.12±0.0050	2958	0.16±0.0090	2958	0.14±0.0040
2922	0.31±0.0070	2921	0.25±0.0100	2921	0.23±0.0030
2893	0.09±0.0060	2892	0.09±0.0100	2895	0.10±0.0100
2874	0.09±0.0100	2875	0.09±0.0090	2877	0.05±0.0090
2852	0.12±0.0030	2852	0.12±0.0070	2852	0.11±0.0080
Amide Region					
Position (cm^{-1}) (23+5d MM 231 SC)	Area	Position (cm^{-1}) (23+10d MM 231 SC)	Area	Position (cm^{-1}) (23+15d MM 231 SC)	Area
1686	0.18±0.0030	1686	0.18±0.0200	1686	0.23±0.0100
1652	6.43±0.1000	1648	7.44±0.0600	1648	7.95±0.0500
1594	3.01±0.2300	1592	3.12±0.1000	1592	3.81±0.1700
1538	1.83±0.1700	1538	1.47±0.0100	1539	1.26±0.1200
1511	0.89±0.0400	1512	0.90±0.0300	1513	0.88±0.0900
Nucleic Acid Region					
Position (cm^{-1}) (23+5d MM 231 SC)	Area	Position (cm^{-1}) (23+10d MM 231 SC)	Area	Position (cm^{-1}) (23+15d MM 231 SC)	Area
1156	0.06±0.0300	1156	0.07±0.0100	1156	0.03±0.0030
1120	0.36±0.0400	1120	0.45±0.0200	1120	0.68±0.0100
1092	1.55±0.1900	1092	1.74±0.0500	1092	1.74±0.0800
1056	1.54±0.3700	1056	1.56±0.0700	1056	1.54±0.0500
1026	0.29±0.0300	1026	0.27±0.0200	1026	0.24±0.0100
988	0.33±0.0100	985	0.33±0.0100	985	0.42±0.0300
966	0.16±0.0800	964	0.12±0.0100	964	0.12±0.0100

Table 6.5. Major components of lipid, amide, nucleic acid region in MM 231 MC

Lipid Region					
Position (cm^{-1}) (5d MM 231 MC)	Area	Position (cm^{-1}) (10d MM 231 MC)	Area	Position (cm^{-1}) (15d MM 231 MC)	Area
2958	0.15±0.0100	2958	0.14±0.0100	2957	0.12±0.0100
2922	0.39±0.0100	2922	0.35±0.0100	2922	0.32±0.0100
2893	0.09±0.0200	2894	0.08±0.0100	2895	0.07±0.0100
2873	0.10±0.0200	2873	0.09±0.0100	2873	0.07±0.0100
2852	0.13±0.0100	2851	0.12±0.0010	2850	0.11±0.0100
Amide Region					
Position (cm^{-1}) (5d MM 231 MC)	Area	Position (cm^{-1}) (10d MM 231 MC)	Area	Position (cm^{-1}) (15d MM 231 MC)	Area
1686	0.09±0.0020	1686	0.10±0.0200	1686	0.10±0.0100
1652	3.58±0.0200	1650	4.21±0.0700	1650	4.92±0.1600
1590	1.21±0.0600	1590	1.41±0.0200	1590	1.79±0.3400
1539	1.17±0.0500	1539	1.37±0.0500	1539	1.60±0.2300
1510	0.59±0.0300	1511	0.66±0.0800	1510	0.85±0.0400
Nucleic Acid Region					
Position (cm^{-1}) (5d MM 231 MC)	Area	Position (cm^{-1}) (10d MM 231 MC)	Area	Position (cm^{-1}) (15d MM 231 MC)	Area
1160	0.08±0.0030	1160	0.07±0.0020	1160	0.03±0.0100
1120	0.36±0.0100	1120	0.40±0.0400	1120	0.57±0.0200
1090	1.66±0.1100	1090	1.34±0.0300	1089	1.33±0.1900
1056	1.40±0.2400	1056	1.06±0.0200	1060	0.79±0.0400
1026	0.53±0.1000	1026	0.57±0.0600	1024	0.74±0.0600
995	0.21±0.0400	995	0.20±0.0400	987	0.21±0.0200
966	0.19±0.0030	966	0.18±0.0100	966	0.22±0.0100

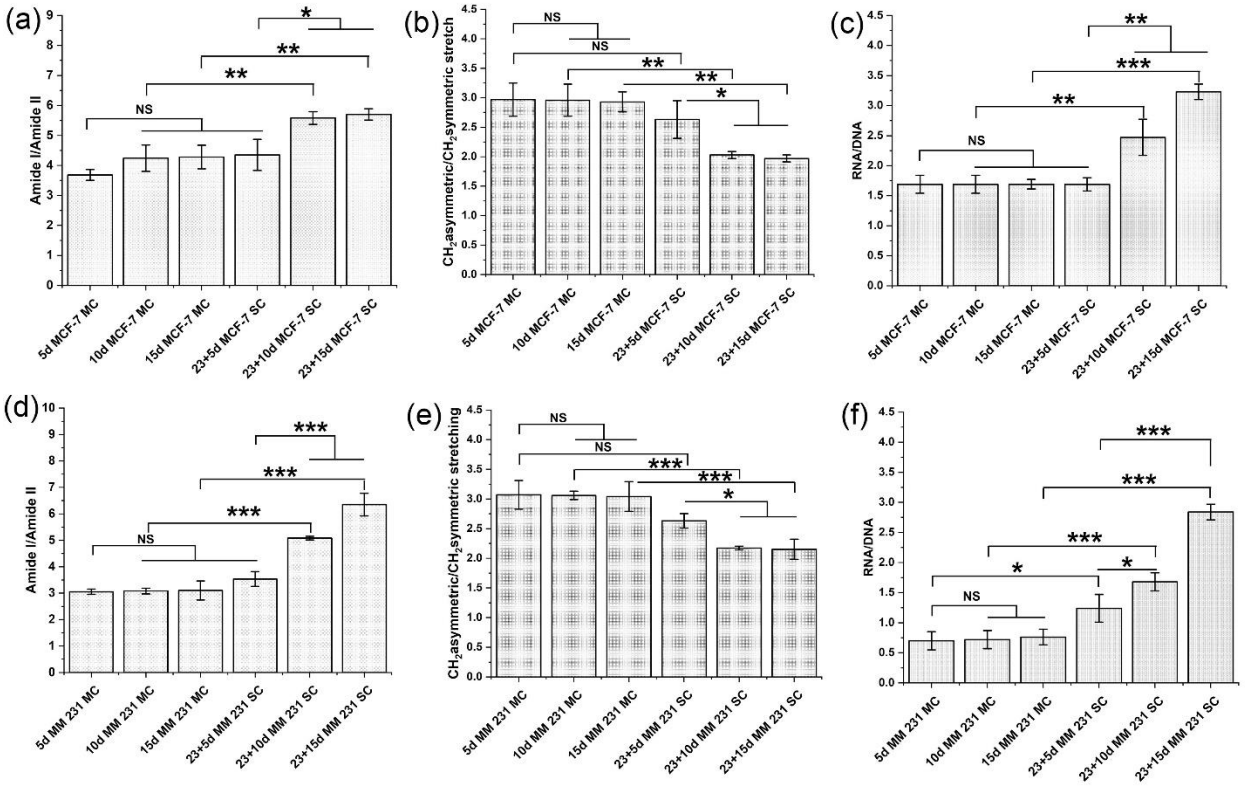

Figure 6.8. Intensity ratios of Amide I/Amide II (a and d), CH_2 asymmetric/ CH_2 symmetric stretch (b and e), RNA/DNA (c and f) of monocultures (MC) and sequential cultures of MCF-7 and MM 231, respectively, at different incubation time. (n=3, two-way ANOVA followed by *post hoc* Tukey test,*$p<0.05$, **$p<0.01$, and ***$p<0.001$).

It is noteworthy to mention that the O-P-O band shift from 1232 cm^{-1} (positive loadings) to 1262 cm^{-1} could be associated with the change of conformation of DNA (B- DNA to A-DNA) [115]. The band at 1082 cm^{-1} (positive loading) further strengthens our claim of change in DNA conformation. The loading plot also reveals that the discriminating wavenumbers associated with PC-1 appear in the high-wavenumber region and include the asymmetric and symmetric stretching vibrations of the methylene and methyl groups at 2921 and 2851 cm^{-1}, respectively. They are positively correlated and thus specific for monoculture suggesting lipid decomposition due to the progression of cancer. This observation is in good agreement with results discussed in 6.3.2.1. Positive loadings at 1738, 1445 cm^{-1} also suggest decomposition of lipids

macromolecules while the band at 1392 cm^{-1} indicates the presence of free of amino acids in the monoculture.

6.3.3.2. MM 231 MC versus MM 231 SC

Figure 6.9c illustrates sample grouping for the monoculture and sequential culture of MM 231 in the 3100-2800 and 2000-930 cm^{-1} regions. Almost all (99%) the spectral variance was explained by data reported. The loading plot shown in Figure 6.9d reveals that discrimination of both groups is mainly associated with proteins. The major discriminants in PC-1 are positively correlated bands at 1652, 1538 and negatively correlated bands at 1702, 1610, and 1564. The bands at 1702 and 1609 cm^{-1} can be attributed to C=O stretching of ring bases (guanine and adenine) of nucleic acids while 1564 cm^{-1} can be attributed to N-H bending of proteins. Our PCA also indicates that clustering is associated with lipids. Positive loadings for the monoculture at 2922, 2854, 1738, and 1445 cm^{-1} suggest decomposition of these macromolecules due to cancer progression. Wavenumbers that also contribute to separation of monoculture and sequential culture are found at 966, 1060 and 1232/ 1092 cm^{-1} in positive loadings of the monoculture. These indicate that both nucleic acids, DNA, RNA, and lipids are also involved in biochemical processes associated with cancer progression.

6.3.3.3. MM 231 SC versus MCF-7 SC

We further used PCA to identify the segregating biochemical entities between sequential culture of MM 231 and MCF-7. The score plot presented in Figure 6.9e not only shows perfect cluster segregation of sequential cultures also explains 99% of the total spectral variance. The major discriminants in the PC-2 loading plot are positively correlated bands at 1630 and 1717 cm^{-1} and negatively correlated bands at 1692, 1660, 1609 and 1554 cm^{-1}. It is noteworthy to mention that segregation of sequential cultures is dominated by the presence of C=O stretching

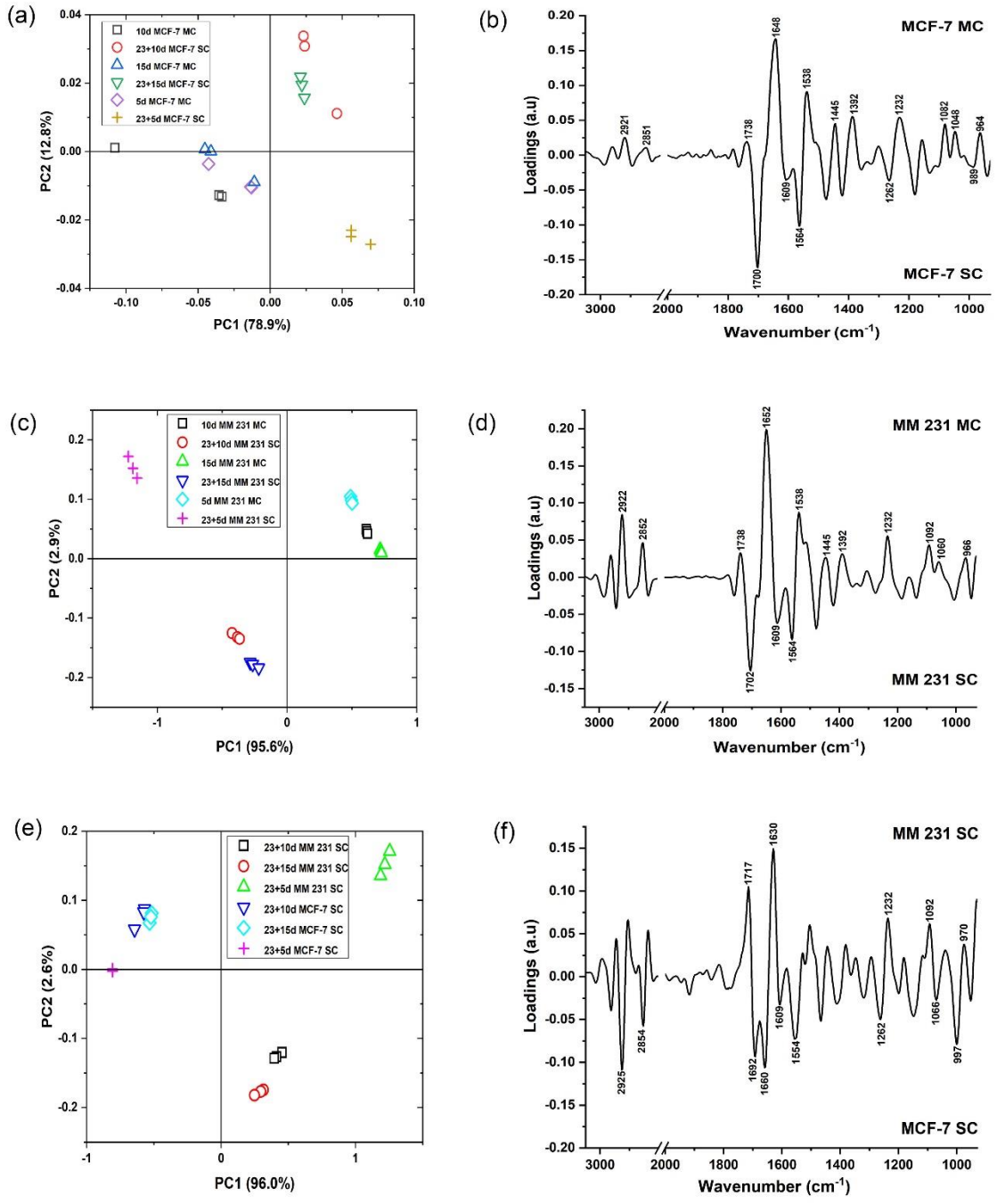

Figure 6.9. The results of PCA applied to 2 groups of second derivative spectra (MCF-7 MC and MCF-7 SC) in the region of 3050-2800 and 2000-930 cm^{-1} (a), and a PC-1 correlation loading plot (b); the results of PCA applied to 2 groups of second derivative spectra (MM 231 MC and MCF-7 SC) in the region of 3050-2800 and 2000-930 cm^{-1} (c), and a PC-1 correlation loading plot (d); the results of PCA applied to 2 groups of second derivative spectra (MM 231 SC and MCF-7 SC) in the region of 3050-2800 and 2000-930 cm^{-1} (e), and a PC-2 correlation loading plot (f).

of nucleic acid bases [1609 (Adenine), 1717 (thymine) cm^{-1}], proteins (amide I) (1630, 1660, and 1692 cm^{-1}) and N-H bending (amide II) (1554 cm^{-1}) of proteins. Differences between sequential culture of MM 231 and MCF-7 regarding lipid composition are revealed by negative loadings at 2925 and 2854 cm^{-1}, suggesting that cancer cells from sequential culture contain a lower concentration of lipids further validating our observation in section 6.3.2.1. A few discriminators are found in the region below 1250 cm^{-1}. The most pronounced feature is a shift of the O–P–O asymmetric stretching band from 1232 cm^{-1} for MM 231 SC to 1262 cm^{-1} for MCF-7 SC. Such a shift was associated with the conformation change for the B-DNA to A-DNA transition [115]. The presence of a positive loading at 1092 and 970 cm^{-1} for MM 231 SC can additionally support a hypothesis that the DNA changes its conformation in the case of MCF-7 SC as compared to the MM 231 SC. Also, MCF-7 SC exhibits a higher content of RNA (negative loadings at 1066 and 997 cm^{-1}).

6.4. Conclusion

In the present study, FTIR spectroscopy was used to identify spectral biomarkers of cancer progression on 3D *in vitro* model of breast cancer bone metastasis. Absorption bands in IR spectra of control monoculture and sequential culture of cancer cells all received contributions from proteins, lipids, and nucleic acids. Selected intensity ratios from the lipid region as well as the fingerprint region showed significant differences between monoculture and sequential cultures. Significant changes are reported in the spectral correlations in the metastasis to bone by use of low metastatic (MCF-7) and highly metastatic (MDA-MB-231) cell lines indicating that the proposed spectroscopy method can be useful in capturing prognosis of nature of cancer progression. Combining intensity ratios in FT-IR spectroscopy with principal component analysis provided a method for monitoring of cancer progression on 3D *in vitro*

model. This method provides an understanding of the molecular composition of different IR absorption regions and could serve as a useful non-invasive and cost-effective tool in the clinical diagnosis of breast cancer bone metastasis.

6.5. Acknowledgements

Authors acknowledge support from NDSU Grand Challenges grant for 'CECT-Center for Engineered Cancer Test-Beds'. Instrumentation obtained from National Science Foundation MRI grants is acknowledged for enabling experiments conducted in this work. Authors would like to acknowledge assistance in electron microscopy laboratory from Dr. Scott Payne. Support from ND EPSCoR for tissue engineering laboratory is also acknowledged.

6.6. References

[1] N. Howlader, A. Noone, M. Krapcho, J. Garshell, D. Miller, S.F. Altekruse, C.L. Kosary, M. Yu, J. Ruhl, Z. Tatalovich, A. Mariotto, D.R. Lewis, H.S. Chen, E.J. Feuer, K.A. Cronin, SEER Cancer Statistics Review, 1975-2012, National Cancer Institute. Bethesda, MD, 2015.

[2] R.L. Siegel, K.D. Miller, A. Jemal, Cancer statistics, 2018, CA: a cancer journal for clinicians 68(1) (2018) 7-30.

[3] A. Lipton, R. Uzzo, R.J. Amato, G.K. Ellis, B. Hakimian, G.D. Roodman, M.R. Smith, The science and practice of bone health in oncology: managing bone loss and metastasis in patients with solid tumors, Journal of the National Comprehensive Cancer Network 7(Suppl 7) (2009) S-1.

[4] Y.B. Kang, P.M. Siegel, W.P. Shu, M. Drobnjak, S.M. Kakonen, C. Cordon-Cardo, T.A. Guise, J. Massague, A multigenic program mediating breast cancer metastasis to bone, Cancer Cell 3(6) (2003) 537-549.

[5] A.S.Y. Leong, Z. Zhuang, The changing role of pathology in breast cancer diagnosis and treatment, Pathobiology 78(2) (2011) 99-114.

[6] M. Smolina, E. Goormaghtigh, Infrared imaging of MDA-MB-231 breast cancer cell line phenotypes in 2D and 3D cultures, Analyst 140(7) (2015) 2336-2343.

[7] C. Sotiriou, S.-Y. Neo, L.M. McShane, E.L. Korn, P.M. Long, A. Jazaeri, P. Martiat, S.B. Fox, A.L. Harris, E.T. Liu, Breast cancer classification and prognosis based on gene expression profiles from a population-based study, Proceedings of the National Academy of Sciences 100(18) (2003) 10393-10398.

[8] T. Sørlie, R. Tibshirani, J. Parker, T. Hastie, J.S. Marron, A. Nobel, S. Deng, H. Johnsen, R. Pesich, S. Geisler, Repeated observation of breast tumor subtypes in independent gene expression data sets, Proceedings of the National Academy of Sciences 100(14) (2003) 8418-8423.

[9] P.K. Tan, T.J. Downey, E.L. Spitznagel Jr, P. Xu, D. Fu, D.S. Dimitrov, R.A. Lempicki, B.M. Raaka, M.C. Cam, Evaluation of gene expression measurements from commercial microarray platforms, Nucleic acids research 31(19) (2003) 5676-5684.

[10] D.E. Ingber, Can cancer be reversed by engineering the tumor microenvironment?, Elsevier, pp. 356-364.

[11] C. Gu, D.R. Katti, K.S. Katti, Microstructural and Photoacoustic Infrared Spectroscopic Studies of Human Cortical Bone with Osteogenesis Imperfecta, Jom 68(4) (2016) 1116-1127.

[12] R. Bogan, R.C. Riddle, Z. Li, S. Kumar, A. Nandal, M.C. Faugere, A. Boskey, S.E. Crawford, T.L. Clemens, A Mouse Model for Human Osteogenesis Imperfecta Type VI, Journal of Bone and Mineral Research 28(7) (2013) 1531-1536.

[13] J. Wegrzyn, J.P. Roux, D. Farlay, H. Follet, R. Chapurlat, The role of bone intrinsic properties measured by infrared spectroscopy in whole lumbar vertebra mechanics: Organic rather than inorganic bone matrix?, Bone 56(2) (2013) 229-233.

[14] C. Gu, D.R. Katti, K.S. Katti, Photoacoustic FTIR spectroscopic study of undisturbed human cortical bone, Spectrochimica Acta Part A: Molecular and Biomolecular Spectroscopy 103 (2013) 25-37.

[15] N.T. Khanarian, M.K. Boushell, J.P. Spalazzi, N. Pleshko, A.L. Boskey, H.H. Lu, FTIR-I Compositional Mapping of the Cartilage-to-Bone Interface as a Function of Tissue Region and Age, Journal of Bone and Mineral Research 29(12) (2014) 2643-2652.

[16] D. Verma, K. Katti, D. Katti, Nature of water in nacre: A 2D Fourier transform infrared spectroscopic study, Spectrochimica Acta Part a-Molecular and Biomolecular Spectroscopy 67(3-4) (2007) 784-788.

[17] I. Rehman, R. Smith, L.L. Hench, W. Bonfield, Structural evaluation of human and sheep bone and comparison with synthetic hydroxyapatite by FT-Raman spectroscopy, Journal of Biomedical Materials Research Part A 29(10) (1995) 1287-1294.

[18] A. Boskey, N.P. Camacho, FT-IR imaging of native and tissue-engineered bone and cartilage, Biomaterials 28(15) (2007) 2465-2478.

[19] C.A. Lima, V.P. Goulart, L. Côrrea, T.M. Pereira, D.M. Zezell, ATR-FTIR spectroscopy for the assessment of biochemical changes in skin due to cutaneous squamous cell carcinoma, International journal of molecular sciences 16(4) (2015) 6621-6630.

[20] M. Kyriakidou, J. Anastassopoulou, A. Tsakiris, M. Koui, T. Theophanides, FT-IR Spectroscopy Study in Early Diagnosis of Skin Cancer, in vivo 31(6) (2017) 1131-1137.

[21] B. Rigas, P.T.T. Wong, Human colon adenocarcinoma cell lines display infrared spectroscopic features of malignant colon tissues, Cancer Research 52(1) (1992) 84-88.

[22] J. Ramesh, A. Salman, S. Mordechai, S. Argov, J. Goldstein, I. Sinelnikov, S. Walfisch, H. Guterman, FTIR microscopic studies on normal, polyp, and malignant human colonic tissues, Subsurface Sensing Technologies and Applications 2(2) (2001) 99-117.

[23] A. Zwielly, S. Argov, A. Salman, E. Bogomolny, S. Mordechai, Classification of human colonic tissues using FTIR spectra and advanced statistical techniques, International Society for Optics and Photonics, p. 771516.

[24] S.Y. Lee, K.-A. Yoon, S.H. Jang, E.O. Ganbold, D. Uuriintuya, S.-M. Shin, P.D. Ryu, S.-W. Joo, Infrared spectroscopy characterization of normal and lung cancer cells originated from epithelium, Journal of veterinary science 10(4) (2009) 299-304.

[25] C. Krafft, D. Codrich, G. Pelizzo, V. Sergo, Raman and FTIR imaging of lung tissue: bronchopulmonary sequestration, Journal of Raman Spectroscopy 40(6) (2009) 595-603.

[26] C. Krafft, D. Codrich, G. Pelizzo, V. Sergo, Raman mapping and FTIR imaging of lung tissue: congenital cystic adenomatoid malformation, Analyst 133(3) (2008) 361-371.

[27] E.M. Morato, G.R. Morais, F. Sato, A.N. Medina, T.I.E. Svidzinski, M.L. Baesso, L. Hernandes, Morphological and structural changes in lung tissue infected by Paracoccidioides brasiliensis: FTIR photoacoustic spectroscopy and histological analysis, Photochemistry and photobiology 89(5) (2013) 1170-1175.

[28] H.P. Wang, H.C. Wang, Y.J. Huang, Microscopic FTIR studies of lung cancer cells in pleural fluid, Science of the Total Environment 204(3) (1997) 283-287.

[29] S. Rehman, Z. Movasaghi, J.A. Darr, I.U. Rehman, Fourier transform infrared spectroscopic analysis of breast cancer tissues; identifying differences between normal

breast, invasive ductal carcinoma, and ductal carcinoma in situ of the breast, Applied Spectroscopy Reviews 45(5) (2010) 355-368.

[30] S. Khalil, M. Khodeir, R. Hakam, R. El-Monem Rezq, Spectroscopic Study for Detection and Grading of Breast Carcinoma In vitro, Aus tralian Journal of Basic and Applied Sciences 3(3) (2009) 2419-2428.

[31] R. Mehrotra, G. Tyagi, S. Charak, B. Ray, G. Kadayaprath, H. Chaturvedi, U. Mukherjee, A. Abrari, Biospectroscopic analysis of human breast cancer tissue: probing infrared signatures to comprehend biochemical alterations, Journal of Biomolecular Structure and Dynamics 36(3) (2018) 761-766.

[32] R.N. Baker, K.D. Rogers, N. Shepherd, N. Stone, Analysis of breast tissue calcifications using FTIR spectroscopy, Optical Society of America, p. 6628_18.

[33] J. Anastassopoulou, E. Boukaki, C. Conti, P. Ferraris, E. Giorgini, C. Rubini, S. Sabbatini, T. Theophanides, G. Tosi, Microimaging FT-IR spectroscopy on pathological breast tissues, Vibrational Spectroscopy 51(2) (2009) 270-275.

[34] T. Gao, J. Feng, Y. Ci, Human breast carcinomal tissues display distinctive FTIR spectra: implication for the histological characterization of carcinomas, Analytical cellular pathology 18(2) (1999) 87-93.

[35] W.M. Elshemey, A.M. Ismail, N.S. Elbialy, Molecular-level characterization of normal, benign, and malignant breast tissues using FTIR spectroscopy, Journal of Medical and Biological Engineering 36(3) (2016) 369-378.

[36] M. Smolina, E. Goormaghtigh, Gene expression data and FTIR spectra provide a similar phenotypic description of breast cancer cell lines in 2D and 3D cultures, Analyst (2018).

[37] H. Fabian, M. Jackson, L. Murphy, P.H. Watson, I. Fichtner, H.H. Mantsch, A comparative infrared spectroscopic study of human breast tumors and breast tumor cell xenografts, Biospectroscopy 1(1) (1995) 37-45.

[38] P. Venkatachalam, L.L. Rao, N.K. Kumar, A. Jose, S.S. Nazeer, Diagnosis of Breast Cancer Based on FT-IR Spectroscopy, AIP, pp. 144-148.

[39] B. de Groot, C.J. Zuurbier, J.H.G.M. van Beek, Dynamics of tissue oxygenation in isolated rabbit heart as measured with near-infrared spectroscopy, American Journal of Physiology-Heart and Circulatory Physiology 276(5) (1999) H1616-H1624.

[40] V. Zohdi, D.R. Whelan, B.R. Wood, J.T. Pearson, K.R. Bambery, M.J. Black, Importance of tissue preparation methods in FTIR micro-spectroscopical analysis of biological tissues:'traps for new users', PLoS One 10(2) (2015) e0116491.

[41] R. Cheheltani, J.M. Rosano, B. Wang, M.F. Kiani, A.K. Sabri, N. Pleshko, Fourier transform infrared spectroscopic imaging of cardiac tissue to detect collagen deposition after myocardial infarction, Journal of biomedical optics 17(5) (2012) 056014.

[42] O. Bozkurt, F. Severcan, S.H. Bayari, M. Severcan, C. Krafft, J. Popp, Structural alterations in rat liver proteins due to streptozotocin-induced diabetes and the recovery effect of selenium: Fourier transform infrared microspectroscopy and neural network study, Journal of Biomedical Optics 17(7) (2012) 076023.

[43] J. Teller, M. Wolf, M. Keel, H.-U. Bucher, S. Fanconi, O. Baenziger, Can near infrared spectroscopy of the liver monitor tissue oxygenation?, European journal of pediatrics 159(7) (2000) 549-549.

[44] L. Chiriboga, H. Yee, M. Diem, Infrared spectroscopy of human cells and tissue. Part VI: A comparative study of histopathology and infrared microspectroscopy of normal, cirrhotic, and cancerous liver tissue, Applied Spectroscopy 54(1) (2000) 1-8.

[45] M.J. Baker, E. Gazi, M.D. Brown, J.H. Shanks, P. Gardner, N.W. Clarke, FTIR-based spectroscopic analysis in the identification of clinically aggressive prostate cancer, British journal of cancer 99(11) (2008) 1859.

[46] G. Theophilou, K.M.G. Lima, M. Briggs, P.L. Martin-Hirsch, H.F. Stringfellow, F.L. Martin, A biospectroscopic analysis of human prostate tissue obtained from different time periods points to a trans-generational alteration in spectral phenotype, Scientific reports 5 (2015) 13465.

[47] M.J. Baker, E. Gazi, M.D. Brown, J.H. Shanks, N.W. Clarke, P. Gardner, Investigating FTIR based histopathology for the diagnosis of prostate cancer, Journal of biophotonics 2(1-2) (2009) 104-113.

[48] E. Gazi, J. Dwyer, P. Gardner, A. Ghanbari-Siahkali, A.P. Wade, J. Miyan, N.P. Lockyer, J.C. Vickerman, N.W. Clarke, J.H. Shanks, Applications of Fourier transform infrared microspectroscopy in studies of benign prostate and prostate cancer. A pilot study, The Journal of pathology 201(1) (2003) 99-108.

[49] C. Paluszkiewicz, W.M. Kwiatek, Analysis of human cancer prostate tissues using FTIR microspectroscopy and SRIXE techniques, Journal of Molecular Structure 565 (2001) 329-334.

[50] E. Gazi, M. Baker, J. Dwyer, N.P. Lockyer, P. Gardner, J.H. Shanks, R.S. Reeve, C.A. Hart, N.W. Clarke, M.D. Brown, A correlation of FTIR spectra derived from prostate

cancer biopsies with Gleason grade and tumour stage, European urology 50(4) (2006) 750-761.

[51] M.A. Mackanos, C.H. Contag, FTIR microspectroscopy for improved prostate cancer diagnosis, Trends in biotechnology 27(12) (2009) 661-663.

[52] N. Fujioka, Y. Morimoto, T. Arai, M. Kikuchi, Discrimination between normal and malignant human gastric tissues by Fourier transform infrared spectroscopy, Cancer Detection and Prevention 28(1) (2004) 32-36.

[53] Q.-B. Li, X.-J. Sun, Y.-Z. Xu, L.-M. Yang, Y.-F. Zhang, S.-F. Weng, J.-S. Shi, J.-G. Wu, Use of Fourier-transform infrared spectroscopy to rapidly diagnose gastric endoscopic biopsies, World Journal of Gastroenterology: WJG 11(25) (2005) 3842.

[54] W.-s. Yi, D.-s. Cui, Z. Li, L.-l. Wu, A.-g. Shen, J.-m. Hu, Gastric cancer differentiation using Fourier transform near-infrared spectroscopy with unsupervised pattern recognition, Spectrochimica Acta Part A: Molecular and Biomolecular Spectroscopy 101 (2013) 127-131.

[55] J.G. Wu, Y.Z. Xu, C.W. Sun, R.D. Soloway, D.F. Xu, Q.G. Wu, K.H. Sun, S.F. Weng, G.X. Xu, Distinguishing malignant from normal oral tissues using FTIR fiber-optic techniques, Biopolymers 62(4) (2001) 185-192.

[56] M.L. Naurecka, B.M. Sierakowski, W. Kasprzycka, A. Dojs, M. Dojs, Z. Suszyński, M. Kwaśny, FTIR-ATR and FT-Raman Spectroscopy for Biochemical Changes in Oral Tissue, American Journal of Analytical Chemistry 8(03) (2017) 180.

[57] N. Krishnakumar, R.N. Madhavan, P. Sumesh, P.R. Palaniappan, P. Venkatachalam, C.R. Ramachandran, FT-IR Spectroscopic Analysis of Normal and Malignant Human Oral Tissues, AIP, pp. 149-151.

[58] Y. Fukuyama, S. Yoshida, S. Yanagisawa, M. Shimizu, A study on the differences between oral squamous cell carcinomas and normal oral mucosas measured by Fourier transform infrared spectroscopy, Biospectroscopy 5(2) (1999) 117-126.

[59] S. Mordechai, R.K. Sahu, Z. Hammody, S. Mark, K. Kantarovich, H. Guterman, A. Podshyvalov, J. Goldstein, S. Argov, Possible common biomarkers from FTIR microspectroscopy of cervical cancer and melanoma, Journal of microscopy 215(1) (2004) 86-91.

[60] B.R. Wood, L. Chiriboga, H. Yee, M.A. Quinn, D. McNaughton, M. Diem, Fourier transform infrared (FTIR) spectral mapping of the cervical transformation zone, and dysplastic squamous epithelium, Gynecologic oncology 93(1) (2004) 59-68.

[61] Y. Jusman, N.A.M. Isa, R. Adnan, N.H. Othman, Intelligent classification of cervical pre-cancerous cells based on the FTIR spectra, Ain Shams Engineering Journal 3(1) (2012) 61-70.

[62] P.T.T. Wong, S. Lacelle, M.F.K. Fung, M. Senterman, N.Z. Mikhael, Characterization of exfoliated cells and tissues from human endocervix and ectocervix by FTIR and ATR/FTIR spectroscopy, Biospectroscopy 1(5) (1995) 357-364.

[63] R. Gasper, J. Dewelle, R. Kiss, T. Mijatovic, E. Goormaghtigh, IR spectroscopy as a new tool for evidencing antitumor drug signatures, Biochimica et Biophysica Acta (BBA)-Biomembranes 1788(6) (2009) 1263-1270.

[64] A. Mignolet, A. Derenne, M. Smolina, B.R. Wood, E. Goormaghtigh, FTIR spectral signature of anticancer drugs. Can drug mode of action be identified?, Biochimica et Biophysica Acta (BBA)-Proteins and Proteomics 1864(1) (2016) 85-101.

[65] B.-B. Wu, Y.-P. Gong, X.-H. Wu, Y.-Y. Chen, F.-F. Chen, L.-T. Jin, B.-R. Cheng, F. Hu, B. Xiong, Fourier transform infrared spectroscopy for the distinction of MCF-7 cells treated with different concentrations of 5-fluorouracil, Journal of translational medicine 13(1) (2015) 108.

[66] A.V. Rutter, M.R. Siddique, J. Filik, C. Sandt, P. Dumas, G. Cinque, G.D. Sockalingum, Y. Yang, J. Sulé-Suso, Study of gemcitabine-sensitive/resistant cancer cells by cell cloning and synchrotron FTIR microspectroscopy, Cytometry Part A 85(8) (2014) 688-697.

[67] S. Kumar, T.S. Shabi, E. Goormaghtigh, A FTIR imaging characterization of fibroblasts stimulated by various breast cancer cell lines, PloS one 9(11) (2014) e111137.

[68] H. Ghimire, M. Venkataramani, Z. Bian, Y. Liu, A.G.U. Perera, ATR-FTIR spectral discrimination between normal and tumorous mouse models of lymphoma and melanoma from serum samples, Scientific reports 7(1) (2017) 16993.

[69] F. Elmi, A.F. Movaghar, M.M. Elmi, H. Alinezhad, N. Nikbakhsh, Application of FT-IR spectroscopy on breast cancer serum analysis, Spectrochimica Acta Part A: Molecular and Biomolecular Spectroscopy 187 (2017) 87-91.

[70] P.D. Lewis, K.E. Lewis, R. Ghosal, S. Bayliss, A.J. Lloyd, J. Wills, R. Godfrey, P. Kloer, L.A.J. Mur, Evaluation of FTIR spectroscopy as a diagnostic tool for lung cancer using sputum, BMC cancer 10(1) (2010) 640.

[71] D. Sheng, Y. Wu, X. Wang, D. Huang, X. Chen, X. Liu, Comparison of serum from gastric cancer patients and from healthy persons using FTIR spectroscopy, Spectrochimica Acta Part A: Molecular and Biomolecular Spectroscopy 116 (2013) 365-369.

[72] L. Dong, X. Sun, Z. Chao, S. Zhang, J. Zheng, R. Gurung, J. Du, J. Shi, Y. Xu, Y. Zhang, Evaluation of FTIR spectroscopy as diagnostic tool for colorectal cancer using spectral analysis, Spectrochimica Acta Part A: Molecular and Biomolecular Spectroscopy 122 (2014) 288-294.

[73] X. Wang, X. Shen, D. Sheng, X. Chen, X. Liu, FTIR spectroscopic comparison of serum from lung cancer patients and healthy persons, Spectrochimica Acta Part A: Molecular and Biomolecular Spectroscopy 122 (2014) 193-197.

[74] V. Rai, R. Mukherjee, A. Routray, A.K. Ghosh, S. Roy, B.P. Ghosh, P.B. Mandal, S. Bose, C. Chakraborty, Serum-based diagnostic prediction of oral submucous fibrosis using FTIR spectrometry, Spectrochimica Acta Part A: Molecular and Biomolecular Spectroscopy 189 (2018) 322-329.

[75] D. Sheng, X. Liu, W. Li, Y. Wang, X. Chen, X. Wang, Distinction of leukemia patients' and healthy persons' serum using FTIR spectroscopy, Spectrochimica Acta Part A: Molecular and Biomolecular Spectroscopy 101 (2013) 228-232.

[76] M. Khanmohammadi, K. Ghasemi, A.B. Garmarudi, M. Ramin, Diagnostic prediction of renal failure from blood serum analysis by FTIR spectrometry and chemometrics, Spectrochimica Acta Part A: Molecular and Biomolecular Spectroscopy 136 (2015) 1782-1785.

[77] A.H. Ambre, D.R. Katti, K.S. Katti, Biomineralized hydroxyapatite nanoclay composite scaffolds with polycaprolactone for stem cell-based bone tissue engineering, Journal of Biomedical Materials Research Part A 103(6) (2015) 2077-2101.

[78] D. Sikdar, S.M. Pradhan, D.R. Katti, K.S. Katti, B. Mohanty, Altered phase model for polymer clay nanocomposites, Langmuir 24(10) (2008) 5599-5607.

[79] D. Sikdar, K.S. Katti, D.R. Katti, Molecular interactions alter clay and polymer structure in polymer clay nanocomposites, Journal of Nanoscience and Nanotechnology 8(4) (2008) 1638-1657.

[80] D. Sikdar, D.R. Katti, K.S. Katti, The role of interfacial interactions on the crystallinity and nanomechanical properties of clay–polymer nanocomposites: a molecular dynamics study, Journal of applied polymer science 107(5) (2008) 3137-3148.

[81] D. Sikdar, D. Katti, K. Katti, B. Mohanty, Effect of organic modifiers on dynamic and static nanomechanical properties and crystallinity of intercalated clay–polycaprolactam nanocomposites, Journal of applied polymer science 105(2) (2007) 790-802.

[82] K.S. Katti, M. Molla, F. Karandish, M.K. Haldar, S. Mallik, D.R. Katti, Sequential culture on biomimetic nanoclay scaffolds forms three-dimensional tumoroids, Journal of Biomedical Materials Research Part A 104(7) (2016) 1591-1602.

[83] K.S. Katti, D.R. Katti, M.S. Molla, S. Kar, Evaluation of Cancer Tumors in 3D Porous Bone Mimetic Scaffolds, Poromechanics VI, pp. 881-888.

[84] S. Molla, D.R. Katti, K.S. Katti, In vitro design of mesenchymal to epithelial transition of prostate cancer metastasis using 3D nanoclay bone-mimetic scaffolds, Journal of Tissue Engineering and Regenerative Medicine 12(3) (2018) 727-737.

[85] K.S. Katti, A.H. Ambre, N. Peterka, D.R. Katti, Use of unnatural amino acids for design of novel organomodified clays as components of nanocomposite biomaterials, Philosophical Transactions of the Royal Society of London A: Mathematical, Physical and Engineering Sciences 368(1917) (2010) 1963-1980.

[86] A. Ambre, K.S. Katti, D.R. Katti, In situ mineralized hydroxyapatite on amino acid modified nanoclays as novel bone biomaterials, Materials Science and Engineering: C 31(5) (2011) 1017-1029.

[87] A.H. Ambre, K.S. Katti, D.R. Katti, Nanoclay based composite scaffolds for bone tissue engineering applications, Journal of Nanotechnology in Engineering and Medicine 1(3) (2010) 031013.

[88] Y. Yang, J. Sulé-Suso, G.D. Sockalingum, G. Kegelaer, M. Manfait, A.J. El Haj, Study of tumor cell invasion by Fourier transform infrared microspectroscopy, Biopolymers 78(6) (2005) 311-317.

[89] D. Naumann, FT-infrared and FT-Raman spectroscopy in biomedical research, Applied Spectroscopy Reviews 36(2-3) (2001) 239-298.

[90] G.I. Dovbeshko, N.Y. Gridina, E.B. Kruglova, O.P. Pashchuk, FTIR spectroscopy studies of nucleic acid damage, Talanta 53(1) (2000) 233-246.

[91] G. Shetty, C. Kendall, N. Shepherd, N. Stone, H. Barr, Raman spectroscopy: elucidation of biochemical changes in carcinogenesis of oesophagus, British journal of cancer 94(10) (2006) 1460.

[92] R. Eckel, H. Huo, H.-W. Guan, X. Hu, X. Che, W.-D. Huang, Characteristic infrared spectroscopic patterns in the protein bands of human breast cancer tissue, Vibrational Spectroscopy 27(2) (2001) 165-173.

[93] S. Yoshida, M. Miyazaki, K. Sakai, M. Takeshita, S. Yuasa, A. Sato, T. Kobayashi, S. Watanabe, H. Okuyama, Fourier transform infrared spectroscopic analysis of rat brain microsomal membranes modified by dietary fatty acids: possible correlation with altered learning behavior, Biospectroscopy 3(4) (1997) 281-290.

[94] D. Naumann, Infrared and NIR Raman spectroscopy in medical microbiology, in: H.H. Mantsch, M. Jackson (Eds.) Infrared Spectroscopy: New Tool in Medicine, SPIE,, International Society for Optics and Photonics, Bellingham, 1998, pp. 245-258.

[95] G.I. Dovbeshko, V.I. Chegel, N.Y. Gridina, O.P. Repnytska, Y.M. Shirshov, V.P. Tryndiak, I.M. Todor, G.I. Solyanik, Surface enhanced IR absorption of nucleic acids from tumor cells: FTIR reflectance study, Biopolymers 67(6) (2002) 470-486.

[96] I. Iloro, D. Narváez, N. Guillén, C.M. Camacho, L. Guillén, E. Cora, B. Pastrana-Ríos, The kinetics of the hydrogen/deuterium exchange of epidermal growth factor receptor ligands, Biophysical journal 94(10) (2008) 4041-4055.

[97] B.R. Wood, M.A. Quinn, F.R. Burden, D. McNaughton, An investigation into FTIR spectroscopy as a biodiagnostic tool for cervical cancer, Biospectroscopy 2(3) (1996) 143-153.

[98] B.R. Wood, M.A. Quinn, B. Tait, M. Ashdown, T. Hislop, M. Romeo, D. McNaughton, FTIR microspectroscopic study of cell types and potential confounding variables in screening for cervical malignancies, Biospectroscopy 4(2) (1998) 75-91.

[99] L. Chiriboga, P. Xie, H. Yee, V. Vigorita, D. Zarou, D. Zakim, M. Diem, Infrared spectroscopy of human tissue. I. Differentiation and maturation of epithelial cells in the human cervix, Biospectroscopy 4(1) (1998) 47-53.

[100] K. Malek, B.R. Wood, K.R. Bambery, FTIR imaging of tissues: techniques and methods of analysis, Optical spectroscopy and computational methods in biology and medicine, Springer2014, pp. 419-473.

[101] B.R. Wood, The importance of hydration and DNA conformation in interpreting infrared spectra of cells and tissues, Chemical Society Reviews 45(7) (2016) 1980-1998.

[102] S. Liyanage, R.S. Dassanayake, A. Bouyanfif, E. Rajakaruna, L. Ramalingam, N. Moustaid-Moussa, N. Abidi, Optimization and validation of cryostat temperature conditions for trans-reflectance mode FTIR microspectroscopic imaging of biological tissues, MethodsX 4 (2017) 118-127.

[103] R.K. Sahu, S. Argov, A. Salman, M. Huleihel, N. Grossman, Z. Hammody, J. Kapelushnik, S. Mordechai, Characteristic absorbance of nucleic acids in the Mid-IR region as possible common biomarkers for diagnosis of malignancy, Technology in cancer research & treatment 3(6) (2004) 629-638.

[104] P.G.L. Andrus, R.D. Strickland, Cancer grading by Fourier transform infrared spectroscopy, Biospectroscopy 4(1) (1998) 37-46.

[105] M.F.K. Fung, M.K. Senterman, N.Z. Mikhael, S. Lacelle, P.T.T. Wong, Pressure-tuning fourier transform infrared spectroscopic study of carcinogenesis in human endometrium, Biospectroscopy 2(3) (1996) 155-165.

[106] N.A. Al-Muslet, E.E. Ali, Spectroscopic analysis of bladder cancer tissues using Fourier transform infrared spectroscopy, Journal of Applied Spectroscopy 79(1) (2012) 139-142.

[107] J.-S. Wang, J.-S. Shi, Y.-Z. Xu, X.-Y. Duan, L. Zhang, J. Wang, L.-M. Yang, S.-F. Weng, J.-G. Wu, FT-IR spectroscopic analysis of normal and cancerous tissues of esophagus, World journal of gastroenterology 9(9) (2003) 1897.

[108] L. Li, X. Bi, H. Sun, S. Liu, M. Yu, Y. Zhang, S. Weng, L. Yang, Y. Bao, J. Wu, Characterization of ovarian cancer cells and tissues by Fourier transform infrared spectroscopy, Journal of ovarian research 11(1) (2018) 64.

[109] H. Yao, X. Shi, Y. Zhang, The use of FTIR-ATR spectrometry for evaluation of surgical resection margin in colorectal cancer: a pilot study of 56 samples, Journal of Spectroscopy 2014 (2014).

[110] J. Wang, J. Zhang, W. Wu, X. Duan, S. Wang, M. Zhang, S. Zhou, F. Mo, Y. Xu, J. Shi, Evaluation of gallbladder lipid level during carcinogenesis by an infrared spectroscopic method, Digestive diseases and sciences 55(9) (2010) 2670-2675.

[111] S.E. Glassford, B. Byrne, S.G. Kazarian, Recent applications of ATR FTIR spectroscopy and imaging to proteins, Biochimica et Biophysica Acta (BBA)-Proteins and Proteomics 1834(12) (2013) 2849-2858.

[112] W.K. Surewicz, H.H. Mantsch, D. Chapman, Determination of protein secondary structure by Fourier transform infrared spectroscopy: a critical assessment, Biochemistry 32(2) (1993) 389-394.

[113] A. Salman, V. Erukhimovitch, M. Talyshinsky, M. Huleihil, M. Huleihel, FTIR spectroscopic method for detection of cells infected with herpes viruses, Biopolymers 67(6) (2002) 406-412.

[114] H. Wiseman, B. Halliwell, Damage to DNA by reactive oxygen and nitrogen species: role in inflammatory disease and progression to cancer, Biochemical Journal 313(Pt 1) (1996) 17.

[115] L. Dostál, C.-Y. Chen, A.H.J. Wang, H. Welfle, Partial B-to-A DNA transition upon minor groove binding of protein Sac7d monitored by Raman spectroscopy, Biochemistry 43(30) (2004) 9600-9609.

CHAPTER 7. LABEL-FREE DISCRIMINATION OF CANCER CELLS AT DIFFERENT STAGES OF TUMORIGENESIS USING 3D IN VITRO BONE METASTASIS MODEL OF PROSTATE CANCER BY RAMAN IMAGING[6]

This chapter demonstrates Raman spectroscopy as a powerful imaging method for prostate cancer bone metastasis diagnosis. The contents of this chapter are going to be submitted for publication.

7.1. Introduction

Prostate cancer is the most frequently diagnosed cancer amongst men. According to recent statistics, the 5- year survival rate of patients with primary prostate cancer is 100% while it declines to 30 % in the case of metastases [1]. Metastatic prostate cancer colonizes in the bone marrow to pave the way for bone metastasis, leading to cytoskeletal complications and is associated with poor prognosis and morbidity. In recent years, there has been an increasing need for translational models that recapitulate bone metastasis of prostate cancer to understand the mechanisms that underlie bone metastasis due to lack of availability of human prostate cancer metastasized bone samples and *in vivo* mouse models for spontaneous prostate cancer bone metastasis. Moreover, the complexity of this disease itself poses a challenge for the diagnosis and assessment of populations with therapeutic resistance. The current gold standard for determining the prognosis of prostate cancer in patients is a basic histopathological examination. Immunohistopathology has also been used extensively for the analysis of biopsy samples in the last decade. Nevertheless, the use of immunohistochemistry is restricted owing to the scarcity of

[6] This chapter was co-authored by S. Kar, K. S. Katti, J. W. Kang, R. R. Dasari, P. T. C. So, J. Eswara, R. Paulmurugan, D. Liepmann, R. Venkatesan, and D. R. Katti. Sumanta Kar conducted all the spectral analyses and drafted the chapter. Experimental design was led by K.S. Katti. Computational design as well as design of codes for spectral analysis were written by D.R. Katti. Raman imaging experiments were conducted by J.W. Kang, R. Venkatesan, R.R. Dasari and P.T.C. So. Consultations with J. Eswara were used for the clinical perspective of the analysis. Kalpana Katti and Dinesh Katti directed the research orientation and revised this chapter.

large volume of tissue sections for staining and the inability to detect multiple signals at once. Also, the reproducibility and robustness of genomic data remain a concern due to the heterogeneity of tumors. It is, therefore, necessary to develop robust diagnostic and classification tools that have reproducibility and clinical potential.

Raman spectroscopy is an inelastic scattering phenomenon that is used to probe molecular vibrations, thus providing a molecular fingerprint that is especially suited for biological macromolecules. This technique is based on a change in polarizability of a molecule on the absorption of photons, whereas the complementary infrared (IR) spectroscopy depends on a change in the dipole moment. Raman spectroscopy is an information-rich spectroscopic method, like FT-IR, capable of detecting specific groups and the environment-sensitive cell surface composition of biological macromolecules consisting of carbohydrates, proteins, and lipids, among others [2-4]. A recent study demonstrated the feasibility of complementary vibrational spectroscopy technique for accurate and precise chemical analysis of organic liquids by combining IR and Raman [5]. Raman spectroscopy has been widely used to differentiate between nonmalignant, normal, and malignant cell lines, such as breast [6, 7], colorectal [8], gastrointestinal [9], lung [10], and prostate cancer cells/tissues while a few studies addressed stage-based classification [11, 12]. A recent study demonstrates the use of Raman mapping to evaluate subcellular responses in prostate cancer cells (PC-3) to x-ray exposure also elucidating the advantage of Raman mapping techniques over single point measurement [13]. Furthermore, most of the previous studies using Raman spectroscopy in the realm of prostate cancer research are based on two-dimensional (2D) culture models [11, 14]. It has been reported that in the 2D system, cells lose their *in vivo* morphology, resulting in poor cell-cell and cell-matrix interactions [15]. In contrast, three-dimensional (3D) *in vitro* models recapitulate a physiological

environment that mimics *in vivo* conditions, leading to improved predictions[16]. The primary goal of this study is to evaluate Raman spectroscopy as a potential tool for monitoring cancer progression using nanoclay-based 3D *in vitro* model of prostate cancer bone metastasis. For this purpose, we developed a 3D *in vitro* model [17] using nanoclay-based scaffolds [18] along with osteogenically differentiated human mesenchymal stem cells (MSCs) and human prostate cancer cells. Our group has investigated nanoclays extensively for the preparation of polymer clay nanocomposites [19, 20] using both experimental and simulation-based studies, with applications towards bone tissue engineering scaffolds [21]. In our previous studies, we have shown osteogenic differentiation of human MSCs into osteoblasts, and MSCs mediated mineralization through the biomimetic process of vesicular delivery on nanoclay based scaffolds without the use of osteogenic supplements [18, 22]. Recently, we have reported the late stage of prostate and breast cancer pathogenesis to the bone using the sequential culture of MSCs with human prostate and breast cancer cells on nanoclay based scaffolds [23-26]. In another study, Wnt/ β-catenin Signaling has been shown to play a key role in osteogenesis in 3D *in vitro* model of breast cancer bone metastasis [27]. In another study, we showed the influence of prostate cancer phenotype on bone mineralization at metastases [28]. In a related study from our laboratory, we have evaluated the feasibility of FT-IR spectroscopy for monitoring breast cancer progression on 3D *in vitro* model of breast cancer bone metastasis [29].

In the present study, we describe the feasibility of Raman spectroscopy as a powerful imaging method for prostate cancer bone metastasis diagnosis using 2D and 3D cell culture models in conjunction with application of principal component analysis (PCA) and cluster analysis. The present work addresses the: (1) potential of Raman imaging to discriminate between cancer cells from different stages of tumorigenesis; and (2) determination of key

biochemical components that account for the differences observed in the cells at different stages of cancer progression.

7.2. Materials and Methods

7.2.1. Modification of MMT clay

The detailed procedure for the modification of Na-MMT clay is described elsewhere [30, 31]. In brief, the 5-aminovaleric acid solution was added to preheated (60 ^{o}C) MMT suspension, and the mixture solution was kept for stirring. After one hour, the obtained slurry was centrifuged and washed to remove chloride ions followed by drying at 70 ^{o}C, grinding, and sieving to obtain a fine powder. Na-MMT clay was procured from Clay Minerals Respiratory at the University of Missouri, Columbia. 5-aminovaleric acid was obtained from Sigma-Aldrich.

7.2.2. Preparation of *in situ* HAPclay

We have followed the procedure described in our previous studies to prepare *in situ* HAP clay [21]. Briefly, the organically modified MMT clay powder was dissolved into Na_2HPO_4 solution (23.8 mM) by stirring at room temperature for two hours. Further, 39.8 mM of $CaCl_2$ solution was added, and this suspension was stirred vigorously for eight hours (pH 7.4). The obtained precipitate was centrifuged, dried (70 ^{o}C), and subsequently ground and sieved to obtain a fine powder. Na_2HPO_4 and $CaCl_2$ were purchased from J.T. Baker.

7.2.3. Preparation of Polycaprolactone (PCL)/*in situ* HAPClay Scaffolds

3D PCL/*in situ* HAPClay scaffolds were prepared according to the procedure described in earlier studies [18]. 3D PCL scaffolds were prepared with 10 wt. % *in situ* HAP clay. In a typical procedure, the PCL solution was prepared by dissolving 3.6 g of polymer in 40 ml of 1,4-dioxane. Another solution was prepared by dissolving 0.4 g of prepared *in situ* HAPclay in 20 ml of 1,4-dioxane, followed by sonicating for 18 min. Freshly prepared *in situ* HAPclay solution

was added to the polymer solution and stirred it for two hours. We used the freeze extraction method to obtain 3D scaffolds. The chemicals PCL and 1, 4-dioxane were purchased from Sigma Aldrich.

7.2.4. Cell Culture

Human MSCs (PT-2501) (Lonza) were maintained in MSCGM™ Bulletkit™ medium (Lonza, PT-3001). Human prostate cancer cell line MDA-PCa-2b (PCa) is purchased from ATCC and maintained in 80% BRFF-HPC-1 (AthenaES) and 20% FBS (ATCC). For 2D cultures, cells are seeded on tissue culture treated Petri dishes. For sequential culture, MSCs were seeded at a density of 5 x 10^4 cells per scaffold and cultured for 23 days to allow bone tissue formation. Further, prostate cancer cells PCa were seeded on newly formed bone tissue in the 3D scaffolds at a density of 5 x 10^4 cells and maintained in 1:1 MSCs and PCa medium (Figure 7.1). All cell cultures were maintained at 37 ºC and 5% CO_2 in a humidified incubator.

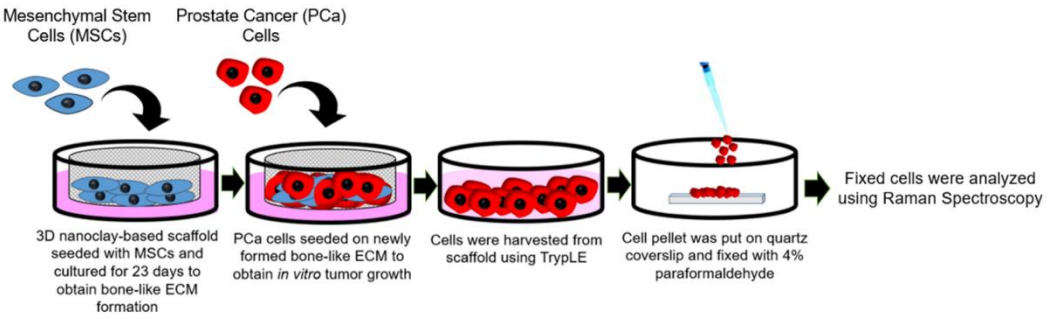

Figure 7.1. Schematic showing sequential culture of MSCs/prostate cancer cells and the workflow of Raman experiment.

7.2.5. Raman Imaging

Raman spectra were acquired using a custom-built NIR confocal Raman microscopy system [32]. The excitation source comprises a 785 nm wavelength from Ti: Sapphire laser (3900S, Spectra-Physics). The laser beam is focused onto the sample, and backscattered light is collected by the same objective lens (1.2 NA, × 60, Olympus UPLASPO60XWIR). Raman

signal is collected after series of Rayleigh rejection filters by a collection fiber, which is connected to a high-throughput imaging spectrograph (HoloSpec f/1.8i, Kaiser Optical Systems) with a thermoelectric-cooled, back-illuminated, and deep depleted CCD (PIXIS: 100BR_eXcelon, Princeton Instruments).

The primary goal of the present study is to investigate biochemical nuances at the cellular level, and thus a collection of cells in pellets from both 2D and 3D cultures was analyzed using point spectroscopic measurements. Briefly, after replacing culture medium with PBS, cell pellets were formed by centrifugation and placed on top of the quartz coverslip followed by fixation with 4% paraformaldehyde for 10 min at room temperature, washing with phosphate-buffered saline (PBS) for 2-3 times before performing Raman experiments (Figure 7.1). Raman spectra were recorded from three locations from each sample. Spectra were collected from 76 μm × 76 μm areas in each location with about 2 μm step size. From each location, 1600 (40 ×40) spectra were acquired with 3 second integration time. Wavelength calibration was performed before spectral acquisition by acquiring spectra from 4-acetamidophenol, a Raman scatterer with well-characterized peak positions. The 700-1800 cm^{-1} fingerprint region was used for the ensuing analysis (spectral resolution of 8 cm^{-1}). Specially developed codes in MATLAB™ were used for simultaneous baseline correction of all Raman spectra in each image. The open-source Raman Tool Set was used for mapping the spectra. Subsequently, additional MATLAB™ codes were utilized for contour map development to allow for uniform scaling across all maps generated for a given band. MATLAB™ codes were also developed to enable data to be transferred between Raman Tool Set and MATLAB™. Cosmic ray removal was also implemented before the spectra were used to create maps for predefined Raman bands in MATLAB (Mathworks Inc.). Further, twenty cell spectra from each sample were selected for intensity calculation of chosen Raman

bands, and principal component analysis. All spectra were normalized to DNA band 780 cm^{-1} before analysis.

7.2.6. Principal Component Analysis (PCA)

Principal Component Analysis (PCA) is an unsupervised statistical method that reduces variability by generating principal components (PCs). PCs are originated from a linear combination of original variables and arranged based on the variance in the original dataset to explain correlation to one another. The first two PCs, i.e., PC1 and PC2, are generally used to explain most of the data variance and generate a score plot. In a score plot, samples are positioned according to PC scores. For instance, samples with similar scores will take up a similar position while those with different scores will be placed in distance, thus making it easier to classify among samples [33].

PCA was conducted to determine whether spectra could be differentiated with respect to overall class 2D and 3D cultures. Before conducting PCA analysis, Raman spectra were imported and stored in a data matrix containing 867 rows (Raman shifts) and 80 columns (spectral intensities). PCA was performed in the spectral region of 700-1800 cm^{-1} using a covariance matrix. (PCA for Spectroscopy, Origin Pro 2018).

7.2.7. Cluster Analysis

Cluster analysis is the method of grouping sets of objects into clusters of similar objects to distinguish and segregate a large volume of dissimilar data [34]. It is extensively used in data mining, machine learning, pattern recognition, image analysis, bioinformatics, and computer graphics in fields as diverse as astronomy, ecology, social sciences, and biology. Although there are many ways of conducting cluster analysis, we have used cluster analysis in combination with PCA to analyze spectral data from Raman mapping. Unsupervised algorithms such as principal

component analysis and cluster analysis have been recently investigated for disease identification, including epithelial tissue tumors, brain tumors, skin tumors, bone diseases, atherosclerosis, kidney stones, gallstones, diabetes, and osteoarthritis [35]. For cluster analysis, a digital stripe of 5 μm width and 76 μm length is created outside of the Raman image. The digital stripe is made of uniformly distributed pixels containing the reference spectra obtained separately for the pure constituents (actin or myosin). The reference spectra obtained from the Raman instrument is baseline corrected and scaled to the average cellular spectra using the 1444 cm^{-1} band for actin and 1002 cm^{-1} band for myosin. PCA was used to identify the different principal components. These principal components were then used to build clusters of the Raman data, followed by mapping. Specifically, we chose principle components PC1 to PC6 for actin and PC1 to PC9 for myosin. Next, the clusters were constructed using the CDP Rodriguez method [36] in the Raman Toolset software. We used pure component spectra that were obtained from commercial sources of actin and myosin.

7.2.8. Statistical Analysis

All the data expressed as mean ± standard deviation (n=20) and the statistical significance (p-value) were verified by one-way ANOVA followed by *post hoc* Tukey test for multiple comparisons (GraphPad Prism, v7.04). $p<0.05$ was considered statistically significant.

7.3. Results and Discussion

In this manuscript, the sequential culture samples are referred to as 3D d(X+Y) MSCs + PCa SC, while 2D cancer culture is referred to as 2D PCa, where X=23 days of MSCs culture and Y= 5, 10, and 15 days of cancer cell culture after 23 days. The mean Raman spectra of 2D PCa, 3D d (23+5) MSCs+PCa SC, 3D d (23+10) MSCs+PCa SC, and 3D d (23+15) MSCs+PCa SC are shown in Figure 7.2A. As seen, prominent Raman bands are observed in both 2D and 3D

cultures of prostate cancer cells at the following peak positions with tentative biochemical assignments: 780 cm^{-1} (ring breathing of cytosine and thymine), 850 cm^{-1} (ν(C–C) ring breathing of tyrosine and proline), 935 cm^{-1} (ν(C–C) of α-helix conformation for proteins), 1002 cm^{-1} (ν(C–C) ring breathing of phenylalanine), 1080 cm^{-1} (ν(C–C) of lipids), 1124 cm^{-1} (ν(C–O) in carbohydrates), 1261 cm^{-1} (amide III δ(N–H) of proteins), 1296 cm^{-1} (δ(CH_2) deformations of lipids and proteins), 1336 cm^{-1} (CH_3CH_2 twisting of nucleic acids), 1444 cm^{-1} (δ(CH_2) of proteins and lipids), and 1654 cm^{-1} (amide I ν(C=O) of proteins, α- helical conformation) [14, 37-42] (Table 7.1). The corresponding difference spectra of different cultures (i.e., 2D and 3D) (Figure 7.2B) reveal the significant Raman spectral changes, particularly in the spectral ranges of 780-850 cm^{-1}, 935-1124 cm^{-1}, 1261-1336 cm^{-1}, 1440-1450 cm^{-1}, and 1500-1800 cm^{-1} which primarily correspond to proteins, DNA, and lipids.

To evaluate spectral variance across the samples studied, we used principal component analysis whose score and loading plots showed subtle differences, as shown in Figure 7.3. Figure 7.3A displays a score plot for the first two PCs illustrating good clustering for different cultures of PCa, while Figure 7.3B shows the first two PC loadings (i.e., PC1 and PC2) accounting for the largest Raman spectral variance (84.9% and 8.0%) and generally represent variations in the six sub-region bands at 1002 cm^{-1}, 1261 cm^{-1}, 1444 cm^{-1}, and 1654 cm^{-1} in the Raman spectra. A comparison of the Raman intensities ± SD at each of the four identified spectral sub-regions for all sample types studied is illustrated in the bar-chart (Figure 7.4). There was no appreciable change observed in intensities at all four bands (1002 cm^{-1} , 1261 cm^{-1}, 1444 cm^{-1}, and 1654 cm^{-1}) between 2D PCa and 3D d(23+5) MSCs+PCa SC; however, we observed a significant reduction in intensities at all four bands for 3D d(23+10) MSCs+PCa SC and 3D d(23+15) MSCs+PCa SC, as compared to both 2D PCa and 3D d(23+5) MSCs+PCa SC [Figure 7.4(A-D)].

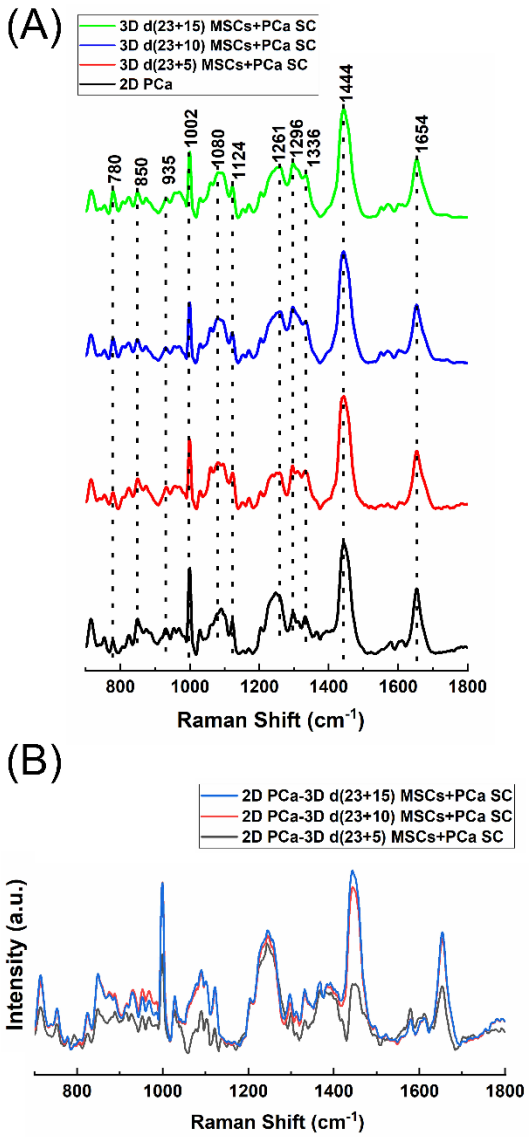

Figure 7.2. (A) Mean Raman spectra of 2D PCa (n=20) and 3D MSCs + PCa SCs (n=20). (B) The corresponding difference spectra calculated from the mean Raman spectra between 2D culture and three different 3D cultures.

To visually identify the chosen Raman bands with higher specificity in the set of samples, we created surface Raman maps shown in Figure 7.5, while optical micrographs for the set of same samples are shown in Figure 7.6A. In a Raman map, only a relative determination of concentrations is possible for multi-constituent biological samples such as cells. Hence, pseudo-

coloring is used for visualizing each concentration, which is proportional to the intensity of the constituent peak detected.

Table 7.1. Band assignments for Raman spectra for prostate cancer cells [14, 37-42].

Raman Shift (cm^{-1})	Band assignment
780	Ring breathing of cytosine and thymine
850	*ν*(C–C) ring breathing of tyrosine and proline
935	*ν*(C–C) of α-helix conformation for proteins
1002	*ν*(C–C) ring breathing of phenylalanine
1080	*ν*(C–C) of lipids
1124	*ν*(C–O) in carbohydrates
1261	amide III δ(N–H) of proteins
1296	$\delta(CH_2)$ deformations of lipids and proteins
1336	CH_3CH_2 twisting of nucleic acids
1444	$\delta(CH_2)$ of proteins and lipids
1654	amide I *ν*(C=O) of proteins, α- helical conformation

We observed a substantial reduction in 1002 cm^{-1} signal in 3D d(23+10) MSCs+PCa SC and 3D d(23+15) MSCs+PCa SC, as opposed to 3D d(23+5) MSCs+PCa SC or 2D PCa, indicating a decrease in the amount of phenylalanine relative to the total Raman-active constituents in cancer cells during cancer progression (Figures 7.5A, 7.4A). Previous studies have reported a reduction in Raman signal at 1002 cm^{-1} in cancerous nasopharyngeal tissue compared to non-cancerous counterparts [43]. The change in the Raman band at 1002 cm^{-1} is attributed to the alteration in protein content and conformation. Furthermore, the Raman band at 1002 cm^{-1} has previously been demonstrated as a prominent and stable signal [43]. In a recent study, it was shown that advance stage nasopharyngeal cancer blood samples had lower phenylalanine content compared to that of early-stage [44].

Therefore, the band at 1002 cm^{-1} has the potential to serve as a biomarker to differentiate between stages of cancer progression at the bone site. In recent years, the cytoplasmic lipid droplets in cancer cells have received a great deal of attention owing to their ability to provide

energy storage that can be accessed by cells without the need for extra energy investment in biosynthesis [45]. These lipids droplets get absorbed, metabolized, and transformed by the cancer cells into cell membranes and other components needed for their further proliferation [46]. In line with these observations, we found a significant reduction in intensity of lipid-related band at 1444 cm^{-1} in 3D d(23+10) MSCs+PCa SC and 3D d(23+15) MSCs+PCa SC as opposed to 3D d(23+5) MSCs+PCa SC (Figures 7.4C, 7.5C), indicating a reduction in saturated CH_2 bonds in lipids during cancer progression [47]. Raman intensity changes at bands 1261 cm^{-1} and 1654 cm^{-1} [Figures 7.4(B, D) & 7.5(B, D)] are associated with a change in the relative amount of proteins in the α-helical conformation. In the present study, we observed a significant reduction in intensities of the bands mentioned above in 3D d(23+10) MSCs+PCa SC and 3D d(23+15) MSCs+PCa SC as compared to 3D d(23+5) MSCs+PCa SC. This reduction in intensity suggests a change in protein conformation or secondary structure i.e., α-helix to random coil conversion, during cancer progression [48].

A new computational technique was developed to rapidly identify specific constituents by obtaining a pure spectrum of the component (actin and myosin). A strip of the pure spectra is then created digitally outside of the Raman image. PCA is conducted for the image, including the component strip. Next, the CDP Rodriguez method [36] is used to cluster data into groups. If data in the specimen image is in the same cluster as the pure component stripe (actin or myosin), those regions within the map were considered similar to the component of the strip.

Figure 7.6B shows the clusters with actin strip at the top for the specimen from 2D, five-day, ten-day, and 15-day tumor samples. Figure 7.6C shows the clusters with myosin strip at the top for the specimen from 2D, five-day, ten-day, and 15-day tumor samples.

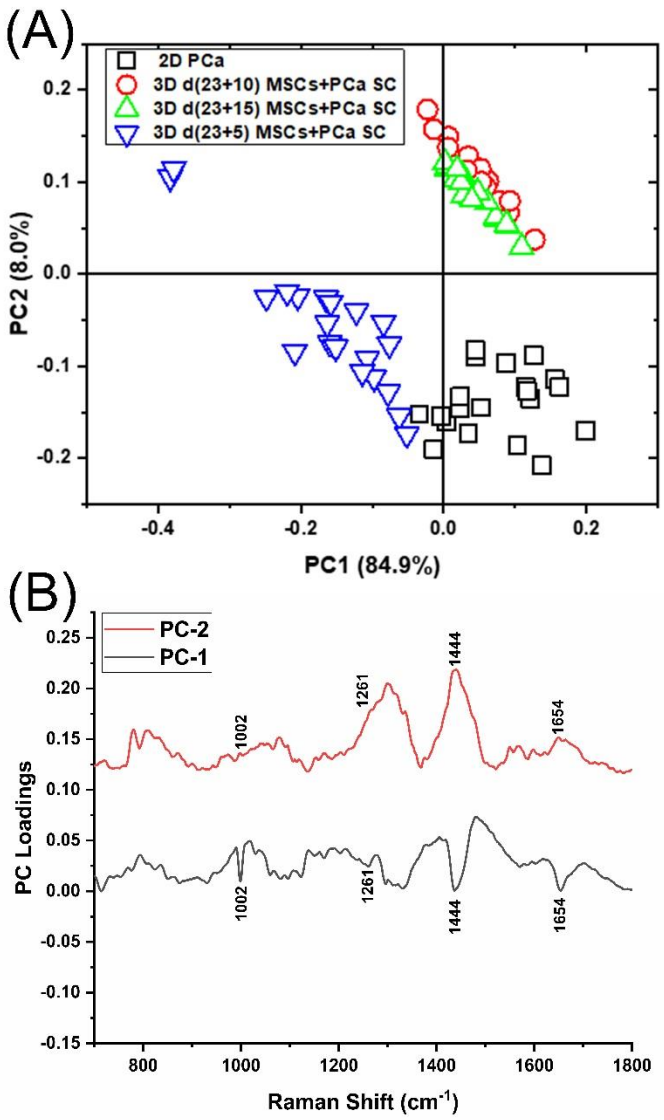

Figure 7.3. (A) PCA score plot spanned by PC1, and PC2 illustrating the intrinsic clustering of 2D PCa and 3D MSCs + PCa SCs. (B) The first two PCs accounting for 92.9% of the total variation in the Raman spectral dataset, revealing the significant Raman spectral features for the classification of cancer cells.

Both spatial and quantitative changes to the actin cytoskeleton are observed during cancer progression, and actin dynamics leading to reorganization of actin within the cancer cells plays an important role in migration and the EMT/MET transitions [49].

We observed dramatic changes to the actin region and distribution between the 2D PCa cells and the PCa cells that have been seeded on the bone-mimetic scaffolds (Figure 7.6B). We

observed changes to the spatial distribution of both actin and myosin from 2D to the 15-day tumor samples. The uniform actin and myosin distribution within cells, as observed in 2D samples, are disturbed as the tumor grows (Figure 7.6B and 7.6C).

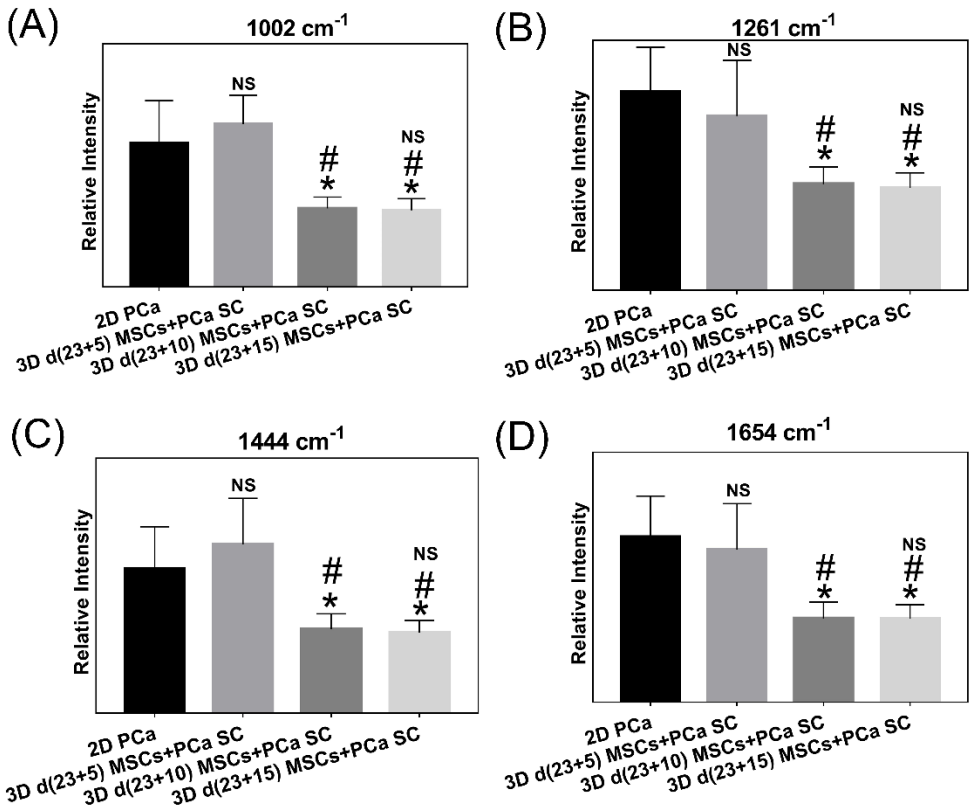

Figure 7.4. Histogram displaying intensities of Raman bands (A) 1002 cm^{-1}, (B) 1261 cm^{-1}, (C) 1444 cm^{-1}, and (D) 1654 cm^{-1} across samples. (n=20, one-way ANOVA followed by *post hoc* Tukey test, *$p<0.05$, **$p<0.01$, and ***$p<0.001$ indicate significant difference between 2D PCa and 3D MSCs + PCa SCs; $^{\#}p<0.05$, $^{\#\#}p<0.01$, and $^{\#\#\#}p<0.001$ indicate significant difference between day (23+5), and other days of 3D MSCs + PCa SCs; $^{\$}p<0.05$, $^{\$\$}p<0.01$, and $^{\$\$\$}p<0.001$ indicate significant difference between day (23+10) 3D MSCs + PCa SC and day (23+15) 3D MSCs + PCa SC).

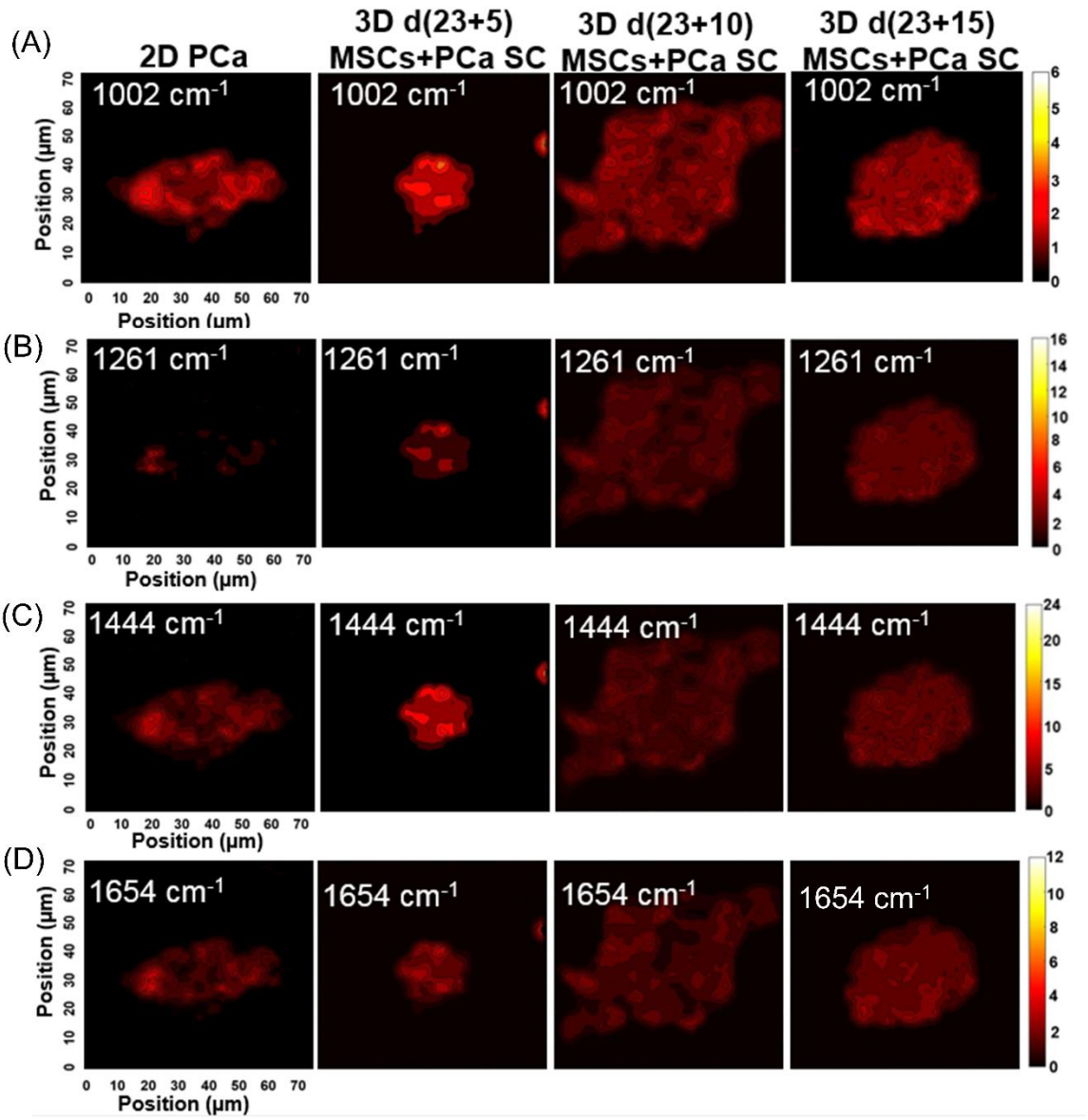

Figure 7.5. Raman mapping images of 2D PCa and three 3D MSCs + PCa SCs for vibrational signatures of: (A) 1002 cm^{-1}, (B) 1261 cm^{-1}, (C) 1444 cm^{-1}, and (D) 1654 cm^{-1}.

The actin region in the cells five days, ten, and 15 days after seeding on the bone-mimetic scaffolds are smaller than the 2D PCa cells. The actin regions in the cells that were seeded on the bone-mimetic samples for ten days and 15 days not only show reduced size of the actin region compared but were also scattered and not localized.

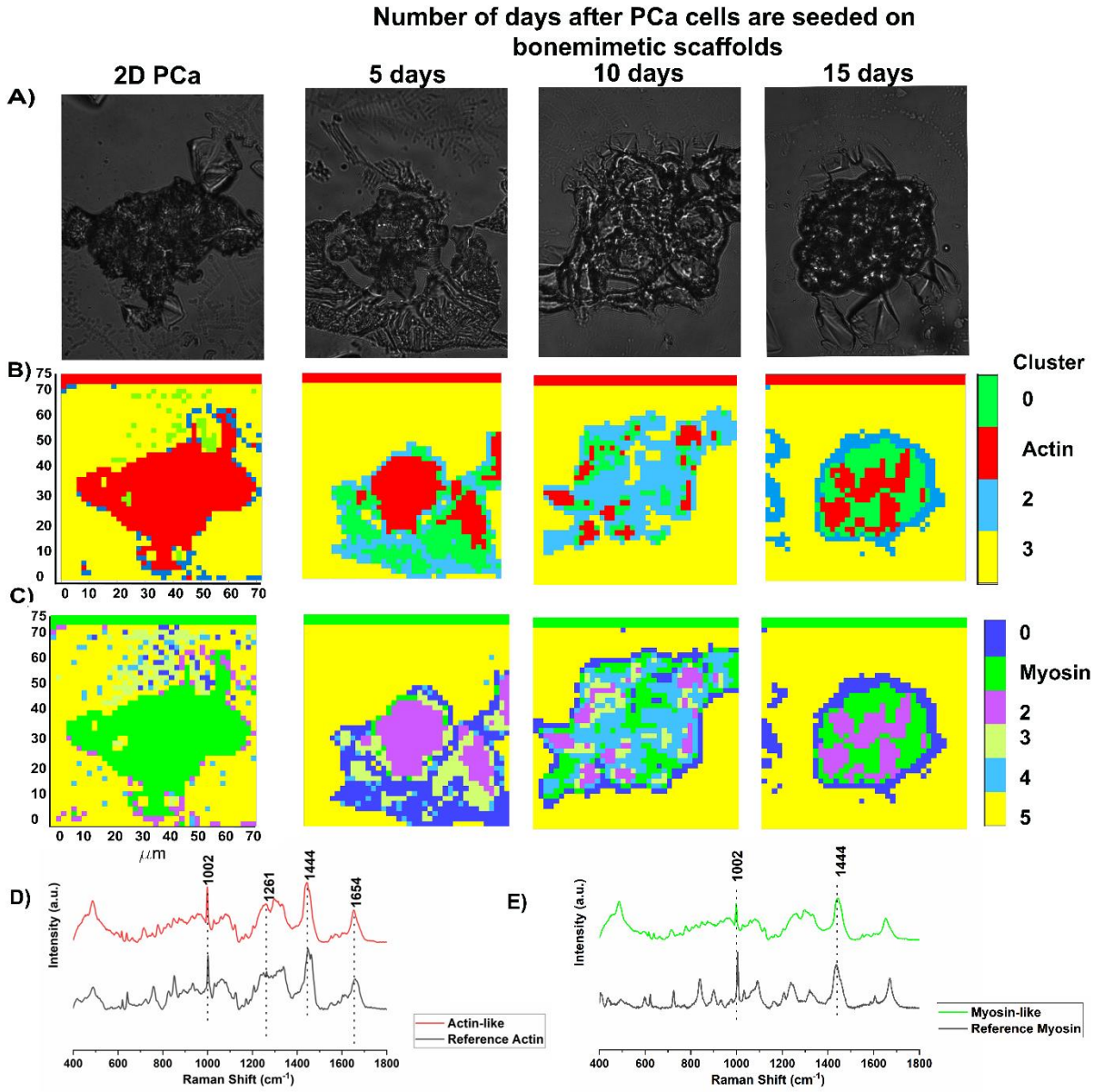

Figure 7.6. Cluster analysis of 2D PCa and PCa cells seeded on bone-mimetic scaffolds for 5, 10 and 15 days, (A) optical images of samples used in Raman Imaging, (B) clusters indicating actin-rich regions colored in red and the red stripe on the top of the image constitutes digitally introduced reference actin, (C) clusters indicating DNA rich regions colored in blue and the blue stripe on the top of the image constitutes digitally introduced reference DNA, (D) average spectra from ten randomly collected spectra from the actin-rich regions on day 15 and the reference spectra for actin, (E) average spectra from ten randomly collected spectra from the DNA rich regions on day 15 and the reference spectra for actin. The bone-mimetic scaffolds are created by seeding MSCs on 3D nanoclay based scaffolds and culturing for 23 days for regeneration of bone tissue. PCa cells are seeded after the MSC culture period of 23 days is completed. The 2D PCa cells indicate PCa cells not seeded on scaffolds.

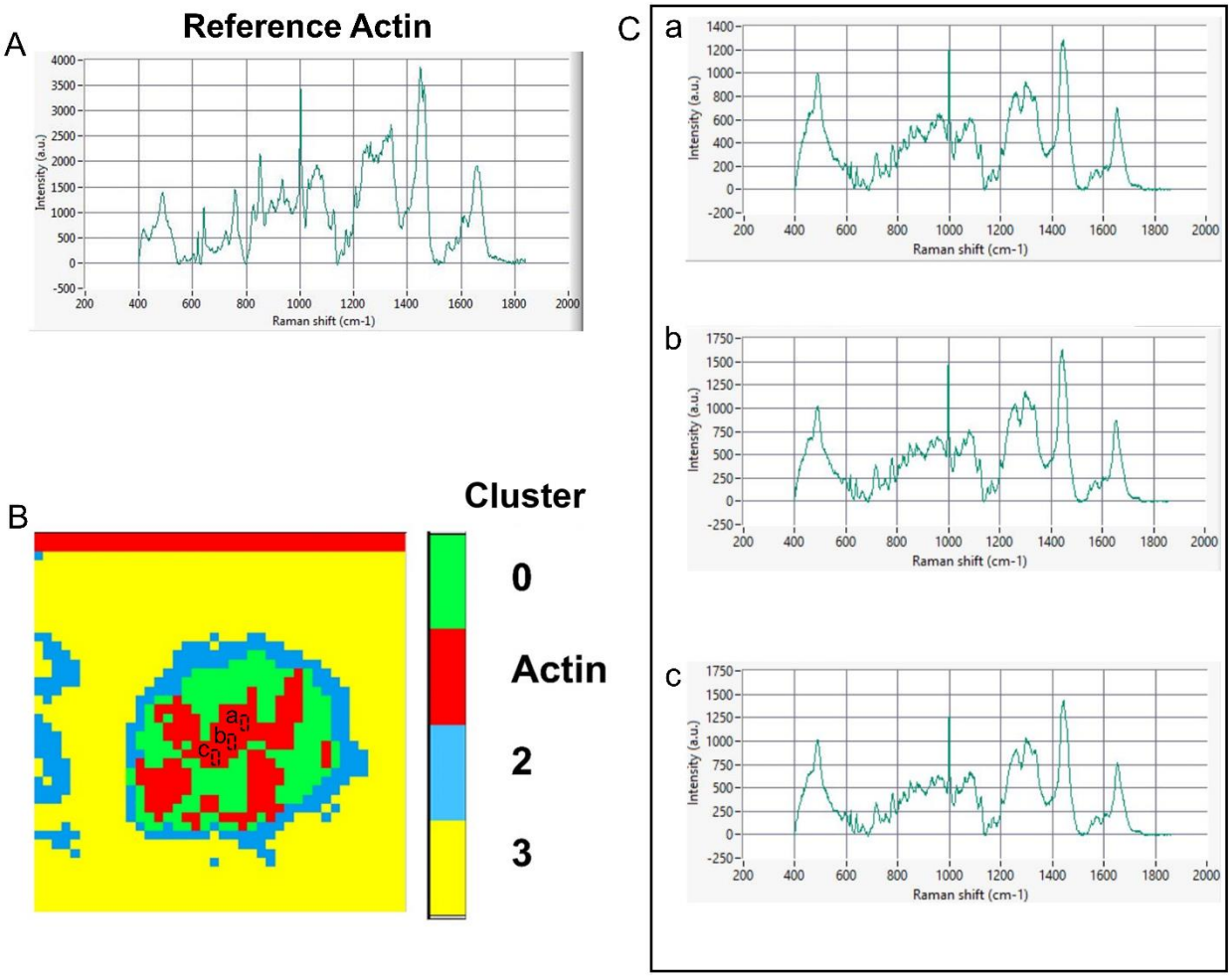

Figure 7.7. (A) Reference Actin spectra used for cluster analysis. (B) Cluster map of 3D d(23+15) MSCs+PCa SC indicating actin-rich regions colored in red and the red stripe on the top of the image constitutes digitally introduced reference actin, boxes (a,b, and c) drawn on the cluster map indicate random location on actin-rich region. (C) Spectra from randomly chosen location on actin-region showing similar features as reference actin.

Figure 7.6D shows pure spectra of actin labeled as reference spectra, and the average spectra of ten spectra obtained from the actin-rich regions in the cluster analysis and are labeled as actin-like spectra. Similarly, Figure 7.6E shows the myosin reference spectra and the myosin-like spectra, an average spectrum obtained from ten spectra in the myosin rich regions in the cluster analysis.

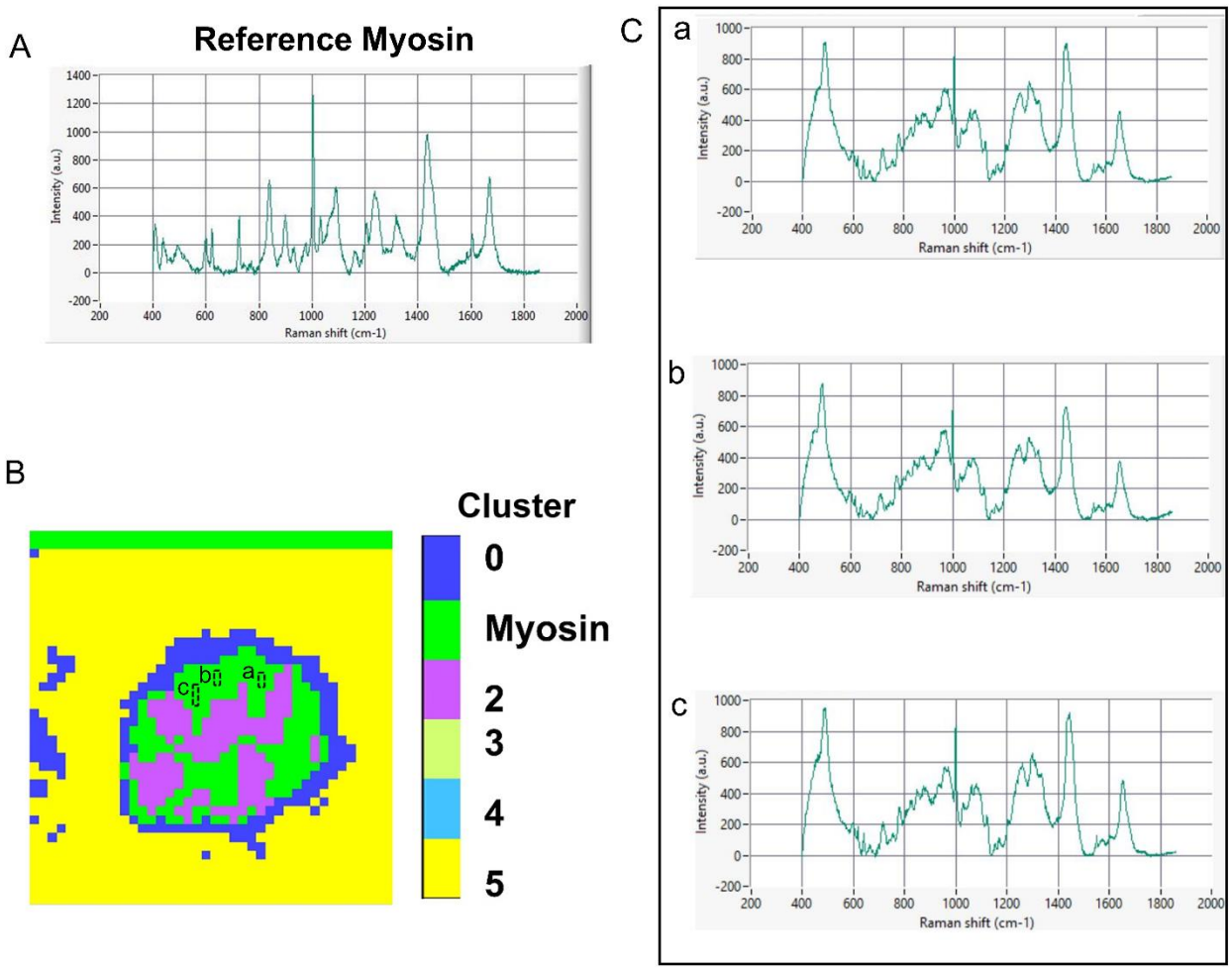

Figure 7.8. (A) Reference Myosin spectra used for cluster analysis. (B) Cluster map of 3D d(23+15) MSCs+PCa SC indicating myosin-rich regions colored in red and the red stripe on the top of the image constitutes digitally introduced reference myosin, boxes (a,b, and c) drawn on the cluster map indicate random location on myosin-rich region. (C) Spectra from randomly chosen location on myosin-region showing similar features as reference myosin.

The actin-like spectra and myosin-like spectra are obtained from the cells extracted from tumors formed 15 days after PCa cells are seeded on the bone-mimetic scaffolds. The spectra from the reference stripes of actin and myosin are not used for obtaining the actin-like and myosin-like spectra. Both the actin-like spectra and the myosin-like spectra are influenced by various other cellular constituents that would likely cause the addition of bands or degradation or amplification of intensities in some spectral regions.

To validate the spectra obtained from actin-rich and myosin-rich region in the cluster analysis, we compared them with pure actin and pure myosin reference spectra and observed actin-related bands at 1002 cm^{-1} (ν(C–C) ring breathing of phenylalanine), 1261 cm^{-1} (amide III δ(N–H) of proteins), 1444 cm^{-1} (δ(CH_2) of proteins), and 1654 cm^{-1} (amide I ν(C=O) of proteins, α-helical conformation) [50] (Figure 7.6D) and myosin-related bands at 1002 cm^{-1} (ν(C–C) ring breathing of phenylalanine), 1444 cm^{-1} (δ(CH_2) of proteins), 1654 cm^{-1} (amide I ν(C=O) of proteins, α-helical conformation) (shifted from 1670 cm-1 in reference myosin spectra) (not shown), and 1336 cm^{-1} (CH_3CH_2 twist) (shifted from 1320 cm^{-1} in reference myosin spectra) (not shown) [50, 51] (Figure 7.6E) in actin-like and myosin-like spectra, respectively. All major bands of actin and myosin are represented in the actin-like and myosin-like spectra, and the actin-like spectra appear to be less influenced by other cellular constituents as compared to myosin. Thus, the cluster analysis can discriminate the actin and myosin regions in the tumor cell clusters during progression. Cluster analysis of actin and myosin rich regions and corresponding spectra are reported in Figures 7.7 and 7.8, respectively.

Collectively, these observations suggest that there are significant changes in the intensities of distinctive biomolecules relative to the total Raman-active constituents in 2D and 3D cultures, suggesting the diagnostic potential of Raman microscopy for prostate cancer bone metastasis.

7.4. Conclusions

The present study marks the first application of Raman spectroscopy to classify 3D *in vitro* prostate cancer bone metastasis and to discriminate between cancer cells at different stages of tumorigenesis. Our results show that lipid, aromatic amino acid, and extracellular matrix components are involved in the staging of prostate cancer at the secondary bone site. Raman

spectroscopic properties of prostate cancer metastasized at bone tissue can be effectively translated into a great wealth of diagnostic information providing new insights into biochemical and architectural changes of prostate cancer cells undergoing different stages to tumorigenesis. Also, from the point of clinical applications, hand-held Raman imaging of tissues for diagnostics at the patient level would be very valuable. Our methods suggest that the incorporation of Raman spectroscopy and statistical techniques, such as PCA, makes the classification of cancer progression straightforward.

7.5. Acknowledgments

Authors acknowledge the support from the NDSU Center for Engineered Cancer testbeds. Support from ND EPSCoR for materials and supplies is also acknowledged. The authors acknowledge MD Shahjahan Molla for preparing the samples used in this work. The Raman imaging conducted in this work is supported by NIH P41-EB015871-33. VR acknowledges Rothschild Foundation, Paris, France and the MIT Center for NIH support as an user.

7.6. References

[1] A.M. Noone, N. Howlader, M. Krapcho, D. Miller, A. Brest, M. Yu, J. Ruhl, Z. Tatalovich, A. Mariotto, D.R. Lewis, SEER cancer statistics review, 1975-2015, Bethesda, MD: National Cancer Institute (2018).

[2] E.C. Le Ru, P.G. Etchegoin, Single-molecule surface-enhanced Raman spectroscopy, Annual review of physical chemistry 63 (2012) 65-87.

[3] K. Kneipp, Y. Wang, H. Kneipp, L.T. Perelman, I. Itzkan, R.R. Dasari, M.S. Feld, Single molecule detection using surface-enhanced Raman scattering (SERS), Physical review letters 78(9) (1997) 1667.

[4] R.S. Das, Y.K. Agrawal, Raman spectroscopy: recent advancements, techniques and applications, Vibrational spectroscopy 57(2) (2011) 163-176.

[5] K. Hashimoto, V.R. Badarla, A. Kawai, T. Ideguchi, Complementary vibrational spectroscopy, Nature Communications 10(1) (2019) 4411.

[6] I. Delfino, G. Perna, M. Lasalvia, V. Capozzi, L. Manti, C. Camerlingo, M. Lepore, Visible micro-Raman spectroscopy of single human mammary epithelial cells exposed to x-ray radiation, Journal of biomedical optics 20(3) (2015) 035003.

[7] F.S. Manciu, J.D. Ciubuc, K. Parra, M. Manciu, K.E. Bennet, P. Valenzuela, E.M. Sundin, W.G. Durrer, L. Reza, G. Francia, Label-free Raman imaging to monitor breast tumor signatures, Technology in cancer research & treatment 16(4) (2017) 461-469.

[8] K. Chen, Y. Qin, F. Zheng, M. Sun, D. Shi, Diagnosis of colorectal cancer using Raman spectroscopy of laser-trapped single living epithelial cells, Optics letters 31(13) (2006) 2015-2017.

[9] X.-L. Yan, R.-X. Dong, L. Zhang, X.-J. Zhang, Z.-W. Zhang, Raman spectra of single cell from gastrointestinal cancer patients, World Journal of Gastroenterology: WJG 11(21) (2005) 3290.

[10] Z. Huang, A. McWilliams, H. Lui, D.I. McLean, S. Lam, H. Zeng, Near-infrared Raman spectroscopy for optical diagnosis of lung cancer, International journal of cancer 107(6) (2003) 1047-1052.

[11] S. Corsetti, T. Rabl, D. McGloin, G. Nabi, Raman spectroscopy for accurately characterizing biomolecular changes in androgen-independent prostate cancer cells, Journal of biophotonics 11(3) (2018) e201700166.

[12] L. Wang, D. He, J. Zeng, Z. Fuan, Q. Dang, X. Wang, J. Wang, L. Huang, P. Cao, G. Zhang, Raman spectroscopy, a potential tool in diagnosis and prognosis of castration-resistant prostate cancer, Journal of biomedical optics 18(8) (2013) 087001.

[13] M. Roman, T.P. Wrobel, A. Panek, E. Efeoglu, J. Wiltowska-Zuber, C. Paluszkiewicz, H.J. Byrne, W.M. Kwiatek, Exploring subcellular responses of prostate cancer cells to X-ray exposure by Raman mapping, Scientific Reports 9(1) (2019) 8715.

[14] P. Crow, B. Barrass, C. Kendall, M. Hart-Prieto, M. Wright, R. Persad, N. Stone, The use of Raman spectroscopy to differentiate between different prostatic adenocarcinoma cell lines, British journal of cancer 92(12) (2005) 2166.

[15] E. Cukierman, R. Pankov, D.R. Stevens, K.M. Yamada, Taking cell-matrix adhesions to the third dimension, Science 294(5547) (2001) 1708-1712.

[16] C. Fischbach, R. Chen, T. Matsumoto, T. Schmelzle, J.S. Brugge, P.J. Polverini, D.J. Mooney, Engineering tumors with 3D scaffolds, Nature Methods 4(10) (2007) 855-860.

[17] K.S. Katti, M. Molla, F. Karandish, M.K. Haldar, S. Mallik, D.R. Katti, Sequential culture on biomimetic nanoclay scaffolds forms three-dimensional tumoroids, Journal of Biomedical Materials Research Part A 104(7) (2016) 1591-1602.

[18] A.H. Ambre, D.R. Katti, K.S. Katti, Biomineralized hydroxyapatite nanoclay composite scaffolds with polycaprolactone for stem cell-based bone tissue engineering, Journal of Biomedical Materials Research Part A 103(6) (2015) 2077-2101.

[19] D. Sikdar, S.M. Pradhan, D.R. Katti, K.S. Katti, B. Mohanty, Altered phase model for polymer clay nanocomposites, Langmuir 24(10) (2008) 5599-5607.

[20] D. Sikdar, K.S. Katti, D.R. Katti, Molecular interactions alter clay and polymer structure in polymer clay nanocomposites, Journal of Nanoscience and Nanotechnology 8(4) (2008) 1638-1657.

[21] A.H. Ambre, D.R. Katti, K.S. Katti, Nanoclays mediate stem cell differentiation and mineralized ECM formation on biopolymer scaffolds, Journal of Biomedical Materials Research Part A 101(9) (2013) 2644-2660.

[22] K.S. Katti, A.H. Ambre, S. Payne, D.R. Katti, Vesicular delivery of crystalline calcium minerals to ECM in biomineralized nanoclay composites, Materials Research Express 2(4) (2015) 13.

[23] S. Molla, D.R. Katti, K.S. Katti, In vitro design of mesenchymal to epithelial transition of prostate cancer metastasis using 3D nanoclay bone-mimetic scaffolds, Journal of tissue engineering and regenerative medicine 12(3) (2018).727-737.

[24] S. Kar, M.D.S. Molla, D.R. Katti, K.S. Katti, Tissue-engineered nanoclay-based 3D in vitro breast cancer model for studying breast cancer metastasis to bone, Journal of tissue engineering and regenerative medicine 13(2) (2019) 119-130.

[25] M.D.S. Molla, D.R. Katti, K.S. Katti, An in vitro model of prostate cancer bone metastasis for highly metastatic and non-metastatic prostate cancer using nanoclay bone-mimetic scaffolds, MRS Advances 4(21) (2019) 1207-1213.

[26] S. Kar, K.S. Katti, D.R. Katti, Engineered nanoclay based bone-mimetic 3D in vitro test-bed for bone metastasis of breast cancer, Transactions of the Annual Meeting of the Society for Biomaterials and the Annual International Biomaterials Symposium 40 (2019) 641.

[27] S. Kar, H. Jasuja, D.R. Katti, K.S. Katti, Wnt/β-catenin Signaling Pathway Regulates Osteogenesis for Breast Cancer Bone Metastasis: Experiments in an in vitro Nanoclay Scaffold Cancer Testbed, ACS Biomaterials Science & Engineering (2019). https://doi.org/10.1021/acsbiomaterials.9b00923

[28] M.D.S. Molla, D.R. Katti, J. Iswara, R. Venkatesan, R. Paulmurugan, K.S. Katti, Prostate cancer phenotype influences bone mineralization at metastasis: A study using an in vitro prostate cancer metastasis testbed, JBMR Plus.4(2) (2020).e10256

[29] S. Kar, D.R. Katti, K.S. Katti, Fourier transform infrared spectroscopy based spectral biomarkers of metastasized breast cancer progression, Spectrochimica Acta Part A: Molecular and Biomolecular Spectroscopy 208 (2019) 85-96.

[30] K.S. Katti, A.H. Ambre, N. Peterka, D.R. Katti, Use of unnatural amino acids for design of novel organomodified clays as components of nanocomposite biomaterials, Philosophical Transactions of the Royal Society of London A: Mathematical, Physical and Engineering Sciences 368(1917) (2010) 1963-1980.

[31] A. Ambre, K.S. Katti, D.R. Katti, In situ mineralized hydroxyapatite on amino acid modified nanoclays as novel bone biomaterials, Materials Science and Engineering: C 31(5) (2011) 1017-1029.

[32] J.W. Kang, N. Lue, C.-R. Kong, I. Barman, N.C. Dingari, S.J. Goldfless, J.C. Niles, R.R. Dasari, M.S. Feld, Combined confocal Raman and quantitative phase microscopy system for biomedical diagnosis, Biomedical optics express 2(9) (2011) 2484-2492.

[33] L. Ericksson, E. Johansson, N. Kettaneh-Wold, S. Wold, Multi-and Megavariate Data Analysis: Principles and Applications, Umetrics Academ, Umea (2001).

[34] N. Saitou, M. Nei, The neighbor-joining method - a new for reconstructing phylogenetic tress, Molecular Biology and Evolution 4(4) (1987) 406-425.

[35] C. Krafft, G. Steiner, C. Beleites, R. Salzer, Disease recognition by infrared and Raman spectroscopy, Journal of Biophotonics 2(1-2) (2009) 13-28.

[36] A. Rodriguez, A. Laio, Clustering by fast search and find of density peaks, Science 344(6191) (2014) 1492-1496.

[37] N. Stone, C. Kendall, J. Smith, P. Crow, H. Barr, Raman spectroscopy for identification of epithelial cancers, Faraday discussions 126 (2004) 141-157.

[38] I.I. Patel, F.L. Martin, Discrimination of zone-specific spectral signatures in normal human prostate using Raman spectroscopy, Analyst 135(12) (2010) 3060-3069.

[39] N. Huang, M. Short, J. Zhao, H. Wang, H. Lui, M. Korbelik, H. Zeng, Full range characterization of the Raman spectra of organs in a murine model, Optics express 19(23) (2011) 22892-22909.

[40] V. Renugopalakrishnan, L.A. Carreira, T.W. Collette, J.C. Dobbs, G. Chandraksasan, R.C. Lord, Non-uniform triple helical structure in chick skin type I collagen on thermal denaturation: Raman spectroscopic study, Zeitschrift für Naturforschung C 53(5-6) (1998) 383-388.

[41] S. Cui, S. Zhang, S. Yue, Raman spectroscopy and imaging for cancer diagnosis, Journal of healthcare engineering 2018 (2018).

[42] Y. Kumamoto, Y. Harada, T. Takamatsu, H. Tanaka, Label-free molecular imaging and analysis by Raman spectroscopy, Acta histochemica et cytochemica 51(3) (2018) 101-110.

[43] Y. Li, J. Pan, G. Chen, C. Li, S. Lin, Y. Shao, S. Feng, Z. Huang, S. Xie, H. Zeng, Micro-Raman spectroscopy study of cancerous and normal nasopharyngeal tissues, Journal of biomedical optics 18(2) (2013) 027003.

[44] D. Lin, J. Pan, H. Huang, G. Chen, S. Qiu, H. Shi, W. Chen, Y. Yu, S. Feng, R. Chen, Label-free blood plasma test based on surface-enhanced Raman scattering for tumor stages detection in nasopharyngeal cancer, Scientific reports 4 (2014) 4751.

[45] H. Abramczyk, J. Surmacki, M. Kopeć, A.K. Olejnik, K. Lubecka-Pietruszewska, K. Fabianowska-Majewska, The role of lipid droplets and adipocytes in cancer. Raman imaging of cell cultures: MCF10A, MCF7, and MDA-MB-231 compared to adipocytes in cancerous human breast tissue, Analyst 140(7) (2015) 2224-2235.

[46] H. Abramczyk, B. Brozek-Pluska, New look inside human breast ducts with Raman imaging. Raman candidates as diagnostic markers for breast cancer prognosis: mammaglobin, palmitic acid and sphingomyelin, Analytica chimica acta 909 (2016) 91-100.

[47] I. Anna, P. Bartosz, P. Lech, A. Halina, Novel strategies of Raman imaging for brain tumor research, Oncotarget 8(49) (2017) 85290.

[48] J. Anastassopoulou, M. Kyriakidou, S. Kyriazis, T. Kormas, A.F. Mavrogenis, V. Dritsa, P. Kolovou, T. Theophanides, An FT-IR spectroscopic study of metastatic cancerous bone, Infrared Spectroscopy-Anharmonicity of Biomolecules, Crosslinking of Biopolymers, Food Quality and Medical Applications, InTech, Europa, Chapt 5 (2015) 89-100.

[49] M. Izdebska, W. Zielińska, D. Grzanka, M. Gagat, The Role of Actin Dynamics and Actin-Binding Proteins Expression in Epithelial-to-Mesenchymal Transition and Its

Association with Cancer Progression and Evaluation of Possible Therapeutic Targets, BioMed research international 2018 (2018) 4578373-4578373.

[50] Z. Movasaghi, S. Rehman, I.U. Rehman, Raman spectroscopy of biological tissues, Applied Spectroscopy Reviews 42(5) (2007) 493-541.

[51] E.B. Carew, I.M. Asher, H.E. Stanley, Laser raman spectroscopy--new probe of myosin substructure, Science 188(4191) (1975) 933-936.

CHAPTER 8. SUMMARY AND CONCLUSIONS

- In this dissertation, we report development of a biologically relevant, 3D tissue-engineered breast cancer model tumor model that provides a unique microenvironment mimicking the physiological cell-cell and cell-matrix interactions, leading to more appropriate BrCa cell behavior in the later stage of cancer metastasis in bone. The unique and distinct behavior of various cells lines including the high metastatic MDA-MB-231 and the low metastatic MCF-7 was observed at the bone metastasis site. The changes to migratory capabilities and invasiveness of MDA-MB-231 in comparison to tumor growth with MCF-7 was directly observed on the 3D model. Also, the model was able to be mimic MET stage of cancer metastasis, thus providing a platform for studying later stage of breast cancer pathogenesis in bone.
- In this dissertation, we showed that 3D *in vitro* model allows investigation of the interactions between breast cancer cells and bone and facilitates quantification of bone formation with different breast cancer cells. MCF-7 cells secrete ET-1, which promotes osteoblastic differentiation via Wnt/β-catenin signaling and induces bone-forming activity, leading to increased bone formation. Inactivation of Wnt/β-catenin signaling by MDA-MB-231 secreted DKK-1 leads to inhibited bone formation through down-regulation of osteoblast differentiation. Most importantly, the model exhibited both inhibited and excessive bone formation with different cell lines, mimicking bone lesions observed in breast cancer patients. Therefore, this model is suitable for studying cellular mechanisms underlying the change during bone metastasis. However, it should be noted that our model does not take the early phases of bone metastases, such as local invasion, intravasation, dissemination via

circulation, and extravasation into consideration. Thus, our data suggest that Wnt/β-catenin pathway regulates osteogenesis at secondary bone site.

- In this dissertation, we observed enhanced drug resistance to paclitaxel at the bone metastasis site as compared to the cells not at the bone site. Our results showed that breast cancer cells grown at 3D metastatic bone site not only require higher drug concentrations than 2D cultures to achieve a comparable reduction in cell viability but also exhibited increased resistance to apoptosis in response to paclitaxel. Upon exploring the underlying mechanism of drug resistance, we noticed that elevated levels of IL-6 secretion in the breast cancer culture at 3D metastatic bone site activated STAT3 signaling, which inhibited apoptosis by upregulating expression of anti-apoptotic Bcl-2 along with a substantial reduction in expression of tumor suppressor gene p53 and upregulated expression of multidrug resistance-related genes (MRP1, ABCG2) rendering cancer cells grown in 3D cultures drug-resistant. Taken together, our data demonstrate that the 3D bone-mimetic nanoclay scaffolds-based *in vitro* tumor model is a promising testbed for screening new therapeutics for breast cancer bone metastasis. Also, our results indicate that the bone interface at metastasis of breast cancer modulates drug resistance in breast cancer cells.
- In this dissertation, we reported the evolution of nanomechanical properties of breast cancer cells at metastases using quasi-static and dynamic nanoindentation methods. We found that scaffolds-grown MCF-7 cells exhibited dramatic changes in elastic modulus and demonstrated liquid-like behavior over time compared to MCF-7 as received cells. In contrast, scaffolds-grown MM 231 cells neither showed significant differences in elastic modulus nor exhibited liquid-like behavior over time as

compared to as-received MM 231 cells. Scaffolds-grown MCF-7 cells were softer and had a larger loss tangent (a measure of liquid-like behavior) than as-received MCF-7 cells, whereas elastic moduli and loss tangent values were similar for as-received and scaffolds-grown MM 231 cells. From immunofluorescence and gene expression analysis results, we observed that the significant reduction in elastic modulus together with increased liquid-like behavior of scaffolds-derived MCF-7 cells compared to MCF-7 as received cells, was induced by depolymerization and reorganization of F-actin to the adherens junctions. In contrast, scaffolds-derived MM 231 cells showed insignificant changes in F-actin reorganization over time, as opposed to their as-received counterparts. The significant reduction of F-actin during progression of metastasis in MCF-7 cells at bone indicates a critical role of the highly viscoelastic cytoplasm in MCF-7, leading to overall increase in loss tangent. The MM-231 cell line does not exhibit this behavior. It is interesting to note that the pathogenesis of the two cell cells is quite different clinically and here we demonstrate the use of a bone scaffold testbed to create metastasis that can be captured through nanomechanical evolution. Collectively, our data indicate that the nanomechanical properties of breast cancer cells could be used as a possible biomarker of breast cancer progression at metastases.

- In this dissertation, we used FT-IR spectroscopy to identify spectral biomarkers of cancer progression on 3D *in vitro* model of breast cancer bone metastasis. Results demonstrate absorption bands in IR spectra of control monoculture and sequential culture of cancer cells all received contributions from proteins, lipids, and nucleic acids. Selected intensity ratios from the lipid region as well as the fingerprint region

showed significant differences between monoculture and sequential cultures. Significant changes were observed in the spectral correlations in the metastasis to bone by use of MCF-7 and MDA-MB-231 cell lines, indicating that the proposed spectroscopy method can be useful in capturing prognosis of nature of cancer progression. Combining intensity ratios in FT-IR spectroscopy with principal component analysis provided a method for monitoring of cancer progression on 3D *in vitro* model. This method provides an understanding of the molecular composition of different IR absorption regions and could serve as a useful non-invasive and cost-effective tool in the clinical diagnosis of breast cancer bone metastasis.

- In this dissertation, we employed Raman spectroscopy to classify 3D *in vitro* prostate cancer bone metastasis model and to discriminate between MDA-PCa-2b prostate cancer cells at different stages of tumorigenesis. Our results show that lipid, aromatic amino acid, and extracellular matrix components are involved in the staging of prostate cancer at the secondary bone site. Raman spectroscopic properties of prostate cancer metastasized at bone tissue can be effectively translated into a great wealth of diagnostic information providing new insights into biochemical and architectural changes of prostate cancer cells undergoing different stages to tumorigenesis. Our methods suggest that the incorporation of Raman spectroscopy and statistical techniques, such as PCA, makes the classification of cancer progression straightforward.

CHAPTER 9. FUTURE DIRECTIONS

In this study, we report the development of a biologically relevant, 3D tissue-engineered breast cancer model for studying bone metastasis using nanoclay based scaffolds. This study provides a lot of new insight into the crosstalk between bone and metastatic breast cancer cells. Based on the understanding gained about the interactions between breast cancer cells and bone microenvironment during this work, the following suggestions can be made for future research.

- In this dissertation, we have reported the mimicking the last stage of breast cancer bone metastasis. Further experiments need to be carried out to verify the suitability of our model for studying initial stages in metastatic progression, i.e., cellular/tumoral dormancy. Besides, the complexity of our system can be increased by incorporating immunological, hematopoietic, and vascular elements that are known to have critical roles in regulating metastatic progression. Furthermore, incorporation of dynamic fluid flow with the help of a bioreactor would help us understand the role of shear stress on the phenotypic switch of breast cancer cells. Also, usage of patient-derived breast cancer cells in the 3D *in vitro* model might help us to predict possible patient outcomes to specific therapeutics.
- In this dissertation, we showed that osteogenesis in the 3D *in vitro* model of breast cancer bone metastasis is mediated by Wnt/β-catenin signaling pathway. MCF-7 cells secrete ET-1, which promotes osteoblastic differentiation via Wnt/β-catenin signaling and includes bone-forming activity, leading to increased bone formation. Inactivation of Wnt/β-catenin signaling by MM 231 secreted DKK-1 leads to inhibited bone formation through the down-regulation of osteoblast differentiation. Further, 3D *in vitro* model exhibited mixed bone lesions with different cell types, mimicking bone

lesions observed in breast cancer patients. However, it should be noted that our model does not take the early phases of bone metastases, such as local invasion, intravasation, dissemination via circulation, and extravasation into consideration. Thus, our data suggested that the Wnt/β-catenin pathway regulates osteogenesis at the secondary bone site. Further experiments need to be carried out to evaluate whether this pathway also governs in the early phases of breast cancer bone metastasis. Also, this study opens a window for targeting DKK1 and ET-1 as a therapeutic approach for breast cancer mediated bone metastasis. Further studies could be planned to use anti-DKK1 neutralizing antibodies such as BHQ880 (Novartis Pharmaceuticals), and DKN-01 (Leap Therapeutics) to see if they could bring about a change in the outcome of bone metastasis as they are already in use in clinical trials of multiple myeloma and advanced biliary cancer, respectively [1, 2]. The therapeutic strategy for blocking ET-1 has been in use for decades, mainly for pulmonary arterial hypertension (PAH), by targeting ETAR or both ETAR and ETBR with small molecule antagonists, selective peptide agonists/antagonists, and monoclonal antibody antagonists [3]. Blocking ET-1 has also been effective in various cancers. Therefore, blocking ET-1 using strategies mentioned above could have potential as a therapeutic approach for bone metastasis.

- In this dissertation, our results showed that breast cancer cells grown in 3D metastatic bone site exhibited altered physiological and biochemical properties including increased drug resistance, inhibited rate of apoptosis, enhanced expression of multidrug resistance-related genes, and elevated levels of cytokine IL-6 and its downstream effectors (STAT3) associated with drug resistance, as opposed to 2D

monolayer cultures. Most importantly, STAT3, a potential biomarker for chemoresistance in many cancers, was activated in our 3D breast cancer bone metastasis model. Further studies need to be carried out by blocking either IL-6 or STAT3 by anti-IL-6 mAb and Stattic, a small-molecule inhibitor of STAT3 activation and dimerization, respectively [4].

- In this dissertation, we have investigated the nanomechanical properties of breast cancer cells during the disease progression at the secondary metastatic site using the 3D *in vitro* model that we have developed. We have shown that breast cells become softer with the disease progression at the bone microenvironment due to F-actin reorganization during establishment of cell-cell adhesion between adjacent cells. Therefore, further studies need to be carried out using both experimental and modeling approaches to investigate deformation behavior of F-actin at phases of organization. Katti et al. showed the influence of the various cellular components on mechanical behavior cells with the help of computational models [5]. Furthermore, methods described in the dissertation could be translated into clinical studies in the form of elastography. Elastography is a non-invasive medical imaging technique that maps the stiffness and elastic properties of a tissue. It uses low frequency vibration during ultrasound or magnetic resonance imaging (MRI) to measure stiffness of organs inside the body.
- In this dissertation, we evaluated the feasibility of vibrational spectroscopy approaches such IR and Raman spectroscopy as diagnostic tools for bone metastasis of breast and prostate cancer, respectively. FTIR-based method provided an understanding of the molecular composition of different IR absorption regions and

could serve as a useful non-invasive and cost-effective tool in the clinical diagnosis of breast cancer bone metastasis. Raman spectroscopic properties of prostate cancer metastasized at bone tissue can be effectively translated into a great wealth of diagnostic information providing new insights into biochemical and architectural changes of prostate cancer cells undergoing different stages of tumorigenesis. Also, from the point of clinical applications, hand-held Raman imaging of tissues for diagnostics at the patient level would be very valuable. Fiber-optic probes for *in vivo* diagnostics by IR and Raman spectroscopy have been in use as optical tools for guided biopsies, and disease characterization [6, 7]. These methods could be used in conjunction with our spectroscopic markers to develop a robust, specific, and relatively non-invasive technique for early detection of bone metastasis.

9.1. References

[1] S.P. Iyer, J.T. Beck, A.K. Stewart, J. Shah, K.R. Kelly, R. Isaacs, S. Bilic, S. Sen, N.C. Munshi, A Phase IB multicentre dose-determination study of BHQ 880 in combination with anti-myeloma therapy and zoledronic acid in patients with relapsed or refractory multiple myeloma and prior skeletal-related events, British journal of haematology 167(3) (2014) 366-375.

[2] J. Eads, S. Stein, A. El-Khoueiry, G. Manji, T. Abrams, A.A. Khorana, R. Miksad, D. Mahalingam, C. Sirard, A.X. Zhu, Phase I study of DKN-01 (D), an anti-DKK1 monoclonal antibody, in combination with gemcitabine (G) and cisplatin (C) in patients (pts) with advanced biliary cancer (ABC), Annals of Oncology 27(suppl_6) (2016).

[3] A.P. Davenport, R.E. Kuc, C. Southan, J.J. Maguire, New drugs and emerging therapeutic targets in the endothelin signaling pathway and prospects for personalized precision medicine, Physiological research 67 (2018).

[4] D.E. Johnson, R.A. O'Keefe, J.R. Grandis, Targeting the IL-6/JAK/STAT3 signalling axis in cancer, Nature reviews Clinical oncology 15(4) (2018) 234.

[5] D.R. Katti, K.S. Katti, Cancer cell mechanics with altered cytoskeletal behavior and substrate effects: A 3D finite element modeling study, Journal of the mechanical behavior of biomedical materials 76 (2017) 125-134.

[6] C. Krafft, S. Dochow, I. Latka, B. Dietzek, J. Popp, Diagnosis and screening of cancer tissues by fiber-optic probe Raman spectroscopy, Biomedical Spectroscopy and Imaging 1(1) (2012) 39-55.

[7] M.A. Mackanos, C.H. Contag, Fiber-optic probes enable cancer detection with FTIR spectroscopy, Trends in biotechnology 28(6) (2010) 317-323.

APPENDIX

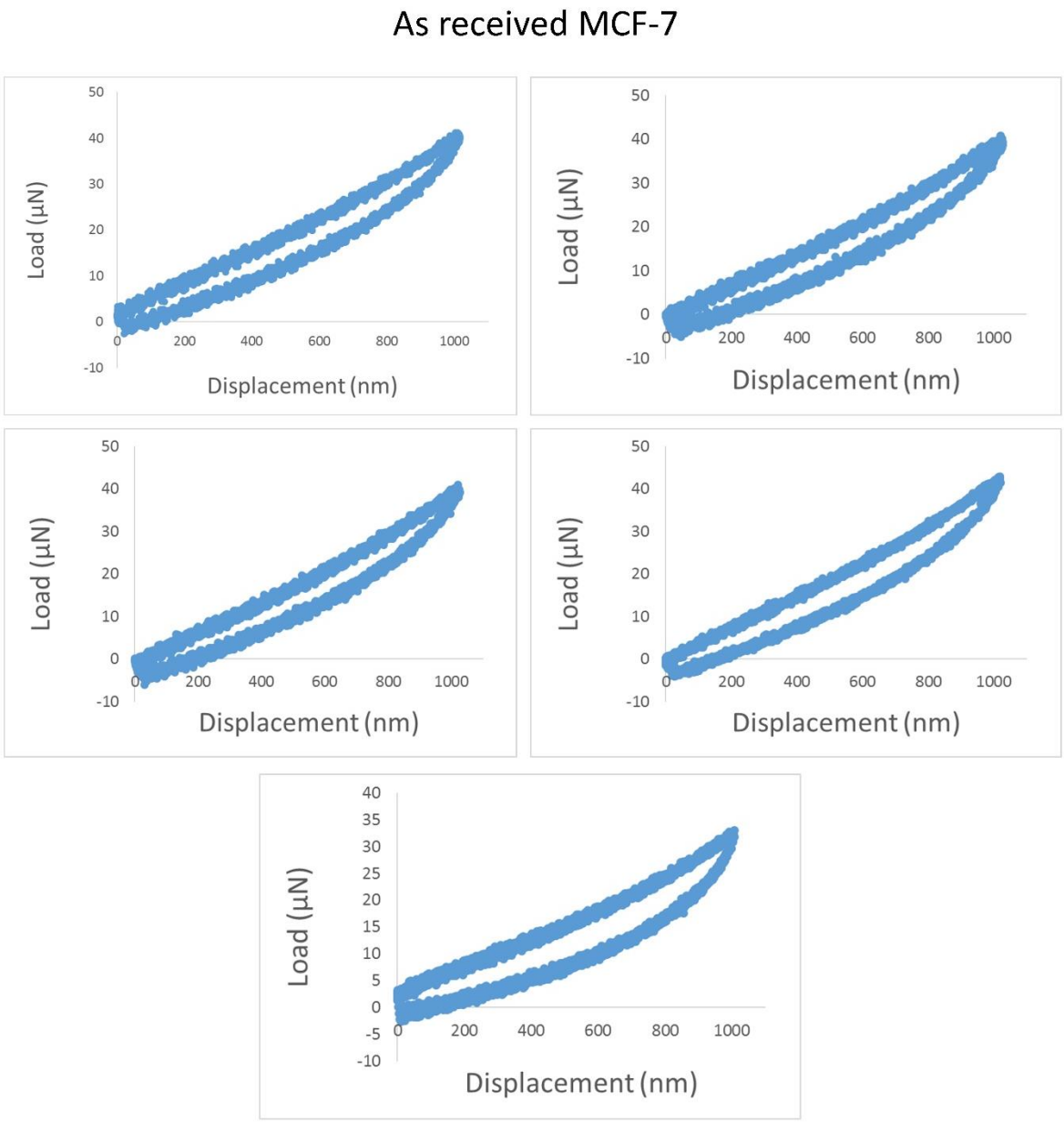

Figure A1. L-D curves of as received MCF-7 cells at maximum displacement of 1000 nm.

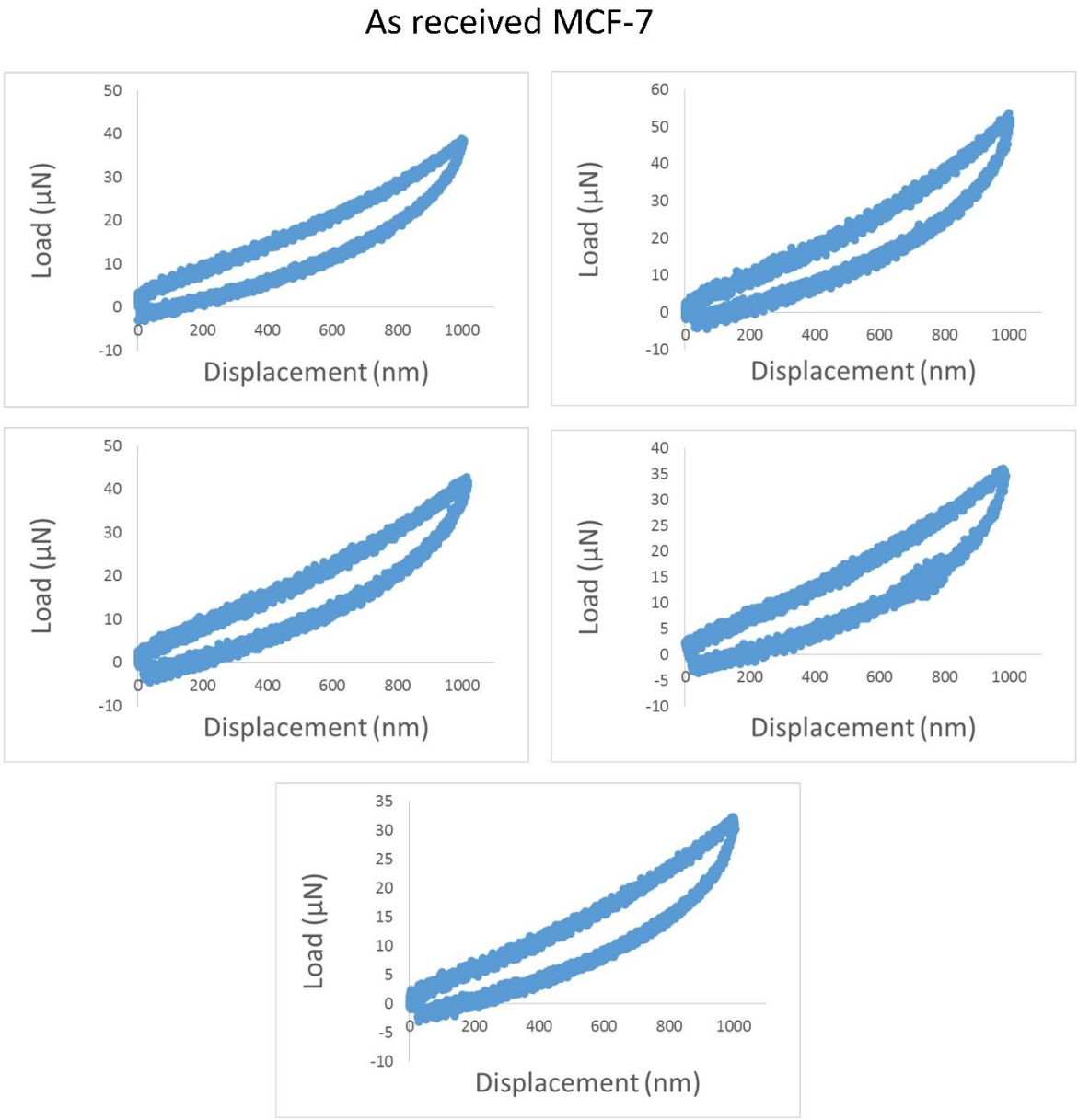

Figure A1. L-D curves of as received MCF-7 cells at maximum displacement of 1000 nm (Continued).

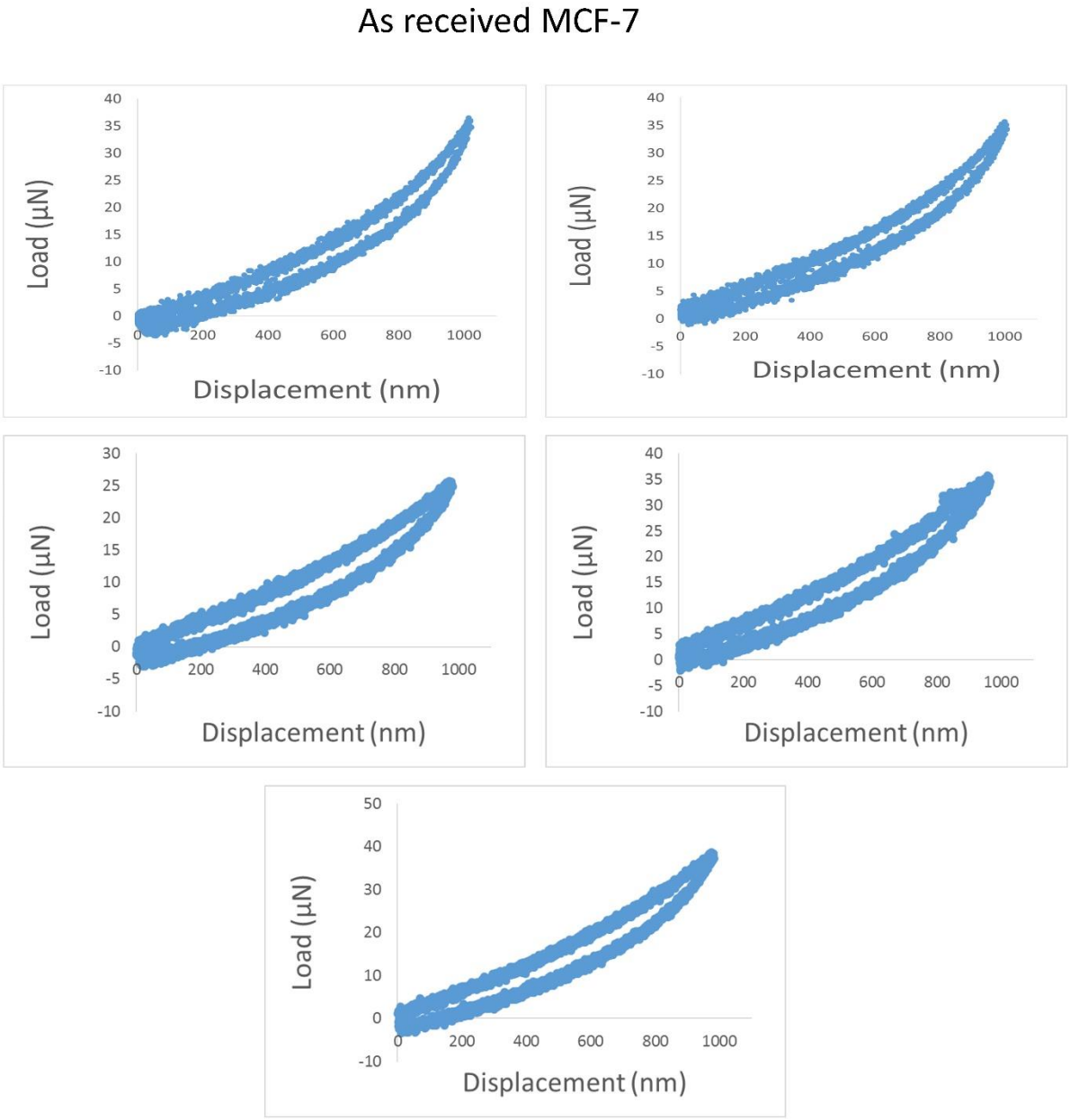

Figure A1. L-D curves of as received MCF-7 cells at maximum displacement of 1000 nm (Continued).

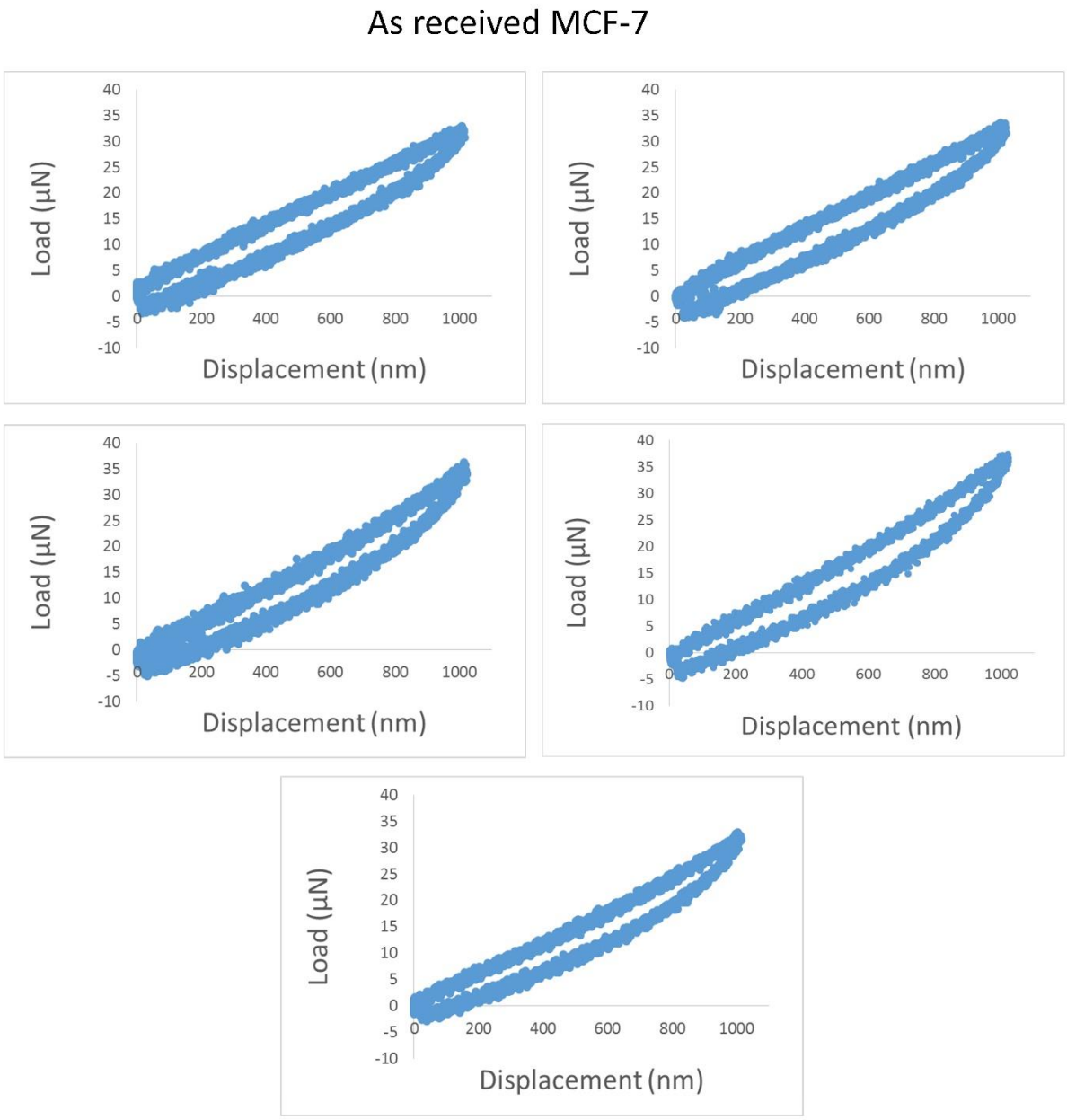

Figure A1. L-D curves of as received MCF-7 cells at maximum displacement of 1000 nm (Continued).

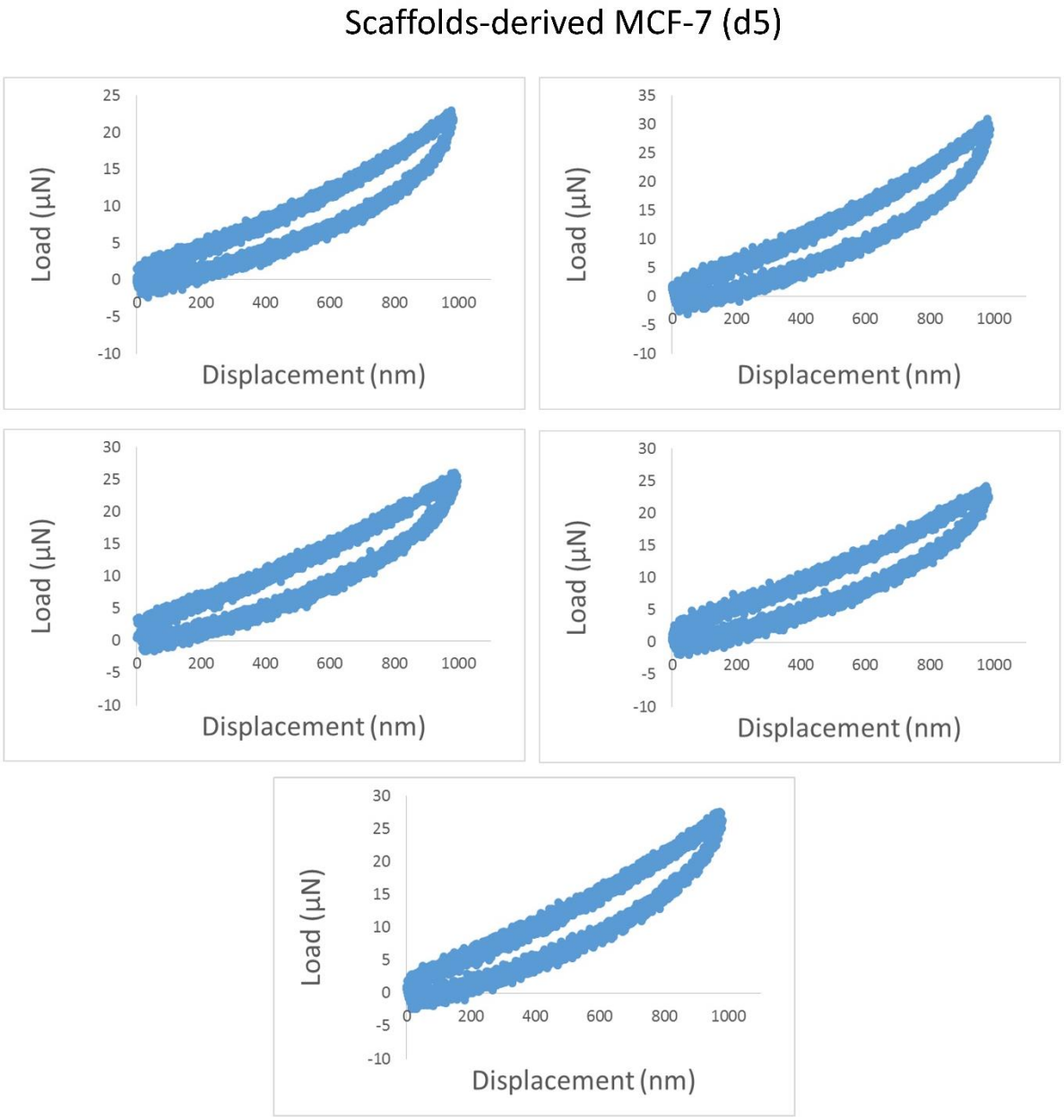

Figure A2. L-D curves of scaffolds-derived MCF-7 cells (d5) at maximum displacement of 1000 nm.

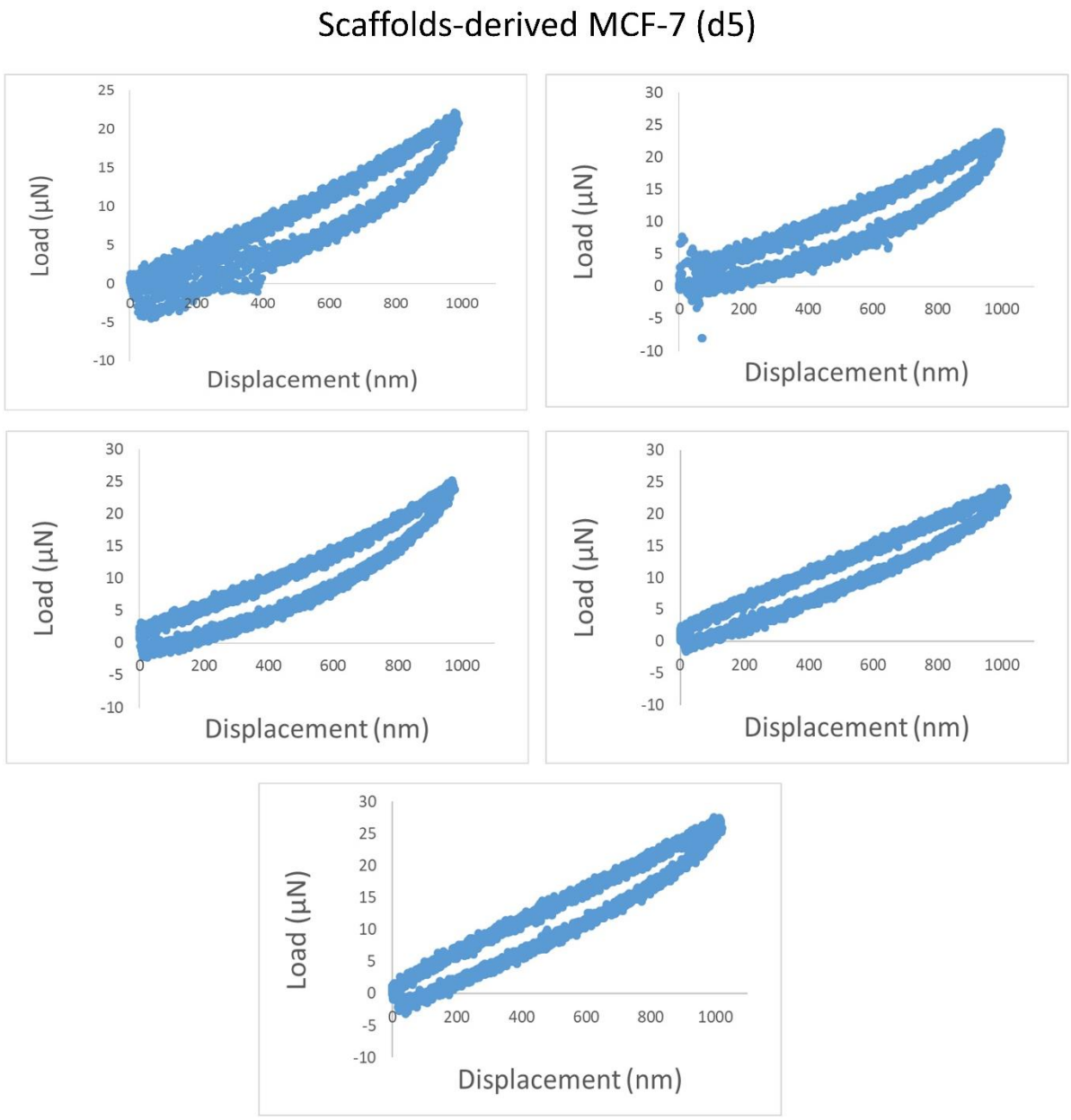

Figure A2. L-D curves of scaffolds-derived MCF-7 cells (d5) at maximum displacement of 1000 nm (Continued).

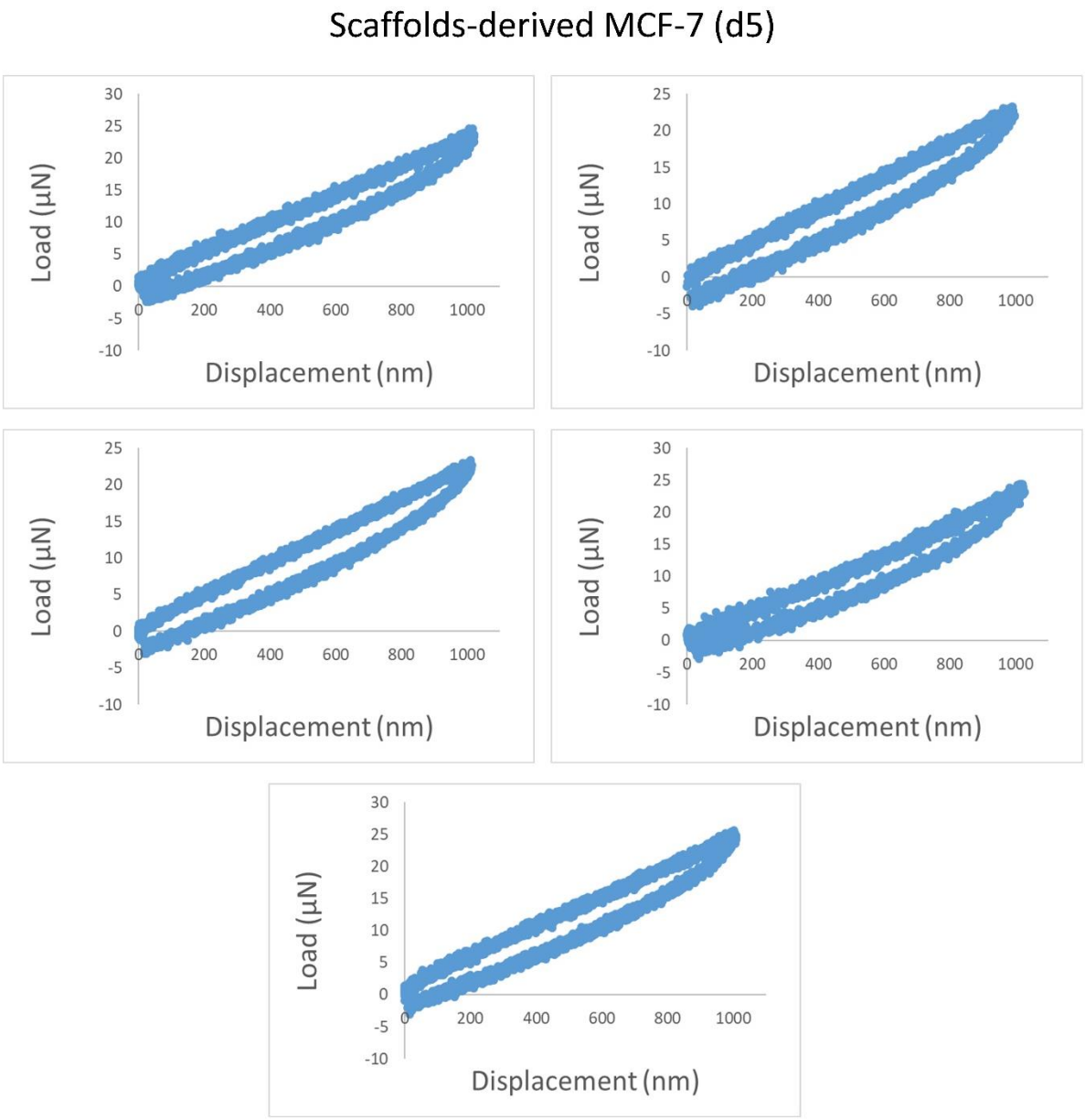

Figure A2. L-D curves of scaffolds-derived MCF-7 cells (d5) at maximum displacement of 1000 nm (Continued).

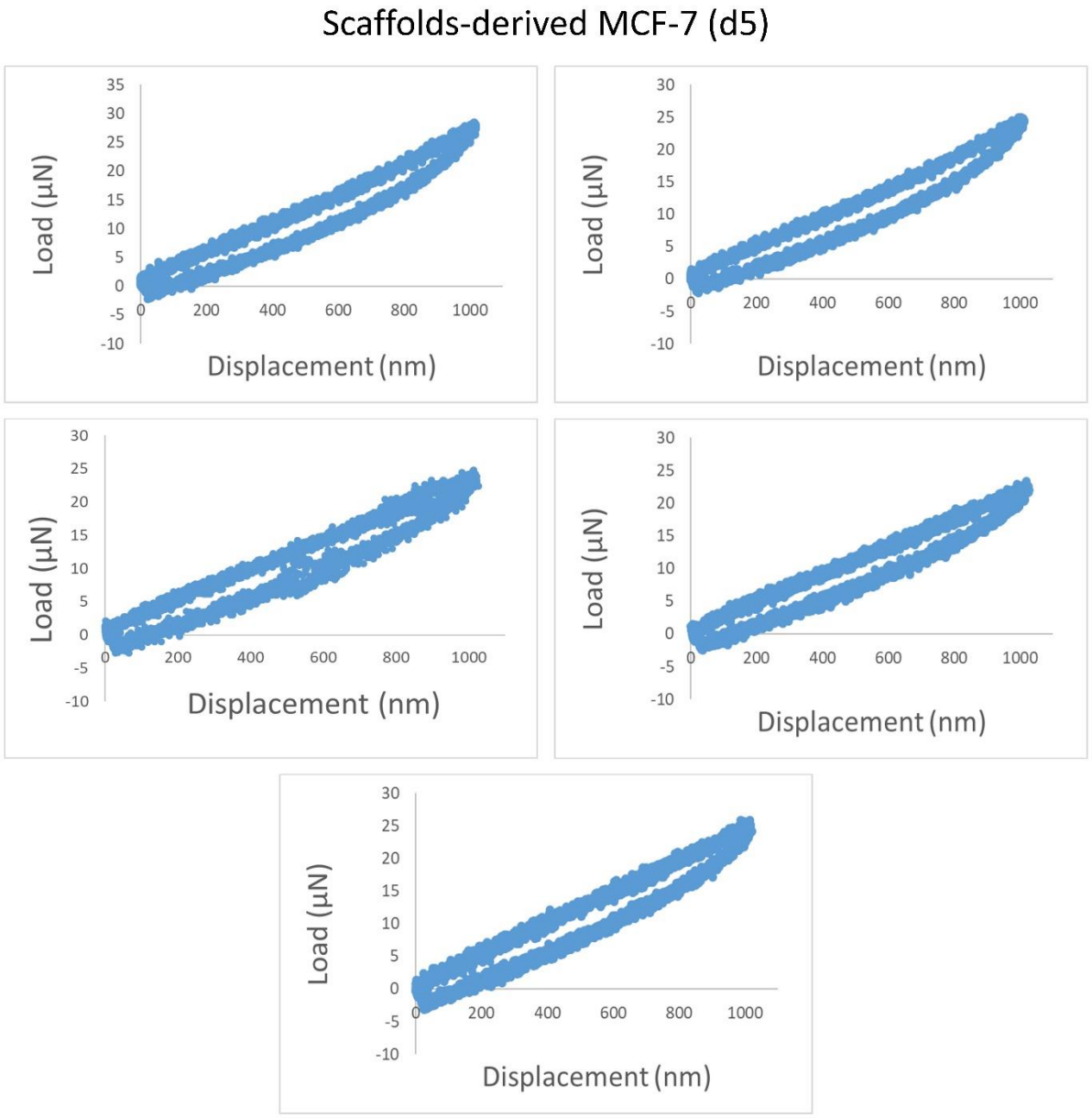

Figure A2. L-D curves of scaffolds-derived MCF-7 cells (d5) at maximum displacement of 1000 nm (Continued).

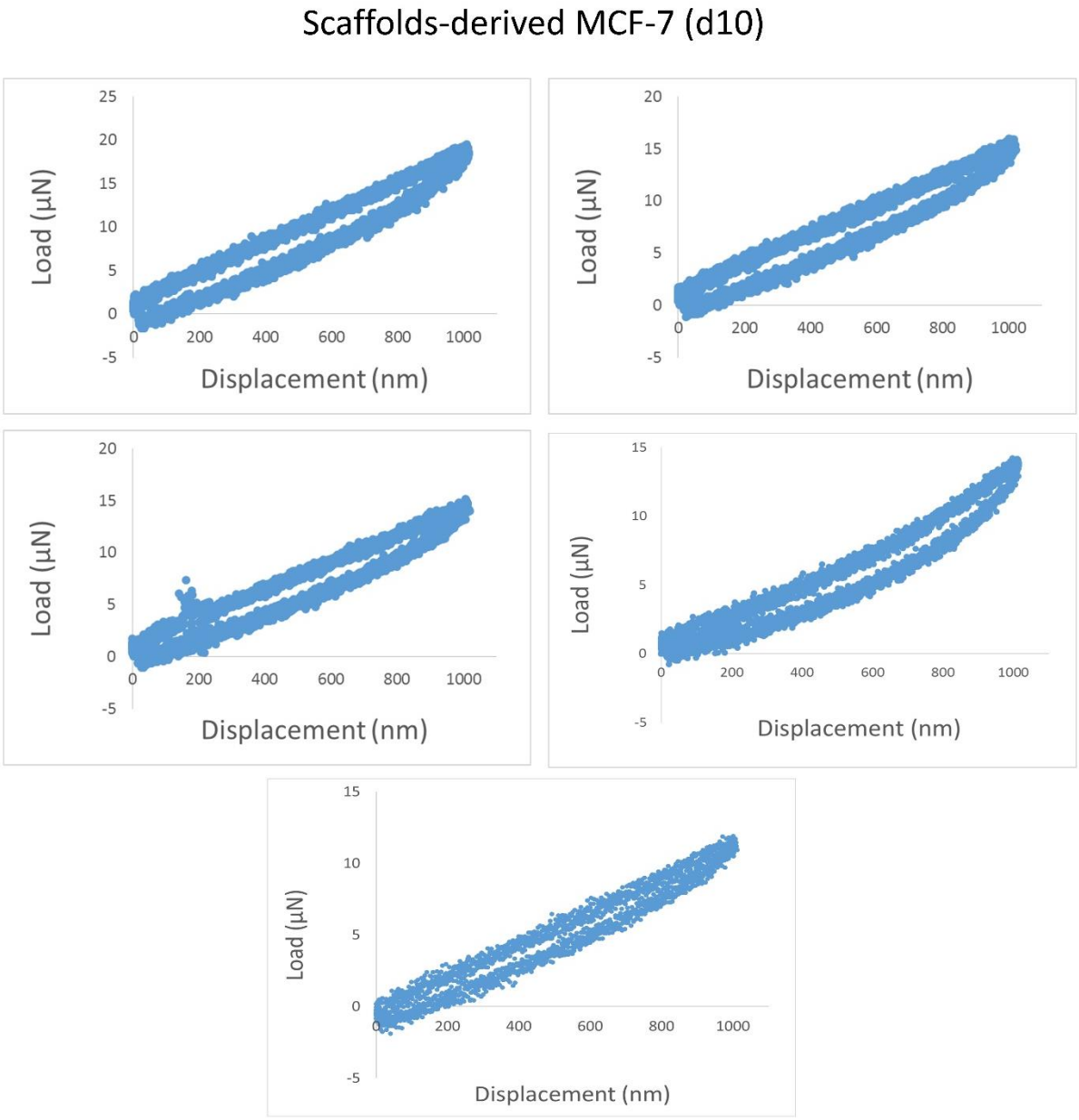

Figure A3. L-D curves of scaffolds-derived MCF-7 cells (d10) at maximum displacement of 1000 nm.

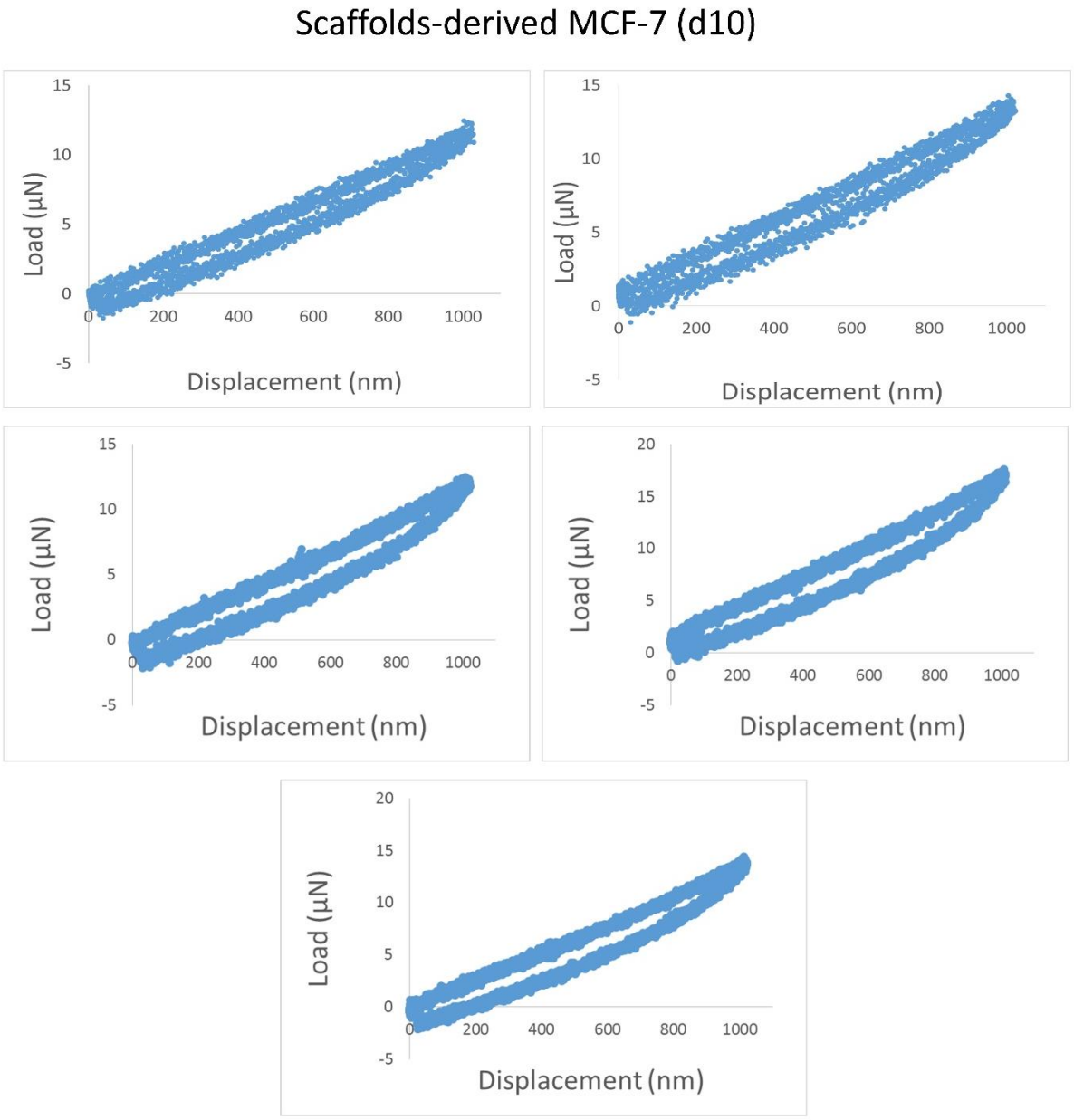

Figure A3. L-D curves of scaffolds-derived MCF-7 cells (d10) at maximum displacement of 1000 nm (Continued).

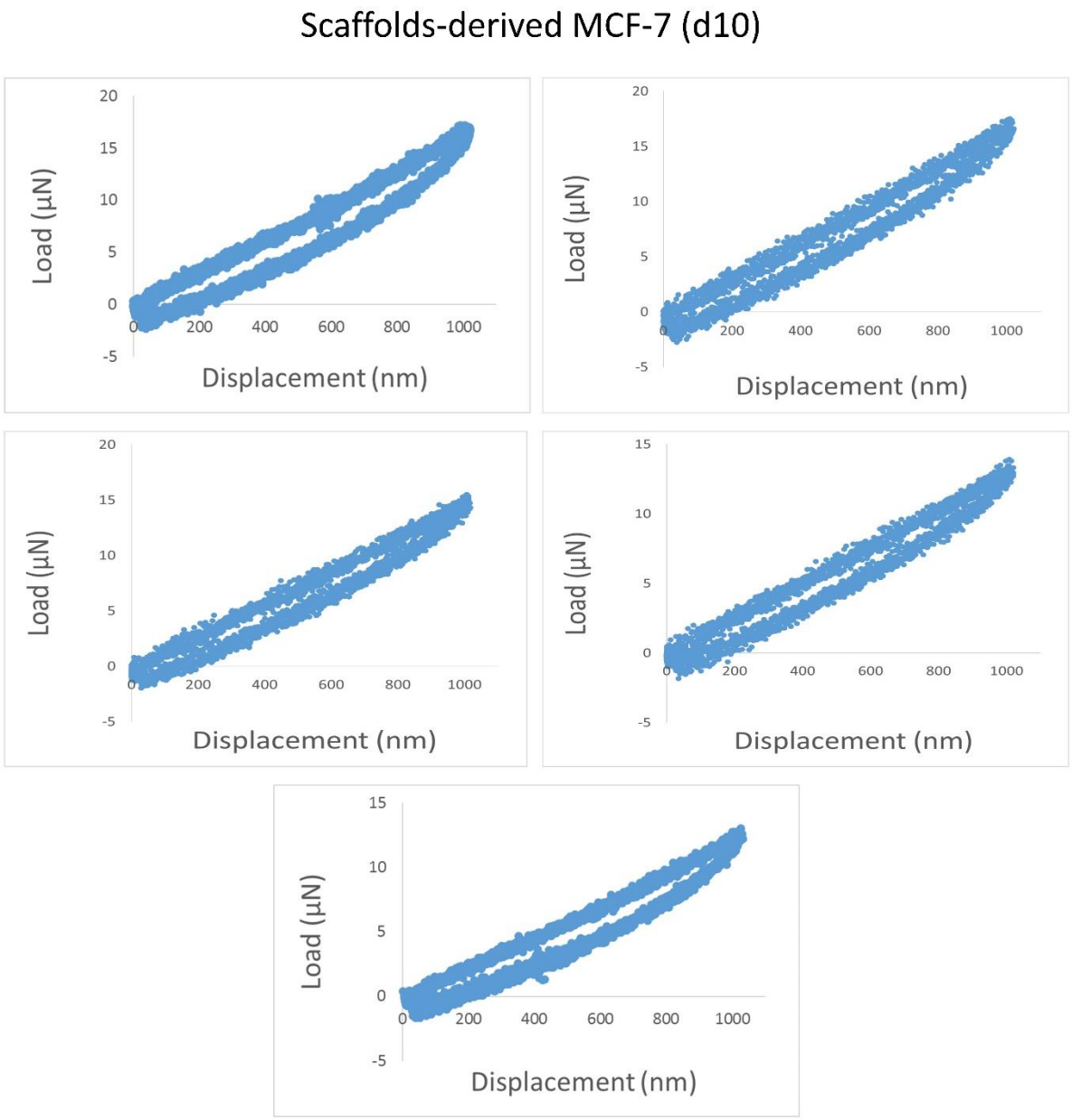

Figure A3. L-D curves of scaffolds-derived MCF-7 cells (d10) at maximum displacement of 1000 nm (Continued).

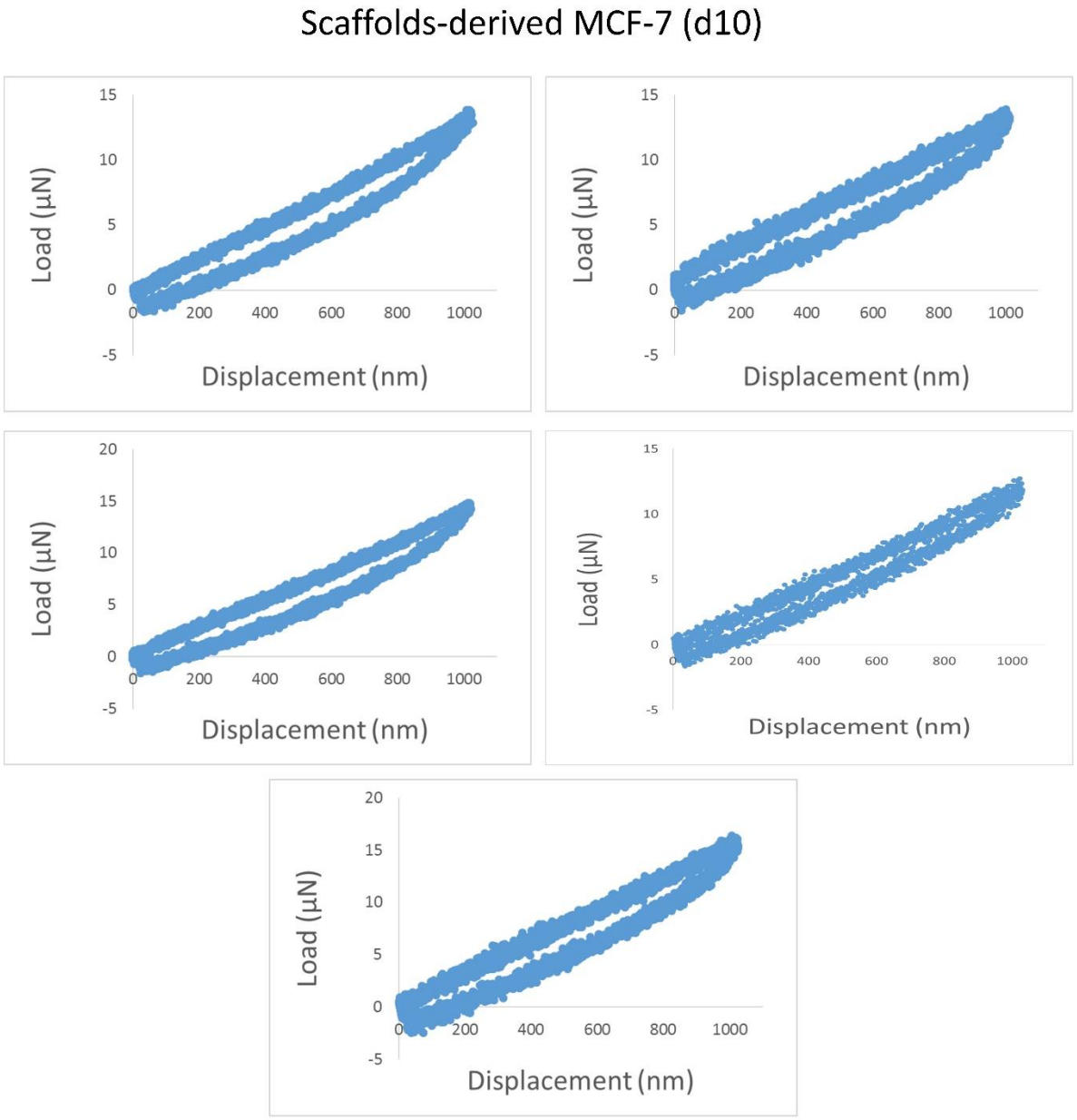

Figure A3. L-D curves of scaffolds-derived MCF-7 cells (d10) at maximum displacement of 1000 nm (Continued).

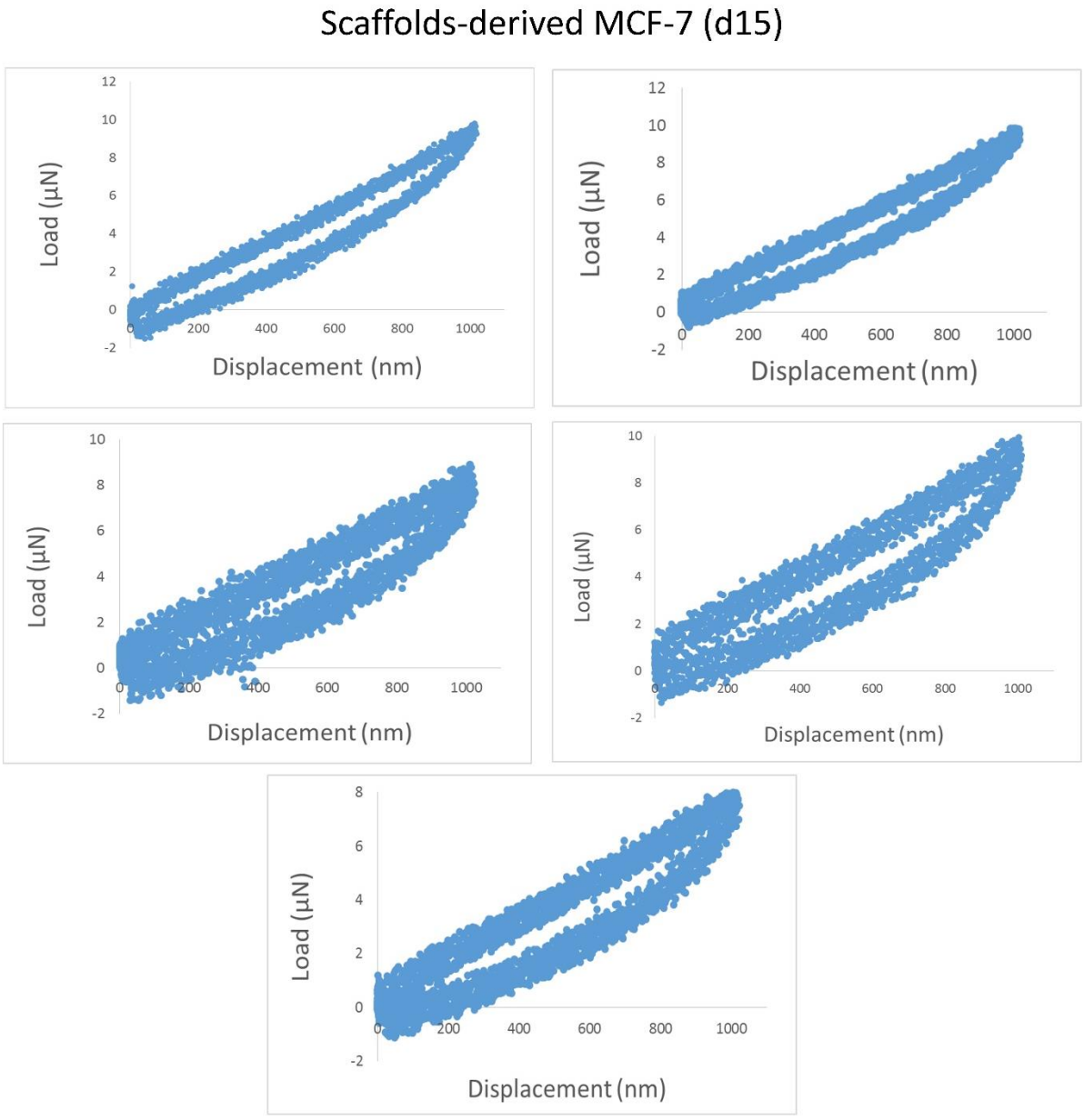

Figure A4. L-D curves of scaffolds-derived MCF-7 cells (d15) at maximum displacement of 1000 nm.

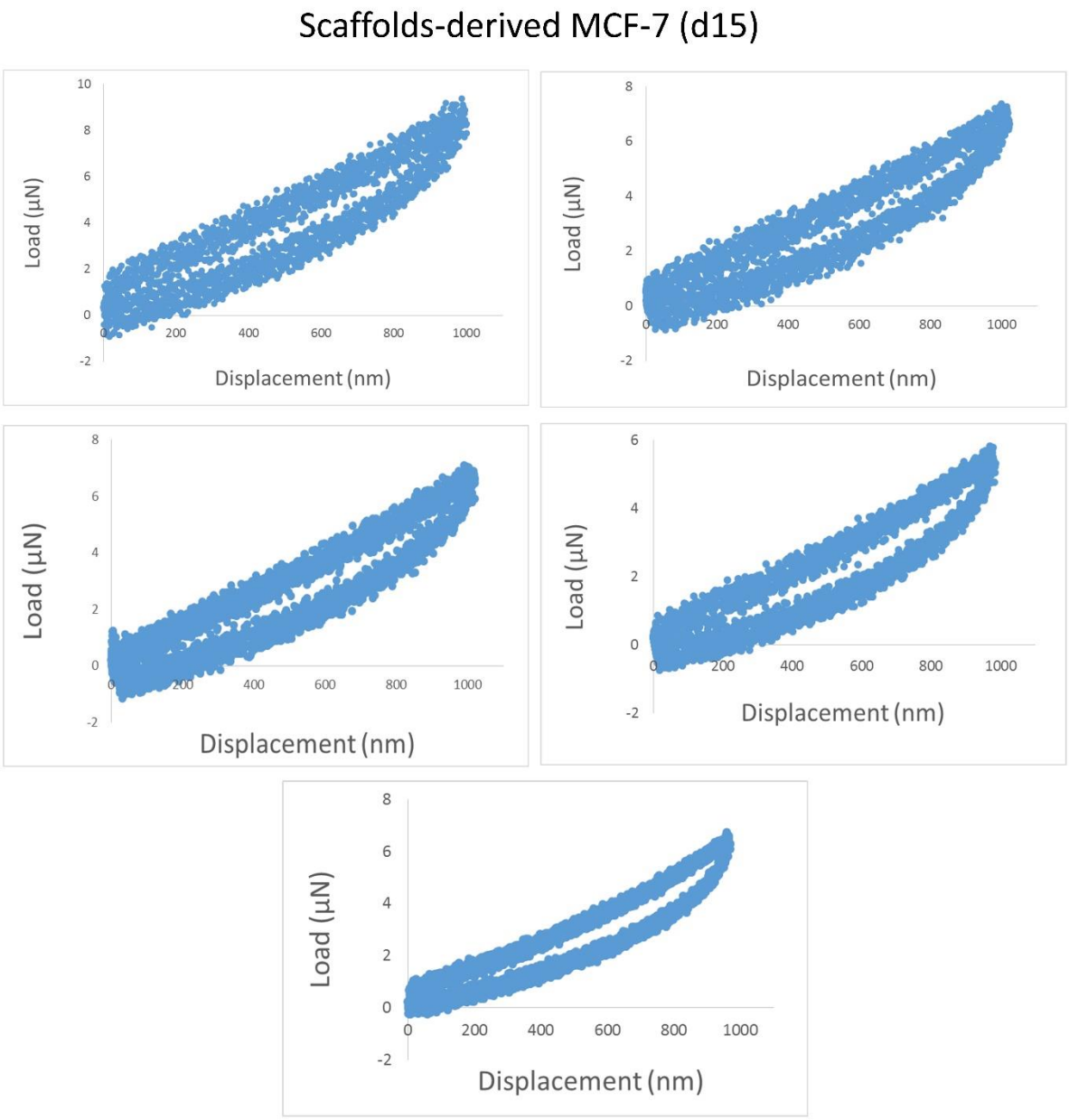

Figure A4. L-D curves of scaffolds-derived MCF-7 cells (d15) at maximum displacement of 1000 nm (Continued).

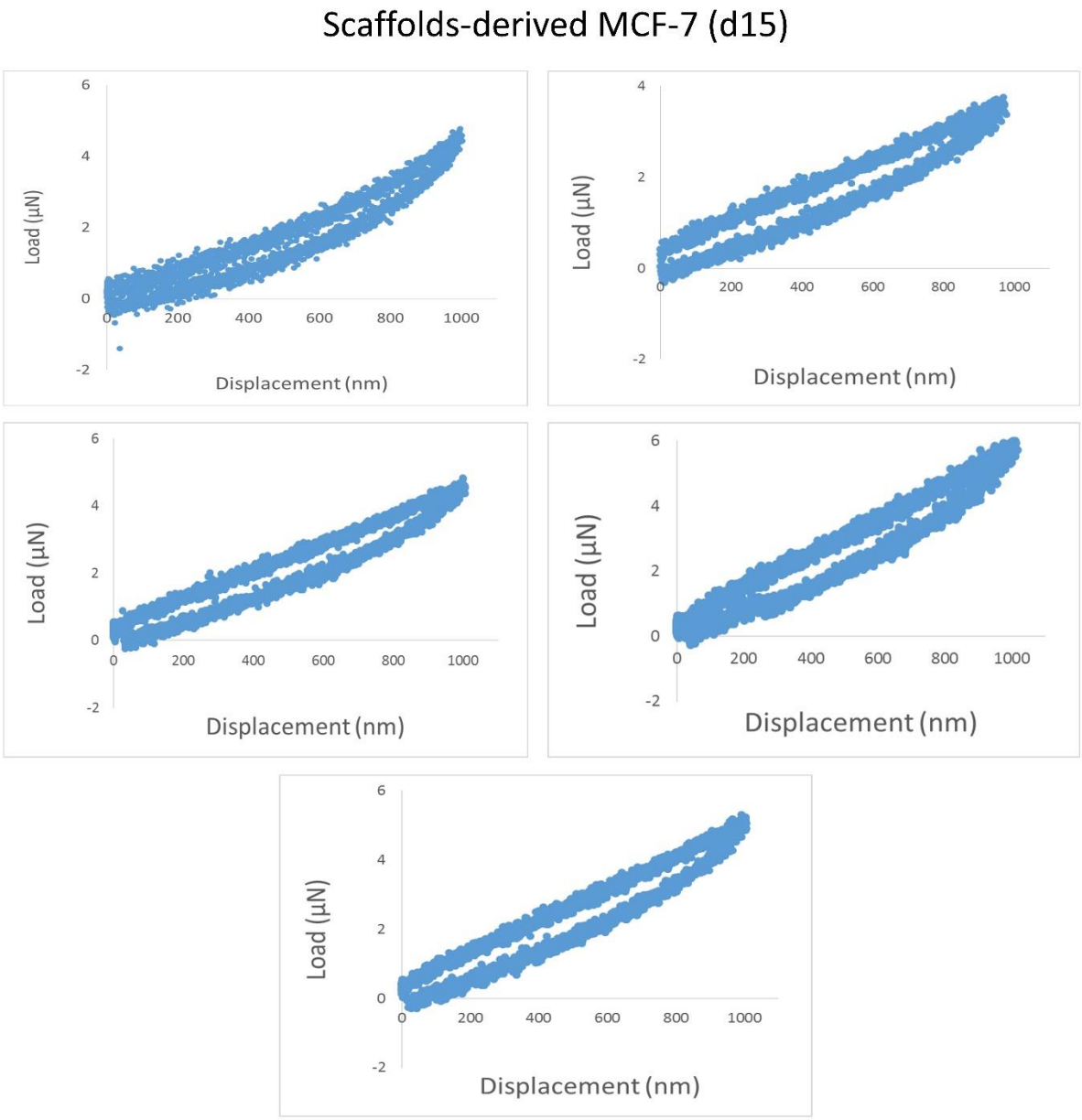

Figure A4. L-D curves of scaffolds-derived MCF-7 cells (d15) at maximum displacement of 1000 nm (Continued).

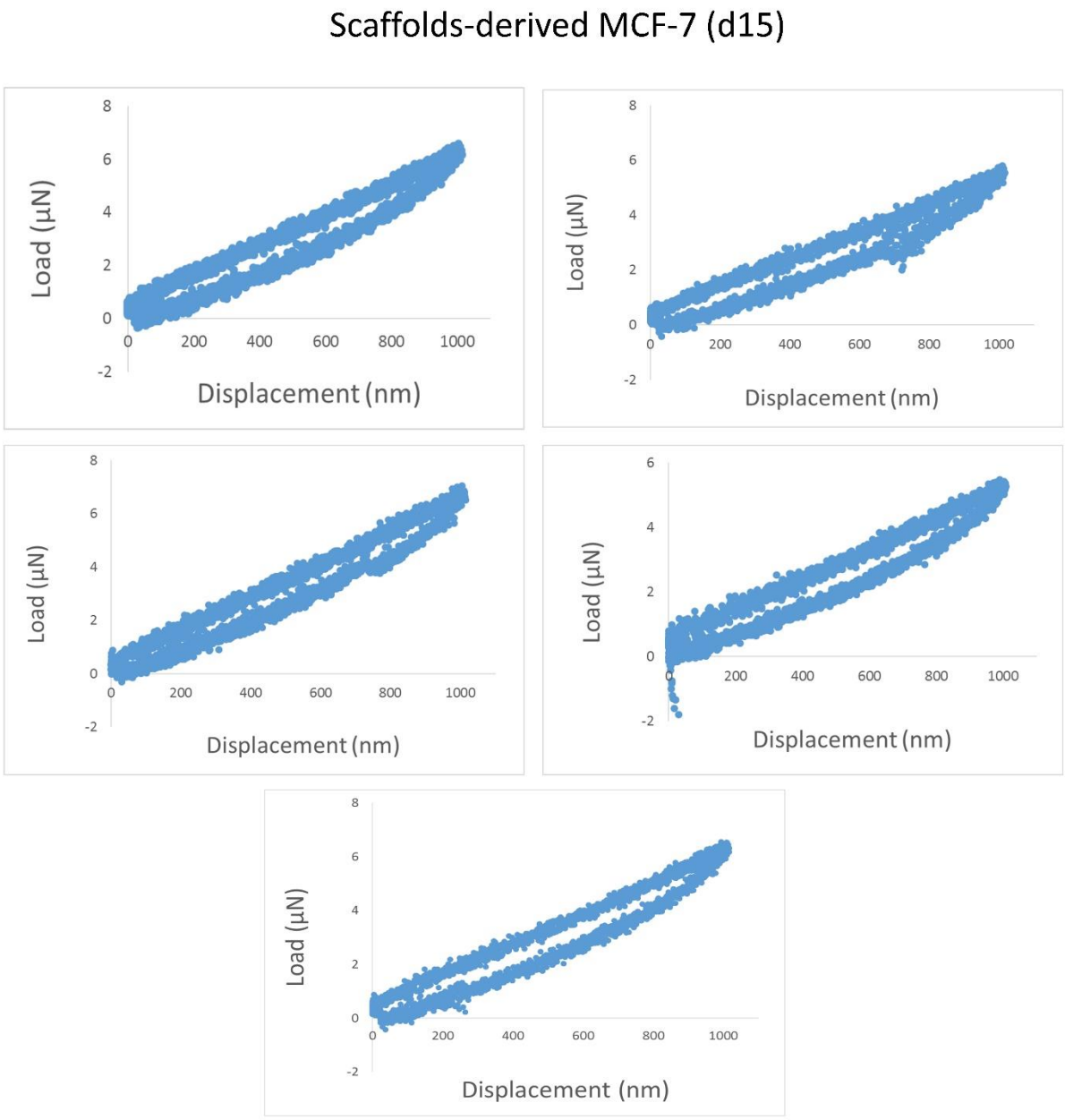

Figure A4. L-D curves of scaffolds-derived MCF-7 cells (d15) at maximum displacement of 1000 nm (Continued).

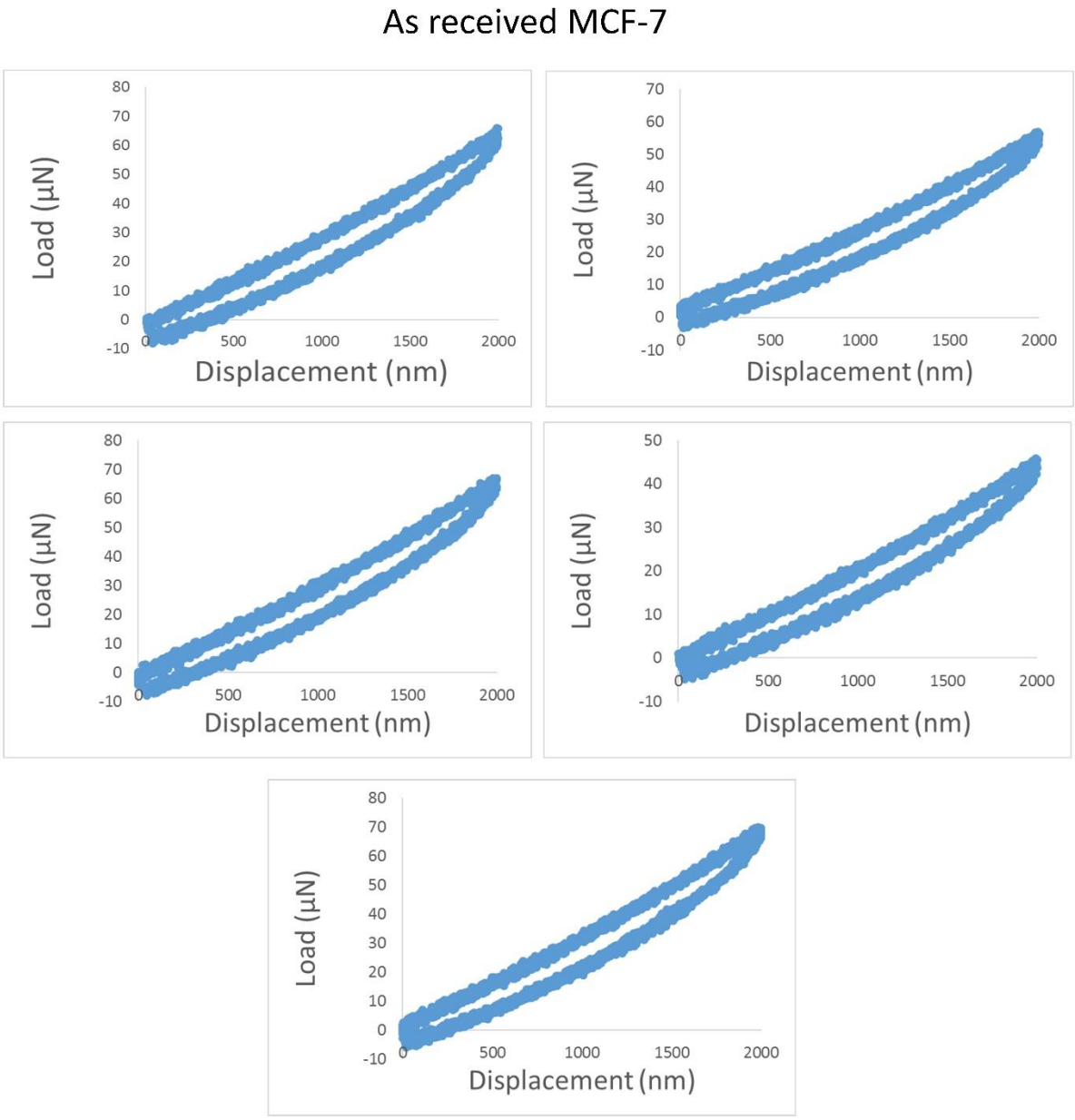

Figure A5. L-D curves of as received MCF-7 cells at maximum displacement of 2000 nm.

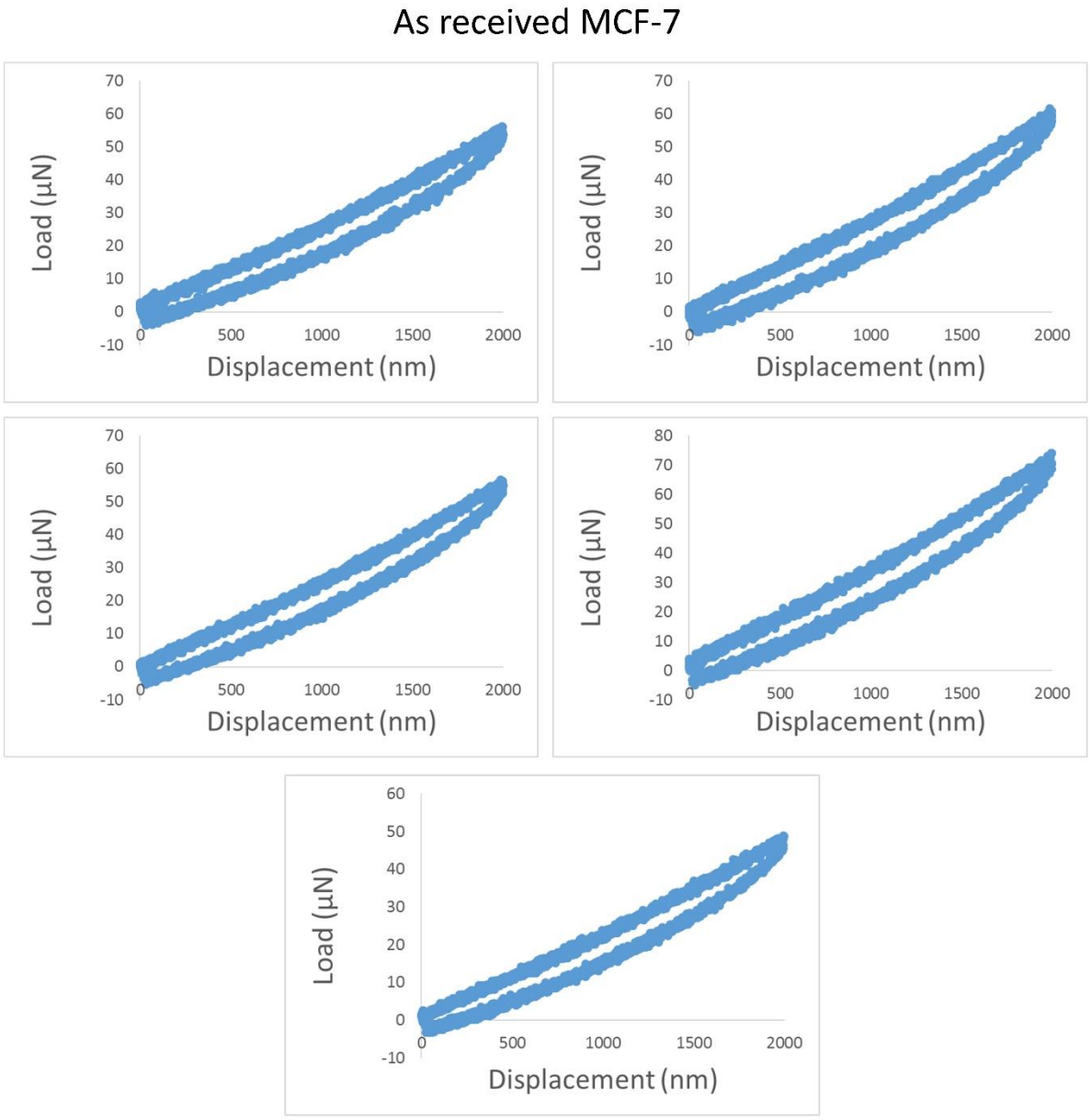

Figure A5. L-D curves of as received MCF-7 cells at maximum displacement of 2000 nm (Continued).

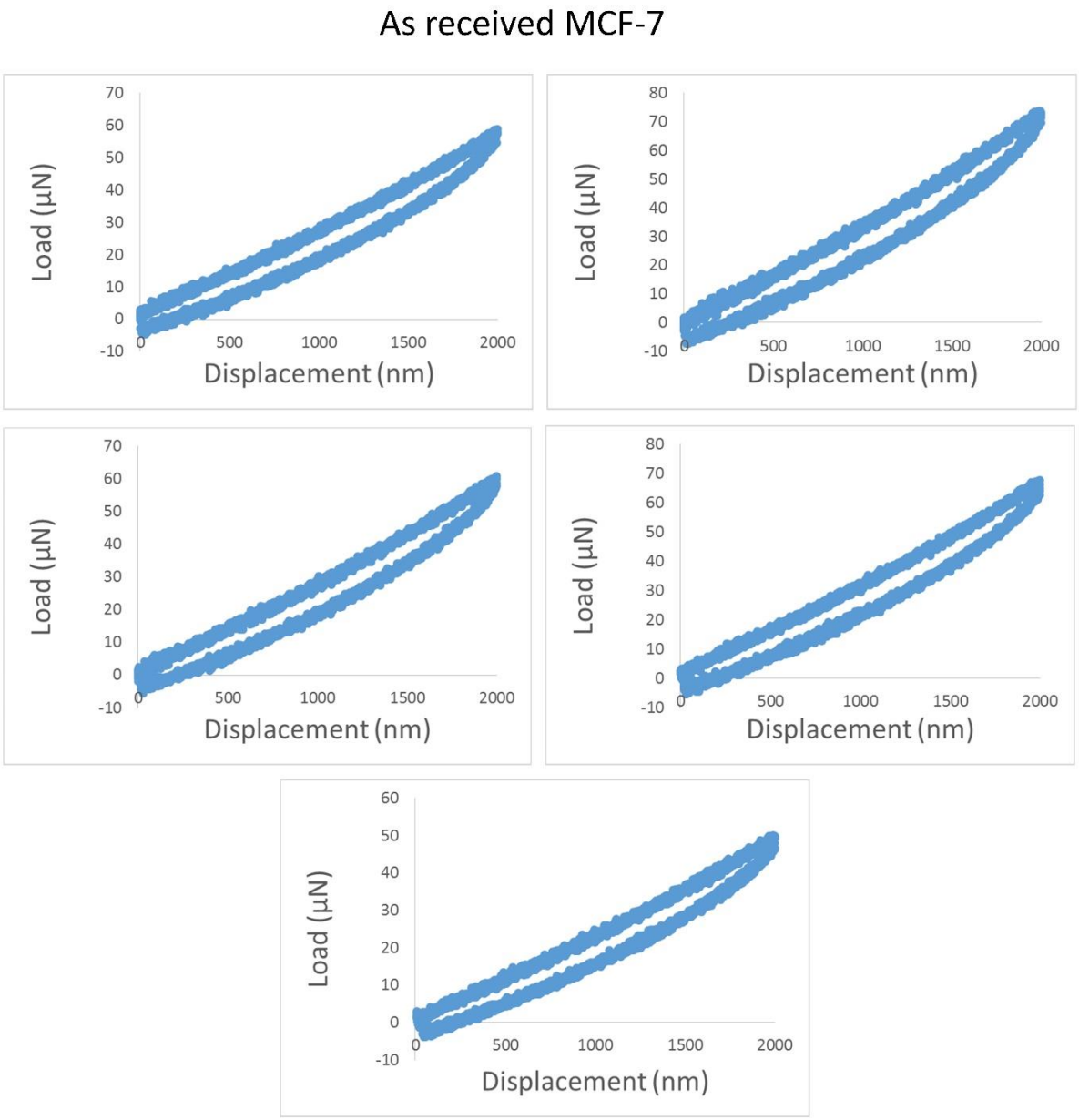

Figure A5. L-D curves of as received MCF-7 cells at maximum displacement of 2000 nm (Continued).

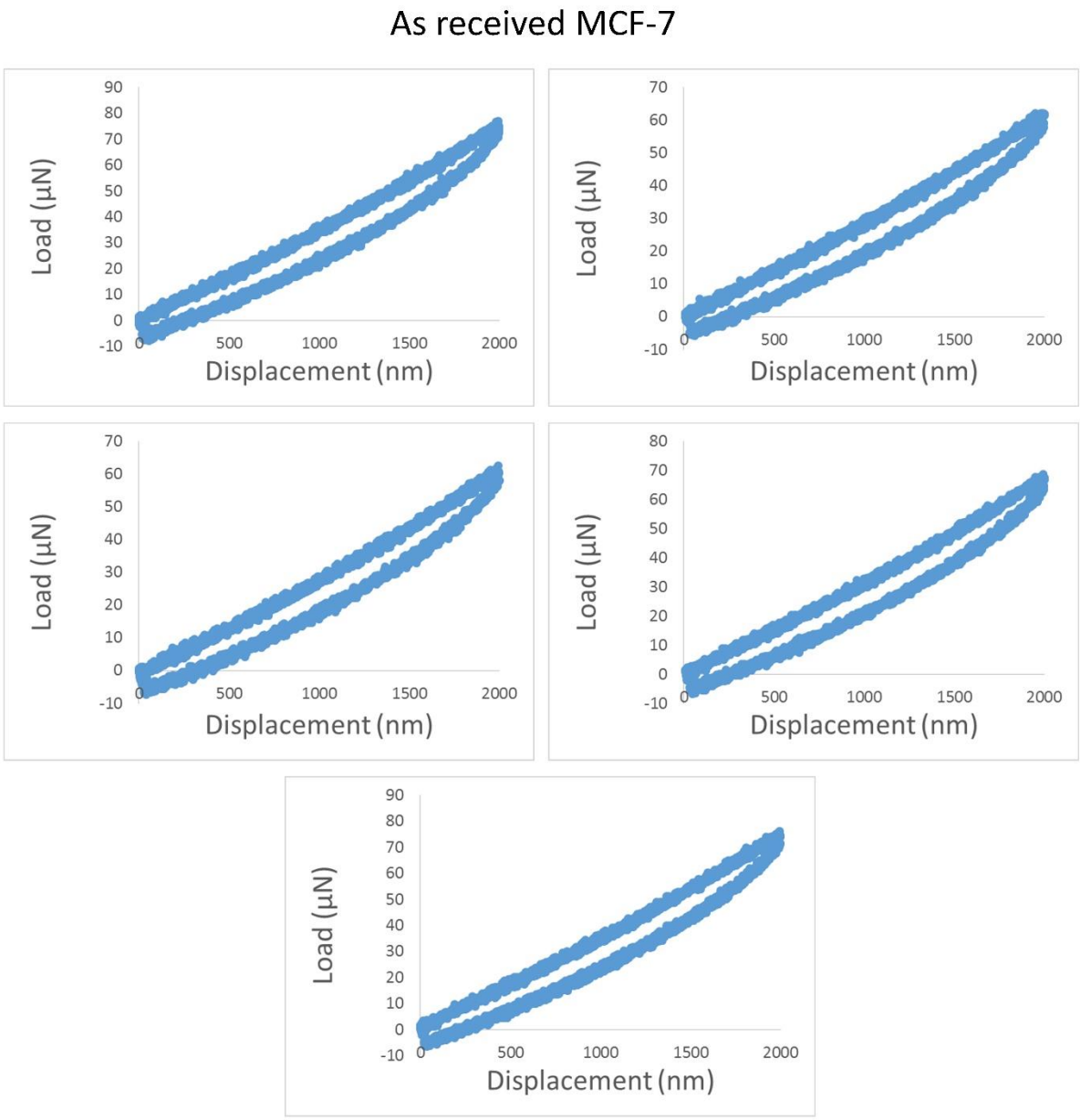

Figure A5. L-D curves of as received MCF-7 cells at maximum displacement of 2000 nm (Continued).

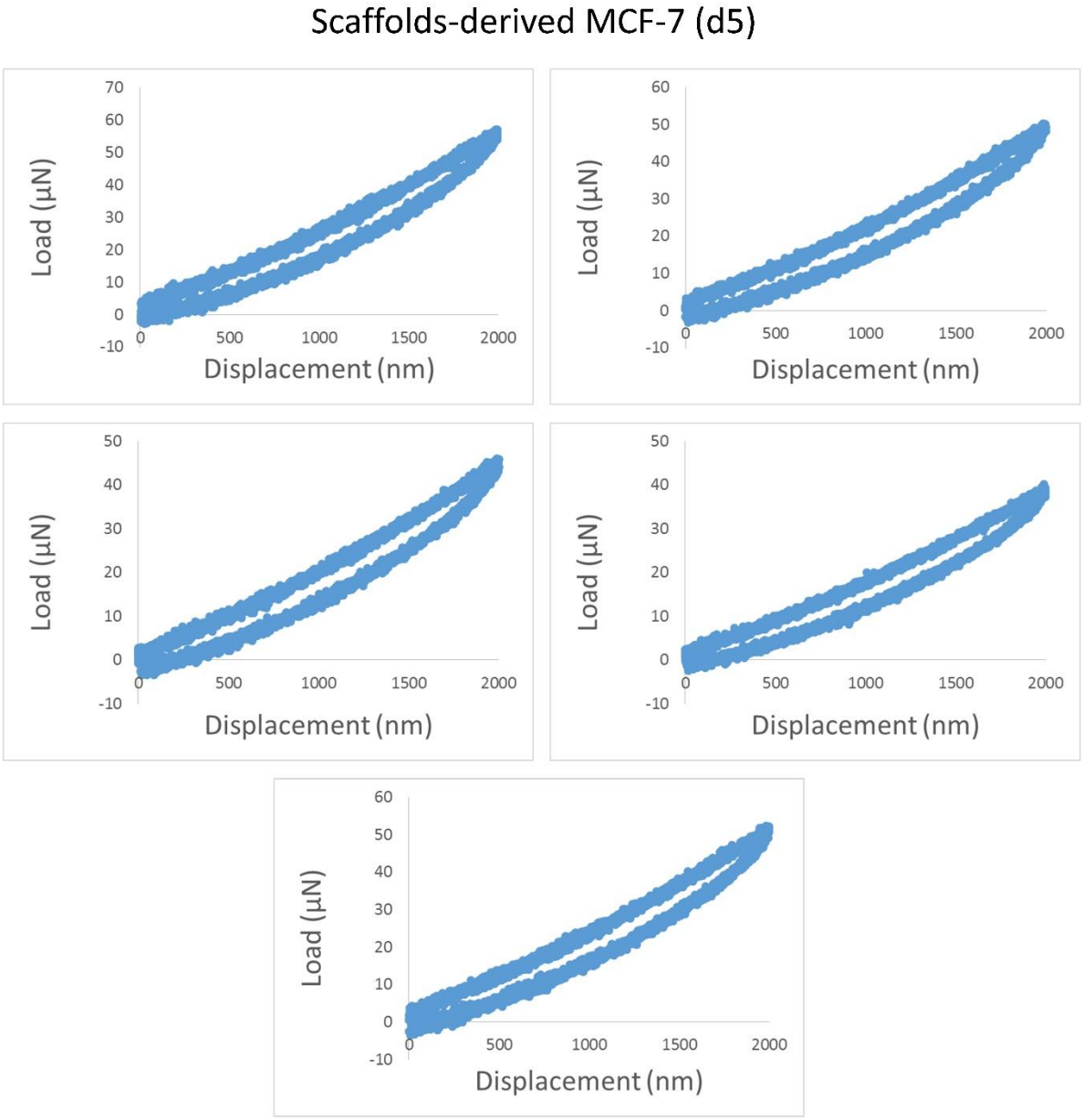

Figure A6. L-D curves of scaffolds-derived MCF-7 cells (d5) at maximum displacement of 2000 nm.

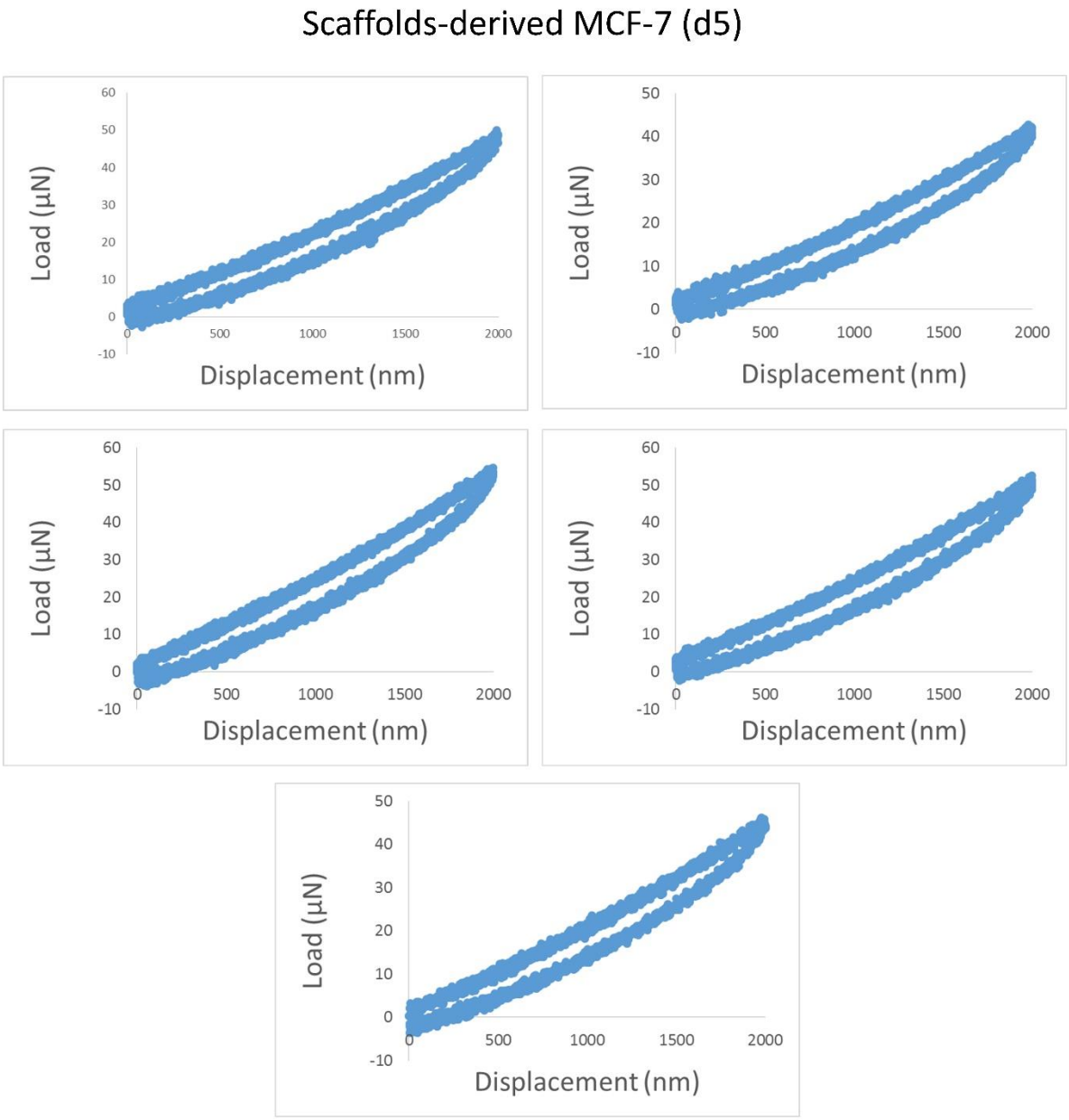

Figure A6. L-D curves of scaffolds-derived MCF-7 cells (d5) at maximum displacement of 2000 nm (Continued).

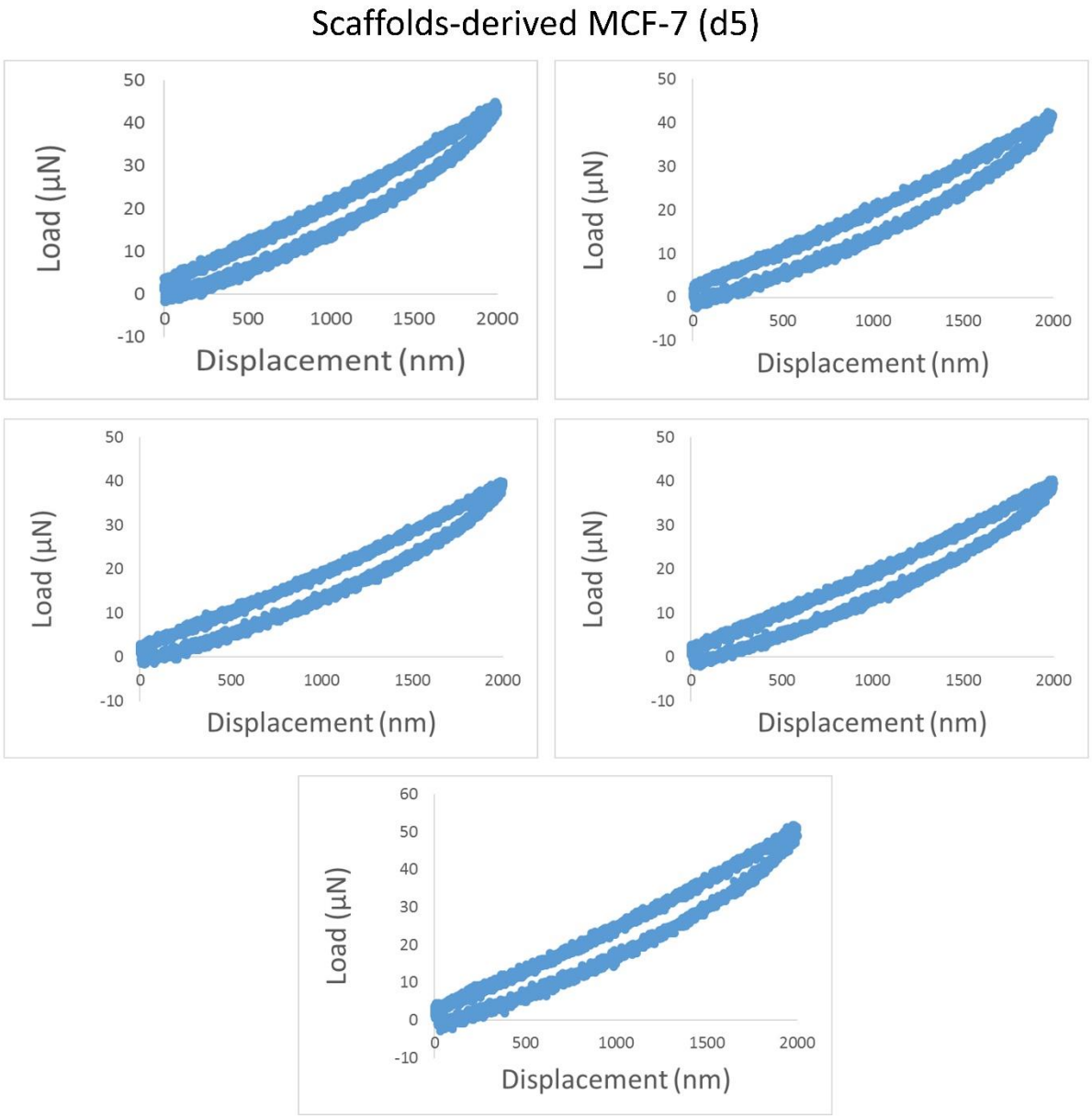

Figure A6. L-D curves of scaffolds-derived MCF-7 cells (d5) at maximum displacement of 2000 nm (Continued).

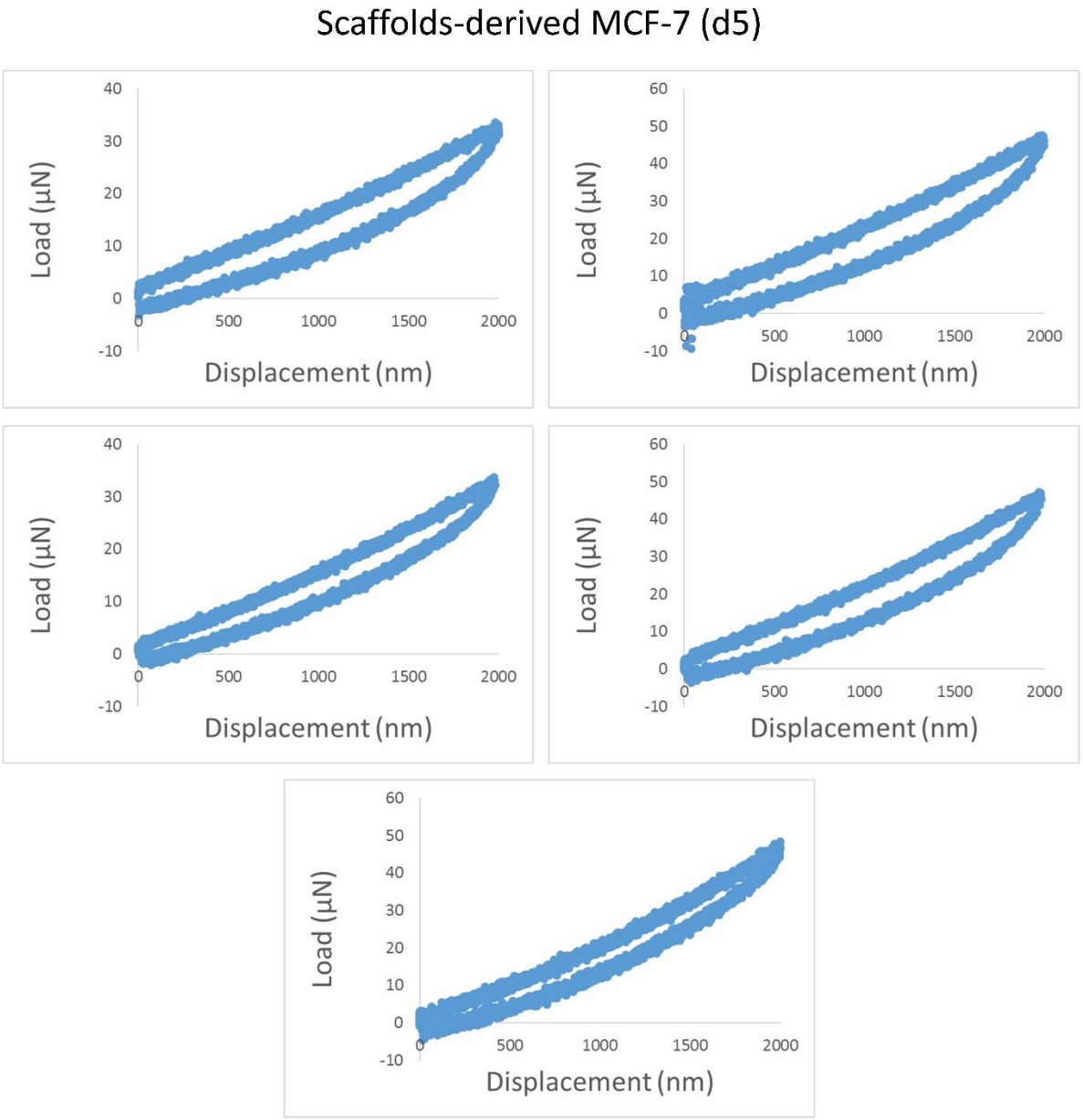

Figure A6. L-D curves of scaffolds-derived MCF-7 cells (d5) at maximum displacement of 2000 nm (Continued).

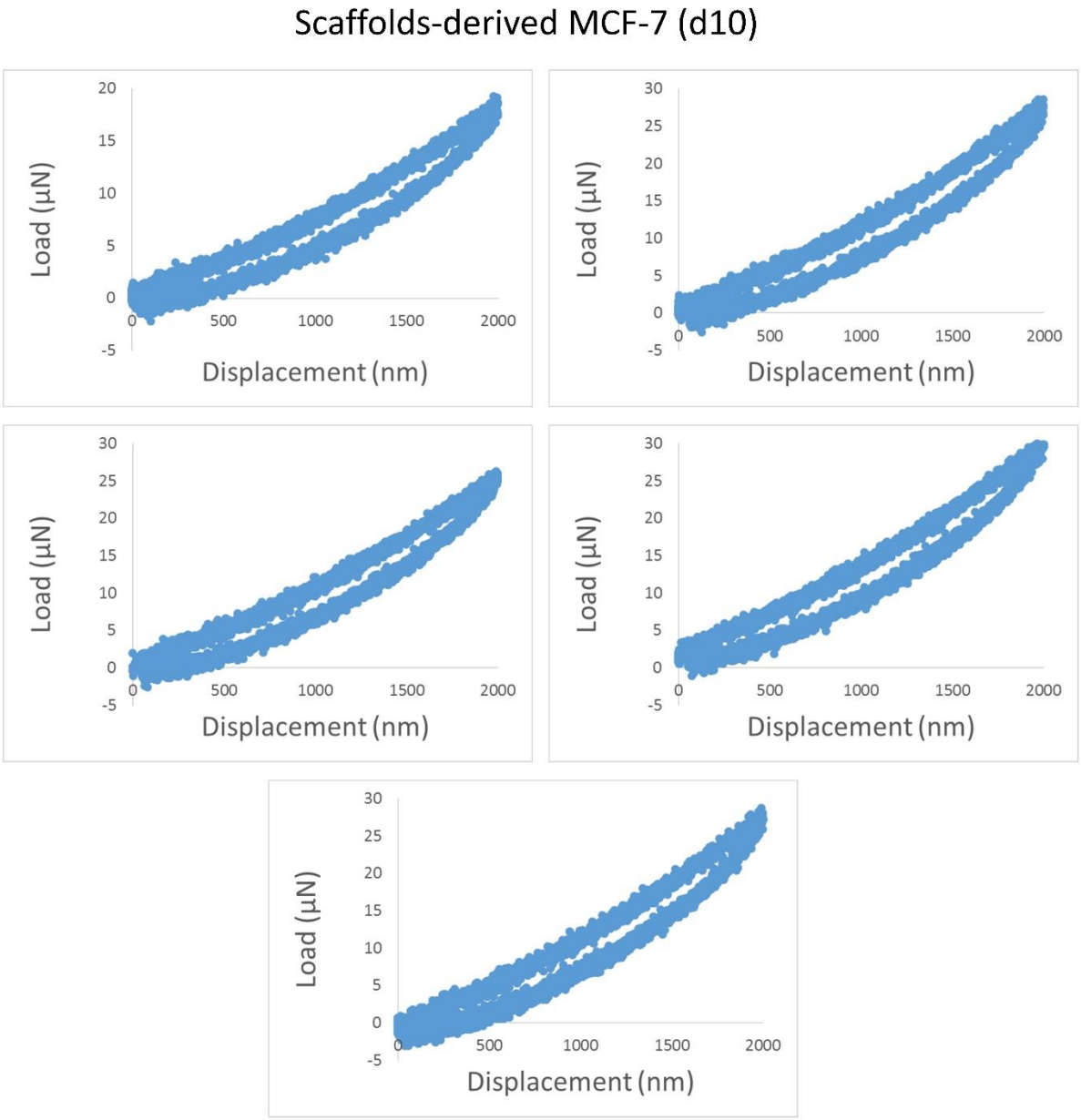

Figure A7. L-D curves of scaffolds-derived MCF-7 cells (d10) at maximum displacement of 2000 nm.

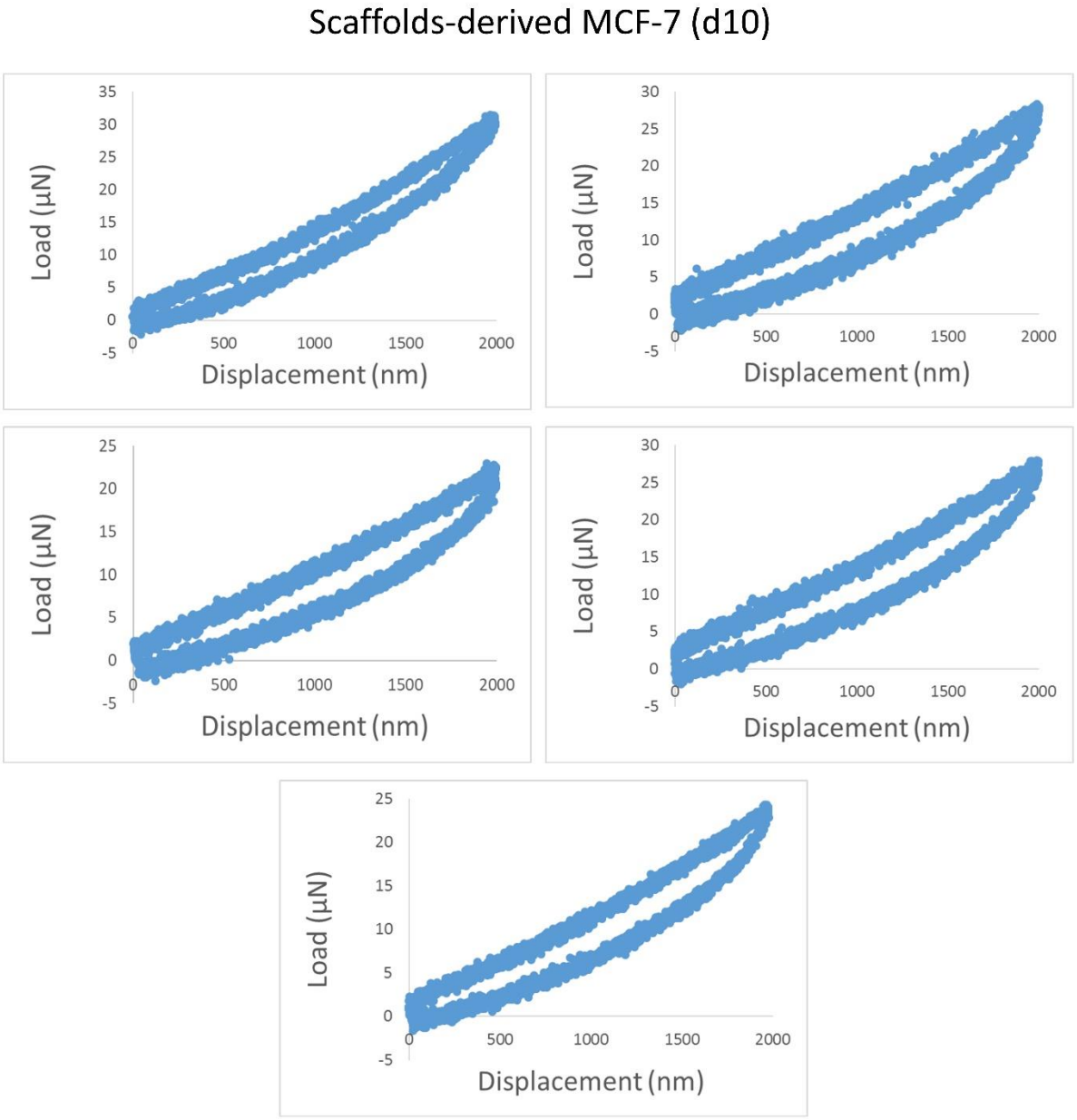

Figure A7. L-D curves of scaffolds-derived MCF-7 cells (d10) at maximum displacement of 2000 nm (Continued).

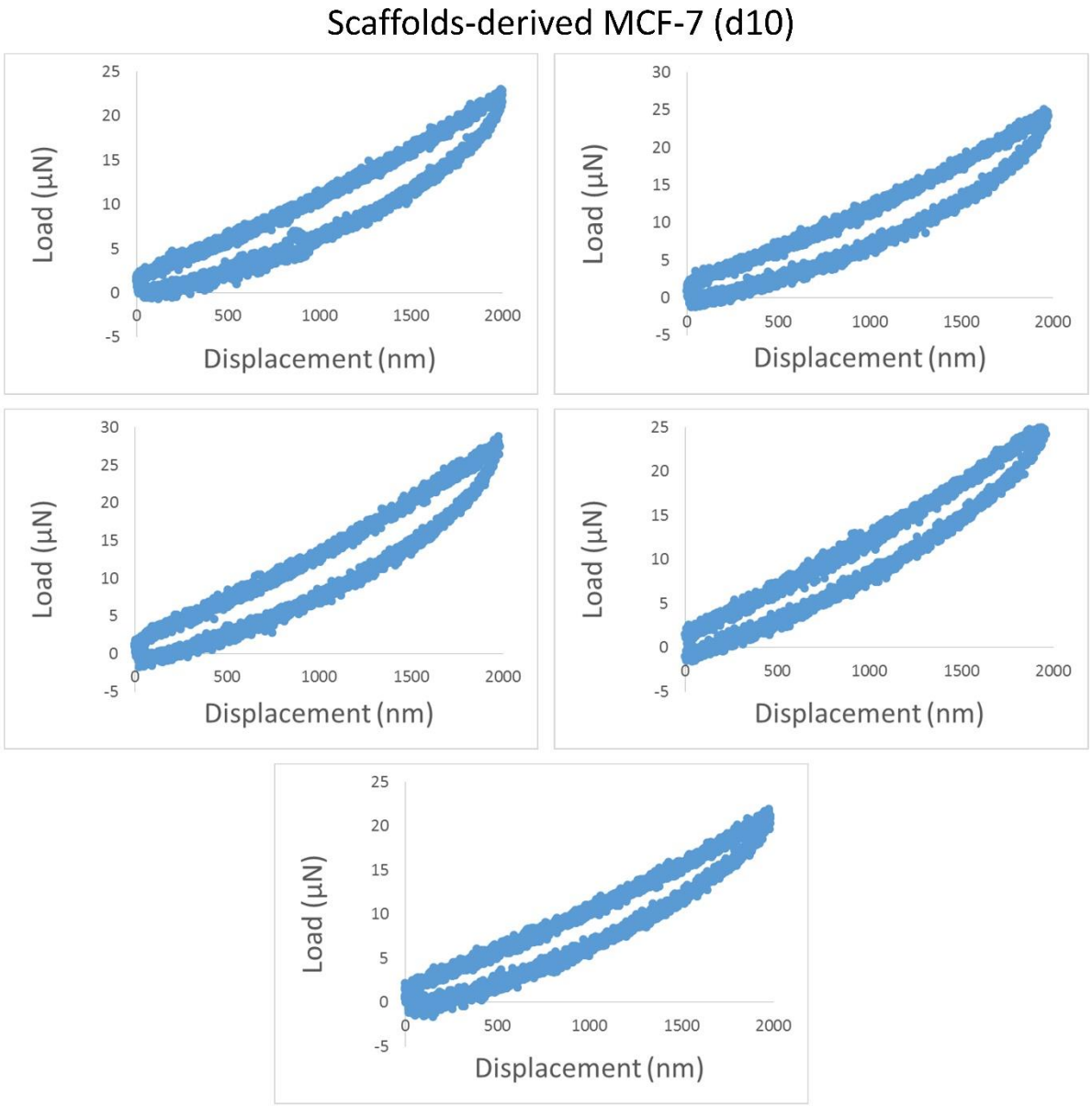

Figure A7. L-D curves of scaffolds-derived MCF-7 cells (d10) at maximum displacement of 2000 nm (Continued).

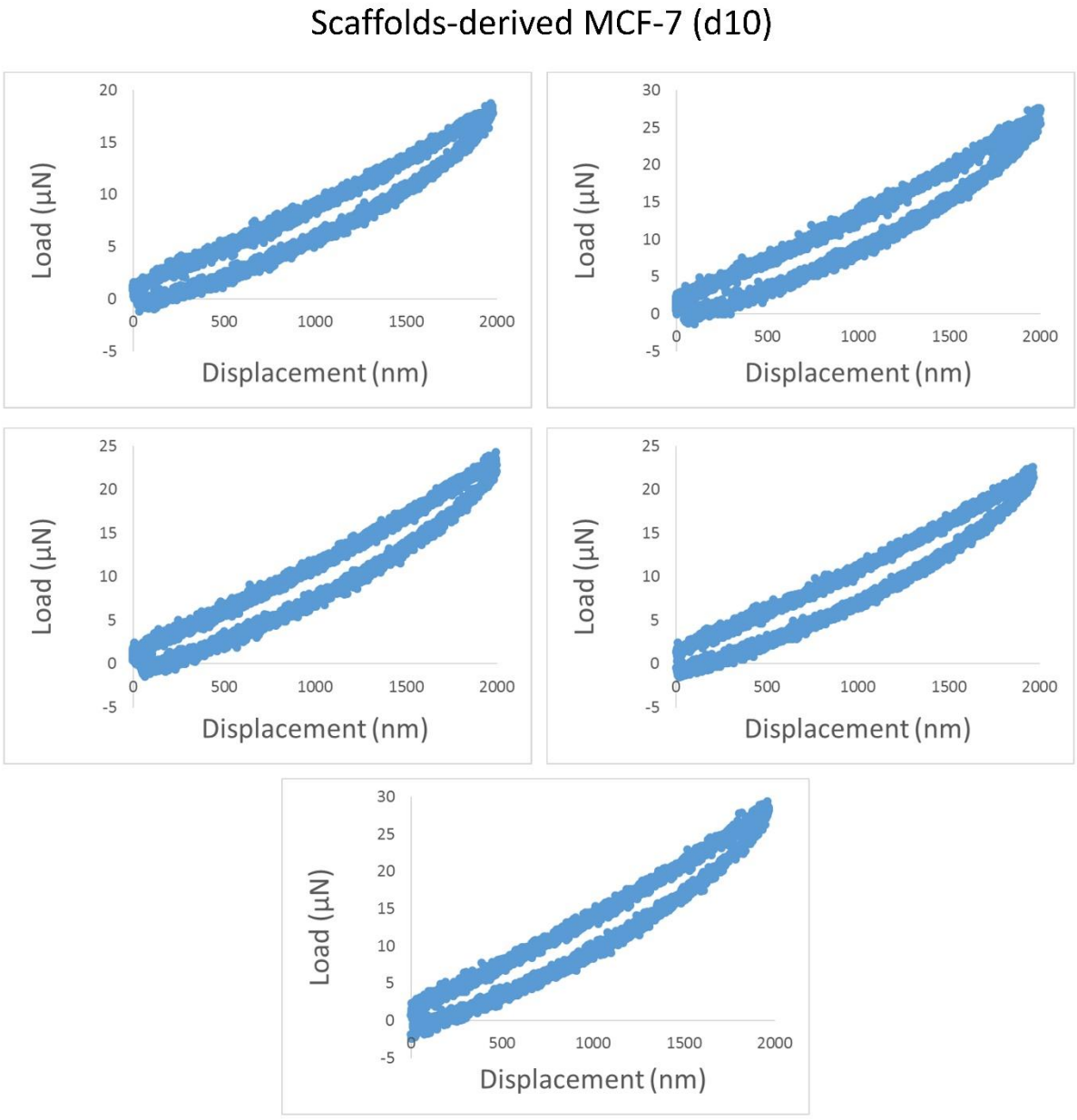

Figure A7. L-D curves of scaffolds-derived MCF-7 cells (d10) at maximum displacement of 2000 nm (Continued).

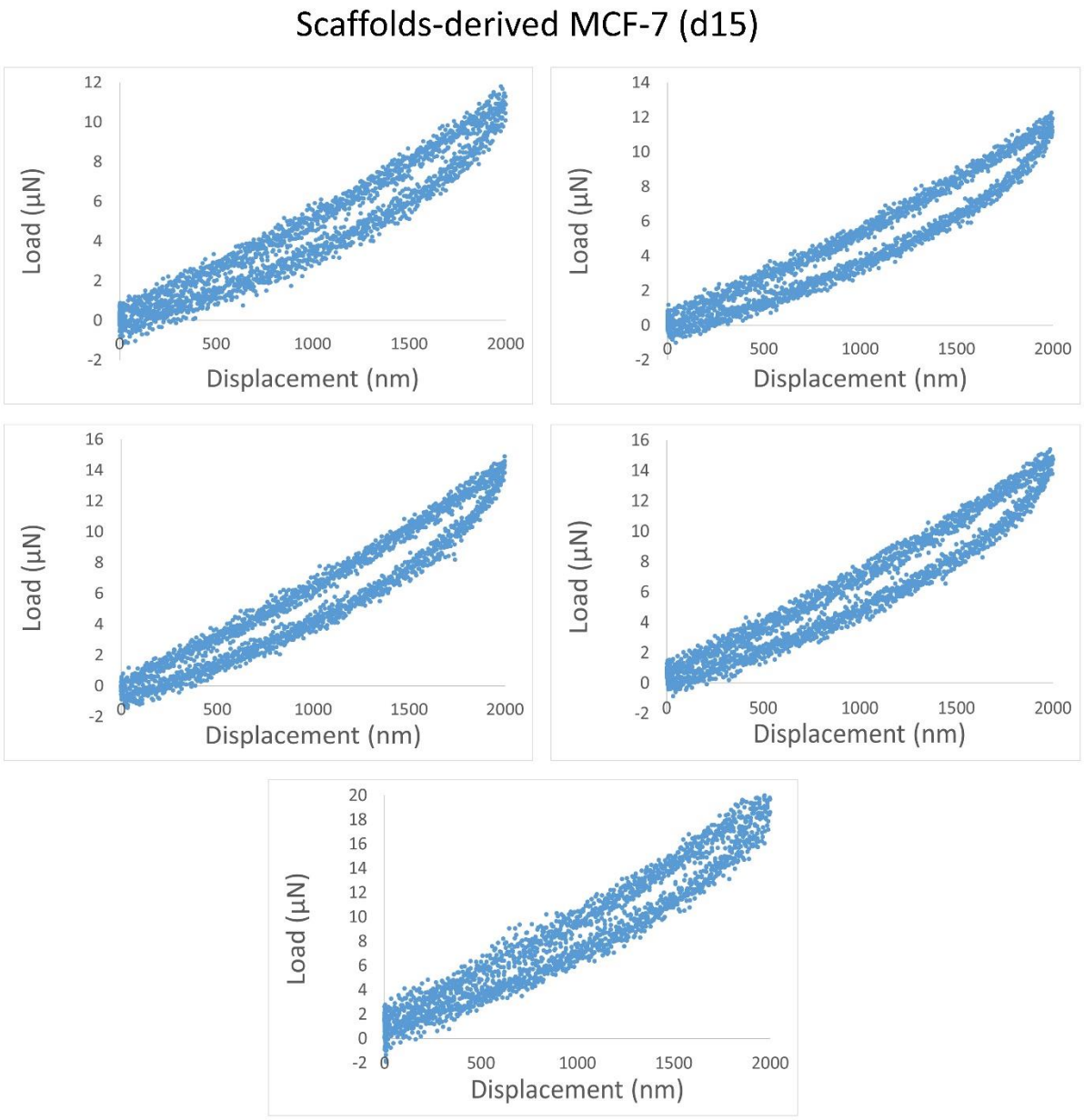

Figure A8. L-D curves of scaffolds-derived MCF-7 cells (d15) at maximum displacement of 2000 nm.

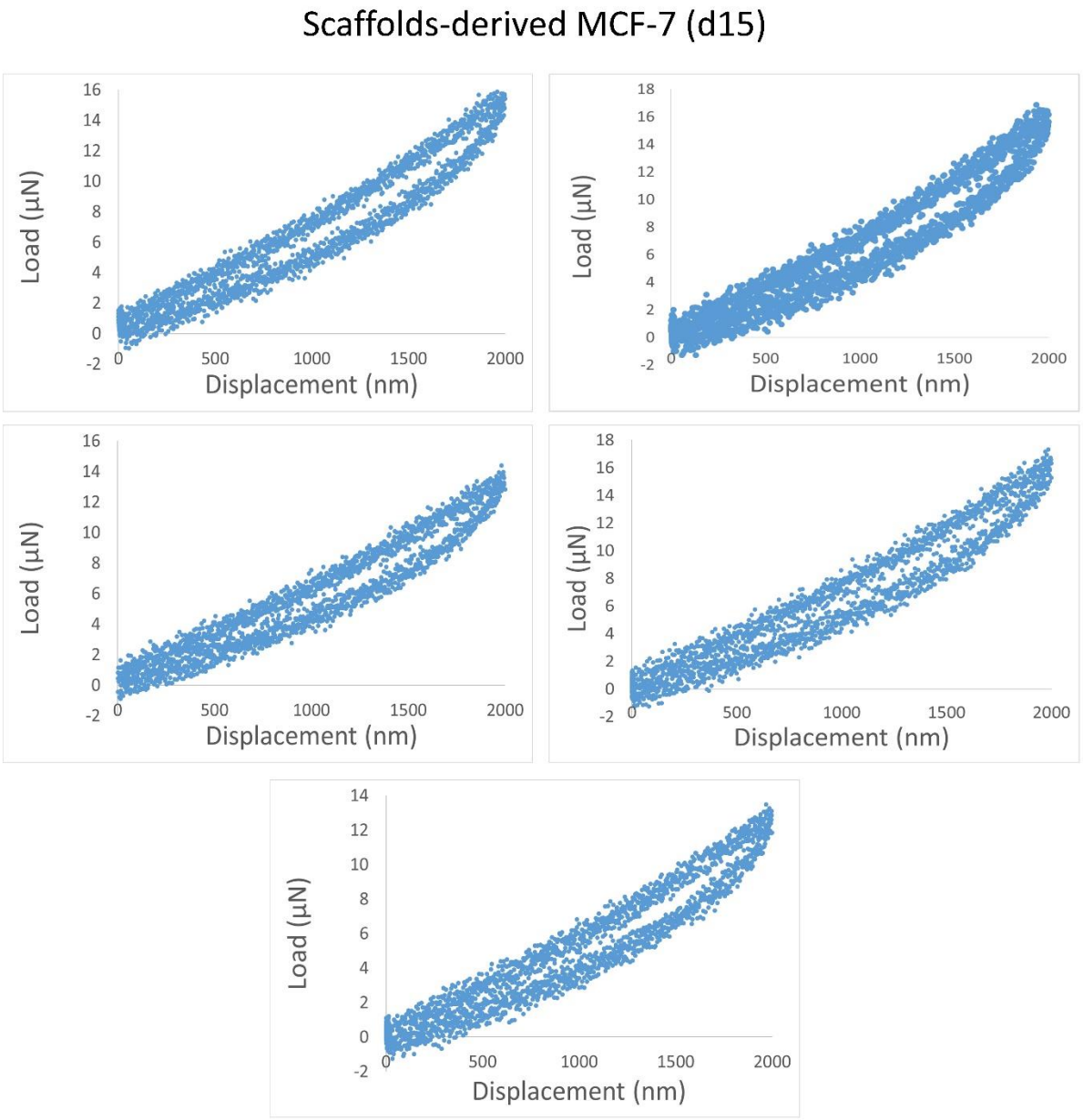

Figure A8. L-D curves of scaffolds-derived MCF-7 cells (d15) at maximum displacement of 2000 nm (Continued).

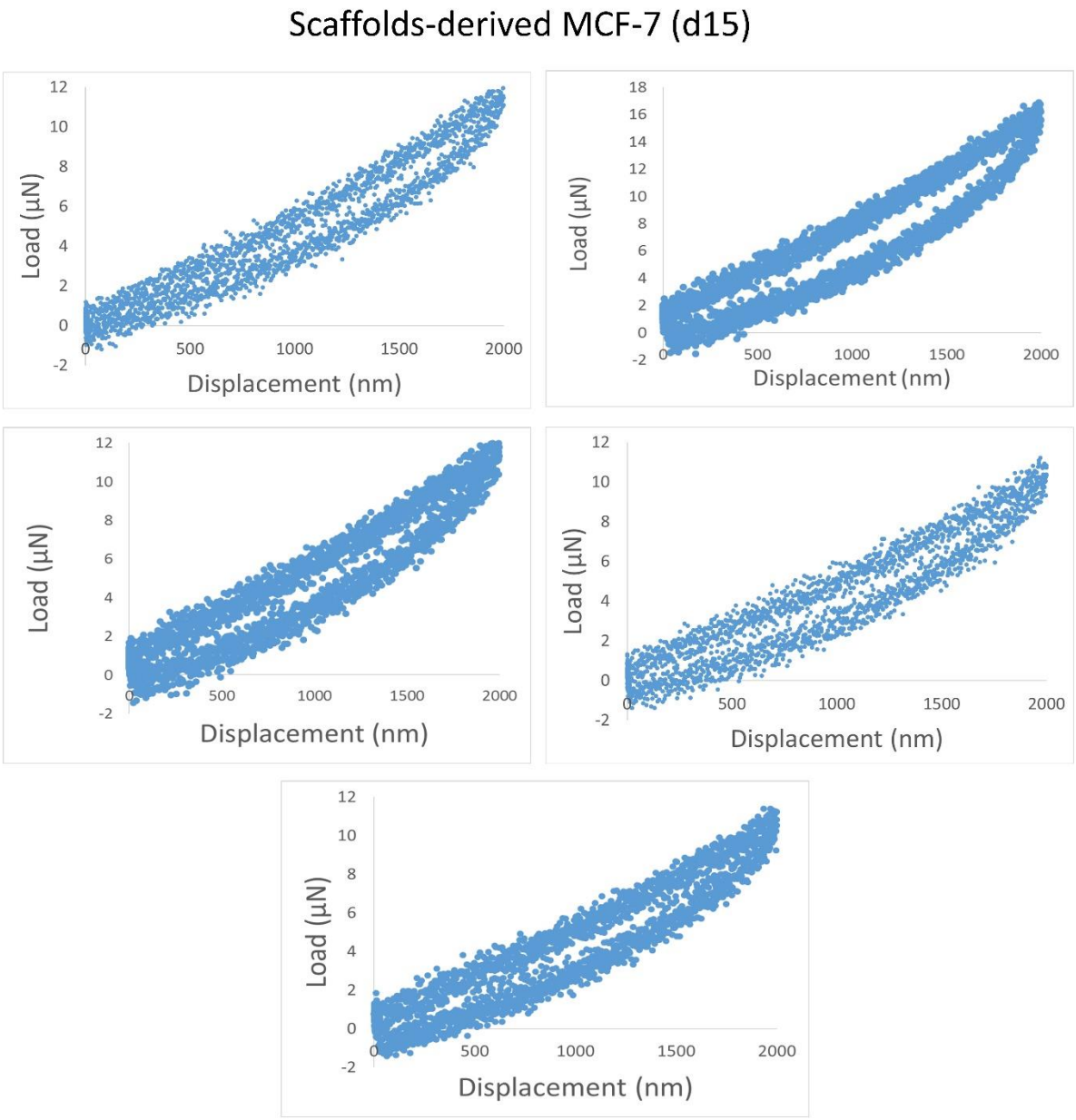

Figure A8. L-D curves of scaffolds-derived MCF-7 cells (d15) at maximum displacement of 2000 nm (Continued).

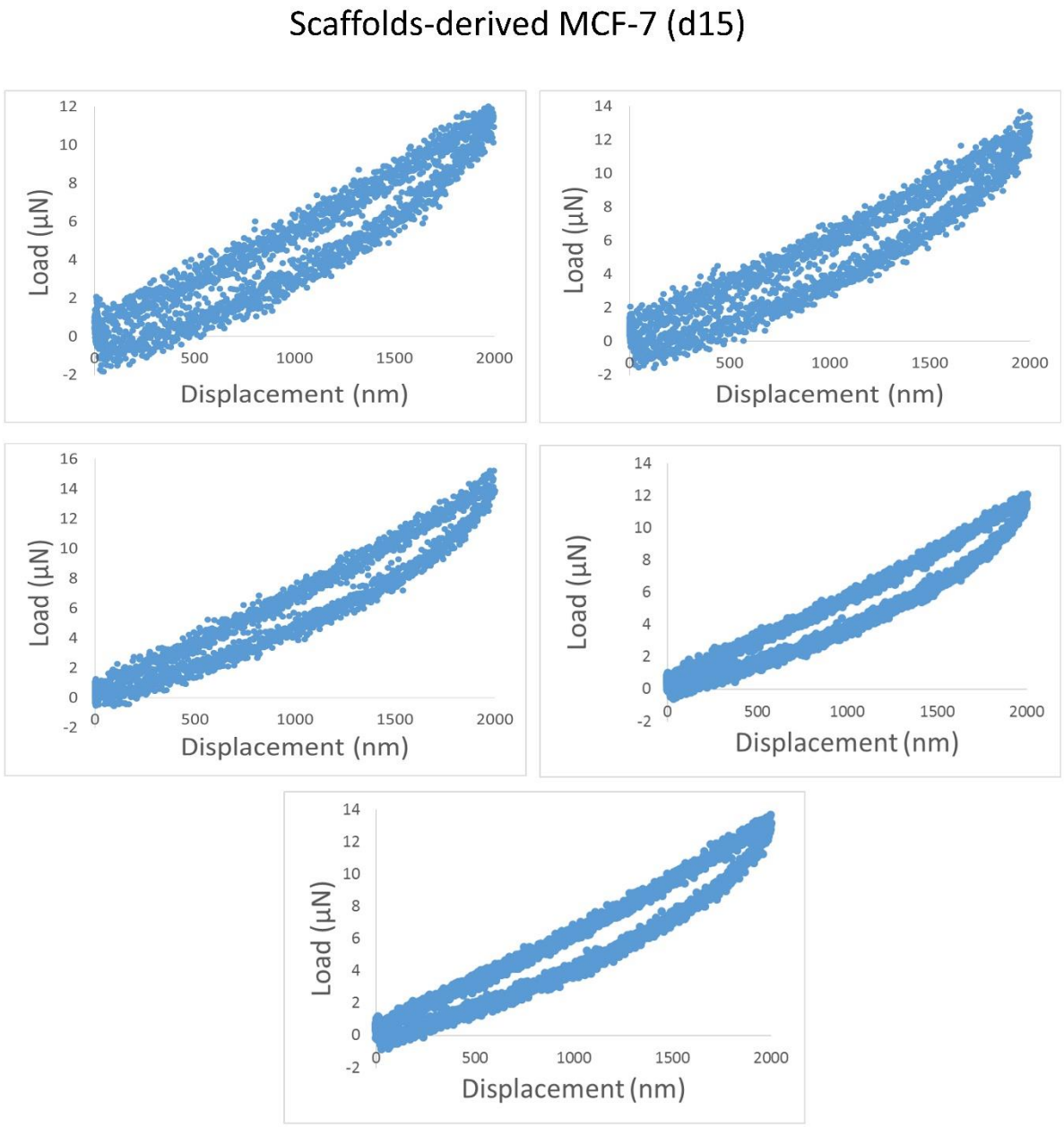

Figure A8. L-D curves of scaffolds-derived MCF-7 cells (d15) at maximum displacement of 2000 nm (Continued).

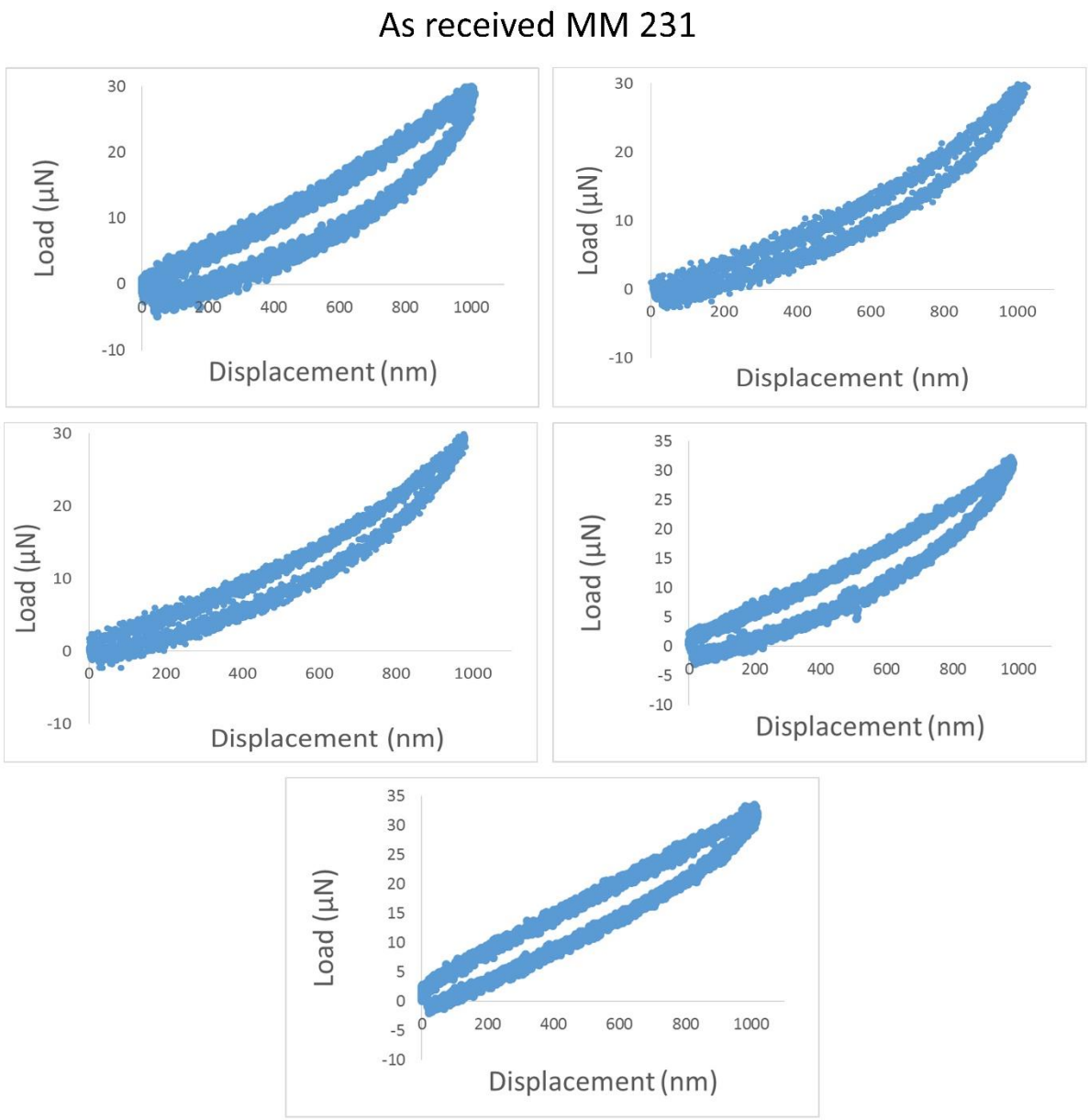

Figure A9. L-D curves of as received MM 231 cells at maximum displacement of 1000 nm.

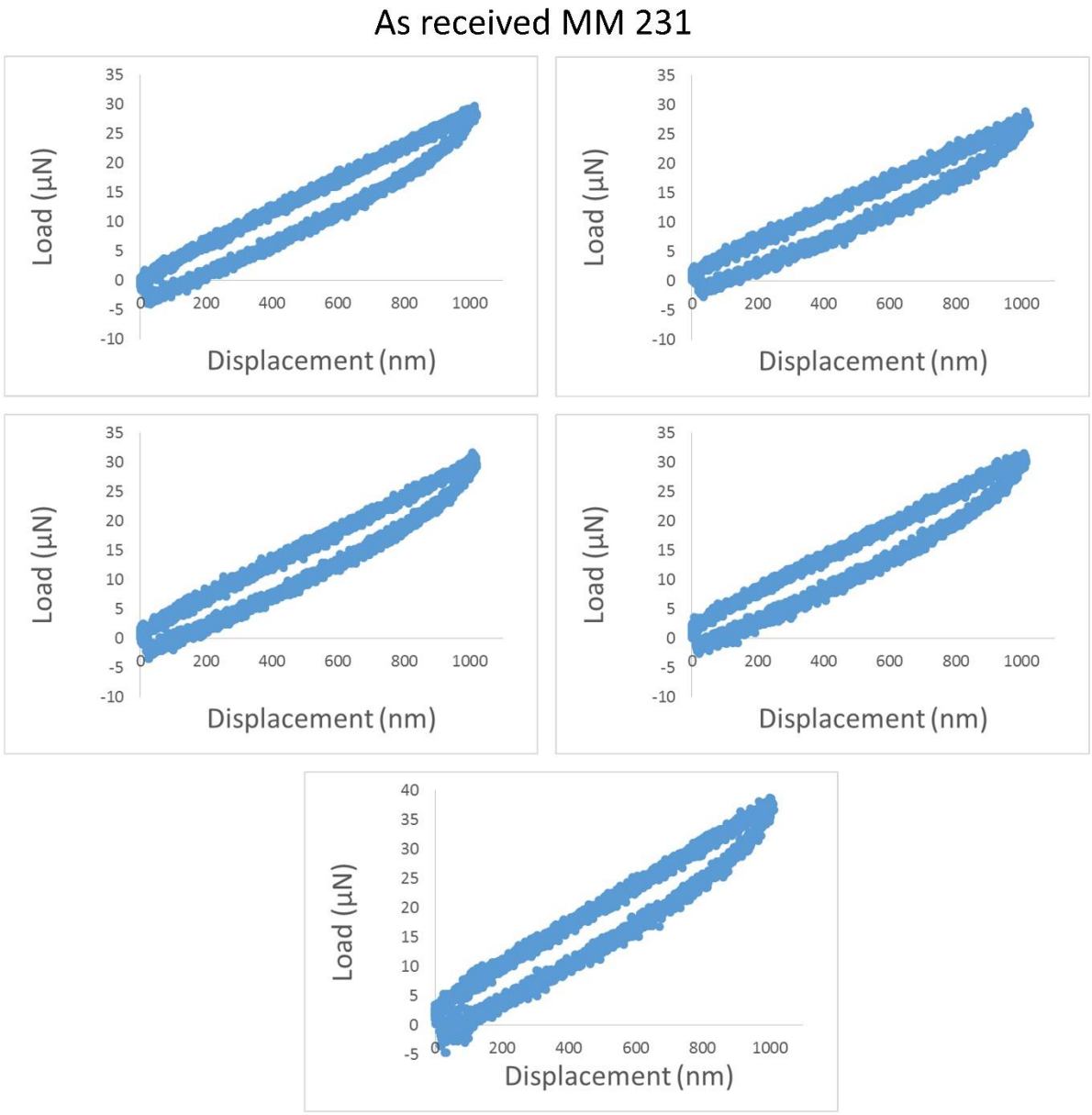

Figure A9. L-D curves of as received MM 231 cells at maximum displacement of 1000 nm (Continued).

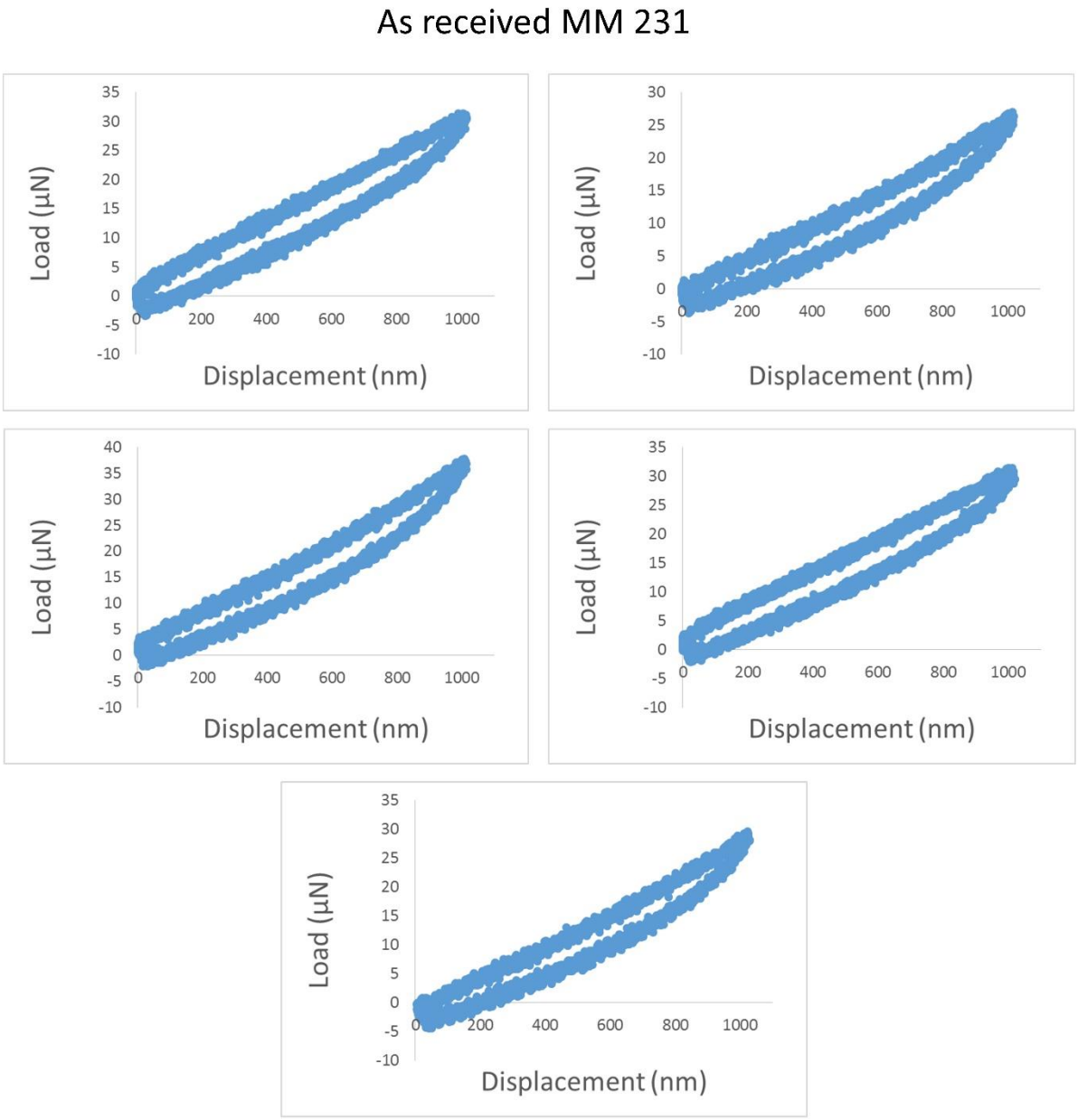

Figure A9. L-D curves of as received MM 231 cells at maximum displacement of 1000 nm (Continued).

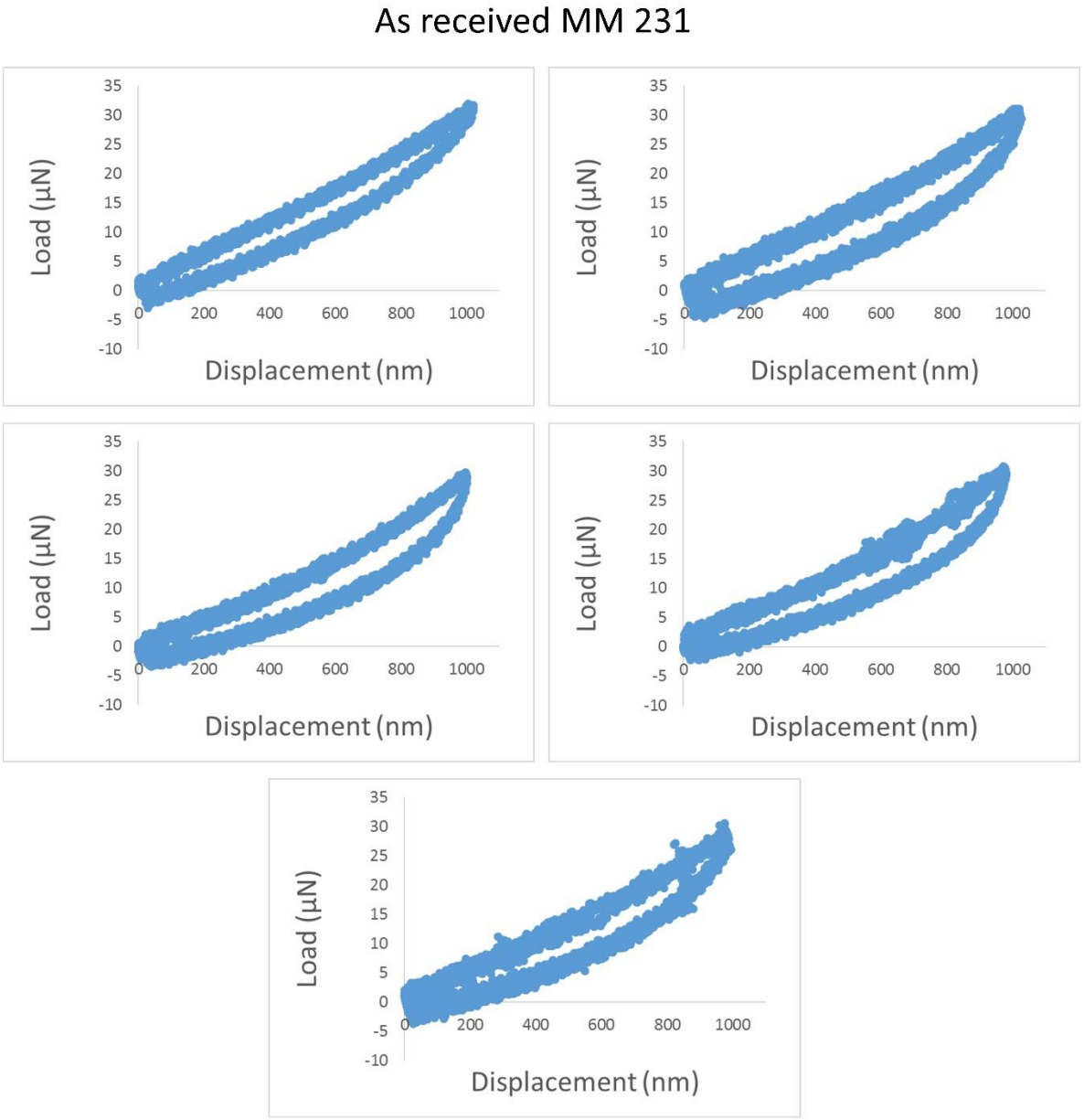

Figure A9. L-D curves of as received MM 231 cells at maximum displacement of 1000 nm (Continued).

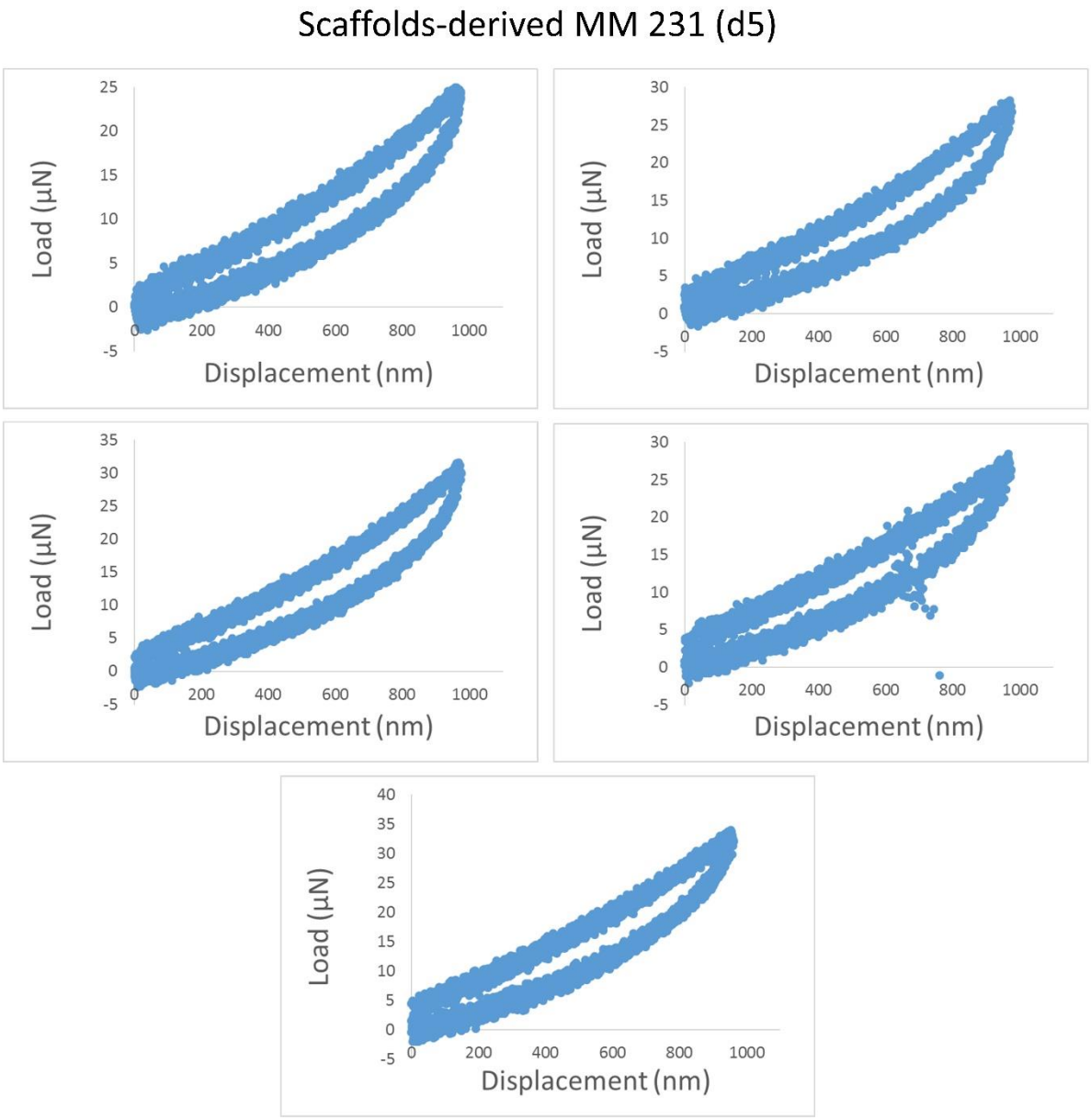

Figure A10. L-D curves of scaffolds-derived MM 231 cells (d5) at maximum displacement of 1000 nm.

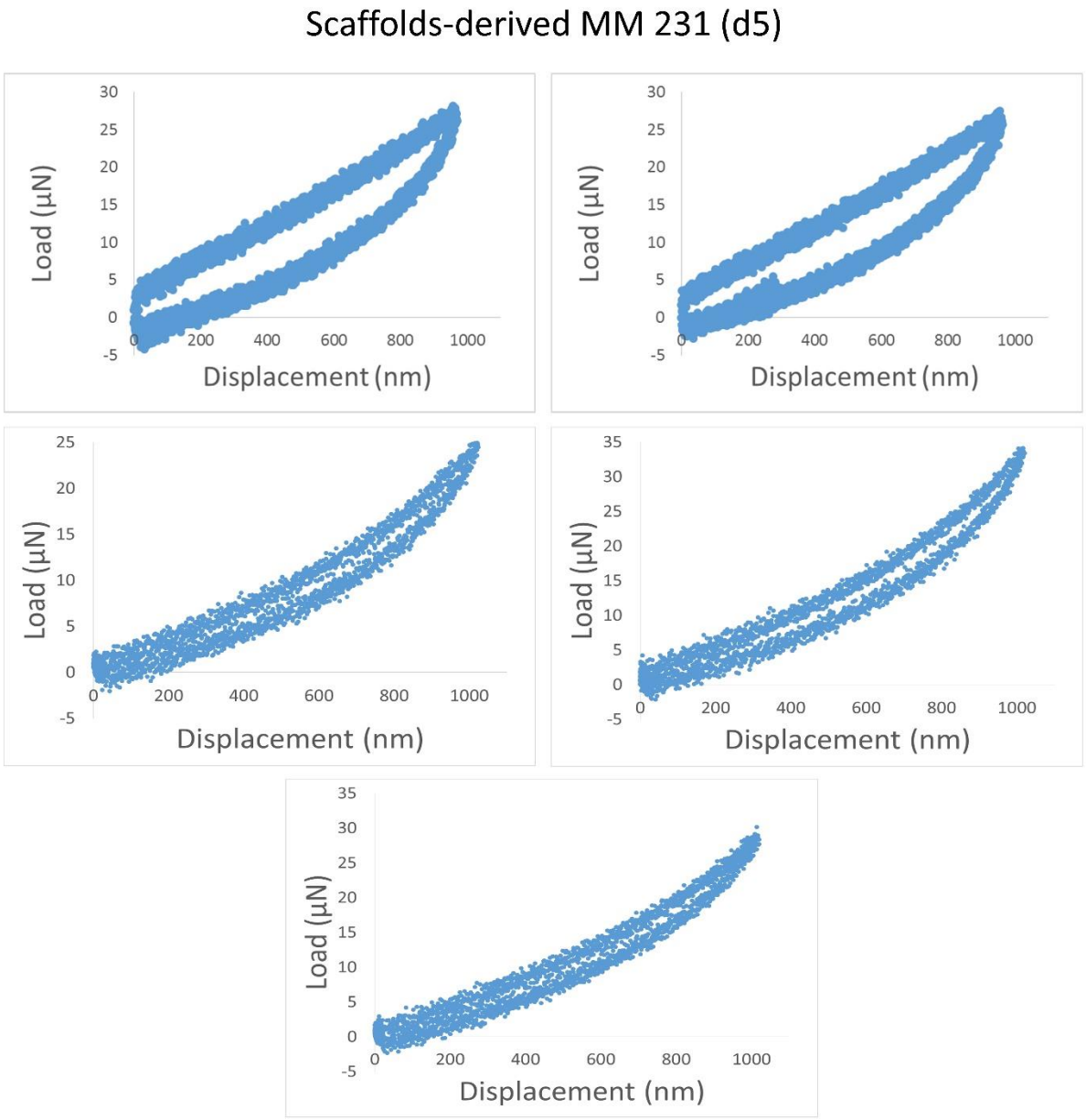

Figure A10. L-D curves of scaffolds-derived MM 231 cells (d5) at maximum displacement of 1000 nm (Continued).

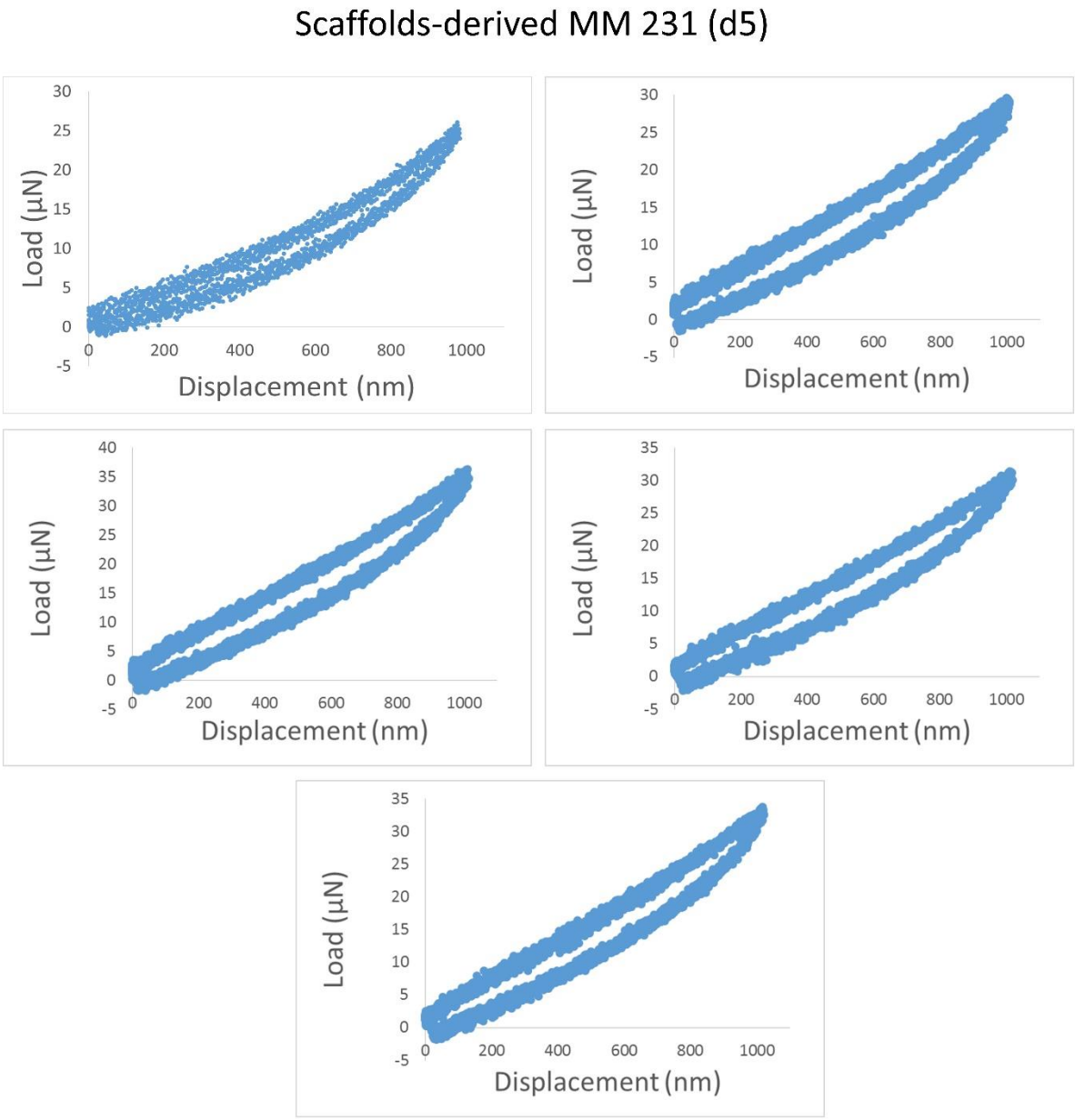

Figure A10. L-D curves of scaffolds-derived MM 231 cells (d5) at maximum displacement of 1000 nm (Continued).

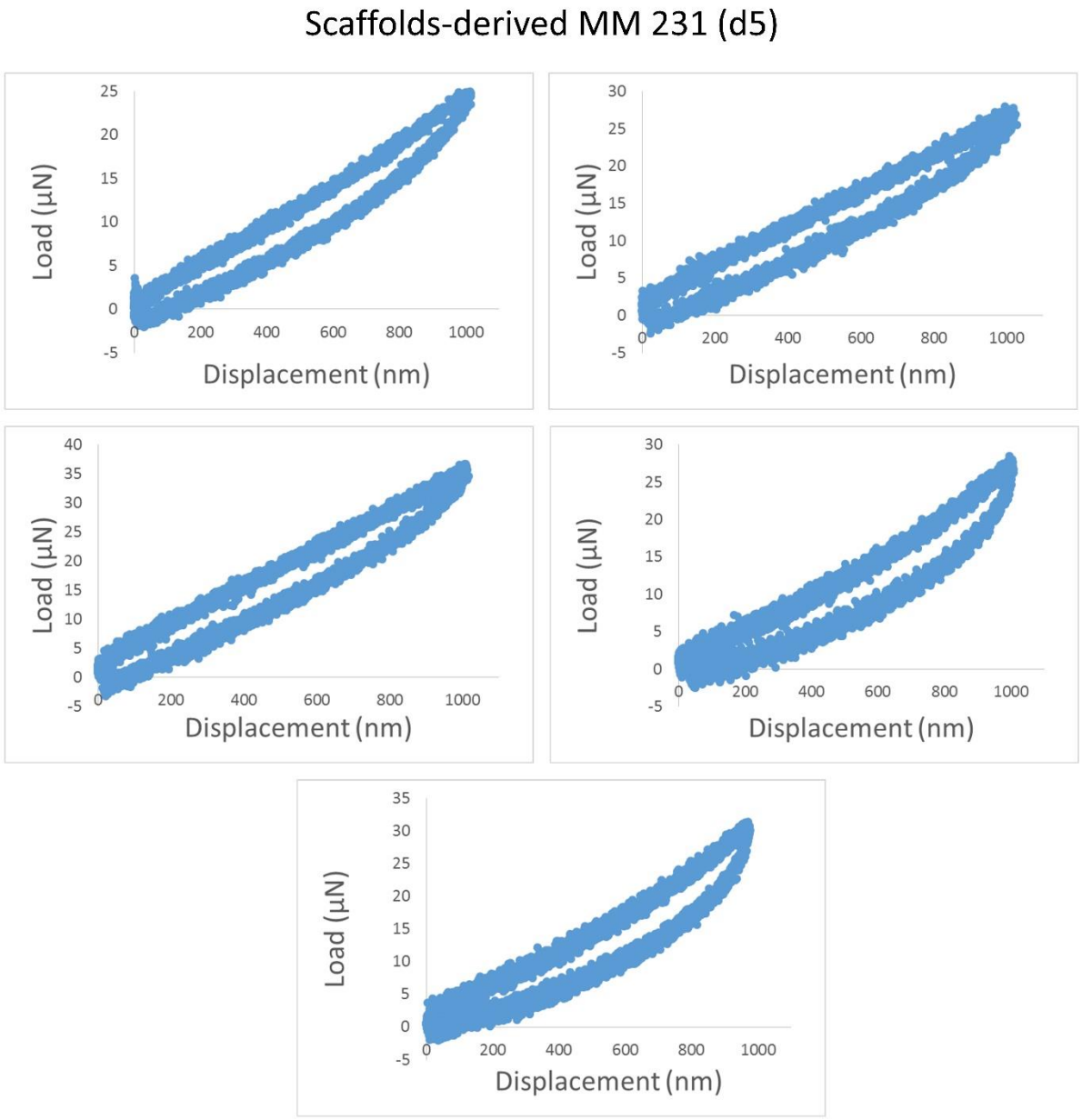

Figure A10. L-D curves of scaffolds-derived MM 231 cells (d5) at maximum displacement of 1000 nm (Continued).

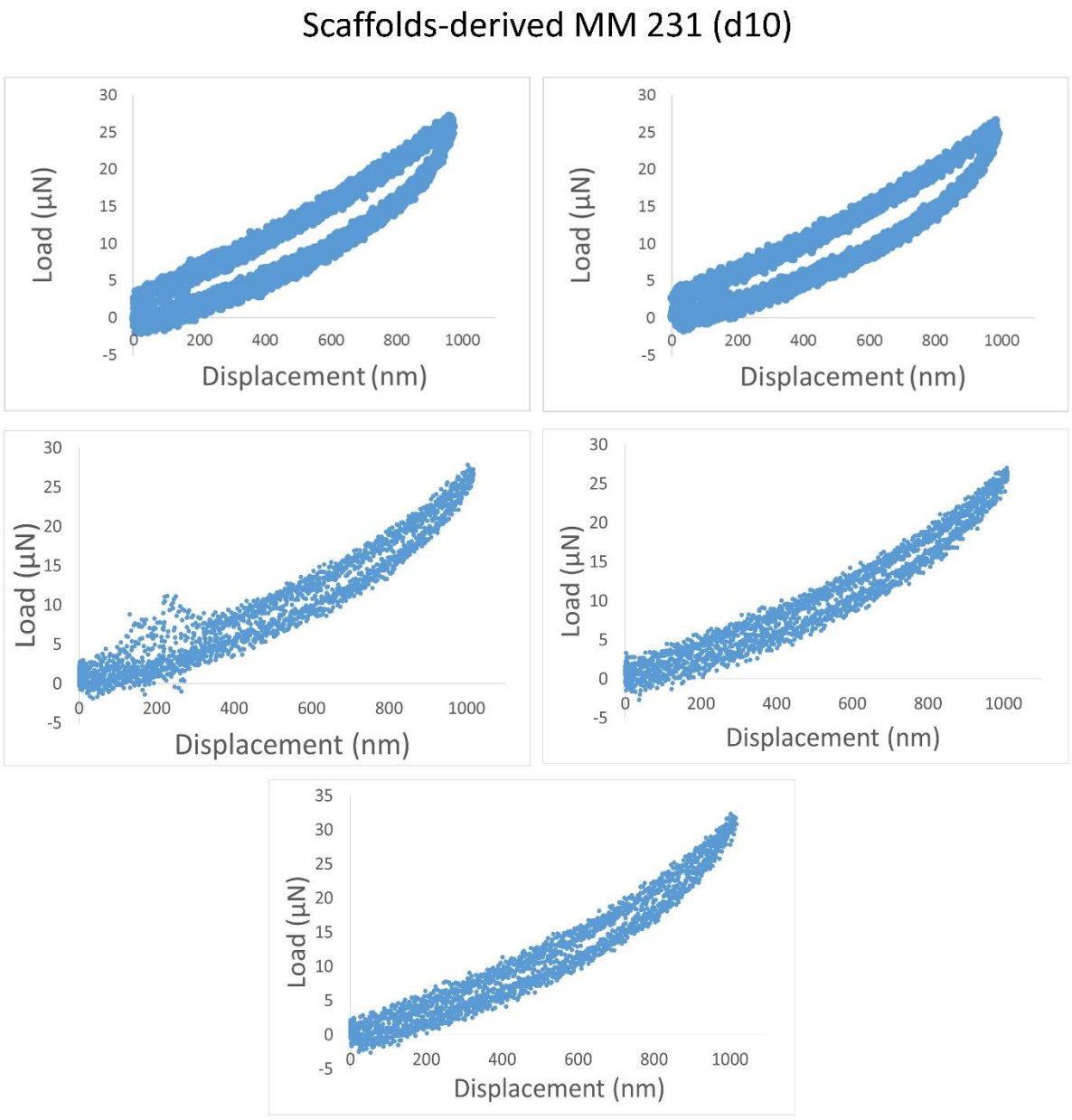

Figure A11. L-D curves of scaffolds-derived MM 231 cells (d10) at maximum displacement of 1000 nm.

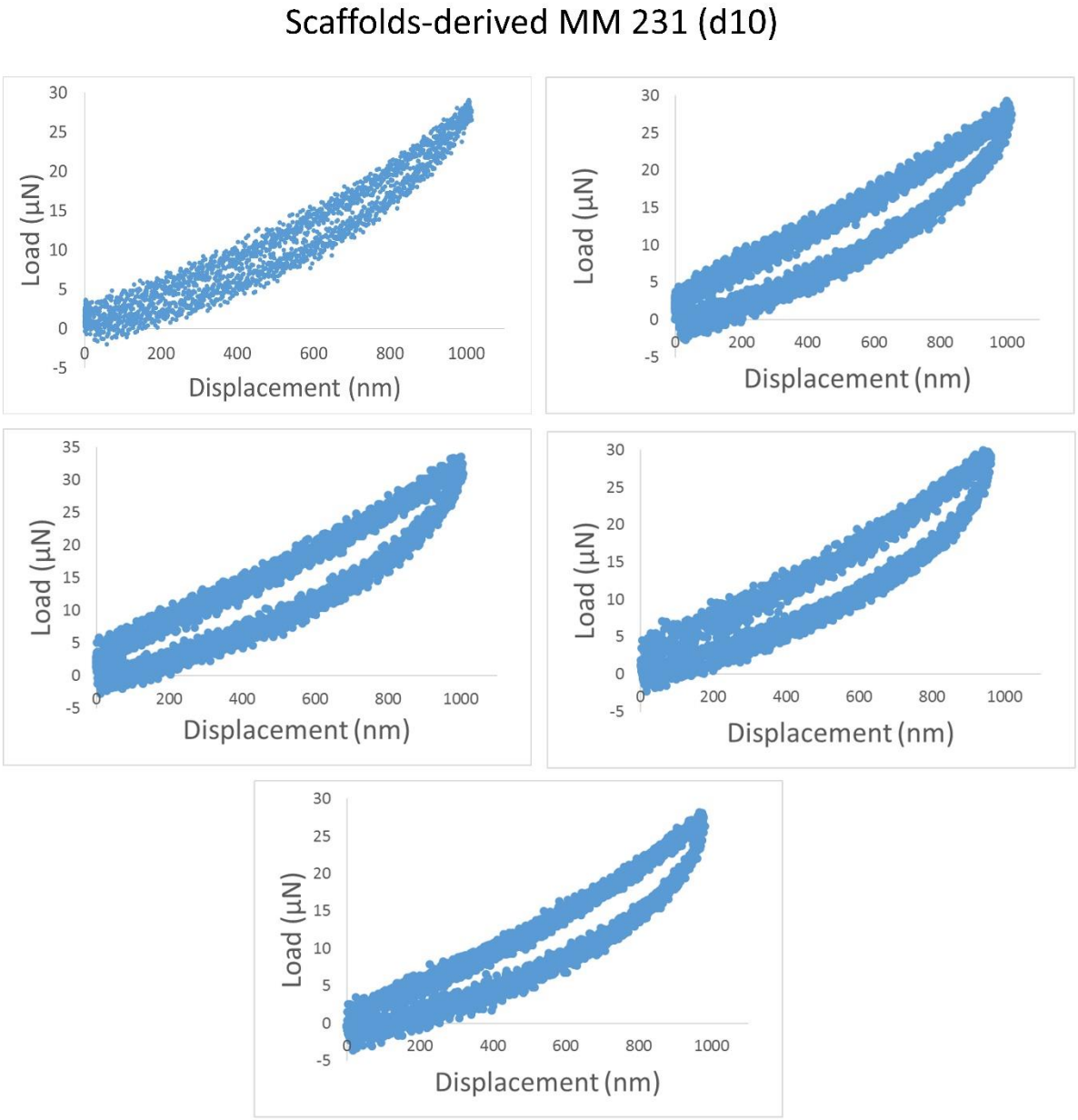

Figure A11. L-D curves of scaffolds-derived MM 231 cells (d10) at maximum displacement of 1000 nm (Continued).

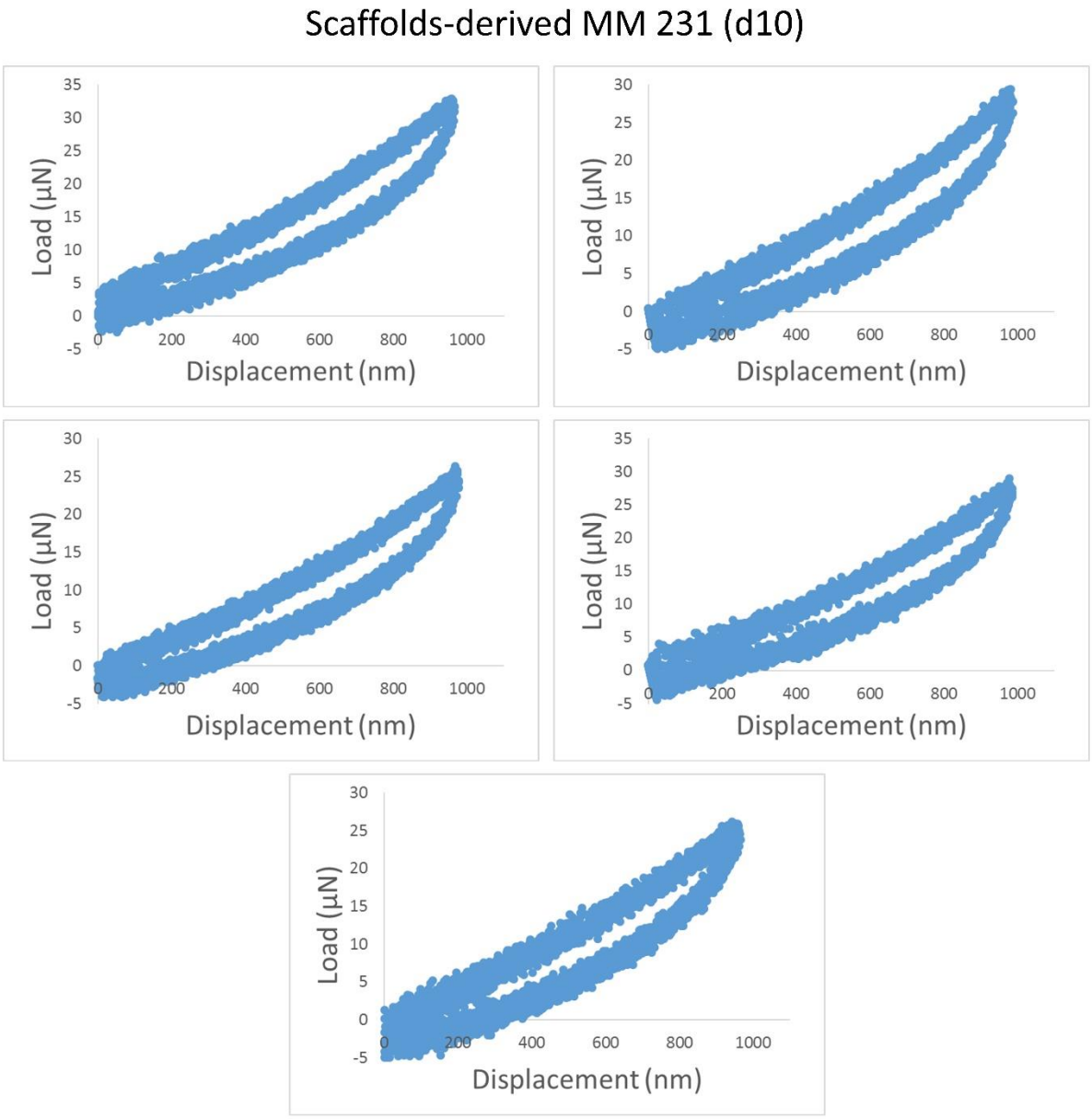

Figure A11. L-D curves of scaffolds-derived MM 231 cells (d10) at maximum displacement of 1000 nm (Continued).

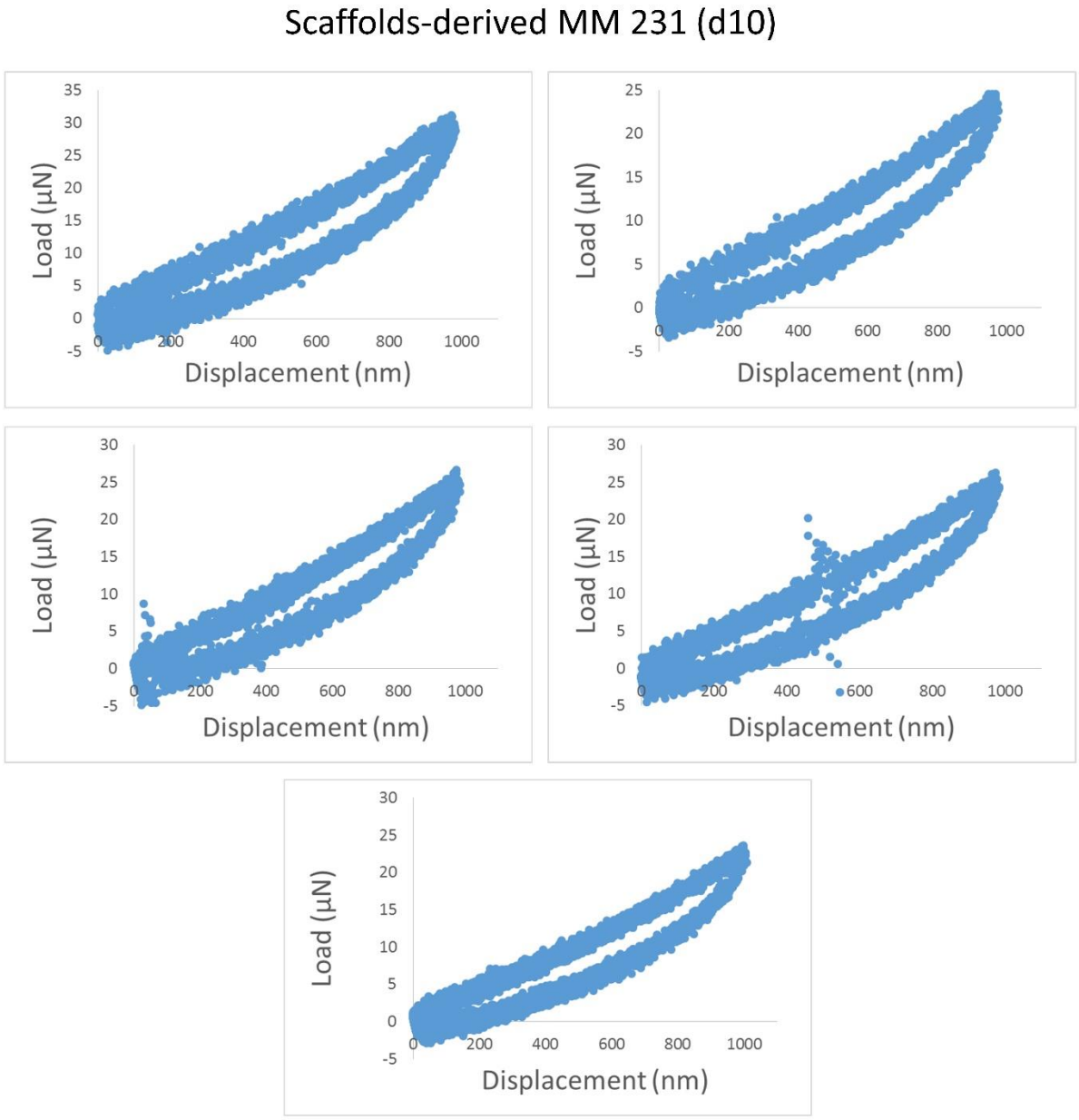

Figure A11. L-D curves of scaffolds-derived MM 231 cells (d10) at maximum displacement of 1000 nm (Continued).

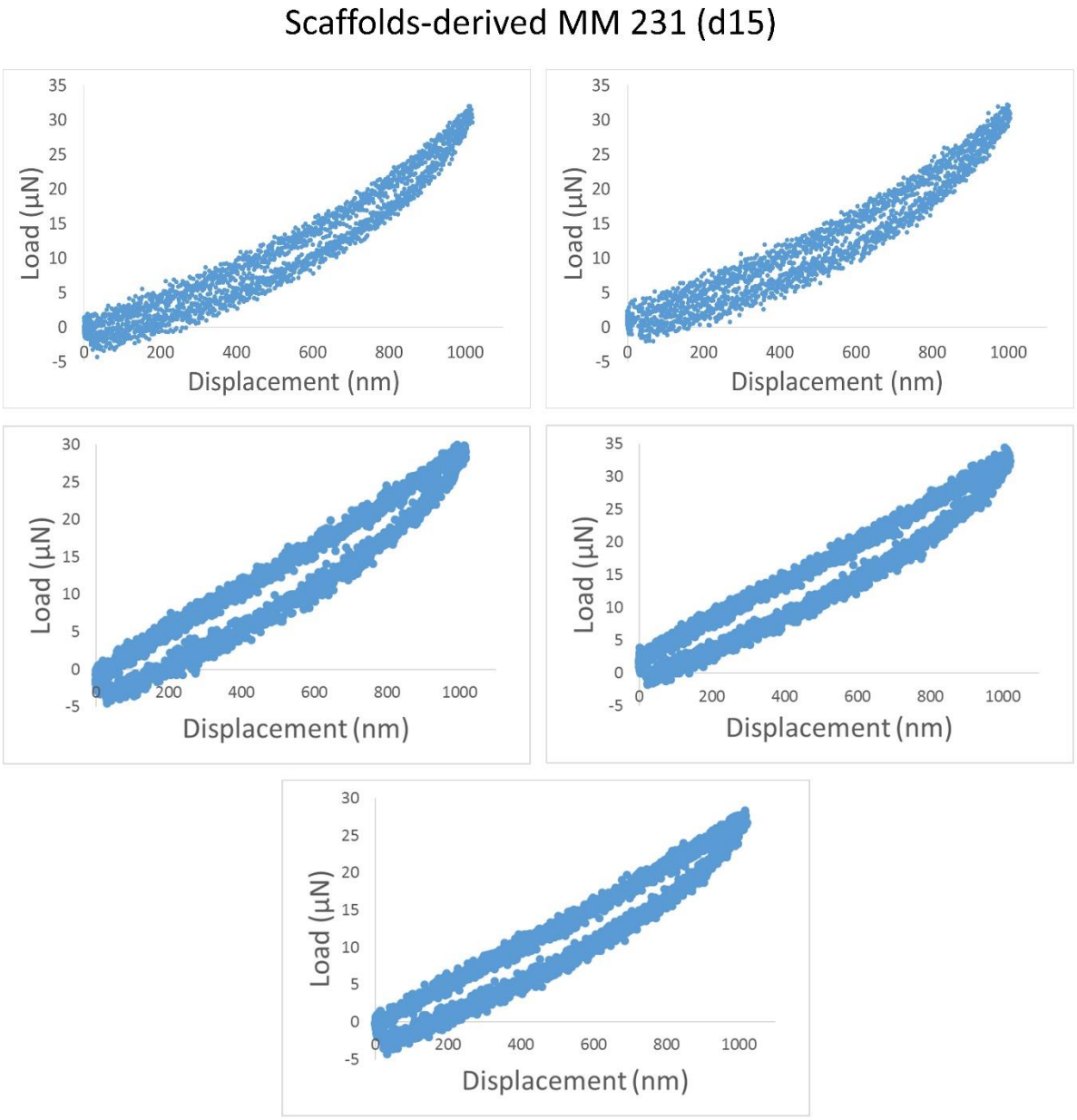

Figure A12. L-D curves of scaffolds-derived MM 231 cells (d15) at maximum displacement of 1000 nm.

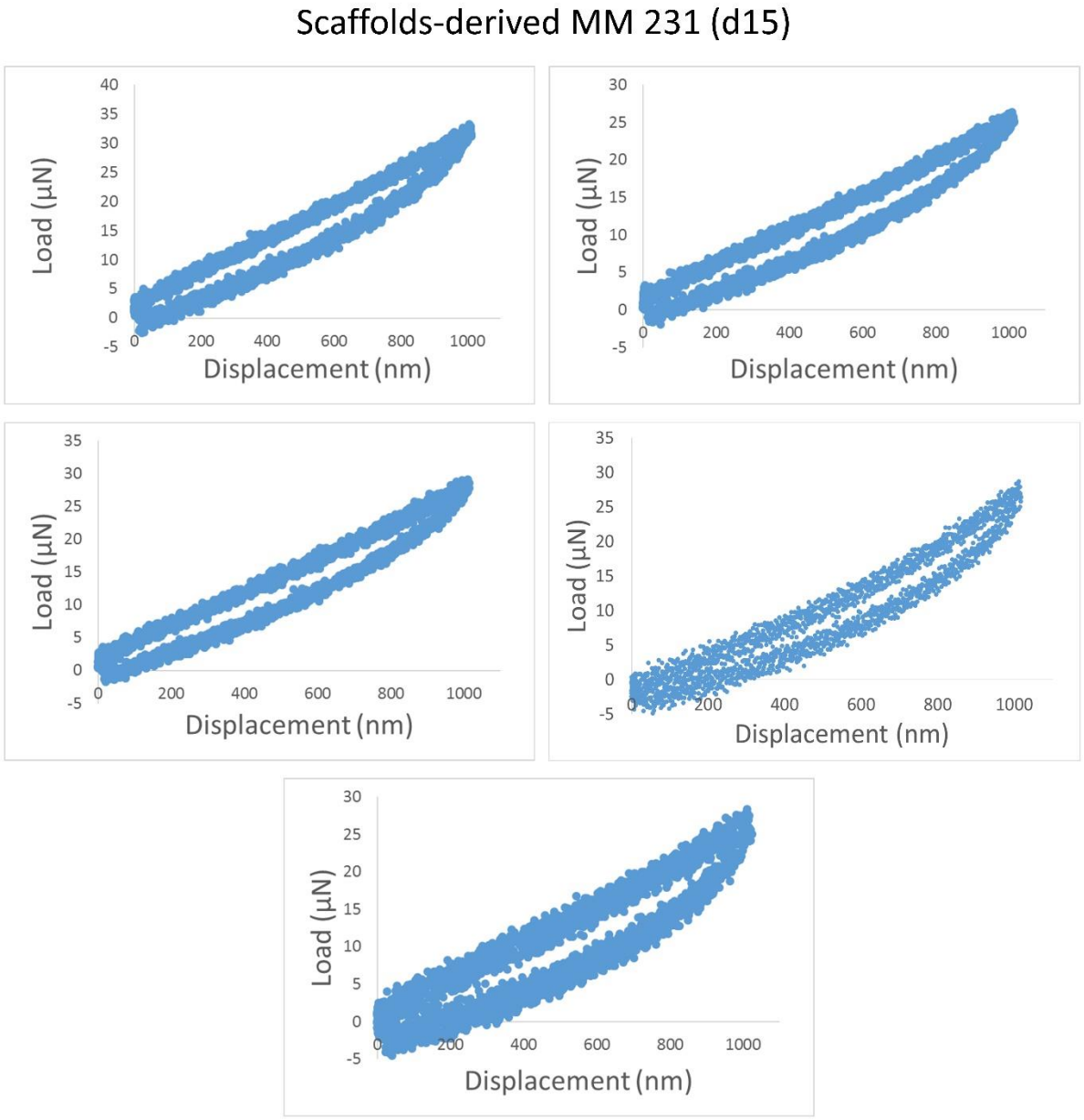

Figure A12. L-D curves of scaffolds-derived MM 231 cells (d15) at maximum displacement of 1000 nm (Continued).

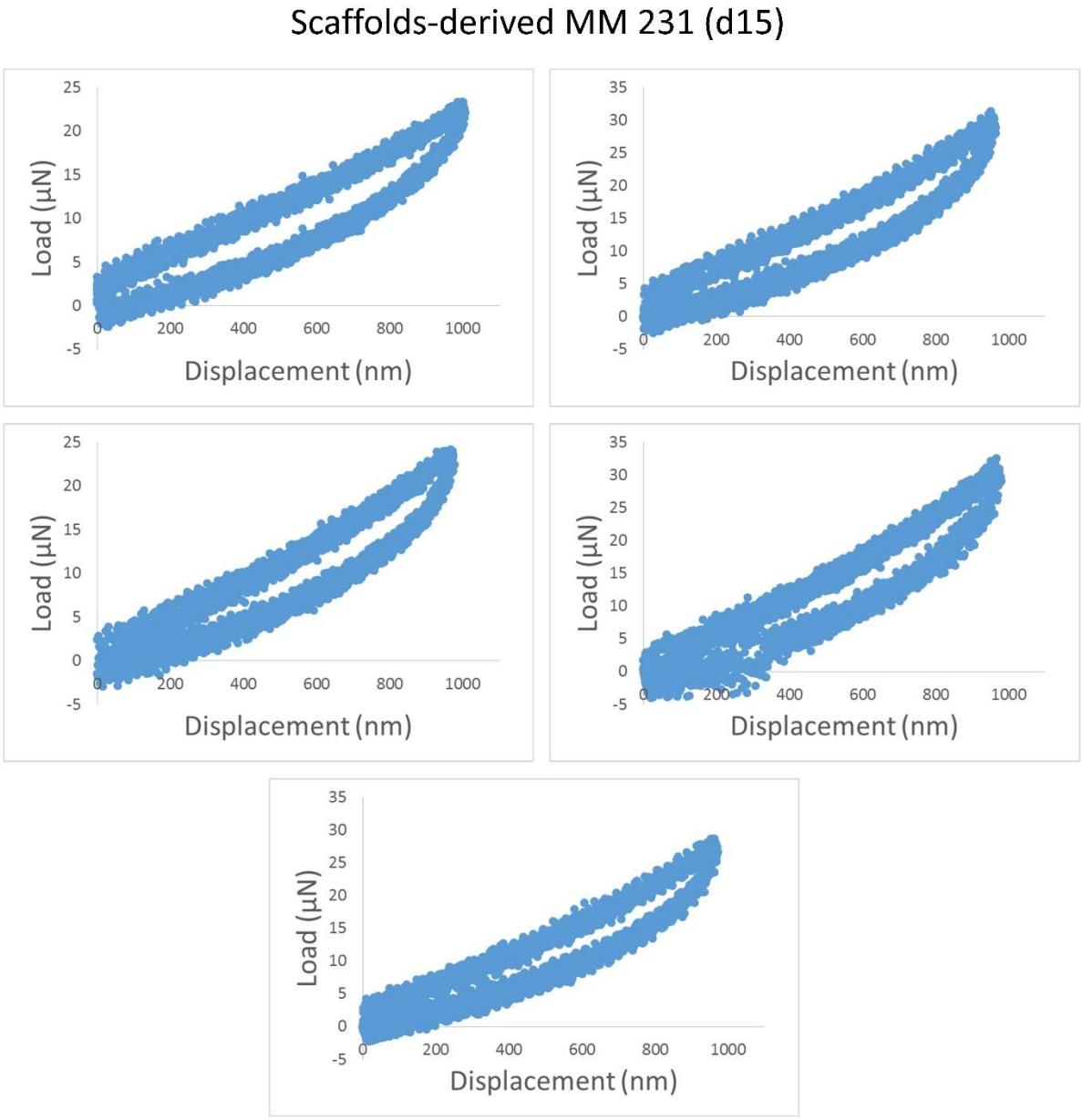

Figure A12. L-D curves of scaffolds-derived MM 231 cells (d15) at maximum displacement of 1000 nm (Continued).

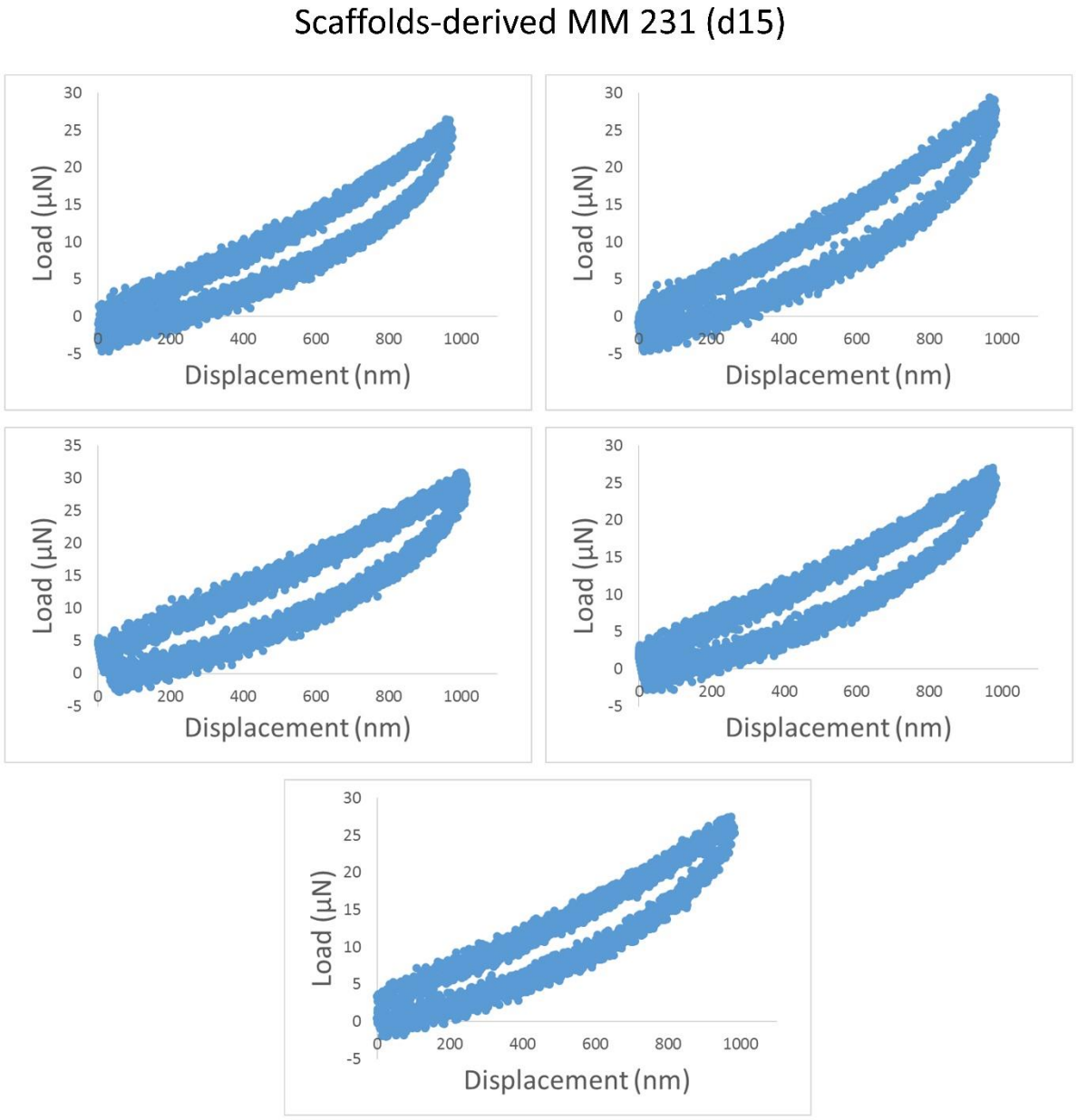

Figure A12. L-D curves of scaffolds-derived MM 231 cells (d15) at maximum displacement of 1000 nm (Continued).

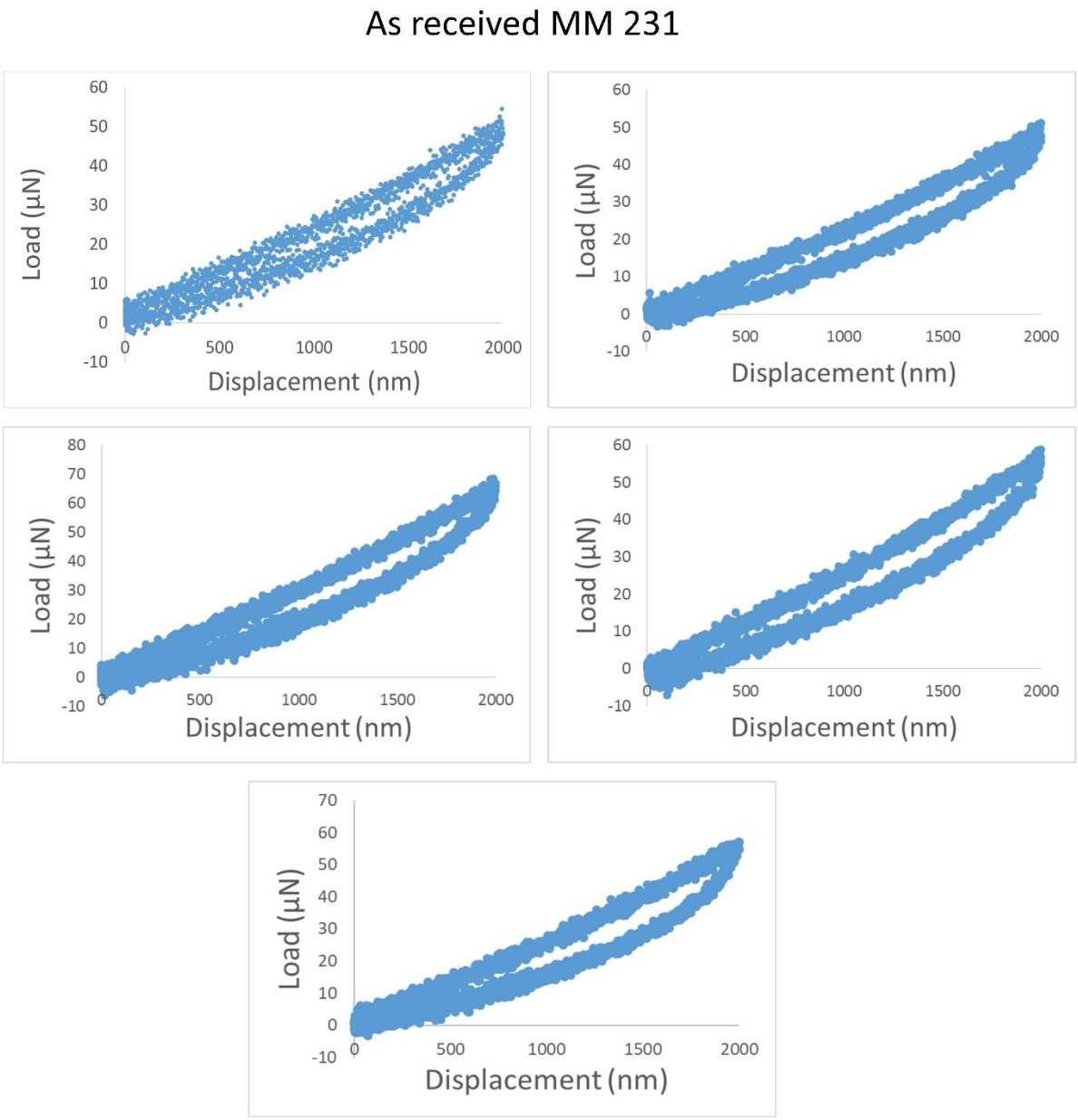

Figure A13. L-D curves of as received MM 231 cells at maximum displacement of 2000 nm.

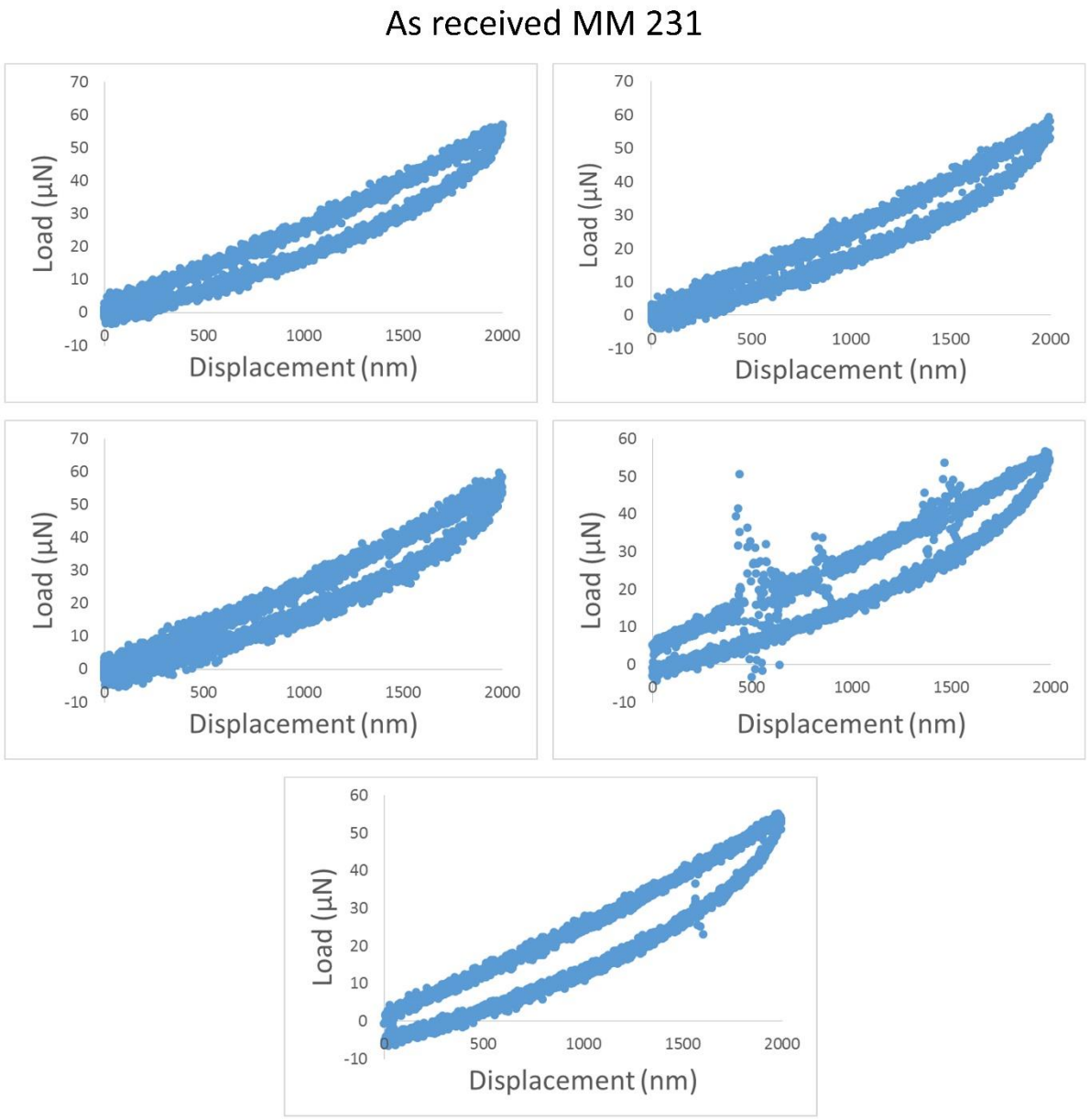

Figure A13. L-D curves of as received MM 231 cells at maximum displacement of 2000 nm (Continued).

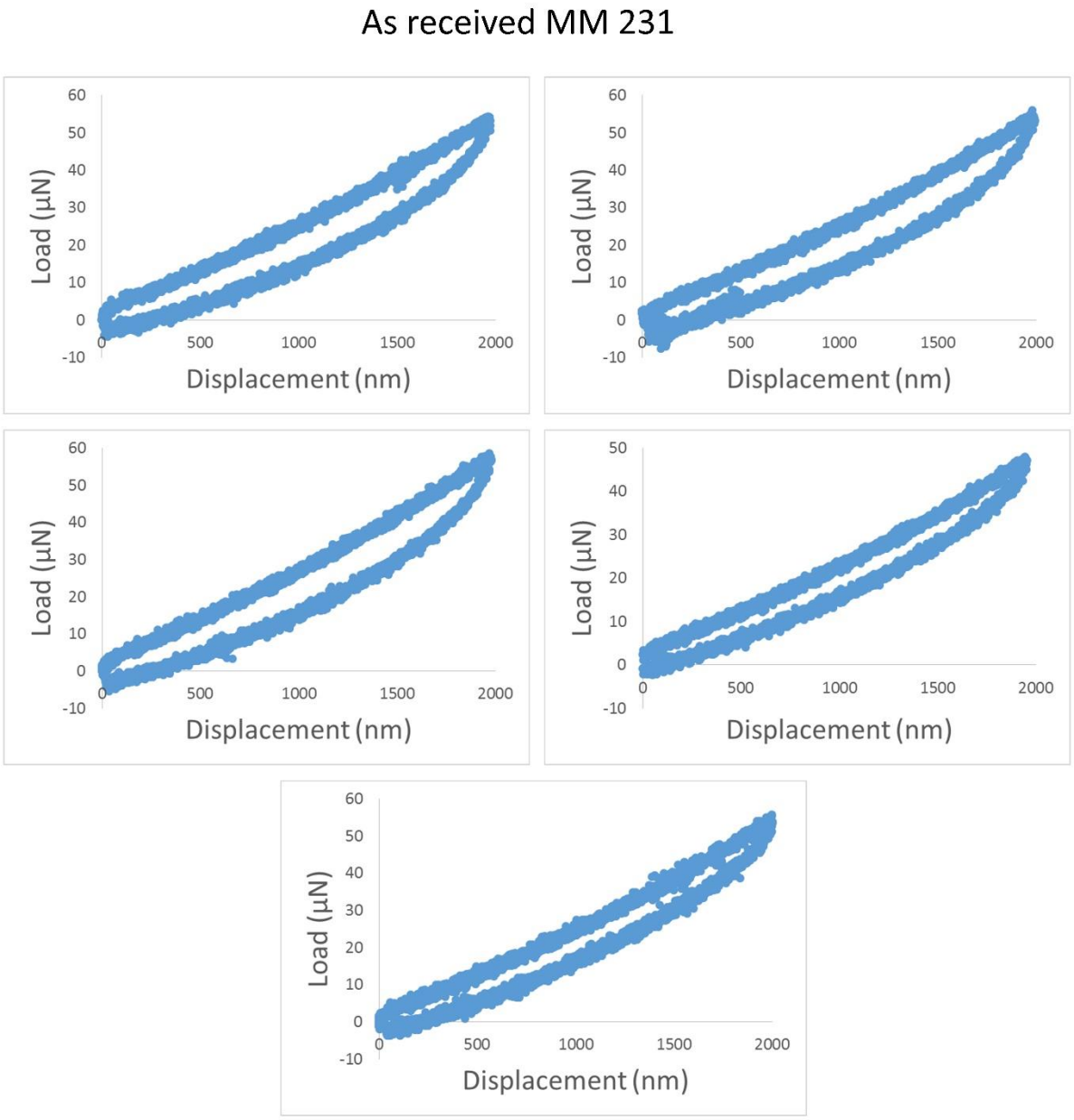

Figure A13. L-D curves of as received MM 231 cells at maximum displacement of 2000 nm (Continued).

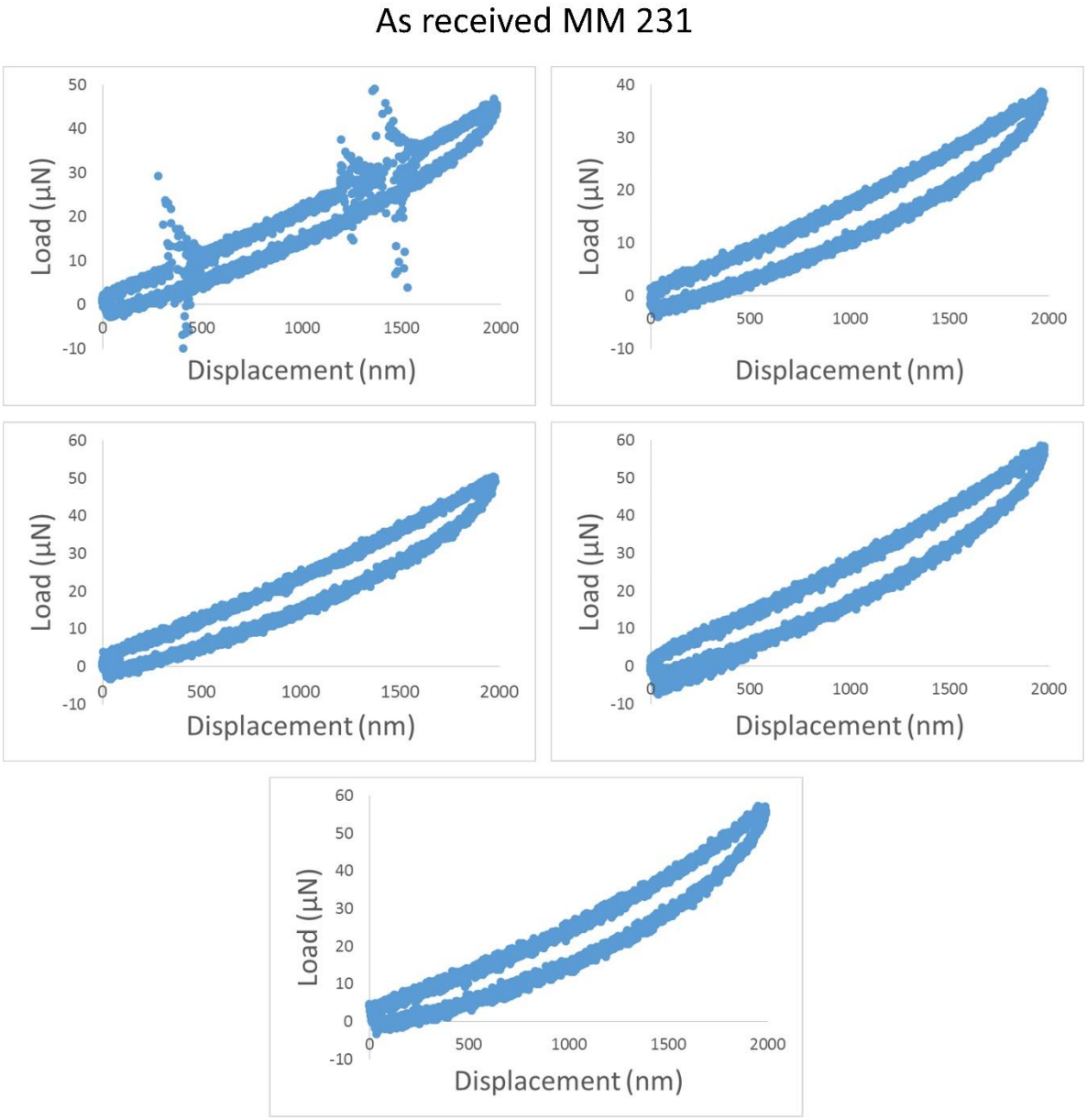

Figure A13. L-D curves of as received MM 231 cells at maximum displacement of 2000 nm (Continued).

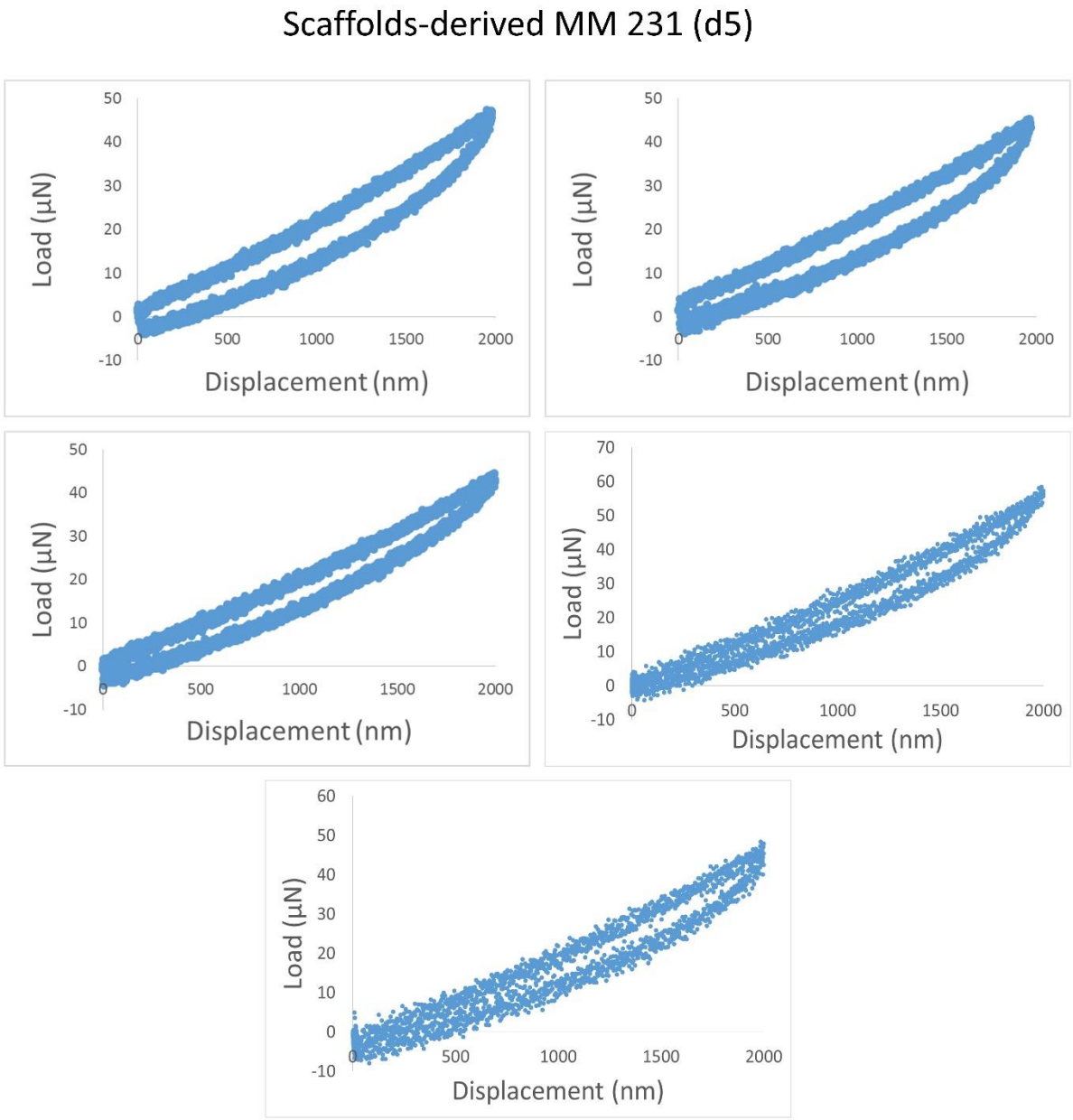

Figure A14. L-D curves of scaffolds-derived MM 231 cells (d5) at maximum displacement of 2000 nm.

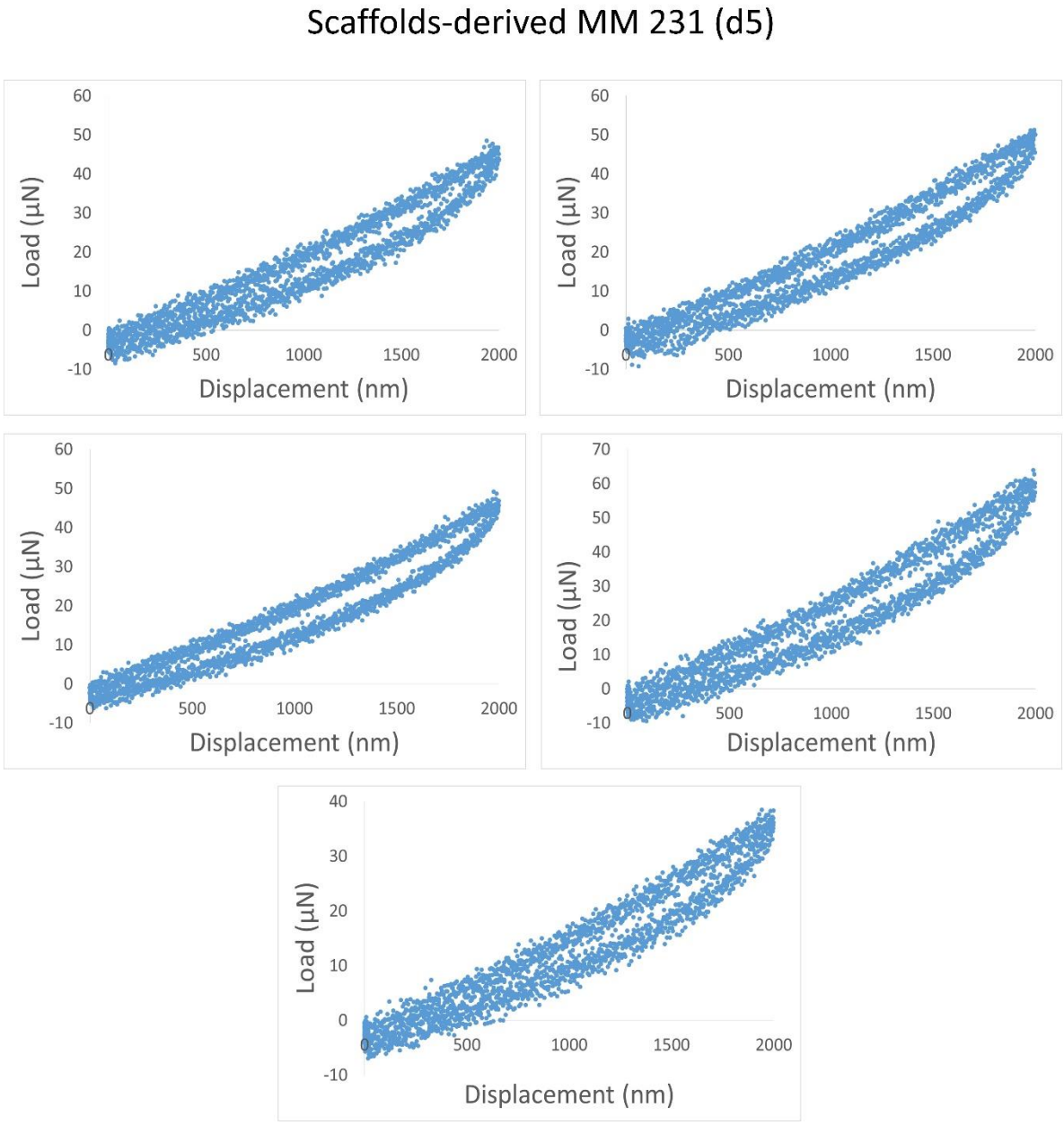

Figure A14. L-D curves of scaffolds-derived MM 231 cells (d5) at maximum displacement of 2000 nm (Continued).

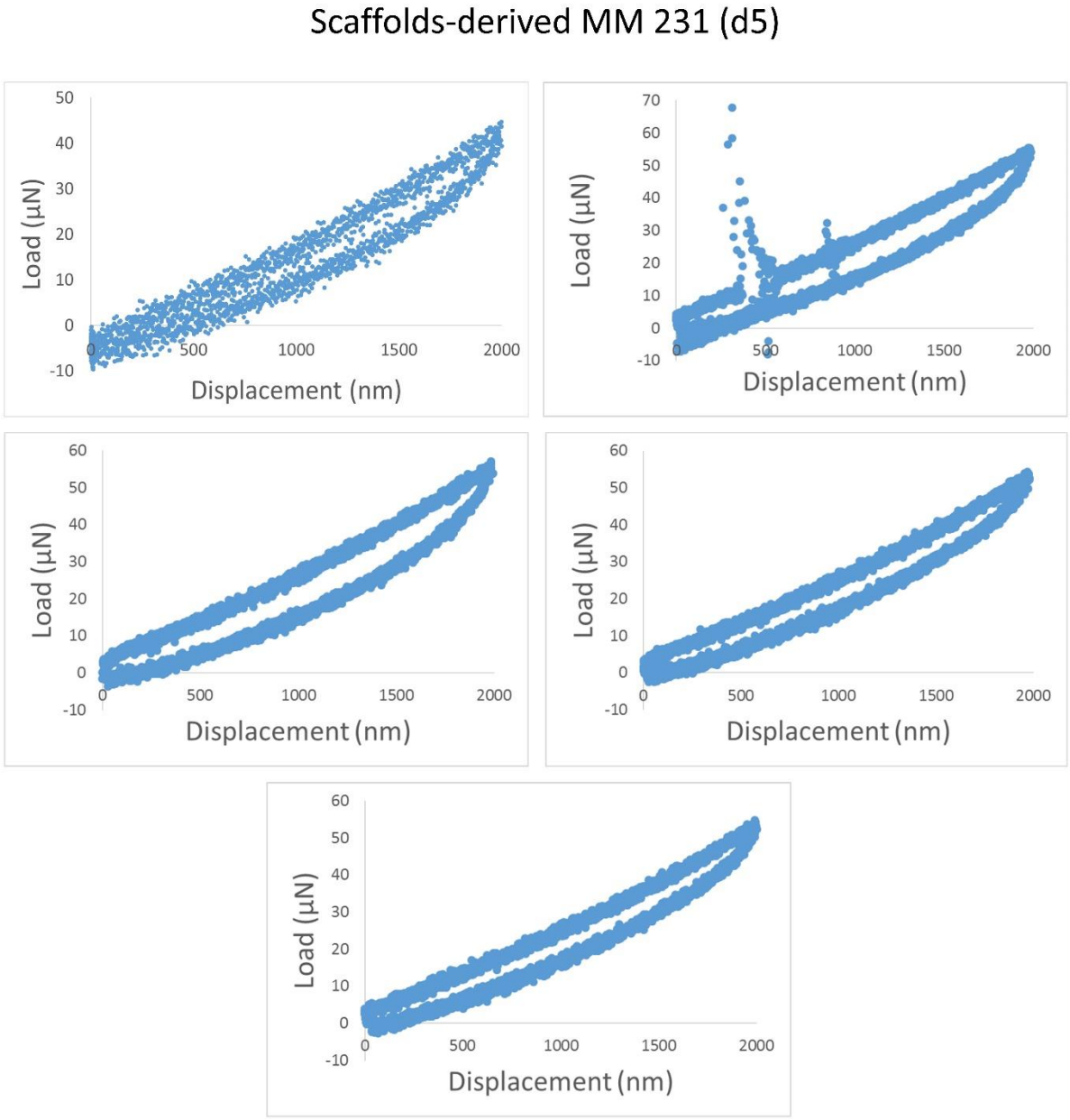

Figure A14. L-D curves of scaffolds-derived MM 231 cells (d5) at maximum displacement of 2000 nm (Continued).

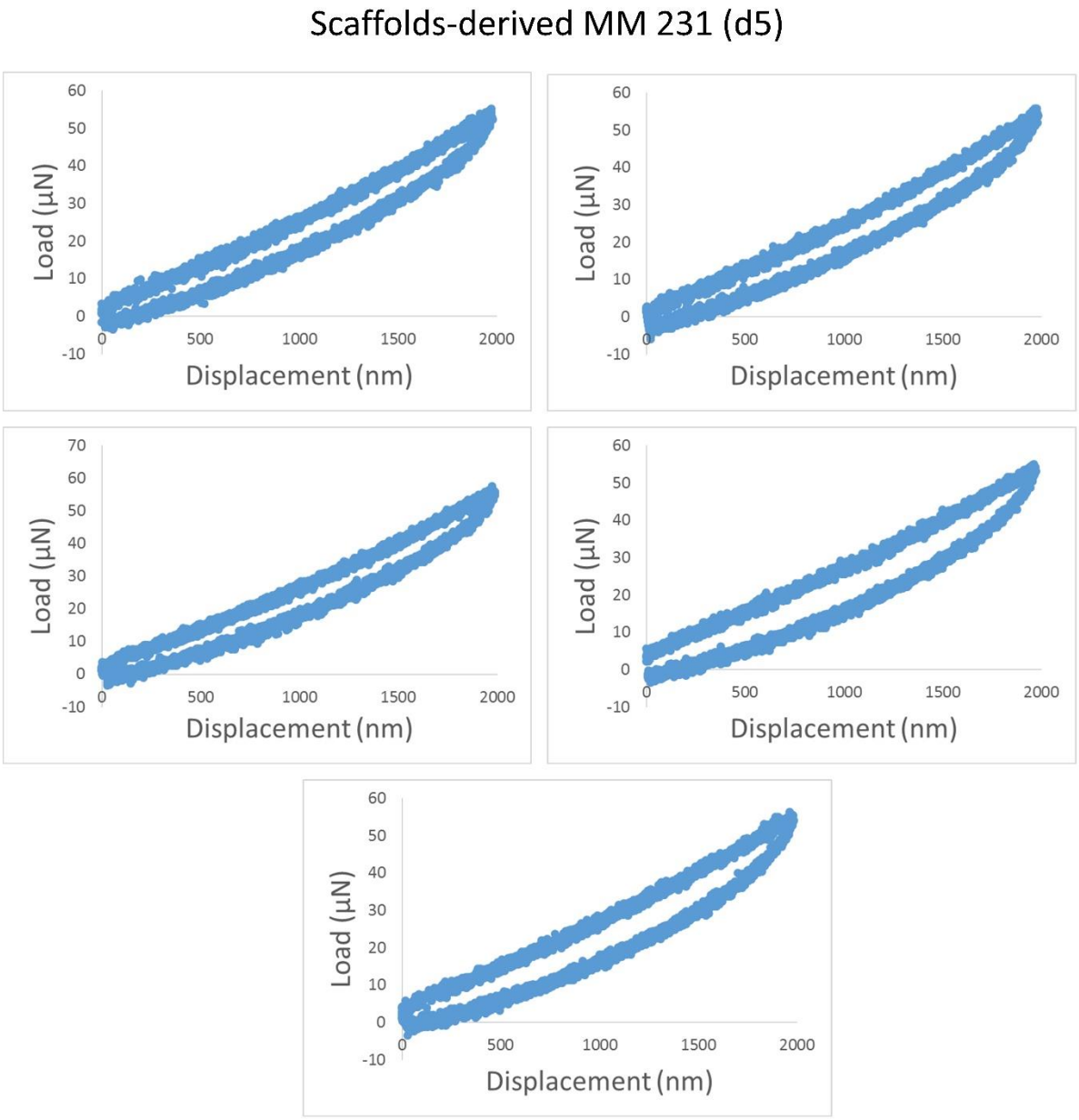

Figure A14. L-D curves of scaffolds-derived MM 231 cells (d5) at maximum displacement of 2000 nm (Continued).

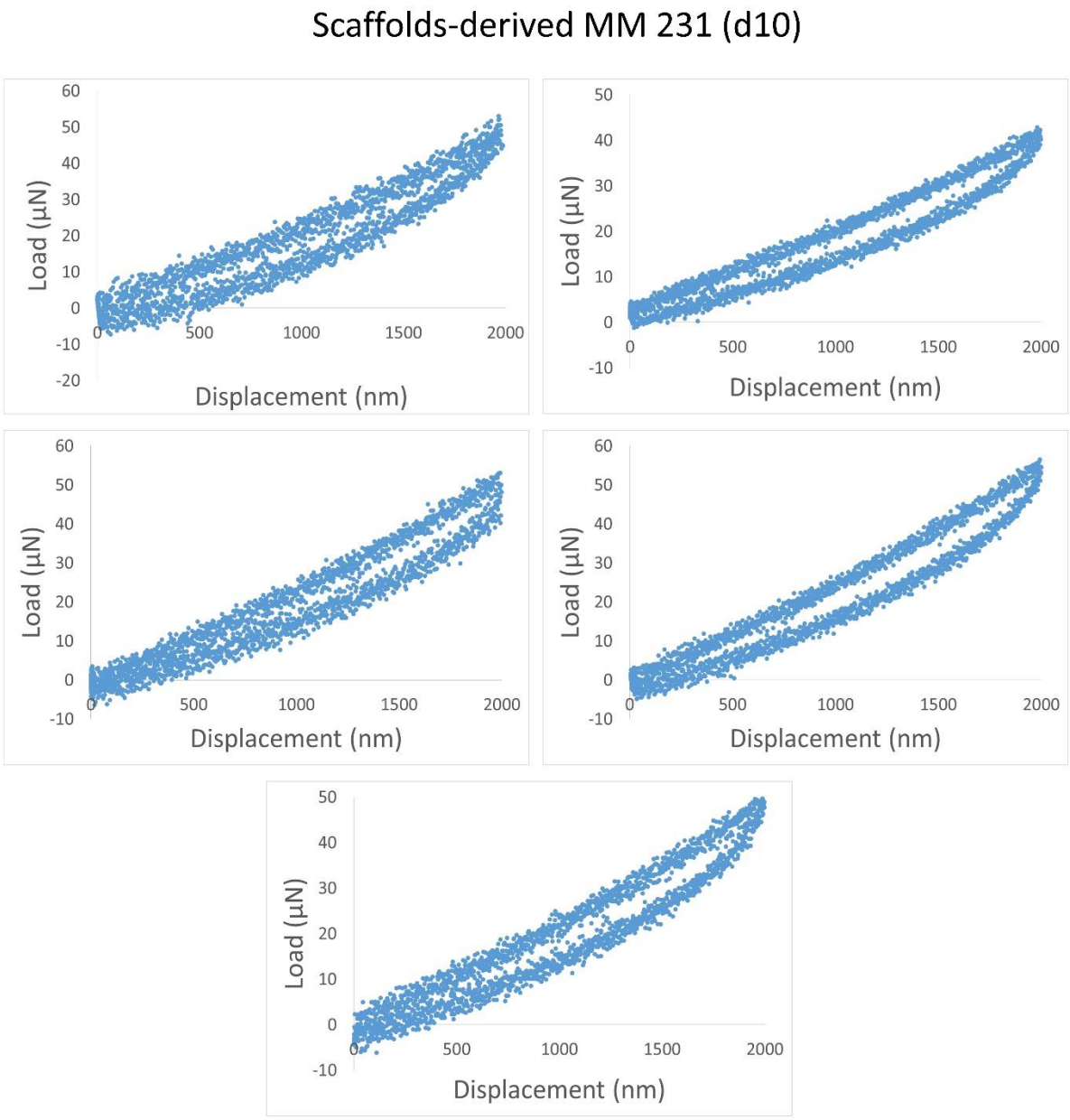

Figure A15. L-D curves of scaffolds-derived MM 231 cells (d10) at maximum displacement of 2000 nm.

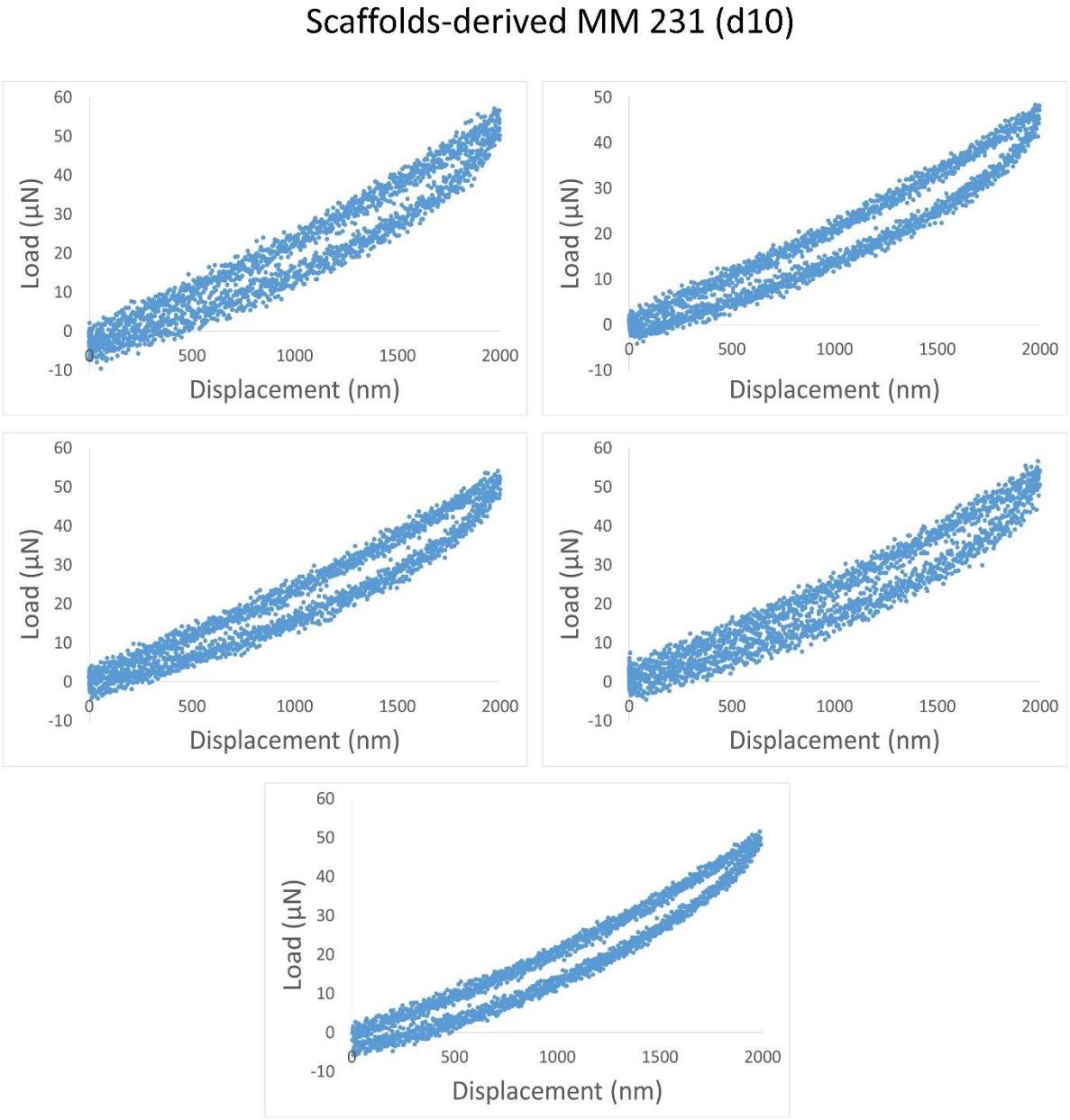

Figure A15. L-D curves of scaffolds-derived MM 231 cells (d10) at maximum displacement of 2000 nm (Continued).

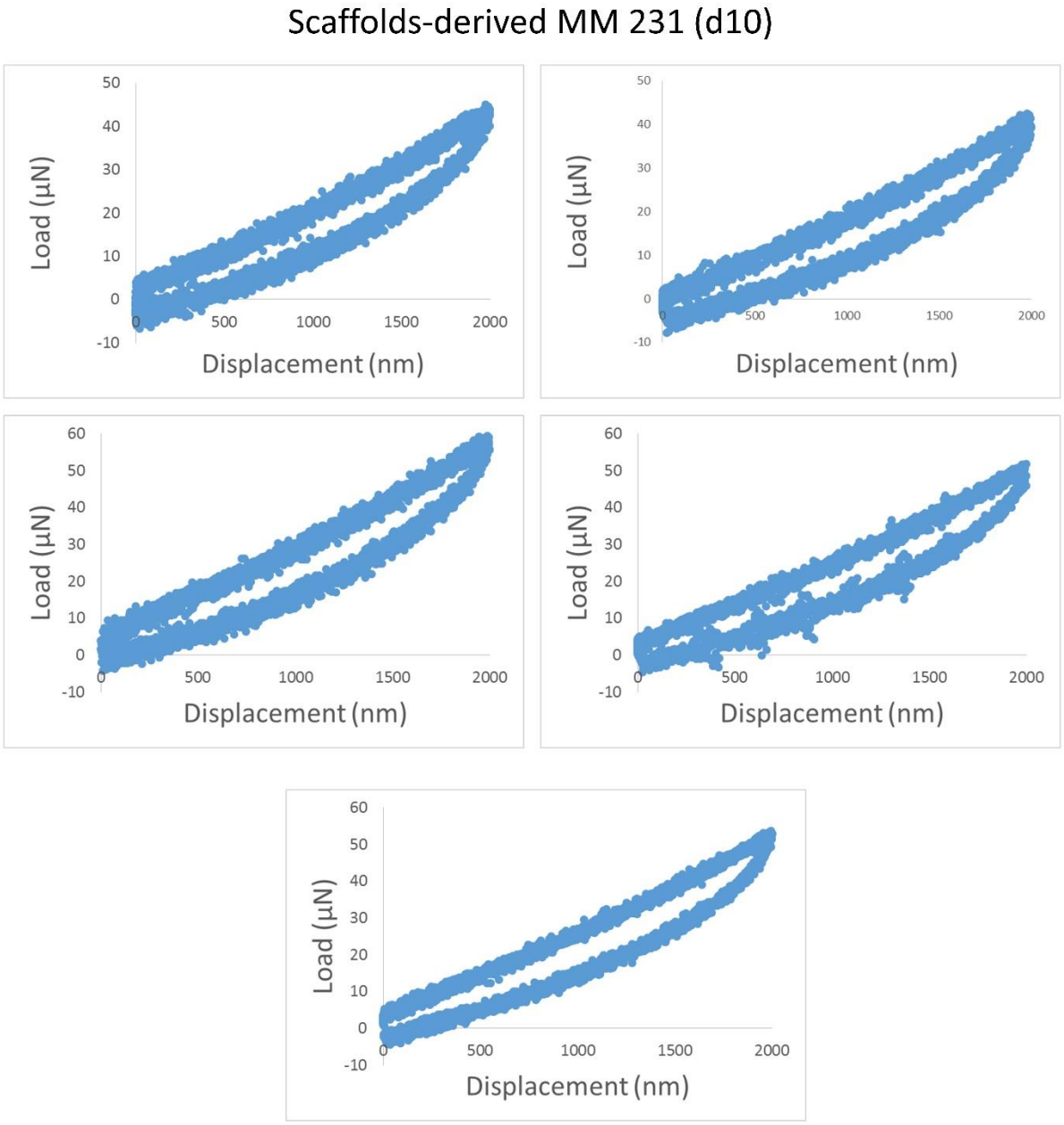

Figure A15. L-D curves of scaffolds-derived MM 231 cells (d10) at maximum displacement of 2000 nm (Continued).

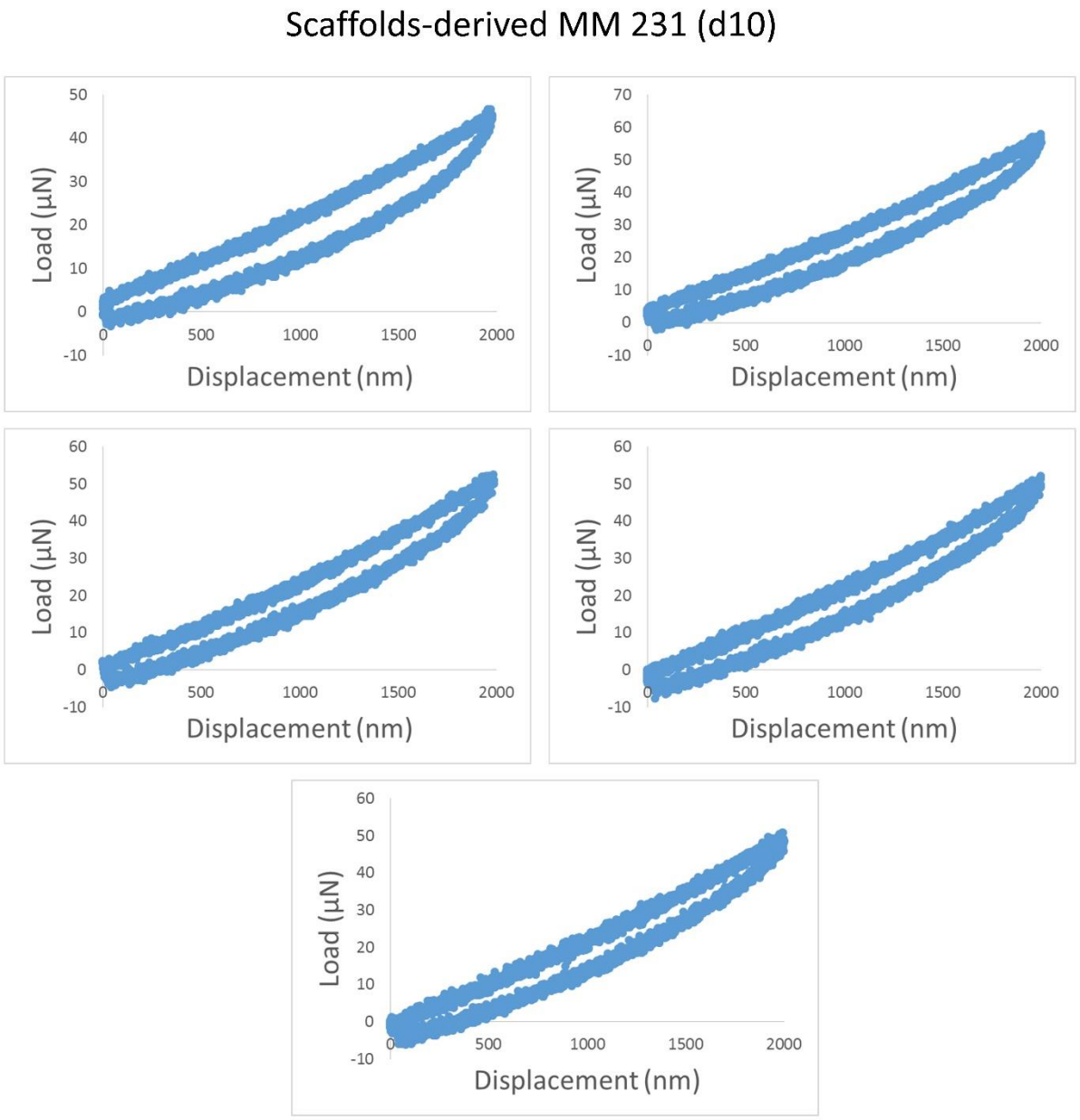

Figure A15. L-D curves of scaffolds-derived MM 231 cells (d10) at maximum displacement of 2000 nm (Continued).

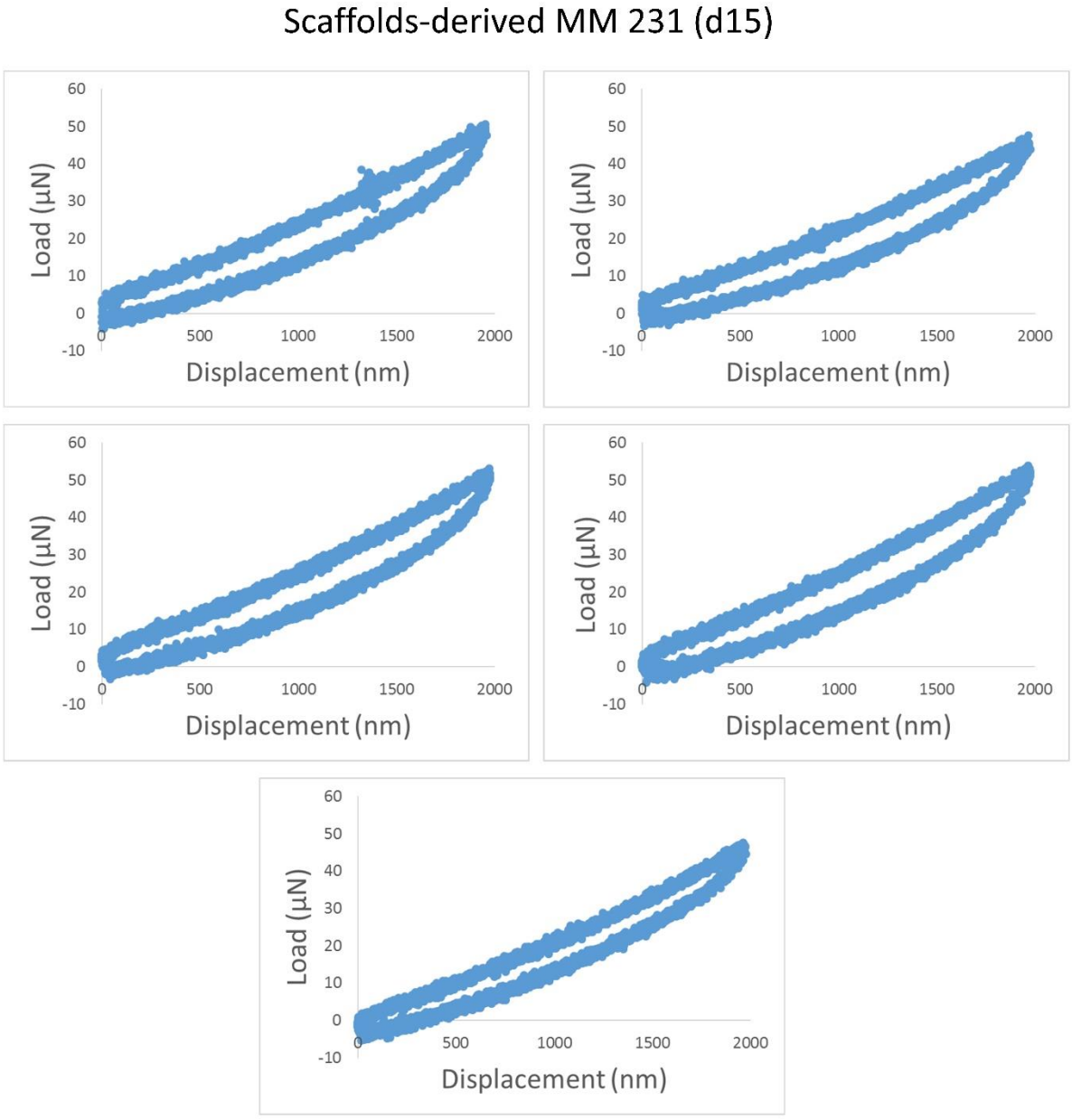

Figure A16. L-D curves of scaffolds-derived MM 231 cells (d15) at maximum displacement of 2000 nm.

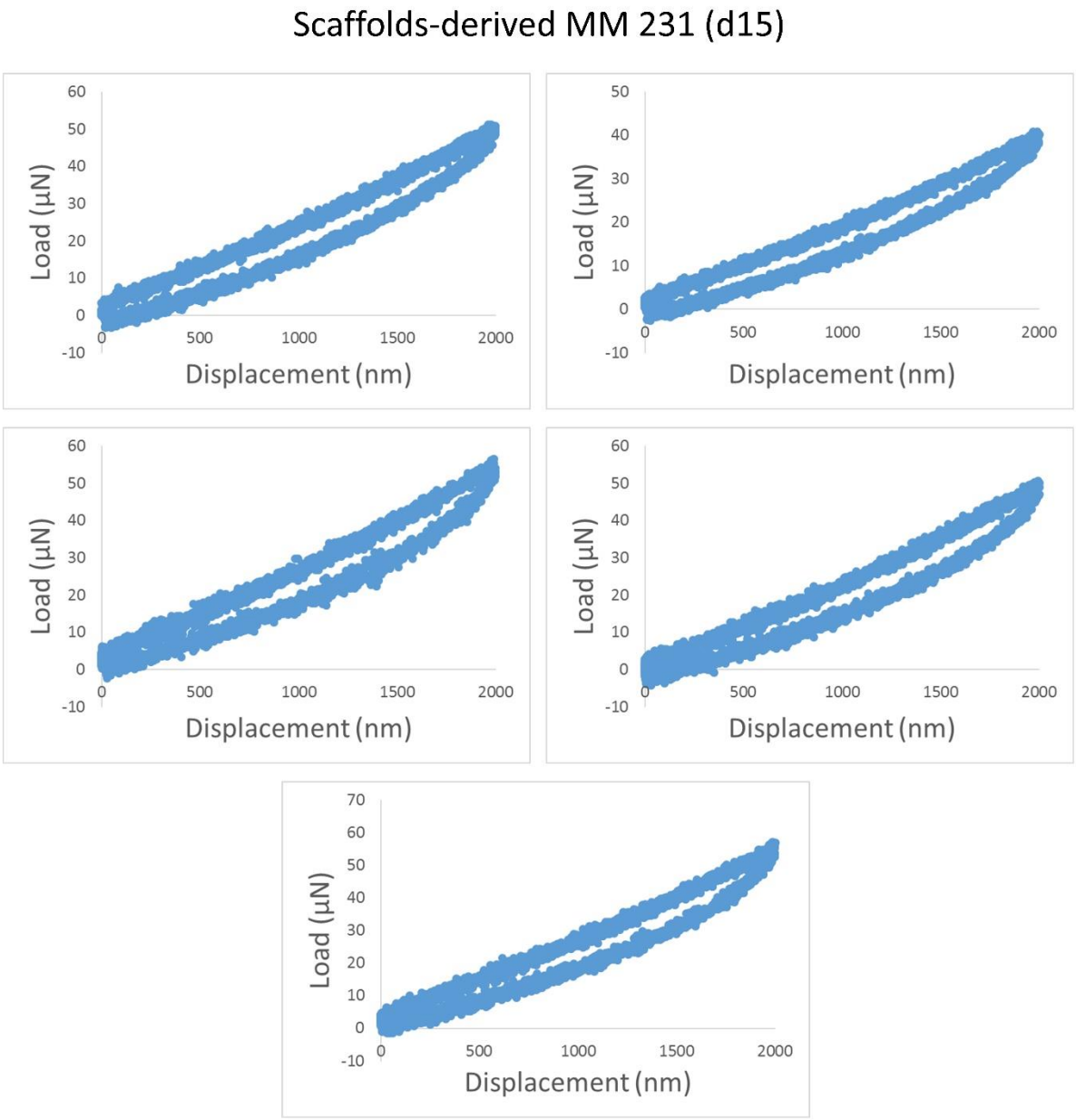

Figure A16. L-D curves of scaffolds-derived MM 231 cells (d15) at maximum displacement of 2000 nm (Continued).

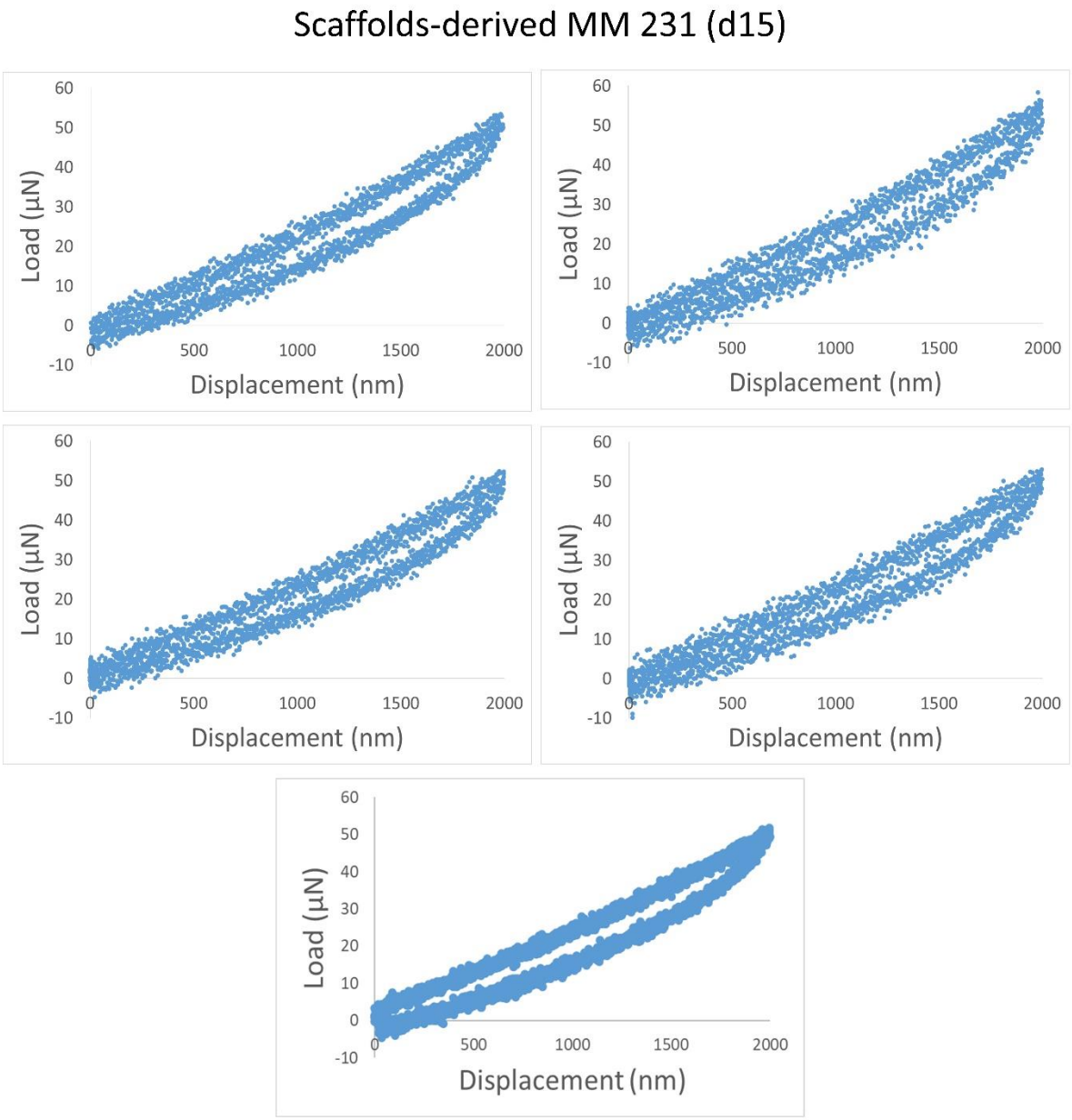

Figure A16. L-D curves of scaffolds-derived MM 231 cells (d15) at maximum displacement of 2000 nm (Continued).

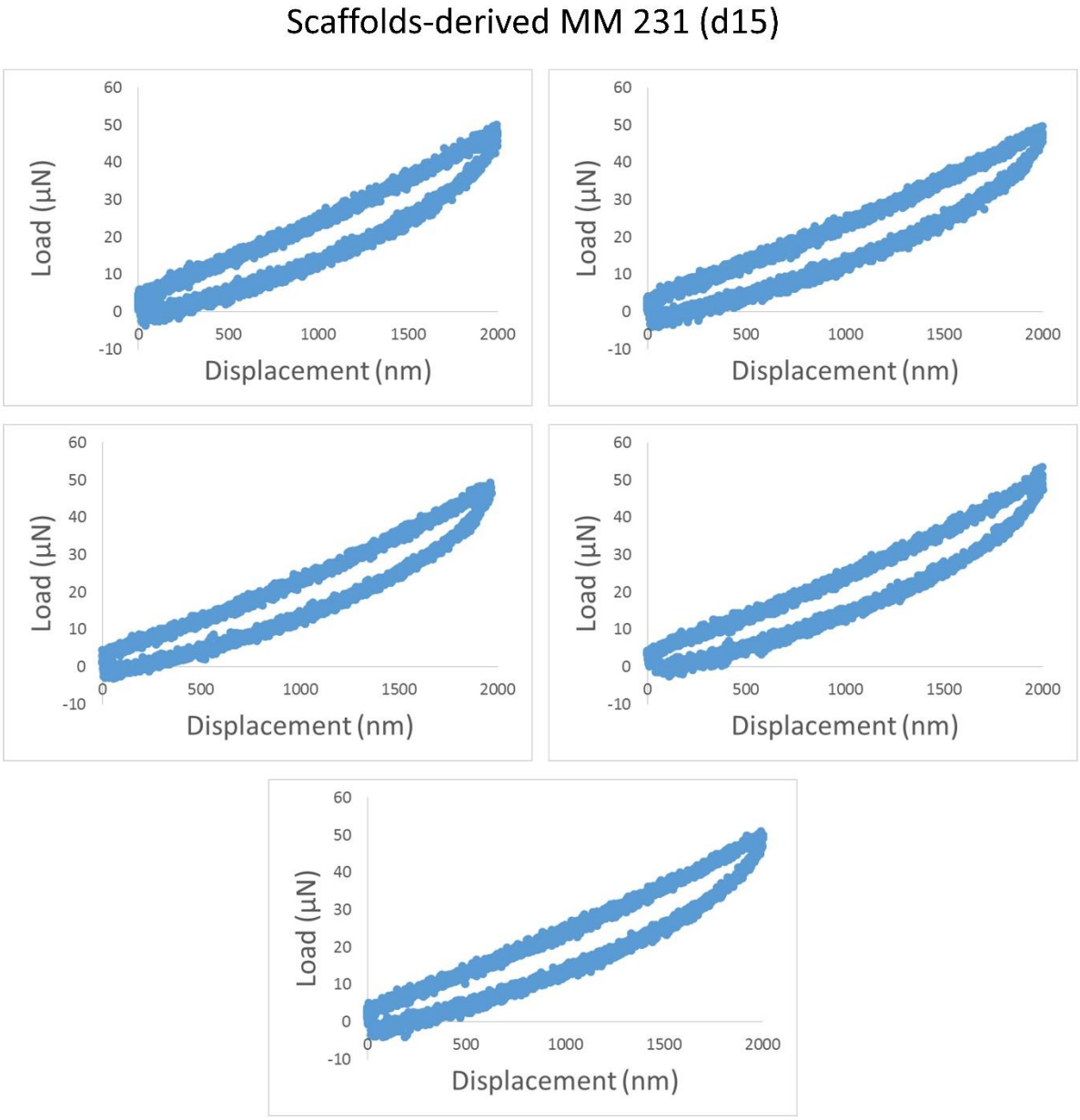

Figure A16. L-D curves of scaffolds-derived MM 231 cells (d15) at maximum displacement of 2000 nm (Continued).